

---

**METALS  
AND SUPERCONDUCTORS**

---

## Influence of the Size Distribution of Granules and of Their Attractive Interaction on the Percolation Threshold in Granulated Alloys

**A. B. Khanikaev, A. B. Granovskii, and J. P. Clerc**

*Moscow State University, Vorob'evy gory, Moscow, 119899 Russia*

*e-mail: alhany@magn.ru, granov@magn.ru*

Received September 17, 2001

**Abstract**—Numerical simulation was applied to study the influence of the size distribution of granules and the interaction between them on the percolation threshold in granulated metal–insulator alloys. An alloy model was considered in which metal granules have two characteristic sizes,  $l$  and  $L$  (with  $L > l$ ), and the size distribution of granules of greater size  $L$  having an average value of approximately  $L_0$  is described by a normal distribution with a standard deviation  $d$ , by a step function with a halfwidth  $d$ , or by a delta function. A model with attraction between granules and mechanisms of trapping of an additional granule by an already developed cluster with a characteristic trapping range  $R$  was also considered. The percolation threshold significantly grows with the ratio  $L_0/l$  and with  $R$  for both two- and three-dimensional cases and tends to flattening at large  $L/l$  or  $R$ . The calculated results make it possible to explain the high percolation threshold observed for the majority of granulated alloys.  
© 2002 MAIK “Nauka/Interperiodica”.

1. A granulated metal–insulator alloy represents a system consisting of metal granules dispersed in the insulator host. A metal–insulator transition takes place in the vicinity of a critical volume concentration  $p_c$  of a metal, referred to as the percolation threshold, such that the system is characterized by metal conduction at  $p > p_c$  and is an insulator at  $p < p_c$  [1–3]. Granulated alloys with a composition close to  $p_c$  are characterized by unique properties [1–3]. Magnetic granulated alloys for which the tunnel-type giant magnetoresistance [4], giant anomalous Hall effect [5], enhanced magneto-optical effects, etc. have relatively recently been detected are of particular interest.

The most important characteristic of a granulated alloy is the percolation threshold  $p_c$ . The effective-field theory developed for a three-dimensional (3D) system of a spherical metal and insulator particles gives  $p_c = 0.33$  [1–3]. Numerical calculations yield  $p_c \approx 0.32$  within the site-percolation model for a simple cubic lattice and lower values of  $p_c$  for other lattices and within the bond-percolation model [1–3].

Experiments [6] on powders of spherical particles alike in diameter yielded  $p_c = 0.27 \pm 0.05$ , which conforms to the theoretical predictions. At the same time, in deposited granulated systems, the values of  $p_c$  have been found to lie in the range 0.5–0.6 [4, 5, 7]. Since  $p_c$  can depend on many factors, including the particle shape [8], the character of short- and long-range order [1–3], and film thickness [6], different standpoints have been advanced on the observed high values of  $p_c$ ; however, none of the hypotheses is consistent with experi-

mental data. For example, according to numerous microscopic studies, the shape of particles is close to spherical, tunneling should decrease  $p_c$ , and the two-dimensional character of films 1–2  $\mu\text{m}$  thick with nanometer-sized granules affects  $p_c$  only slightly [6].

In this paper, we suggest a simple explanation for high values of  $p_c$  in granulated films which is based on the size distribution of granules. In Section 2, the presence of granules of significantly different sizes is postulated. By using the Monte Carlo method, it is shown that this assumption leads to increased values of  $p_c$  in both 2D and 3D cases. In Section 3, we perform a computer simulation of the formation of large clusters (including nonspherical ones) due to attractive interaction between granules and consider the influence of this attraction on  $p_c$ . In earlier papers (see [3, 9] and references therein), the attraction, considered only at distances shorter than the granule radius, was shown to decrease  $p_c$  [9], because the attraction between granules improves electrical contact between them. It was shown in [10] that an increase in  $p_c$  can take place even if the attraction range is small, because more compact granules form from fine ones and the system becomes discontinuous.

In this study, we consider the case of a large interaction range in which the latter tendency is dominant and  $p_c$  significantly increases. The attraction between granules can be due to both Coulomb forces and magnetic interaction. It is evident that most of the small granules in nanocomposites are charged; consequently, granules can be drawn to one another. Furthermore, small parti-

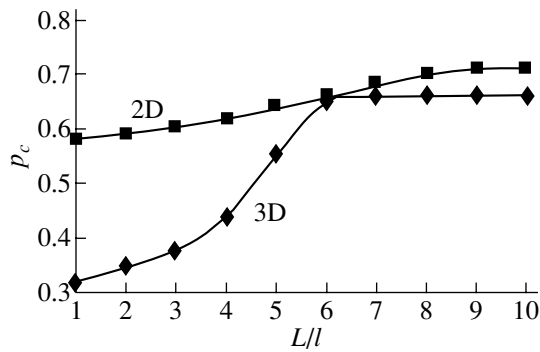


Fig. 1. Dependence of the percolation threshold  $p_c$  on the relative size  $L/l$  of large granules for the 2D and 3D cases.

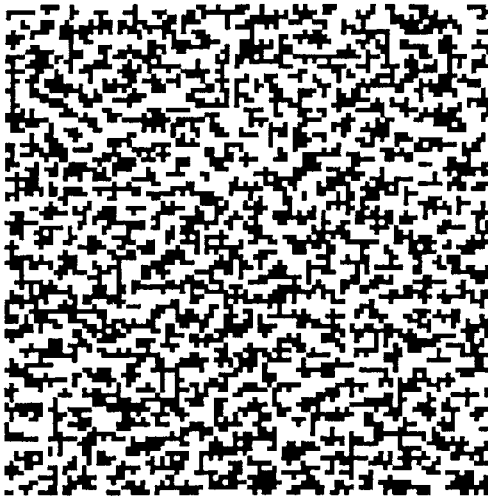


Fig. 2. Example of configurations found in the model with attraction in the 2D case.

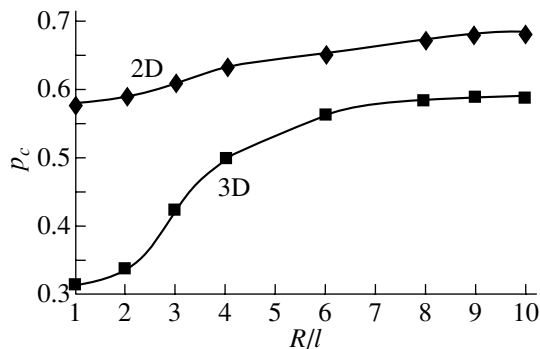


Fig. 3. Dependence of the percolation threshold on the trapping range  $R$  in the 2D and 3D cases.

cles possessing a charge are attracted to one another due to electrostatic image forces. In magnetic systems, single-domain particles tend to form sufficiently large

aggregates or chains with magnetic-flux closure. As a result of these interactions, sufficiently large clusters arise along with fine ones in granulated alloys, which causes  $p_c$  to increase.

2. Now, we consider a granulated metal–insulator alloy characterized by two types of metal granules (particles) of diameters  $l$  and  $L > 1$ . We assume that small particles have a well-defined diameter  $l$  coinciding with the cell size of the lattice percolation problem, while the size distribution of large particles about the average  $L_0$  is described by (i) the delta function  $f(L) = A\delta(L - L_0)$ , or (ii) the normal distribution  $f(L) = B\exp[-(L - L_0)^2/(2d)^2]$ , or (iii) a uniform distribution in a certain range  $2d$  wide:

$$f(L) = \begin{cases} C: L_0 - d < L < L_0 + d \\ 0: L_0 + d < L; \quad L_0 - d > L. \end{cases}$$

Various versions of  $f(L)$  are taken to find the functional dependence of  $p_c$  on the size distribution. Let the distribution parameters  $A$ ,  $B$ , and  $C$  be determined from the normalization conditions such that the number of granules of the second type is always ten times smaller than the number of granules of the first type.

In our numerical experiment, granules were randomly distributed over the sample volume. The boundaries of granules distributed in the preceding iteration cycles were not crossed. After the granules had been distributed over the volume, discretization was carried out. For this purpose, the sample volume was partitioned into cells of size  $l$ ; the cells that fell within clusters were considered to be occupied, and the cells that fell outside of the clusters were considered to be empty. The percolation threshold for the sample was determined by the Hoschen–Kapelmann method (also known as the cluster-labeling method) [8]. The percolation probability was found by performing 50 iterations for each concentration.

In the 2D and 3D cases, the sample size was  $100l$  and  $50l$ , respectively. The calculated dependences of the percolation threshold  $p_c$  on the relative size  $L/l$  of large particles are shown in Fig. 1 for a ratio of the numbers of small and large granules equal to  $n = 10$ .

For particles of the same size  $L = l$ , we found  $p_c = 0.32$  and  $0.58$  in the 2D and 3D cases, respectively, which coincides with the published data [1–3]. The value of  $p_c$  increases with the ratio  $L/l$  to a greater extent in the 3D case, tending to flattening at large  $L/l$ . It is noteworthy that the size  $L$  of large particles is much smaller than the size of the sample (lattice); therefore, the effect of boundary conditions is insignificant.

This result can be readily understood from simple geometrical considerations or using the Scher–Zallen invariant [11]. According to the Scher–Zallen condition [11] in percolation problems, the product  $Zp_c$  remains invariant for any packing of particles. Here,  $Z$  is the effective coordination number or the number of good

electric contacts between the nearest neighbor particles. In the presence of large particles,  $Z$  decreases; hence,  $p_c$  should depend not only on the ratio  $L/l$  but also on the relative number  $n^{-1}$  of large particles.

It follows that the function  $p_c(n)$  has a maximum at a certain value of  $L/l$ . This conclusion is fully confirmed by calculations. It also follows that the value of  $p_c(L/l)$  depends only weakly on the size distribution of large granules. Indeed, to within the error of the numerical experiment, the results shown in Fig. 1 are virtually identical for any size distribution of granules.

**3.** Large granules can also be nonspherical. Let us elucidate whether the percolation threshold increases in this case. To model the formation of large clusters numerically, we assume that all the granules are of the same size  $l$  and are attracted to each other at a certain distance  $R$ . In the course of the numerical experiment, the coordinates of the occupied cells were randomly generated in successive iteration cycles. When the distance from a cell to the cells filled in the preceding iteration was shorter than  $R$ , its coordinates were exchanged with the coordinates of the empty cell nearest to the center of mass of the cluster generated in the next iteration. In this case, the parameter  $R$  characterizes the attraction strength or the particle trapping range and clusters represent branched parts of a fractal structure rather than compact spherical formations. One of the clusters obtained in the 2D case is shown in Fig. 2. The calculated dependences of the percolation threshold on the ratio  $R/l$  for the 2D and 3D cases are displayed in Fig. 3. These dependences exhibit the same behavior as the dependence of the percolation threshold on the particle size  $L/l$  (Fig. 1); i.e., the percolation threshold also significantly increases, reaching a value of  $p_c = 0.58$  in the 3D case.

Thus, the high percolation thresholds observed in granulated alloys can be due to rather large spherical and nonspherical clusters present in these systems.

#### ACKNOWLEDGMENTS

This work was supported by the Russian Foundation for Basic Research, project no. 00-02-17797.

#### REFERENCES

1. B. I. Shklovskii and A. L. Efros, *Electronic Properties of Doped Semiconductors* (Nauka, Moscow, 1979; Springer, New York, 1984).
2. J. P. Clerc, G. Giraund, and J. M. Laugier, *Adv. Phys.* **3**, 191 (1990).
3. M. B. Isichenko, *Rev. Mod. Phys.* **64**, 961 (1992).
4. S. Mitani, H. Fujimori, and K. Takahashi, *J. Magn. Magn. Mater.* **198–199**, 179 (1999).
5. A. B. Pakhomov and X. Yan, *Solid State Commun.* **99**, 139 (1996).
6. J. P. Clerc, G. Giraud, S. Alexander, and E. Guyon, *Phys. Rev. B* **22**, 2489 (1980).
7. C. L. Chien, *J. Appl. Phys.* **69**, 5267 (1991).
8. E. W. Brouer, *J. Phys. C* **19**, 7183 (1986).
9. L. R. Bug, S. A. Safran, G. S. Grest, and I. Webman, *Phys. Rev. Lett.* **55**, 1896 (1985).
10. H. Gould and J. Tobochnik, *An Introduction to Computer Simulation Methods. Applications to Physical Systems* (Addison-Wesley, Reading, 1988; Mir, Moscow, 1990).
11. H. Scher and R. Zallen, *J. Chem. Phys.* **53**, 3759 (1970).

*Translated by A. Kazantsev*

## SEMICONDUCTORS AND DIELECTRICS

# Polarization Dependence of the Spontaneous Radiation of Hot Electrons

V. M. Bondar, O. G. Sarbey, and P. M. Tomchuk

*Institute of Physics, National Academy of Sciences of Ukraine, pr. Nauki 46, Kiev, 03028 Ukraine*

*e-mail: sarbey@iop.kiev.ua*

Received June 9, 2001

**Abstract**—This paper reports on the results of investigations into the polarization dependence of the spontaneous radiation of hot electrons due to their intervalley redistribution in multivalley semiconductors. It is demonstrated that the radiation is predominantly polarized normally to the electric field and the direction of polarization and its intensity can vary according to the degree of electron redistribution, the electron concentration, and the heating electric field. © 2002 MAIK “Nauka/Interperiodica”.

### 1. INTRODUCTION

The spontaneous radiation of charge carriers of crystals with cubic symmetry is not polarized. However, the cubic symmetry of the electron distribution in the space of wave vectors can be broken by a heating electric field. The symmetry breaking can be governed by different mechanisms. In particular, Vas’ko [1] and Malevich [2] considered a number of mechanisms associated with radiation polarization and absorption anisotropy.

In the present work, we investigated the polarization dependence of the spontaneous radiation of hot electrons due to their intervalley redistribution in multivalley semiconductors. It is well known that absorption and radiation of free electrons become possible only in the presence of a “third body.” Under normal conditions, the role of a third body is played by phonons and impurities providing the law of conservation of quasi-momentum. Note that scattering by phonons and impurities is substantially anisotropic in multivalley semiconductors (germanium, silicon, etc.). This leads to a polarization dependence of the spontaneous radiation upon nonuniform population of the valleys.

### 2. FORMULATION OF THE PROBLEM. ACOUSTIC SCATTERING

Let us first consider anisotropic scattering of an electron by acoustic vibrations of the lattice in multivalley semiconductors. We proceed from the collision integral of electrons scattered by acoustic phonons in which the effect of the field of a high-frequency electro-

magnetic wave on the collision event is taken into account; that is,

$$\begin{aligned} \hat{I}f = & \sum_{(s)} \sum_q \sum_{l=-\infty}^{\infty} W^{(s)}(\mathbf{q}) I_l^2 \left( \frac{eV}{m\omega c} \right) \\ & \times [f(\mathbf{p} + \hbar\mathbf{q})(N_{\mathbf{q}}^{(s)} \pm 1) - f(\mathbf{p})N_{\mathbf{q}}^{(s)}] \\ & \times \delta[\varepsilon_{\mathbf{p} + \hbar\mathbf{q}} - \varepsilon_{\mathbf{p}} - \hbar\omega_{\mathbf{q}}^{(s)} - l\hbar\omega] + f(\mathbf{p} - \hbar\mathbf{q})N_{\mathbf{q}}^{(s)} \\ & - f(\mathbf{p})(N_{\mathbf{q}}^{(s)} + 1)\delta[\varepsilon_{\mathbf{p} - \hbar\mathbf{q}} - \varepsilon_{\mathbf{p}} + \hbar\omega_{\mathbf{q}}^{(s)} - l\hbar\omega], \end{aligned} \quad (1)$$

where  $f(\mathbf{p})$  is the distribution function of the electron momenta  $\mathbf{p}$ ,  $N^{(s)}$  is the distribution function of phonons of the  $s$ th branch,  $\hbar\omega_{\mathbf{q}}^{(s)}$  is the phonon energy,  $\hbar\omega$  is the photon energy,  $W^{(s)}(\mathbf{q})$  is the scattering probability,  $I_l$  is the Bessel function of the  $l$ th order,  $m_{\perp}$  is the transverse electron mass,  $c$  is the velocity of light, and  $\gamma$  is the quantity defined by the formula

$$\gamma = \mathbf{A}\mathbf{q} + \left( \frac{m_{\parallel}}{m_{\perp}} - 1 \right) (\mathbf{A}\mathbf{l}_0)(\mathbf{q}\mathbf{l}_0). \quad (2)$$

Here,  $\mathbf{l}_0$  is the unit vector of the rotation axis of the mass ellipsoid of the  $i$ th valley and  $\mathbf{A}$  is the vector-potential of the electromagnetic wave.

It is assumed that the scattering is quasi-elastic and that

$$N_{\mathbf{q}}^{(s)} + 1 \approx N_{\mathbf{q}}^{(s)} \approx \frac{\theta}{\hbar\omega_{\mathbf{q}}^{(s)}},$$

where  $\theta$  is the lattice temperature expressed in units of energy.

The total probability of electron scattering by all the three acoustic branches is defined by the expression

$$W(\mathbf{q}) = \sum_{s=1}^3 W^{(s)}(\mathbf{q}) = \frac{2\pi\theta}{\rho V \hbar s_{\parallel}^2} \left[ \Sigma_d + \Sigma_u \left( \frac{\mathbf{l}_0 \mathbf{q}}{q} \right)^2 \right]^2 + \frac{\Sigma_u^2}{s_{\perp}^2} \left[ 1 - \left( \frac{\mathbf{l}_0 \mathbf{q}}{q} \right)^2 \right] \left( \frac{\mathbf{l}_0 \mathbf{q}}{q} \right)^2, \quad (3)$$

where  $s_{\parallel}$  is the longitudinal velocity of sound,  $s_{\perp}$  is the transverse velocity of sound,  $V$  is the volume,  $\rho$  is the density of the material, and  $\Sigma_d$  and  $\Sigma_u$  are the constants of the deformation potential.

According to formula (1), the energy transferred from electrons to the lattice in a unit time in the presence of an electromagnetic wave can be represented by the expression

$$P = \int \varepsilon(\mathbf{p}) \hat{I} f(\mathbf{p}) d\mathbf{p} = P_0 - \frac{V}{(2\pi\hbar)^3} \hbar\omega \times \sum_{l=-\infty}^{\infty} l \int d\mathbf{p} f(\mathbf{p}) \int d\mathbf{p}' W(\mathbf{q}) I_l^2 \left( \frac{e\gamma}{m_{\perp} \omega c} \right) \times \delta[\varepsilon_{\mathbf{p}'} - \varepsilon_{\mathbf{p}} - l\hbar\omega], \quad (4)$$

where  $P_0$  is the transferred energy in the absence of the electromagnetic wave and  $\mathbf{p}' = \mathbf{p} + \hbar\mathbf{q}$ .

We will restrict our consideration to the case of one-quantum processes (i.e.,  $l = \pm 1$ ).

The estimates indicate that the argument of the Bessel function is considerably less than unity for virtually all the frequencies in the optical range. On this basis, the correction to the energy transferred to the lattice in the presence of the electromagnetic wave field can be written in the following form:

$$\Delta P^{(\pm)} = P - P_0 = \mp \frac{V \hbar \omega}{(2\pi\hbar)^3} \int d\mathbf{p} f(\mathbf{p}) \times \int d\mathbf{p}' W(\mathbf{q}) \left( \frac{e\gamma}{2m_{\perp} \omega c} \right)^2 \delta[\varepsilon_{\mathbf{p}'} - \varepsilon_{\mathbf{p}} \mp \hbar\omega]. \quad (5)$$

After the transition, the electron energy is determined as  $\varepsilon_{\mathbf{p}'} = \varepsilon_{\mathbf{p}} \pm \hbar\omega$ . Hence, it follows that  $\Delta P^{(+)}$  describes the processes associated with photon absorption, whereas  $\Delta P^{(-)}$  characterizes the processes due to photon emission.

Expression (5) is accepted as a basis for the calculation of both the absorption caused by the electromagnetic wave field and the wave-field-induced radiation. As will be shown below, the spontaneous radiation of interest can be easily obtained from the expression for radiation induced by an electromagnetic wave field.

It is convenient to perform integration in expression (5) in distorted coordinates in which the initial

ellipsoidal isoenergetic surfaces become spherical; that is,

$$\mathbf{p}_{\perp} = \mathbf{p}_{\perp}^*, \quad p_{\parallel} = \left( \frac{m_{\parallel}}{m_{\perp}} \right)^{1/2} p_{\parallel}^*, \\ \mathbf{q}_{\perp} = \mathbf{q}_{\perp}^*, \quad q_{\parallel} = \left( \frac{m_{\parallel}}{m_{\perp}} \right)^{1/2} q_{\parallel}^*, \quad (6)$$

$$\varepsilon_{\mathbf{p}} = \frac{p_{\perp}^2}{2m_{\perp}} + \frac{p_{\parallel}^2}{2m_{\parallel}} = \frac{p^{*2}}{2m_{\perp}}.$$

In these coordinates, the delta function takes the form

$$\delta[\varepsilon_{\mathbf{p}'} - \varepsilon_{\mathbf{p}} \pm \hbar\omega] = \delta \left[ \frac{(\hbar q^*)^2}{2m_{\perp}} + \frac{\hbar}{m_{\perp}} p^* q^* \cos v^* \mp \hbar\omega \right], \quad (7)$$

where  $v^*$  is the angle between  $p^*$  and  $q^*$ .

By using the delta function, it is easy to carry out the integration in expression (5) with respect to  $v^*$ . In this case, we have

$$\cos v^* = \left[ \pm \hbar\omega - \frac{(\hbar q^*)^2}{2m_{\perp}} \right] / \frac{\hbar q^* p^*}{m_{\perp}}, \quad (8) \\ |\cos v^*| \leq 1.$$

Relationship (8) and the condition  $|\cos v^*| \leq 1$  determine the limits of integration with respect to  $q^*$ . As a result, we obtain

$$\int d\mathbf{p} f(\mathbf{p}) \int d\mathbf{p}' W(\mathbf{q}) \gamma^2 \delta[\varepsilon_{\mathbf{p}'} - \varepsilon_{\mathbf{p}} - \hbar\omega] \\ = \frac{m_{\parallel}}{m_{\perp}} \hbar^3 \int d\mathbf{p}^* f_0(\varepsilon_{\mathbf{p}^*}) \int d\mathbf{q}^* W(\mathbf{q}^*) \gamma^2 \delta \\ \times \left[ \frac{(\hbar q^*)^2}{2m_{\perp}} + \frac{\hbar}{m_{\perp}} p^* q^* \cos v^* - \hbar\omega \right] = 2\pi \frac{m_{\parallel}}{m_{\perp}} \hbar^3 \frac{m_{\perp}}{\hbar} \\ \times \int_0^{\infty} dp^* p^* f_0(\varepsilon_{p^*}) \int_{q_{\min}}^{q_{\max}} dq^* q^* \int d\Omega_{q^*}^* W(\mathbf{q}^*) \gamma^2.$$

Here,  $d\Omega_{q^*}^*$  is the solid angle in the  $q^*$  space and the quantities  $q_{\min}$  and  $q_{\max}$  can be determined from condition (8) and, in the case of absorption, take the form

$$\hbar q_{\max} = p^* + \sqrt{p^{*2} + 2m_{\perp} \hbar\omega}, \quad (10) \\ \hbar q_{\min} = -p^* + \sqrt{p^{*2} + 2m_{\perp} \hbar\omega}.$$

In relationship (9), we used the symmetric function  $f_0(\varepsilon)$  instead of the function  $f(\bar{\mathbf{p}})$ .

It follows from formula (3) that

$$W(\mathbf{q}) = W(\mathbf{v}^*) = \frac{2\pi\theta}{\rho V \hbar} \left\{ \frac{1}{s_{\parallel}^2} [\Sigma_d + \cos^2 \mathbf{v}^*]^2 + \frac{\Sigma_u^2}{s_{\perp}^2} [1 - \cos^2 \mathbf{v}^*]^2 \cos^2 \mathbf{v}^* \right\}. \quad (11)$$

Here,  $\mathbf{v}^*$  is the angle between the vector  $\mathbf{q}^*$  and the unit vector  $\bar{\mathbf{l}}_0$ . Since the probability  $W$  does not depend on the modulus  $q^*$  and the quantity  $\gamma^2$  [as can be seen from relationship (2)] is proportional to  $q^{*2}$ , the integration can be easily performed with respect to both  $dq^*$  and  $d\Omega_{q^*} = \cos \mathbf{v}^* d\mathbf{v}^* d\varphi^2$ . The remaining integral over  $p^*$  is given by

$$\int_0^{\infty} dp^* p^{*2} (\hbar\omega + \varepsilon)^{1/2} (\hbar\omega + 2\varepsilon) f_0(\varepsilon) = \frac{n_i(\theta_i)}{2} \left(\frac{\theta_i}{\pi}\right)^{3/2} \times \int_0^{\infty} dx \left\{ x \left(\frac{\hbar\omega}{\theta_i} + x\right) \right\}^{1/2} \left(\frac{\hbar\omega}{\theta_i} + 2x\right) e^{-x}. \quad (12)$$

In expression (12), the Maxwellian function with the effective electron temperature  $\theta_i$  in the  $i$ th valley is taken as  $f_0(\varepsilon)$  and  $n_i$  is the electron concentration in the  $i$ th valley.

Integrals of type (12) can be expressed through the Bessel function of the imaginary argument  $K_1(a)$ :

$$\int_0^{\infty} dx e^{-x} x^n (x^2 + 2ax)^{g-\frac{1}{2}} = (-1)^n \frac{2^g}{\sqrt{\pi}} \Gamma\left(g + \frac{1}{2}\right) \frac{d^n}{da^n} \{a^{-g} e^a K_g(a)\}, \quad (13)$$

where  $\Gamma$  is the gamma function.

In the calculations of the radiation, instead of the limits specified by relationships (10), we should write

$$\begin{aligned} \hbar q_{\max} &= p^* + \sqrt{p^{*2} - 2m_{\perp} \hbar\omega}, \\ \hbar q_{\min} &= p^* - \sqrt{p^{*2} - 2m_{\perp} \hbar\omega} \end{aligned} \quad (14)$$

and the integration with respect to  $p^*$  should be performed within the limits defined by the relationship

$$\sqrt{2m_{\perp} \hbar\omega} \leq p^* \leq \infty.$$

As a consequence, we obtain

$$\begin{aligned} \Delta P_i^{(+)} &= e^2 \left( \frac{A_{\perp}^2}{m_{\perp} \tau_{\perp}^{(0)}} + \frac{A_{\parallel}^2}{m_{\parallel} \tau_{\parallel}^{(0)}} \right) \frac{2}{3\sqrt{\pi}} \frac{n_i \theta_i^{3/2}}{\sqrt{\theta}} \\ &\times \frac{1}{c^2 \hbar \omega} \left\{ a_i^3 e^{a_i} \frac{d}{da_i} \left( \frac{K_1(a_i)}{a_i} \right) \right\}, \end{aligned} \quad (15)$$

$$\begin{aligned} \Delta P_i^{(-)} &= -\exp\left(\frac{\hbar\omega}{\theta_i}\right) \Delta P_i^{(+)}, \\ a_i &= \frac{\hbar\omega}{2\theta_i}. \end{aligned} \quad (16)$$

In relationship (15),  $\tau_{\perp}^{(0)}$  and  $\tau_{\parallel}^{(0)}$  are the transverse and longitudinal components of the tensor of the relaxation time at  $\varepsilon = \theta$ , respectively, due to electron scattering by acoustic phonons.

By using formulas (15) and (16), it is easy to deduce a general expression for the absorption coefficient related to the acoustic scattering; that is,

$$K = \frac{\sum_i (\Delta P_i^{(+)} + \Delta P_i^{(-)})}{\Pi}, \quad (17)$$

where

$$\Pi = \frac{c\sqrt{\varepsilon_0}}{4\pi} \mathbf{E}^2 = \frac{c\sqrt{\varepsilon_0}}{4\pi} \left(\frac{\omega}{c}\right)^2 \frac{A_0^2}{2} \quad (18)$$

is the flux incident on the semiconductor,  $\varepsilon_0$  is the static permittivity,  $E$  is the electric field of the electromagnetic wave,  $A_0$  is the amplitude of the vector-potential defined by the formula

$$\mathbf{A} = \mathbf{q}_0 A_0 \cos(\omega t - xz), \quad (19)$$

$\mathbf{q}_0$  is the unit vector specifying the polarization of the wave, and  $x$  is the wave vector.

Next, we take into account that the polarization-dependent factor in relationship (15) can be reduced to the form

$$\begin{aligned} &\frac{A_{\perp}^2}{m_{\perp} \tau_{\perp}^{(0)}} + \frac{A_{\parallel}^2}{m_{\parallel} \tau_{\parallel}^{(0)}} \\ &= A_0^2 \left\{ \frac{1}{m_{\perp} \tau_{\perp}^{(0)}} + \left[ \frac{1}{m_{\parallel} \tau_{\parallel}^{(0)}} - \frac{1}{m_{\perp} \tau_{\perp}^{(0)}} \right] (\mathbf{q}_0 \mathbf{l}_0)^2 \right\}. \end{aligned} \quad (20)$$

As a result, from expression (17) with due regard for formulas (15), (16), and (18), we obtain a general rela-

tionship for the absorption coefficient in the following form:

$$K = \frac{16\sqrt{\pi} e^2}{3 c \hbar} \sum_{(i)} \frac{n_i \theta_i^{3/2}}{\sqrt{\theta \omega}} \times \left\{ \frac{1}{m_{\perp} \tau_{\perp}^{(0)}} + \left[ \frac{1}{m_{\parallel} \tau_{\parallel}^{(0)}} - \frac{1}{m_{\perp} \tau_{\perp}^{(0)}} \right] (\mathbf{q}_0 \mathbf{l}_0)^2 \right\} \times \left( 1 - \exp\left(\frac{-\hbar \omega}{\theta_i}\right) \right) \left[ a_i^3 e^{a_i} \frac{d}{da_i} \left( \frac{K_1(a_i)}{a_i} \right) \right], \quad (21)$$

$$a_i = \frac{\hbar \omega}{2\theta_i}.$$

Equation (21) holds in the classical limit ( $\theta_i \gg \hbar \omega$ ) and in the quantum limit ( $\theta_i \ll \hbar \omega$ ). In the limiting cases, the general formula can be substantially simplified and, as a result, we obtain

$$K = \frac{32\sqrt{\pi}}{3} \frac{e^2}{\sqrt{\epsilon} c \omega^2} \sum_{(i)} n_i \sqrt{\frac{\theta_i}{\theta}} \times \left\{ \frac{1}{m_{\perp} \tau_{\perp}^{(0)}} + \left[ \frac{1}{m_{\parallel} \tau_{\parallel}^{(0)}} - \frac{1}{m_{\perp} \tau_{\perp}^{(0)}} \right] (\mathbf{q}_0 \mathbf{l}_0)^2 \right\} \quad (22)$$

at  $\theta_i \gg \hbar \omega$  and

$$K = \frac{4\pi}{3} \frac{e^2}{\sqrt{\epsilon_0} c \omega^2} \left( \frac{\hbar \omega}{\theta} \right)^{1/2} \times \sum_{(i)} n_i \left\{ \frac{1}{m_{\perp} \tau_{\perp}^{(0)}} + \left[ \frac{1}{m_{\parallel} \tau_{\parallel}^{(0)}} - \frac{1}{m_{\perp} \tau_{\perp}^{(0)}} \right] (\mathbf{q}_0 \mathbf{l}_0)^2 \right\} \quad (23)$$

at  $\theta_i \ll \hbar \omega$ .

It is evident that, in the general case, when the valley populations  $n_i$  are not equal to each other or the electron temperatures  $\theta_i$  in different valleys differ, the absorption coefficient depends on the polarization of the electromagnetic wave. The difference in the valley populations can be associated either with the different degrees of electron heating in the valleys or with the uniaxial deformations of the sample.

For isotropic acoustic scattering, the relaxation time  $\tau(\epsilon)$  is a scalar quantity and has the standard form

$$\frac{1}{\tau(\epsilon)} = \frac{\sqrt{2} m^{3/2} \theta \Sigma_d^2}{\pi \rho s^2 \hbar^4} \sqrt{\epsilon}. \quad (24)$$

In this case, instead of formula (22), we have

$$K \approx \frac{32\sqrt{\pi}}{3\sqrt{\epsilon} c m \tau(\theta) \omega^2} e^2 n. \quad (25)$$

Formula (25) differs from the classical Drude formula by the factor  $\frac{8}{3\sqrt{\pi}}$ . This insignificant difference is

due to the fact that, in the classical Drude theory, the energy dependence of the relaxation time is ignored. In the quantum limit, when the scattering is anisotropic, instead of formula (23), we obtain

$$K = \frac{4\pi n}{3mc \sqrt{\epsilon_0} \omega^2 \tau(\hbar \omega)}. \quad (26)$$

To avoid confusion, we recall that, in formulas (25) and (26),  $n$  is the total electron concentration, whereas  $n_i$  involved in formulas (22) and (23) is the electron concentration in the  $i$ th valley ( $n = \Sigma n_i$ ).

Expression (16) determines the radiation induced by the wave field. The spontaneous radiation of hot electrons under consideration can easily be obtained formally from expression (16). For this purpose, we normalize the vector-potential of the electromagnetic wave [defined by expression (19)] in such a manner that there will be  $N_{ph}$  photons in the volume  $V$ ; i.e., we use the condition

$$\frac{1}{V} N_{ph} \hbar \omega = \frac{\mathbf{E}^2}{4\pi}, \quad (26a)$$

from which it follows that

$$A_0 = c \left( \frac{2\pi \hbar}{v \omega} N_{ph} \right)^{1/2}. \quad (27)$$

By substituting expression (27) into relationship (16), assuming that  $N_{ph} = 1$ , and multiplying the resultant expression by the density of final states of the field, we obtain the formula for the spontaneous radiation.

The density of final states of the field in a unit frequency interval at the solid angle  $d\Omega$  is given by

$$d\rho(\omega) = \frac{V k^2 dk d\Omega}{(2\pi \hbar)^3 d\omega} = \frac{V}{(2\pi c)^3} \omega^2 d\Omega. \quad (28)$$

After the above transformations, we obtain the following expression for the contribution made by hot electrons of the  $i$ th valley to the spontaneous radiation:

$$W^{(-)} = -\frac{V e^2 n_i \theta_i^{3/2}}{6\pi^{5/2} \sqrt{\theta} c^3} \times \left\{ \frac{1}{m_{\perp} \tau_{\perp}^{(0)}} + \left[ \frac{1}{m_{\parallel} \tau_{\parallel}^{(0)}} - \frac{1}{m_{\perp} \tau_{\perp}^{(0)}} \right] (\mathbf{q}_0 \mathbf{l}_0)^2 \right\} \quad (29)$$

$$\times \left\{ a_i^3 e^{a_i} \frac{d}{da_i} \left( \frac{K_1(a_i)}{a_i} \right) \right\} d\Omega,$$

$$a_i = \frac{\hbar \omega}{2\theta_i}.$$

In the quantum range of frequencies, i.e., for frequencies at which  $a_i = \frac{\hbar\omega}{2\theta_i} \gg 1$ , expression (29) has a simple form,

$$W^{(-)} \approx \frac{V}{24\pi^2} \left\{ \frac{1}{m_{\perp}\tau_{\perp}^{(0)}} + \left[ \frac{1}{m_{\parallel}\tau_{\parallel}^{(0)}} - \frac{1}{m_{\perp}\tau_{\perp}^{(0)}} \right] (\mathbf{q}_0 \mathbf{l}_0)^2 \right\} \times \frac{e^2 n_i (\hbar\omega)^{3/2}}{\sqrt{\theta} c^3} \exp\left(-\frac{\hbar\omega}{\theta_i}\right) d\Omega. \quad (30)$$

In this range of frequencies, the spontaneous radiation exponentially depends on the electron temperature. A different situation occurs in the classical range of frequencies ( $a_i \ll 1$ ). In this case, we have

$$W^{(-)} \approx \frac{V}{3\pi^{5/2}} \left\{ \frac{1}{m_{\perp}\tau_{\perp}^{(0)}} + \left[ \frac{1}{m_{\parallel}\tau_{\parallel}^{(0)}} - \frac{1}{m_{\perp}\tau_{\perp}^{(0)}} \right] (\mathbf{q}_0 \mathbf{l}_0)^2 \right\} \times \frac{e^2 n_i \theta^{3/2}}{\sqrt{\theta} c^3} d\Omega. \quad (31)$$

### 3. IMPURITY SCATTERING

For impurity scattering, the power induced by the field of the electromagnetic wave, which is absorbed or radiated by electrons, has the form of expression (5) with the only difference that, instead of formula (3), the scattering probability  $W(q)$  is defined by the expression

$$W(\mathbf{q}) = \frac{(2\pi\hbar)^3 4e^4 N}{V x_0^2} \left\{ (\hbar q)^2 + \left(\frac{\hbar}{r_0}\right)^2 \right\}^{-2}. \quad (32)$$

Here,  $N$  is the concentration of ionized impurities,  $r_0$  is the shielding length, and  $x_0$  is the statistical permittivity. The scattering probability (32) is calculated for the case of scattering of an electron by the screened Coulomb potential.

Let us dwell briefly on a procedure of calculating the required integrals [see expression (5)]. We begin with the calculation of integral (9) for the case of impurity scattering. Integral (9) corresponds to the case of absorption of the photon energy  $\hbar\omega$ . Now, we consider the case of emission of the photon energy  $\hbar\omega$ .

Taking into account expressions (6) and (7), by analogy with integral (9), we obtain

$$\int d\mathbf{p} f(\mathbf{p}) \int d\mathbf{p}' W(\mathbf{q}) \gamma^2 \delta\{\varepsilon_{\mathbf{p}'} - \varepsilon_{\mathbf{p}} + \hbar\omega\} = 2\pi\hbar^2 m_{\parallel} m_{\perp} \int_{\hbar\omega}^{\infty} d\varepsilon f(\varepsilon) \int_{q_{\min}}^{q_{\max}} dq^* q^* \int d\Omega_{q^*} W(\mathbf{q}^*) \gamma^2. \quad (33)$$

Relationship (33) accounts for the fact that photons can be emitted only by electrons with energies  $\varepsilon \geq \hbar\omega$ . Moreover, the quantities  $q_{\max}$  and  $q_{\min}$  in formula (32)

for the radiation are determined by expressions (14). When calculating integrals (9) for acoustic scattering, we performed the integration with respect to the modulus  $q^*$ .

This treatment was convenient because the scattering probability  $W(\mathbf{q}^*)$  did not depend on the magnitude of the vector  $\mathbf{q}^*$  and was dependent on the angles alone. In the case of photon emission, as follows from formula (32), the scattering probability depends on the modulus of the transferred momentum. Hence, it is assumed that  $f(\varepsilon)$  is the Maxwellian function of the  $i$ th valley with the temperature  $\theta_i$  and concentration  $n_i$ :

$$f(\varepsilon) = \frac{n_i}{(2\pi\theta_i)^{(3/2)} m_{\perp} \sqrt{m_{\parallel}}} \exp\left(-\frac{\varepsilon}{\theta_i}\right). \quad (34)$$

In relationship (33), we shift the limits of integration with respect to the energy ( $\varepsilon = \varepsilon' + \hbar\omega$ ) and take the integral by parts with respect to the variable  $\varepsilon'$ . As a result, relationship (33) can be transformed into the expression

$$\int d\mathbf{p} f(\mathbf{p}) \int d\mathbf{p}' W(\mathbf{q}) \gamma^2 \delta\{\varepsilon_{\mathbf{p}'} - \varepsilon_{\mathbf{p}} + \hbar\omega\} = \frac{n_i \theta_i m_{\perp} \exp\left(-\frac{\hbar\omega}{\theta_i}\right)_{\infty}}{(2\pi\theta_i)^{3/2} \sqrt{m_{\parallel}}} \int_0 d\varepsilon' \exp\left(-\frac{\varepsilon'}{\theta_i}\right) \times q^* \int [d\Omega_{q^*} W(\mathbf{q}^*) \gamma^2]_{q^* = q'_{\max}} \frac{dq'_{\max}}{d\varepsilon'} - [q^* \int d\Omega_{q^*} W(\mathbf{q}^*) \gamma^2]_{q^* = q'_{\min}} \frac{dq'_{\min}}{d\varepsilon'}. \quad (35)$$

Here, the quantities  $q'_{\max}$  and  $q'_{\min}$  coincide (owing to the energy shift) with those determined by expression (10). It follows from relationship (35) that the case of radiation differs from the case of absorption only in the factor  $e^{-\frac{\hbar\omega}{\theta_i}}$ . Consequently, relationship (16) also holds for impurity scattering.

The calculation of the integrals with respect to the angles  $\int d\Omega_{q^*} W(\mathbf{q}^*) \gamma^2$  presents no problems, and we easily obtain

$$\int d\Omega_{q^*} W(\mathbf{q}^*) \gamma^2 = \frac{(2\pi\hbar)^3 4e^4}{V x_0^2} \left(\frac{m_{\perp}}{m_{\parallel} - m_{\perp}}\right)^2 \frac{\pi N}{(\hbar q^*)^2} \times \left\{ A_0^2 B_1(q^*) + A_{\parallel}^2 \left[ -B_1(q^*) + 2 \frac{m_{\perp}}{m_{\parallel}} B_2(q^*) \right] \right\}. \quad (36)$$

Here, we introduced the following designations:

$$\begin{aligned} B_1(q^*) &= \frac{1}{b^2} + \frac{1-b^2}{b^3} \arctan \frac{1}{b}, \\ B_2(q^*) &= -\frac{1}{1+b^2} + \frac{1}{b} \arctan \frac{1}{b}, \\ b^2 &= \frac{m_\perp}{m_\parallel - m_\perp} \left( 1 + \frac{1}{(r_0 q^*)^2} \right). \end{aligned} \quad (37)$$

Next, we change over to the dimensionless variables  $x = \frac{\varepsilon}{\theta_i}$  in relationship (35) and substitute expression (36) into relationship (35). We take into account that, in the new variables,

$$\begin{aligned} q'_{\max} &= \frac{(2m_\perp \theta_i)^{1/2}}{\hbar} \left\{ x^{1/2} + \left( x + \frac{\hbar \omega}{\theta_i} \right)^{1/2} \right\}, \\ q'_{\min} &= \frac{(2m_\perp \theta_i)^{1/2}}{\hbar} \left\{ -x^{1/2} + \left( x + \frac{\hbar \omega}{\theta_i} \right)^{1/2} \right\}. \end{aligned} \quad (38)$$

As a consequence, from relationship (35), we obtain

$$\begin{aligned} &\int d\mathbf{p} f(\mathbf{p}) \int d\mathbf{p}' W(\mathbf{q}) \gamma^2 \delta\{\varepsilon_{\mathbf{p}'} - \varepsilon_{\mathbf{p}} + \hbar \omega\} \\ &= \frac{(2\pi \hbar)^3 e^4 N n_i}{V x_0^2} \left( \frac{2\pi m_\parallel}{\theta_i} \right)^{1/2} \left( \frac{m_\perp}{m_\parallel - m_\perp} \right)^2 \\ &\times A_0^2 \int \frac{dx e^{-x} \{\Psi(q'_{\max}) + \Psi(q'_{\min})\}}{\sqrt{s \left( x + \frac{\hbar \omega}{\theta_i} \right)}}, \end{aligned} \quad (39)$$

where

$$\Psi(q^*) = B_1(q^*) + (\mathbf{q}_0 \mathbf{l}_0)^2 \left[ -B_1(q^*) + 2 \frac{m_\perp}{m_\parallel} B_2(q^*) \right]. \quad (40)$$

Recall that, in formula (40),  $\mathbf{q}_0$  is the unit vector specifying the polarization of the electromagnetic wave and  $\mathbf{l}_0$  is the unit vector directed along the axis of rotation of the mass ellipsoid of the  $i$ th valley.

From relationship (39), we easily determine the corrections to the power transferred to (or removed from) the electron subsystem due to the action of the electromagnetic wave.

According to expressions (5) and (39), we obtain the formulas

$$\begin{aligned} \Delta P_i^{(+)} &= -\frac{e^6 N n_i \hbar \left( \frac{2\pi m_\parallel}{\theta_i} \right)^{1/2}}{4 x_0^2 c^2 \omega (m_\parallel - m_\perp)^2} A_0^2 \\ &\times \int_0^\infty \frac{dx e^{-x} \{\Psi(q'_{\max}) + \Psi(q'_{\min})\}}{\sqrt{x \left( x + \frac{\hbar \omega}{\theta_i} \right)}}, \\ \Delta P_i^{(-)} &= -\exp\left(-\frac{\hbar \omega}{\theta_i}\right) \Delta P_i^{(+)}. \end{aligned} \quad (41)$$

By using relationship (41), we obtain a general expression for the coefficient of light absorption by free electrons in the case when anisotropic impurity scattering in multivalley semiconductors plays a dominant role. Form formulas (17) and (41), we derive the expression

$$\begin{aligned} K &= (2\pi)^{3/2} - \frac{e^6 N m_\parallel^{1/2} \hbar}{x_0^{5/2} c (m_\parallel - m_\perp)^2 \omega^3} \\ &\times \sum \frac{n_i}{\sqrt{\theta_i}} \left( 1 - \exp\left(-\frac{\hbar \omega}{\theta_i}\right) \right) \int_0^\infty \frac{dx e^{-x} \{\Psi(q'_{\max}) + \Psi(q'_{\min})\}}{\sqrt{x \left( x + \frac{\hbar \omega}{\theta_i} \right)}}. \end{aligned} \quad (42)$$

Expression (42) can be substantially simplified in different limiting cases. For example, at  $\frac{\hbar \omega}{\theta_i} \gg 1$ , the quantities  $q'_{\max}$  and  $q'_{\min}$  in the integrand in expression (42) can be taken as

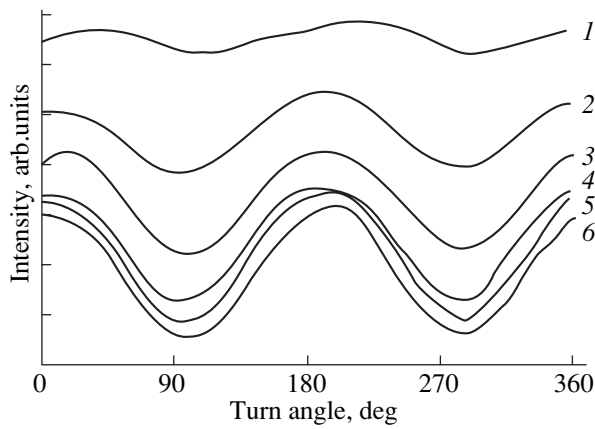
$$q'_{\max} \approx q'_{\min} \approx \left( \frac{2m_\perp \omega}{\hbar} \right)^{1/2} \equiv q'.$$

Then,

$$\int_0^\infty \frac{dx e^{-x} \{\Psi(q'_{\max}) + \Psi(q'_{\min})\}}{\sqrt{x \left( x + \frac{\hbar \omega}{\theta_i} \right)}} \approx 2\sqrt{\pi} \Psi(q') \sqrt{\frac{\theta_i}{\hbar \omega}}.$$

Let us now write a general expression for the radiation of hot electrons of the  $i$ th valley in the case of impurity scattering. By using relationship (41) and repeating the procedures used to derive formula (29), we easily obtain

$$\begin{aligned} W^{(-)} &= \frac{e^6 N n_i \sqrt{m_\parallel} \hbar^2 d\Omega}{4(2\pi)^{3/2} x_0^2 c^3 \sqrt{\theta_i} (m_\parallel - m_\perp)^2} \exp\left(-\frac{\hbar \omega}{\theta_i}\right) \\ &\times \int_0^\infty \frac{dx e^{-x} \{\Psi(q'_{\max}) + \Psi(q'_{\min})\}}{\sqrt{x \left( x + \frac{\hbar \omega}{\theta_i} \right)}}. \end{aligned} \quad (43)$$



Dependences of the radiation intensity of *n*-Ge on the turn angle of the polarizer. Uniaxial pressure, *P*, kbar/cm<sup>2</sup>: (1) 0, (2) 1.0, (3) 2.0, (4) 3.0, (5) 4.0, and (6) 6.0.

#### 4. RESULTS AND DISCUSSION

Equations (29) and (43) describe the electromagnetic radiation of electrons of a single valley. The structure of these equations is such that both equations and their sum can be written in the form

$$W^{(-)} = R + Q^2(\mathbf{q}_0, \mathbf{i}_0). \quad (44)$$

For a multivalley semiconductor, it is necessary to carry out summation of the radiation over all equivalent valleys:

$$W_s^{(-)} = \sum_i [R_i + Q_i^2(\mathbf{q}_0, \mathbf{i}_0)], \quad (44a)$$

where  $R_i$  and  $Q_i$  depend on the lattice temperature, impurity concentration, electron temperatures, and electron concentrations in the valleys. As an example, we consider germanium, because the radiation of hot electrons from germanium has been studied in a number of works [3–5]. It is assumed that the electric field is directed along the [111] axis of the crystal. In this case, all the valleys can be divided into two groups with different electron temperatures and different electron concentrations in the valleys. The first group contains a single valley located on the [111] axis, and the second group consists of three valleys located on the  $[\bar{1}11]$ ,  $[1\bar{1}1]$ , and  $[11\bar{1}]$  axes.

After summation in formula (44a), in the case under consideration, we obtain

$$W_s^{(-)} = R_1 + 3R_2 + \frac{Q_1}{3} + Q_2 + \frac{2}{3}(q_{0x}q_{0y} + q_{0y}q_{0z} + q_{0x}q_{0z})(Q_1 - Q_2). \quad (45)$$

It can easily be shown that extreme values of the anisotropic part are reached at  $q_{0x} = q_{0y} = q_{0z} = \frac{1}{\sqrt{3}}$  with the constraint  $q_{0x} + q_{0y} + q_{0z} = 0$ , i.e., in the [111] direction and in the plane perpendicular to this direction, which, what more, follows from symmetry considerations.

For definiteness, we assume that the propagation wave vector is directed along the  $[\bar{1}10]$  axis; consequently, the polarization vector lies in the  $(\bar{1}10)$  plane. The sense of the polarization vector in this plane can be specified, for example, by the angle  $\alpha$  the vector makes with the [111] axis. After simple transformations, formula (45) is rearranged to the form

$$W_s^{(-)} = R_1 + 3R_2 + \frac{4}{3}Q_2 + (Q_1 - Q_2)\cos^2(\alpha) \quad (45a)$$

and the degree of polarization is represented by the formula

$$P = \frac{W_s^{(-)}|_{\alpha=0} - W_s^{(-)}|_{\alpha=\pi/2}}{W_s^{(-)}|_{\alpha=0} + W_s^{(-)}|_{\alpha=\pi/2}} = \frac{Q_1 - Q_2}{2(R_1 + 3R_2) + Q_1 + \frac{5}{3}Q_2}. \quad (46)$$

It follows from expressions (29) and (43) that  $R > 0$ ,  $Q < 0$ , and  $|R| \approx |Q|$  for germanium characterized by the ratio  $\frac{m_{\perp}}{m_{\parallel}} \approx 0.05$ . Consequently, according to formula

(46), the radiation polarization reaches a maximum value close to 100% and the polarization vector is predominantly directed across the electric field at  $Q_2 \ll Q_1$ . This means that, in the case when a single valley located on the [111] axis is populated by electrons, the electromagnetic waves with polarization along the minor axis of the energy ellipsoid are predominantly emitted independently of the emission wavelength, the electric field strength, and the electron scattering mechanism. For  $Q_1 = Q_2$ , i.e., when the electron temperatures and electron concentrations in valleys of both groups are equal to each other, the polarization is absent. At  $Q_2 > Q_1$ , the radiation is predominantly polarized along the electric field and the degree of polarization reaches a maximum value of about 25% at  $Q_2 \gg Q_1$ . When the partial populations of valleys in both groups differ, the radiation polarization depends on the electric field, the emission wavelength, the degree of crystal doping, etc.

As an illustration, the figure presents the results of the radiation polarization measurements carried out by V.M. Bondar<sup>1</sup> for germanium crystals doped with antimony at a concentration of  $10^{15}$  cm<sup>-3</sup>. The measure-

<sup>1</sup> Detailed description of the experimental procedure and experimental data will be published in a separate paper.

ments were performed at a temperature of about 5 K in an electric field with a strength of 50 V/cm in the wavelength range 80–120  $\mu\text{m}$ . In this figure, zero corresponds to such a configuration of the polarizer and the sample when the polarization lines are directed along the electric field. Different curves were obtained at different uniaxial pressures applied parallel to the electric field as aligned along the [111] axis. In this case, the electrons predominantly occupy the [111] valley both in the heating field and under the applied pressure. At a maximum pressure (about 7  $\text{tn/cm}^2$ ), virtually all the electrons are located in this valley.

It is seen from the figure that, at all the pressures, the radiation is polarized perpendicularly to the electric field and, in accordance with the developed theory, the degree of polarization increases with an increase in the pressure, i.e., when the electrons are transferred into the [111] valley. However, the maximum degree of polarization (about 25%) is substantially less than that predicted from the theory. Moreover, the degree of polarization depends on the heating field. There are several reasons for this discrepancy between the theory and experiment. First, the insignificant decrease in the measured degree of polarization is associated with imperfections in the polarization analyzer. Second, a certain depolarization takes place when the radiation leaves the crystal. Third, one of the main reasons is that, at low temperatures of the crystal, the polarization occurs through the competing mechanism with its preferential

direction along the electric field. It is well known that, at low temperatures, the asymmetric part of the distribution function becomes significant and comparable to the symmetric part. Proper allowance made for this circumstance can lead to better agreement between the theoretical and available experimental results. On the other hand, it is expedient to perform measurements of the radiation polarization of hot electrons at higher temperatures of the lattice (for example, at  $T = 77$  K) for which the assumptions underlying the theory hold good.

#### REFERENCES

1. F. T. Vas'ko, *Fiz. Tekh. Poluprovodn. (Leningrad)* **24** (4), 682 (1990) [*Sov. Phys. Semicond.* **24**, 428 (1990)].
2. V. P. Malevich, *Fiz. Tekh. Poluprovodn. (Leningrad)* **16** (8), 2035 (1982) [*Sov. Phys. Semicond.* **16**, 1313 (1982)].
3. V. M. Bondar, A. V. Kuznetsov, and P. M. Tomchuk, *Ukr. Fiz. Zh.* **36** (4), 517 (1991).
4. I. Ferretti, A. Abramo, R. Brunetti, and C. Jacoboni, *Phys. Status Solidi B* **204** (1), 538 (1997).
5. V. M. Bondar, A. V. Kuznetsov, and A. S. Khanenko, *Ukr. Fiz. Zh.* **36** (3), 344 (1991).
6. V. M. Bondar, A. V. Kuznetsov, P. M. Tomchuk, and A. S. Khanenko, *Ukr. Fiz. Zh.* **36** (6), 824 (1991).

*Translated by O. Moskalev*

---

---

SEMICONDUCTORS  
AND DIELECTRICS

---

---

## Transport Properties of the $\text{LaSrNiO}_{4 \pm \delta}$ Ceramics

T. A. Ivanova\*, I. Jacyna-Onyszkiewicz\*\*, and Yu. V. Yablokov\*\*\*

\*Kazan Physicotechnical Institute, Russian Academy of Sciences, Kazan, 420029 Russia

e-mail: alex@dionis.kfti.knc.ru

\*\*Adam Mickiewicz University, Poznan, 61-614 Poland

\*\*\*Institute of Molecular Physics, Polish Academy of Sciences, Poznan, 60-179 Poland

Received October 3, 2001

**Abstract**—The temperature dependence of electrical resistivity in  $\text{LaSrNiO}_{4 \pm \delta}$  ceramics synthesized using various techniques and subjected to heat treatment is studied. The occurrence of a metal–semiconductor transition is shown to be accounted for by the Anderson carrier localization originating from the random arrangement of oxygen vacancies. © 2002 MAIK “Nauka/Interperiodica”.

### 1. INTRODUCTION

Investigation of superconducting oxide ceramics and of their structural analogs shows that their conduction is due, to a large extent, to inhomogeneities in their microstructure (structural defects, charge nonstoichiometry, microphase inhomogeneity), which might depend substantially on the actual conditions of preparation and heat treatment. The nickel-containing oxides  $\text{La}_{2-x}\text{Sr}_x\text{NiO}_4$ , which are isostructural to superconducting cuprates, reveal, in addition to many features which make these compounds similar to cuprates (similarity between the electronic spectra of the Ni and Cu  $3d$  states, the possibility of changing the valence state, susceptibility of the low-spin  $\text{Ni}^{3+}$  and  $\text{Cu}^{2+}$  ions to Jahn–Teller distortions), some specific transport properties; moreover, they have not thus far been shown to be superconducting. Substitution of strontium for lanthanum was found [1] to change the properties of  $\text{La}_{2-x}\text{Sr}_x\text{NiO}_4$  from those of an antiferromagnetic insulator to those of a metallic conductor, but much slower than occurs in  $\text{La}_{2-x}\text{Sr}_x\text{CuO}_4$ ; indeed, metallic conduction sets in the nickelates for temperatures  $>100$  K only at  $x = 1$ . At the same time, the conduction in  $\text{LaSrNiO}_4$  has a semiconducting character within the temperature interval 10–300 K [2]. To establish the mechanism of the onset of metallic conduction in the nickelates, we studied the transport properties of the  $\text{LaSrNiO}_{4 \pm \delta}$  ceramics (synthesized using various techniques) and their variation under heat treatment.

$\text{LaSrNiO}_{4 \pm \delta}$  belongs to the class of layered perovskites with a  $\text{K}_2\text{NiF}_4$ -type lattice. The nickel ions in the  $\text{LaSrNiO}_4$  structure do not produce an EPR signal [3, 4]. The weak EPR signals sometimes observed in this compound are due to various paramagnetic defects originating from charge or structural nonstoichiometry [5, 6].

### 2. SAMPLE PREPARATION AND MEASUREMENT TECHNIQUES

The  $\text{LaSrNiO}_4$  ceramics were synthesized using standard solid-phase technology. Spectroscopically pure  $\text{La}_2\text{O}_3$ ,  $\text{NiO}$ , and  $\text{SrCO}_3$  were taken in a 1 : 1 : 1 stoichiometric ratio and crushed in a Pulversette 6 (Fritsch) ball mill (with an agate container). The powder was heated in a corundum crucible at  $1150^\circ\text{C}$  in air for 12 h and subsequently cooled slowly to room temperature. The product thus obtained was again crushed, pressed in pellets, sintered in air at  $1150^\circ\text{C}$  for 12 h, and then cooled to room temperature (sample A1). Part of sample A1 was annealed at 850 K for 10 h in a pure oxygen flow (sample B1). Samples A1 and B1 were additionally annealed in air at  $500^\circ\text{C}$  for 1 h (regime I, samples A2 and B2) and at  $700^\circ\text{C}$  for 4 h (regime II, samples A3 and B3); in both cases, the samples were cooled slowly to room temperature in air. Sample C was synthesized by nitrate decomposition using the technique described in [7], and a preliminary study of it was reported in [2]. All samples were found to be single-phase within the x-ray diffraction sensitivity and to belong to the  $\text{K}_2\text{NiF}_4$  structural type. The lattice parameters extracted from the x-ray diffraction patterns are listed in Table 1.

The temperature dependence of the electrical resistivity was measured using the conventional four-probe method within the temperature interval 15–340 K. The measurements were carried out on a computerized system combined with a CS-202 helium cryostat (APD Cryogenics USA). Indium was used as contacts. The reliability of measurements was ensured by repeated reversal of the dc current direction at each temperature point.

The EPR measurements were performed on an ERS-230 EPR spectrometer in the X range at temperatures from 10 to 300 K.

**Table 1.** Lattice parameters and some data on the electrical resistivity of the  $\text{LaSrNiO}_{4\pm\delta}$  ceramics

Sample	$a$ , Å	$c$ , Å	$T_{tr}$ , K	$\rho_{100\text{ K}}$ , $10^{-3}\ \Omega\ \text{cm}$	$\rho_0$ , $10^{-3}\ \Omega\ \text{cm}$	$(d\rho/dT)_{T>T_{tr}}$ , $10^{-6}\ \Omega\ \text{cm/K}$
A1	3.832	12.376	155	1.67	1.13	2.18
A2			150	1.61	1.02	2.58
A3	3.829	12.419	–	4.67	–	–
B1	3.827	12.374	152	1.87	1.45	2.00
B2			152	2.51	1.86	2.68
B3	3.832	12.413	–	3.80	–	–
C	3.827	12.510	–	52.56	–	–

### 3. EXPERIMENTAL RESULTS

Measurements of the temperature dependence of electrical resistivity  $\rho$  revealed a transition from the semiconducting to metallic conduction at a temperature  $T_{tr} \sim 150$  K in samples A1 and B1 (Fig. 1). The resistivity of sample B1 was found to be higher than that of A1 at the same temperatures. No EPR signal was detected in either sample.

Heat treatment of sample A1 at  $500^\circ\text{C}$  did not change, on the whole, the behavior of  $\rho(T)$ ; sample B1 subjected to the same treatment also exhibited the metal–semiconductor transition, but the resistivities increased slightly (curves A2, B2 in Fig. 1). Samples A2 and B2 at temperatures below  $\sim 100$  K produced a type-I EPR signal, namely, an axial-symmetry spectrum with  $S = 1/2$  and parameters  $g_{\parallel} = 2.098$  and  $g_{\perp} = 2.022$ , which

are characteristic of  $\text{O}_2^-$ -type oxygen defects [8]. The concentration of such centers is rather low (a few hundredths of a percent) and is comparable to the expected defect content.

Samples A1 and B1 subjected to heating at  $700^\circ\text{C}$  exhibited a semiconducting character of conduction throughout the temperature interval covered (curves A3, B3 in Fig. 1). EPR spectra of sample A3 revealed a broad type-II line in addition to type-I signals (Fig. 2). The type-II signal is observed in the range 10–293 K. As seen from Fig. 2, the effective, peak-to-peak width of the signal decreases from  $\sim 200$  to  $\sim 30$  mT with increasing temperature and  $g_{\text{eff}}$  measured at the crossing with the zero line varies from 2.75 to 2.03. At low temperatures, the line shape is close to symmetrical; however, above 116 K, the spectrum takes on a more

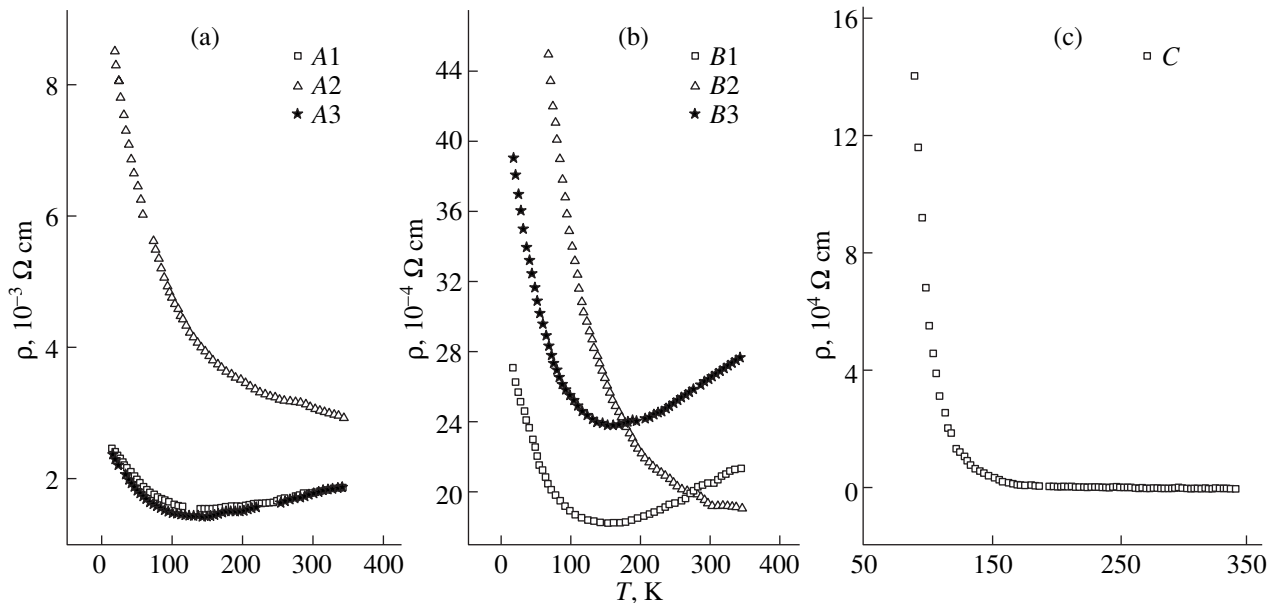


**Fig. 1.** Temperature dependence of the electrical resistivity of  $\text{LaSrNiO}_{4\pm\delta}$  samples prepared using various methods: (a) standard solid-phase technology in air; (b) same conditions as in (a) but with additional annealing in an oxygen flow; and (c) nitrate decomposition. A1 and B1 are starting samples; A2 and B2 are samples after annealing at  $T = 500^\circ\text{C}$  for 1 h; and A3 and B3 are samples after annealing at  $T = 700^\circ\text{C}$  for 4 h.

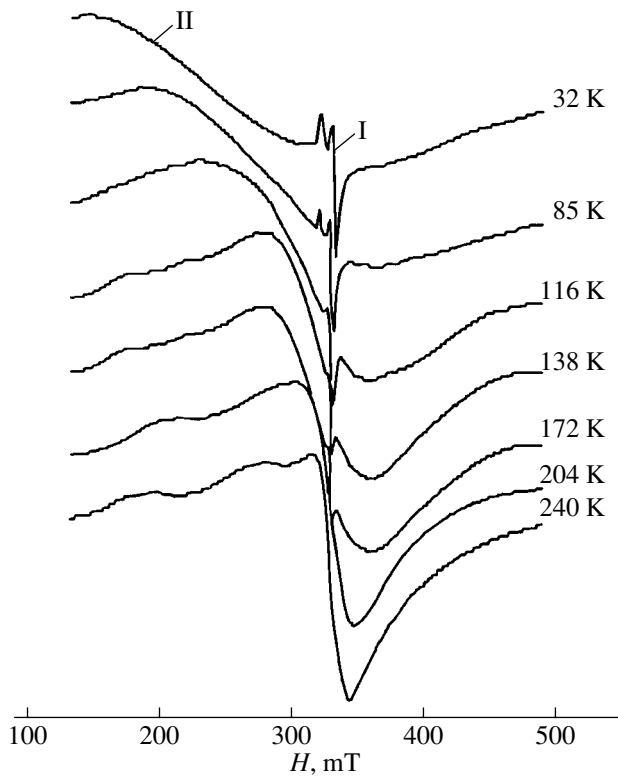


**Fig. 2.** Temperature behavior of the EPR spectra of sample A3.  $\nu = 9.32$  GHz.

complex shape, which implies superposition of several signals.

The temperature dependence of the electrical resistivity obtained on sample C over the whole range 14–340 K exhibits a semiconducting character, with the

resistivities considerably exceeding (by several orders of magnitude) those of samples A1 and B1.

The results obtained in an analysis of the temperature dependence of the electrical resistivity of the samples are presented in Tables 1 and 2 and Fig. 3.

The  $\rho(T)$  dependence for samples A1, A2, B1, and B2 follows a linear character in the metallic-conduction range, i.e., for  $T > T_{tr}$ :  $\rho(T) = \rho_0 + (dp/dT)T$ , its slope increases slightly after annealing at 500°C (for the oxygen-annealed samples B, this increase is somewhat larger than that for the A samples).

The temperature dependence of the electrical resistivity  $\rho(T)$  of samples A3 and B3 and the semiconducting-type  $\rho(T)$  relation of samples A1, B1, A2, and B2 at low temperatures is fitted satisfactorily by Mott's law (variable-range hopping conduction)  $\rho(T) = \rho_0 \exp\{(T_0/T)^{1/4}\}$ . As the temperature increases, the  $\rho(T)$  relation for these samples takes on an activated character,  $\rho(T) = \rho_0 \exp(\alpha/T)$ . The temperature at which  $\rho(T)$  crosses over to activated behavior increases with increasing heat treatment temperature, particularly in the B sample series. Sample C exhibits good agreement with Mott's law throughout the temperature range covered. As seen from Table 2, heat treatment increases the parameter  $T_0$  (for samples B, this increase is quite substantial). The values of  $T_0$  for sample C are comparable with the data available for isostructural cuprates [9], while being considerably larger than those for samples A and B.

Measurements of the sign of the thermopower showed the conduction in all the samples to be of electronic type, which agrees with the data [4, 10] reported for ceramics of the same composition.

**Table 2.** Fitting parameters for the experimental  $\rho(T)$  relations obtained on samples A3, B3, and C and on samples A1, A2, B1, and B2 in the temperature range where these samples are semiconductors

Sample	Best-fit forms of $\rho(T)$	$\Delta T$	$T_0$ , K	$\alpha$ , K	$\ln \rho_0$
A1	$\ln \rho = \ln \rho_0 + (T_0/T)^{1/4}$	14–42	3.46	17.8	–6.710
	$\ln \rho = \ln \rho_0 + \alpha/T$	42–150			
A2	$\ln \rho = \ln \rho_0 + (T_0/T)^{1/4}$	14–48	15.00	18.1	–6.683
	$\ln \rho = \ln \rho_0 + \alpha/T$	48–130			
A3	$\ln \rho = \ln \rho_0 + (T_0/T)^{1/4}$	14–50	26.36	57.4	–5.864
	$\ln \rho = \ln \rho_0 + \alpha/T$	50–340			
B1	$\ln \rho = \ln \rho_0 + (T_0/T)^{1/4}$	14–46	1.95	14.5	–6.526
	$\ln \rho = \ln \rho_0 + \alpha/T$	46–130			
B2	$\ln \rho = \ln \rho_0 + (T_0/T)^{1/4}$	30–85	77.20	19.7	–6.916
	$\ln \rho = \ln \rho_0 + \alpha/T$	85–140			
B3	$\ln \rho = \ln \rho_0 + (T_0/T)^{1/4}$	63–99	$2.2 \times 10^3$	84.32	–7.847
	$\ln \rho = \ln \rho_0 + \alpha/T$	99–340			
C	$\ln \rho = \ln \rho_0 + (T_0/T)^{1/4}$	87–340	$82 \times 10^6$		–19.244

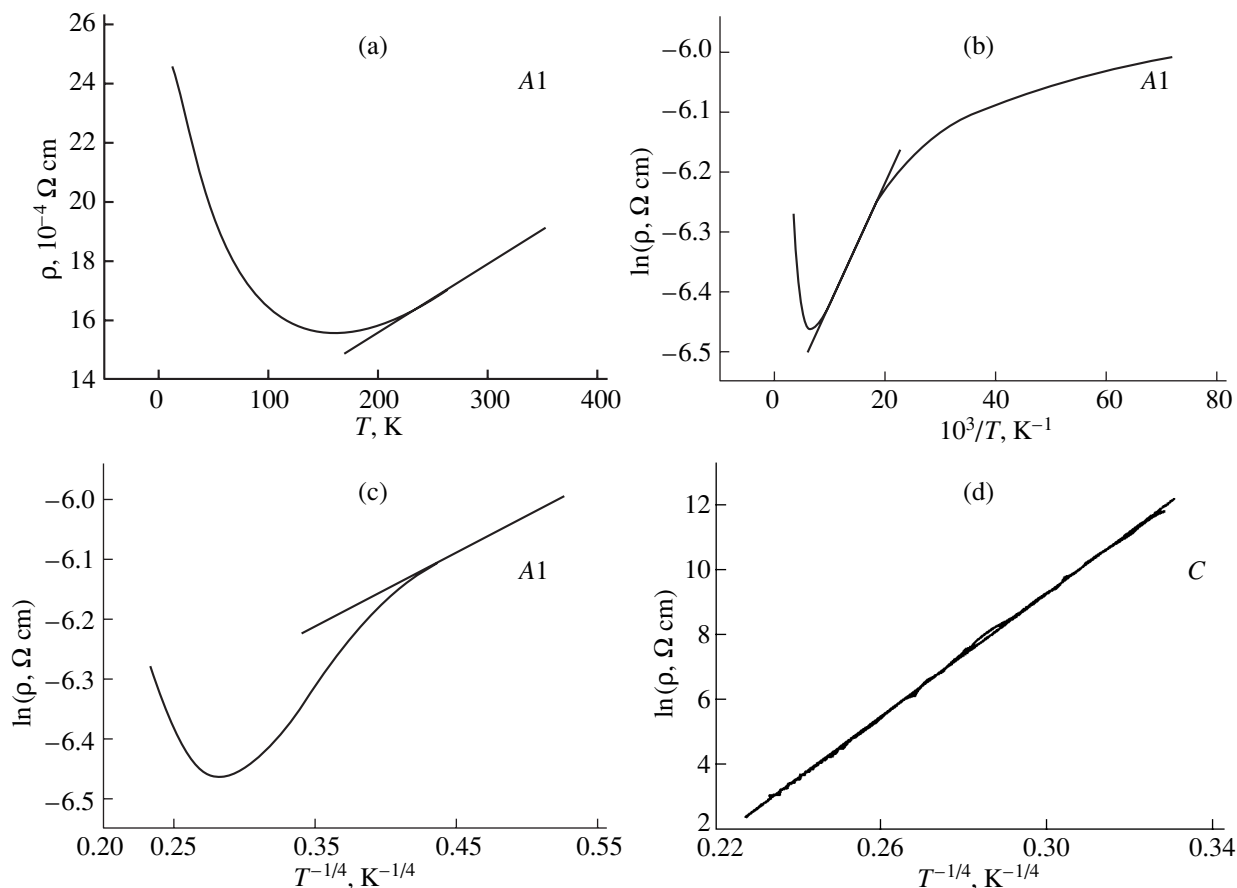


**Fig. 3.** Illustration of the fitting of the experimental  $\rho(T)$  relations by the models specified in Table 2 (a–c) for sample A1 in the regions of the metallic, activated, and Mott's conduction, respectively, and (d) for sample C exhibiting Mott's conduction throughout the temperature range covered.

#### 4. DISCUSSION OF RESULTS

As follows from an analysis of the dependence of the electrical resistivity on the conditions of preparation (see Table 1 for samples A1, B1, C), the electrical conductivity  $\sigma = 1/\rho$  correlates with the content of oxygen vacancies in the sample. Indeed, sample A1 exhibits the highest electrical conductivity. It was prepared under conditions precluding the formation of oxygen vacancies. Synthesis from the oxides and carbonates proceeds by the reaction  $(1/2)\text{La}_2\text{O}_3 + \text{SrCO}_3 + \text{NiO} = \text{LaSrNiO}_{3.5} + \text{CO}_2$ . Although the oxygen balance levels off in the course of sintering and cooling, the compound we obtained is most likely  $\text{LaSrNiO}_{4-\delta}$ , which contains the largest number of vacancies  $\delta$  as compared with the other samples. Heat treatment in an oxygen flow reduces  $\delta$  (sample B1), and the electrical resistivity increases slightly. Synthesis from nitrates produces a more oxygen-enriched compound:  $\text{La}(\text{NO}_3)_3 + \text{Sr}(\text{NO}_3)_2 + \text{NiO} = \text{LaSrNiO}_4 + 5\text{NO}_2 + \text{O}_2$ . One might, therefore, expect the value of  $\delta$  in sample C to be substantially smaller. As a result, the electrical resistivity of sample C should be higher than that of A1 and B1. The formation of oxygen vacancies gives rise to a

decrease in the number of negatively charged sites in the structure. The charge neutrality of the sample is provided by additional electrons, which can be either localized on the vacancy or delocalized over the sample volume. One may also expect a decrease in the positive charge on a part of the nickel ions, i.e., the formation of some amount of  $\text{Ni}^{2+}$  ions. It may be conjectured that the electronic conduction of the samples studied is primarily due to the electrons freed in the formation of defects of the type of oxygen vacancies. This conjecture is borne out indirectly by x-ray structural measurements. Assuming the binding energy of the apical oxygen to be smaller than that of the oxygen in the planes, the vacancies should form predominantly in the apical positions. Then, an increase in the number of oxygen vacancies should bring about a decrease in the parameter  $c$ , which is in accord with the structural measurements (Table 1).

We assume that the oxygen vacancies efficiently localize the carriers. The character of the temperature dependence of electrical resistivity, as well as the activation energy and the constant  $T_0$  in Mott's law, is sensitive to the vacancy content in a compound; this is usu-

ally observed in doped semiconductors. The oxygen vacancies apparently act as a donor impurity and form an impurity band located close to the conduction-band bottom. The acceptors required for the operation of the hopping mechanism in the impurity band are most likely  $\text{Ni}^{2+}$  ions. The random potential associated with charged point defects gives rise to the formation of an energy range of localized states near the bottom of the conduction band. We denote the energy separating the localized from nonlocalized states (the carrier mobility edge) by  $E_C$  and the lower boundary of the energy range of localized states by  $E_A$ . The Fermi level lies in the impurity band and is separated from the mobility edge by the distance  $\Delta = E_C - E_F$  and from the lower boundary of the region of localized states by the distance  $\Delta' = E_A - E_F$ .

Let us estimate the maximum carrier concentration in the samples under study. According to the literature data [11, 12], the largest value of  $\delta$  obtained in such samples is 0.04, which corresponds to 0.02 vacancies per unit cell. Then, our estimates suggest that there are  $2.4 \times 10^{19}$  vacancies per cubic centimeter and that the average distance between donors at their maximum concentration is  $\sim 16.7 \text{ \AA}$ , which exceeds the lattice constant  $a$  by a factor of 4.4. Hence, in all the cases studied, the samples remain lightly doped and one can expect the impurity band to be fairly narrow.

At low temperatures, the hopping conduction is described by Mott's law; in other words, variable-range hopping between localized states with an energy close to the Fermi level provides a major contribution to the semiconducting behavior.

At higher temperatures, the conduction is realized via hopping to localized states near the band edge. The crossover point to activated conduction increases with increasing anneal temperature and under annealing in an oxygen flow. This is probably associated with the vacancies becoming partially compensated under annealing because of the oxygen being supplied by thermal diffusion from the surrounding medium or from microregions containing excess oxygen. A decrease in the number of structural defects reduces the energy range of localized states near the impurity band edge and, accordingly, makes the energy interval  $\Delta'$  smaller. The nonactivated behavior of sample *C* (or the shift of the crossover to the activated character toward high temperatures beyond the measurement range covered) implies that the magnitude of  $\Delta'$  in this sample is larger than 340 K.

Thermal excitation of carriers above the energy corresponding to the boundary separating the localized from nonlocalized states gives rise to the onset of metallic conduction. The small temperature coefficient  $dp/dT$  (Table 1) indicates that the mean free path is equal in order of magnitude to the interatomic separation [13].

The vanishing of the metal–semiconductor transition after heat treatment following regime II implies an

increase in the interval  $\Delta$ . This increase is most probably associated with a downward shift of the Fermi level as a result of increased donor compensation. This annealing regime apparently initiates the transfer of an additional amount of  $\text{Ni}^{3+}$  ions to the  $\text{Ni}^{2+}$  state. This conjecture is argued for by sample A3 producing a type-II EPR signal. This signal indicates the formation of magnetic clusters with an odd total spin which contain both  $\text{Ni}^{3+}$  and  $\text{Ni}^{2+}$  ions. In particular, the decrease in the linewidth from 150–200 mT to a few tens of milliteslas with increasing temperature [14], a feature characteristic of intermediate-valence clusters, is also observed to occur in our case. Refined interpretation of the type-II signals requires additional experiments.

In samples annealed in regime I ( $T = 500^\circ\text{C}$ ), the change in the state of the carriers primarily involves the centers lying close to the surface. Therefore, the parameters of sample A2 virtually do not change as compared to those of sample A1. This conjecture is borne out by the observation of a type-I EPR signal in sample A2, which is usually assigned to  $\text{O}_2^-$  oxygen radicals forming on the surface of oxides [15]. Heat treatment at  $500^\circ\text{C}$  results in a certain change in the parameters of the  $\rho(T)$  relation for sample B2 as compared to those for sample B1, although the metal–semiconductor transition in sample B2 persists. This may be due to the fact that the electrical resistivity was increased during the prolonged oxygen annealing that transferred sample A1 to B1, but the surface layers retained a higher density of additional oxygen than the bulk of the sample did. Oxygen diffusion from the surface layers into the bulk of the sample in the course of annealing of sample B1 in regime I brings about a change in the parameters of the  $\rho(T)$  dependence in sample B2 as compared to those in B1.

In conclusion, we note that in this case there is apparently one more example of the metal–semiconductor transition associated with the Anderson localization of carriers. As in other compounds [16–18], the random potential initiating Anderson localization near the energy band edge is formed because of charged point defects (oxygen vacancies in our case, cerium vacancies in the cerium sulfide and oxygen “holes” in cuprates with  $x < 0.05$ ) being randomly distributed over the sample.

#### ACKNOWLEDGMENTS

This study was supported by the Russian Foundation for Basic Research, project no. 01-03-32266.

#### REFERENCES

1. R. J. Cava, B. Batlogg, T. T. Palstra, *et al.*, *Phys. Rev. B* **43** (1), 1229 (1991).
2. A. E. Usachev, V. E. Petrashen', Yu. V. Yablokov, *et al.*, *Fiz. Tverd. Tela (St. Petersburg)* **39** (6), 985 (1997) [*Phys. Solid State* **39**, 884 (1997)].

3. Yu. V. Yablokov, T. A. Ivanova, S. Yu. Shipunova, *et al.*, *Appl. Phys. Res.* **2**, 547 (1991).
4. K. K. Singh, P. Ganguly, P. P. Edwards, and J. B. Goodenough, *J. Phys.: Condens. Matter* **3**, 2479 (1991).
5. R. D. Sanches, M. T. Causa, M. J. Sayagues, *et al.*, *Physica B (Amsterdam)* **190**, 177 (1993).
6. T. A. Ivanova, I. Jacyna-Onyszkiewicz, J. Mroziński, *et al.*, *Physica B (Amsterdam)* **304**, 246 (2001).
7. T. A. Ivanova, E. F. Kukovitskiĭ, A. E. Usachev, and Yu. V. Yablokov, *Sverkhprovodimost: Fiz., Khim., Tekh.* **5** (5), 860 (1992).
8. P. W. Atkins and M. C. R. Symons, *Structure of Inorganic Radicals* (American Elsevier, New York, 1967; Mir, Moscow, 1970).
9. M. A. Kastner, R. J. Birgenau, C. Y. Chen, *et al.*, *Phys. Rev. B* **37** (1), 111 (1988).
10. J. Copalkrishnan, G. Colsmann, and B. Reuter, *J. Solid State Chem.* **22**, 145 (1977).
11. Y. Takeda, R. Kanno, M. Sdakano, *et al.*, *Mater. Res. Bull.* **25**, 293 (1990).
12. J. D. Jorgensen, B. Dabrowski, Sh. Pei, *et al.*, *Phys. Rev. B* **40** (4), 2187 (1989).
13. N. F. Mott and E. A. Davis, *Electronic Processes in Non-Crystalline Materials* (Clarendon, Oxford, 1971; Mir, Moscow, 1974).
14. V. K. Voronkova, J. Mrozinski, and Yu. V. Yablokov, *Z. Phys. Chem.* **201**, 181 (1997).
15. A. A. Davydov, *J. Chem. Soc., Faraday Trans.* **87** (6), 913 (1991).
16. M. Cutler and N. F. Mott, *Phys. Rev.* **181** (3), 1336 (1969).
17. I. G. Mikhaïlov, D. P. Moiseev, S. K. Tolpygo, and S. K. Uvarova, *Fiz. Nizk. Temp.* **13** (9), 985 (1987) [*Sov. J. Low Temp. Phys.* **13**, 562 (1987)].
18. B. Ellman, H. M. Jaeger, D. P. Katz, *et al.*, *Phys. Rev. B* **39** (13), 9012 (1989).

*Translated by G. Skrebtsov*

# Neutron Diffraction Study of the Pressure-Driven Structural Transition in the $\text{HgTe}_{0.85}\text{S}_{0.15}$ Ternary Compound

D. P. Kozlenko\*, V. V. Shchennikov\*\*, V. I. Voronin\*\*,  
V. P. Glazkov\*\*\*, and B. N. Savenko\*

\*Joint Institute for Nuclear Research, Dubna, Moscow oblast, 141980 Russia  
e-mail: [denk@nf.jinr.ru](mailto:denk@nf.jinr.ru)

\*\*Institute of Metal Physics, Ural division, Russian Academy of Sciences,  
ul. S. Kovalevskoi 18, Yekaterinburg, 620219 Russia

\*\*\* Russian Research Centre Kurchatov Institute, pl. Kurchatova 1, Moscow, 123182 Russia

Received October 26, 2001

**Abstract**—The structure of the  $\text{HgTe}_{0.85}\text{S}_{0.15}$  ternary mercury compound was studied by neutron diffraction at high pressures of up to 40 kbar. A phase transition from the cubic (sphalerite-type) to the hexagonal (cinnabar-type) structure was established to occur with increasing pressure and to be accompanied by an abrupt change in the unit-cell volume and interatomic distances. The unit cell parameters, the positions of the Hg and Te/S atoms in the hexagonal cinnabar phase, and their pressure dependences were found. © 2002 MAIK “Nauka/Interperiodica”.

## 1. INTRODUCTION

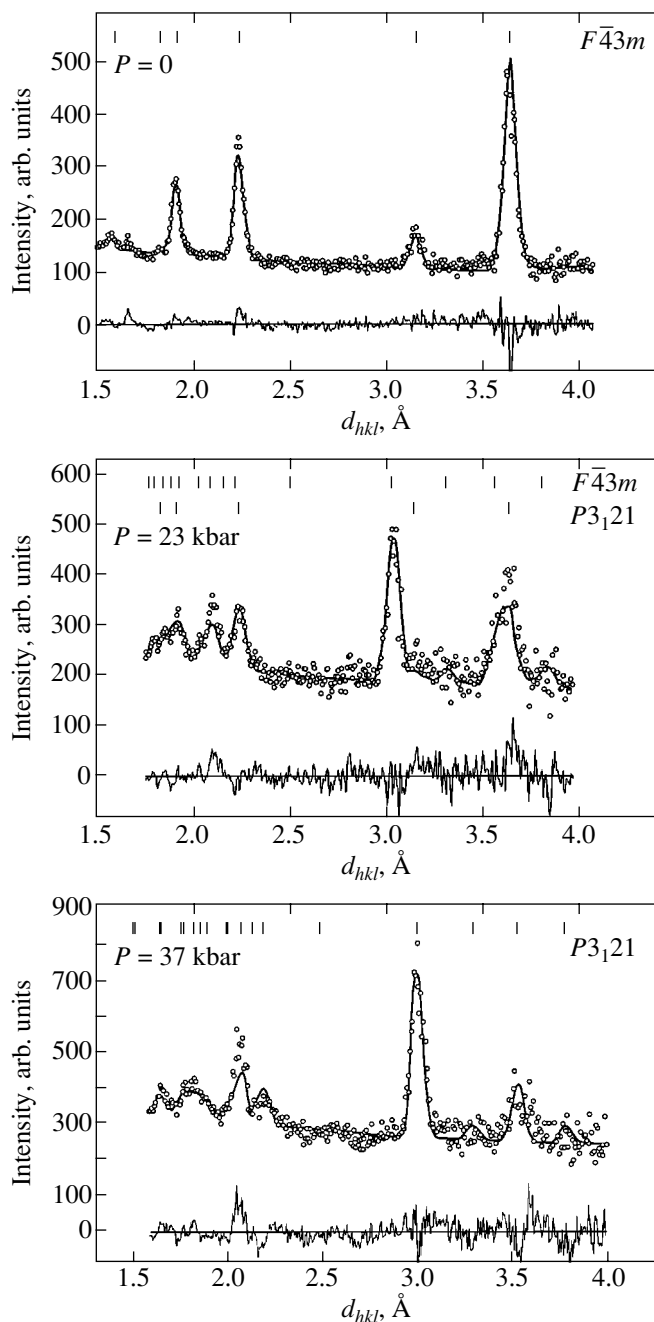
Investigation of the semiconductor–metal-type (S–M) phase transformations is an important field of condensed-state physics offering a broad range of applications [1, 2]. The ternary mercury chalcogenides  $\text{HgSe}_{1-x}\text{S}_x$  and  $\text{HgTe}_{1-x}\text{S}_x$ , with substitutional atoms on the cation or anion sublattice, are of interest in this respect, because they undergo reversible S–M pressure-driven phase transformations. By properly varying the composition, one can change the electrophysical parameters of the initial and final phases and the phase transition pressure [3–5]. However, our knowledge of the structural changes associated with such phase transitions is still incomplete. These changes are assumed to be similar to the phase transformations occurring in the HgSe and HgTe binary mercury compounds [6–8]. In the case of the  $\text{HgSe}_{1-x}\text{S}_x$  system, this assumption was checked with neutron diffraction measurements on the high-pressure phases [9]. We report here on a similar investigation of a ternary compound of another type, namely,  $\text{HgTe}_{1-x}\text{S}_x$ . Unlike the  $\text{HgSe}_{1-x}\text{S}_x$  system, which has the electrical properties of a semimetal [4], the  $\text{HgTe}_{1-x}\text{S}_x$  compound with a low sulfur content ( $x < 0.2$ ) is a gapless semiconductor with a negative exponent of the temperature dependence of electrical resistivity ( $\rho(T) \sim T^{-3/2}$ ) and becomes a semimetal only for  $x > 0.3$  [10, 11]. The contribution of the electronic component to the total lattice energy can noticeably affect the phase stability at high pressures [3]. In this study, we used a crystal with  $x = 0.15$ , which is, like HgTe, a gapless semiconductor [10, 11].

## 2. EXPERIMENTAL TECHNIQUE

The technique employed in the sample preparation was described in [10, 11], and the sample composition was measured with a Superprobe-JCXA-733 x-ray spectrometer. Neutron diffraction measurements were carried out on an IBR-2 pulsed high-flux reactor (JINR, Dubna) with a DN-12 spectrometer [12] using high-pressure sapphire-anvil chambers [13]. The samples were  $V \sim 2 \text{ mm}^3$  in volume. The diffraction spectra were obtained at a scattering angle  $2\theta = 90^\circ$ , for which the diffractometer resolution at the wavelength  $\lambda = 2 \text{ \AA}$  was  $\Delta d/d = 0.02$ . The time taken to measure one spectrum was typically 20 h. The chamber pressure was derived from the shift of the ruby luminescence line to within 0.5 kbar. All measurements were made at room temperature.

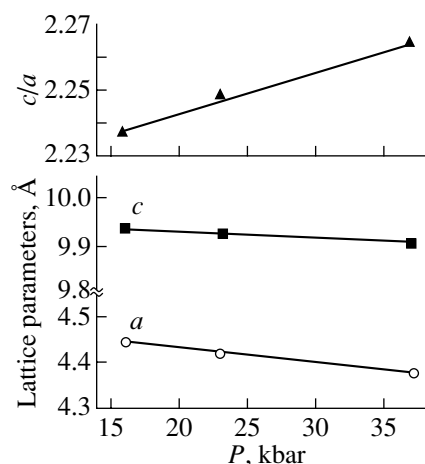
## 3. RESULTS AND DISCUSSION

Figure 1 shows parts of the diffraction spectra of  $\text{HgTe}_{0.85}\text{S}_{0.15}$  measured at normal and high pressures. The spectrum obtained at  $P = 0$  belongs to the cubic sphalerite structure. Starting from  $P = 16$  kbar, new diffraction peaks began to appear, whose intensity grew with a further increase in pressure, and the intensity of the original sphalerite phase reflections decreased. A Rietveld refinement [14] of the diffraction data showed the new peaks to correspond to the hexagonal cinnabar structure [3–5]. At  $P = 37$  kbar, the diffractograms revealed a single-phase cinnabar structure. Within a pressure interval of 16 to 24 kbar,  $\text{HgTe}_{0.85}\text{S}_{0.15}$  revealed the presence of a two-phase state; the concentration of the cinnabar phase increased and the concentration of



**Fig. 1.** Parts of the  $\text{HgTe}_{0.85}\text{S}_{0.15}$  diffraction spectra measured with a DN-12 spectrometer at 0, 23, and 37 kbar and refined by the Rietveld procedure. The spectra feature experimental points, the calculated profile, and the difference curve (at the bottom of each panel).

the original sphalerite decreased with a rise in pressure. This phenomenon was observed earlier in x-ray structural studies of the HgSe and HgTe binary systems [15, 16], as well as in neutron diffraction measurements carried out on the  $\text{HgSe}_{1-x}\text{S}_x$  ternary systems at high pressures [9]. The formation of a two-phase state is tentatively attributed to a low rate of the phase transformation [16]. The HgTe and HgSe binary compounds also



**Fig. 2.** Lattice parameters  $a$  and  $c$  of the hexagonal cinnabar phase of  $\text{HgTe}_{0.85}\text{S}_{0.15}$  and their ratio  $c/a$  plotted as functions of pressure. Solid lines are linear interpolations of experimental data.

exhibited (near the sphalerite–cinnabar structural transition) weak reflections which could be assigned to the cristobalite structure [15, 16]. In the present study, this phase was not observed.

The Rietveld analysis of neutron diffraction data by the MRJA code [14] was based on well-known structural models [15], namely, space group  $F\bar{4}3m$  for the original cubic sphalerite phase and space group  $P3_121$  for the high-pressure phase with the hexagonal cinnabar structure. In accordance with the measurements made on the binary mercury chalcogenide systems HgSe, HgTe, and HgS [15–20], it was assumed that the Hg atoms in the cinnabar structure occupy positions  $3a$  ( $u, 0, 1/3$ ) and the Te/S atoms are in positions  $3b$  ( $v, 0, 5/6$ ) of the space group. The structural parameters of  $\text{HgTe}_{0.85}\text{S}_{0.15}$  found at various pressures are given in the table. The typical values of the  $R$  factors for the  $\text{HgTe}_{0.85}\text{S}_{0.15}$  diffraction spectrum measured at  $P = 37$  kbar and corresponding to the cinnabar phase (Fig. 1) were  $R_p = 14.5\%$  and  $R_{wp} = 12.8\%$ . As seen from the table, the coordination number of the cinnabar structure of  $\text{HgTe}_{0.85}\text{S}_{0.15}$  and HgTe is  $4 + 2$  [20]. In HgS, the cinnabar structure has another coordination type, namely,  $2 + 4$  [15, 20].

With increasing pressure, the unit cell parameter of the hexagonal cinnabar phase decreases almost linearly and the  $c/a$  ratio increases (Fig. 2). The value  $c/a = 0.264$  found at  $P = 37$  kbar is smaller than that for HgTe ( $c/a = 0.287$ ) measured at a similar pressure,  $P = 36$  kbar [20]. As in the HgSe and HgTe binary compounds [6–8, 21], the cubic-to-hexagonal phase transition is accompanied by a jump in the unit-cell volume  $\Delta V/V \approx 10\%$  (Fig. 3). The pressure corresponding to the onset of the phase transition in  $\text{HgTe}_{0.85}\text{S}_{0.15}$  is in accord with the value  $P \approx 15$  kbar derived from the electrical resistivity measurements [5, 10, 11]. Linear interpola-

Structural parameters of  $\text{HgTe}_{0.85}\text{S}_{0.15}$  at normal and high pressures for the sphalerite (unit cell parameter  $a$ , Hg–X interatomic distance) and cinnabar (unit cell parameters  $a$ ,  $c$ ; positional parameters  $u$ ,  $v$ ; the distances between nearest neighbor atoms Hg1–X, Hg2–X, Hg3–X) phases. In the cinnabar phase, the Hg atoms occupy positions of the  $(u, 0, 1/3)$  type and atoms  $X = \text{Te/S}$  are in positions of the  $(v, 0, 5/6)$  type

Parameter	$P$ , kbar				
	0	14	16	23	37
Cubic sphalerite phase					
$a_c$ , Å	6.382(5)	6.329(5)	6.313(5)	6.300(5)	
Hg–X, Å	2.763	2.740	2.734	2.728(5)	
Hexagonal cinnabar phase					
$a$ , Å			4.441(5)	4.415(5)	4.375(5)
$c$ , Å			9.930(9)	9.927(9)	9.904(9)
$c/a$			2.236	2.248	2.264
$u$			–	0.597(5)	0.609(5)
$v$			–	0.549(8)	0.541(9)
Hg1–X, Å			–	2.73(2)	2.68(2)
Hg2–X, Å			–	2.90(2)	2.92(2)
Hg3–X, Å			–	3.66(2)	3.62(2)

tion of the pressure dependence of the cell volume per formula unit (Fig. 3) yields  $B_0 = VdP/dV|_{V=V_0} = 673$  kbar for the bulk modulus of the cinnabar phase. The cell volume per formula unit used in the calculations,  $V_0 = 57.89 \text{ Å}^3$ , was obtained by extrapolation to  $P = 0$ . The calculated value of  $B_0$  is in agreement with the compressibility data [22] ( $B_0 = 656$  kbar) and is slightly in excess of the value  $B_0 = 410$  kbar from [21].

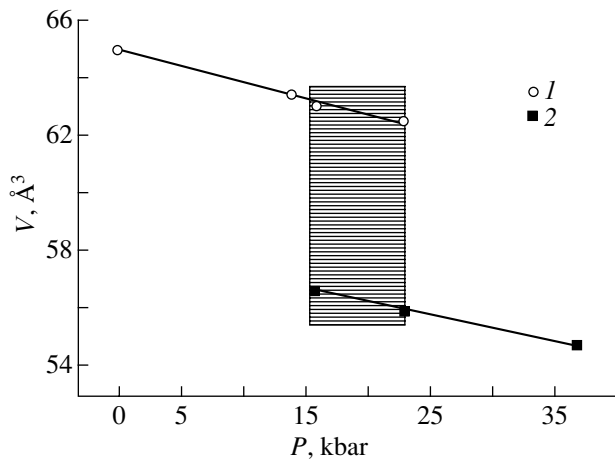


**Fig. 3.** Cell volume per formula unit in the (1) sphalerite and (2) cinnabar phases of  $\text{HgTe}_{0.85}\text{S}_{0.15}$  plotted as functions of pressure. Solid lines are linear interpolations of experimental data. The hatched area specifies the region of existence of the two-phase state.

The observed changes in the atomic positions and in the lattice parameters of  $\text{HgTe}_{0.85}\text{S}_{0.15}$  with pressure increasing from 23 to 37 kbar (see table) correspond to an increase in the X–Hg–X angle  $\alpha_1$  from  $156.5^\circ$  to  $158.2^\circ$  and to a decrease in the Hg–X–Hg angle  $\alpha_2$  from  $111.8^\circ$  to  $111.7^\circ$  in the helical chains formed by the Hg and X atoms ( $X = \text{Te, S}$ ) in the cinnabar structure [21]. Because the cinnabar structure can be considered a distorted NaCl structure, this change in the interatomic angles with increasing pressure reflects a gradual rearrangement of the hexagonal lattice to the cubic NaCl structure, for which  $\alpha_1 = 180^\circ$  and  $\alpha_2 = 90^\circ$ . A similar pattern was observed in HgTe, where  $\alpha_1$  and  $\alpha_2$  at  $P = 34.5$  kbar are closer to the limiting angles corresponding to the NaCl structure [21]; in other words, the lattice in this case is distorted less than in the ternary compound  $\text{HgTe}_{0.85}\text{S}_{0.15}$ . Therefore, the phase transition from the cinnabar structure to the NaCl-type lattice in  $\text{HgTe}_{0.85}\text{S}_{0.15}$  should occur at higher pressures than in HgTe ( $P \approx 80$  kbar) [18–25]. As shown by electrical-resistance and thermopower measurements [26], the pressure at which the semiconductor–metal electronic transition takes place in  $\text{HgTe}_{1-x}\text{S}_x$  shifts toward higher values with increasing  $x$ . In the HgTe and HgSe binary systems, this electronic phase transition occurs at the cinnabar–NaCl structural transformation.

#### 4. CONCLUSION

As shown in our study, the phase transition occurs in the ternary mercury-chalcogenide system  $\text{HgTe}_{0.85}\text{S}_{0.15}$  with increasing pressure and the cubic sphalerite structure transforms into the hexagonal cinnabar structure characterized by the coordination number  $4 + 2$ , as in the HgSe and HgTe binary compounds. The structural transformation of the cinnabar phase under pressure can be considered to be its gradual rearrangement to a cubic NaCl-type lattice. At higher pressures, the  $\text{HgTe}_{1-x}\text{S}_x$  ternary systems should apparently also undergo the cinnabar–NaCl structural transition, as was observed to occur in HgTe at  $P \approx 80$  kbar [21].

#### ACKNOWLEDGMENTS

The authors are indebted to V.M. Frasnuyak and N.P. Gavaleshko for providing the samples.

This study was supported by the Russian Foundation for Basic Research, project nos. 00-02-17199 and 01-02-17203.

#### REFERENCES

1. A. A. Bugaev, B. P. Zakharchenya, and F. A. Chudnovskii, *Metal–Semiconductor Phase Transition and Its Application* (Nauka, Leningrad, 1979).
2. G. Wicker, *MICRO/MEMS'99: Technical Program* (Royal Pines Resort, Queensland, Australia, 1999), p. 3.

3. S. Narita, M. Egawa, K. Suizu, *et al.*, *Appl. Phys.* **2** (3), 151 (1973).
4. V. V. Shchennikov, N. P. Gavaleshko, and V. M. Frasnuyak, *Fiz. Tverd. Tela (St. Petersburg)* **37**, 3532 (1995) [*Phys. Solid State* **37**, 1943 (1995)].
5. V. V. Shchennikov, N. P. Gavaleshko, and V. M. Frasnuyak, *Fiz. Tverd. Tela (St. Petersburg)* **35**, 389 (1993) [*Phys. Solid State* **35**, 199 (1993)].
6. P. W. Bridgman, *Proc. Am. Acad. Arts Sci.* **74** (3), 21 (1940).
7. J. A. Kafalas, H. G. Gatos, M. C. Lavine, and M. D. Banus, *J. Phys. Chem. Solids* **23** (11), 1541 (1962).
8. A. N. Mariano and E. P. Warekois, *Science* **142**, 672 (1963).
9. V. I. Voronin, V. V. Shchennikov, I. F. Berger, *et al.*, *Fiz. Tverd. Tela (St. Petersburg)* **43**, 2076 (2001) [*Phys. Solid State* **43**, 2165 (2001)].
10. V. V. Shchennikov, A. E. Kar'kin, N. P. Gavaleshko, and V. M. Frasnuyak, *Fiz. Tverd. Tela (St. Petersburg)* **42**, 210 (2000) [*Phys. Solid State* **42**, 215 (2000)].
11. Yu. S. Ponosov, V. V. Shchennikov, V. E. Mogilenskikh, *et al.*, *Phys. Status Solidi B* **223**, 275 (2001).
12. V. L. Aksenov, A. M. Balagurov, V. P. Glazkov, *et al.*, *Physica B (Amsterdam)* **265**, 258 (1999).
13. V. P. Glazkov and I. N. Goncharenko, *Fiz. Tekh. Vys. Davleniĭ* **1**, 56 (1991).
14. V. B. Zlokazov and V. V. Chernyshev, *J. Appl. Crystallogr.* **25**, 447 (1992).
15. M. I. McMahon and R. J. Nelmes, *Phys. Status Solidi B* **198** (1), 389 (1996).
16. M. I. McMahon, R. J. Nelmes, H. Liu, and S. A. Belmonte, *Phys. Rev. Lett.* **77**, 1781 (1996).
17. A. Werner, H. D. Hochheimer, K. Strössner, and A. Jayaraman, *Phys. Rev. B* **28** (6), 3330 (1983).
18. A. San-Miguel, A. Polian, and J. P. Itié, *J. Phys. Chem. Solids* **56** (3/4), 555 (1995).
19. T. L. Huang and A. L. Ruoff, *Phys. Rev. B* **31**, 5976 (1985).
20. N. G. Wright, M. I. McMahon, R. J. Nelmes, and A. San-Miguel, *Phys. Rev. B* **48**, 13 111 (1993).
21. A. San-Miguel, N. G. Wright, M. I. McMahon, and R. J. Nelmes, *Phys. Rev. B* **51** (14), 8731 (1995).
22. C. M. J. Rooymans, *Philips Res. Rep. Suppl.*, No. 5, 1 (1968).
23. V. V. Shchennikov and N. G. Gluzman, *Fiz. Tverd. Tela (Leningrad)* **23** (10), 3091 (1981) [*Sov. Phys. Solid State* **23**, 1800 (1981)].
24. I. M. Tsidil'kovskii, V. V. Shchennikov, and N. G. Gluzman, *Fiz. Tverd. Tela (Leningrad)* **24**, 2658 (1982) [*Sov. Phys. Solid State* **24**, 1507 (1982)].
25. A. Ohtani, T. Seike, M. Motobayashi, and A. Onodera, *J. Phys. Chem. Solids* **43** (7), 627 (1982).
26. V. V. Shchennikov, V. I. Osotov, N. P. Gavaleshko, and V. M. Frasnuyak, in *High Pressure Science and Technology*, Ed. by W. A. Trzeciakowski (World Scientific, Singapore, 1996), pp. 493–495.

*Translated by G. Skrebtsov*

---

SEMICONDUCTORS  
AND DIELECTRICS

---

# Absorption of Electromagnetic Radiation by Electrons of a Nanosphere

D. V. Bulaev and V. A. Margulis

Mordovian State University, Bol'shevistskaya ul. 68, Saransk, 430000 Russia

e-mail: theorphysics@mrsu.ru

Received November 19, 2001

**Abstract**—The electrodynamic response of an electron gas on the surface of a nanosphere is investigated. An analytical relationship for the absorption of electromagnetic radiation by the nanosphere is derived. It is demonstrated that the absorption curve at low temperatures has two resonance peaks. The shape, position, and intensity of the peaks are examined. The dependence of the absorption on the radiation frequency exhibits kinks associated with the degeneracy of the electron gas. The number and position of the kinks and the absorption jumps at these kinks are analyzed. Consideration is given to the cases of an isolated sphere and a sphere exchanging electrons with a reservoir. © 2002 MAIK "Nauka/Interperiodica".

## 1. INTRODUCTION

Recent considerable progress achieved in nanotechnology has provided a way of producing spherical nanostructures with sizes from several nanometers to hundreds of nanometers [1–3]. Investigation of spherical nanostructures has revealed that these objects possess interesting spectral [4] and optical [5–7] properties. In a number of works [5–8], it has been shown that the absorption of optical radiation by a spherical metallic nanostructure can be adequately described in the framework of the classical approach. The optical properties of a nanoparticle depend on its size and geometry. Albe *et al.* [9] studied the influence of the nanoparticle shape on the absorption spectrum. It was demonstrated that closely packed nanospheres can form three-dimensional crystals. The collective optical properties of closely packed nanospheres were considered in [3, 10–12]. Note that these crystals have a photonic band gap and can be treated as photonic crystals [13–15]. In recent years, it has become possible to cover spherical nanostructures with metallic or semiconducting shells. In particular, Hines and Guyot-Sionnest [16] prepared crystals from nanospheres based on a CdSe core covered with a ZnS shell. There is a number of works concerned with the optical properties of Au<sub>2</sub>S dielectric cores covered with a gold shell [17–20]. These spherical nanoshell structures can be produced by mixing HAuCl<sub>4</sub> and Na<sub>2</sub>S aqueous solutions. The sizes of the spheres thus obtained are equal to several tens of nanometers. Zhou *et al.* [17] and Averitt *et al.* [18] investigated the absorption of electromagnetic radiation in a medium containing nanoshell structures and demonstrated that, in the optical range, the absorption spectrum exhibits a resonance peak associated with the absorption of radiation by nanoshell structures. A theoretical model for describing the optical properties of

spherical nanoshells was developed on the basis of the Mie classical theory [8]. It was established that the absorption peak corresponds to plasma resonance of electrons in the system and that the position and the intensity of this peak depend on the metallic shell thickness and the diameter of the dielectric core [17, 18]. Investigation into the optical absorption in nanostructures provided a deep insight into the growth kinetics of nanostructures [18] and made it possible to determine important parameters such as the electron relaxation time and the electron–phonon coupling constant [17]. Analysis of the nonlinear optical response of nanoshell spherical and spheroidal systems proved that the nanoshell can substantially enhance the nonlinear optical response of the system [21–23]. It should be noted that, in the case of thin metallic or semiconducting shells (of the order of several atomic layers thick), quantum effects become significant and can make a considerable contribution to the properties of the system; hence, the classical model cannot be used to describe the optical absorption in the nanoshell [17].

The aim of the present work was to investigate the intraband optical transitions in a nanosphere. Note that the study of the intraband optical transitions provides important information on the parameters of the energy spectrum and the Fermi surface of electrons [24–28]. The model of a sphere can be applied to analyzing different physical properties of a metallic or semiconducting shell whose thickness is appreciably less than the size of the structure. This model was successfully used to investigate the spectral [29, 30], magnetic [31–34], and transport [35] properties of spherical or spheroidal nanostructures and to examine the influence of the electron–electron [36] and spin–orbit [37] interactions on the spectral properties of electrons in spherical systems.

## 2. ABSORPTION OF ELECTROMAGNETIC RADIATION

Let us consider a system of noninteracting electrons confined to the surface of a nanosphere. The eigenfunctions and eigenvalues of the Hamiltonian for this system are well known and have the form

$$\Psi_{l,m}(\vartheta, \varphi) = Y_{l,m}(\vartheta, \varphi), \quad E_l = \frac{\hbar\Omega}{2}l(l+1),$$

where  $l$  and  $m$  are the orbital and magnetic quantum numbers, respectively;  $\Omega = \hbar/m^*R^2$  and  $Y_{l,m}(\vartheta, \varphi)$  are the spherical harmonics;  $m^*$  is the effective mass; and  $R$  is the sphere radius. The absorption of electromagnetic radiation can be determined using the perturbation theory for the interaction of electrons with a high-frequency electromagnetic field [38]. In the case of a degenerate electron gas, the absorption by a nanosphere can be represented by the relationship

$$\begin{aligned} \Gamma &= \frac{\sqrt{\varepsilon(\omega)}}{2c\hbar R^2 N_f} (1 - e^{-\hbar\omega/T}) \\ &\times \sum_{l,m} \sum_{l',m'} f_0(E_l) [1 - f_0(E_l + \hbar\omega)] \\ &\times |\langle l', m', -\mathbf{f} | H_R | l, m, 0 \rangle|^2 \delta(E_l - E_{l'} + \hbar\omega), \end{aligned} \quad (1)$$

where  $\varepsilon(\omega)$  is the real part of the permittivity (the dispersion is assumed to be absent in the frequency range under consideration),  $N_f$  is the concentration of photons (with the frequency  $\omega$ ) incident on the nanosphere,  $\mathbf{f}$  is the photon wave vector,  $f_0(E_l)$  is the electron distribution function, and  $[1 - \exp(-\hbar\omega/T)]$  is the multiplier accounting for the induced photon emission. The electron-photon interaction operator can be written in the form

$$H_R = \frac{|e|\hbar}{m^*} \sqrt{\frac{2\pi\hbar N_f}{\varepsilon(\omega)\omega}} \mathbf{e}_f \mathbf{p},$$

where  $\mathbf{e}_f$  is the polarization vector of the photon.

The matrix elements of the operator  $H_R$  are calculated by assuming three to be a uniform electromagnetic field; i.e., the photon wavelength is taken to be considerably larger than the sphere radius.

Let the  $Oz$  axis be aligned along the polarization vector of the photon. In the dipole approximation, the transition matrix elements are defined as

$$\begin{aligned} &\langle l', m', -\mathbf{f} | H_R | l, m, 0 \rangle \\ &= \frac{|e|\hbar}{m^*} \sqrt{\frac{2\pi\hbar N_f}{\varepsilon(\omega)\omega}} \langle l', m' | p_z | l, m \rangle = \frac{|e|\hbar}{m^* R} \sqrt{\frac{2\pi\hbar N_f}{\varepsilon(\omega)\omega}} \delta_{m',m} \\ &\times \left[ (l+1) \sqrt{\frac{l^2 - m^2}{4l^2 - 1}} \delta_{l',l-1} + l \sqrt{\frac{(l+1)^2 - m^2}{4(l+1)^2 - 1}} \delta_{l',l+1} \right]. \end{aligned} \quad (2)$$

It follows from expression (2) that, in the dipole approximation, the transitions are allowed only between adjacent levels ( $l' = l \pm 1$ ). Substitution of expression (2) into relationship (1) gives

$$\begin{aligned} \Gamma &= \frac{\pi e^2}{3cm^* R^2 \sqrt{\varepsilon(\omega)}} \frac{\Omega}{\omega} (1 - e^{-\hbar\omega/T}) \\ &\times \sum_{l=0}^{\infty} f_0(E_l) [1 - f_0(E_l + \hbar\omega)] l(l+1) \\ &\times [(l+1)\delta(\omega + \Omega l) + l\delta(\omega - \Omega(l+1))]. \end{aligned} \quad (3)$$

It is seen from relationship (3) that the dependence  $\Gamma(\omega)$  is resonant in character. Resonances arise at the frequencies of electromagnetic radiation  $\omega = \Omega(l+1)$  for the orbital quantum numbers  $l$  at which the distribution function  $f_0(E_l)[1 - f_0(E_l + \hbar\Omega(l+1))]$  is not a small quantity.

In order to take into account the broadening of the resonance peaks due to scattering, we introduce the Lorentzian broadening of delta-shaped peaks according to the formula

$$\delta_\tau(x) = \frac{(\pi\tau)^{-1}}{\tau^{-2} + x^2}, \quad (4)$$

where  $\tau$  is the phenomenological relaxation time. With due regard for expression (4), relationship (3) can be written as the sum of two terms:  $\Gamma = \Gamma_1 + \Gamma_2$ , where

$$\begin{aligned} \frac{\Gamma_1}{\Gamma_0} &= \frac{\Omega}{\omega} (1 - e^{-\hbar\omega/T}) \\ &\times \sum_{l=1}^{\infty} \frac{f_0(E_l) [1 - f_0(E_l + \hbar\omega)] l(l+1)^2}{1 + \tau^2(\omega + \Omega l)^2}, \\ \frac{\Gamma_2}{\Gamma_0} &= \frac{\Omega}{\omega} (1 - e^{-\hbar\omega/T}) \\ &\times \sum_{l=1}^{\infty} \frac{f_0(E_l) [1 - f_0(E_l + \hbar\omega)] l^2(l+1)}{1 + \tau^2[\omega - \Omega(l+1)]^2}. \end{aligned}$$

Here,  $\Gamma_0 = e^2\tau/3cm^*R^2\sqrt{\varepsilon(\omega)}$ .

The nonresonant term  $\Gamma_1$  describes the processes associated with photon emission and satisfies the condition  $\Gamma_1 = O(\Gamma_2/(\tau\omega)^2)$  in the vicinity of the resonance point. Therefore, in the case of a high-frequency field, the contribution of the nonresonant term  $\Gamma_1$  to the absorption in the vicinity of the resonance can be ignored. By omitting the nonresonant term, we obtain

$$\begin{aligned} \frac{\Gamma}{\Gamma_0} &= \frac{\Omega}{\omega} (1 - e^{-\hbar\omega/T}) \\ &\times \sum_{l=1}^{\infty} \frac{f_0(E_l) [1 - f_0(E_l + \hbar\omega)] l^2(l+1)}{1 + \tau^2[\omega - \Omega(l+1)]^2}. \end{aligned} \quad (5)$$

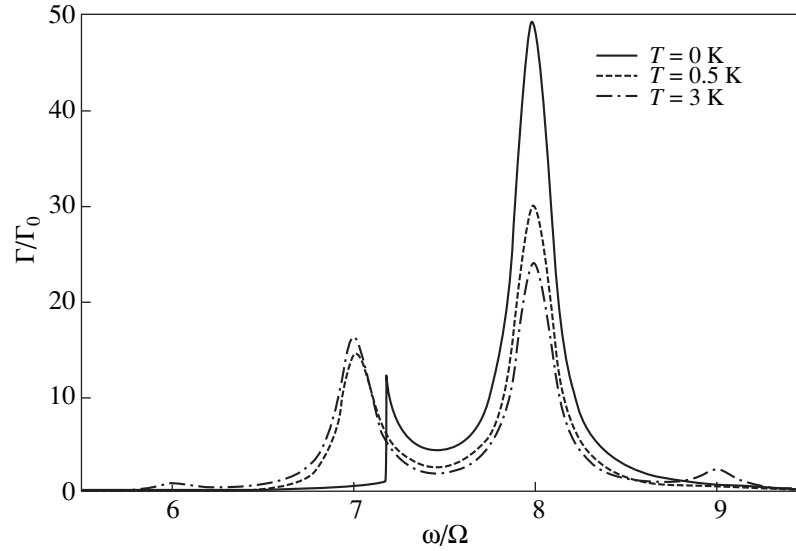


**Fig. 1.** Appearance of new resonance peaks in the absorption curve with increasing temperature.  $R = 10^{-5}$  cm,  $\tau = 5 \times 10^{-11}$  s, and  $\mu = 5.15 \times 10^{-15}$  erg.

It follows from relationship (1) that, at a sufficiently low temperature, only electrons whose energy falls within the range  $[\mu - \hbar\omega, \mu]$  participate in the absorption. Note that, in the case when the frequency of electromagnetic radiation changes, the line  $(\mu - \hbar\omega)$  can cross an electron energy level. As a result, the number of electrons involved in the absorption changes and a kink appears in the dependence of the absorption  $\Gamma$  on the frequency  $\omega$ .

From the condition for the appearance of kinks ( $\mu - \hbar\omega = E_l$ ), we found that the kinks can arise at the frequency of electromagnetic radiation

$$\omega_{\text{kink}}(l) = \frac{\mu}{\hbar} - \frac{\Omega}{2}l(l+1). \quad (6)$$

Hence, the separation between the adjacent kinks is determined by the formula  $\omega_{\text{kink}}(l) - \omega_{\text{kink}}(l-1) = \Omega l$ .

The absorption jump at the kink  $\Delta_l$  at temperatures close to zero can be estimated from the expression

$$\Delta_l \approx \Gamma_0 \frac{\Omega l^2(l+1)}{[\mu/\hbar - \Omega l(l+1)/2] \{1 + \tau^2 [\mu/\hbar - \Omega(l+1)(l+2)/2]^2\}}. \quad (7)$$

As is known, the thermodynamic properties of a three-dimensional electron gas (for example, the Landau diamagnetism) are virtually independent of whether the number of particles in the system is constant ( $N = \text{const}$ ) or whether the chemical potential is constant ( $\mu = \text{const}$ ). This circumstance is primarily associated with the fact that the effect of the method chosen to describe the system on its thermodynamic properties is of the order of  $N^{-1/3}$  [39], and this effect can be ignored when the number of particles is very large.

In the case of an electron gas on a nanosphere, the number of particles in the system is small; hence, the physical properties of the nanosphere essentially depend on the method chosen to describe the system [34]. In this respect, we will consider two cases, namely, the case of a constant chemical potential and the case of a constant number of electrons on the

sphere, and perform a detailed analysis of the differences in absorption between these cases.

### 3. THE NANOSPHERE IN A THERMOSTAT

We assume that the nanosphere is in contact with a reservoir characterized by the chemical potential  $\mu$  and the temperature  $T$ .

For further analysis, it is convenient to introduce the quantum number  $l_0$  such that  $E_{l_0} \leq \mu < E_{l_0+1}$ . At zero temperature,  $l_0$  is the orbital quantum number of the upper level filled by electrons and the absorption resonance arises upon transition of electrons from the  $l_0$ th level to the  $(l_0 + 1)$ th level at the electromagnetic radiation frequency  $\Omega(l_0 + 1)$  (the solid line in Fig. 1). As the temperature increases, the contribution of the electron transitions from the  $(l_0 - 1)$ th level to the  $l_0$ th level

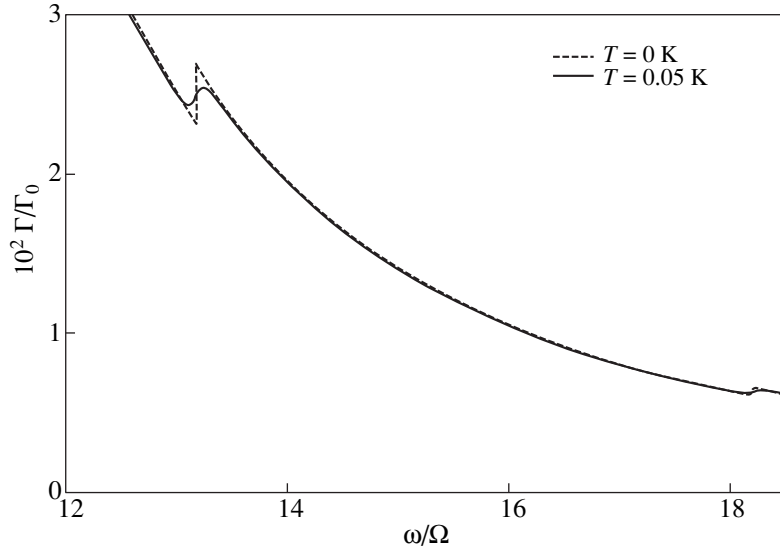


**Fig. 2.** Temperature smearing of kinks on the right wing of the second resonance peak.  $R = 10^{-5}$  cm,  $\tau = 5 \times 10^{-11}$  s, and  $\mu = 5.15 \times 10^{-15}$  erg.

becomes significant and the resonance peak appears at the frequency  $\Omega l_0$  (the dashed line in Fig. 1). A further increase in the temperature gives rise to absorption maxima due to electron transitions from the  $(l_0 - 2)$ th level to the  $(l_0 - 1)$ th level or from the  $(l_0 + 1)$ th level to the  $(l_0 + 2)$ th level (the dot-dashed line in Fig. 1) and so on.

The intensities of the first (at  $\omega = \Omega l_0$ ) and second [at  $\omega = \Omega(l_0 + 1)$ ] peaks can be estimated from the following formulas:

$$\Gamma(\omega = \Omega l_0) = \Gamma_0(1 - e^{-\hbar\Omega l_0/T})f_0(E_{l_0-1}) \times [1 - f_0(E_{l_0})](l_0 - 1)^2 + O(1/(\tau\Omega)^2), \quad (8)$$

$$\Gamma(\omega = \Omega(l_0 + 1)) = \Gamma_0(1 - e^{-\hbar\Omega(l_0+1)/T})f_0(E_{l_0}) \times [1 - f_0(E_{l_0+1})]l^2 + O(1/(\tau\Omega)^2). \quad (9)$$

Note that an increase in the temperature results in a decrease in the intensity of the largest peak [at  $\omega = \Omega(l_0 + 1)$ ] and an increase in the intensities of the other peaks.

At  $T = 0$  K, the absorption curve in Fig. 1 exhibits a kink corresponding to the intersection of the line  $(\mu - \hbar\omega)$  with the sixth electron energy level. As can be seen from Fig. 1, this kink is completely smoothed at a temperature of 0.5 K. The next two kinks, which appear on the right wing of the second resonance peak due to the intersection of the line  $(\mu - \hbar\omega)$  with the fifth and fourth energy levels, are displayed in Fig. 2. It is seen from this figure that an increase in the temperature does not

affect the position of the kinks; however, even a small increase in the temperature leads to their noticeable smoothing.

Let us now examine the kink corresponding to the intersection of the line  $(\mu - \hbar\omega)$  with the  $(l_0 - 1)$ th energy level. As follows from relationships (6) and (7), the closer the chemical potential to the energy  $E_{l_0}$  of the electronic level, the closer the frequency  $\omega_{\text{kink}}$  to the frequency  $\Omega l_0$  and the larger the absorption jump at this kink. In particular, at  $\mu \approx E_{l_0}$ , the absorption jump at the kink is equal to  $\Gamma_0(l_0 - 1)^2$  (Fig. 3). It should be noted that, since the change in the chemical potential leads only to a change in the position of the kink and in the absorption jump at the kink, the absorption curves coincide on both sides of the kink. According to relationship (7), the absorption jump  $\Delta_l$  at other kinks decreases with a decrease in the quantum number  $l$  (Fig. 2).

Next, we evaluate the absorption at zero temperature. In the range of electromagnetic radiation frequencies close to the resonance frequency  $\Omega(l_0 + 1)$ , only two terms with  $l = l_0 - 1$  and  $l_0$  in expression (5) make substantial contributions. Then, by retaining only these terms in expression (5) and tending the temperature to zero, we obtain

$$\frac{\Gamma(T = 0)}{\Gamma_0} \approx \frac{\Omega}{\omega} \left[ \frac{l_0^2(l_0 + 1)}{1 + \tau^2[\omega - \Omega(l_0 + 1)]^2} + \frac{(l_0 - 1)^2 l_0}{1 + \tau^2(\omega - \Omega l_0)^2} \Theta(E_{l_0-1} + \hbar\omega - \mu) \right], \quad (10)$$

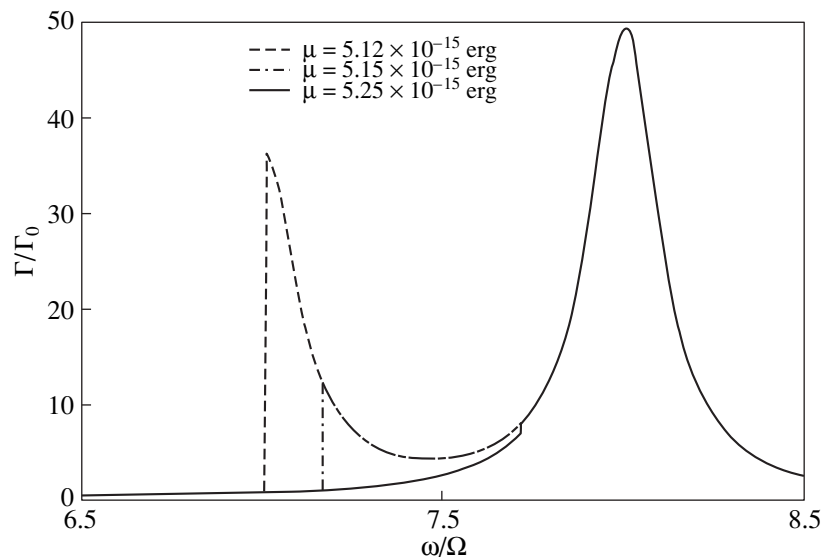


**Fig. 3.** Changes in the kink position and in the absorption jump at the kink in the absorption curve at different chemical potentials. The kink appearing at the intersection of the line  $(\mu - \hbar\omega)$  and the  $(l_0 - 1)$ th energy level is shown.  $R = 10^{-5}$  cm,  $T = 0$  K, and  $\tau = 5 \times 10^{-11}$  s.

where  $\Theta(x)$  is the step function defined as

$$\Theta(x) = \begin{cases} 0, & \text{at } x \leq 0 \\ 1, & \text{at } x > 0. \end{cases}$$

In relationship (10), the first term describes the resonance absorption peak at the frequency  $\omega = \Omega(l_0 + 1)$  and the second terms characterizes the kink at the frequency  $\omega = \mu/\hbar - \Omega(l_0 - 1)l_0/2$ . It follows from relationship (10) that, at  $T = 0$ , no absorption resonance occurs at the electromagnetic radiation frequency  $\Omega l_0$ . This stems from the fact that the  $l_0$ th level at zero temperature is filled [ $f_0(E_{l_0}) = 1$ ]; hence, electron transitions from the  $(l_0 + 1)$ th level to the  $l_0$ th level become impossible. An increase in the temperature results in the appearance of a resonance peak at the frequency  $\Omega l_0$  {owing to the multiplier  $[1 - f_0(E_{l_0})]$  in expression (8)} (Fig. 1).

It is seen from formula (9) that, at  $T = 0$ , the peak at the frequency  $\omega = \Omega(l_0 + 1)$  has the highest intensity, because  $f_0(E_{l_0})[1 - f_0(E_{l_0+1})] = 1$ . Therefore, from relationship (10), we obtain the expression

$$\frac{\Gamma(\omega = \Omega(l_0 + 1))}{\Gamma_0} = l_0^2 + \frac{(l_0 - 1)^2 l_0}{(l_0 + 1)(1 + \tau^2 \Omega^2)} \Theta(E_{l_0} + \hbar\Omega - \mu). \tag{11}$$

Here, we take into account that  $E_{l_0-1} + \hbar\Omega(l_0 + 1) = E_{l_0} + \hbar\Omega$ . According to expression (11), the intensity

of the absorption peak at zero temperature and the electromagnetic radiation frequency  $\omega = \Omega(l_0 + 1)$  has the form

$$\frac{\Gamma(\omega = \Omega(l_0 + 1))}{\Gamma_0} = l_0^2 + \frac{(l_0 - 1)^2 l_0}{(l_0 + 1)(1 + \tau^2 \Omega^2)} \tag{12}$$

at  $\mu < E_{l_0} + \hbar\Omega$ , i.e., when the  $(l_0 - 1)$ th kink is located to the left of the resonance frequency  $\Omega(l_0 + 1)$ , and

$$\Gamma(\Omega(l_0 + 1)) = \Gamma_0 l_0^2$$

at  $\mu > E_{l_0} + \hbar\Omega$ , i.e., when the  $(l_0 - 1)$ th kink is located to the right of the resonance frequency  $\Omega(l_0 + 1)$ .

An increase in the temperature leads to a decrease in the multiplier  $f_0(E_{l_0})[1 - f_0(E_{l_0+1})]$  in formula (9) and, consequently, to a decrease in the intensity of the absorption peak (Fig. 1). Note that the resonance frequencies are completely determined by the chemical potential and the sphere radius. Indeed, it can be seen from relationship (5) that the low-temperature resonances arise at the frequencies  $\Omega l_0$  and  $\Omega(l_0 + 1)$ ; i.e., their positions depend on  $R$  and  $l_0$ ; in turn, the quantum number  $l_0$  is governed by the chemical potential.

#### 4. THE ISOLATED NANOSPHERE

For the isolated nanosphere, the number of electrons in the system remains unchanged ( $N = \text{const}$ ) and the chemical potential is determined from the normalizing condition. Figure 4 shows the dependences of the potential  $\mu$  on  $N$  at different temperatures. Analysis of

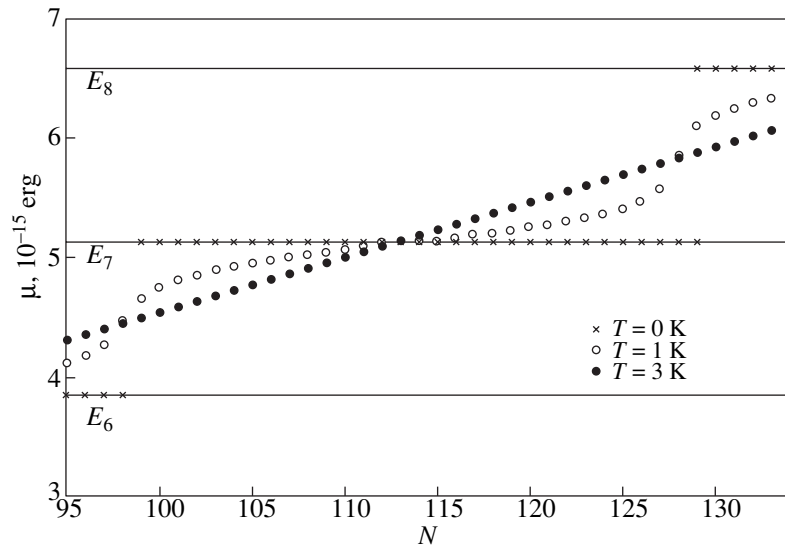


Fig. 4. Dependences of the chemical potential of the system on the number of electrons on a sphere of radius  $R = 10^{-5}$  cm.

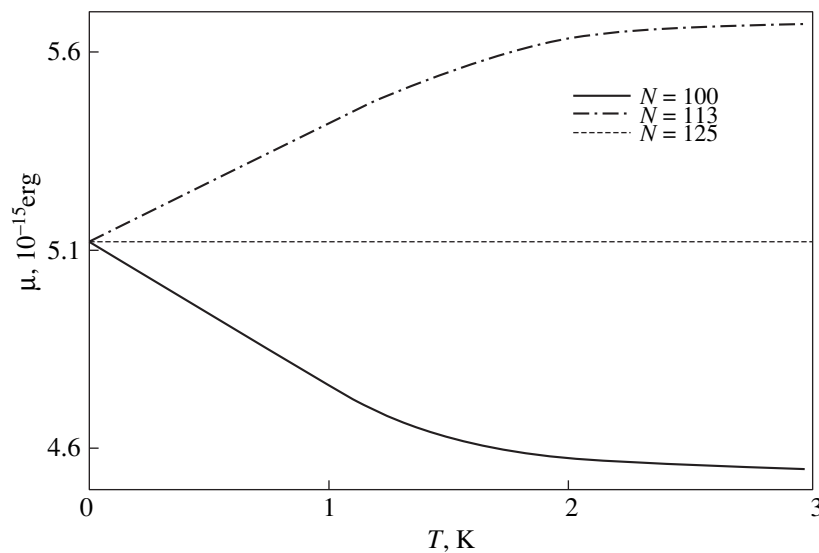
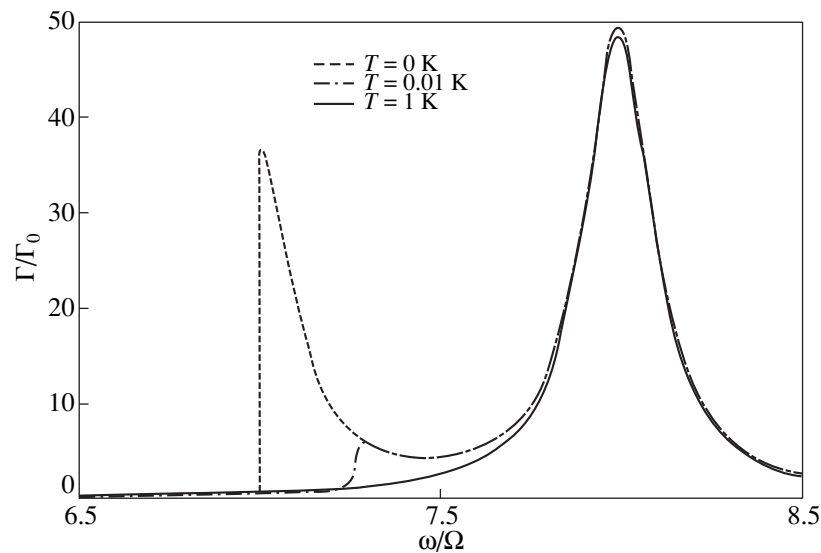


Fig. 5. Temperature dependences of the chemical potential of the electron gas on a sphere of radius  $R = 10^{-5}$  cm.

these dependences indicates that the chemical potential at  $T \approx 0$  K is very close to the energy of the upper filled level. In the case when the  $l_0$ th energy level is filled by less than half ( $N - 2l_0^2 < 2l_0 + 1$ ), we have  $\mu < E_{l_0}$ . If the number of electrons at the  $l_0$ th level is larger than half the degeneracy multiplicity of this level ( $N - 2l_0^2 > 2l_0 + 1$ ), the reverse inequality  $\mu > E_{l_0}$  holds. When a change in the number of electrons in the system leads to a change in the quantum number  $l_0$ , there occurs an

abrupt jump in the dependence  $\mu(N)$  at  $T \approx 0$ . As is seen from Fig. 4, an increase in the temperature to  $T = 1$  K brings about a substantial smoothing of the step dependence. With a further increase in the temperature to  $T = 3$  K, the steps disappear completely and the dependence  $\mu(N)$  exhibits an almost linear behavior.

Figure 5 displays the temperature dependences of the chemical potential. It is worth noting that, when the  $l_0$ th level is filled by less than half ( $N - 2l_0^2 < 2l_0 + 1$ ), the chemical potential is a decreasing function of the



**Fig. 6.** Change in the position of the kink in the absorption curve at different temperatures (the case of the upper completely filled electron shell).  $R = 10^{-5}$  cm,  $\tau = 5 \times 10^{-11}$  s, and  $N = 128$ .

temperature. At  $(N - 2l_0^2 > 2l_0 + 1)$ , the chemical potential increases with an increase in the temperature. In the case when  $N - 2l_0^2 = 2l_0 + 1$ , the chemical potential is virtually independent of temperature. It can be seen from Fig. 5 that the dependence  $\mu(T)$  is linear at sufficiently low temperatures ( $T < 1$  K). As the temperature increases, the linear dependence changes over to a weak monotonic dependence of the potential  $\mu$  on  $T$ . Judging from the data presented in Fig. 5 and formula (6), at sufficiently low temperatures, the position of the kinks changes with an increase in  $T$  due to the dependence of the chemical potential on the temperature.

Now, we dwell on the case of an upper filled electron shell. The number of electrons is determined by the formula  $N = 2(2l_0 + 1)^2$ . At  $T = 0$ , the distribution function is defined as  $f_0(E_{l_0}) = 1$ ; hence, relationships (10) and (11) hold for the case under consideration.

At  $T = 0$ , the chemical potential is given by  $\mu = E_{l_0}$ . As a consequence, we have

$$\omega_{\text{kink}}(l) = \frac{\Omega}{2}[l_0(l_0 + 1) - l(l + 1)]. \quad (13)$$

As follows from this expression, the  $(l_0 - 1)$ th kink in the absorption curve arises at the electromagnetic radiation frequency  $\omega = \Omega l_0$ .

Analysis of the dependence  $\mu(T)$  (Fig. 5) demonstrates that, for the closed electron shell, the chemical potential exceeds the energy of the  $l_0$ th electronic level and the difference between  $\mu$  and  $E_{l_0}$  increases with an increase in the temperature. Consequently, an increase

in the temperature leads to a shift of the kinks toward the high-frequency range (Figs. 6, 7). The kinks at a sufficiently low but nonzero temperature transform into peaks which are considerably smoothed with an increase in the temperature.

With due regard for relationships (10) and (13), the absorption at zero temperature can be estimated from the expression

$$\frac{\Gamma(T = 0)}{\Gamma_0} \approx \frac{\Omega}{\omega} \left[ \frac{l_0^2(l_0 + 1)}{1 + \tau^2[\omega - \Omega(l_0 + 1)]^2} + \frac{(l_0 - 1)^2 l_0}{1 + \tau^2(\omega - \Omega l_0)^2} \Theta(\omega - \Omega l_0) \right]. \quad (14)$$

According to expression (14), the intensity of the absorption peak at the resonance frequency  $\omega = \Omega(l_0 + 1)$  is identical to that found for the constant chemical potential at  $\mu < E_{l_0} + \hbar\Omega$  [formula (12)]. As is seen from expression (9), an increase in the temperature results in a decrease in the intensity of the second resonance peak. Note that, owing to the temperature dependence of the chemical potential at a constant number of electrons, the temperature dependence of the intensity of the second peak is weaker than that in the case of a constant chemical potential (Figs. 1, 6).

At low temperatures, the absorption jump at the kink can be evaluated from the expression

$$\Delta_l \approx 2\Gamma_0 \frac{l^2(l+1)}{[l_0(l_0+1) - l(l+1)]\{1 + \tau^2\Omega^2[l_0(l_0+1) - (l+1)(l+2)]^2/4\}}$$

As follows from this expression, the absorption jump at the  $(l_0 - 1)$  kink can be estimated by the formula

$$\Delta_{l_0-1} \approx \Gamma_0(l_0 - 1)^2.$$

Next, we consider the case of an upper partly filled electron shell. As is known, the broadening of a step Fermi function is of the order of  $T$ . Let us assume that the temperature broadening of the distribution function is considerably less than the energy level spacing; i.e.,  $\hbar\Omega l_0/T \gg 1$ . Then, from the normalizing condition, we obtain

$$f_0(E_{l_0}) \approx \frac{N - 2l_0^2}{2(2l_0 + 1)}. \tag{15}$$

Here,  $2(2l_0 + 1)$  is the degeneracy multiplicity of the upper filled level and  $N - 2l_0^2$  is the number of electrons at the  $l_0$ th level.

From relationship (15), we found

$$\mu \approx E_{l_0} + T \ln \frac{N - 2l_0^2}{2(l_0 + 1)^2 - N}. \tag{16}$$

This formula adequately describes the behavior of the chemical potential at  $T \leq 1$  K (Fig. 5). It is easy to show that  $2(l_0 + 1)^2 - N$  is the number of free states at the  $l_0$ th level. It follows from formula (16) that, when the upper

level is half filled ( $N = 2l_0^2 + 2l_0 + 1$ ), the chemical potential is determined as  $\mu = E_{l_0}$ . If the number of electrons at the  $l_0$ th level is larger than half the degeneracy multiplicity of this level ( $N - 2l_0^2 > 2l_0 + 1$ ), we obtain  $\mu > E_{l_0}$ ; otherwise, we have  $\mu < E_{l_0}$  (Fig. 4).

Making allowance for relationship (15), the absorption at low temperatures can be evaluated by the expression

$$\frac{\Gamma}{\Gamma_0} \approx \frac{\Omega}{\omega} \left[ \frac{(N - 2l_0^2)l_0^2(l_0 + 1)}{2(2l_0 + 1)\{1 + \tau^2[\omega - \Omega(l_0 + 1)]^2\}} + \frac{[1 - f_0(E_{l_0-1} + \hbar\omega)](l_0 - 1)^2 l_0}{1 + \tau^2(\omega - \Omega l_0)^2} \right]. \tag{17}$$

According to formula (17), the intensities of the absorption peaks can be estimated using the following relationships:

$$\frac{\Gamma(\omega = \Omega l_0)}{\Gamma_0} \approx \frac{(N - 2l_0^2)l_0(l_0 + 1)}{2(2l_0 + 1)[1 + (\tau\Omega)^2]} + \frac{[2(l_0 + 1)^2 - N](l_0 - 1)^2}{2(2l_0 + 1)},$$

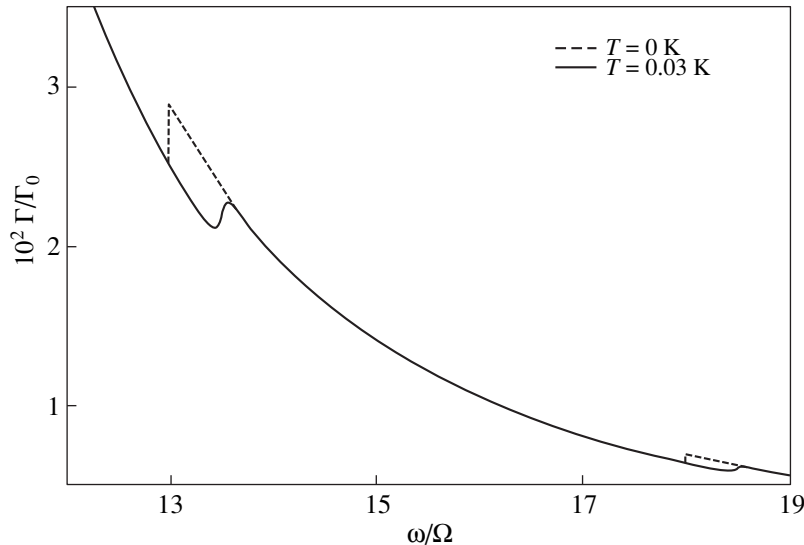


**Fig. 7.** Shift of the kinks in the absorption curve toward the high-frequency range with increasing temperature (the case of the upper completely filled electron shell).  $R = 10^{-5}$  cm,  $\tau = 5 \times 10^{-11}$  s, and  $N = 128$ .

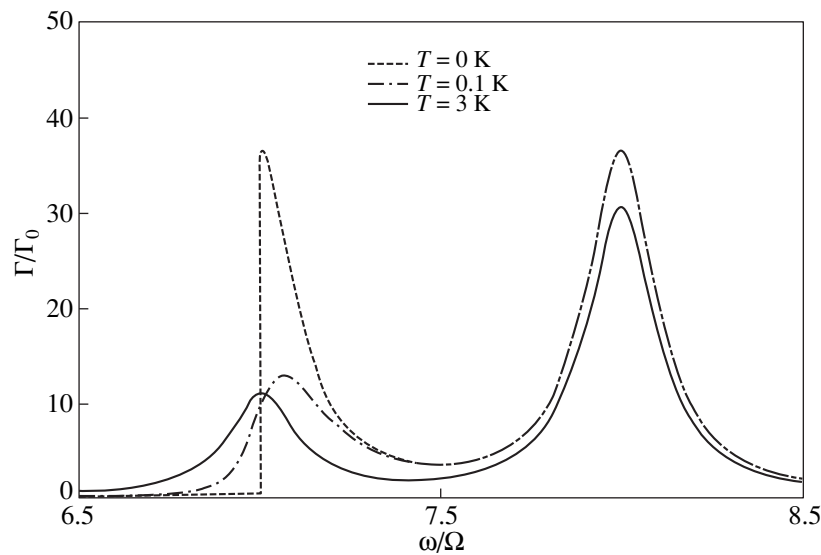


**Fig. 8.** Absorption curves at different temperatures of the electron gas on the nanosphere (the case of the upper partly filled electron shell).  $R = 10^{-5}$  cm,  $\tau = 5 \times 10^{-11}$  s, and  $N = 120$ .

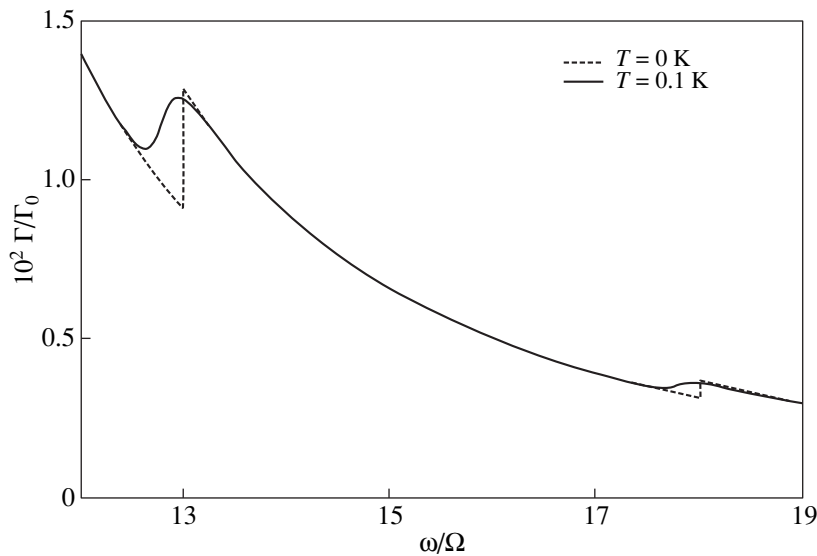


**Fig. 9.** Shift of the kinks in the absorption curve toward the low-frequency range with increasing temperature (the number of electrons at the  $l_0$ th energy level is less than half the degeneracy multiplicity of this level).  $R = 10^{-5}$  cm,  $\tau = 5 \times 10^{-11}$  s, and  $N = 100$ .

$$\frac{\Gamma(\omega = \Omega(l_0 + 1))}{\Gamma_0} \approx \frac{N - 2l_0^2}{2(2l_0 + 1)} l_0^2 + \frac{l_0(l_0 - 1)^2}{(l_0 + 1)[1 + (\tau\Omega)^2]}$$

linear, i.e., in which formula (16) holds. A further increase in the temperature is attended by a decrease in the intensity of the second absorption peak (Fig. 8).

It is worth noting that, at zero temperature, we observed a kink with the absorption jump  $\Gamma_0(l_0 - 1)^2$  rather than the first peak (Fig. 8). As follows from the estimated intensities of the peaks, the intensity of the second peak is independent of the temperature in the range in which the temperature dependence of the chemical potential is

### 5. RESULTS AND DISCUSSION

Let us now consider the case when the system is characterized by a constant chemical potential. As was noted above, the absorption curve at zero temperature has one resonance peak at the frequency  $\omega = \Omega(l_0 + 1)$ .

The intensity of the peak is determined by the orbital quantum number  $l_0$  of the upper filled shell, the sphere radius  $R$ , and the relaxation time  $\tau$ . An increase in the temperature leads to a decrease in the intensity of this peak and the appearance of new resonance peaks due to electron transitions from the  $(l_0 - 1)$ th level to the  $l_0$ th level, from the  $(l_0 - 2)$ th level to the  $(l_0 - 1)$ th level or from the  $(l_0 + 1)$ th level to the  $(l_0 + 2)$ th level, and so on (Fig. 1). At zero temperature, the absorption curve exhibits sharp kinks arising when the line  $(\mu - \hbar\omega)$  crosses the electron energy levels. The position of the kinks depends on the chemical potential and the quantum number of the electronic level. If the change in the chemical potential does not affect the quantum number  $l_0$ , it leads only to a change in the position of the kink and in the absorption jump at the kink. Consequently, the absorption curves at different chemical potentials  $\mu$  coincide on both sides of the kink (Fig. 3). An increase in the temperature is not accompanied by a change in the position of the kinks; however, even a small increase in the temperature leads to their noticeable smoothing (Fig. 2).

The difference in the behavior of the absorption in the cases when  $\mu = \text{const}$  and  $N = \text{const}$  results primarily from two circumstances. First, when the number of particles is constant, the chemical potential depends on the temperature. For the isolated sphere and the upper completely filled electron shell, the intensity of the peak at the resonance frequency  $\omega = \Omega(l_0 + 1)$  and  $T = 0$  is identical to that for the sphere in the thermostat at  $\mu < E_{l_0} + \hbar\Omega$  [formula (12)]. An increase in the temperature brings about an increase in the chemical potential (Fig. 5). As a result, unlike the case of the sphere in the thermostat, the intensity of the peak at  $\omega = \Omega(l_0 + 1)$  is virtually independent of the temperature in the range of the linear dependence  $\mu(T)$  (Figs. 1, 6). Since the chemical potential for the upper filled electron shell increases with an increase in the temperature, the kinks shift toward the high-frequency range as the temperature increases (Figs. 6, 7). Note that the kink position at  $\mu = \text{const}$  does not depend on the temperature (Fig. 2).

Second, in contrast with the case of a constant chemical potential, the upper energy level at a constant number of particles can be partly filled by electrons at zero temperature. If the electron shell with  $l = l_0$  is partly filled, the intensity of the absorption peaks at zero temperature depends on the number of electrons in this shell  $(N - 2l_0^2)$ . For  $N - 2l_0^2 < 2l_0 + 1$  (the number of electrons at the  $l_0$ th level is less than half the degeneracy multiplicity of the level), an increase in the temperature is accompanied by a decrease in the chemical potential and, hence, by a shift of the kinks toward the low-frequency range (Fig. 9). At  $N - 2l_0^2 > 2l_0 + 1$ , the behavior of the kinks is the same as in the case of the upper filled shell (Figs. 6, 7). When the  $l_0$ th level is half

filled ( $N = 2l_0^2 + 2l_0 + 1$ ), the chemical potential satisfies the condition  $\mu \approx E_{l_0}$  and the kink position is independent of the temperature.

#### ACKNOWLEDGMENTS

This work was supported by the Russian Foundation for Basic Research (project no. 01-02-16564), DFG (project no. 436 RUS 113/572), and the "Russian Universities" Program (project no. 015.01.01.049).

#### REFERENCES

1. C. B. Murray, D. J. Norris, and M. G. Bawendi, *J. Am. Chem. Soc.* **11**, 8706 (1993).
2. R. C. Salvarezza, L. Vázquez, H. Miguez, *et al.*, *Phys. Rev. Lett.* **77** (22), 4572 (1996).
3. Yu. A. Vlasov, V. N. Astratov, O. Z. Karimov, *et al.*, *Phys. Rev. B* **55** (20), R13357 (1997).
4. J. B. Xia and J. Li, *Phys. Rev. B* **60** (16), 11540 (1999).
5. S. S. Martinos, *Phys. Rev. B* **39** (2), 1363 (1989).
6. R. Rupp, *Phys. Rev. B* **45** (19), 11209 (1992).
7. B. M. Smirnov and H. Weidele, *Zh. Éksp. Teor. Fiz.* **116** (6), 1903 (1999) [*JETP* **89**, 1030 (1999)].
8. G. Mie, *Ann. Phys. (Leipzig)* **25**, 377 (1908).
9. V. Albe, C. Jouanin, and D. Bertho, *Phys. Rev. B* **58** (8), 4713 (1998).
10. F. Claro and R. Fuchs, *Phys. Rev. B* **33** (12), 7956 (1986).
11. A. Taleb, V. Russier, A. Courty, and M. P. Pileni, *Phys. Rev. B* **59** (20), 13350 (1999).
12. D. J. Bergman, O. Levy, and D. Stroud, *Phys. Rev. B* **49** (1), 129 (1994).
13. H. Miguez, A. Blanco, F. Meseguer, *et al.*, *Phys. Rev. B* **59** (3), 1563 (1999).
14. V. Yannopapas, A. Modinos, and N. Stefanou, *Phys. Rev. B* **60** (8), 5359 (1999).
15. K. Ohtaka, Y. Suda, S. Nagano, *et al.*, *Phys. Rev. B* **61** (8), 5267 (2000).
16. M. A. Hines and P. Guyot-Sionnest, *J. Phys. Chem.* **100**, 468 (1996).
17. H. S. Zhou, I. Honma, H. Komiyama, and J. W. Haus, *Phys. Rev. B* **50** (16), 12052 (1994).
18. R. D. Averitt, D. Sarkar, and N. J. Halas, *Phys. Rev. Lett.* **78** (22), 4217 (1997).
19. R. D. Averitt, S. L. Westcott, and N. J. Halas, *Phys. Rev. B* **58** (16), R10203 (1998).
20. J. J. Diao and G. D. Chen, *J. Phys. D* **34**, L79 (2001).
21. N. Kalyaniwalla, J. W. Haus, R. Inguva, and M. H. Birnboim, *Phys. Rev. A* **42** (9), 5613 (1990).
22. L. Fu and L. Resca, *Phys. Rev. B* **56** (17), 10963 (1997).
23. R. Rojas, F. Claro, and R. Fuchs, *Phys. Rev. B* **37** (12), 6799 (1988).
24. L. Brey, N. F. Johnson, and B. I. Halperin, *Phys. Rev. B* **40** (15), 10647 (1989).
25. V. A. Margulis, *Zh. Éksp. Teor. Fiz.* **111** (3), 1092 (1997) [*JETP* **84**, 603 (1997)].

26. N. G. Galkin, V. A. Margulis, and A. V. Shorokhov, *Fiz. Tverd. Tela (St. Petersburg)* **43** (3), 511 (2001) [*Phys. Solid State* **43**, 530 (2001)].
27. V. A. Geyler, V. A. Margulis, and A. V. Shorokhov, *Phys. Rev. B* **63**, 245316 (2001).
28. V. Ya. Demikhovskii and A. A. Perov, *Zh. Éksp. Teor. Fiz.* **114** (5), 1795 (1998) [*JETP* **87**, 973 (1998)].
29. D. N. Aristov, *Pis'ma Zh. Éksp. Teor. Fiz.* **70** (6), 405 (1999) [*JETP Lett.* **70**, 410 (1999)].
30. P. Malits and I. D. Vagner, *J. Phys. A* **32**, 1507 (1999).
31. H. Aoki and H. Suezawa, *Phys. Rev. A* **46** (3), R1163 (1992).
32. Ju. H. Kim, I. D. Vagner, and B. Sundaram, *Phys. Rev. B* **46** (15), 9501 (1992).
33. D. N. Aristov, *Phys. Rev. B* **59** (9), 6368 (1999).
34. D. V. Bulaev, V. A. Geyler, and V. A. Margulis, *Phys. Rev. B* **62** (17), 11517 (2000).
35. C. L. Foden, M. L. Leadbeater, and M. Pepper, *Phys. Rev. B* **52** (12), R8646 (1995).
36. A. Wójs and J. J. Quinn, *Physica E (Amsterdam)* **3**, 181 (1998).
37. M. V. Entin and L. I. Magarill, *Phys. Rev. B* **64**, 085330 (2001).
38. F. G. Bass and I. B. Levinson, *Zh. Éksp. Teor. Fiz.* **49** (3), 914 (1965) [*Sov. Phys. JETP* **22**, 635 (1966)].
39. I. A. Kvasnikov, *Thermodynamics and Statistical Physics: The Theory of Equilibrium Systems* (Mosk. Gos. Univ., Moscow, 1991).

*Translated by O. Borovik-Romanova*

SEMICONDUCTORS  
AND DIELECTRICS

## An EXAFS Study of the Local Structure of the $\text{Pb}_x\text{Sn}_{1-x}\text{S}$ Solid Solution

A. I. Lebedev\*, I. A. Sluchinskaya\*, and I. H. Munro\*\*

\*Moscow State University, Vorob'evy gory, Moscow, 119899 Russia

e-mail: swan@mch.chem.msu.su

\*\*Daresbury Laboratory, Warrington, WA4 4AD UK

Received November 20, 2001

**Abstract**—The local lead-atom environment in the  $\text{Pb}_x\text{Sn}_{1-x}\text{S}$  solid solutions with cubic and orthorhombic structure was studied by EXAFS spectroscopy. The shortest Pb–S distance in samples with orthorhombic structure was found to be smaller by  $\approx 0.2$  Å than that in cubic-lattice samples, which is a sign of stereochemical activity of the two paired  $6s^2$  electrons of a Pb atom. The metal atom arrangement reveals strong short-range order, which results in the formation of –Pb–Sn–Pb–Sn–... zigzag chains aligned with the  $c$  axis (in the  $Pbnm$  system) in orthorhombic samples. It was shown that the onset of such short-range order in  $\text{Pb}_{0.5}\text{Sn}_{0.5}\text{S}$  can initiate the formation of superstructures belonging to the  $C_{2v}^2$  or  $C_{2v}^7$  space groups. © 2002 MAIK “Nauka/Interperiodica”.

### 1. INTRODUCTION

One of the problems encountered in studies of solid solutions is establishment of the relation between the deviation of a solid solution from its ideal structure and its physical properties.

The available scarce information on solid solutions in the SnS–PbS system is fairly contradictory. This system forms a limited number of solid solutions, because SnS has an orthorhombic structure (space group  $D_{2h}^{16}$  –  $Pbnm$ ) while PbS has an NaCl-type cubic structure. The limiting solubility of SnS in PbS is  $\approx 10$  mol %, and that of PbS in SnS is about 50 mol % [1–3]. There is no consensus on whether the  $\text{Pb}_{0.5}\text{Sn}_{0.5}\text{S}$  composition (existing in nature in the mineral form of teallite [4]) in this system is an individual phase or a SnS-based solid solution. Some authors consider this composition to be an individual phase crystallizing in space group  $D_{2h}^{16}$  [2, 5, 6] or space groups  $D_{2h}^{13}$  or  $C_{2v}^7$  [2, 6]. Others believe this material to be an SnS-based solid solution [1, 3, 7, 8]. To resolve this contradiction, coordinated studies of the short- and long-range order in samples of this composition are needed.

Our interest in the SnS–PbS system is connected with the off-centering of large-radius impurity ions, which was revealed earlier in the  $\text{Ge}_{1-x}\text{Pb}_x\text{Te}$  and  $\text{Ge}_{1-x}\text{Sn}_x\text{Te}$  semiconducting solid solutions [9]. The displacement of Pb and Sn atoms in these compounds to off-center positions was explained as being due to a deformation of the spherically symmetric electron-density distribution of the two paired  $s^2$  electrons in these atoms. Being energetically favorable, this deformation

produced chemical bonds of unequal length. As concerns Pb atoms, this came as a surprise, because the  $6s^2$  lone pair in compounds of divalent lead is typically stereochemically inactive, as a result of which the local Pb environment in crystals is usually symmetric (as in PbS). It appeared, therefore, of interest to see whether the local environment of Pb atoms in SnS is distorted and whether it is associated with the stereochemical activity of their  $6s^2$  electron pairs. In addressing this problem, we chose EXAFS spectroscopy. This modern x-ray method for investigating local structure is widely used in studies of the structure of solid solutions.

### 2. EXPERIMENTAL TECHNIQUE

#### 2.1. Samples

Samples of the  $\text{Pb}_x\text{Sn}_{1-x}\text{S}$  solid solution with  $x = 0.1, 0.2, 0.35, 0.5,$  and  $0.95$  were prepared by synthesizing PbS and SnS and melting them in evacuated quartz ampules, with subsequent annealing of the alloys at  $645^\circ\text{C}$  for 70–96 h. The phase homogeneity of the samples was checked by x-ray diffraction. At 300 K, the crystal structure of the samples with  $x \leq 0.5$  corresponded to the orthorhombic phase and the structure of the  $x = 0.95$  sample was cubic. Immediately before EXAFS spectral measurements, the alloys were ground to powder, sieved, and deposited on adhesive tape. The optimum absorber thickness for spectral measurements was obtained by repeatedly folding the tape.

The EXAFS spectra were obtained at the Pb  $L_{\text{III}}$  absorption edge (13.055 keV) at 80 K in transmission geometry on station 7.1 at the Daresbury Laboratory (Great Britain). The radiation was made monochro-

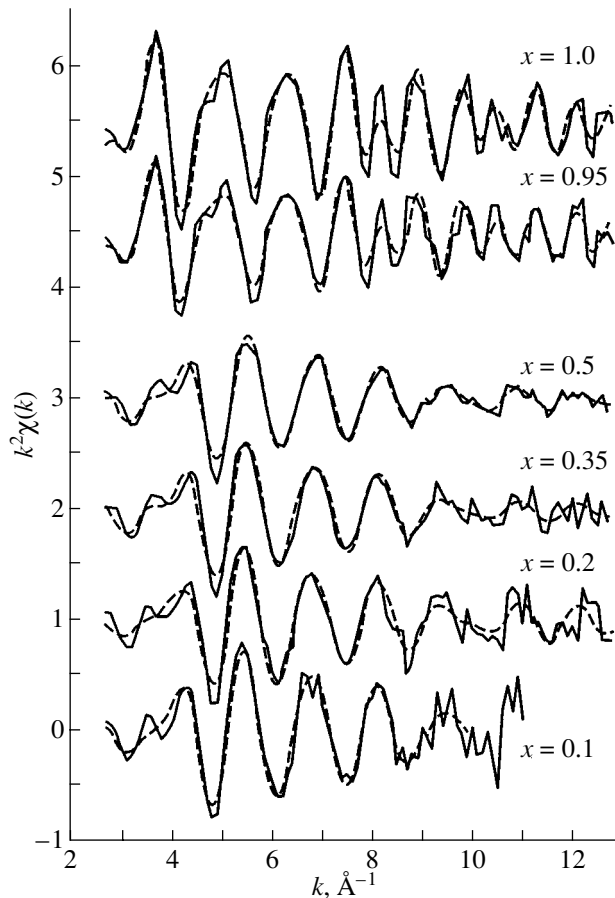


**Fig. 1.** Typical Pb  $L_{III}$  EXAFS spectra of lead obtained for  $Pb_xSn_{1-x}S$  samples (solid lines) and their theoretical approximation (dashed lines).

matic by using a Si(111) double-crystal monochromator, and the intensity of the radiation incident on and transmitted through a sample was measured with ionization chambers. Two spectra were recorded for each sample.

### 2.2. Processing Technique

The EXAFS function  $\chi(k)$  was extracted from  $\mu x(E)$  transmission spectra as was done in [10]. After subtraction of the background caused by the absorption of radiation by atoms other than Pb, the monotonic part of atomic absorption  $\mu x_0(E)$  was isolated by spline fitting and the dependence of  $\chi = (\mu x - \mu x_0)/\mu x_0$  on wave vector  $k = \sqrt{2m(E - E_0)}/\hbar$  was calculated. The photoelectron energy  $E_0$  was reckoned from the inflection point at the absorption edge. The jump at the absorption edge varied from 0.10 to 1.5.

The information on the first three coordination shells of interest to us here was extracted by taking direct and inverse Fourier transforms of the  $\chi(k)$  curves thus obtained using a modified Hanning window. The

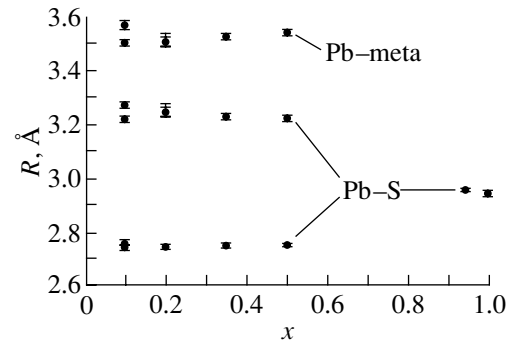


**Fig. 2.** Interatomic distances for the three nearest coordination shells of Pb atoms in the  $Pb_xSn_{1-x}S$  solid solution plotted vs. composition parameter  $x$ .

range of isolation in the  $R$  space was typically 1.2–3.7 Å. The  $R_j$  distances, the coordination numbers  $N_j$ , and the Debye–Waller factor  $\sigma_j^2$  for each of the three coordination shells ( $j = 1-3$ ) were derived by minimizing the rms deviation between the experimental and calculated  $k^2\chi(k)$  curves. The parameters  $R_j$ ,  $N_j$ , and  $\sigma_j^2$ , as well as the origin displacement along the energy axis  $dE_0$ , were varied. To reduce the number of variable parameters, known relations between the coordination numbers in the SnS and NaCl structures were taken into account. The number of variable parameters (eight) was about two times smaller than that of independent parameters (15 or 16) in the  $2\Delta R\Delta k/\pi$  data. The errors in determination of the parameters reported in the paper were found from the covariance matrix and correspond to a 95% confidence interval of their variation.

The dependences of the backscattering amplitude and phase, of the central-atom phase, and of the photoelectron mean free path on  $k$ , which are necessary to construct theoretical  $\chi(k)$  curves, were calculated using the FEFF code [11].

### 3. EXPERIMENTAL RESULTS

Figure 1 shows typical  $k^2\chi(k)$  relations obtained for all  $Pb_xSn_{1-x}S$  samples. The curves for samples with cubic ( $x \geq 0.95$ ) and orthorhombic ( $x \leq 0.5$ ) structure differ qualitatively in pattern, which indicates different characters of the local Pb environment in these samples. An analysis of the data reveals that lead atoms in the  $x = 0.95$  solid solution and PbS are surrounded by six sulfur atoms located at the same distance (see table and Fig. 2). The spectra obtained for samples with orthorhombic structure are described well only by the model according to which, in the first coordination shell, three S atoms sit at one distance from the central atom ( $R_1$ ) and the other three sit at another distance ( $R_2$ ). Thus, the nearest neighbor environment of Pb in SnS differs from that in PbS. As follows from the table, as  $x$  increases from 0.1 to 0.5, distance  $R_1$  remains

Local Pb environment parameters for  $\text{Pb}_x\text{Sn}_{1-x}\text{S}$  samples

Parameter	$x$						SnS*
	0.1	0.2	0.35	0.5	0.95	1	
$R_1, \text{\AA}$	2.750(8)	2.745(8)	2.752(4)	2.752(4)	2.954(8)	2.942(6)	2.660(3)
$\sigma_1^2, \text{\AA}^2$	0.0066(13)	0.0053(10)	0.0087(6)	0.0079(6)	0.0095(11)	0.0086(9)	0.0036(4)
$R_2, \text{\AA}$	3.246(16)	3.243(16)	3.233(7)	3.232(8)	4.175(7)	4.184(6)	3.301(8)
$\sigma_2^2, \text{\AA}^2$	0.0174(35)	0.0120(26)	0.0178(14)	0.0187(16)	0.0064(7)	0.0066(6)	0.0059(8)
$R_3, \text{\AA}$	3.534(13)	3.500(15)	3.522(7)	3.535(10)			3.481(7)
$\sigma_3^2, \text{\AA}^2$	0.0081(16)	0.0090(15)	0.0118(8)	0.0141(12)			0.0067(6)

\*The EXAFS data for the local environment of an Sn atom in SnS were obtained at the Sn  $K$  edge.

unchanged to within experimental error, whereas  $R_2$  decreases slightly. Note also the fairly large value of the Debye–Waller factors for the longer Pb–S bond length.

In samples with orthorhombic structure, the metal atoms (Pb, Sn) in the second coordination shell are located at an average distance  $R_3 \approx 3.5 \text{\AA}$ , which grows insignificantly with  $x$ . The Debye–Waller factors for this shell ( $\sigma_3^2$ ) turn out to be even smaller than ( $\sigma_2^2$ ) (see table); however, their values grow noticeably with  $x$ .

As seen from the table, the Debye–Waller factors are the largest for the longer Pb–S bond length and depend only weakly on composition. To separate the contributions from thermal motion and static lattice distortions to the Debye–Waller factors, we measured the temperature dependences of EXAFS spectra for the  $\text{Pb}_{0.8}\text{Sn}_{0.2}\text{S}$  sample within the temperature interval 80–300 K. An analysis of the data obtained showed that the temperature dependence of the Debye–Waller factor ( $\sigma_2^2$ ) is stronger. One may thus conclude that the main

contribution to ( $\sigma_2^2$ ) is due not to static lattice distortions but rather to thermal vibrations. This suggests that the corresponding chemical bonding is weak.

Because solid solutions often exhibit short-range order, we decided to check whether this order is reflected in the metal atom arrangement in the second coordination shell. To check this possibility, we compared the experimental EXAFS spectra with the curves calculated for various ratios of Pb and Sn concentrations in the second coordination shell of lead under the assumption that the values of  $R_3$  and ( $\sigma_3^2$ ) for atoms of both types are equal. Figure 3 plots the sum of the squares of deviations,  $S_{\min}$ , for all the measured spectra as a function of the local Sn atom concentration in the second coordination shell of Pb atoms. We readily see that the minimum in the curves for samples with  $x = 0.2, 0.35,$  and  $0.5$  lies at a local Sn concentration considerably in excess of its average concentration in the sample; the local concentration averaged over several

spectra for each of the samples studied is close to 100%. In our opinion, the short-range order in which Pb atoms are surrounded predominantly by atoms of Sn may be accounted for by the deformation interaction between metal atoms, which precludes two large-radius lead atoms from sitting close to one another.

#### 4. DISCUSSION OF RESULTS

According to the neutron diffraction data available for SnS [12], the six S atoms in the first coordination shell of tin lie at four different distances: 2.627  $\text{\AA}$  (one atom), 2.665  $\text{\AA}$  (two atoms), 3.290  $\text{\AA}$  (two atoms), and 3.388  $\text{\AA}$  (one atom). The two shortest distances are so close to each other that their separation in EXAFS spectra is impossible. The same applies to the two longest distances. For this reason, the nearest environment of metal atoms in EXAFS spectra should be represented

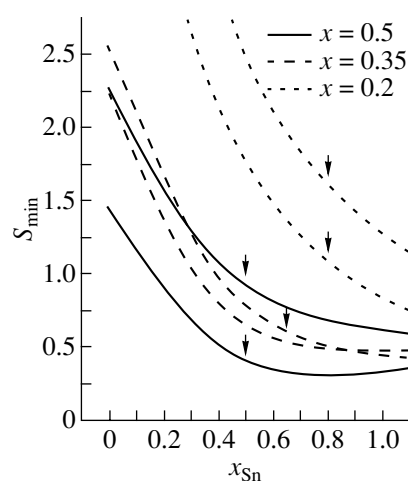
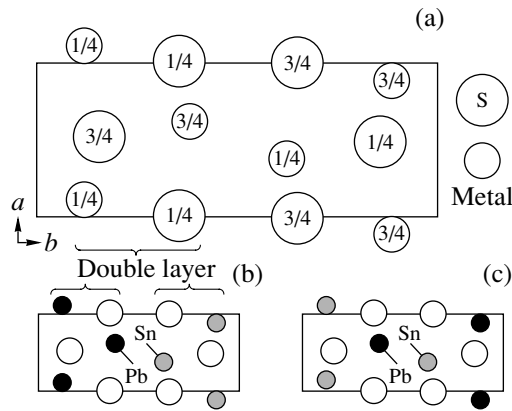


Fig. 3. Sum of the squares of deviations plotted vs. local Sn concentration in the second coordination shell of Pb atoms. Curves of one type belong to two spectra measured on samples of the same composition. Arrows identify the average Sn concentration in a sample.



**Fig. 4.** (a) Projection of the SnS structure on the  $ab$  plane, and (b, c) two possible schemes of superstructural ordering of metal atoms in the  $\text{Pb}_{0.5}\text{Sn}_{0.5}\text{S}$  solid solution. The space groups of the superstructures are (b)  $C_{2v}^7$  and (c)  $C_{2v}^2$ .

by three short and three long distances, each of them being determined by the averaged length of the constituent bonds. It is this that is observed experimentally.

As follows from a comparison of EXAFS data obtained for the local environment of Pb impurity atoms in SnS with those available for Sn atoms in pure SnS (see table), the shorter Pb–S bond length turns out to be  $\approx 0.1$  Å longer than the corresponding Sn–S bond length in SnS and the longer Pb–S bond length is shorter by  $\approx 0.07$  Å than the corresponding Sn–S distance in SnS.

Another result, which we believe to be most important, is that the short Pb–S bond length in samples with orthorhombic structure turned out to be noticeably shorter (by  $\approx 0.2$  Å) than that in PbS (2.94 Å). The decrease in this bond length and the splitting of the first coordination shell into two components indicate that Pb atoms in SnS occupy off-center positions. A comparison of our data with the results obtained in the study of the  $\text{Ge}_{1-x}\text{Pb}_x\text{Te}$  solid solution [9] shows that, in both systems, the Pb–chalcogen bond lengths become different, with the decrease in the short bond length being nearly equal in both systems ( $\approx 0.2$  Å). Significantly, the decrease in the Pb–chalcogen bond length is considerably smaller than the difference between the ionic radii of  $\text{Pb}^{2+}$  and  $\text{Pb}^{4+}$  (0.5 Å). This suggests that the two paired  $6s^2$  electrons are not involved in chemical bonding, and we have here only a deformation in the density distribution of these paired electrons, i.e., a crossover to a stereochemically active state. In view of the fact that Pb is observed in off-center positions in SnS and GeTe, whereas introduction of Pb atoms into cubic SnTe does not entail, as we have seen, any local distortion of the symmetric environment, one can conclude that lead atoms become off-center only when they enter lattices with symmetry lower than cubic. Thus, the density distribution of the paired  $6s^2$  electrons of a

Pb atom is mobile enough to be able to transfer from the inactive (as in PbS, PbSe, PbTe) to an active state under certain conditions. This feature of the paired lead electrons could account for the structural instability and phase transitions observed to occur in many lead compounds.

Our results also permit certain conclusions as to the structure of the solid solutions studied. According to our data, all the bond lengths in the nearest neighbor environment of Pb atoms in the  $\text{Pb}_x\text{Sn}_{1-x}\text{S}$  solid solution vary monotonically with  $x$ . This suggests that the  $\text{Pb}_{0.5}\text{Sn}_{0.5}\text{S}$  composition in the SnS–PbS system should be considered to be an SnS-based solid solution.

Consider now the short-range order observed in this system. The SnS structure is known to consist of double-layer packets (Fig. 4a). The formation of a well-defined short-range order, in which Pb atoms in one double-layer packet are surrounded predominantly by Sn atoms of the neighboring packet, suggests that under certain conditions a superstructural metal-atom ordering observed in minerals (teallite) can set in in  $\text{Pb}_{0.5}\text{Sn}_{0.5}\text{S}$  crystals.

Assuming the local tin atom concentration in the second coordination shell of lead atoms to be 100%, we may expect that completely ordered zigzag chains  $\dots\text{Pb}\text{--}\text{Sn}\text{--}\text{Pb}\text{--}\text{Sn}\text{--}\dots$  aligned with the  $c$  axis (perpendicular to the plane of Fig. 4a) will form in  $\text{Pb}_{0.5}\text{Sn}_{0.5}\text{S}$  samples. However, even if atoms in one such chain are fully ordered, three-dimensional long-range order (superstructure) can form only in the case where the atomic arrangements in neighboring chains are correlated. We note that the formation of zigzag chains destroys the inversion center in the crystal, which in the SnS structure lies midway between the two nearest neighbor tin atoms. This means that the space group of the superstructure must be a subgroup of space group  $D_{2h}^{16}$  and contain point group  $C_{2v}$  as a subgroup. Restricting oneself to analysis of superstructures without any change in unit cell volume, two types of atomic ordering in the superstructure can be conceived: (1) one packet contains atoms of one species (space group  $C_{2v}^7\text{--}P2_1nm$ , Fig. 4b), and (2) one packet contains atoms of both species (space group  $C_{2v}^2\text{--}Pb2_1m$ , Fig. 4c). Superstructures of the first type allow (00 $l$ ) superstructure reflections with odd  $l$ , while superstructures of the second type allow (00 $l$ ) and (100) reflections with odd  $l$ .

Electron diffraction patterns of thin  $\text{Pb}_{0.5}\text{Sn}_{0.5}\text{S}$  films grown on substrates of alkali halide crystals at 200°C [8] exhibited reflections characteristic of a  $C_{2v}^2$  superstructure. In an attempt to reproduce this result, we annealed a volume  $\text{Pb}_{0.5}\text{Sn}_{0.5}\text{S}$  sample at 240°C for a month. X-ray studies of the annealed sample did not reveal any superstructural reflections. In our opinion, this may be due to the fact that the coupling energy of

neighboring chains (in which the shortest interatomic distance is  $\approx 4.1$  Å) is too low; therefore, annealing at lower temperatures is required. Thus, well-defined short-range order and the absence of long-range order in our samples indicates that interlayer coupling between metal atoms in the SnS-based solid solution under study is stronger than the intralayer coupling. This is in accord with the relative magnitude of the corresponding bond lengths (3.5, 4.1 Å).

Thus, the strong short-range order manifesting itself in the distribution of metal atoms permits one to consider the structure of the SnS–PbS solid solution to be in the form of randomly arranged fragments of zigzag chains aligned with the *c* axis of the structure. The clearly pronounced anisotropy of the local structure may account for the unusual physical properties of these solid solutions.

The short-range order in the arrangement of metal atoms is also directly reflected in the phase diagram of the SnS–PbS system. As already mentioned, the extent of the single-phase region in the phase diagram of the solid solution on the SnS side is  $\approx 50\%$ . Our analysis suggests that this concentration corresponds to the limiting case where all metal atoms are ordered in zigzag chains. At higher Pb atom concentrations, Pb–Pb pairs should inevitably appear in the chains, whose formation is energetically unfavorable. It is this factor that determines the boundary of existence of the solid solution in the system studied.

## REFERENCES

1. I. S. Morozov and C.-F. Li, Zh. Neorg. Khim. **8** (7), 1688 (1963).
2. V. G. Kuznetsov and C.-F. Li, Zh. Neorg. Khim. **9** (5), 1201 (1964).
3. H. von Krebs and D. Langner, Z. Anorg. Allg. Chem. **334** (1–2), 37 (1964).
4. *Minerals: A Handbook* (Akad. Nauk SSSR, Moscow, 1960), Vol. 1, pp. 370–373.
5. T. Baak, E. D. Dietz, M. Shouf, and J. A. Walmsley, J. Chem. Eng. Data **11** (4), 587 (1966).
6. A. D. Bigvava, É. D. Kunchuliya, S. S. Moiseenko, and B. B. Anisimov, Izv. Akad. Nauk SSSR, Neorg. Mater. **10** (2), 539 (1974).
7. Z. M. Latypov, N. R. Faizullina, V. N. Savel'ev, and R. Yu. Davletshin, Izv. Akad. Nauk SSSR, Neorg. Mater. **12** (2), 206 (1976).
8. I. R. Nuriev, É. Yu. Salaev, and R. N. Nabiev, Izv. Akad. Nauk SSSR, Neorg. Mater. **22** (2), 204 (1986).
9. A. I. Lebedev, I. A. Sluchinskaya, V. N. Demin, and I. H. Munro, Phys. Rev. B **55** (22), 14770 (1997).
10. A. I. Lebedev, I. A. Sluchinskaya, V. N. Demin, and I. H. Munro, Fiz. Tverd. Tela (St. Petersburg) **41** (8), 1394 (1999) [Phys. Solid State **41**, 1275 (1999)].
11. J. Mustre de Leon, J. J. Rehr, S. I. Zabinsky, and R. C. Albers, Phys. Rev. B **44** (9), 4146 (1991).
12. T. Chattopadhyay, J. Pannetier, and H. G. von Schnering, J. Phys. Chem. Solids **47** (9), 879 (1986).

*Translated by G. Skrebtsov*

---

---

**SEMICONDUCTORS  
AND DIELECTRICS**

---

---

## Optical Characterization of Synthetic Opals

**A. V. Baryshev\*, A. V. Ankudinov\*, A. A. Kaplyanskiĭ\*, V. A. Kosobukin\*,  
M. F. Limonov\*, K. B. Samusev\*, and D. E. Usvyat\*\***

\**Ioffe Physicotechnical Institute, Russian Academy of Sciences, Politekhnikeskaya ul. 26, St. Petersburg, 194021 Russia*  
*e-mail: alex.baryshev@pop.ioffe.rssi.ru*

\*\**St. Petersburg Institute of Precision Mechanics and Optics, St. Petersburg, 197101 Russia*

Received October 30, 2001

**Abstract**—The results of a structural-optical characterization of synthetic opals are presented. Information on the growth-induced features of the opal structure was derived from an analysis of the position and width of the one-dimensional photonic band gap. The structure of the samples was found to vary substantially along the growth axis coinciding with the [111] direction of the fcc lattice. It was shown that the regions corresponding to early stages in the opal structure growth are typically strongly disordered, which manifests itself, in particular, in the crystallites being misoriented relative to the sample growth axis. It was concluded that the regions of synthetic opals most suitable for application as photonic crystals are those corresponding to later growth stages.  
© 2002 MAIK “Nauka/Interperiodica”.

### 1. INTRODUCTION

Starting from the publication of studies [1, 2], the investigation and synthesis of photonic band-gap structures [3] (photonic crystals [4]) have been an important area in solid-state physics. One usually understands photonic crystals to be weakly absorbing dielectric structures possessing the following two properties [4]: (i) periodic modulation of the dielectric permittivity on a scale comparable to the wavelength of electromagnetic waves and (ii) the existence of a complete photonic band gap in three-dimensional space [1], or, at least, of a photonic band gap in prescribed crystallographic directions (the stop band) associated with the periodicity of the structure [4, 5]. The latter property means that within a given spectral range, light of any polarization cannot enter a sample or leave it in any direction. By analogy with the electronic band structure, the formation of a band gap in the photonic spectrum is connected with Bragg diffraction of Bloch light waves from a dielectric grating. It is believed that the existence of a complete photonic band gap will suppress spontaneous emission from a sample [1] and give rise to other important optical effects [3].

A complete photonic band gap was first observed in the microwave range in an artificial fcc lattice formed by crossing cylindrical holes drilled in a dielectric [6]. The problem of detecting a complete photonic band gap in the optical spectral region apparently remains open [7]. At the same time, properties characteristic of a one-dimensional photonic structure have been observed in the optical region in a number of materials, in particular, in synthetic opals [5] and colloidal structures made up of spherical  $\text{TiO}_2$  microparticles [8]. Opal-based inverted structures are considered to be the most prom-

ising materials from the standpoint of formation of a complete band gap in the optical range [7, 9].

Monodisperse spherical  $\text{SiO}_2$  particles in synthetic opals form close-packed layers parallel to the growth surface. These layers can alternate in the sequence ABCABC... characteristic of an fcc lattice or ABA-BAB... typical of a hexagonal close-packed (hcp) structure. Numerical simulation of a perfect crystal consisting of rigid spheres suggests that the fcc structure is more stable [10, 11]. It is generally believed that real opals represent a random mixture of fcc and hcp structures. The growth technologies used in various laboratories to obtain synthetic photonic structures, including opals, produce samples varying in properties and degree of lattice perfection. In this connection, investigation of the effect of the real crystal structure of materials on the photonic band gap parameters is an urgent problem [12, 13].

The purpose of this work was to analyze the structure of synthetic opals and characterize them by optical methods. It was established that in most of the samples studied, regions with different optical properties, which are associated with differences in the defects in the structures, form along the growth axis. Each of these regions was characterized based on an analysis of transmission and reflection spectra obtained in visible light over a broad spectral range, as well as on studying the diffraction of laser monochromatic light. The paper is organized as follows. Section 2 describes the characterization of the samples using transmission electron and atomic-force microscopy, Section 3 presents the results of optical measurements, Section 4 gives a theoretical analysis of the one-dimensional photonic band gap, and Section 5 sums up the results obtained.

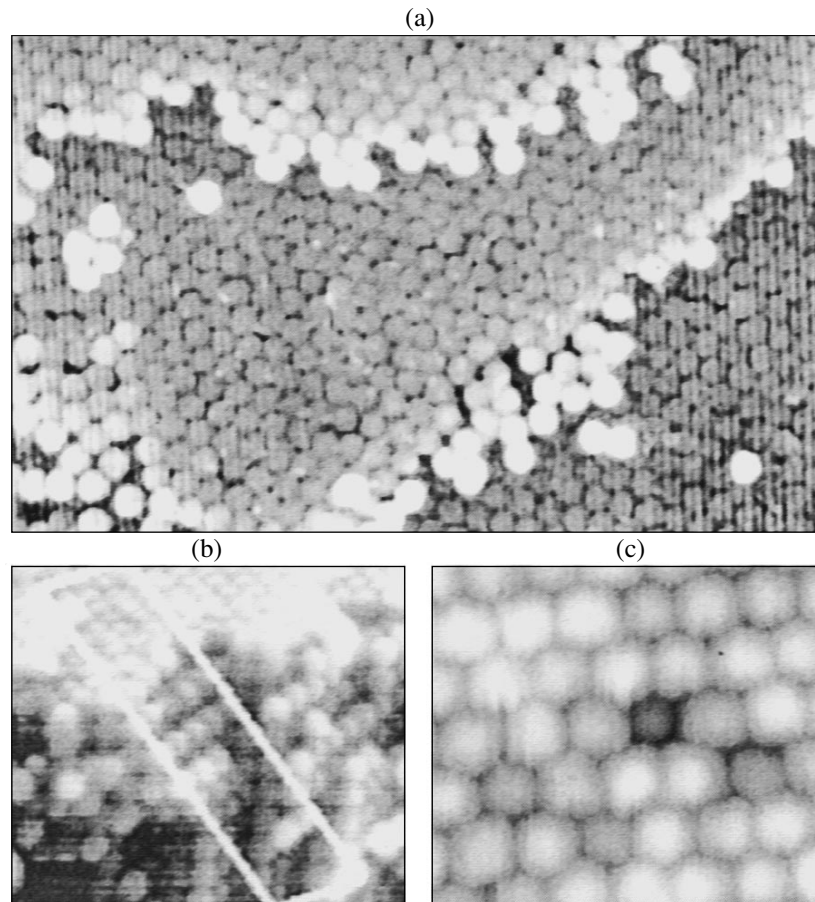


**Fig. 1.** Opal surface imaged by (a, b) electron and (c) atomic-force microscopy; (a) (111) growth plane, (b) cleaved surface featuring a sequence of (111) planes forming the fcc structure, and (c) point defect (vacancy) in a (111)-type layer.

## 2. SAMPLE PREPARATION AND SURFACE MORPHOLOGY STUDIES

The samples of synthetic opals studied in this work were prepared using the technology described in [14]. In the first stage of the technological process, a mono-disperse suspension (size dispersion ~5%) of spherical  $\text{SiO}_2$  particles, whose average diameter can vary in the range 200–800 nm, is synthesized. Next, a water solution of this suspension is prepared and placed in a cell for an extended period of time (up to nine months).  $\text{SiO}_2$  particles in the cell settle to the bottom under gravity and form a three-dimensional periodic structure through self-organization. The sediment thus obtained is dried and annealed to impart a higher density and hardness to the sample. The samples have a porous structure with a continuous array of voids separating the  $\text{SiO}_2$  spheres. The lattice parameter of the opals thus formed lies in the visible wavelength range, and the samples measure a few centimeters on their base and up to one centimeter in height.

During the growth of synthetic opals, hexagonal close-packed layers perpendicular to the growth direc-

tion  $Z$  form. In a real structure, these layers are parallel to the (111) plane of the fcc lattice. It is essential that the system of growth layers perpendicular to the growth axis  $Z$  in the synthesized samples differs physically from layers with orientations determined by the system of the other three fcc lattice planes, namely,  $(\bar{1}11)$ ,  $(1\bar{1}1)$ , and  $(11\bar{1})$ . The reason for this lies in the fact that in synthetic opals, there are stacking faults along the growth axis  $Z$ , thus differentiating this axis from the other three equivalent [111] directions in the fcc lattice, which are perpendicular to the crystallographic planes mentioned above.

The orientation of crystallographic planes relative to the sample faces was determined through direct visualization of the sphere packing patterns using transmission electron microscopy (Hitachi SEM-2700 electron microscope) and atomic-force microscopy (P4-SPM microscope). The results obtained in visualization of the opal crystal structure using these methods are presented in Fig. 1. As seen from Fig. 1a, the growth surface of the crystal is formed by hexagonal close-packed layers. The pattern of mutual arrangement of  $\text{SiO}_2$

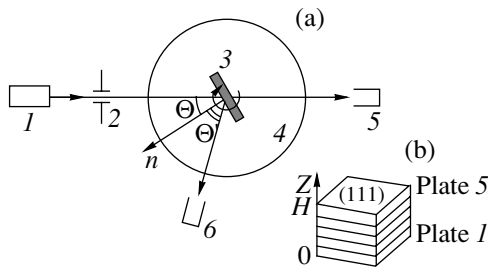


**Fig. 2.** (a) Experimental setup: (1) light source, (2) collimator, (3) opal plate, (4) spherical vessel, and (5, 6) radiation detectors; (b) cutting of a sample into plates.

spheres in several layers lying one upon another suggests that, near the sample surface, the ABC...-type layer stacking, as a rule, corresponding to the opal fcc lattice is formed. We also readily see that (111)-type growth layers of the fcc lattice retain long-range order in the sphere arrangement, unlike natural opals, in which micron-scale ordered regions are misoriented with respect to one another [15]. Figure 1b features an image of a (100)-type cleaved surface of the fcc lattice indicating cubic opal structure. All samples exhibit point lattice defects [see the image of the (111) surface in Fig. 1c] with a concentration of about 1 defect per square micron, as well as edge and screw dislocations. Atomic-force microscopy images show that the diameter of the  $\text{SiO}_2$  spheres varies from 240 to 300 nm. The  $\text{SiO}_2$  sphere diameter in each of the original samples is the same over the volume, and the defect concentration

is higher in the regions corresponding to earlier growth stages.

### 3. OPTICAL EXPERIMENTS

For the experimental investigation of the structural features and optical properties of synthetic opals, we chose the most optically homogeneous original samples, which were oriented using an atomic-force microscope. Next, the samples were cut, as shown in Fig. 2b, into plates of thickness not more than 0.5 mm perpendicular to the crystal growth axis  $Z$ . We shall call such plates the (111) plates, with the plates cut from the upper and lower parts of the original sample (which correspond to the later and earlier growth stages) being referred to as the upper and lower plates, respectively.

The optical spectra of the (111) plates were studied in the transmission and reflection geometries under the condition that the reflecting surface coincided with the growth plane of the opal. The spectra were measured on a setup as shown schematically in Fig. 2a. The source of white light was an incandescent lamp (1) whose light beam was collimated with a diaphragm and a lens (2) to reach a beam divergence of  $2^\circ$ – $4^\circ$ . Next, the beam was directed onto an opal plate (3) placed in a spherical vessel (4) filled with immersion liquid to reduce incoherent scattering from the surface. The transverse cross section of the beam on the sample surface was  $1$ – $1.5 \text{ mm}^2$ . The transmitted (5) or reflected (6) light was directed onto the entrance slit of a DFS-12 spectrometer (spectral resolution  $0.5 \text{ nm}$ ) through a fiber  $2 \text{ mm}$  in diameter, thus obtaining an angular resolution of about  $1^\circ$ .

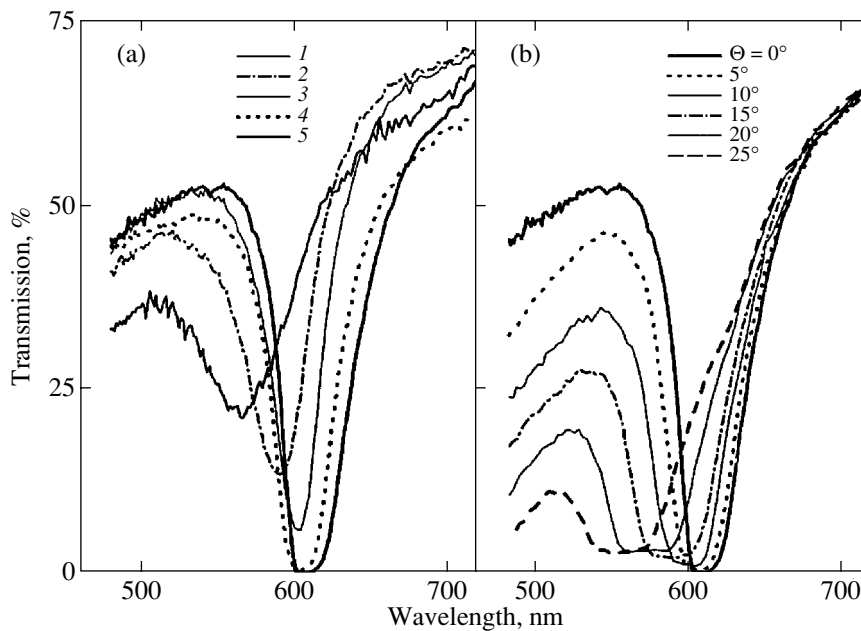


**Fig. 3.** Absorption spectra of opal plates. (a) Spectra obtained at normal incidence for the following plates (Fig. 2b): (1) the lowest plate in the sample, (2–4) plates from the central part, and (5) the top plate. (b) Transmission spectra of plate 5 obtained at different incidence angles  $\Theta$ .

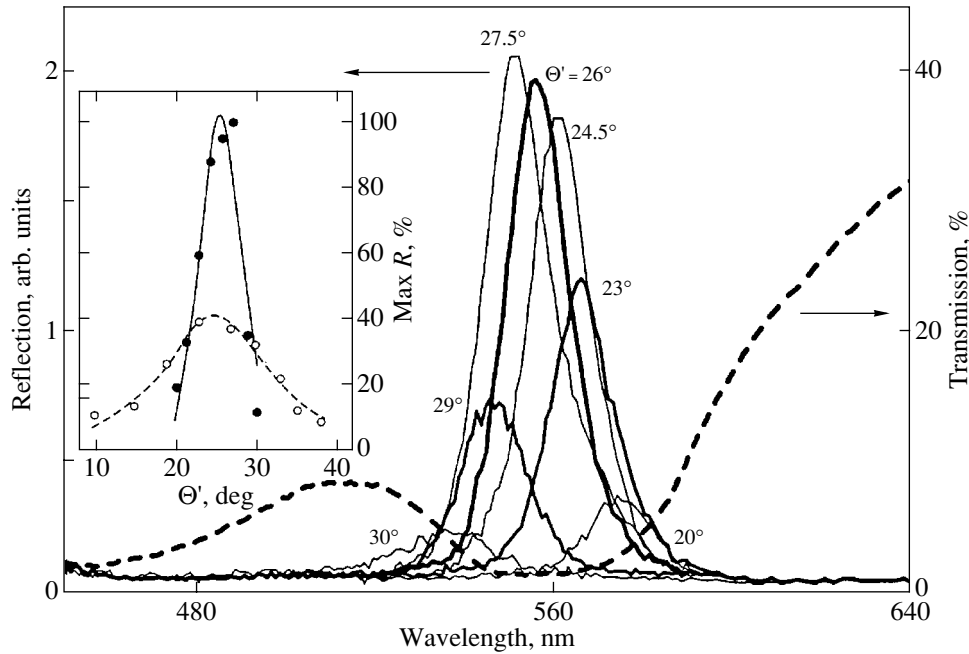


**Fig. 4.** Reflection spectra of plate 1 measured at different reflection angles  $\Theta'$  (solid lines) and transmission spectrum of the same plate obtained with the light incident at  $\Theta = 25^\circ$  (dashed line). Inset: dependence of the maximum reflection band intensity on the angle  $\Theta'$  at which the corresponding spectrum was measured (filled circles refer to the top plate; open ones, to the bottom plate).

Figure 3a presents the spectra of unpolarized white light transmitted through (111) plates. These spectra were taken with the light propagating normally to the plate surface (i.e., in the  $\Gamma \rightarrow L$  direction from the  $\Gamma$  to the  $L$  point of the Brillouin zone of the fcc lattice). The spectra of all the plates exhibited a characteristic band whose position, width, and depth were strongly dependent on the plate number, i.e., on the coordinate  $Z$  in the original sample (Fig. 2). The spectrum of the bottom plate (curve 1 in Fig. 3a), corresponding to an early stage in growth, has a characteristic band with the smallest dip and the largest width. As one crosses over to the upper plates of the sample, which correspond to later growth stages, the position of the band minimum shifts toward longer wavelengths, its width decreases, and the depth of the spectral dip increases. Figure 3b shows reflection spectra for a (111) plate cut from the top part of the sample obtained at different light incidence angles  $\Theta$ , with the  $\Theta = 0^\circ$  angle corresponding to the beam striking the growth surface along its normal. It can readily be seen that, as the beam deviates from the normal, the band in the transmission spectra measured in the beam direction (Fig. 2a) shifts toward shorter wavelengths while broadening noticeably.

The Bragg angle of light scattering inside an opal sample is given by the well-known theoretical equation  $b^2 = -2\mathbf{k} \cdot \mathbf{b}$ , where  $\mathbf{k}$  is the quasi-wave vector of a Bloch electromagnetic wave in the crystal and  $\mathbf{b}$  is the reciprocal-lattice vector. For the Bragg wavelength in vacuum, this yields the relation  $\lambda_B = 2dn\cos\delta$ , where  $\delta$  is the angle of light incidence inside the crystal on the

crystallographic plane perpendicular to vector  $\mathbf{b}$ ,  $n$  is the refractive index, and  $d = 2\pi/b$  is the interplanar distance in the direction of vector  $\mathbf{b}$ . Because the quantities  $\delta$  and  $n$  are not measured in the experiment, we will use the relation

$$\lambda_B = 2d\bar{n}\cos\Theta. \quad (1)$$

Here,  $\lambda_B$  is expressed through the experimentally measured angle of light incidence on the sample  $\Theta$  and the effective refractive index  $\bar{n}$ . Thus, the wavelength determining the position of the minima in the opal transmission spectra (the position of the stop band) as a function of the incidence angle  $\Theta$  is described by Eq. (1), where, in the case of light diffraction from the (111) opal plane,  $d = R\sqrt{8/3}$  is determined by the radius  $R$  of  $\text{SiO}_2$  spheres. Substitution of the position of the band minimum in the transmission spectrum of the top (111) plate obtained at normal incidence (curve 5 in Fig. 3a) into Eq. (1) yielded a reasonable value of  $\bar{n} = 1.36$  for the effective refractive index.

In addition to transmission spectra, we also measured reflection spectra under oblique incidence of white light on a (111) plate. Each spectrum was taken at an angle  $\Theta'$  (Fig. 2) close to the direction of mirror reflection ( $\Theta' = \Theta$ ) specified by the light incidence angle  $\Theta$ . Figure 4 presents spectra measured in an interval of angles  $\Theta'$  for a fixed incidence angle  $\Theta \approx 25^\circ$  on the plate cut from the top part of the sample (plate 5). To permit identification of the origin of the bands in the transmission (Fig. 3b) and reflection (Fig. 4) spectra,

Fig. 4 also displays a transmission spectrum of the plate obtained at an incidence angle near  $25^\circ$  (dashed line). All reflection spectra are seen to lie in the region of one stop band, which implies that the bands revealed in the transmission and reflection spectra are of the same origin. The inset to Fig. 4 shows the intensities at the maxima of reflection bands as functions of angle  $\Theta'$  for two plates cut from the top and bottom parts of the sample. We readily see that the reflection is maximum and the angular width of the peak is minimum ( $\approx 5^\circ$ ) for the top plate (filled circles), while for the bottom plate, the angular width of the reflected beam is considerably larger ( $\approx 15^\circ$ , open circles). This means that, due to strong structural imperfections in the lower plates, the diffuse light scattering from them is substantially larger than that from the upper plates.

The same set of (111) plates was subjected, in addition to white-light experiments, to measurements of the reflected intensity component under monochromatic illumination using a narrow He–Ne and Ar laser beam directed under different incidence angles  $\Theta$ . In this case, at the angles  $\Theta$  satisfying condition (1), diffracted light in the direction of mirror reflection is observed. The diameter of the diffraction spot depends on the degree of perfection of the crystal structure. For the top plate, the angular width of this reflection is the smallest,  $5^\circ$ , while for the lower plates this reflection is broadened, thus corroborating the above conclusion on strong diffuse scattering of light from the lower plates.

#### 4. ANALYSIS OF THE ONE-DIMENSIONAL BAND GAP

Because the stacking of hexagonal layers in opals is well ordered only along the growth axis  $Z$  [the normal to the growth plane (111) of the fcc lattice], the one-dimensional periodic model of the photonic crystal is applicable to investigation of the optical properties of opals near this direction. In this section, we will make a theoretical analysis of the one-dimensional photonic band gap (stop band).

As already mentioned, the formation of photonic band gaps in the presence of a periodic modulation of dielectric properties is initiated by coherent Bragg scattering of light waves. The electromagnetic eigenwaves in photonic crystals have the form of Bloch waves. The propagation of a light wave in such a structure can be considered a result of its multiple elastic scattering involving Umklapp processes with all possible combinations of the reciprocal-lattice vectors of the photonic crystal. In experiments on light scattering performed in the mirror-scattering and transmission geometry, the directions of propagation of the waves striking the crystal and scattered from it are fixed. The detected secondary radiation is a sum of the contributions due to the coherent Bragg scattering processes in which the resultant reciprocal-lattice vector of the Umklapp processes (tangent to the plate surface) is zero. In all other scattering processes, the energy is removed from the

detected beam. Thus, in general, the attenuation of the light beam propagating through a photonic crystal has the character of extinction and reflects a combined manifestation of both irreversible scattering of light and its absorption.

All this was taken into account in analyzing the transmission and reflection of opals, which was performed in terms of the dielectric superlattice model (one-dimensional photonic crystal [4]). An infinite structure made of periodically alternating layers with dielectric permittivities  $\epsilon_A$  and  $\epsilon_B$  can be described by a dispersion relation,

$$\cos(qd) = \cos(k_A a) \cos(k_B b) - \frac{1}{2} \left( \sqrt{\frac{\epsilon_A}{\epsilon_B}} + \sqrt{\frac{\epsilon_B}{\epsilon_A}} \right) \sin(k_A a) \sin(k_B b). \quad (2)$$

This equation relates to Bloch electromagnetic waves, which are characterized by a quasi-wave number  $q$  and are linearly polarized in the layer plane of the superlattice. Here,  $k_i = \sqrt{\epsilon_i k_0^2 - Q^2}$ ;  $Q$  is the tangential component of the wave vector, which is preserved in this model;  $a$  and  $b$  are the thicknesses of uniform layers which have dielectric permittivities  $\epsilon_A$  and  $\epsilon_B$  and represent a close-packed layer of spheres in the opal and the space between them, respectively; and  $d = a + b$  is the structure period. It is essential that Eq. (2) predicts the formation of a one-dimensional band gap (stop band) in the presence of any weak periodic modulation of the dielectric permittivity. Within the one-dimensional model discussed here, the effect of extinction on the photonic band structure is included subsequently by introducing an imaginary part into the dielectric permittivities  $\epsilon_A$  and  $\epsilon_B$ .

Following [12], we simulate the opal structure periodicity in the growth direction by means of an effective dielectric function,

$$\epsilon_{\text{eff}}(z) = \epsilon_s S(z) + \epsilon_v [1 - S(z)]. \quad (3)$$

This function is obtained by averaging the dielectric permittivities in the planes perpendicular to the [111] growth direction of the opal fcc lattice, with the  $S(z)$  function determining the part of the cross section (specified by the coordinate  $z$ ) occupied by  $\text{SiO}_2$  spheres. In Eq. (3),  $\epsilon_s$  and  $\epsilon_v$  denote the dielectric permittivities of the materials filling the volume of the spheres in the opal and the volume of the voids separating them, respectively; if these volumes are filled nonuniformly by the dielectric, the corresponding volume-averaged values of  $\epsilon_s$  and  $\epsilon_v$  should be used in the calculations.

The specific features of the one-dimensional photonic band gap in an infinite structure were analyzed qualitatively with the use of Eq. (1) for a superlattice aligned with the [111] growth direction of an opal fcc lattice having a period  $d = R\sqrt{8/3} = 1.63R$ , with  $R$  being the sphere radius. The constants  $\epsilon_A$  and  $\epsilon_B$  enter

ing Eq. (2) were approximated using the function  $\varepsilon_{\text{eff}}(z)$  from Eq. (3), with the ratio  $\beta = b/a$  and the period  $d = a + b$  assumed to be fixed. The same assumptions were used in calculating the transmission and reflection spectra of a one-dimensional photonic crystal formed by a finite number of layers  $N$  and bounded by uniform nonabsorbing dielectric media in the  $Z$  axis direction. As in deriving Eq. (2), the close-packed layer of the opal spheres was simulated by a dielectric layer with the coefficients of reflection  $r_1$  and transmission  $t_1$  and width  $b$ . By properly using the transfer matrices (see, e.g., [16]), we come to the following expression for the transmission coefficient [17]:

$$T_N = |t_N \tau_I \tau_{II} / \Delta_N|^2. \quad (4)$$

Here,

$$t_N = (\cos Nqd - H \sin Nqd / \sin qd),$$

$$r_N = \frac{r_1 \sin Nqd}{t_1 \sin qd} t_N$$

are the coefficients of transmission and reflection, respectively, for a periodic structure of  $N$  layers; the dielectric permittivity of the outer medium is accepted equal to  $\varepsilon_A$ ;

$$\Delta_N = 1 + (\rho_I - \rho_{II}) r_N + \rho_I \rho_{II} (t_N^2 - r_N^2);$$

$\tau_I(\rho_I)$  and  $\tau_{II}(\rho_{II})$  are the coefficients of transmission (reflection) of light, taken with the corresponding phases, for the real front and rear dielectric boundaries of the finite periodic structure, respectively; and

$$H = \frac{1}{2t_1}$$

$$\times \{ (t_1^2 - r_1^2 - 1) \cos(kd) + i(t_1^2 - r_1^2 + 1) \sin(kd) \}.$$

The results of numerical calculations of the light transmission coefficient  $T_N(\omega)$  from Eq. (4) made using the dielectric structure parameters characteristic of opals are presented in Fig. 5. Curve 1 shows that if light strikes the layers of the structure with  $N \gg 1$  normally, the  $T_N(\omega)$  spectrum has a frequency band within which the transmission is zero even in the case of negligible losses. Outside the dip,  $T_N(\omega)$  undergoes oscillations originating from light interference at the outer boundaries of the structure. In its position and width, the dip in the  $T_N(\omega)$  transmission spectrum agrees well with the band gap found in the one-dimensional dispersion relation of electromagnetic waves  $\omega(q)$ , which was derived from Eq. (2). On the other hand, the specific features of the dip in the theoretical  $T_N(\omega)$  spectrum are in quantitative agreement with the parameters of an experimental transmission spectrum obtained at  $\Theta = 0$  (curve 5 in Fig. 3a). Thus, the dip observed in the opal transmission spectrum is indeed due to the existence of a photonic band gap along the normal to the (111) plate surface.

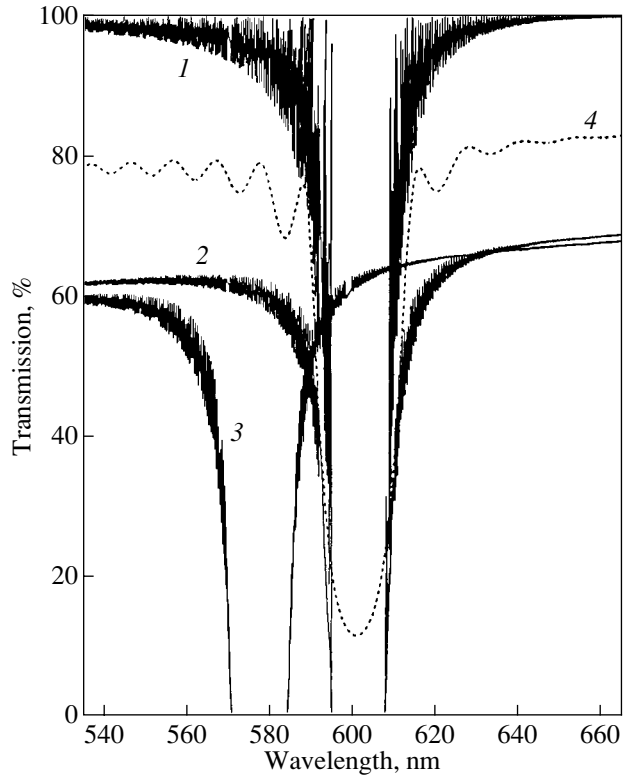


**Fig. 5.** Light transmission coefficient calculated for a one-dimensional photonic crystal. The curves are plotted for the following sets of parameters  $(\Theta, N, \varepsilon_{\text{eff}}'')$ : (1)  $(0^\circ, 1000, 10^{-6})$ , (2)  $(0^\circ, 2000, 2 \times 10^{-4})$ , (3)  $(20^\circ, 2000, 2 \times 10^{-4})$ , and (4)  $(0^\circ, 50, 2 \times 10^{-3})$ , where  $N$  is the number of layers in the photonic crystal (plate),  $\Theta$  is the angle of light incidence on the plate, and  $\varepsilon_{\text{eff}}''$  is an imaginary term that is uniform over the plate volume and is added to the dielectric permittivity expressed by Eq. (3). The one-dimensional lattice period  $d = R\sqrt{8/3}$  is equal to the interplanar distance of the opal fcc lattice in the [111] direction. The opal parameters used are as follows:  $R = 150$  nm,  $\varepsilon_s = 1.37$  ( $\text{SiO}_2$ ), and  $\varepsilon_v = 1$  (vacuum). The oscillations seen in all four curves are associated with light interference at the boundaries of the structure of finite thickness.

Curves 2 and 3 in Fig. 5 illustrate the extinction effect, which was simulated by adding an imaginary term  $\varepsilon_{\text{eff}}''$ , uniform over the plate volume, to function (3). Curve 3 differs from curve 2 only in that it relates to oblique incidence of light ( $\Theta = 20^\circ$ ), a case for which the stop band is observed to shift because of the changed condition of Bragg reflection. As follows from a comparison of curves 2 and 3 with curve 1, at plate thicknesses typical of real samples, the light transmission decreases substantially outside the stop band even for very small  $\varepsilon_{\text{eff}}'' \sim 10^{-4}$ . Also, the characteristics of the band gap do not change noticeably with increasing  $\varepsilon_{\text{eff}}''$  (transition from curve 1 to curves 2, 3). Curve 4 was plotted for a periodic structure with a small number

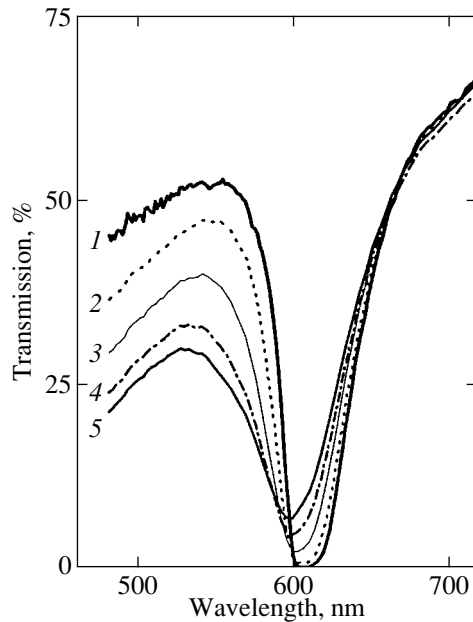


**Fig. 6.** Experimental transmission spectrum of a top (111) plate obtained under normal light incidence,  $\Theta = 0$  (curve 1), and transmission spectra calculated using Eqs. (5) and (6)

for the following standard deviations  $\Delta\vartheta = \sqrt{\langle\vartheta^2\rangle}$  of the crystallite orientation angle relative to the cut plane of the (111) plate: (2)  $5^\circ$ , (3)  $10^\circ$ , (4)  $15^\circ$ , and (5)  $25^\circ$ .

of layers; this curve exhibits the onset of considerable light transmission within the stop band.

In accordance with our model, the weak dependence of the transmission coefficient on the wavelength outside the stop band (curves 2, 3) can be attributed to a decrease in the absorption of the plate (proportional to  $\varepsilon''_{\text{eff}}/\lambda$ ) with increasing wavelength. The onset of transmission in the region of the stop band (curve 4) can be assigned to the coherence of Bloch light waves being destroyed by the introduction of boundary conditions, whose role increases substantially in plates with a small number of layers. We note that this interpretation of both effects differs substantially from the one based on the numerical simulation performed in [12], where these effects were attributed to disorder. Thus, our theoretical interpretation is of a more general character, because it is based on a model of the regular structure and does not require that any additional assumptions be made.

The characterization of opals rests on the following theoretical conclusions established above. (1) The dip observed in transmission spectra is due to the presence of a one-dimensional photonic band gap. (2) The main features of the band gap do not change under oblique light incidence at comparatively small angles to the normal. (3) Any slip in structural coherence gives rise to a finite transmission in the region of the band gap.

## 5. DISCUSSION OF RESULTS

Let us consider the results obtained in characterizing the structure of synthetic opals based on the above data on the properties of the spectral band corresponding to a photonic stop band. As shown earlier (Fig. 3), as one crosses over to later sample growth stages, this band exhibits a long-wavelength shift, an increase in the depth of the corresponding dip in the transmission spectrum, and its narrowing. This evolution of the band (stop band) observed to occur as one transfers from earlier growth stages (the lower part of the original sample) to later stages (the upper part) can be associated with the fact that the upper part of the sample is substantially more perfect in structure than the lower part. One can maintain that the perfect top part is characterized by a structure made up of close-packed layers arranged perpendicular to the growth axis. In this case, the increase in the band width in the lower part of the sample (Fig. 3a) can be accounted for by assuming that in the initial stages of growth, the opal structure is strongly disordered and consists of misoriented crystallites of close-packed layers of  $\text{SiO}_2$  spheres.

The presence of strong disorder in the bottom part of the sample is indicated in the structural-optical analysis of the three-dimensional patterns of Bragg diffraction in opals, which was performed by us on samples illuminated perpendicular to the growth axis. The diffraction pattern obtained from the top part of the sample is a set of reflections caused by Bragg diffraction from several (111)-type fcc planes. This indicates a perfect crystal structure of the opal in this region. The diffraction reflections from the bottom part of the sample broaden, to become circles similar to those observed in x-ray structural analysis of polycrystalline objects.

As follows from Eq. (1), a short-wavelength shift of the stop band can be produced by any deviation of the direction of light incidence on the (111) plane from its normal (i.e., a deviation from  $\Theta = 0$ ) or by a decrease in the quantity  $d\bar{n}$ . We shall use this as a basis for interpretation of the stop band evolution in going from the top to the bottom part of the sample (Fig. 3a). We shall assume that the observed transmission band broadening is inhomogeneous in character and connected with misorientation of micron-sized crystallites in the lower layers of the sample. Assuming the crystallites to have perfect internal packing, we shall define the crystallite orientation by the angle  $\vartheta$  between the normal to its (111) plane and the sample growth axis  $Z$ . Then, in the case of normal light incidence on the plate, the orientation angle of a crystallite  $\vartheta$  is equal to the angle of light incidence  $\Theta$  on the (111) plane of this crystallite. We introduced a distribution function  $g(\vartheta)$  of crystallites into the angles of their orientation with respect to the normal to the (111) plane of the plate and calculated the transmission coefficient taking due account of the inhomogeneous broadening of the spectrum:

$$\langle T(\omega) \rangle = \int T(\omega, \vartheta) g(\vartheta) d\vartheta. \quad (5)$$

We used the Gaussian distribution

$$g(\vartheta) = \frac{1}{\sqrt{2\pi\langle\vartheta^2\rangle}} \exp\left(-\frac{\vartheta^2}{2\langle\vartheta^2\rangle}\right) \quad (6)$$

with a mean  $\langle\vartheta\rangle = 0$  and a variance  $\langle\vartheta^2\rangle$  [standard deviation  $\Delta\vartheta = \sqrt{\langle\vartheta^2\rangle}$ ], the latter being the only statistical parameter determining the inhomogeneous spectral broadening. When using Eqs. (5) and (6) in the calculations, the reference transmission spectra  $T(\omega, \vartheta)$  in Eq. (5) are taken to be spectra obtained on the most perfect sample (plate 5), which are shown in Fig. 3b for some values of  $\Theta(=\vartheta)$ ; we took account of the fact that the experimental reflection spectra are symmetric about the incidence angle  $\Theta$ , namely,  $T(\omega, -\Theta) = T(\omega, \Theta)$ . The results of the calculation of an inhomogeneously broadened transmission spectrum are presented graphically in Fig. 6 for various values of the variance  $\langle\vartheta^2\rangle$ . A comparison of Figs. 3a and 6 shows that the model of inhomogeneous broadening caused by different orientation of crystallites relative to the incident beam accounts quite well, on the whole, for the behavior of the transmission band in going from the ordered top part of the sample to the disordered bottom part. This relates, in particular, to the short-wavelength shift of the band centroid. However, when using the spectra shown in Fig. 3b for reference, the shape of the inhomogeneously broadened spectrum virtually does not change for  $\Delta\vartheta > 20^\circ$ . Hence, the disagreement between the short-wavelength shifts of the spectra displayed in Figs. 3a and 6 in the region  $\lambda < 570$  nm can be associated only with the factor  $d\bar{n}$  entering into Eq. (4). Because parameter  $d$  is the smallest for the [111] growth direction, it cannot account for the short-wavelength shift. Therefore, the additional contribution to the observed short-wavelength shift of the transmission band should be related to a decrease in the refractive index  $\bar{n}$  in the disordered lower part of the sample as compared to the top one, which is of higher perfection. This decrease may be due to an excess fraction of the optically less dense medium (air) in the voids both between the SiO<sub>2</sub> spheres and inside the spheres themselves.

## 6. CONCLUDING REMARKS

We have demonstrated that measurement of the optical reflection and transmission spectra in the region of the photonic band gap is an efficient method of characterizing synthetic opals. It was shown that by analyzing the parameters of the one-dimensional band gap (stop band), one can obtain important information on the growth features of the structure. It was established that the natural growth anisotropy of opals gives rise to the formation of regions with an essentially different structure along the growth axis  $Z$ . The structure of these

regions is characterized by (1) different opal lattice defect concentrations, (2) crystallite misorientation relative to the sample growth axis, and (3) nonuniform dielectric filling of the voids between the SiO<sub>2</sub> spheres and inside them. The regions corresponding to earlier stages in the structure growth are the most disordered; therefore, the parts of the sample produced in later growth stages are more suitable for use as photonic crystals.

## ACKNOWLEDGMENTS

The authors are indebted to S.M. Samoïlovich for providing the samples for measurements.

This study was supported by the Russian Foundation for Basic Research, project nos. 99-02-18284 and 00-02-16924.

## REFERENCES

1. E. Yablonovitch, Phys. Rev. Lett. **58**, 2059 (1987).
2. S. John, Phys. Rev. Lett. **58**, 2486 (1987).
3. E. Burstein and C. Weisbuch, *Confined Electrons and Photons. New Physics and Applications* (Plenum, New York, 1995).
4. J. D. Joannopoulos, R. D. Mead, and J. D. Winn, *Photonic Crystals. Molding of Flow of Light* (Princeton Univ. Press, Princeton, 1995).
5. V. N. Astratov, V. N. Bogomolov, A. A. Kaplyanskii, *et al.*, Nuovo Cimento D **17**, 1349 (1995).
6. E. Yablonovitch, T. J. Gmitter, and K. M. Leung, Phys. Rev. Lett. **67**, 2295 (1991).
7. A. Blance *et al.*, Nature **405**, 437 (2000).
8. J. E. G. J. Wijnhoven and W. L. Vos, Science **281**, 802 (1998).
9. K. Busch and S. John, Phys. Rev. E **58**, 3896 (1998).
10. L. V. Woodcock, Nature **385**, 141 (1997).
11. A. D. Bruce, N. B. Wilding, and G. J. Ackland, Phys. Rev. Lett. **79**, 16 (1997).
12. Yu. A. Vlasov, M. A. Kaliteevski, and V. V. Nikolaev, Phys. Rev. B **60** (3), 1555 (1999).
13. Yu. A. Vlasov, V. N. Astratov, A. V. Baryshev, *et al.*, Phys. Rev. E **61** (5), 5784 (2000).
14. N. D. Deniskina, D. V. Kalinin, and L. K. Kazantseva, *Precious Opals, Their Synthesis and Natural Genesis* (Nauka, Novosibirsk, 1988), p. 353.
15. J. V. Sanders, Acta Crystallogr. A **24**, 427 (1968).
16. V. A. Kosobukin, Fiz. Tverd. Tela (St. Petersburg) **34** (10), 3107 (1992) [Sov. Phys. Solid State **34**, 1662 (1992)].
17. V. A. Kosobukin, Phys. Status Solidi B **208** (1), 271 (1998).

Translated by G. Skrebtsov

# The Hartree–Fock Method and Density-Functional Theory as Applied to an Infinite Crystal and to a Cyclic Cluster

R. A. Évarestov and I. I. Tupitsyn

Research Institute for Physics, St. Petersburg State University, ul. Pervogo maya 100, Petrodvorets,  
St. Petersburg, 198904 Russia

e-mail: evarest@hm.csa.ru

e-mail: tup@tup.usr.pu.ru

Received October 24, 2001; in final form, November 13, 2001

**Abstract**—The basic properties of the one-electron density matrix of a crystal are considered. It is shown that when the Brillouin zone special-point technique, developed earlier for calculating the electron density and local exchange potentials, is directly applied to the case of a nonlocal exchange potential, the calculated density matrix is not idempotent and physically meaningless divergences appear. To surmount these difficulties, a scheme is developed for interpolating the density matrix over the Brillouin zone in reciprocal space. A modification of the Hartree–Fock method for an infinite crystal is proposed in which the equations of the cyclic-cluster model are satisfied automatically. The electronic structures of perfect crystals of  $\text{BN}_{\text{hex}}$ , silicon, and rutile are calculated using the Hartree–Fock method and the density-functional theory. © 2002 MAIK “Nauka/Interperiodica”.

## 1. INTRODUCTION

The theory of the electronic structure of a crystal is based on the assumption of the translation symmetry of the crystal, i.e., of the invariance of the energy operator under translations through vectors  $\mathbf{R}_n$ . Strictly speaking, only an infinite crystal possesses translational symmetry; in fact, such a crystal is kept in mind when the one-electron-Hamiltonian approximation is used and the electron–electron interaction is not included explicitly in the energy operator. In this approach, the calculated one-electron energies  $\varepsilon_i(\mathbf{k})$  form a continuum and the one-electron Bloch functions  $\psi_{i,\mathbf{k}}$ , which do not vanish at infinity, are normalized to unity within a primitive cell. Calculations are performed independently for each of the values of wave vector  $\mathbf{k}$  chosen.

Self-consistent schemes for calculating the electronic structure within the Hartree–Fock (HF) approach and density-functional theory (DFT) have been extensively used in recent years. The fundamental difficulty in such calculations for crystals is that the number of electrons in the system is very large (formally, infinite). Indeed, the one-electron density matrix (DM) in the basis of crystal orbitals can be calculated only if the number of electrons is finite and the orbitals can be normalized to unity in all space. At the same time, the translational and point symmetry of the one-electron energy operator must not be broken. These two conditions are met in a cyclic-cluster model representing a crystal fragment which has a finite volume but is unbounded [1] because its one-electron wave functions are subject to cyclic boundary conditions. A cyclic cluster is usually taken to be the so-called basic domain of

the crystal, in which the number of primitive cells is so large that the cyclic boundary conditions imposed on the end atoms virtually do not affect the electron density distribution in the bulk of the crystal. In actual practice, self-consistent calculations also suffer from a lack of proper balance between the summations over direct and reciprocal lattices, because a fixed number of states differing in wave vector  $\mathbf{k}$  are involved in self-consistent calculations. (In calculating the DM, summation over a set of points in the Brillouin zone (BZ) is performed in each iterative cycle of the self-consistent procedure.) However, a finite set of wave vectors  $\mathbf{k}$  corresponds, in fact, to a particular choice of the cyclic cluster of the direct lattice, which restricts the summation region in calculating lattice sums [2]. Further refinement should be done by simultaneously extending the set of vectors  $\mathbf{k}$  and the summation region of the direct lattice. Unfortunately, this requirement is not always met in self-consistent calculations of the electronic structure of crystals. Within the Hartree–Fock approach, the imbalance between the summations over the direct lattice and BZ leads to divergence of the exchange energy [2–4] and complicates the application of the BZ special-point technique [5] developed for calculating the electronic structure in terms of the diagonal elements of the density matrix of the crystal in the framework of such methods as the DFT.

In this paper, we propose a self-consistent method for calculating the electronic structure of a crystal in which an infinite crystal is approximated by a progressively enlarging cyclic cluster placed in the Madelung field produced by the remainder of the crystal. A criterion for convergence of this procedure is proposed; the

criterion is based on the fact that the density matrix of the cyclic cluster, which is a finite system in an infinite crystal, must be idempotent. By using the large-unit-cell (LUC) method [6, 7], a relationship between the symmetries of the infinite crystal and of the cyclic cluster is established and a correlation is made between a specific set of wave vectors  $\mathbf{k}$  (involved in summation over the BZ) and the corresponding summation region of the direct lattice when calculating the DM of the crystal.

In Section 2, the general properties of the one-electron density matrix of the crystal (e.g., symmetry properties) are considered using the single-determinant Hartree–Fock approximation to the many-electron wave function and it is shown that the DM is idempotent in the coordinate and quasi-momentum representations.

In Section 3, we introduce the CO-LCAO approximation (for crystal orbitals as linear combinations of atomic orbitals) and derive relations which allow one to establish the accuracy to which the density matrix is approximately calculated using a specific set of wave vectors  $\mathbf{k}$  in the BZ.

In Section 4, the DM of the basic domain of the crystal is approximately calculated using a method based on a transformation of the large unit cell that gives a set of  $\mathbf{k}$  points in the BZ between which the DM is analytically interpolated in the BZ. This method allows one to test the successive approximations to the DM for convergence.

The CO-LCAO approximation within the Hartree–Fock approach and DFT and the specific features of the approximate calculation of the DM of the crystal within each of these methods are discussed in Section 5. An intimate relationship is established between the interpolation of the DM of the infinite crystal in the BZ and the LUC (cyclic cluster) which generates the given set of  $\mathbf{k}$  points.

Finally, in Section 6, the proposed approach is applied to a number of specific crystals differing in symmetry and in the nature of the electron density distribution, namely, a hexagonal boron nitride crystal in the single-layer model, a tetragonal rutile crystal, and a cubic silicon crystal with diamond structure.

## 2. THE ONE-ELECTRON DENSITY MATRIX OF A CRYSTAL

Let the basic domain (cyclic cluster) of an infinite crystal consist of  $N = N_1 \times N_2 \times N_3$  primitive cells of volume  $V_a = \mathbf{a}_1[\mathbf{a}_2 \times \mathbf{a}_3]$  each, where  $\mathbf{a}_i$  ( $i = 1, 2, 3$ ) are the primitive direct-lattice vectors; therefore, the volume of the basic region is  $V_N = NV_a$  and the primitive translations of the corresponding cyclic system are  $\mathbf{A}_i = N_i \mathbf{a}_i$  ( $i = 1, 2, 3$ ). In the case of an infinite crystal, the translation group is infinite and its irreducible representations are specified by the wave vector  $\mathbf{k}$ , which varies continuously in the BZ. The replacement of the crystal by the cyclic cluster (basic domain) implies that any

translation of the cluster as a unit is equivalent to the identity translation. In this case, the translation group and the number of its irreducible representations become finite. Therefore, the latter are specified by a finite number ( $N$ ) of values of the wave vector, which now varies discretely in the BZ. These values are defined by the relation  $\exp(i\mathbf{k}\mathbf{A}_i) = 1$  and given by

$$\mathbf{k} = \sum_{i=1}^3 \kappa_i \mathbf{g}_i, \quad \text{where } \kappa_i = 0, \frac{1}{N_i}, \dots, \frac{N_i - 1}{N_i}$$

and  $\mathbf{g}_i$  are primitive reciprocal lattice vectors.

The infinite crystal can be considered a basic limitlessly expanding domain, in which case the numbers  $N_i$  tend to infinity. We will treat the basic domain of the crystal as a many-electron system containing  $M = Nn$  electrons ( $n$  is the number of electrons per primitive cell).

As is well known, the energy of a system within the single-determinant Hartree–Fock approximation and DFT can be expressed in terms of the one-electron density matrix. The one-electron spinless DM  $\rho(\mathbf{R}, \mathbf{R}')$  is defined as

$$\rho(\mathbf{R}, \mathbf{R}') = \int_{V_N} \psi(\mathbf{R}, \mathbf{R}_2, \dots, \mathbf{R}_M) \quad (1)$$

$$\times \psi^*(\mathbf{R}', \mathbf{R}_2, \dots, \mathbf{R}_M) d^3 \mathbf{R}_2 d^3 \mathbf{R}_3 \dots d^3 \mathbf{R}_M,$$

where the electron position vectors  $\mathbf{R}$  and  $\mathbf{R}'$  vary within the basic domain of a crystal of volume  $V_N$ . The DM of the infinite crystal is obtained from the DM of the basic domain by taking the limit  $N \rightarrow \infty$ . In its translational symmetry, the DM is periodic on the direct lattice:

$$\rho(\mathbf{R}, \mathbf{R}') = \rho(\mathbf{R} + \mathbf{R}_n, \mathbf{R}' + \mathbf{R}_n), \quad (2)$$

where  $\mathbf{R}_n$  is an arbitrary translation vector of the Bravais lattice.

We will represent the electron position vector  $\mathbf{R}$  in the form  $(\mathbf{r}, \mathbf{R}_n)$ , where  $\mathbf{R}_n$  specifies the primitive cell within which the tip of the vector  $\mathbf{R}$  lies and  $\mathbf{r}$  is the position vector of an electron within this primitive cell. Therefore, we have  $\mathbf{R} = \mathbf{r} + \mathbf{R}_n$ . Using Eq. (2), the density matrix can be written in the form

$$\begin{aligned} \rho(\mathbf{R}, \mathbf{R}') &= \rho(\mathbf{r} + \mathbf{R}_n, \mathbf{r}' + \mathbf{R}_n) \\ &= \rho(\mathbf{r}, \mathbf{r}' + \mathbf{R}_n - \mathbf{R}_n) = \rho_{\mathbf{r}, \mathbf{r}'}(\mathbf{R}_n - \mathbf{R}_n). \end{aligned} \quad (3)$$

The notation  $\rho_{\mathbf{r}, \mathbf{r}'}(\mathbf{R}_n)$  for the one-electron DM in the coordinate representation implies that the indices  $\mathbf{r}$  and  $\mathbf{r}'$  of the matrix vary continuously only within the primitive cell. Therefore, there is an analogy between the properties of the DM in the coordinate representation and the properties of the DM represented in terms of a set of basis functions, for example, in terms of Bloch sums of atomic orbitals (AOs) or plane waves.

As is known, the diagonal elements of the one-electron DM in the coordinate representation are equal to the electron density:

$$\rho(\mathbf{R}) = \rho(\mathbf{R}, \mathbf{R}) = \rho_{r,r}(0). \quad (4)$$

From the normalization condition for the many-electron wave function within the basic domain, it follows that

$$\begin{aligned} \int_{V_N} \rho(\mathbf{R}, \mathbf{R}) d^3\mathbf{R} &= Nn \\ &= \sum_{\mathbf{R}_n} \int_{V_a} \rho_{r,r}(0) d^3\mathbf{r} = N \int_{V_a} \rho_{r,r}(0) d^3\mathbf{r}. \end{aligned} \quad (5)$$

Therefore, the electron density is normalized to the number of electrons per primitive cell,

$$\int_{V_a} \rho_{r,r}(0) d^3\mathbf{r} = n. \quad (6)$$

By using the single-determinant approximation to the many-electron wave function, the DM can be expressed through the one-electron wave functions (crystal orbitals):

$$\rho(\mathbf{R}, \mathbf{R}') = \sum_i \sum_{\mathbf{k}} n_i(\mathbf{k}) \psi_{i\mathbf{k}}(\mathbf{R}) \psi_{i\mathbf{k}}^*(\mathbf{R}'), \quad (7)$$

where the index  $i$  specifies the energy bands and  $n_i(\mathbf{k})$  are the occupation numbers. In insulators, the energy bands are either completely filled or empty; therefore,  $n_i(\mathbf{k})$  are independent of  $\mathbf{k}$  and  $n_i = 0, 2$ .

The one-electron DM is invariant under any orthogonal transformation in the space of occupied states. In particular, in insulators, we can go over from the orthonormal set of extended Bloch states  $\psi_{i\mathbf{k}}(\mathbf{R})$  to the orthonormal set of localized Wannier functions:

$$u_i(\mathbf{R} - \mathbf{R}_n) = \sqrt{\frac{1}{N}} \sum_{\mathbf{k}} e^{i\mathbf{k}\mathbf{R}_n} \psi_{i\mathbf{k}}(\mathbf{R}). \quad (8)$$

In this case, Eq. (7) for the DM takes the form

$$\rho(\mathbf{R}, \mathbf{R}') = \sum_i n_i \sum_{\mathbf{R}_m} u_i(\mathbf{R} - \mathbf{R}_m) u_i^*(\mathbf{R}' - \mathbf{R}_m) \quad (9)$$

or

$$\rho_{r,r}(\mathbf{R}_n) = \sum_i n_i \sum_{\mathbf{R}_m} u_i(\mathbf{r} - \mathbf{R}_m) u_i^*(\mathbf{r}' - \mathbf{R}_m + \mathbf{R}_n). \quad (10)$$

It is well known that the Wannier functions  $u_i(\mathbf{R})$  vanish exponentially as  $|\mathbf{R}| \rightarrow \infty$  in crystals with completely filled bands. Since the vectors  $\mathbf{r}$  and  $\mathbf{r}'$  lie in the zeroth primitive cell, the products of the Wannier functions on the right-hand side of Eq. (10) fall off exponentially with increasing  $|\mathbf{R}_n|$ . Therefore, we may expect the total lattice sum in Eq. (10) for the off-diagonal ele-

ments  $\rho_{r,r}(\mathbf{R}_n)$  of the DM to also vanish exponentially with increasing  $|\mathbf{R}_n|$  (see [8, 9] for further details). It should be noted that in metals, the DM decays according to a power law.

Under translation through a lattice vector, according to Bloch's theorem, the crystal orbitals transform according to irreducible representations of the translation group:

$$\psi_{i\mathbf{k}}(\mathbf{R} + \mathbf{R}_n) = \exp(i\mathbf{k}\mathbf{R}_n) \psi_{i\mathbf{k}}(\mathbf{R}). \quad (11)$$

This condition is satisfied for both the infinite crystal and the basic domain; only the sets of values of the wave vector  $\mathbf{k}$  for which Eq. (11) is satisfied are different in these two cases.

By applying Bloch's theorem (11) to the wave functions in Eq. (7) for the one-electron DM of the basic domain, we obtain

$$\begin{aligned} \rho_{r,r}(\mathbf{R}_n) &= \sum_i \sum_{\mathbf{k}} n_i(\mathbf{k}) \psi_{i\mathbf{k}}(\mathbf{r}) \psi_{i\mathbf{k}}^*(\mathbf{r}' + \mathbf{R}_n) \\ &= \frac{1}{N} \sum_{\mathbf{k}} \exp(-i\mathbf{k}\mathbf{R}_n) P_{r,r}(\mathbf{k}), \end{aligned} \quad (12)$$

where  $P_{r,r}(\mathbf{k})$  is the density matrix in  $\mathbf{k}$  space, which is defined as

$$P_{r,r}(\mathbf{k}) = N \sum_i n_i(\mathbf{k}) \psi_{i\mathbf{k}}(\mathbf{r}) \psi_{i\mathbf{k}}^*(\mathbf{r}'). \quad (13)$$

From the familiar orthogonality relations for columns and rows of the matrices in the irreducible representations of the Abelian translation group, it follows that

$$\frac{1}{N} \sum_{\mathbf{R}_n} e^{i\mathbf{k}\mathbf{R}_n} = \delta_{\mathbf{k}, \mathbf{g}}, \quad (14a)$$

$$\frac{1}{N} \sum_{\mathbf{k}} e^{-i\mathbf{k}\mathbf{R}_n} = \delta_{\mathbf{R}_n, \mathbf{A}}, \quad (14b)$$

where  $\mathbf{g}$  is a reciprocal lattice vector and  $\mathbf{A}$  is a primitive translation of the basic domain as a whole. Using Eq. (14b), it is easy to derive an inverse relation of Eq. (12),

$$P_{r,r}(\mathbf{k}) = \sum_{\mathbf{R}_n} \exp(i\mathbf{k}\mathbf{R}_n) \rho_{r,r}(\mathbf{R}_n). \quad (15)$$

It follows from Eq. (15) that  $P_{r,r}(\mathbf{k})$  is a periodic function in the reciprocal space:

$$P_{r,r}(\mathbf{k} + \mathbf{g}_m) = P_{r,r}(\mathbf{k}). \quad (16)$$

Using the hermiticity of the DM

$$\rho(\mathbf{R}, \mathbf{R}') = \rho^*(\mathbf{R}', \mathbf{R}), \quad (17)$$

we find that

$$\rho_{\mathbf{r},\mathbf{r}'}(\mathbf{R}_n) = \rho_{\mathbf{r}',\mathbf{r}}^*(-\mathbf{R}_n), \quad P_{\mathbf{r},\mathbf{r}'}(\mathbf{k}) = P_{\mathbf{r}',\mathbf{r}}^*(-\mathbf{k}). \quad (18)$$

From Eq. (6), the normalization condition for the DM in  $\mathbf{k}$  space can easily be found to be

$$\int_{V_a} P_{\mathbf{r},\mathbf{r}'}(\mathbf{k}) d^3\mathbf{r} = n. \quad (19)$$

Here, integration is performed over a primitive cell of volume  $V_a$ .

In the case where the many-electron wave function is calculated in the single-determinant approximation, the spinless DM is idempotent:

$$\int_{V_N} \rho(\mathbf{R}, \mathbf{R}'') \rho(\mathbf{R}'', \mathbf{R}') d^3\mathbf{R}'' = 2\rho(\mathbf{R}, \mathbf{R}') \quad (20)$$

$(n_i = 0, 2).$

Similar relations also hold for the matrices  $\rho_{\mathbf{r},\mathbf{r}'}(\mathbf{R}_n)$  and  $P_{\mathbf{r},\mathbf{r}'}(\mathbf{k})$ :

$$\sum_{\mathbf{R}_m} \int_{V_a} d^3\mathbf{r}'' \rho_{\mathbf{r},\mathbf{r}''}(\mathbf{R}_m) \rho_{\mathbf{r}'',\mathbf{r}}(\mathbf{R}_n - \mathbf{R}_m) = 2\rho_{\mathbf{r},\mathbf{r}}(\mathbf{R}_n), \quad (21)$$

$$\int_{V_a} d^3\mathbf{r}'' P_{\mathbf{r},\mathbf{r}''}(\mathbf{k}) P_{\mathbf{r}'',\mathbf{r}}(\mathbf{k}) = 2P_{\mathbf{r},\mathbf{r}}(\mathbf{k}). \quad (22)$$

### 3. THE ONE-ELECTRON DENSITY MATRIX OF THE CRYSTAL IN THE LCAO APPROXIMATION

In the CO-LCAO approximation, a one-electron Bloch function  $\psi_{i\mathbf{k}}(\mathbf{R})$  (crystal orbital, CO) is expanded in Bloch sums  $\chi_{\mu\mathbf{k}}(\mathbf{R})$  of AOs:

$$\psi_{i,\mathbf{k}}(\mathbf{R}) = \sum_{\mu} C_{\mu i}(\mathbf{k}) \chi_{\mu,\mathbf{k}}(\mathbf{R}), \quad (23)$$

where

$$\chi_{\mu,\mathbf{k}}(\mathbf{R}) = \frac{1}{\sqrt{N}} \sum_{\mathbf{R}_n} e^{i\mathbf{k}\mathbf{R}_n} \phi_{\mu}(\mathbf{R} - \mathbf{R}_n). \quad (24)$$

In Eqs. (23) and (24), the index  $\mu$  labels all AOs in the zeroth primitive cell ( $\mu = 1, 2, \dots, M$ ) and the index  $i$  numbers the energy bands ( $i = 1, 2, \dots, M$ ). The Bloch sums, as well as the AOs, do not compose an orthonormal basis; that is, the overlap integrals

$$S_{\mu\nu}(\mathbf{k}) = \int d^3\mathbf{R} \chi_{\mu,\mathbf{k}}^*(\mathbf{R}) \chi_{\nu,\mathbf{k}}(\mathbf{R}), \quad (25)$$

$$s_{\mu\nu}(\mathbf{R}_n) = \int d^3\mathbf{R} \phi_{\mu}^*(\mathbf{R}) \phi_{\nu}(\mathbf{R} - \mathbf{R}_n)$$

are not equal to  $\delta_{\mu\nu}$ .

The crystal orbitals  $\psi_{i,\mathbf{k}}(\mathbf{r})$  compose an orthonormal set from which the following orthonormality relations can be derived for the elements of the matrix  $C(\mathbf{k})$  involved in Eq. (23):

$$\{C(\mathbf{k})S(\mathbf{k})C(\mathbf{k})\}_{ij} = \delta_{ij}. \quad (26)$$

In terms of the Bloch sums of AOs, the DM elements  $P_{\mu\nu}(\mathbf{k})$  can be expressed as

$$P_{\mu\nu}(\mathbf{k}) = \sum_i n_i(\mathbf{k}) C_{\mu i}(\mathbf{k}) C_{\nu i}^*(\mathbf{k}). \quad (27)$$

Within the LCAO approximation, the DM elements in the coordinate space are given by an expression similar to Eq. (12),

$$\rho_{\mu\nu}(\mathbf{R}_n) = \frac{1}{N} \sum_{\mathbf{k}} e^{-i\mathbf{k}\mathbf{R}_n} P_{\mu\nu}(\mathbf{k}), \quad (28)$$

and the DM in the reciprocal space is related to the DM in the coordinate space through a relation similar to Eq. (15),

$$P_{\mu\nu}(\mathbf{k}) = \sum_{\mathbf{R}_n} \exp(i\mathbf{k}\mathbf{R}_n) \rho_{\mu\nu}(\mathbf{R}_n). \quad (29)$$

In the reciprocal space, the analog of the normalization condition (19) for the DM in the AO representation is the relation

$$\text{Tr}(P(\mathbf{k})S(\mathbf{k})) = \sum_{\mu,\nu} P_{\mu\nu}(\mathbf{k}) S_{\mu\nu}(\mathbf{k}) = n. \quad (30)$$

The normalization condition for the DM in the coordinate space [analog of Eq. (6)] is

$$\sum_{\mathbf{R}_n} \text{Tr}[\rho(\mathbf{R}_n)s(-\mathbf{R}_n)] = n. \quad (31)$$

The idempotency relation for the density matrix  $P(\mathbf{k})$  in the reciprocal space (with allowance for the nonorthogonality of the AO basis) has the form [ $n_i(\mathbf{k}) = 0, 2$ ]

$$P(\mathbf{k})S(\mathbf{k})P(\mathbf{k}) = 2P(\mathbf{k}). \quad (32)$$

In the coordinate space, the idempotency relation for the DM is written as

$$\sum_{\mathbf{R}_m, \mathbf{R}_n} \rho(\mathbf{R}_m) S(\mathbf{R}_m' - \mathbf{R}_m) \rho(\mathbf{R}_n - \mathbf{R}_m') = 2\rho(\mathbf{R}_n). \quad (33)$$

In various semiempirical versions of the Hartree-Fock approximation, the orthonormal set of Lowdin atomic orbitals (LAOs) rather than the nonorthogonal AO basis is used; the LAOs are defined as

$$\chi_{\mu,\mathbf{k}}^L(\mathbf{R}) = \sum_{\nu} S_{\mu\nu}^{-1/2}(\mathbf{k}) \chi_{\nu\mathbf{k}}(\mathbf{R}). \quad (34)$$

In this basis, the normalization condition for the density matrix  $P^L(\mathbf{k})$  is simplified; instead of Eqs. (30) and (31), we have

$$\text{Tr}P^L(\mathbf{k}) = n, \quad \text{Tr}[\rho^L(0)] = n. \quad (35)$$

In the LAO basis, the idempotency relations for the DM in the coordinate and reciprocal spaces are similar to Eqs. (21) and (22) for the DM in the coordinate representation; in the reciprocal space, we have

$$P^L(\mathbf{k})P^L(\mathbf{k}) = 2P^L(\mathbf{k}), \quad (36)$$

and in the coordinate space, the relation has the form

$$\sum_{\mathbf{R}_m} \rho^L(\mathbf{R}_m)\rho^L(\mathbf{R}_n - \mathbf{R}_m) = 2\rho^L(\mathbf{R}_n). \quad (37)$$

In particular, for the zeroth primitive cell ( $\mathbf{R}_n = 0$ ), with allowance for the hermiticity of the DM, we have

$$\sum_{\mathbf{R}_n} \rho^L(\mathbf{R}_n)\rho^{L*}(\mathbf{R}_n) = 2\rho^L(0). \quad (38)$$

The off-diagonal elements of the DM in the AO basis determine the quantities

$$W_{AB}(\mathbf{R}_n) = \sum_{\mu \in A, \nu \in B} |\rho_{\mu\nu}^L(\mathbf{R}_n)|^2, \quad (39)$$

which are called the Wiberg indices of the crystal [10, 11]. The Wiberg indices  $W_{AB}(\mathbf{R}_n)$  can be interpreted as chemical-bond indices (orders) between atoms  $A$  and  $B$ . These indices are subject to a relation that is a consequence of the idempotency of the DM. To derive this relation, we consider the diagonal matrix elements of Eq. (38) and carry out summation over all AO indices of atom  $A$ . The result is

$$\sum_{B \neq A} \sum_{\mathbf{R}_n} W_{AB}(\mathbf{R}_n) = 2p_A^L - \sum_{\mu \in A} \rho_{\mu\mu}^L(\mathbf{0}). \quad (40)$$

Here,  $p_A^L$  is the total electron population (in Lowdin's sense) of atom  $A$ ,

$$p_A^L = \sum_{\mu} \rho_{\mu\mu}^L(\mathbf{0}). \quad (41)$$

Let us define the covalence  $C_A$  of atom  $A$  as the sum of the chemical-bond orders (Wiberg indices) between atom  $A$  and all other atoms of the crystal. Using the idempotency relation (40), we have

$$C_A = \sum_{B, \mathbf{R}_n \neq A, 0} W_{AB}(\mathbf{R}_n) = 2p_A^L - \sum_{\mu \in A} \rho_{\mu\mu}^L(\mathbf{0}). \quad (42)$$

It follows from Eq. (42) that the covalence of atom  $A$  in the crystal can be calculated either by summing the bond indices between atom  $A$  and all other atoms of the crystal or by using only single-center DM elements related to atom  $A$ . This property of the covalence is a consequence of the idempotency of the DM.

The above consideration holds for the density matrix of the basic domain of the crystal; that is, it is assumed that the number  $N$  of primitive cells in this domain is so large that the introduction of cyclic bound-

ary conditions virtually does not affect the density matrix of the infinite crystal.

#### 4. APPROXIMATE ONE-ELECTRON DENSITY MATRIX OF THE CRYSTAL

##### 4.1. Large-Unit-Cell Method for Generating a Set of Special Points in the Brillouin Zone

In actual practice, the electronic structure of a crystal is calculated using one-electron wave functions found at a finite (relatively small) number  $L$  of points  $\{\mathbf{k}_j\}$  in the BZ ( $j = 1, 2, \dots, L$ ). This raises the question of how the sum over  $\mathbf{k}$  points in the BZ should be approximately calculated in Eq. (12) for the one-electron DM of the crystal.

We consider a set of points  $\{\mathbf{k}_j\}$  generated by the large-unit-cell (LUC) method [6, 7]. In this method, the primitive lattice vectors  $\mathbf{a}_i$  ( $i = 1, 2, 3$ ) are transformed with the help of a matrix  $l$  whose elements are integers:

$$\mathbf{a}_j^L = \sum_{i=1}^3 l_{ji} \mathbf{a}_i, \quad L = |\det l|. \quad (43)$$

The basis vectors  $\mathbf{a}_j^L$  determine an LUC and a new Bravais superlattice. The LUC thus constructed has volume  $V_L = LV_a$  and consists of  $L$  primitive cells. The superlattice vectors  $\mathbf{A}$  are linear combinations (with integral-valued coefficients) of the basis vectors  $\mathbf{a}_i^L$ . The matrix  $l$  is chosen such that the point symmetry of the new superlattice is identical to that of the original lattice [7] (the corresponding transformation (43) is called a symmetric extension). The type of the direct lattice can be changed if there are several types of lattice with the given point symmetry. The LUC is conveniently chosen in the form of a Wigner-Seitz (WS) cell, which possesses the point symmetry of the lattice.

We introduce the cyclic boundary conditions for the crystal domain coinciding with the LUC; that is, we assume that all translations through the superlattice vectors  $\mathbf{A}$  are equivalent to the identity translation. Thus, we have a system of finite size, i.e., a cyclic cluster belonging to the symmetry group  $G^L = T^L F$  [12] (we consider only symmetric extensions). Here, the subgroup  $T^L$  includes  $L$  translations through the vectors  $\mathbf{R}_n^0$  of the original direct lattice that lie within the LUC or fall on its boundary. The lattice sites lying on the boundary of the LUC are connected by superlattice vectors  $\mathbf{A}$ . These lattice sites should be counted only once, because they belong simultaneously to several LUCs.

For the cyclic cluster thus constructed, the following orthogonality relations hold:

$$\frac{1}{L} \sum_{\mathbf{R}_n^0} e^{i\mathbf{k}_j \cdot \mathbf{R}_n^0} = \delta_{\mathbf{k}_j, \mathbf{g}}, \quad (44a)$$

$$\frac{1}{L} \sum_{\mathbf{k}_j} e^{-i\mathbf{k}_j \mathbf{R}_n^0} = \delta_{\mathbf{R}_n^0, \mathbf{A}}. \quad (44b)$$

These relations are a generalization of the analogous equations in (14) for the basic domain of the crystal. Equations (44) are more general, because the cyclic cluster is obtained with the help of transformation (43), in which the matrix  $l$  can be nondiagonal. The vectors  $\mathbf{k}_j$  in Eqs. (44) label  $L$  different irreducible representations of the group  $T^L$  and can be found from the relation

$$\exp(i\mathbf{k}_j \mathbf{A}) = 1 \quad (j = 1, 2, \dots, L). \quad (45)$$

Equation (44a) is a consequence of the orthogonality of the characters of irreducible representations of the translation group to the character of the unit representation ( $\mathbf{k}_j = 0$ ), while Eq. (44b) means that the characters of a regular representation of the group are equal to zero for all elements of the group except for the identity element (i.e., except for the identity translation and equivalent translations through the superlattice vectors  $\mathbf{A}$ ).

#### 4.2. Interpolation Procedure for Constructing an Approximation to the Density Matrix

Let the density matrix  $P(\mathbf{k})$  be known at a finite set of points  $\{\mathbf{k}_j\}$  ( $j = 1, \dots, L$ ) determined by the LUC method and, therefore, satisfying Eq. (45). Our aim is to approximate the DM at an arbitrary point  $\mathbf{k}$  in the BZ. The interpolation procedure discussed in this subsection is appropriate for calculations in both the coordinate representation and the AO basis. For this reason, we drop the indices on the DM, keeping in mind that these indices are  $\mathbf{r}$  and  $\mathbf{r}'$  in the coordinate representation and  $\mu$  and  $\nu$  in the AO or orthogonalized-AO representation.

The expansions of the density matrix  $P(\mathbf{k})$  given by Eqs. (15) and (29) can be rewritten in the form

$$P(\mathbf{k}) = \sum_{\mathbf{R}_n^0} e^{i\mathbf{k}\mathbf{R}_n^0} \rho(\mathbf{R}_n^0) + \sum_{\mathbf{A} \neq 0} \sum_{\mathbf{R}_n^0} e^{i\mathbf{k}(\mathbf{R}_n^0 + \mathbf{A})} \rho(\mathbf{R}_n^0 + \mathbf{A}), \quad (46)$$

where the translations ( $\mathbf{R}_n^0 + \mathbf{A}$ ) lie in the basic domain of the crystal. As mentioned above, the off-diagonal elements of the density matrix  $\rho(\mathbf{R}_n^0 + \mathbf{A})$  fall off with distance as Wannier functions (exponentially in the case of insulators). Therefore, as the LUC grows in size and the values of  $|\mathbf{A}|$  become sufficiently large, the second term in Eq. (46) will be small in magnitude. With

this in mind, we will approximate the density matrix  $\tilde{P}(\mathbf{k})$  of the crystal as follows [2]. In the expansion given by Eq. (46), we drop the sum over the superlattice sites with  $\mathbf{A} \neq 0$  and take the remaining expression as an interpolation formula for determining the DM at any  $\mathbf{k}$  point in the BZ; we rewrite this expression in the form

$$\tilde{P}(\mathbf{k}) = \sum_{\mathbf{R}_n^0} e^{i\mathbf{k}\mathbf{R}_n^0} \rho^0(\mathbf{R}_n^0). \quad (47)$$

This formula was proposed in [13] for the interpolation of an arbitrary periodic function  $f(\mathbf{k})$  (see also [2, 14, 15]). The interpolation coefficients  $\rho^0(\mathbf{R}_n^0)$  (the number of which is  $L$ ) can be found from the condition

$$\tilde{P}(\mathbf{k}_j) = \sum_{\mathbf{R}_n^0} e^{i\mathbf{k}_j \mathbf{R}_n^0} \rho^0(\mathbf{R}_n^0) = P(\mathbf{k}_j). \quad (48)$$

Using the orthogonality relation (44b), the interpolation coefficients can be found to be

$$\rho^0(\mathbf{R}_n^0) = \frac{1}{L} \sum_{\mathbf{k}_j} e^{-i\mathbf{k}_j \mathbf{R}_n^0} P(\mathbf{k}_j). \quad (49)$$

The coefficients  $\rho^0(\mathbf{R}_n^0)$  can also be represented as a sum of the DM elements  $\rho(\mathbf{R}_n^0)$  over the superlattice sites. Indeed, substituting Eq. (46) for  $P(\mathbf{k}_j)$  into Eq. (49) and using Eq. (44b), we have

$$\rho^0(\mathbf{R}_n^0) = \sum_{\mathbf{A}} \rho(\mathbf{R}_n^0 + \mathbf{A}). \quad (50)$$

It should be noted that the matrix  $\rho^0(\mathbf{R}_n^0)$  can be defined for all vectors  $\mathbf{R}_n^0$  of the Bravais lattice by using the appropriate extensions of Eqs. (49) and (50). It is easy to see that  $\rho^0(\mathbf{R}_n^0)$  is a periodic function of period  $\mathbf{A}$ .

Substituting Eq. (49) for the coefficients  $\rho^0(\mathbf{R}_n^0)$  into Eq. (47), we obtain an interpolation formula for the DM in the reciprocal space,

$$\tilde{P}(\mathbf{k}) = \sum_{\mathbf{k}_j} P(\mathbf{k}_j) \Omega_j(\mathbf{k}), \quad (51)$$

$$\Omega_j(\mathbf{k}) = \frac{1}{L} \sum_{\mathbf{R}_n^0} e^{i(\mathbf{k} - \mathbf{k}_j) \mathbf{R}_n^0}.$$

Here,  $\Omega_j(\mathbf{k})$  are interpolation weights, the sum of which is equal to unity (the normalization natural for weight-

ing factors). Indeed, using Eq. (44b), we find

$$\begin{aligned} \sum_{\mathbf{k}_j} \Omega_j(\mathbf{k}) &= \sum_{\mathbf{R}_n^0} e^{i\mathbf{k}\mathbf{R}_n^0} \left[ \frac{1}{L} \sum_{\mathbf{k}_j} e^{-i\mathbf{k}_j\mathbf{R}_n^0} \right] \\ &= \sum_{\mathbf{R}_n^0} e^{i\mathbf{k}\mathbf{R}_n^0} \delta_{\mathbf{R}_n^0, 0} = 1. \end{aligned} \quad (52)$$

For the appropriate DM in the coordinate space, one can write equations similar to Eqs. (12) and (28):

$$\begin{aligned} \tilde{\rho}(\mathbf{R}_n) &= \frac{1}{N} \sum_{\mathbf{k}} \exp(-i\mathbf{k}\mathbf{R}_n) \tilde{P}(\mathbf{k}) \\ &= \sum_{\mathbf{R}_n^0} \rho^0(\mathbf{R}_n^0) \left[ \frac{1}{N} \sum_{\mathbf{k}} e^{i\mathbf{k}(\mathbf{R}_n^0 - \mathbf{R}_n)} \right]. \end{aligned} \quad (53)$$

According to Eq. (14b), the expression in the square brackets on the right-hand side of Eq. (53) is equal to unity if the vector  $\mathbf{R}_n$  belongs to the set of vectors  $\{\mathbf{R}_n^0\}$  (i.e., if this vector lies within the LUC or on its boundary) and vanishes otherwise. Therefore, the appropriate DM can be represented in the form

$$\tilde{\rho}(\mathbf{R}_n) = \omega(\mathbf{R}_n) \rho^0(\mathbf{R}_n), \quad (54)$$

where  $\omega(\mathbf{R}_n)$  is the so-called weighting function [2, 3],

$$\omega(\mathbf{R}_n) = \frac{1}{N} \sum_{\mathbf{k}} e^{i\mathbf{k}(\mathbf{R}_n^0 - \mathbf{R}_n)} = \begin{cases} 1 & \mathbf{R}_n \in \{\mathbf{R}_n^0\} \\ 0 & \mathbf{R}_n \notin \{\mathbf{R}_n^0\}. \end{cases} \quad (55)$$

We note that the procedure described above for interpolating the DM in the BZ is not uniquely determined, because the LUC (i.e., the set of vectors  $\{\mathbf{R}_n^0\}$ ) can be variously chosen for the same superlattice. Furthermore, the LUC can be chosen differently for the pairs of DM indices  $\mathbf{r}$ ,  $\mathbf{r}'$  and  $\mu$ ,  $\nu$ . In this paper, the LUC is taken to be the Wigner–Seitz cell, because only this cell has a symmetry identical to the point symmetry of the superlattice in all cases. In order to correlate the LUC with a cyclic cluster, we choose the LUC to be dependent of the pair of DM indices as follows. In the coordinate representation, the LUC ( $V_A$  region) is centered at the point  $(\mathbf{r} - \mathbf{r}')$ ; therefore, we have

$$\begin{aligned} \omega_{\mathbf{r}, \mathbf{r}'}(\mathbf{R}_n) &= \omega(\mathbf{R}_n + \mathbf{r}' - \mathbf{r}) \\ &= \begin{cases} 1 & \mathbf{R}_n + \mathbf{r}' - \mathbf{r} \in V_A \\ 0 & \mathbf{R}_n + \mathbf{r}' - \mathbf{r} \notin V_A. \end{cases} \end{aligned} \quad (56)$$

In the AO representation, the LUC is centered at the point  $(\mathbf{d}_\mu - \mathbf{d}_\nu)$ , where  $\mathbf{d}_\mu$  and  $\mathbf{d}_\nu$  are the position vectors

of the two atoms to which the AOs with indices  $\mu$  and  $\nu$  belong, respectively. Thus, we have

$$\begin{aligned} \omega_{\mu\nu}(\mathbf{R}_n) &= \omega(\mathbf{R}_n + \mathbf{d}_\nu - \mathbf{d}_\mu) \\ &= \begin{cases} 1 & \mathbf{R}_n + \mathbf{d}_\nu - \mathbf{d}_\mu \in V_A \\ 0 & \mathbf{R}_n + \mathbf{d}_\nu - \mathbf{d}_\mu \notin V_A. \end{cases} \end{aligned} \quad (57)$$

The weighting function  $\omega_{\mu\nu}(\mathbf{R}_n)$  of Eq. (57) introduced into expressions for the DM specifies the cyclic boundary conditions and the cyclic cluster. Indeed, let an arbitrarily chosen LUC be fixed and let us consider the orbitals of atoms  $A$  and  $B$  in this LUC ( $\mu \in A$ ,  $\nu \in B$ ). Out of all matrix elements  $\tilde{\rho}_{\mu\nu}(\mathbf{R}_n + \mathbf{A})$  with indices  $\mu$  and  $\nu$  kept fixed and the vector  $\mathbf{A}$  running over the superlattice, only one matrix element is nonzero. For this matrix element, the vector  $(\mathbf{d}_\nu + \mathbf{R}_n + \mathbf{A})$  (the position vector of atom  $B$ ) falls into the Wigner–Seitz cell centered at the atom- $A$  site. This matrix element exactly equals the matrix element  $\rho_{\mu\nu}^0(\mathbf{R}_n)$ .

#### 4.3. Essential Features of the Approximate Density Matrix

According to Eq. (54), the approximate density matrix  $\tilde{\rho}(\mathbf{R}_n)$  found by interpolation in the BZ contains the weighting function of Eqs. (55)–(57) as a factor. This function ensures the proper behavior of the off-diagonal elements of the approximate DM as  $|\mathbf{R}_n| \rightarrow \infty$ . As already mentioned, the matrix  $\rho^0(\mathbf{R}_n)$  without a weighting factor is a periodic (not vanishing at infinity) function,

$$\rho^0(\mathbf{R}_n + \mathbf{A}) = \rho^0(\mathbf{R}_n). \quad (58)$$

However, this DM is frequently used in many calculations based on the Hartree–Fock approximation or its semiempirical versions for crystals (the CNDO and INDO methods). In those calculations, all summations over the lattice sites are usually truncated by introducing interaction ranges. The nondecaying density matrix  $\rho^0(\mathbf{R}_n)$  gives rise to a divergent exchange term in the Fock matrix [2]. In other words, as the corresponding interaction range increases in size at a fixed number of involved  $\mathbf{k}$  points, the results do not converge to a certain limit and the total energy of the system sharply decreases. In order to avoid these divergences, the exchange interaction range should be chosen such that the corresponding sphere differs only slightly from the Wigner–Seitz cell of the superlattice, which generates precisely the set of  $\mathbf{k}$  points used in the calculations. In this case, the size of the summation domain in the coordinate space is in accord with the number of  $\mathbf{k}$  points used in the calculations and the exchange term in the Fock operator does not diverge. The approximate density matrix  $\tilde{\rho}(\mathbf{R}_n)$  is not subject to these drawbacks, and the balance between the size of the summation domain

in the coordinate space and the number of  $\mathbf{k}_j$  points involved occurs automatically [2].

It should be noted that in the versions of the density-functional theory in which the exchange-correlation term depends on the electron density alone, both approaches are equivalent. Indeed, the electron density  $\rho(\mathbf{R}, \mathbf{R}) = \rho_{r,r}(0)$  depends only on the diagonal elements of the DM; therefore, the weighting function of Eqs. (55) and (56) is equal to unity in this case.

In general, the approximate DM does not satisfy all the conditions to which the exact DM is subject. Let us elucidate which of the relations presented in Section 2 holds for the approximate DM and which do not.

The normalization conditions (5), (31), and (35) are very important. The approximate DM in the coordinate representation and in the LAO basis meets these conditions because the weighting function for the diagonal elements of the DM is equal to unity. In the nonorthogonal AO basis, a modified normalization condition is satisfied,

$$\sum_{\mathbf{R}_n} \text{Tr}[\tilde{\rho}(\mathbf{R}_n)\tilde{s}(-\mathbf{R}_n)] = n, \quad (59)$$

where  $\tilde{s}(\mathbf{R}_n)$  is an approximate overlap-integral matrix, which is obtained by interpolating in the BZ in much the same way as the approximate DM was obtained and has the form

$$\begin{aligned} \tilde{s}_{\mu\nu}(\mathbf{R}_n) &= \omega(\mathbf{R}_n + \mathbf{d}_\nu - \mathbf{d}_\mu)s_{\mu\nu}^0(\mathbf{R}_n), \\ s_{\mu\nu}^0(\mathbf{R}_n) &= \frac{1}{L} \sum_{\mathbf{k}_j} e^{-i\mathbf{k}_j \cdot \mathbf{R}_n} S(\mathbf{k}_j) = \sum_{\mathbf{A}} s(\mathbf{R}_n + \mathbf{A}). \end{aligned} \quad (60)$$

It is easy to verify that in all cases the approximate DM is Hermitian; i.e., it obeys relations identical to Eqs. (17) and (18).

In general, the approximate DM is not idempotent, because Eq. (22) holds only at points  $\mathbf{k} = \mathbf{k}_j$  ( $j = 1, 2, \dots, L$ ) and is not satisfied at other points of the BZ. For this reason, Eqs. (21) and (37) in the coordinate space do not generally hold. However, in the important particular case where the vector  $\mathbf{R}_n$  in these equations is zero, the idempotency relation is satisfied. In the coordinate space and in the LAO representation, we have

$$\sum_{\mathbf{R}_m} \tilde{\rho}(\mathbf{R}_m)\tilde{\rho}(-\mathbf{R}_m) = 2\tilde{\rho}(0). \quad (61)$$

Therefore, the relation important for the Wiberg indices (42) is also satisfied.

We note that the matrix  $\rho^0(\mathbf{R}_n)$  obeys the relation

$$\sum_{\mathbf{R}_m^0} \rho^0(\mathbf{R}_m^0)\rho^0(\mathbf{R}_n^0 - \mathbf{R}_m^0) = 2\rho^0(\mathbf{R}_n^0). \quad (62)$$

In the strict sense, Eq. (62) is not an idempotency relation, because summation is carried out only over the vectors  $\mathbf{R}_m^0$  lying within the LUC, whereas the vector difference  $(\mathbf{R}_n^0 - \mathbf{R}_m^0)$  can lie outside the LUC. If we perform summation over all Bravais lattice vectors, the right-hand side of Eq. (62) will diverge, because  $\rho^0(\mathbf{R}_n)$  does not vanish at infinity.

For the approximate DM to have the proper point symmetry, the LUC should be taken to be the Wigner–Seitz (WS) cell. In this case, however, the symmetry can be broken if, on the boundary of the WS cell, there are atoms of the crystal. Indeed, if an atom lies on the WS cell boundary, then there is one or several equivalent atoms that also lie on the boundary of the cell and their position vectors differ from that of the former atom by a superlattice vector  $\mathbf{A}$ . When constructing the approximate density matrix  $\tilde{\rho}$ , we assigned only one of several equivalent atoms to the WS cell. In other words, in the set  $\{\mathbf{R}_n^0\}$ , there are no two vectors that differ from each other by a superlattice vector  $\mathbf{A}$ . In this case, if a point-symmetry operation takes one boundary atom into another atom assigned to another WS cell, then the point symmetry of the density matrix  $\tilde{\rho}$  is broken, because the symmetry of the weighting function  $\omega_{\mu\nu}(\mathbf{R}_n)$  of Eq. (57) is broken.

Since it is desirable to preserve the point symmetry when calculating the electronic structure, the approximate DM can be replaced by an averaged density matrix  $\rho^s$  (see also [14, 16–18]):

$$\rho^s(\mathbf{R}_n) = \frac{1}{N_s} \sum_{\alpha=1}^{N_s} \tilde{\rho}^\alpha(\mathbf{R}_n) = \omega^s(\mathbf{R}_n)\rho^0(\mathbf{R}_n). \quad (63)$$

Here, the index  $\alpha = 1, 2, \dots, N_s$  labels all  $N_s$  possible ways in which one of the equivalent boundary atoms can be assigned to a given WS cell and the symmetrical weighting function  $\omega^s(\mathbf{R}_n)$  is defined as

$$\begin{aligned} \omega_{\mu\nu}^s(\mathbf{R}_n) &= \frac{1}{N_s} \sum_{\alpha=1}^{N_s} \omega_{\mu\nu}^\alpha(\mathbf{R}_n) \\ &= \begin{cases} \frac{1}{n_{\mu\nu}^s} & \mathbf{R}_n + \mathbf{d}_\nu - \mathbf{d}_\mu \in V_A \\ 0 & \mathbf{R}_n + \mathbf{d}_\nu - \mathbf{d}_\mu \notin V_A, \end{cases} \end{aligned} \quad (64)$$

where  $n_{\mu\nu}^s$  is the number of atoms in the WS cell (including its boundary) that are translationally equivalent to atom  $B$  ( $\nu \in B$ ) in the case where the WS cell is centered at the atom- $A$  site ( $\mu \in A$ ). In other words,  $n_{\mu\nu}^s$  is the number of WS cells that have atom  $B$  in common. If atom  $B$  is strictly inside the WS cell, then  $n_{\mu\nu}^s = 1$  and Eq. (64) is identical to Eq. (57). We note that the density

matrix  $\rho^s(\mathbf{R}_n)$  does not satisfy idempotency relation (61) and corresponds to a mixed state of the system. However, as the LUC enlarges, the effect of the boundary atoms decreases and the density matrix  $\rho^s(\mathbf{R}_n)$  approaches the idempotent density matrix  $\rho(\mathbf{R}_n)$ .

### 5. HARTREE–FOCK METHOD AND DENSITY-FUNCTIONAL THEORY IN THE CO-LCAO APPROXIMATION

The energy of the crystal (per primitive cell) as calculated within the Hartree–Fock (HF) approximation ( $E_{\text{HF}}$ ) and DFT ( $E_{\text{DFT}}$ ) can be expressed in terms of the one-electron DM:

$$\begin{aligned} E_{\text{HF}}[\rho] &= E_0[\rho] + E_H[\rho] + E_X[\rho], \\ E_{\text{DFT}}[\rho] &= E_0[\rho] + E_H[\rho] + E_{XC}[\rho], \end{aligned} \quad (65)$$

where  $E_0[\rho]$  is the one-electron energy, which is defined as the expectation value of the one-electron operator  $\hat{h}(\mathbf{R})$ ,

$$E_0[\rho] = \frac{1}{N} \int_{V_N} d^3\mathbf{R} \hat{h}(\mathbf{R}) \rho(\mathbf{R}, \mathbf{R}') \Big|_{\mathbf{R}'=\mathbf{R}}; \quad (66)$$

$E_H[\rho]$  is the Coulomb (Hartree) energy,

$$E_H[\rho] = \frac{1}{N} \int_{V_N} d^3\mathbf{R} \int_{V_N} d^3\mathbf{R}' \frac{\rho(\mathbf{R}, \mathbf{R})\rho(\mathbf{R}', \mathbf{R}')}{|\mathbf{R}-\mathbf{R}'|}; \quad (67)$$

$E_X[\rho]$  is the HF exchange energy,

$$E_X[\rho] = -\frac{1}{2} \frac{1}{N} \int_{V_N} d^3\mathbf{R} \int_{V_N} d^3\mathbf{R}' \frac{|\rho(\mathbf{R}, \mathbf{R}')|^2}{|\mathbf{R}-\mathbf{R}'|}; \quad (68)$$

and  $E_{XC}[\rho]$  is the exchange-correlation energy,

$$E_{XC}[\rho] = \frac{1}{N} \int_{V_N} d^3\mathbf{R} \rho(\mathbf{R}, \mathbf{R}) \varepsilon_{XC}[\rho]. \quad (69)$$

In Eq. (69),  $\varepsilon_{XC}[\rho]$  is the exchange-correlation energy per electron as calculated within the uniform electron gas approximation.

In the HF approximation and DFT, the crystal orbitals are solutions to the equations

$$\hat{F}(\mathbf{k})\psi_{i,\mathbf{k}} = \varepsilon_i(\mathbf{k})\psi_{i,\mathbf{k}}, \quad (70)$$

where the one-electron operator  $\hat{F}$  is either the HF operator  $\hat{F}^{\text{HF}}(\mathbf{k})$ ,

$$\hat{F}^{\text{HF}}(\mathbf{k}) = \hat{H}(\mathbf{k}) + \hat{J}(\mathbf{k}) + \hat{X}(\mathbf{k}), \quad (71)$$

or the Kohn–Sham operator  $\hat{F}^{\text{DFT}}(\mathbf{k})$ ,

$$\hat{F}^{\text{DFT}}(\mathbf{k}) = \hat{H}(\mathbf{k}) + \hat{J}(\mathbf{k}) + \hat{V}_{XC}(\mathbf{k}). \quad (72)$$

Here,  $\hat{H}(\mathbf{k})$  is a one-electron operator which describes the motion of an electron in the crystal and is equal to the sum of the kinetic-energy operator and the Coulomb interaction operator between the electron and fixed atomic nuclei and  $\hat{J}(\mathbf{k})$  and  $\hat{X}(\mathbf{k})$  are the Coulomb and exchange operators, respectively, which describe the interaction of the given electron with the other electrons of the crystal. In the LCAO basis, the Hartree–Fock and Kohn–Sham operators in the reciprocal space are represented by the Fock matrices  $F_{\mu\nu}^{\text{HF}}(\mathbf{k})$  and Kohn–Sham matrices  $F_{\mu\nu}^{\text{DFT}}(\mathbf{k})$ , which are related to the matrices in the coordinate space by the relations

$$F_{\mu\nu}^{\text{HF}}(\mathbf{k}) = \sum_{\mathbf{R}_n} e^{i\mathbf{k}\mathbf{R}_n} [h_{\mu\nu}(\mathbf{R}_n) + j_{\mu\nu}(\mathbf{R}_n) + x_{\mu\nu}(\mathbf{R}_n)], \quad (73)$$

$$F_{\mu\nu}^{\text{DFT}}(\mathbf{k}) = \sum_{\mathbf{R}_n} e^{i\mathbf{k}\mathbf{R}_n} [h_{\mu\nu}(\mathbf{R}_n) + j_{\mu\nu}(\mathbf{R}_n) + v_{\mu\nu}^{XC}(\mathbf{R}_n)],$$

where  $h_{\mu\nu}(\mathbf{R}_n)$ ,  $j_{\mu\nu}(\mathbf{R}_n)$ , and  $x_{\mu\nu}(\mathbf{R}_n)$  are the one-electron, Coulomb, and exchange parts of the Fock matrix in the coordinate space, respectively. The Coulomb part  $j_{\mu\nu}(\mathbf{R}_n)$  of the Fock matrix is defined as

$$\begin{aligned} j_{\mu\nu}(\mathbf{R}_n) &= \sum_{\lambda, \sigma} \sum_{\mathbf{R}_m, \mathbf{R}_m'} \rho_{\lambda\sigma}(\mathbf{R}_m) \int d^3\mathbf{R} \int d^3\mathbf{R}' \phi_{\mu}(\mathbf{R}) \\ &\times \phi_{\nu}(\mathbf{R}-\mathbf{R}_n) \frac{1}{|\mathbf{R}-\mathbf{R}'|} \phi_{\lambda}(\mathbf{R}'-\mathbf{R}_m) \phi_{\sigma}(\mathbf{R}'-\mathbf{R}_m-\mathbf{R}_m'). \end{aligned} \quad (74)$$

The exchange part of the Fock matrix can be obtained from Eq. (74) by interchanging the electron position vectors  $\mathbf{R}$  and  $\mathbf{R}'$  in the arguments of functions  $\phi_{\nu}(\mathbf{R}-\mathbf{R}_n)$  and  $\phi_{\lambda}(\mathbf{R}'-\mathbf{R}_m)$ :

$$\begin{aligned} x_{\mu\nu}(\mathbf{R}_n) &= -\frac{1}{2} \sum_{\lambda, \sigma} \sum_{\mathbf{R}_m, \mathbf{R}_m'} \rho_{\lambda\sigma}(\mathbf{R}_m) \int d^3\mathbf{R} \int d^3\mathbf{R}' \phi_{\mu}(\mathbf{R}) \\ &\times \phi_{\lambda}(\mathbf{R}-\mathbf{R}_m) \frac{1}{|\mathbf{R}-\mathbf{R}'|} \phi_{\nu}(\mathbf{R}'-\mathbf{R}_n) \phi_{\sigma}(\mathbf{R}'-\mathbf{R}_m-\mathbf{R}_m'). \end{aligned} \quad (75)$$

In the DFT, instead of the nonlocal-exchange interaction matrix  $x_{\mu\nu}(\mathbf{R}_n)$ , the exchange-correlation matrix  $v_{\mu\nu}^{XC}(\mathbf{R}_n)$  is used, with different exchange-correlation-functional approximations being employed in various versions of the DFT. In particular, in the local-density approximation (LDA), it is assumed that

$$\begin{aligned} v_{\mu\nu}^{XC}(\mathbf{R}_n) &= \int d^3\mathbf{R} \phi_{\mu}(\mathbf{R}) v^{XC}(\mathbf{R}) \phi_{\nu}(\mathbf{R}-\mathbf{R}_n), \\ v^{XC}(\mathbf{R}) &= \frac{\partial}{\partial \rho} \varepsilon[\rho(\mathbf{R})]. \end{aligned} \quad (76)$$

Here,  $\rho(\mathbf{R}) = \rho(\mathbf{R}, \mathbf{R})$  is the electron density. In the DFT, the exchange-correlation potential depends only on the electron density and, therefore, has no off-diagonal elements in the coordinate representation. In more accurate (than LDA) versions of the DFT, a gradient correction is added to the energy functional.

In the DFT, the electronic structure of a crystal is calculated, as a rule, in the plane-wave basis [19]. Recently, CO-LCAO calculations have been performed using the Crystal-95 computer code [20], which is based on both the HF method and DFT and allows one not only to make a comparison between the results obtained within these two approximations but also to employ a combination of these approximations. For example, the HF self-consistent electron density of the crystal can be used to calculate correlation corrections to the total HF energy *a posteriori*. Self-consistent calculations of the electronic structure of a crystal are also carried out using the so-called hybridized operator, which includes both the nonlocal HF exchange operator and the correlation potential derived from the density functional. The other terms in operators (71) and (72) are calculated in this case within the same approximations. In the LCAO approximation, the exchange-correlation potential  $v^{XC}(\mathbf{R})$  is expanded in the Gaussian AOs and the expansion coefficients are found self-consistently by fitting to an analytical expression in each iterative cycle.

In actual practice, calculations are performed for a relatively small number of points  $\mathbf{k}_j$  ( $j = 1, 2, \dots, L$ ), which are usually chosen using the LUC method with a diagonal [21] or nondiagonal matrix  $l$  [22] (see Eq. (43)). Such a set of wave vectors is chosen when constructing an approximate DM of the crystal. In the Crystal-95 computer code [20], the periodic (not vanishing at infinity) matrix  $\rho_{\mu\nu}^0(\mathbf{R}_n)$  is taken, in fact, as the approximate DM. Therefore, particular attention should be given to calculating lattice sums like Eqs. (74) and (75) in this case. We will consider this problem in more detail following [20].

In the Crystal-95 code [20], the accuracy to which the overlap-integral and kinetic-energy lattice sums are computed is controlled by parameter  $t_1$ ; the summation is terminated when the product of AOs at different centers becomes less than  $10^{-t_1}$ . The accuracy to which the Coulomb lattice sum  $j_{\mu\nu}(\mathbf{R}_n)$  is computed is also determined by parameter  $t_1$  and, in addition, by parameter  $t_2$ . When the overlap of the electron densities of different atoms becomes less than  $10^{-t_2}$ , the corresponding Coulomb interaction is treated as that of point multipoles.

The sums over  $\mathbf{R}_{m'}$  and  $\mathbf{R}_m$  in Eq. (75) for the exchange energy are convergent; the corresponding summation is controlled by parameter  $t_3$  and terminated when the  $\phi_\mu(\mathbf{R})\phi_\lambda(\mathbf{R} - \mathbf{R}_{m'})$  and  $\phi_\nu(\mathbf{R}' - \mathbf{R}_n)\phi_\sigma(\mathbf{R}' - \mathbf{R}_m - \mathbf{R}_{m'})$  AO overlap becomes less than  $10^{-t_3}$ . However,

when the periodic (not vanishing at infinity) matrix  $\rho^0(\mathbf{R}_n)$  is taken as the approximate DM, the matrix elements  $x_{\mu\nu}(\mathbf{R}_n)$  do not tend to zero as  $|\mathbf{R}_n| \rightarrow \infty$ . This can be easily verified by putting  $\mathbf{R}_{m'} = 0$  and  $\mathbf{R}_m = \mathbf{R}_n$  in the sums over  $\mathbf{R}_m$  and  $\mathbf{R}_{m'}$  in Eq. (75) and taking into account that the function  $1/|\mathbf{R} - \mathbf{R}'|$  slowly decreases with increasing  $|\mathbf{R} - \mathbf{R}'|$ . Because of this improper asymptotic behavior of  $x_{\mu\nu}(\mathbf{R}_n)$ , the exchange part of the Fock operator in the reciprocal space diverges at  $\mathbf{k} = 0$  and the total energy of the crystal also becomes divergent. In order to avoid these divergences, the appropriate interaction ranges (determined by parameters  $t_4$  and  $t_5$ ) are introduced in the Crystal-95 code; the DM elements  $\rho_{\mu\nu}(\mathbf{R}_n)$  and  $\rho_{\lambda\sigma}(\mathbf{R}_m)$  in Eq. (75) are taken equal to zero if the  $\phi_\mu(\mathbf{R})\phi_\nu(\mathbf{R} - \mathbf{R}_n)$  and  $\phi_\lambda(\mathbf{R})\phi_\sigma(\mathbf{R} - \mathbf{R}_m)$  AO products become less than  $10^{-t_4}$  and  $10^{-t_5}$ , respectively.

Such a scheme for calculating the lattice sums involved in the matrix elements of the energy operator was employed in [20] within both the HF approximation and DFT. In the former approach, the accuracy of computation of integrals was controlled by all of the parameters  $t_1$  to  $t_5$ ; in the latter, only by  $t_1$  and  $t_2$ .

We propose three different versions of the HF method in which the approximate density matrix  $\rho^s(\mathbf{R}_n)$  is used instead of the matrix  $\rho^0(\mathbf{R}_n)$  not vanishing at infinity.

In the first version, the density matrix  $\rho_{\lambda\sigma}(\mathbf{R}_m)$  in Eq. (75) for the exchange part  $x_{\mu\nu}(\mathbf{R}_n)$  of the Fock matrix is replaced by the approximate DM  $\rho_{\lambda\sigma}^s(\mathbf{R}_n)$ , which differs from  $\rho_{\lambda\sigma}^0(\mathbf{R}_n)$  in that the former contains the weighting factor  $\omega_{\lambda\sigma}^s(\mathbf{R}_n)$  [see Eq. (63)]. The introduction of this factor removes the divergence of the exchange energy of the crystal and the imbalance between the number of  $\mathbf{k}$  points in the BZ involved in calculations and the summation procedure over the direct lattice in Eq. (75). In this case, there is no need to introduce artificial cutoffs determined by parameters  $t_4$  and  $t_5$ . This version allows one to calculate the electronic structure of the infinite crystal (or its basic domain) by using a proper DM rapidly vanishing at infinity in constructing the exchange potential.

In the second version, the density matrix  $\rho_{\lambda\sigma}^s(\mathbf{R}_m)$  is substituted not only into the exchange part of the Fock matrix in Eq. (75) but also into the Coulomb part  $j_{\mu\nu}(\mathbf{R}_n)$  of the Fock matrix in Eq. (74). In this case, however, one should redefine the overlap integral matrix  $\tilde{s}_{\mu\nu}(\mathbf{R}_n)$  in accordance with Eq. (60) in order to preserve the normalization relation (59). This version, as well as the first, corresponds to calculation of the elec-

tronic structure of the infinite crystal (or its basic domain).

In the third version, the approximate DM  $\rho_{\lambda\sigma}^s(\mathbf{R}_m)$  is substituted into the total energy of the crystal in Eq. (65) and both the HF energy  $E_{\text{HF}}[\rho^s]$  and DFT energy  $E_{\text{DFT}}[\rho^s]$  are calculated. Equations for the crystal orbitals can be found by minimizing the energies  $E_{\text{HF}}[\rho^s]$  and  $E_{\text{DFT}}[\rho^s]$ . The distinctive feature of this version is that the cutoff weighting function  $\omega_{\mu\nu}^s(\mathbf{R}_n)$  is also involved as a factor in all lattice sums for the one-electron and two-electron parts of the Fock matrix in Eq. (73):

$$F_{\mu\nu}^{\text{HF}}(\mathbf{k}) = \sum_{\mathbf{R}_n} e^{i\mathbf{k}\mathbf{R}_n} \omega_{\mu\nu}^s(\mathbf{R}_n) \times [h_{\mu\nu}(\mathbf{R}_n) + j_{\mu\nu}(\mathbf{R}_n) + x_{\mu\nu}(\mathbf{R}_n)]. \quad (77)$$

Thus, in the third version, the cutoff factor  $\omega_{\lambda\sigma}^s(\mathbf{R}_n)$  is introduced in all lattice sums, in particular, in the overlap integral matrices and kinetic-energy matrix. The introduction of a cutoff factor in these sums is equivalent to considering a cyclic cluster placed in an external electric field (Madelung field) produced by various (finite-size) multipoles. The field due to charges and multipoles is determined by the diagonal DM elements  $\rho_{\mu\mu}^s(0)$  for which the weighting function  $\omega_{\mu\mu}^s(0)$  equals unity. Thus, there is an intimate relationship between the interpolation procedure proposed for calculating the DM of the infinite crystal in the  $\mathbf{k}$  space and a cyclic cluster equal to the LUC in size.

In this paper, we employed the first version of modified HF equations. In the next section, we discuss the electronic structures of a number of crystals computed by means of the Crystal-95 code without and with allowance for the weighting function.

## 6. CALCULATED ELECTRONIC STRUCTURES OF $\text{BN}_{\text{hex}}$ , Si, AND RUTILE $\text{TiO}_2$ CRYSTALS

From the above discussion of calculations of the electronic structure of an infinite crystal and a cyclic cluster by using the HF and DFT methods, we can draw some practically important conclusions. Such calculations are performed first for a set of points  $\mathbf{k}_j$  ( $j = 1, 2, \dots, L$ ) chosen in the BZ and then for enlarged sets  $\{\mathbf{k}_j\}$  until the results become convergent. In this paper, we investigated the convergence of quantities such as the total energy per primitive cell, the energies corresponding to the top of the valence band and the bottom of the conduction band, the band width, and the atomic charges and covalences.

The calculations are performed for (i) hexagonal BN (in the single-layer model) having two atoms per primitive cell and belonging to the double-periodic

symmetry group  $D_{3h}^1$ , (ii) a cubic Si crystal having two atoms per primitive cell and belonging to the space group  $O_h^7$  ( $Fd3m$ ), and (iii) a rutile-structure  $\text{TiO}_2$  crystal having a tetragonal lattice and belonging to the space group  $D_{4h}^{14}$  ( $P4_2/mnm$ ). By choosing these crystals, we can compare the convergence of calculations for crystals with different chemical-bond covalence (a pure covalent Si crystal, a BN crystal with weakly distributed charge, and an essentially ionic  $\text{TiO}_2$  crystal).

We employed the Crystal-95 computer code [20], which allows one to perform computations within the LCAO approximation by using the HF and DFT methods. The lattice parameters are taken to be equal to their theoretical values for  $\text{BN}_{\text{hex}}$  ( $a = 2.504 \text{ \AA}$ ), Si ( $c = 5.460 \text{ \AA}$ ), and  $\text{TiO}_2$  ( $a = 4.555 \text{ \AA}$ ,  $c = 2.998 \text{ \AA}$ ) calculated in [23–25], respectively. The AO bases for Si, Ti, and O are also taken from those papers. For  $\text{BN}_{\text{hex}}$ , the STO-3G basis is used. In the DFT calculations, we used the Becke–Lyp exchange-correlation potential [26], which includes a gradient correction.

As indicated in Section 5, the accuracy of calculations of lattice sums in the Crystal-95 code is controlled by parameters  $t_1, t_2, \dots, t_5$  in the HF method and by  $t_1$  and  $t_2$  in DFT. In our computations, we put  $t_1 = t_2 = t_3 = t_4 = 6$  and  $t_5 = 12$ . For such values of the parameters, summations over the direct lattice cover domains of radius  $R_s$ , equal to 9.03, 11.17, and 8.16  $\text{\AA}$  for  $\text{BN}_{\text{hex}}$ , Si, and  $\text{TiO}_2$  crystals, respectively.

The results are listed in Tables 1–3. In the first columns, the transformation matrices  $l$  defined by Eq. (43) are presented; these matrices determine the direct-lattice domains and the corresponding sets of  $L$  vectors  $\{\mathbf{k}_j\}$ . Columns 2 to 10 present the following: the number  $J$ , which is the number of the translation-vector shell determining the LUC (the number of points  $\mathbf{k}_j$  and, hence, the accuracy of calculations of the approximate DM  $\tilde{\rho}$  are increased with increasing  $J$ ); the radii  $R_j$  and  $R_X$ , which characterize the localization region of the Wannier functions for the diagonal and off-diagonal DM elements, respectively [see Eq. (10)]; next, the energy characteristics are listed (the total energy per primitive cell  $E_{\text{tot}}$ , the energy of the top of the valence band  $E_v$ , and the band gap width  $\Delta E_g$ ); and the atomic charges  $Q$  (Ti atom charge in the case of  $\text{TiO}_2$ ) and the chemical-bond orders  $W_{AB}$  (Wiberg indices) for the nearest neighbors as calculated from the LAO populations using Eq. (39). For the Si crystal (in which we have  $Q_{\text{Si}} = 0$ ), the covalence  $C_A$  of the Si atom is presented. The calculations are performed using three methods: the standard HF method ignoring the weighting function [20], the HF method with allowance for the

**Table 1.** Electronic structure of the  $\text{BN}_{\text{hex}}$  crystal ( $R_s = 9.03 \text{ \AA}$ )

Matrix $l$	$J$	$R_J (\text{\AA})$	$R_X (\text{\AA})$	Method	$E_{\text{tot}}$	$E_v$	$\Delta E_g$ (a.u.)	$ Q $	$W_{\text{B-N}}$
$\begin{pmatrix} 2 & 1 \\ -1 & 1 \end{pmatrix}$ $L = 3$	2	4.34	2.50	HF	-81.192	-0.992	1.381	0.356	0.987
				$\text{HF}_\omega$	-78.311	-0.260	0.558	0.353	1.047
				DFT	-78.632	-0.031	0.097	0.298	1.042
$\begin{pmatrix} 3 & 0 \\ 0 & 3 \end{pmatrix}$ $L = 9$	5	7.51	3.82	HF	-78.299	-0.268	0.617	0.356	1.120
				$\text{HF}_\omega$	-78.286	-0.239	0.508	0.353	1.123
				DFT	-78.693	-0.083	0.153	0.298	1.137
$\begin{pmatrix} 4 & 2 \\ -2 & 2 \end{pmatrix}$ $L = 12$	6	8.67	4.34	HF	-78.295	-0.252	0.564	0.258	1.116
				$\text{HF}_\omega$	-78.290	-0.245	0.516	0.259	1.116
				DFT	-78.694	-0.082	0.153	0.167	1.133
$\begin{pmatrix} 6 & 3 \\ -3 & 3 \end{pmatrix}$ $L = 27$	12	13.01	6.62	HF	-78.291	-0.241	0.508	0.260	1.123
				$\text{HF}_\omega$	-78.291	-0.241	0.507	0.260	1.123
				DFT	-78.697	-0.087	0.157	0.156	1.141
$\begin{pmatrix} 6 & 0 \\ 0 & 6 \end{pmatrix}$ $L = 36$	15	15.02	7.51	HF	-78.291	-0.240	0.504	0.259	1.124
				$\text{HF}_\omega$	-78.291	-0.240	0.504	0.259	1.124
				DFT	-78.697	-0.087	0.158	0.153	1.143

weighting function in the exchange part of the Fock matrix ( $\text{HF}_\omega$  method), and the DFT method.

The data presented in Tables 1 to 3 allow one to draw the following conclusions, which are applicable to all three crystals under study:

(1) In spite of the differences in the crystallographic structure and in the AO basis used, the convergence of the results for all three crystals sets in at parameter  $R_X$  values close to one another (7.51, 11.58, 8.99  $\text{\AA}$ ). In [27], the variations of the diagonal DM elements with distance were investigated for valence AOs in  $\text{BN}_{\text{hex}}$  and Si crystals. In those calculations, sets of points  $\{\mathbf{k}_j\}$  were used for which the convergence of HF computations already took place. It was found that these DM elements are close to zero for interatomic distances 7–10  $\text{\AA}$ , which correlates with the values of  $R_J$  calculated in this paper. The last statement does not contradict the fact that the approximate DM  $\rho^0$  without the weighting function is a periodic function of distance [see Eq. (58)] and does not vanish at infinity, because the spatial periods (superlattice parameters) for the given sets of  $\{\mathbf{k}_j\}$  are far larger than the interatomic distances under discussion. We also note that the values of the parameters  $R_x$  and  $R_s$  are close to each other when the convergence of calculations sets in. This is no surprise, because the calculations become convergent when the size of the localization region of Wannier functions (parameter  $R_x$ ) is close to the size of the region of crystal-lattice summation (parameter  $R_s$ ).

(2) For sets of  $\{\mathbf{k}_j\}$  relatively small in number ( $L = 3, 9$  for  $\text{BN}_{\text{hex}}$ ;  $L = 4, 8$  for Si;  $L = 2, 4, 9$  for  $\text{TiO}_2$ ), HF calculations not involving a weighting function lead to significantly lower values of the total energy of the crystal in comparison with the total energy calculated using  $\{\mathbf{k}_j\}$  sets large in number. The reason for this is that the DM  $\rho^0(\mathbf{R}_n)$  exhibits improper asymptotic behavior at large distances  $|\mathbf{R}_n|$  and, hence, is not idempotent. Because of the divergence mentioned in Section 4, the negative exchange energy becomes large in magnitude and the total energy of the crystal is considerably decreased. Such an artificial decrease in the total energy is particularly noticeable for large values of the parameters  $t_4$  and  $t_5$ , which truncate the lattice sums in the exchange energy. In calculations involving the weighting function, there are no artificial divergences and, when wave-vector sets small in number are used, the total energy is virtually always an upper-bound estimate, as it must be in variational calculations. We note that, in the case of the Si crystal, the introduction of the weighting function leads to the formation of a nonzero band gap for any  $\{\mathbf{k}_j\}$  set small in number. In HF calculations not involving a weighting function, the electronic structure is found to correspond to a metal in the case of  $L = 8$ , whereas in  $\text{HF}_\omega$  calculations, the electron density distribution is obtained to be close to the “exact” result even for  $\{\mathbf{k}_j\}$  sets very small in number.

(3) Because of the absence of nonlocal exchange terms in the Hamiltonian, the DFT method gives an upper-bound (typical of variational methods) estimate

**Table 2.** Electronic structure of the Si crystal ( $R_y = 11.17 \text{ \AA}$ )

Matrix $l$	$J$	$R_J (\text{\AA})$	$R_X (\text{\AA})$	Method	$E_{\text{tot}}$	$E_v$	$\Delta E_g$ (a.u.)	$C_A$	$W_{\text{Si-Si}}$
$\begin{pmatrix} 1 & -1 & -1 \\ -1 & 1 & -1 \\ -1 & -1 & 1 \end{pmatrix}$ $L = 4$	2	5.46	3.86	HF	-10.154	-4.900	1.602	3.647	0.816
				$\text{HF}_\omega$	-7.557	-0.216	0.285	4.146	0.999
				DFT	-7.643	-0.098	0.041	4.173	0.996
$\begin{pmatrix} 2 & 0 & 0 \\ 0 & 2 & 0 \\ 0 & 0 & 2 \end{pmatrix}$ $L = 8$	4	7.72	3.86	HF	-	Metal	0.0	-	-
				$\text{HF}_\omega$	-7.515	-0.230	0.293	4.160	0.998
				DFT	-7.645	-0.109	0.042	4.188	0.995
$\begin{pmatrix} 3 & -1 & -1 \\ -1 & 3 & -1 \\ -1 & -1 & 3 \end{pmatrix}$ $L = 16$	6	9.46	5.46	HF	-7.537	-0.208	0.308	4.176	0.952
				$\text{HF}_\omega$	-7.534	-0.216	0.251	4.154	0.964
				DFT	-7.724	-0.138	0.046	4.180	0.947
$\begin{pmatrix} -2 & 2 & 2 \\ 2 & -2 & 2 \\ 2 & 2 & -2 \end{pmatrix}$ $L = 32$	8	10.92	5.46	HF	-7.535	-0.223	0.254	4.149	0.967
				$\text{HF}_\omega$	-7.537	-0.228	0.247	4.165	0.955
				DFT	-7.727	-0.139	0.046	4.179	0.941
$\begin{pmatrix} 4 & 0 & 0 \\ 0 & 4 & 0 \\ 0 & 0 & 4 \end{pmatrix}$ $L = 64$	15	15.44	7.72	HF	-7.537	-0.226	0.260	4.155	0.966
				$\text{HF}_\omega$	-7.537	-0.227	0.257	4.157	0.966
				DFT	-7.728	-0.140	0.047	4.178	0.939
$\begin{pmatrix} 6 & 0 & 0 \\ 0 & 6 & 0 \\ 0 & 0 & 6 \end{pmatrix}$ $L = 216$	34	23.16	11.58	HF	-7.540	-0.223	0.230	4.155	0.961
				$\text{HF}_\omega$	-7.540	-0.223	0.230	4.155	0.961
				DFT	-7.733	-0.143	0.036	4.174	0.928
$\begin{pmatrix} 8 & 0 & 0 \\ 0 & 8 & 0 \\ 0 & 0 & 8 \end{pmatrix}$ $L = 512$	59	30.88	15.44	HF	-7.541	-0.222	0.228	4.155	0.961
				$\text{HF}_\omega$	-7.541	-0.222	0.230	4.155	0.961
				DFT	-7.734	-0.144	0.034	4.173	0.925

of the total energy of the crystal for any set of  $\mathbf{k}$  points. In this case, as is evident from numerous calculations available in the literature, the calculated band gap width  $\Delta E_g$  is always less than that given by the HF method. Allowance for correlation effects in DFT leads to a more covalent electron density distribution (in comparison with that given by the HF method); it follows from

Tables 1 and 3 that the atomic charges become noticeably smaller in the case of  $\text{BN}_{\text{hex}}$  and  $\text{TiO}_2$ .

(4) As the  $\{\mathbf{k}_j\}$  set is enlarged, calculations of the local characteristics of the electron density (atomic charges, chemical-bond orders) converge more rapidly than calculations of the energy characteristics do in all three methods.

**Table 3.** Electronic structure of the TiO<sub>2</sub> crystal ( $R_s = 8.16 \text{ \AA}$ )

Matrix $l$	$J$	$R_J (\text{\AA})$	$R_X (\text{\AA})$	Method	$E_{\text{tot}}$	$E_v$	$\Delta E_g (\text{a.u.})$	$Q_{\text{Ti}}$	$W_{\text{Ti-O}}$
$\begin{pmatrix} 0 & 1 & 1 \\ 1 & 0 & 1 \\ 1 & 1 & 0 \end{pmatrix}$ $L = 2$	3	5.45	2.99	HF	-70.171	-0.633	0.452	-0.033	0.630
				HF <sub><math>\omega</math></sub>	-69.732	-0.303	0.409	1.768	0.512
				DFT	-71.885	-0.222	0.363	2.605	0.364
$\begin{pmatrix} 0 & 1 & 2 \\ 1 & 0 & 2 \\ 1 & 1 & 0 \end{pmatrix}$ $L = 4$	5	6.44	3.45	HF	-69.790	-0.316	0.406	1.602	0.580
				HF <sub><math>\omega</math></sub>	-69.772	-0.303	0.397	1.697	0.556
				DFT	-71.323	-0.133	0.057	1.137	0.657
$\begin{pmatrix} -1 & 1 & 2 \\ 1 & -1 & 2 \\ 1 & 1 & -2 \end{pmatrix}$ $L = 8$	6	8.80	4.55	HF	-69.778	-0.307	0.391	1.719	0.560
				HF <sub><math>\omega</math></sub>	-69.775	-0.305	0.389	1.728	0.558
				DFT	-71.341	-0.135	0.057	1.110	0.656
$\begin{pmatrix} 2 & 0 & 0 \\ 0 & 2 & 0 \\ 0 & 0 & 3 \end{pmatrix}$ $L = 12$	9	8.99	4.55	HF	-69.775	-0.305	0.389	1.728	0.557
				HF <sub><math>\omega</math></sub>	-69.775	-0.304	0.389	1.729	0.556
				DFT	-71.349	-0.138	0.057	1.117	0.649
$\begin{pmatrix} 2 & 0 & 0 \\ 0 & 2 & 0 \\ 0 & 0 & 4 \end{pmatrix}$ $L = 16$	10	9.11	4.55	HF	-69.775	-0.303	0.387	1.730	0.557
				HF <sub><math>\omega</math></sub>	-69.775	-0.304	0.387	1.730	0.557
				DFT	-71.344	-0.138	0.055	1.112	0.649
$\begin{pmatrix} 2 & 0 & 0 \\ 0 & 2 & 0 \\ 0 & 0 & 6 \end{pmatrix}$ $L = 24$	10	9.11	4.55	HF	-69.775	-0.303	0.387	1.729	0.557
				HF <sub><math>\omega</math></sub>	-69.775	-0.304	0.387	1.729	0.557
				DFT	-71.343	-0.135	0.055	1.108	0.649
$\begin{pmatrix} 4 & 0 & 0 \\ 0 & 4 & 0 \\ 0 & 0 & 4 \end{pmatrix}$ $L = 64$	18	11.99	5.99	HF	-69.776	-0.303	0.386	1.728	0.557
				HF <sub><math>\omega</math></sub>	-69.776	-0.303	0.386	1.728	0.557
				DFT	-71.347	-0.139	0.058	1.103	0.650
$\begin{pmatrix} 6 & 0 & 0 \\ 0 & 6 & 0 \\ 0 & 0 & 6 \end{pmatrix}$ $L = 216$	45	17.99	8.99	HF	-69.776	-0.303	0.386	1.727	0.557
				HF <sub><math>\omega</math></sub>	-69.776	-0.303	0.386	1.727	0.557
				DFT	-71.348	-0.139	0.058	1.101	0.650

## 7. CONCLUSION

Thus, the results presented in this paper allow one to better understand the features of Hartree-Fock self-

consistent calculations of the electronic structure of an infinite crystal with a nonlocal exchange potential determined by the off-diagonal elements of the one-electron density matrix. It has been shown that the

number of  $\mathbf{k}$  points chosen in the BZ for calculations should be in accord with the size of the interaction range in the coordinate space. In other words, there should be a correlation between summations over the Bravais lattice in the coordinate space and over the BZ in the reciprocal space. It was also shown that when the Fock operator or the Kohn–Sham operator contains off-diagonal DM elements, the BZ special-point technique should be modified. By performing calculations for particular systems, it was shown that the introduction of the weighting function  $\omega(\mathbf{R}_n)$  in the direct-lattice sums entering the exchange term establishes the necessary balance and removes the artificial divergences.

The comparison made between the HF operators in the infinite-crystal and cyclic-cluster models in Section 5 makes it possible to understand the relation between these models. The equations derived within the cyclic-cluster model by using the variational method are different from the equations following from the HF equations for an infinite crystal in which the weighting function is introduced. This important problem will be the subject of our next publication.

#### ACKNOWLEDGMENTS

The authors are grateful to Professor I.V. Abarenkov and Dr. A.V. Leko for helpful discussions.

This study was supported by the Russian Foundation for Basic Research, project no. 99-03-33255.

#### REFERENCES

1. M. I. Petrashen', N. N. Kristofel', and I. V. Abarenkov, *Vestn. Leningr. Univ., Ser. Fiz., Khim.*, No. 10, 5 (1963).
2. R. Evarestov and I. Tupitsyn, *Russ. J. Phys. Chem.* **74**, Suppl. 2, S363 (2000).
3. R. A. Evarestov, V. A. Lovchikov, and I. I. Tupitsyn, *Phys. Status Solidi B* **117**, 417 (1983).
4. R. A. Évarestov, V. A. Lovchikov, and I. I. Tupitsyn, *Fiz. Tverd. Tela (Leningrad)* **25**, 625 (1983) [*Sov. Phys. Solid State* **25**, 355 (1983)].
5. D. J. Chadi and M. J. Cohen, *Phys. Rev. B* **8**, 5747 (1973).
6. R. A. Evarestov and V. P. Smirnov, *Site Symmetry in Crystals: Theory and Applications* (Springer, Heidelberg, 1997, 2nd ed.), Springer Series in Solid State Sciences, Vol. 108.
7. R. A. Evarestov and V. P. Smirnov, *J. Phys.: Condens. Matter* **9**, 3023 (1997).
8. J. des Cloizeaux, *Phys. Rev.* **135**, A685 (1964); **135**, A698 (1964).
9. E. K. Kudinov, *Fiz. Tverd. Tela (St. Petersburg)* **41**, 1582 (1999) [*Phys. Solid State* **41**, 1450 (1999)].
10. K. B. Wiberg, *Tetrahedron* **24**, 1083 (1968).
11. V. A. Veryazov, A. V. Leko, and R. A. Évarestov, *Fiz. Tverd. Tela (St. Petersburg)* **41**, 1407 (1999) [*Phys. Solid State* **41**, 1286 (1999)].
12. R. A. Evarestov, A. V. Leko, and V. P. Smirnov, *Phys. Status Solidi B* **128**, 275 (1985).
13. R. A. Evarestov and V. P. Smirnov, *Phys. Status Solidi B* **119**, 9 (1983).
14. C. Pisani, E. Apra, and M. Causa, *Int. J. Quantum Chem.* **38**, 395 (1990).
15. C. Pisani, R. Dovesi, and C. Roetti, *Hartree-Fock ab initio Treatment of Crystalline Systems* (Springer, Berlin, 1988), Lecture Notes in Chemistry, Vol. 48.
16. T. Bredow, R. A. Evarestov, and K. Jug, *Phys. Status Solidi B* **222**, 495 (2000).
17. T. Bredow, G. Geudtner, and K. Jug, *J. Comput. Chem.* **22**, 89 (2001).
18. P. Deak, *Phys. Status Solidi B* **217**, 9 (2000).
19. M. C. Payne, M. P. Teter, D. C. Alan, *et al.*, *Rev. Mod. Phys.* **64**, 1045 (1992).
20. R. Dovesi, V. R. Saunders, C. Roetti, N. M. Harrison, R. Orlando, and E. Apra, *Crystal-95 Manual* (Torino, 1996).
21. H. J. Monkhorst and J. D. Pack, *Phys. Rev. B* **13**, 5188 (1976).
22. J. Moreno and J. M. Soler, *Phys. Rev. B* **45**, 13891 (1992).
23. R. Dovesi, C. Pisani, and C. Roetti, *Int. J. Quantum Chem.* **17**, 517 (1980).
24. M. Causa, R. Dovesi, and C. Roetti, *Phys. Rev. B* **43**, 11937 (1991).
25. B. Silvi, N. Fourati, R. Nada, and C. R. Catlow, *J. Phys. Chem. Solids* **52**, 1005 (1991).
26. A. D. Becke, *J. Chem. Phys.* **88**, 2547 (1988).
27. C. Pisani, E. Apra, M. Causa, and R. Orlando, *Int. J. Quantum Chem.* **38**, 419 (1990).

*Translated by Yu. Epifanov*

---

---

**DEFECTS, DISLOCATIONS,  
AND PHYSICS OF STRENGTH**

---

---

# Nonradiative Relaxation of Photoexcited $O_1^0$ Centers in Glassy $SiO_2$

A. F. Zatsepin, D. Yu. Biryukov, V. S. Kortov, and S. O. Cholakh

Ural State Technical University, ul. Mira 19, Yekaterinburg, 620002 Russia

e-mail: zats@dpt.ustu.ru

Received December 3, 2001

**Abstract**—The processes involved in the excited-state relaxation of hole  $O_1^0$  centers at nonbridging oxygen atoms in glassy  $SiO_2$  were studied using luminescence, optical absorption, and photoelectron emission spectroscopy. An additional nonradiative relaxation channel, in addition to the intracenter quenching of the 1.9-eV luminescence band, was established to become operative at temperatures above 370 K. This effect manifests itself in experiments as a negative deviation of the temperature-dependent luminescence intensity from the well-known Mott law and is identified as thermally activated external quenching with an energy barrier of 0.46 eV. Nonradiative transitions initiate, within the external quenching temperature interval, the migration of excitation energy, followed by the creation of free electrons. In the final stages, this relaxation process becomes manifest in the form of spectral sensitization of electron photoemission, which is excited in the hole  $O_1^0$ -center absorption band. © 2002 MAIK “Nauka/Interperiodica”.

## 1. INTRODUCTION

Silicon dioxide plays a significant part in conventional and integrated optics, electronics, and microelectronics. The operating characteristics of the various  $SiO_2$ -based devices depend substantially on the presence of photosensitive defects in the  $SiO_2$  structure. Structural defects form in the material in the course of its preparation (for instance, in crystal growth or quartz-glass fiber drawing) or under bombardment by high-energy radiation.

The nonbridging oxygen, which is a component of the complementary pair of a broken silicon–oxygen bond, is an important kind of native defect in glassy  $SiO_2$ . The hole  $O_1^0$  centers associated with nonbridging oxygen atoms form efficiently in amorphous  $SiO_2$  modifications, and their observation in crystals is an indication of structural amorphization of the material [1].

Despite extensive studies of defects of this type, some of the problems related to their properties still remain unsolved. In particular, mechanisms operating in the relaxation of excited states of the  $O_1^0$  centers require more comprehensive investigation. These centers in  $SiO_2$  are usually associated with the optical-absorption bands at 4.75 eV (oscillator strength  $f = 0.048$ ) and 2.0 eV ( $f = 0.001$ ) and with red luminescence at 1.9 eV [1–3]. It was observed that Mott’s law is insufficient for adequate description of the quenching of the 1.9-eV luminescence in samples warmed to room temperature and higher. This point requires a special

analysis, because the above disagreement may be caused by various reasons. One of them could be the structural disorder in glassy  $SiO_2$ , which makes an activation-energy distribution of intracenter photoluminescence quenching possible [1]. At the same time, one cannot exclude the possibility of existence of other energy dissipation channels, for instance, of the recombination type, which become operative at elevated temperatures. In other words, there is an obvious divergence in the description of thermal quenching of the luminescence produced by native defects in  $SiO_2$ , which implies a lack of clear understanding of the processes involved in the nonradiative relaxation of excited states.

The present communication reports on an integrated investigation of photoluminescence (PL) and of the excitation, optical absorption (OA), and optically stimulated electron emission (OSEE) spectra of glassy quartz containing radiation-induced defects undertaken with the purpose of obtaining more detailed information on the specific features of nonradiative transitions in photoexcited  $O_1^0$  centers.

## 2. SAMPLES AND EXPERIMENTAL TECHNIQUES

We studied polished samples of KV-grade optical quartz glass. Defect centers in the structure of the samples under study were produced by irradiating them with 10-MeV electrons on an M-20 microtron. The electron fluence  $\Phi$  was  $2.4 \times 10^{16} \text{ cm}^{-2}$ .

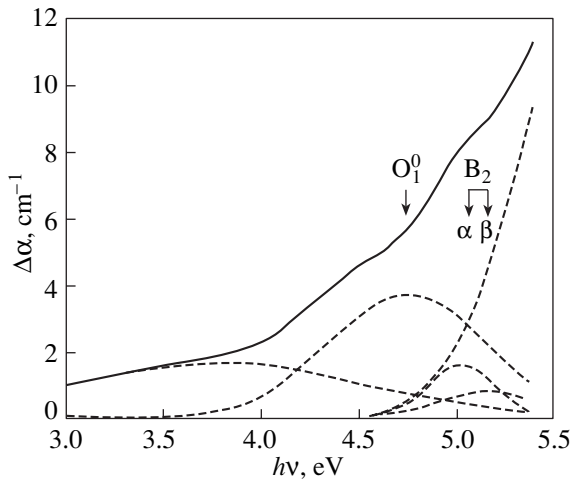


**Fig. 1.** OA spectrum of quartz glass obtained after fast-electron irradiation ( $2.4 \times 10^{16} \text{ cm}^{-2}$ , 10 MeV) and its decomposition into Gaussian constituents (dashed lines).

The OA spectra were measured with a Specord-40M spectrophotometer. The PL spectra were obtained with an FEU-71 PM tube interfaced with a DMR-4 double crystal monochromator. The luminescence was excited with a DRK-120 mercury lamp or a DDS-400 deuterium lamp through a DMR-4 monochromator.

OSEE spectra were measured in the wavelength range 200–600 nm. The UV radiation was produced by a DDS-400 lamp, with the required energy interval cut out by a monochromator. The light beam formed in this way was focused into a  $3 \times 0.5$ -mm spot on the sample surface. The OSEE intensity was measured in a vacuum of  $10^{-4}$  Pa with a VÉU-6 secondary-electron multiplier. The OSEE temperature behavior was studied with the use of a device providing sample temperature variation within the range 80–800 K. The heater was of double-helical design, thus precluding the electromagnetic field induced by the heater current from exerting defocusing action on the electron beam. The system permitted the carrying out of measurements under linear heating at a preset rate or in the thermostating regime.

The OSEE spectral response curves obtained in the experiment were normalized to the light flux and treated subsequently by a technique described elsewhere [4–6]. The spectral-response treatment procedure used by us is based on the assumption that the OSEE spectrum of an irradiated sample can be presented as a superposition of an exponential described by the Urbach rule and a set of Gaussians corresponding to various species of point defects. This model permitted us to obtain refined OSEE response curves which, as shown in [4–6], are emission counterparts of induced OA spectra. The OSEE data thus obtained can be used to determine the spectral parameters and concentration of photosensitive defects in the emission-active layer of a material [5–7].

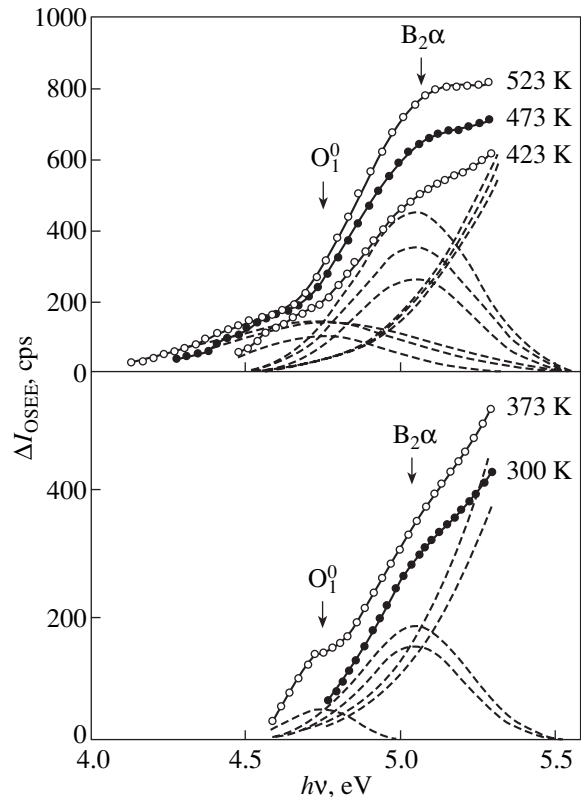


**Fig. 2.** OSEE spectra of radiation centers in quartz glass obtained after fast-electron irradiation (10 MeV,  $2.4 \times 10^{16} \text{ cm}^{-2}$ ) and its decomposition into Gaussian constituents (dashed lines).

### 3. EXPERIMENTAL RESULTS

#### 3.1. Optical-Absorption and Optically Stimulated Electron Emission Spectra

Figure 1 shows induced OA spectra of quartz glass samples irradiated by fast electrons. Decomposition of OA spectra in the 4.0- to 5.3-eV region into the constituent Gaussians revealed three maxima located at 4.75 eV (half-width at full maximum  $\Delta = 0.9$  eV), 5.02 eV ( $\Delta = 0.4$  eV), and 5.15 eV ( $\Delta = 0.55$  eV), with spectral parameters permitting their assignment to the  $O_1^0$ ,  $B_2\alpha$ , and  $B_2\beta$  centers, respectively [1, 2, 8]. The curve rising with energy in the range 4.7–5.4 eV originates apparently from the long-wavelength part of the  $E'$ -center absorption band [1, 8].

The OSEE spectral cutoff for the sample irradiated at room temperature lies near 4.8 eV. Heating the sample shifts the cutoff toward lower photon energies, with a simultaneous steepening of the exponential slope of the OSEE response curves.

When treated by the technique described in [4–6], the OSEE spectra of the irradiated samples exhibited the presence of selective bands (Fig. 2), which permits their identification with similar bands in the induced OA spectra (Fig. 1). The OSEE spectra obtained at suf-

ficiently low temperatures are dominated by an emission maximum at 5.02 eV, whose spectral parameters coincide with those of the  $\alpha$  component of the  $B_2$ -center OA band [8]. At temperatures above 370 K, an additional emission band at 4.75 eV appears in OSEE spectra (Fig. 2). When heated still further, this band grows in intensity and, in addition, undergoes strong thermal broadening (with  $\Delta$  increasing from 0.23 to 0.8 eV). Taking into account the optical absorption data (Fig. 1), we assigned the 4.75-eV OSEE band to photoexcited  $O_1^0$  centers. This assignment is supported by the observation that at elevated temperatures, the spectral parameters of the corresponding OSEE and OA bands become nearly identical.

### 3.2. Photoluminescence Spectra

Luminescence studies of the nonbridging oxygen atom centers yielded additional data which permitted us to refine the nature of the OSEE maximum near 4.75 eV. In this experiment, the PL was excited by the 256-nm line (4.85 eV) of the mercury lamp spectrum, which corresponds to the absorption band of the  $O_1^0$  centers. As seen from Fig. 3a, the  $O_1^0$  emission spectrum has a narrow band peaking at 1.9 eV. As the temperature is increased from 80 to 530 K, the luminescence intensity drops by more than an order of magnitude. At the same time, the maximum of the luminescence band shifts from 1.9 to 2.02 eV while simultaneously broadening from 0.18 to 0.2 eV, which is in full accord with the data reported in [1–3].

The excitation spectra were measured with a deuterium lamp. The excitation spectrum of the 1.9-eV luminescence in the temperature range 80–515 K is dominated by a broad band peaking at 4.75 eV (Fig. 3b). As the temperature increases, the intensity of the 4.75-eV excitation band varies in correlation with that of the corresponding luminescence peak. We note that this band in the excitation spectrum does not undergo thermal broadening ( $\Delta = 0.8$  eV) or a noticeable shift in the position of the maximum.

The parameters of the PL excitation spectrum (the width and position of the maximum) agree well with the photoelectron emission data. For  $T > 520$  K, the half-widths of the corresponding bands in the excitation and OSEE spectra are close in magnitude. This gives us grounds to assume that the 1.9-eV photoluminescence and the OSEE processes excited by 4.75-eV photons are intimately connected and actually represent various relaxation channels of the same excited state of the  $O_1^0$  centers. The relaxation probabilities can undergo substantial redistribution among the channels with variations in temperature.

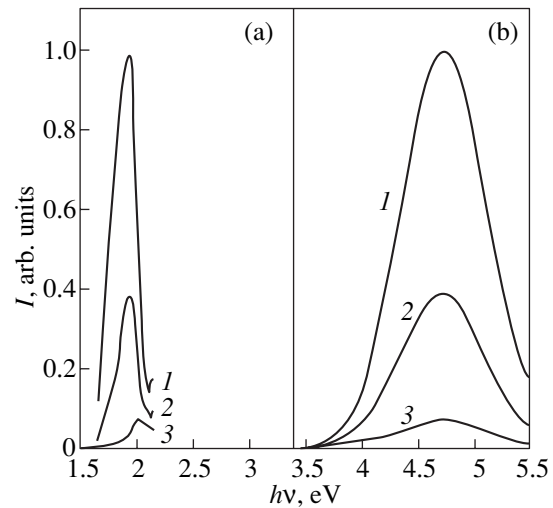


**Fig. 3.** (a) Emission spectra and (b) excitation spectra of the  $O_1^0$  radiation centers localized on nonbridging oxygen atoms at various temperatures  $T$ : (1) 80, (2) 300, and (3) 515 K.

### 3.3. Thermal Quenching of the Luminescence

Studies of the thermal quenching of the PL permitted us to determine the quantitative characteristics of radiative and nonradiative relaxation of the optically excited  $O_1^0$  centers, as well as to confirm the involvement of these centers in the OSEE effect. The luminescence quenching was studied under heating from the liquid-nitrogen temperature up (Fig. 4). It was taken into account that the radiative transition probability is only weakly dependent on temperature [9]. The temperature dependence of the luminescence intensity  $I_1(T)$ , considered with inclusion of the luminescence quantum yield  $\eta_L$ , can be written as

$$I_1(T) = I_0 \eta_L(T) = \frac{I_0}{1 + \frac{p_0^I}{P_L} e^{\frac{E_I}{kT}}}, \quad (1)$$

where  $I_0$  is the PL intensity for  $T \rightarrow 0$ ,  $P_L$  is the luminescence probability, and  $E_I$  and  $p_0^I$  are the activation barrier and the frequency factor of intracenter luminescence quenching, respectively.

Equation (1) is the well-known Mott law [1, 9] for intracenter quenching. Fitting the experimental  $I(T)$  curve by Eq. (1) shows that the quenching of the  $O_1^0$  PL is well reproduced by Mott's law only for temperatures  $T \leq 370$  K (dashed line in Fig. 4). At higher temperatures, a negative deviation from Mott's law is observed to exist; it appears only logical to assign this deviation to the operation of an additional quenching channel.

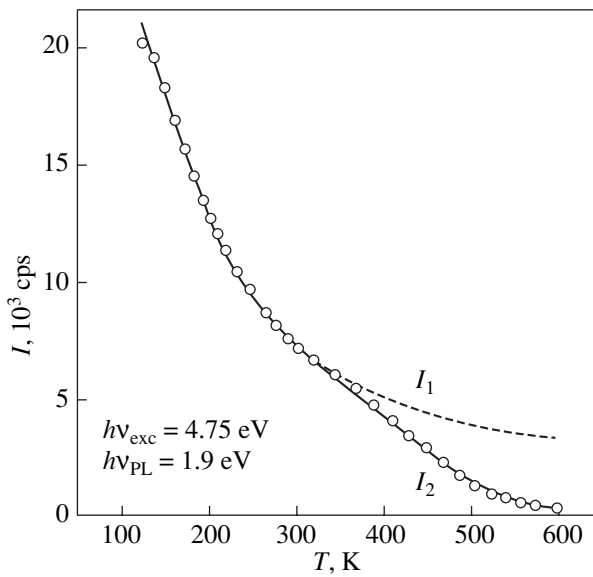


**Fig. 4.** Temperature dependence of the 1.9-eV luminescence intensity of  $O_1^0$  centers produced in quartz glass by electron bombardment. Circles are experiment, dashed line is fitting by Mott's relation ( $I_1$ ), and solid line is fitting with inclusion of external quenching ( $I_2$ ).

Assuming this process to be thermally activated, Eq. (1) can be rewritten in the form

$$I_2(T) = \frac{I_0}{1 + \frac{1}{P_L}(P_I + P_E)} = \frac{I_0}{1 + \frac{1}{P_L}(p_0^I e^{-\frac{E_I}{kT}} + p_0^E e^{-\frac{E_E}{kT}})}, \quad (2)$$

where  $I_2(T)$  is the temperature-dependent luminescence intensity with inclusion of the additional quenching;  $P_E$  and  $E_E$  are the probability and activation energy of the additional quenching, respectively; and  $p_0^E$  is a prefactor which is inversely proportional to the shortest characteristic time of the process.

The calculated curve described by Eq. (2) shows a good fit to the experimental relation (solid line in Fig. 4). Because luminescence is the dominant relaxation channel of the  $O_1^0$  centers, the radiative transition probability  $P_L$  can be found as  $1/\tau$ , where  $\tau \sim 20 \mu\text{s}$  [1] is the lifetime of the excited state. Knowing  $P_L$ , one can find the prefactors  $p_0^I$  and  $p_0^E$ . The parameters  $I_0$ ,  $E_I$ , and  $p_0^I/P_L$  were calculated from Eq. (1) using the part

Parameters of  $O_1^0$  center luminescence quenching

$I_0$ , cps	$P_L$ , $\text{s}^{-1}$	$p_0^I$ , $\text{s}^{-1}$	$E_I$ , eV	$p_0^E$ , $\text{s}^{-1}$	$E_E$ , eV
24000	$5 \times 10^4$	$10^6$	0.05	$2 \times 10^{10}$	0.46

of the experimental curve that obeys Mott's law. The results of the fitting are given in the table.

An analysis of the shape of the experimental  $I(T)$  curve in Fig. 4 shows immediately that the initiation of the additional quenching channel coincides in temperature (370 K) with the appearance of the 4.75-eV band in the OSEE spectra (Fig. 2). This observation should be considered as independent evidence that the processes responsible for the deviation from Mott's law (1) and for excitation of the photoelectron emission are interrelated.

#### 4. DISCUSSION OF RESULTS

To understand the processes underlying the relaxation of excited  $O_1^0$  centers, as well as to establish the part played by these centers in the photoelectron emission, it appears appropriate to consider their electronic structure. According to the model proposed in [1, 2], the absorption and luminescence bands of the  $O_1^0$  centers at 2.0 and 1.9 eV, respectively, derive from electronic transitions between the split  $2p$  states of the nonbridging oxygen atom. One of these states is the filled  $2p_x$  orbital, and the other is the  $2p_y$  orbital with one unpaired electron. The origin of the  $2p$  state splitting can be explained in terms of the dynamic Jahn-Teller effect; the nonbridging atom occupying a corner of the oxygen tetrahedron precesses and forms additional chemical bonds with other oxygen atoms in the same tetrahedron. According to [1, 2], the electronic transitions responsible for the absorption at 2 eV and luminescence at 1.9 eV are forbidden, which is in accord with experimental results; indeed, the oscillator strength of the 2-eV absorption band is small and the decay time of the 1.9-eV luminescence band ( $\tau \sim 20 \mu\text{s}$ ) is substantially larger than the corresponding values for allowed transitions ( $\tau < 0.01 \mu\text{s}$ ).

Considered within this model, the experimentally observed 4.75-eV band can be associated with a transition from the  $\sigma$ -bonding orbital to the  $2p_y$  antibonding orbital with an unpaired electron. The allowed character of the transition is in accord with the large amplitude of the 4.75-eV band observed in the OA, luminescence excitation, and OSEE spectra (Figs. 1–3). The luminescence at 1.9 eV is excited after the  $\sigma \rightarrow 2p_y$  transition has been followed by a fast nonradiative  $2p_x \rightarrow \sigma$  transition and, subsequently, by a radiative  $2p_y \rightarrow 2p_x$  transition. The Mott intracenter quenching of the 1.9-eV luminescence is associated in this case with the increased probability of nonradiative transitions of the  $2p_y \rightarrow 2p_x$  type with an activation barrier of 0.05 eV (see table). The process of additional quenching occurs with a considerably higher barrier of 0.46 eV. To confirm the external character of the luminescence quenching and its relation to the formation of the 4.75-eV OSEE band, it appears appropriate to compare the quantitative characteristics of these processes.

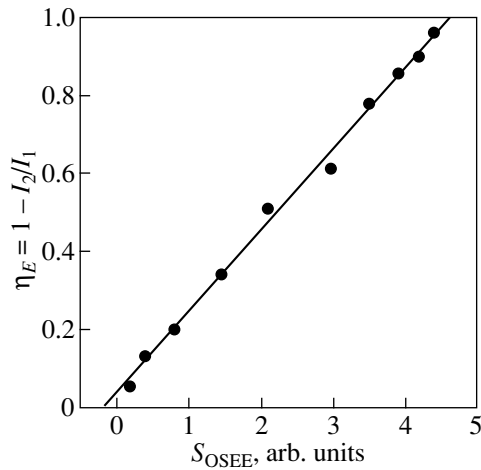


**Fig. 5.** Correlation between quantum efficiency of external luminescence quenching and integrated OSEE intensity of the  $O_1^0$  centers in the temperature range 373–600 K.

The quantum efficiency of the additional quenching  $\eta_E$  can be derived from the PL temperature dependence (Fig. 4). As follows from a comparison of Eqs. (1) and (2),

$$1 - \frac{I_2(T)}{I_1(T)} = \frac{P_E}{P_L + P_I + P_E} = \eta_E(T). \quad (3)$$

Using Eq. (3), one can compare the numerical values of the quenching efficiency  $\eta_E$  and integrated intensity of the 4.75-eV OSEE band (see Fig. 5). As is evident from Fig. 5, the relation constructed in this manner is linear and demonstrates an intimate correlation (with a coefficient of 0.99) between the nonradiative relaxation processes and the OSEE. This result can be considered an argument supporting the external character of the high-temperature luminescence quenching and, accordingly, the involvement of  $O_1^0$  centers in the photoelectron emission.

Auger recombination may be one of the possible mechanisms by which hole centers can be involved in electron emission [10]. This mechanism, however, assumes that the hole is released from the  $O_1^0$  center. At the same time, an analysis of the electronic structure of this center suggests that 0.46 eV is too small an energy for such a process to be realized (see table). In our case, resonant transfer of the energy of the  $2p_y \rightarrow 2p_x$  electronic transition from  $O_1^0$  to the centers donating electrons appears to be the most probable mechanism. The generation of free electrons, which occurs at temperatures above 370 K, is completed in the final stages of the relaxation process by their escaping from the surface into vacuum. According to [11], the observed phenomenon should be treated as spectral sensitization of photoelectron emission in the hole center excitation band. The activated character of this process may be due to thermal broadening with a subsequent overlap of

the emission and absorption bands between centers releasing and absorbing energy [12].

## 5. CONCLUSION

Thus, we have shown that photoexcited nonbridging-oxygen centers in glassy  $\text{SiO}_2$  can undergo relaxation, in general, over three channels. In addition to the radiative transitions accounting for the 1.9-eV luminescence band, there are two channels involving nonradiative transitions  $2p_y \rightarrow 2p_x$  between sublevels of the photoexcited  $2p$  state of the  $O_1^0$  center. One of these nonradiative channels transforms the excitation energy into thermal lattice vibrations and is actually an intracenter quenching process ( $E_I = 0.05$  eV) obeying Mott's law. The other nonradiative recombination channel ( $E_E = 0.46$  eV) involves external quenching with excitation transfer to emission-active electronic centers and manifests itself at certain temperatures in the form of spectrally sensitized photoelectron emission.

## ACKNOWLEDGMENTS

The authors are indebted to V.A. Pustovarov for his assistance in the experiments.

This study was supported by the US Civil Research & Development Foundation, grant no. REC-005.

## REFERENCES

1. A. R. Silin' and A. N. Trukhin, *Point Defects and Elementary Excitations in Crystalline and Vitreous  $\text{SiO}_2$*  (Zinatne, Riga, 1985).
2. L. N. Skuja, *J. Non-Cryst. Solids* **179**, 51 (1994).
3. A. A. Bobyshev and V. A. Radtsig, *Fiz. Khim. Stekla* **14**, 501 (1988).
4. D. Yu. Biryukov, A. F. Zatsepin, and V. S. Kortov, *Inter-university Collection of Works "Problems in Spectroscopy and Spectrometry"* (UGTU-UPI, Yekaterinburg, 1999), p. 27.
5. A. F. Zatsepin, D. Yu. Biryukov, and V. S. Kortov, *Latv. J. Phys. Tech. Sci., Suppl.* **6**, 83 (2000).
6. V. S. Kortov, A. F. Zatsepin, and D. Yu. Biryukov, *Optically Stimulated Electron Emission Spectroscopy of Photoactive Defects of Material Surface, Part 1: Methodic Aspects* (UGTU-UPI, Yekaterinburg, 2001).
7. D. Yu. Biryukov, A. F. Zatsepin, and V. S. Kortov, *Fiz. Khim. Solids* **27** (4), 503 (2001).
8. L. N. Skuja, *J. Non-Cryst. Solids* **239**, 16 (1998).
9. V. V. Antonov-Romanovskii, *Kinetics of Photoluminescence of Phosphor Crystals* (Nauka, Moscow, 1966).
10. A. F. Zatsepin, V. S. Kortov, and J. V. Shchapova, *J. Lumin.* **65**, 355 (1995).
11. I. A. Akimov, Yu. A. Cherkasov, and M. N. Cherkashin, *Sensitized Photoeffect* (Nauka, Moscow, 1980).
12. M. N. Tolstoï, in *Spectroscopy of Crystals: Collection of Articles* (Nauka, Moscow, 1970), p. 124.

Translated by G. Skrebtsov

---

---

**DEFECTS, DISLOCATIONS,  
AND PHYSICS OF STRENGTH**

---

---

# Amplitude-Independent Dislocation Internal Friction under Random External Actions

O. V. Kamaeva and V. M. Chernov

*Leipninskii Institute of Physics and Power Engineering, Russian Federal Research Center,  
pl. Bondarenko 1, Obninsk, Kaluzhskaya oblast, 249033 Russia*

Received June 25, 2001; in final form, December 13, 2001

**Abstract**—The amplitude-independent dislocation absorption (internal friction) is investigated under the joint action of constant and random external forces on the dislocation. The action of random forces of different types are considered with due regard for the inertial properties of the dislocation and the effect of the internal (parabolic) potential relief of the crystal. The dependences of the internal friction on the degree of correlation of random forces and the parameters of the dislocation and the medium are obtained. © 2002 MAIK “Nauka/Interperiodica”.

## 1. INTRODUCTION

Traditionally, the acoustical properties and the microstructure of crystals (internal friction) have been investigated with the use of exciting signals described by a harmonic function. The dislocation motion under external harmonic loads, the associated dynamical properties, and the internal microstructure of crystals have been examined in sufficient detail [1–10]. However, up to now, a number of interesting experimental effects (and, sometimes, their irreproducibility as well) have defied justified explanation. These effects can be associated with the manifestation of random actions on the crystal and its microstructure. External actions on a material cannot be reduced to harmonic loads alone. In practice, the material is often subjected to random mechanical stresses induced by different thermomechanical and radiation processes. In order to describe the behavior of materials under these random loads, it is necessary to elucidate the mechanisms of energy absorption by defects of the crystal lattice with the aim of determining the damping ability of the materials themselves and their internal microstructure.

The use of a random signal (with known statistical characteristics) as an exciting action in experiments on internal friction can also provide a way of deriving new additional information on the internal structure of the material.

The specific feature of the action of random loads is that the correlation of these loads can have a pronounced effect on the dislocation dynamics. In this respect, the dependence of the internal friction on the degree of correlation of external actions (in addition to the dependence on the frequency) is an important characteristic of the dislocation motion and can be used to obtain new data on the crystal microstructure.

In the present work, we solved a model problem that permitted us to demonstrate clearly how the random

external loads affect the dislocation (amplitude-independent) internal friction and to determine the dynamic properties of crystals and their microstructure under random actions.

## 2. THE EQUATION OF MOTION

Let us consider a dislocation segment that has a length  $L$ , is rigidly fixed at the ends, and executes oscillations under applied constant and random external stresses. Moreover, the segment interacts with the internal-stress field, which can be induced by the interaction of a dislocation with the crystal lattice (the Peierls–Nabarro relief) or with different aggregates of lattice defects (point, linear, and other defects). Without going into the origin of the internal-stress field, we will assume that the interaction between the dislocation and this field is described by a linear force dependence. This dependence corresponds to a parabolic potential well in which the dislocation resides:  $U = \kappa u^2$ . The dislocation displacement  $u(x, t)$  in the glide plane at the point  $x$  and the instant of time  $t$  from an equilibrium position is determined by the standard equation of motion in the elastic-string approximation [1], that is,

$$m \frac{\partial^2 u}{\partial t^2} = T_0 \frac{\partial^2 u}{\partial x^2} - \lambda_{\text{fr}} \frac{\partial u}{\partial t} - b \kappa u + g(t), \quad (1)$$

$$u(0, t) = u(L, t) = 0.$$

Here, the  $x$  axis is parallel to the rectilinear dislocation at the equilibrium position in the absence of external stresses,  $b$  is the magnitude of the Burgers vector of the dislocation,  $m$  is the effective mass per unit length of the dislocation,  $T_0$  is the effective line tension of the dislocation,  $\lambda_{\text{fr}}$  is the coefficient of dislocation dynamic friction,  $g(t) = b f_0 + b \eta(t)$  is the external force acting on the dislocation per unit length,  $f_0$  is the constant com-

ponent of the external stress, and  $\eta(t)$  is the stress produced under random actions of the medium on the dislocation string.

In the case when the dislocation moves, for example, in a valley of the Peierls–Nabarro relief, the coefficient  $\kappa$  can vary from  $\sim 10^{15}$  to  $\sim 10^{19}$   $\text{g}/(\text{cm s})^2$  with a change in the Peierls stress  $\sigma_p$  from  $\sim 10^4 G$  to  $\sim 10^{-2} G$  (where  $G$  is the shear modulus) [7]. The motion in potential wells of another origin can be characterized by similar or different coefficients  $\kappa$ .

The random actions on the crystal have different origins. Correspondingly, the random forces can be described by different models. In the present work, we will use the following processes for modeling typical random actions on a dislocation [11]: the telegraph and generalized telegraph processes, the rectangular-pulsed process with a fixed width and a random amplitude of pulses, and the “exponential-saw” process (see the Appendix). For these processes, the mean amplitude of signals is equal to zero. In this case, the dislocation does not undergo regular displacement under the action of random forces.

The random instants of time  $t_i$  at which the random force suddenly changes its action on the dislocation will be referred to as the flow of events. We will consider the stationary Poissonian flow with the intensity  $\nu$ . This means that the mean number of events per unit time (the mean frequency) is equal to  $\nu$ . The quantity  $\nu$  can be treated as an analog of the frequency of a periodic action. Hence, the quantity  $\nu$  will be termed the frequency of the random action. The probability that the behavior of the force changes  $n$  times on the time interval  $\tau = t_2 - t_1$  is defined by the Poisson formula  $P_{n(t_1, t_2) = n} = a^n \exp(-a)/n!$ , where  $a = \langle n(t_1, t_2) \rangle$  is the ensemble-averaged number of events on the time interval  $(t_1, t_2)$ ,  $\langle n(t_1, t_2) \rangle = \nu\tau$ .

### 3. INTERNAL FRICTION

As is customary, the logarithmic decrement  $\Delta$  is taken as a measure of the internal friction. However, since the external action is a random event, the corresponding quantities are averaged over an ensemble of random forces. Furthermore, in view of the aperiodic external action, the viscous loss is calculated for a time chosen equal to the reciprocal of the mean frequency  $\nu$ . Consequently, the loss  $\Delta$  (damping decrement) is calculated for the effective period  $T_{eq} = \nu^{-1}$  from the relationship  $\Delta = (N\langle A \rangle)/(2\langle U_{e1}^0 \rangle)$ . Here,  $\langle \rangle$  is the operator of averaging over the ensemble of random forces,  $N$  is the number of dislocation segments per unit volume,

$$\langle A \rangle = \int_0^L \lim_{T \rightarrow \infty} \frac{1}{T} \left\langle \int_0^T [bf_0 + b\eta(t)] \frac{\partial u(x, t)}{\partial t} dt \right\rangle dx \quad (2)$$

is the mean energy dissipated by one dislocation segment per unit volume in the case of stationary dislocation motion,  $\langle U_{e1}^0 \rangle = (f_0^2 + \sigma_0^2)/2G$  is the ensemble-averaged vibrational energy per unit volume of the crystal, and  $\sigma_0^2$  is the square of the amplitude (or the variance  $D_v$ ) of the random component of the external force.

Hereafter, without loss of generality, we will consider a typical delta distribution of dislocation segments over lengths. Other distributions can be treated in a similar way.

From relationships (1) and (2), we obtain the expression for the damping decrement [12]

$$\Delta = \frac{8Gb^2\Lambda}{\nu m} \frac{1}{(f_0^2 + \sigma_0^2)^T} \lim_{T \rightarrow \infty} \sum_{n=0}^{\infty} \frac{1}{\pi^2(2n+1)} \times \int_0^T \text{Kor}(S) \exp\left(-\frac{\lambda_{fr}}{2m} S\right) \left\{ \cos(B_n S) - \frac{\lambda_{fr}}{2m} \frac{\sin(B_n S)}{B_n} \right\} dS. \quad (3)$$

Here,

$$B_n = \sqrt{\Omega_n^2 - \frac{\lambda_{fr}^2}{4m^2}}, \quad \Omega_n^2 = \frac{T_0}{m} (2n+1)^2 \left(\frac{\pi}{L}\right)^2 + \frac{b\kappa}{m};$$

$n = 0, 1, 2, \dots$ ;  $\Lambda$  is the dislocation density; and  $\text{Kor}(S)$  is the correlation function of the random component of the external force. Expression (3) indicates that the damping decrement depends on the correlation properties of the random component of the external force.

## 4. ANALYSIS OF THE RESULTS

**4.1. The telegraph process.** The calculations performed with inclusion of the correlation function of the telegraph random process lead to the following relationship for the decrement:

$$\Delta = \frac{2Gb^2\Lambda}{(4\nu^2 m + 2\nu\lambda_{fr} + b\kappa)} \times \frac{1}{[(f_0^2/\sigma_0^2) + 1]} \left[ 1 - \frac{\tanh y_t}{y_t} \right], \quad (4)$$

where

$$y_t = \frac{\pi}{2} \sqrt{\frac{a_*}{b_*}}, \quad a_* = 4\nu^2 m + 2\nu\lambda_{fr} + b\kappa, \\ b_* = T_0 \left(\frac{\pi}{L}\right)^2.$$

Figure 1 shows the frequency dependence of the normalized damping decrement  $\Delta_n$  (where  $\Delta_n = \Delta/\Delta^*$  and  $\Delta^* = \pi G b^2 \Lambda L^2 / 2 T_0$ ) for different damping magnitudes  $D = 2m\Omega_0/\lambda_{fr}$ . The frequency characteristic

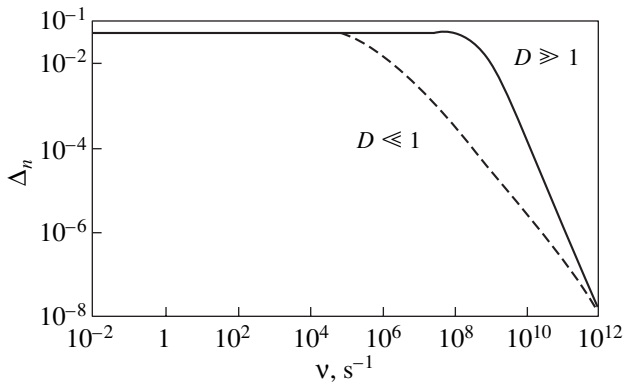


**Fig. 1.** Frequency dependences of the decrement at a constant dislocation length  $L$  and different damping magnitudes  $D$ . The decrement is normalized to the multiplier  $\pi G b^2 \Lambda L^2 / 2 T_0$ .

involves two portions, namely, a frequency-independent plateau and a branch descending with an increase in the frequency. The decrement in the range of the plateau (the low-frequency range) is governed by the elastic properties of the dislocation and the stiffness of the internal relief. A decrease in the decrement in the high-frequency range is associated with the inertial properties of the dislocation and the friction. The plateau width, i.e., the frequency range in which the decrement is independent of the frequency, is determined by the frequency  $\nu_{cr} = \lambda_{fr}(-1 + \sqrt{1 + D^2})/4m$ . The higher the frequency  $\nu_{cr}$ , the wider the plateau. At frequencies of the external random action  $\nu \ll \nu_{cr}$ , the decrement does not depend on the frequency and can be represented by the expression

$$\Delta = \frac{2Gb\Lambda}{\kappa} \frac{1}{[(f_0^2/D\nu) + 1]} \left[ 1 - \frac{\tanh y_1}{y_1} \right], \quad (5)$$

where  $y_1 = \frac{\pi}{2} \sqrt{\frac{a_1}{b_*}}$  and  $a_1 = b\kappa$ .

Two types of the frequency characteristics of the decrement at a constant dislocation length can be observed depending on the damping magnitude  $D$ .

At a light damping ( $D \gg 1$ ), we have  $\nu_{cr} \approx \Omega_0/2$  and the frequency characteristic exhibits a wide plateau extending to nearly half the resonance frequency. At higher frequencies, the decrement in a narrow range varies in inverse proportion to the frequency; i.e.,  $\Delta \sim \nu^{-1}$ . In this range, the dislocation motion is governed by the friction. In the vicinity of the resonance frequency, the decrement sharply decreases as  $\nu^{-2}$ . In this case, the behavior of the decrement is determined by the inertial properties of the dislocation.

An increase in the damping results in a narrowing of the plateau. At  $D^2 \gg 1$ , the frequency  $\nu_{cr}$  decreases compared to that in the preceding case and is deter-

mined by the formula  $\nu_{cr} \approx 0.5(\Omega_0 - \lambda_{fr}/2m)$ . In turn, the descending branch of the frequency characteristic of the decrement, which is associated with the friction, extends over a progressively wider frequency range.

If the damping is heavy ( $D \ll 1$ ), we obtain  $\nu_{cr} = \lambda_{fr}D^2/4m = \Omega_0D/4$ . In this case, the critical frequency is considerably lower than the resonance frequency. The plateau is shifted toward the range of very low frequencies. The frequency characteristic is represented by the curve smoothly descending with an increase in the frequency. At  $\nu \ll \lambda_{fr}/2m$ , the decrement decreases smoothly [ $\Delta \sim (\lambda_{fr\nu})^{-1}$ ] due to the friction. In the range  $\nu \gg \lambda_{fr}/2m$ , the decrement decreases steeply ( $\Delta \sim \nu^{-2}$ ), which is explained by the effect of the inertia. The maximum loss is observed at  $\nu \ll \nu_{cr}$ .

When the internal relief is soft [ $b\kappa \ll T_0(\pi/L)^2$ ], the decrement in the range of the plateau is determined only by the elastic properties and the length of the dislocation and can be written as

$$\Delta = \Delta^* \frac{1}{3\pi[(f_0^2/\sigma_0^2) + 1]}. \quad (6)$$

As follows from relationship (6), the decrement is proportional to the dislocation length squared and does not depend on the friction coefficient  $\lambda_{fr}$ , dislocation mass, and stiffness of the internal relief. Moreover, the decrement does not depend on the amplitude (variance) of the random force in the absence of the constant load ( $f_0 = 0$ ). Note that, in this case, the normalized decrement is a universal quantity equal to  $1/(3\pi)$ .

For the stiff internal relief [ $b\kappa \gg T_0(\pi/L)^2$ ], the decrement in the range of the plateau is represented by the expression

$$\Delta = \frac{2Gb\Lambda}{\kappa} \frac{1}{[(f_0^2/\sigma_0^2) + 1]}. \quad (7)$$

According to expression (7), the decrement does not depend on the length, mass, elastic properties, and coefficient of dynamic friction of the dislocation segment and is governed only by the relief stiffness and dislocation density. Relationship (7) can be used to estimate experimentally the stiffness  $\kappa$  of the internal potential relief in which the dislocation resides.

The influence of the internal-relief stiffness  $\kappa$  on the frequency dependence of the decrement is illustrated in Fig. 2. It can be seen from this figure that the relief affects the decrement only in the range of the plateau and the dependences for different stiffnesses in the high-frequency range virtually coincide with each other. This implies that the dislocation motion at these frequencies of the external action does not depend on the relief and is determined by the friction and inertial properties of the dislocation.

The dependence of the decrement on the dislocation segment length is controlled by the parameter

$$L_{\text{eff}} = \frac{L}{2} \sqrt{\frac{4v^2 m + 2v\lambda_{\text{fr}} + b\kappa}{T_0}}.$$

Under the condition  $L_{\text{eff}} \ll 1$ , the decrement is characterized by a quadratic dependence on the length, that is,

$$\Delta = \frac{Gb^2 \Lambda L^2}{6T_0} \frac{1}{[(f_0^2/\sigma_0^2) + 1]}. \quad (8)$$

At  $L_{\text{eff}} > 1$ , we have

$$\Delta = \frac{2Gb^2 \Lambda}{4v^2 m + 2v\lambda_{\text{fr}} + b\kappa} \frac{1}{[(f_0^2/\sigma_0^2) + 1]} \times \left[ 1 - \frac{2}{L} \sqrt{\frac{T_0}{(4v^2 m + 2v\lambda_{\text{fr}} + b\kappa)}} \right]. \quad (9)$$

As follows from formula (9), an increase in the dislocation length leads to an increase in the decrement  $\Delta \sim 1 - \text{const}L^{-1}$ ; however, this increase is smoother than that observed in the preceding case.

For long dislocation segments with  $L_{\text{eff}} \gg 1$ , we obtain

$$\Delta = \frac{2Gb^2 \Lambda}{(4v^2 m + 2v\lambda_{\text{fr}} + b\kappa)} \frac{1}{[(f_0^2/\sigma_0^2) + 1]}. \quad (10)$$

It is seen from expression (10) that the decrement does not depend on the dislocation segment length and is determined by a relationship identical to that derived for the action of a random force of the telegraph type on a dislocation with free ends [13]. The condition  $L_{\text{eff}} \gg 1$  is satisfied not only for very long dislocations but also in the case of dislocation motion in a stiff relief [ $\kappa > 10^{15} \text{ g/(s cm)}^2$ ] at dislocation segment lengths larger than  $L = 10^2 b$  for any friction coefficient. This condition can also be met for the motion in a softer relief at certain ratios between the dislocation length and the friction coefficient.

In the case when the random force associated with the generalized telegraph process (see the Appendix) acts on the dislocation, the decrement can be represented in the form

$$\Delta = \frac{Gb^2 \Lambda}{(v^2 m + v\lambda_{\text{fr}} + b\kappa)} \frac{1}{[(f_0^2/D_v) + 1]} \left[ 1 - \frac{\tanh y}{y} \right] \quad (11)$$

$$\left( y = \frac{\pi}{2} \sqrt{\frac{p}{b_*}}, \quad p = v^2 m + v\lambda_{\text{fr}} + b\kappa \right).$$

This model is characterized by dependences similar to those obtained for the telegraph process. However, for the model of the generalized telegraph process, the dec-

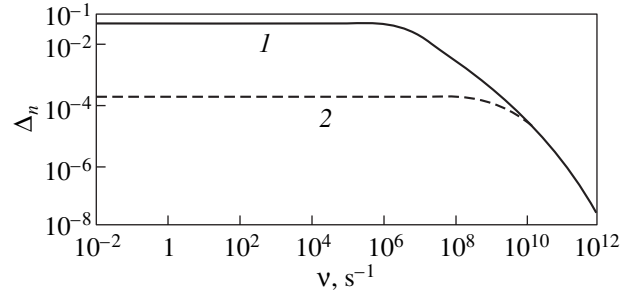


**Fig. 2.** Effect of the lattice relief stiffness  $\kappa$  on the frequency dependence of the normalized decrement  $\Delta_n$  at a constant dislocation length.  $\kappa = (1) 0$  and  $(2) 10^{15} \text{ g/(s cm)}^2$ .

rement becomes smaller, the frequency  $\nu_{\text{cr}}$  is doubled, and the amplitude in the corresponding formulas is replaced by the amplitude variance.

It should be noted that the decrement over the entire frequency range does not depend on the amplitude (variance) of the random force when the dislocation does not experience an additional constant load or its amplitude is substantially less than that of the random force. If the constant load is predominant [its amplitude is considerably larger than the amplitude (variance) of the random force], the decrement becomes proportional to the square of the ratio between the amplitude (variance) of the random component of the external force and the amplitude of the constant load.

Analysis demonstrates that the stronger the correlation of random forces (the lower the frequency  $\nu$ ), the larger the damping decrement. For strongly correlated forces ( $\nu \ll \nu_{\text{cr}}$ ), the decrement does not depend on the degree of correlation.

**4.2. The exponential-saw process.** From formula (3), we obtain the expression for the decrement in the form

$$\Delta = \frac{Gb^2 \Lambda}{(\alpha^2 m + \alpha\lambda_{\text{fr}} + b\kappa)} \times \frac{1}{[(f_0^2/D_v) + 1]} \left[ 1 - \frac{\tanh h}{h} \right], \quad (12)$$

where

$$h = \frac{\pi}{2} \sqrt{\frac{d_*}{b_*}}, \quad d_* = \alpha^2 m + \alpha\lambda_{\text{fr}} + b\kappa,$$

and  $\alpha$  is the attenuation coefficient of the exponential pulse. It is seen from expression (12) that the decrement is independent of the frequency  $\nu$ ; i.e., the frequency of the action of the random force on the dislocation does not affect the decrement. The behavior of the decrement is determined by the attenuation coefficient  $\alpha$  of a single pulse. This coefficient characterizes the degree of correlation of random forces.

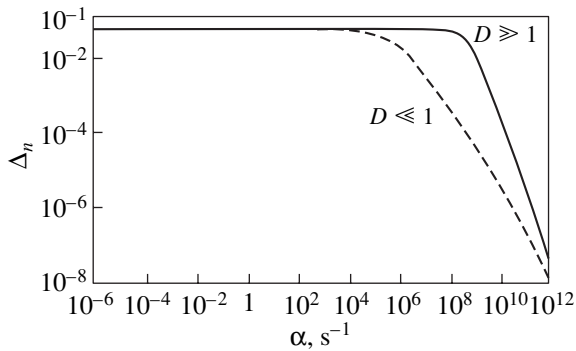


**Fig. 3.** Dependences of the normalized decrement  $\Delta_n$  on the degree of correlation  $\alpha$  of random forces at a constant dislocation length and different damping magnitudes  $D$ .

For  $\alpha \ll \alpha_{cr}$  and the critical coefficient defined by the formula

$$\alpha_{cr} = \frac{\lambda_{fr}}{2m} [-1 + \sqrt{1 + D^2}], \quad (13)$$

the decrement does not depend on the coefficient  $\alpha$  and can be written as

$$\Delta = \frac{Gb\Lambda}{\kappa} \frac{1}{[(f_0^2/D_v) + 1]} \left[ 1 - \frac{\tanh y_1}{y_1} \right]. \quad (14)$$

In this range of coefficients  $\alpha$ , the dislocation behavior is governed only by the length and elastic properties of the dislocation and the internal relief. The relationship for the decrement appears to be identical to that derived in the case of the random low-frequency action modeled by the generalized telegraph process. By ignoring the internal-stress field ( $\kappa = 0$ ) in the description of the dislocation motion, expression (14) for the decrement takes the form

$$\Delta = \frac{Gb^2\Lambda}{12T_0} l^2 \frac{1}{[(f_0^2/D_v) + 1]}. \quad (15)$$

When the damping is sufficiently light ( $D^2 \gg 1$ ), the coefficient  $\alpha_{cr}$  is close to the resonance frequency  $\Omega_0$ ; that is,

$$\alpha_{cr} = \left( -\frac{\lambda_{fr}}{2m} + \Omega_0 \right). \quad (16)$$

The decrement  $\Delta(\alpha)$  remains unchanged at  $\alpha \ll \alpha_{cr}$ . In the range of  $\alpha \sim \alpha_{cr}$ , the decrement decreases gradually due to the friction [ $\Delta \sim (\lambda_{fr}\alpha)^{-1}$ ]. At  $\alpha \gg \alpha_{cr}$ , the decrement decreases sharply ( $\Delta \sim \alpha^{-2}$ ), because the inertial properties of the dislocation in this range make the main contribution. For a very light damping ( $D \gg 1$ ), we have  $\alpha_{cr} = \Omega_0$ . In this case, the range of gradual decrease in the decrement due to the friction is virtually absent. With an increase in  $\alpha$ , the decrement remains

constant almost to the resonance frequency  $\Omega_0$  and then decreases steeply ( $\Delta \sim \alpha^{-2}$ ).

If the damping is not light ( $D^2 \ll 1$ ), the coefficient  $\alpha_{cr} = \Omega_0 D/2$  is substantially less than the resonance frequency. The plateau is shifted toward the range of very low frequencies. At  $\Omega_0 D/2 \ll \alpha < \lambda_{fr}/2m$ , the curve  $\Delta(\alpha)$  falls off smoothly as  $(\lambda_{fr}\alpha)^{-1}$ . Finally, at  $\alpha > \lambda_{fr}/2m$ , the sharp decrease in the decrement ( $\Delta \sim \alpha^{-2}$ ) is governed by the inertial properties of the dislocation. The loss is maximum at  $\alpha \ll \alpha_{cr}$ . The loss associated with this mechanism is observed in the range  $\alpha \ll \Omega_0$  for a light damping and in the range  $\alpha \ll \Omega_0 D/2$  for a heavy damping.

Figure 3 displays the dependences of the normalized decrement on the degree of correlation  $\alpha$  of random forces for different damping magnitudes  $D$ . The dependences of the decrement on the relief stiffness and the dislocation length are similar to those for a random force modeled by the generalized telegraph process.

Over the entire frequency range, the dependence of the decrement on the amplitude variance for the exponential-saw random force exhibits a behavior identical to that for the telegraph random force.

Analysis shows that the stronger the correlation of random forces (the less the parameter  $\alpha$ ), the larger the damping decrement. For strongly correlated forces ( $\alpha \ll \alpha_{cr}$ ), the decrement does not depend on the degree of correlation.

**4.3. The rectangular-pulsed process.** From relationship (3), we obtain the following formula for the decrement:

$$\Delta = \frac{8Gb^2\Lambda}{\pi^2} \frac{1}{[(f_0^2/D_v) + 1]} + \sum_{n=0}^{\infty} \frac{1}{(2n+1)^2} \frac{1}{[b\kappa + T_0(2n+1)^2(\pi/L)^2]} \times \left\{ 1 - \exp\left(-\frac{\lambda_{fr}}{2m}\delta\right) A_n \right\}, \quad (17)$$

where

$$A_n = \left\{ \cos(B_n\delta) + \frac{\lambda_{fr}\delta \sin(B_n\delta)}{2m B_n\delta} \right\}$$

and  $\delta$  is the pulse width.

In this case, the decrement is independent of the frequency. The dependence of the decrement on the dislocation segment length and the pulse width is characterized by a complex behavior (Fig. 4). When the damping is relatively light ( $D^2 > 1$ ), the relationship for the decrement includes trigonometric functions, which, in a number of cases, leads to oscillating dependences of the decrement on the pulse width and the dislocation

length. For a heavy damping ( $D^2 < 1$ ), the trigonometric functions are replaced by the hyperbolic functions and the dependences on the dislocation length and the pulse width become monotonic. Let us analyze the limiting cases of the decrement behavior.

If the inequality  $\lambda_{fr}\delta/2m \gg 1$  is met, at any damping magnitude ( $D > 1$  or  $D < 1$ ) satisfying the condition  $\lambda_{fr}\delta D^2/4m \gg 1$ , the decrement is defined by the expression coinciding with formula (14), which was derived in the case when the dislocation was subjected to a low-frequency random force modeled by the generalized telegraph process or an external random force of the exponential-saw type (at  $\alpha < \alpha_{cr}$ ). Under these conditions, the decrement does not depend on the degree of correlation of external forces (i.e., on the pulse width), friction coefficient  $\lambda_{fr}$ , and inertial properties of the dislocation and is determined only by the stiffness of the internal relief of the lattice and the length and elastic properties of the dislocation.

When the inequality  $\frac{\lambda_{fr}\delta}{2m} \gg 1$  holds, but the damping magnitude is so large ( $D^2 \ll 1$ ) that  $\lambda_{fr}\delta D^2/(4m) \ll 1$ , the decrement is given by

$$\Delta = \frac{Gb^2\Lambda}{\lambda_{fr}} \frac{1}{[(f_0^2/D_v) + 1]} \delta. \quad (18)$$

In this situation, the decrement depends neither on the mass, length, and elastic properties of the dislocation segment nor on the stiffness of the internal relief and is governed by the pulse width and friction.

For  $\lambda_{fr}\delta/2m \sim 1$  and a light damping ( $D^2 \gg 1$ ), we have

$$\begin{aligned} \Delta = & \frac{8Gb^2\Lambda}{\pi^2} \frac{1}{[(f_0^2/D_v) + 1]} \sum_{n=0}^{\infty} \frac{1}{(2n+1)^2} \\ & \times \frac{1}{[b\kappa + T_0(2n+1)^2(\pi/L)^2]} \\ & \times \left\{ 1 - \exp\left(-\frac{\lambda_{fr}\delta}{2m}\right) \cos\left(\frac{\lambda_{fr}\delta}{2m} D_n\right) \right\}, \end{aligned} \quad (19)$$

where

$$D_n = \frac{2m}{\lambda_{fr}} \sqrt{\frac{b\kappa}{m} + \frac{T_0}{m} \left(\frac{\pi}{L}\right)^2} (2n+1).$$

In this case, oscillations are observed in the dependences of the decrement on the dislocation length  $L$  (Fig. 5). The amplitude of these oscillations does not depend on the length  $L$  and is determined by the value of  $\lambda_{fr}\delta/2m$ . The smaller this value, the larger the oscillation amplitude. The oscillation frequency decreases with an increase in the length  $L$ . The dependence of the decrement on the length  $L$  is not periodic, whereas the

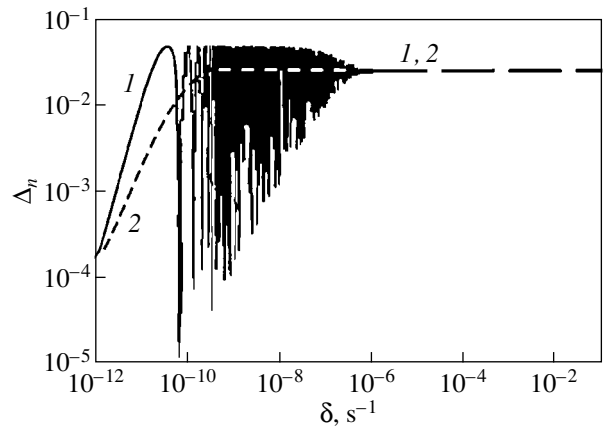


Fig. 4. Dependences of the normalized decrement  $\Delta_n$  on the degree of correlation  $\delta$  of random forces at a constant dislocation length and different friction coefficients  $\lambda_{fr}$ : (1)  $10^{-6}$  and (2)  $10^{-1}$  g/(cm s).

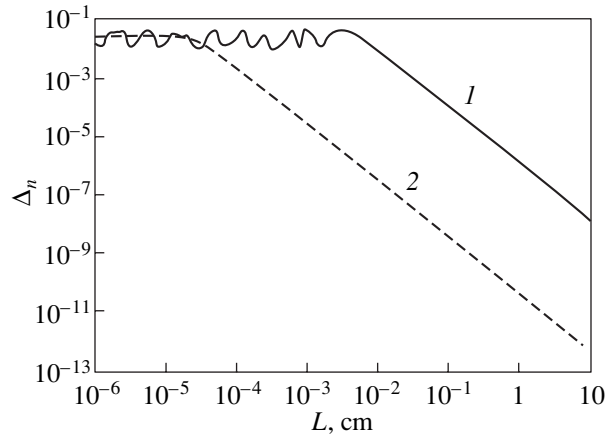


Fig. 5. Dependences of the normalized decrement  $\Delta_n$  on the dislocation length  $L$  at a constant pulse width and different friction coefficients  $\lambda_{fr}$ : (1)  $10^{-6}$  and (2)  $10^{-1}$  g/(cm s).

dependence of the decrement on the pulse width, according to formula (19), is represented by a high-frequency periodic function with an exponentially decaying amplitude.

At a heavy damping ( $D^2 \ll 1$ ), the relationship for the decrement coincides with expression (18).

For  $\lambda_{fr}\delta/2m \ll 1$  and damping magnitudes  $D > 1$  satisfying the inequality  $\lambda_{fr}\delta D/2m \ll 1$ , we obtain

$$\Delta = \frac{Gb^2\Lambda}{2m} \frac{1}{[(f_0^2/D_v) + 1]} \delta^2. \quad (20)$$

Under these conditions, the decrement does not depend on the friction coefficient  $\lambda_{fr}$ , the length and elastic properties of the dislocation segment, and the stiffness

of the internal relief and is proportional to the quantity  $\delta^2 m^{-1}$ .

If the damping is so light ( $D \gg 1$ ) that  $\lambda_{fr} \delta D / (2m) \gg 1$ , the decrement has the form

$$\Delta = \frac{8Gb^2\Lambda}{\pi^2} \frac{1}{[(f_0^2/D_v) + 1]} \sum_{n=0}^{\infty} \frac{1}{(2n+1)^2} \times \frac{1}{[b\kappa + T_0(2n+1)^2(\pi/L)^2]} \left\{ 1 - \cos\left(\frac{\lambda_{fr}\delta}{2m} D_n\right) \right\}. \quad (21)$$

The dependence of the decrement on the dislocation length in this case coincides with that given by relationship (19). The dependence of the decrement on the pulse width is described by a high-frequency periodic function with a constant amplitude.

When the damping is heavy ( $D^2 \ll 1$ ), the expression for the decrement takes the form

$$\Delta = \frac{Gb\Lambda}{2\kappa} \frac{1}{[(f_0^2/D_v) + 1]} \left[ 1 - \frac{\tanh y_1}{y_1} \right] \left( \frac{\lambda_{fr}\delta}{2m} \right)^2. \quad (22)$$

Therefore, at  $\lambda_{fr}\delta/2m \gg 1$  and any damping magnitude ( $D > 1$  or  $D < 1$ ) satisfying the inequality  $\lambda_{fr}\delta D^2/4m \gg 1$ , the decrement does not depend on the degree of correlation of external forces (i.e., on the pulse width), friction, and dislocation mass and coincides with the decrement observed for a random force modeled by the generalized telegraph process (in the

low-frequency range) or an exponential-saw random force (at  $\alpha < \alpha_{cr}$ ).

The amplitude dependence of the decrement is identical to that obtained for random forces modeled by the generalized-telegraph or exponential-saw processes.

### 5. CONCLUSIONS

Thus, the regularities of the energy loss by excitation of the dislocation structure under random external actions essentially differ from those observed under harmonic actions. Unlike the Granato–Lucke classical case of periodic actions on a dislocation, the internal friction in the low-frequency range for the random actions nonlinearly depends on the frequency. The decrement in this frequency range is considerably larger than that under periodic actions. The dependence of the damping decrement on the dislocation segment length is governed by the parameters of the dislocation, the medium, and the random force and can exhibit different behavior in contrast with the corresponding dependence observed under periodic actions ( $\Delta \sim L^4$ ).

The decrement behavior substantially depends on the degree of correlation of random forces. The degree of correlation is considered to mean the quantity characterizing a decrease in the correlation function. This quantity is determined by the parameter  $\nu$  for the telegraph and generalized telegraph processes, the parameter  $\alpha$  for the exponential-saw process, and the pulse width  $\delta$  for the rectangular-pulsed process. The stronger the correlation of external forces, the larger the dec-

### APPENDIX

Types and correlation characteristics of random processes

Process	Relationships describing the process	Correlation function
Telegraph process	$\eta(t) = a(-1)^{n(0,t)}$ , Probability ( $a = \delta_0$ ) = Probability ( $a = -\sigma_0$ ) = 1/2, $\text{Probability } (n(t_1, t_2) = m) = \frac{[\bar{n}(t_1, t_2)]^m}{m!} \exp\{-\bar{n}(t_1, t_2)\}$ , $\bar{n}(t_1, t_2) = \nu t_1 - t_2  = \nu \tau $	$\text{Kor}(\tau) = \sigma_0^2 \exp(-2\nu \tau )$
Generalized telegraph process	$\eta(t) = V_{n(0,t)}$ , $\langle\langle V_i \rangle\rangle = 0, \langle\langle V^2 \rangle\rangle = D_v$	$\text{Kor}(\tau) = D_v \exp(-\nu \tau )$
Exponential-saw process	$\eta(t) = \sum_{i=1}^N V_i \exp(-\alpha(t - t_i))$	$\text{Kor}(\tau) = \frac{\nu D_v}{2\alpha} \exp(-\alpha \tau )$
Rectangular-pulsed process with a fixed width and a random amplitude of pulses	$\eta(t) = \sum_{i=1}^N V_i h(t - t_i)$ , $h(t) = \theta(t) - \theta(t - \delta)$ , $\theta(t) = \begin{cases} 1, & t > 0 \\ 0, & t < 0 \end{cases}$	$\text{Kor}(\tau) = \nu \delta D_v \left(1 - \frac{ \tau }{\delta}\right) \theta\left(1 - \frac{ \tau }{\delta}\right)$

Note:  $n(0, t)$  is the integer random Poissonian flow;  $V_0, V_1, \dots, V_k$  are the random statistically independent quantities with the distribution  $p(V)$ ;  $N$  is the number of random points  $t_i$  on the interval  $(0, t)$  [ $N$  obeys a Poisson distribution with the parameter  $\langle N \rangle = \nu t$ ]; and  $h(t)$  is the pulse shape.

rement. When the degree of correlation exceeds the threshold value, the decrement becomes independent of the type of random process. In this case, the decrement depends neither on the frequency of the action of random forces and the coefficient of dynamic friction, nor on the inertial properties of the dislocation. The threshold degree of correlation is governed by the type of the process modeling the random force and the parameters of the problem.

In the case when the constant load is appreciably larger than the amplitude (variance) of the random force, the decrement depends on the amplitude. The amplitude dependence of the decrement is not associated with hysteresis phenomena.

The inclusion of the internal-stress field results in a change in the damping decrement. The deeper the potential well (the larger the coefficient  $\kappa$ ) in which the dislocation executes a motion, the smaller the decrement.

#### REFERENCES

1. A. Granato and K. J. Lucke, *Appl. Phys.* **27**, 789 (1956).
2. *Physical Acoustics: Principles and Methods*, Vol. III, Part A: *The Effect of Imperfections*, Ed. by W. P. Mason (Academic, New York, 1966; Mir, Moscow, 1969).
3. A. S. Nowick and B. S. Berry, *Inelastic Relaxation in Crystalline Solids* (Academic, New York, 1972; Atomizdat, Moscow, 1975).
4. V. L. Indenbom and V. M. Chernov, *Phys. Status Solidi A* **14**, 347 (1972).
5. V. M. Chernov, *Fiz. Tverd. Tela (Leningrad)* **15** (4), 1159 (1973) [*Sov. Phys. Solid State* **15**, 784 (1973)].
6. V. L. Indenbom and V. M. Chernov, in *Elastic Strain Fields and Dislocation Mobility*, Ed. by V. L. Indenbom and J. Lothe (North-Holland, Amsterdam, 1992), p. 517.
7. V. I. Alshits, in *Elastic Strain Fields and Dislocation Mobility*, Ed. by V. L. Indenbom and J. Lothe (North-Holland, Amsterdam, 1992), p. 625.
8. *Proceedings of the 9th International Conference on Internal Friction and Ultrasonic Attenuation in Solids, Beijing, China, 1989*.
9. J. P. Hirth and J. Lothe, *Theory of Dislocations* (McGraw-Hill, New York, 1967; Atomizdat, Moscow, 1972).
10. S. P. Nikanorov and B. K. Kardashev, *Elasticity and Dislocation Inelasticity of Crystals* (Nauka, Moscow, 1985).
11. W. Feller, *An Introduction to Probability Theory and Its Applications* (Wiley, New York, 1957; Mir, Moscow, 1964).
12. O. V. Kamaeva and V. M. Chernov, Preprint FÉI-2856 (Institute of Physics and Power Engineering, Obninsk, 2000).
13. O. V. Kamaeva and V. M. Chernov, Preprint FÉI-2770 (Institute of Physics and Power Engineering, Obninsk, 1999).

*Translated by O. Borovik-Romanova*

---

## DEFECTS, DISLOCATIONS, AND PHYSICS OF STRENGTH

---

# Discontinuous Deformation and Morphology of Polymers

N. N. Peschanskaya\*, P. N. Yakushev\*, V. M. Egorov\*,  
V. A. Bershtein\*, and L. Bokobza\*\*

\* Ioffe Physicotechnical Institute, Russian Academy of Sciences, St. Petersburg, 194021 Russia  
e-mail: yak@pav.ioffe.rssi.ru

\*\* Laboratoire P.C.S.M., Paris Cedex 05, 75231 France

Received November 20, 2001; in final form, December 14, 2001

**Abstract**—The morphological nature of discontinuous (jumplike) deformation is studied. Recording creep behavior of materials using a laser interferometer permits one to determine the parameters of deformation jumps on a micron scale. The objects of investigation were poly(dimethylsiloxane) (PDMS) and a composite material consisting of PDMS and quartz ( $\text{SiO}_2$ ). It is shown that the height and sharpness of jumps depend on the composition of the material and the stage of deformation. An analysis of differential scanning calorimetry (DSC) curves of the materials in the deformed and initial states suggests that deformation results in ordered domains in rubberlike polymers. This confirms the assumption that deformation jumps reflect the presence and the evolution of structural inhomogeneities in amorphous polymers. © 2002 MAIK “Nauka/Interperiodica”.

## INTRODUCTION

Real bodies, including polymers, have a complex nonuniform structure on various morphological levels. According to modern concepts, the creep behavior of materials at constant external parameters is a process of structural self-organization and macrodeformation is ensured by microdeformations on deeper levels. One of the main features of deformation on various levels is its localization, i.e., its discontinuous, jumplike development, e.g., through the nucleation of disclinations and dislocations, slip lines and bands, the formation of “silvery cracks” in polymers, etc. However, the traditional techniques of recording creep curves level the heterogeneity of the structure and the localization of deformation revealed by microscopic, x-ray diffraction, and other methods, and support the concept of a monotonicity of the process with a gradually changing deformation rate. This contradiction can be eliminated by increasing the resolution of the methods of measuring the deformation rate and using new approaches to the investigation of the kinetics of deformation [1–7]. The use of an interferometer in the scheme of recording creep in materials permitted study of the kinetics (rate) of processes at the level of strain increments beginning from fractions of a micron, i.e., on a mesoscopic structural level, and revealing rate changes (deformation jumps) as a creep property common for various materials. The novelty of the results was in the fact that not only the phenomenon of the nonmonotonic development of deformation on a micron level was established, but also a regular change in the characteristics of the jumps at various stages of creep for amorphous polymers, whose structure had no long-range order, was shown. Usually, the term “discontinuous (jumplike) deformation” referred to macroscopic (on the order of

a few millimeters) shear bands, which are formed upon tensile tests at liquid-helium temperatures [8]. In [7], the deformation is considered as a fundamentally non-monotonic process.

As to the nature of jumps, the following assumption was made already in our first work [1]: the deformation jumps arise because of the existence of nonuniform (strong and weak) interactions between polymer molecules; these interactions are overcome in deformation acts, and the scale of the jumps observed depends on the size of ordered domains typical of a given level. This assumption is confirmed by correlations with molecular characteristics [2, 4, 7] and experiments on model samples of polyethylene [3, 5].

To more completely study the nature of jumplike acts of deformation, it is necessary to investigate polymers with various chemical and supramolecular structure in various physical states. Earlier, main attention was paid to solid amorphous and amorphous–crystalline polymers.

In this work, we consider changes in the rate of deformation on a mesoscopic level for poly(dimethylsiloxane) (PDMS) and a composite consisting of PDMS and  $\text{SiO}_2$ . These materials are interesting since at 300 K the polymer is in a rubberlike state and can crystallize upon cooling.

## 1. EXPERIMENTAL

Samples of cross-linked PDMS as well as PDMS filled with quartz particles (40 wt %  $\text{SiO}_2$ ) were investigated. At 300 K, PDMS is in an amorphous rubberlike state. The samples were deformed at a constant stress in the regime of creep at 300 K. Using an interferometer [1–7], the creep process was recorded as successive

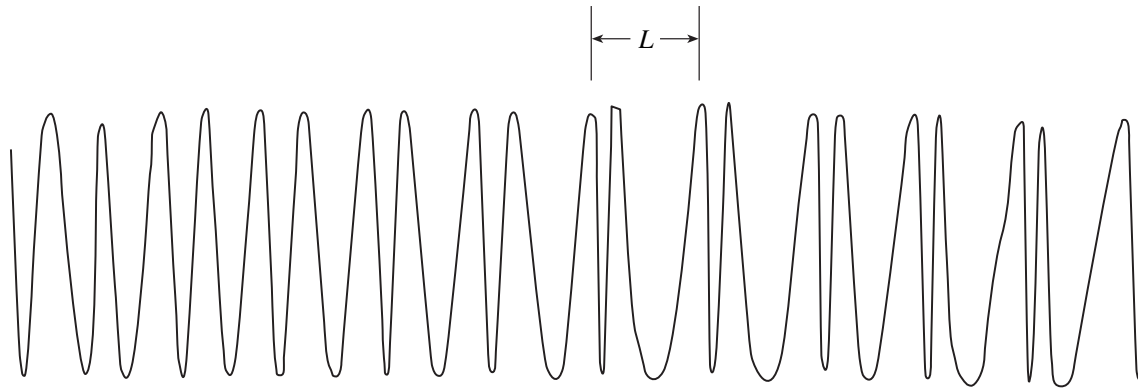


**Fig. 1.** An interferogram of discontinuous creep. The period of the rate variation, or the height of a jump, is  $L = 0.6 \mu\text{m}$ . Each beat is equal to an increment of deformation by  $0.3 \mu\text{m}$ .

beats, each corresponding to a deformation increment of  $0.3 \mu\text{m}$  (Fig. 1). The relative rate of deformation is calculated by the formula  $\dot{\epsilon} = \lambda\nu/2l_0$ , where  $\lambda = 0.63 \mu\text{m}$  is the laser wavelength,  $\nu$  is the beat frequency or an average frequency of several beats, and  $l_0$  is the initial length of the sample. Figure 1 displays an interferogram in which the rate of deformation (frequency of beatings) changes periodically. The period  $L$  of the rate variation expressed as the number of oscillations multiplied by  $0.3 \mu\text{m}$  is equal to the height of the deformation jump. Since the periodicity in the beat frequency is by no means always clearly pronounced, the periods  $L$  were usually determined from the dependence of the rate  $\dot{\epsilon}$  (calculated from the frequencies of successive beat in the interferogram) on the number of beats (Figs. 2–5). The period of the rate changes, or the height of the deformation jump, is equal to the number of points in a period multiplied by  $0.3 \mu\text{m}$ . Another characteristic of a jump is its sharpness  $h$ , i.e., the ratio of the maximum rate to the minimum rate within each period. The table lists the average values of  $L$  and  $h$  for small periods (calculated from five oscillations) and the maximum parameters of the jumps near the general microdeformations indicated in the table.

The tensile samples were 20 mm long and 2 mm thick; the compression samples were 6 mm in height and 4 mm in diameter.

In [9], using the infrared dichroism and birefringence methods, a proportionality was shown to exist between the molecular orientations and the degree of extension of PDMS at 300 K. In this work, for the investigation of changes in the structure of the polymer after deformation, we used the ability of PDMS to crystallize upon cooling. Using differential scanning calorimetry (DSC), we measured the thermal effect upon phase transition [10]. A DSC-2 Perkin–Elmer calorimeter was used; the rates of cooling and heating were 5 K/min. The assumption on the formation of a heterogeneous structure in the process of deformation of the polymer at 300 K was checked as follows. The samples

stretched to 40% at 300 K were cooled to below the melting temperature  $T_m$ ; then, upon heating, we recorded the DSC curve in the melting range of the crystals and compared the DSC curves of the deformed and undeformed samples of PDMS and PDMS +  $\text{SiO}_2$ .

## 2. RESULTS AND DISCUSSION

In the rubberlike state, the main deformation of the polymer is developed during loading, then the creep rate decreases rapidly. To obtain the same degree of deformation, the PDMS samples should be subjected to smaller stresses than the composite samples and to smaller stresses during tensile tests than upon compression tests; therefore, it is impossible to compare the creep behavior of such materials at identical stresses and strains and main attention was paid to deformation under tension. Fragments of creep curves of the materials studied are shown in Figs. 2–5 in the strain–rate–strain coordinates; each point in the curves shown

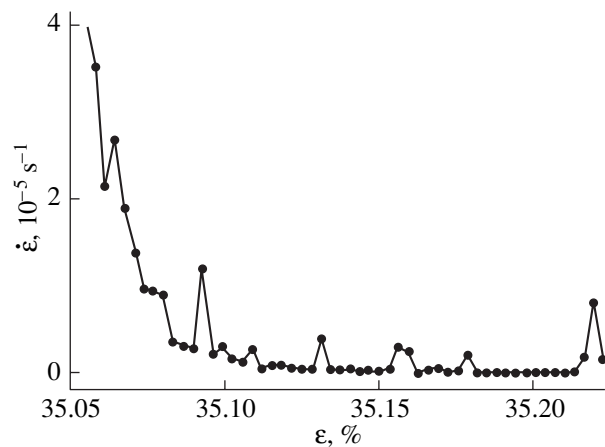


**Fig. 2.** Variation of the creep rate as a function of deformation upon tension for poly(dimethylsiloxane). Each point corresponds to the creep rate within an interval of  $0.3 \mu\text{m}$ . The stress is  $\sigma = 0.15 \text{ MPa}$ .

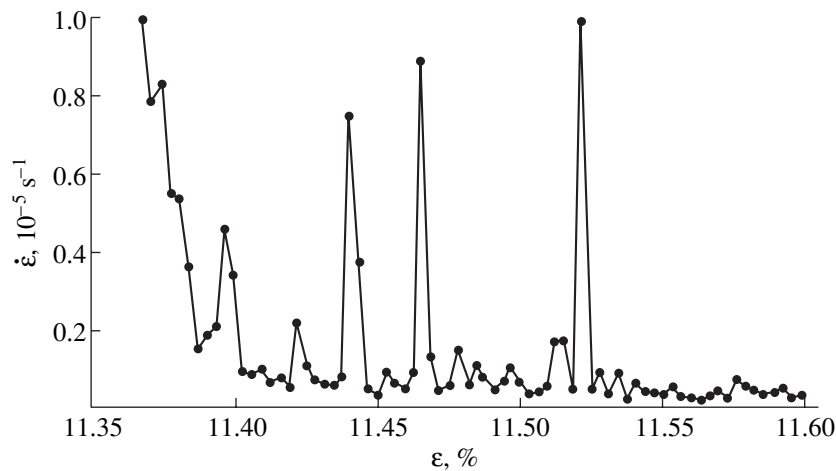


Fig. 3. PDMS + SiO<sub>2</sub>, same as in Fig. 2,  $\sigma = 0.2$  MPa.

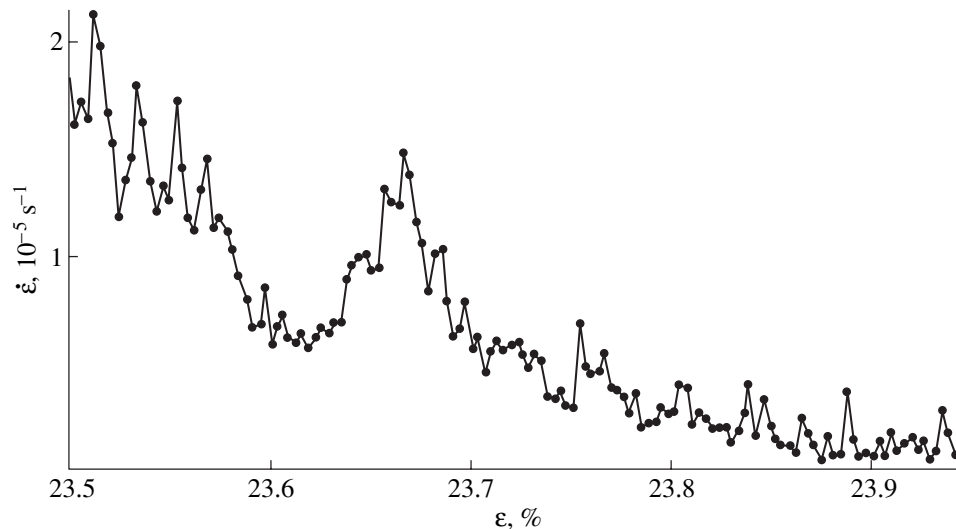


Fig. 4. PDMS + SiO<sub>2</sub>, same as in Fig. 2,  $\sigma = 0.35$  MPa.

refers to a deformation increment of  $0.3 \mu\text{m}$ . The main result of the work is that the deformation jumps (the nonuniform deformation rate) are observed for the polymer in the rubberlike state even at relatively small deformations (Fig. 3). It is seen from Figs. 2–5 and from the table that the periods  $L$  of the variation of the deformation rate, or the deformation jumps, can be divided into two groups. The periods  $L_{\text{min}}$  of the smallest variations are approximately the same upon tension and compression (see table). With increasing deformation  $\epsilon$ , small jumps unite into coarser ones ( $L_{\text{max}}$ ) consisting of smaller jumps (Figs. 4, 5 and table). Upon tension, the amplitude of variations of the deformation rate ( $h$ ) is usually higher than upon compression, which is in general typical of various polymers and various deformation stages. The greater sharpness and the more

complex shape of jumps upon tension can be explained by the formation of microcracks under the effect of tensile stresses. The greatest variety of jumps was observed upon tension of the composite, which can be attributed to shears not only in pure polymer but also in the adhesion layers at polymer–quartz interfaces.

It was shown, using composite samples as an example (see Figs. 3–5 and table), that with increasing deformation (and stress), there occurs an increase in the period  $L$  of jumps and the formation of large jumps from smaller ones. An analogous evolution of the periods of the variations of the deformation rate was observed upon deformation of glassy and crystalline polymers in [1, 3, 5, 7].

By definition, deformation jumps reflect the cooperative behavior of kinetic units and, consequently, are

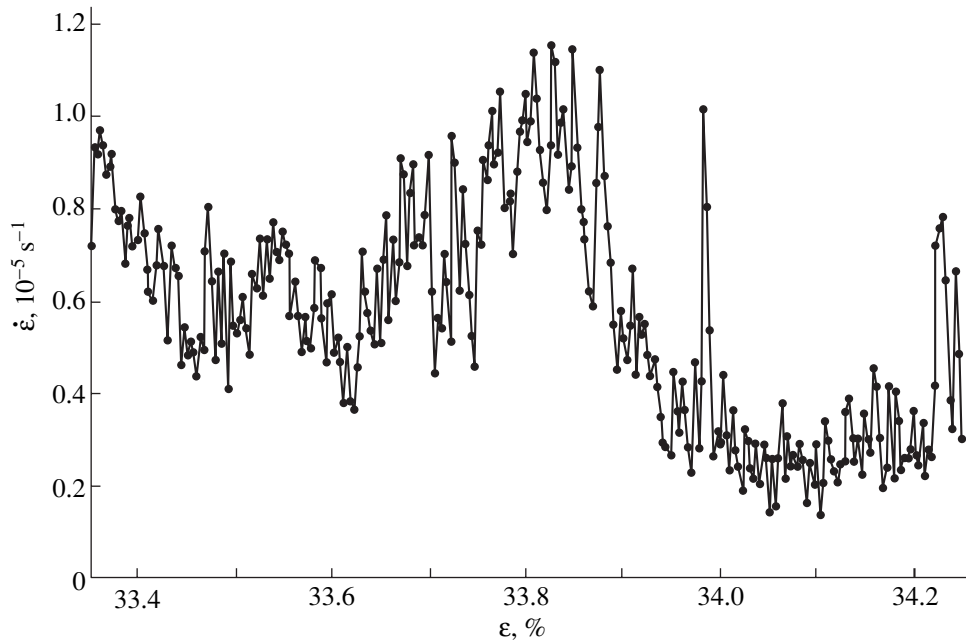


Fig. 5. PDMS + SiO<sub>2</sub>, same as in Fig. 2,  $\sigma = 0.55$  MPa.

related to the heterogeneity of the polymer morphology. The information on the morphology of amorphous polymers is contradictory, but the concept of a cross-linked structure formed by “physical nodes” between fragments of neighboring chains can be considered to be commonly accepted.

Strong interactions between groups of atoms in neighboring molecules and the most densely packed regions of molecular chains can serve as physical nodes. Strong bonds correspond to large relaxation times; weak bonds, to small relaxation times; i.e., the nonuniformity of interactions in amorphous polymers is sufficient grounds for the appearance of a stepped type of motion. It is more difficult to explain what features are associated with the scale of jumps in amorphous polymers, where the presence of clearly pronounced elements of packing of micron size has not yet

been proved. In this case, an analogy with dislocation models can be drawn; these models were not first applied to amorphous bodies, since such bodies do not contain classical dislocations. The situation changed when Gilman suggested the model of the formation, under the action of a force, of a gliding dislocation loop, which travels on the plane in which maximum tangential stresses act. Similarly, we suppose that structural nonuniformities of micron sizes can arise in amorphous polymers under the effect of directional forces and deformations. For PDMS, it was shown in [9] that the molecules become oriented upon deformation. In the process of orientation, ordered domains can arise (because of a greater degree of local orientation of chain fragments and because of their denser packing), similar to the situation where fibrils are formed upon extension of amorphous–crystalline polymers. The

Parameters of deformation jumps for PDMS and PDMS + SiO<sub>2</sub>

Material and loading mode	Stress, MPa	$\epsilon$ , %	Average values of $L_{\min}$ , $\mu\text{m}$	$L_{\max}$ , $\mu\text{m}$	Average values of $h$	$h_{\max}$
PDMS, tension	0.15	35	0.9	1.2	2.5	3
PDMS, compression	0.65	30	0.9	3	1.3	2.2
PDMS + SiO <sub>2</sub> , tension	0.2	11.3	1.0	1.5	6.0	10
	0.25	14.3	1.25	5.4	3.0	4.0
	0.35	23.4	1.25	9.0	2.5	3.0
	0.45	31.3	1.6	9.0	3.0	4.5
	0.55	33.6	1.8	50	3.5	7.0
PDMS + SiO <sub>2</sub> , compression	1.5	26	1.0	1.5	1.4	1.5

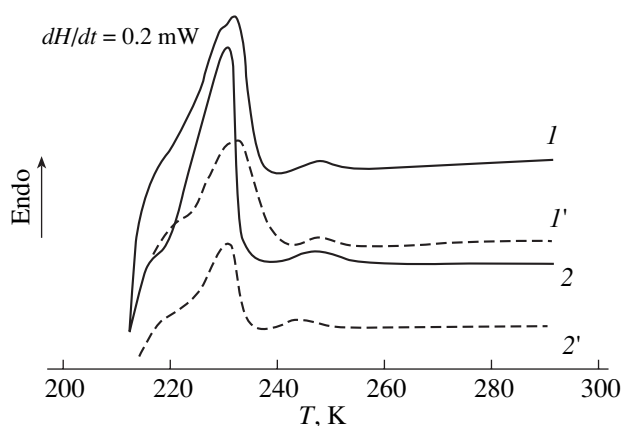


**Fig. 6.** DSC curves: (1, 1') undeformed sample and (2, 2') sample stretched to 40% at 300 K. Solid lines, PDMS; dashed lines, composite.

length of the initial ordered domains in amorphous polymers is supposed to correspond approximately to the length of a stretched molecule (fractions of a micron, microns). Such “amorphous fibrils” can determine the scale of deformation jumps that can be solved using this technique. In the process of deformation, as follows from experiments (Figs. 2–5), coarser jumps are formed from smaller ones and complex jumps appear sometimes [3, 4], which indicates an evolution of the structure that can be called “kinetic.”

The above suggested concepts were confirmed in this work by the investigations (using the DSC technique) of structural change upon deformation. At 300 K, poly(dimethylsiloxane) is in a rubberlike state, but upon cooling it passes into an amorphous–crystalline state (the melting temperature is  $T_m = 230$  K, and the temperature of transition into the glassy state is  $T_g = 150$  K). It turned out that the DSC spectra of PDMS and composite films that were stretched at 300 K and cooled to below  $T_g$  broaden significantly upon heating in the region of  $T_m$  as compared to similar spectra for undeformed samples (Fig. 6).

The effect for the composite is somewhat higher; in addition, a shift of the spectra of deformed samples toward higher temperatures by 2–3 K is noted. The broadening of the DSC lines suggests that the deformation of the polymer in the rubberlike state increases the dispersion of crystallites that are formed at low temperatures; i.e., the structure of a deformed amorphous polymer contains a greater number of nuclei for crystallites than in the undeformed material. In the filled poly-

mer, the number of variations of crystals can increase because of the existence of boundary layers between the polymer and  $\text{SiO}_2$ ; therefore, the DSC line for the composite turns out to be broader than that for a pure polymer. Thus, the data obtained support the assumption on the appearance of heterogeneity in the polymer structure oriented upon deformation even for the rubberlike state when the relaxation times are small. The data on discontinuous creep and the results of DSC are in good agreement; the introduction of a filler increases the variety of the characteristics of jumps and the variation of crystals.

The above results prove that the assumption that it is the heterogeneity of the medium that is the cause of the discontinuous (jumplike) character of creep is also confirmed for amorphous polymers. Therefore, the investigation of the kinetics of deformation on a mesoscopic level gives information on the scale of ordered structural domains and on their evolution during deformation.

## REFERENCES

1. N. N. Peschanskaya and P. N. Yakushev, *Fiz. Tverd. Tela (Leningrad)* **30** (7), 1299 (1988) [*Sov. Phys. Solid State* **30**, 1264 (1988)].
2. N. N. Peschanskaya, *Vysokomol. Soedin., Ser. A* **31** (6), 1182 (1989).
3. N. N. Peschanskaya, L. P. Myasnikova, and A. B. Sinani, *Fiz. Tverd. Tela (Leningrad)* **33** (10), 2948 (1991) [*Sov. Phys. Solid State* **33**, 1665 (1991)].
4. N. N. Peschanskaya, *Fiz. Tverd. Tela (St. Petersburg)* **35** (11), 3019 (1993) [*Phys. Solid State* **35**, 1484 (1993)].
5. N. N. Peschanskaya, P. N. Yakushev, L. P. Myasnikova, *et al.*, *Fiz. Tverd. Tela (St. Petersburg)* **38** (8), 2582 (1996) [*Phys. Solid State* **38**, 1416 (1996)].
6. N. N. Peschanskaya, J. Hristova, and P. N. Yakushev, *Polymer* **42**, 7101 (2001).
7. N. N. Peschanskaya, *Fiz. Tverd. Tela (St. Petersburg)* **43** (8), 1418 (2001) [*Phys. Solid State* **43**, 1478 (2001)].
8. V. V. Shpeĭzman, V. I. Nikolaev, B. I. Smirnov, *et al.*, *Fiz. Tverd. Tela (St. Petersburg)* **42** (6), 1034 (2000) [*Phys. Solid State* **42**, 1066 (2000)].
9. L. Bokobza, F. Clement, L. Monnerie, and P. Laperonne, *The Wiley Polymer Networks Group Review Series* (Wiley, New York, 1998), Vol. 1, p. 321.
10. V. A. Bershteĭn and V. M. Egorov, *Differential Scanning Calorimetry in Physical Chemistry of Polymers* (Khimiya, Leningrad, 1990).

*Translated by S. Gorin*

---

## MAGNETISM AND FERROELECTRICITY

---

# Preparation and Electrical Properties of Cobalt-Containing Carbon Fibers

I. A. Bashmakov, V. A. Dorosinets, M. G. Lukashevich, A. A. Mazanik,  
T. F. Tikhonova, and D. A. Skripka

*Belarussian State University, pr. F. Skoriny 4, Minsk, 220050 Belarus*

Received July 13, 2001

**Abstract**—Carbon fibers with inclusions of cobalt nanoclusters are prepared by heat treatment of carboxylated cellulose containing cobalt cations. The influence of the heat treatment conditions on the structuring of the carbon matrix and cobalt clusters, the magnetization hysteresis loop, the temperature dependence of the conductivity, and the magnetoresistance is investigated. It is established that the cobalt-containing carbon fibers heat treated at  $T_M = 700$  and  $900^\circ\text{C}$  possess superparamagnetic and ferromagnetic properties, respectively. It is shown that fibers heat treated under different conditions are characterized by different conduction mechanisms and can exhibit anisotropic and giant magnetoresistances and also the effects associated with the influence of magnetic field on the processes of weak localization and spin–orbit scattering. © 2002 MAIK “Nauka/Interperiodica”.

### 1. INTRODUCTION

Over the last decades, the electronic properties of granular metals have been extensively investigated by experimental and theoretical methods. Granular ferromagnets belong to the subclass of granular metals in which metallic nanoparticles consisting of a ferromagnetic material are introduced into a nonmagnetic matrix. Either nonmagnetic metals (Ag, Au, and Cu) or dielectrics ( $\text{SiO}_2$  and  $\text{Al}_2\text{O}_3$ ) are traditionally used as nonmagnetic matrices. These materials possess quite different magnetic, magnetoresistive, and transport properties, which can be controlled by choosing the composition of the materials and the shape and structure of magnetic nanoparticles. The size-dependent magnetic characteristics [1] and the giant [2] and tunnel [3] magnetoresistive effects are among the most intriguing properties of these materials. However, the mechanisms of electron transfer in these systems, especially in the vicinity of metal–insulator junctions, are still not clearly understood. In this range, the electrical conductivity is determined, to a large extent, by the properties and structure of thin interlayers between metallic particles, because these interlayers, as a rule, are strongly disordered and can vary in composition.

Investigation into the magnetic and transport properties of these nanostructured materials is not only of purely scientific importance but also of applied significance in respect to the development of magnetic-memory elements with a giant density and magnetic-field pickups on the basis of the giant or tunnel magnetoresistive effects. The giant and tunnel magnetoresistive effects are observed in the cases of metallic and dielectric matrices, respectively. At the same time, the physics of electron transfer processes that are responsible

for the giant and tunnel magnetoresistive effects in a magnetic field calls for further investigation. In order to gain a better insight into the magnetism and the mechanisms of magnetotransport in these systems, it is also important to investigate the structural and electrical properties in the case when the conductivity of the matrix is intermediate between the conductivities of metals and dielectrics.

Granular solids are usually produced by simultaneous or sequential deposition of metal and insulator layers [4, 5], the sol–gel method [6], or a combination of ion-beam sputtering and preparation of a matrix in an inert-gas flow [7]. Alternatively, metallic nanoparticles in the matrix with different electrical conductivities can be prepared by heat treatment of carboxylated cellulose fibers after replacement of protons in COOH groups of the cellulose by metal cations through the ion-exchange sorption. An atomically uniform distribution of metal cations over the fiber bulk in the course of sorption can provide a uniform distribution of metallic nanoparticles in carbon fibers upon heat treatment under the appropriate conditions.

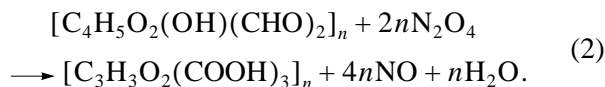
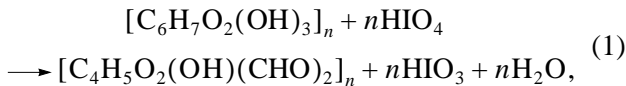
The present paper reports on the results of a systematic investigation into the structural, magnetic-field, and temperature dependences of the electrical conductivity and the magnetoresistance for  $\text{Co}_x\text{C}_{1-x}$  carbon fibers containing cobalt clusters at different concentration ratios between cobalt and carbon. Cobalt, like nickel, is the main metal used for preparing granular ferromagnets. Carbon was chosen as the matrix material, because its conductivity can be easily changed by varying the temperature and conditions of heat treatment.

Effect of the duration of preliminary annealing of the cobalt salt of tricarboxycellulose (the cobalt content in polymeric acid is equal to 2.7 mmol/g) in air at  $T_p = 300^\circ\text{C}$  on the cobalt content in carbon fibers prepared by annealing under vacuum at  $T_M = 700$  and  $900^\circ\text{C}$

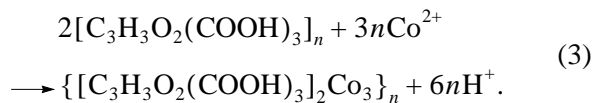
No.	Time $\tau$ of annealing at $300^\circ\text{C}$ in air, h	Mole fraction of cobalt in carbon fibers	
		$T_M = 700^\circ\text{C}$	$T_M = 900^\circ\text{C}$
1	0	0.138	0.146
2	0.5	0.159	0.185
3	1.0	0.177	0.198
4	2.0	0.251	–
5	3.0	0.606	–

## 2. SAMPLE PREPARATION

Cobalt clusters in the carbon matrix were produced by heat treatment of carboxylated cellulose fibers after substitution of cobalt cations for protons in COOH groups of the cellulose through the ion-exchange sorption. Tricarboxycellulose (polymeric acid) was used as carboxylated cellulose. Tricarboxycellulose was obtained by introducing three carboxyl groups into each monomer unit of a cellulose macromolecule according to the reactions



Tricarboxycellulose synthesized through reactions (1) and (2) retained the fibrous structure of the initial cellulose (viscose fibers). As follows from chemical analysis, the content of COOH groups in tricarboxycellulose was equal to 2.8–35.0 wt %. Cobalt cations were introduced into the tricarboxycellulose matrix from aqueous solutions of cobalt acetate at a solid-to-liquid ratio of 1 : 50 and a temperature of  $20.0 \pm 0.2^\circ\text{C}$  through ion-exchange sorption according to the reaction



The concentration of cobalt acetate solutions was 0.125 M, which provided the maximum substitution of cobalt cations for protons of tricarboxycellulose. The cobalt content in tricarboxycellulose varied from 2.5 to 3.1 mmol/g.

The samples were heat treated under vacuum (with a residual pressure of 1.3 Pa) at a heating rate of 3 K/min. After heating to the final heat treatment temperature  $T_M$  (700 or  $900^\circ\text{C}$ ), the samples were isothermally treated for 30 min with the aim of stabilizing

thermochemical transformations in the annealing product. The heat treatment resulted in the formation of carbon fibers that had cobalt inclusions and reproduced the texture of the cellulose precursor. When it is necessary to obtain spatial formations with a complicated configuration, this method offers an advantage, as the initial cellulose fibers possess a high flexibility.

The thermostimulated transformations in tricarboxycellulose fibers under the above conditions led to a considerable decrease in their size and mass (the fiber diameter decreased from 1.5 to 0.5 mm, and the mass loss was as large as 70%) due to the removal of volatile low-molecular products, for the most part, in the form of carbon monoxide and carbon dioxide.

The maximum mole fraction  $x$  of cobalt in the  $\text{Co}_x\text{C}_{1-x}$  fibers prepared from cobalt salts of tricarboxycellulose at the annealing temperatures used did not exceed 0.19. This appeared to be insufficient for reaching the metal–insulator transition. In order to increase the cobalt content in the carbon matrix, we modified the regime of heat treatment of the metallocellulose precursors. Essentially, the modification was as follows: prior to the thermal annealing under vacuum, the metallocellulose fibers were heat treated at  $300^\circ\text{C}$  in air for  $\tau = 0.5\text{--}3$  h. This led to more intensive oxidation reactions in the cellulose matrix and to an increase in the total mass loss in the sample and the cobalt content in the carbon fiber (see table). As can be seen from the table, the preliminary annealing of tricarboxycellulose containing 2.7 mmol/g Co at  $T_p = 300^\circ\text{C}$  for 3 h made it possible to obtain carbon fibers with a mole fraction of cobalt as large as 0.60.

The cobalt content in the  $\text{Co}_x\text{C}_{1-x}$  fibers was independently determined by chemical (gravimetric) analysis and Auger spectroscopy. In the case of gravimetric analysis, the fibers were calcined at a temperature of  $850^\circ\text{C}$  to transformation into  $\text{Co}_3\text{C}_4$  and the cobalt content in the cobalt-containing carbon fibers was calculated from the weight of the reaction product. The cobalt contents determined in the carbon fibers by these two methods were slightly different, possibly, because the chemical method offers an integral estimate, whereas the Auger spectroscopic data refer only to a thin surface layer. For this reason, we presented the data obtained by the chemical method and Auger spectroscopy was used to check the presence of foreign elements in the fibers. The carbon matrix reliably protects the cobalt clusters against oxidation. The stability of the cluster structure in the carbon matrix is indicated by the fact that the electrical and magnetic characteristics of the  $\text{Co}_x\text{C}_{1-x}$  fibers remained constant over the course of a year.

## 3. EXPERIMENTAL TECHNIQUE

The distribution of cobalt clusters over the carbon fiber, their structure, and the influence on the structuring of the carbon matrix were investigated using trans-

mission electron microscopy (TEM) on a Philips CM 300UT-EFG transmission electron microscope at an accelerating voltage of 300 kV with a resolution of about 1.5 Å. The magnetization hysteresis loops were recorded on a Faraday magnetometer. The temperature dependences of the electrical resistance and the magnetoresistance were measured with samples prepared by cutting the fibers into 6- to 8-mm-long pieces to which copper wires were cemented using a silver paste. The current–voltage characteristic in the range covered was linear. The temperature dependences of the resistance and the magnetoresistance were measured in a dc mode in the temperature range 2–300 K at magnetic fields as high as 1.2 T.

## 4. RESULTS

### 4.1. Structuring of the matrix and cobalt clusters.

Examination of the TEM images of fibers (Figs. 1–5) prepared at different heat treatment temperatures revealed that the heat treatment leads to the formation of cobalt clusters inside the carbon fibers. As can be seen from Figs. 1 and 2, the mean size of the cobalt clusters at the heat treatment temperature  $T_M = 700^\circ\text{C}$  is approximately equal to 10 nm. The clusters are rather uniformly distributed over the fiber bulk and have a polycrystalline structure. No structuring of carbon is observed.

A general view of the matrix and clusters in the carbon fiber annealed at  $T_M = 900^\circ\text{C}$  is displayed in Fig. 3. An increase in the annealing temperature leads to an

increase in the cluster size. In this case, the diameter of the cobalt clusters varies from less than 30 to 200 nm or greater and their distribution over the fiber bulk becomes nonuniform.

It is seen from Fig. 4 that the cobalt clusters have a catalytic effect on the formation of graphite planes. This process most intensively occurs in the region between two closely spaced cobalt clusters. It can also be seen from this figure that a layer composed of graphite planes surrounding the cobalt cluster is formed in the matrix. The layer of graphite planes has an imperfect structure in regions far from other clusters. The twisting of the graphite planes around the cobalt clusters induces mechanical stresses in regions between spherical formations, which leads to the appearance of pores in these regions.

Note that the introduction of the cobalt clusters into the amorphous carbon matrix results in the formation of extended regions 100 nm in size or greater with parallel graphite planes, as is shown in Fig. 5. The interplanar distance  $d$  is of the order of 0.370 nm. This is somewhat larger than the corresponding distances in turbostratum carbon, which is characterized by the absence of regular orientation of layers with respect to the hexagonal axis ( $d = 0.344$  nm), and pyrolytic graphite ( $d = 0.335$  nm) but is typical of strongly disordered fibers [8].

**4.2. Magnetization.** The magnetization hysteresis loops measured at room temperature for the cobalt-containing carbon fibers annealed at  $T_M = 700$  and  $900^\circ\text{C}$  are depicted in Fig. 6. The magnetization for a particular magnetic field strength increases with an increase in

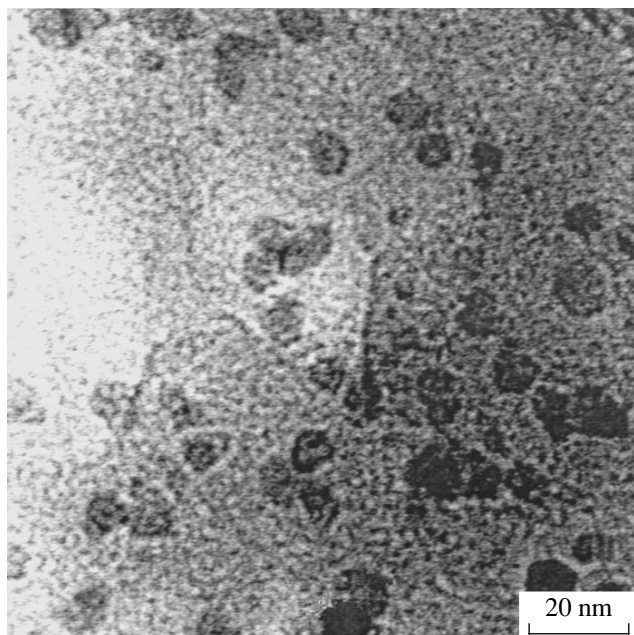


**Fig. 1.** TEM image of the fiber annealed at  $T_M = 700^\circ\text{C}$ .

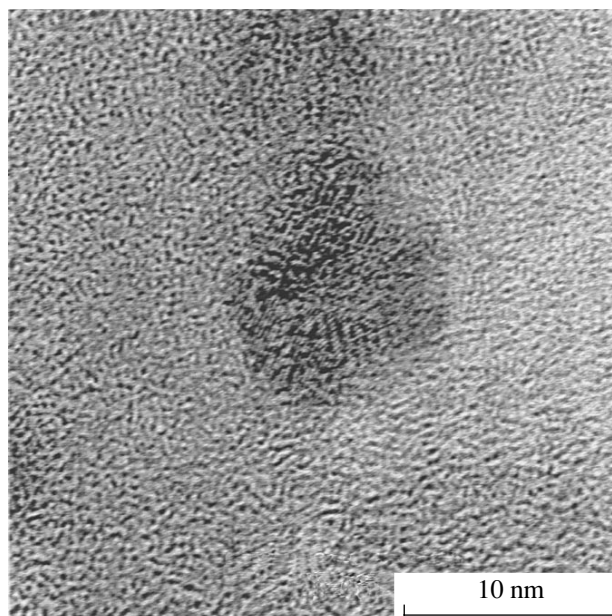


**Fig. 2.** Structure of the cobalt cluster in the fiber annealed at  $T_M = 700^\circ\text{C}$ .

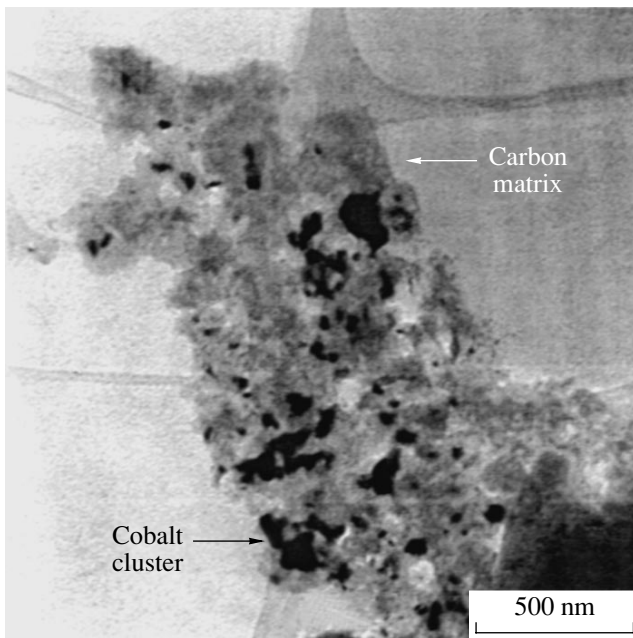


**Fig. 3.** TEM image of the fiber annealed at  $T_M = 900^\circ\text{C}$ .

the heat treatment temperature and the cobalt content in the carbon fibers. It is seen that the fibers annealed at  $T_M = 700^\circ\text{C}$  with  $x = 0.123$  and  $0.157$  do not possess remanent magnetization (Fig. 6, curves 1, 2). This indicates that the blocking temperature of magnetic moments of the clusters is below room temperature; i.e., the system of cobalt clusters at 300 K is in the superparamagnetic state. The blocking temperature

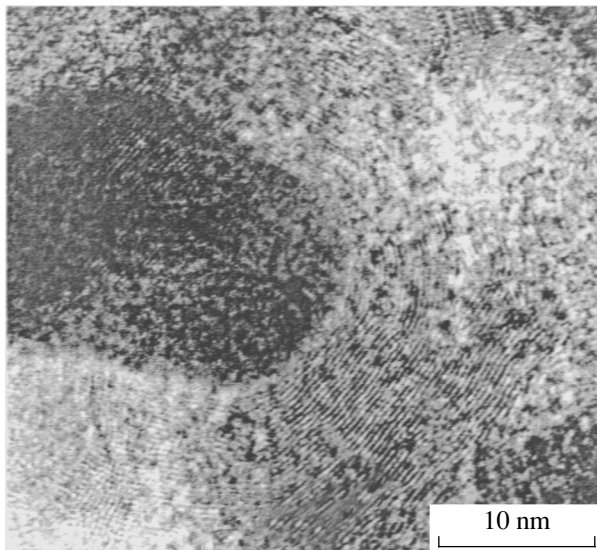


**Fig. 4.** TEM image of a fiber region with structuring of carbon between cobalt clusters upon annealing at  $T_M = 900^\circ\text{C}$ .

estimated according to [9] for the system of cobalt clusters with a cluster diameter of 10 nm, which is most characteristic of this heat treatment temperature (Fig. 1), is less than 100 K.

An increase in the magnetization with an increase in the concentration of cobalt cations in tricarboxycellulose and in the annealing temperature is caused by an increase in the cluster size. The fibers annealed at  $T_M = 900^\circ\text{C}$  with the cobalt contents  $x = 0.146$  and  $0.187$  possess remanent magnetization with the equal coercive force  $B_C = 0.043$  T (Fig. 6, curves 3, 4). The cobalt clusters, whose size in these fibers can be as large as 200 nm or greater (Fig. 3), are in the ferromagnetic state, which explains the remanent magnetization of the carbon fibers annealed at  $T_M = 900^\circ\text{C}$ .

#### 4.3. Temperature dependence of the resistance.

With the use of the above procedures and heat treatment conditions, we prepared three groups of samples exhibiting different behavior of the temperature dependences of the resistance  $R(T)$  and magnetoresistance  $R(B)$ . Since the dependences  $R(T)$  for the samples belonging to each group differed only quantitatively, one sample from each group was chosen for analysis.

Figure 7 shows the temperature dependences of the resistance for three samples on the linear (Fig. 7a), logarithmic (Fig. 7b), and  $T^{1/2}$  (Fig. 7c) scales. The numbering of the samples corresponds to that of the groups of the samples. The samples of the first group ( $0.146 \leq x \leq 0.187$ ) were prepared by the aforementioned technique with annealing under vacuum at  $T_M = 900^\circ\text{C}$  and without intermediate annealing at  $300^\circ\text{C}$  in air. The experimental dependences  $R(T)$  and  $R(B)$  are given for sample no. 1 with  $x = 0.187$ . As is seen from Fig. 7

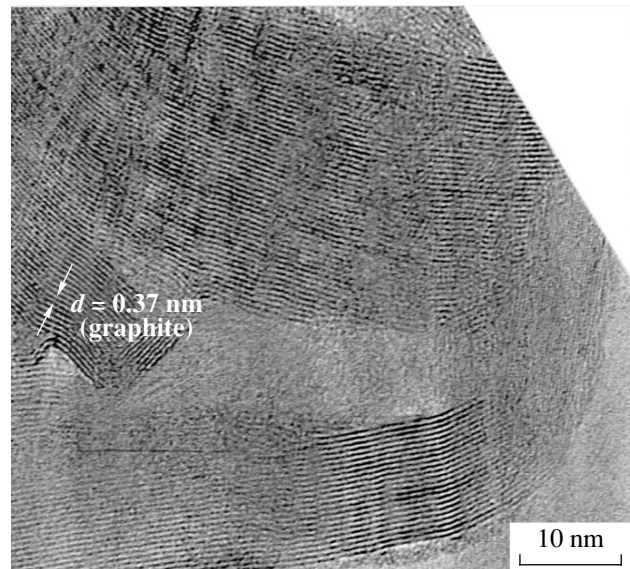


**Fig. 5.** TEM image of a fiber region with structuring of carbon in the form of graphite planes upon annealing at  $T_M = 900^\circ\text{C}$ .

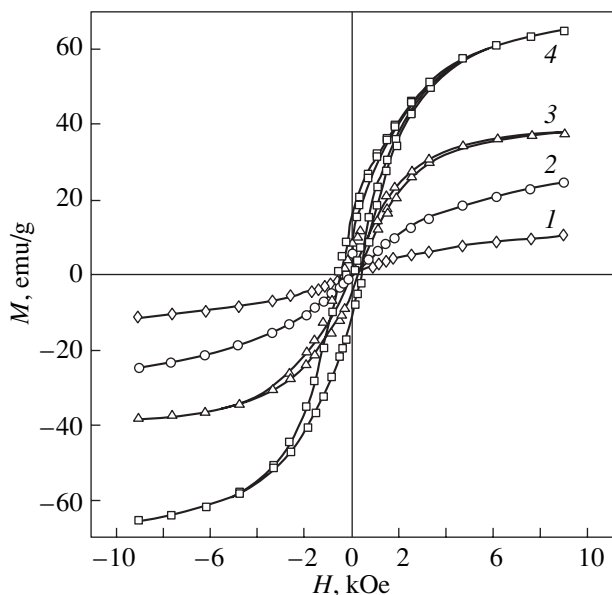


**Fig. 6.** Magnetization hysteresis loops at  $T = 300$  K for cobalt-containing carbon fibers annealed at  $T_M = (1, 2)$  700 and  $(3, 4)$  900°C. Mole fraction  $x$  of cobalt in carbon fibers: (1) 0.123, (2) 0.157, (3) 0.146, and (4) 0.187.

(curve 1), the temperature coefficient of resistance for this sample is negative; hence, we can make the inference that this sample corresponds to the dielectric side of the metal–dielectric transition. The temperature dependence of the resistance is linear on the logarithmic scale (Fig. 7b).

The procedure of preparing sample no. 2 with  $x = 0.198$  involved preliminary annealing at  $T_p = 300^\circ\text{C}$  for 1 h in air followed by annealing under vacuum at  $T_M = 900^\circ\text{C}$  for 0.5 h. The dependence  $R(T)$  for this sample (Fig. 7, curve 2) exhibits a minimum at  $T = 45$  K. The temperature coefficient of resistance is positive in the high-temperature range and negative in the low-temperature range. The minima in the curves  $R(T)$  are observed for all samples of the second group with a change in the low-temperature annealing time in the range  $0.5 \leq \tau \leq 1$  h.

For sample no. 3 with  $x = 0.251$ , the time  $\tau$  of the preliminary annealing at  $T_p = 300^\circ\text{C}$  in air was equal to 2 h and the temperature  $T_M$  of the high-temperature annealing was 700°C. The temperature dependence of the resistance for this sample is typical of “dirty” metals. As the temperature decreases, the resistance decreases and reaches saturation at low temperatures. Other samples of this group with the preliminary annealing time  $\tau$  varying in the range 1–3 h have a similar dependence  $R(T)$ .

The change in the behavior of the dependence  $R(T)$  (when changing over from sample no. 1 to sample no. 3) with a variation in the annealing temperature reflects an increase in the structural perfection of the percolation channels providing the charge transfer.

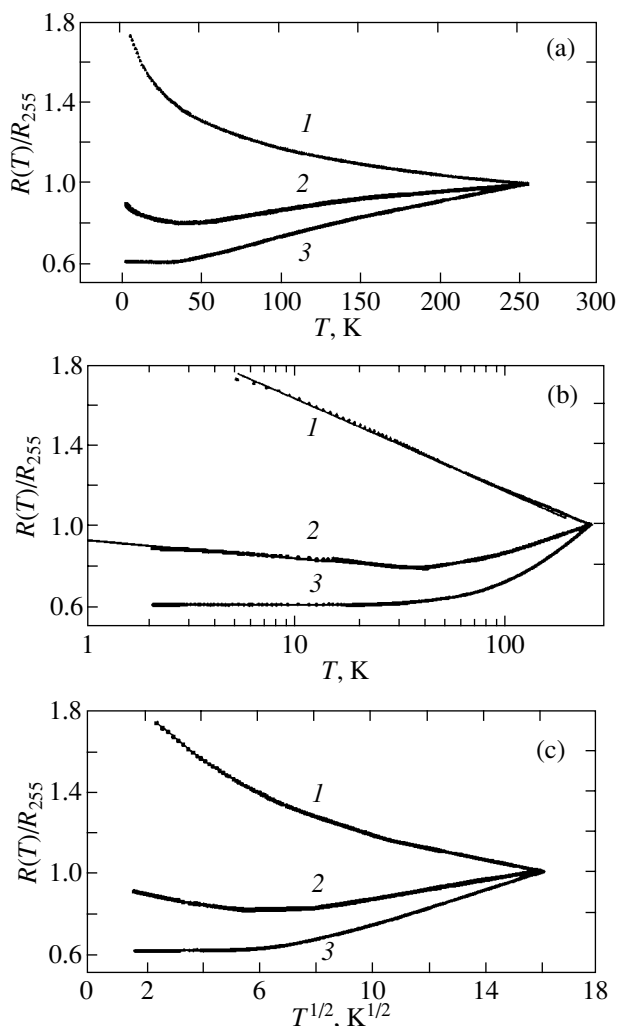


**Fig. 7.** Temperature dependences of the resistance normalized to the resistance at  $T = 255$  K on different scales for fiber samples prepared under different heat treatment conditions: (1)  $T_M = 900^\circ\text{C}$ ,  $x = 0.187$ , without preliminary heat treatment; (2)  $T_M = 900^\circ\text{C}$ ,  $x = 0.198$ ,  $\tau = 1$  h; and (3)  $T_M = 700^\circ\text{C}$ ,  $x = 0.251$ ,  $\tau = 2$  h.

These channels consist of cobalt clusters with a pronounced crystal structure and intercluster regions that are characterized by a considerable degree of disordering and, possibly, include the carbon phase.

**4.4. Magnetoresistive effect.** The magnetic-field dependences of the magnetoresistance  $\Delta R(B)/R(0) = (R(B) - R(0))/R(0)$  for the samples of three groups at different temperatures with the magnetic field applied normally to the fiber are plotted in Figs. 8 and 9. The dependences of the magnetoresistance on the magnetic field for samples of these groups differ significantly. It is worth noting that the magnetoresistance of the samples of all the groups involves a negative magnetoresistance component over the entire studied range of magnetic fields  $-1.2 \leq B \leq 1.2$  T. The negative magnetoresistance component of all the samples increases with a

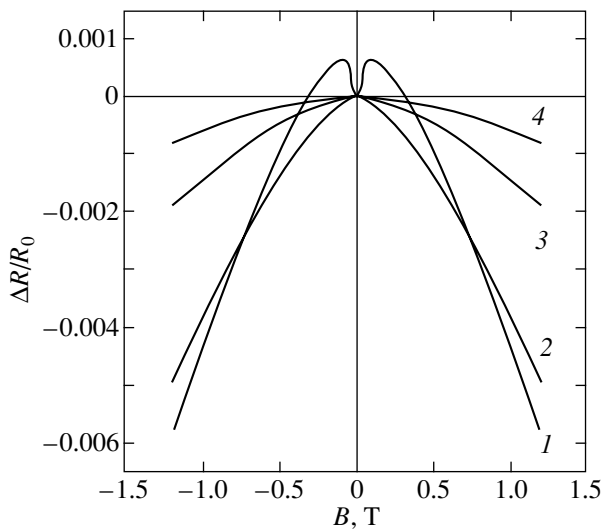


**Fig. 8.** Typical magnetic-field dependences of the magnetoresistance for cobalt-containing carbon fibers of the first group at different temperatures  $T$  (K): (1) 2.2, (2) 10, (3) 50, and (4) 100.

decrease in the temperature and exhibits a similar behavior in the magnetic field. In this respect, the typical magnetic-field dependences of the magnetoresistance are represented only for samples of the first group at different temperatures in Fig. 8. The magnetoresistance of the samples of different groups differs only in weak magnetic fields, in which the positive magnetoresistance component is observed for the fibers of all the groups (Fig. 9). The magnetoresistance of sample no. 1 (Fig. 9a) is positive only in weak magnetic fields at a temperature of 2 K, whereas only the negative component is observed at higher temperatures. No hysteresis is found in the magnetoresistance curves; i.e., the magnetoresistance does not depend on the prehistory and the direction of magnetic field scanning.

The dependence of the magnetoresistance for sample no. 2, which is characterized by the minimum in the temperature dependence of the resistance, also exhibits unusual behavior. As for the samples of the first group, the magnetoresistance of this sample, in the low-temperature range is positive without hysteresis. An increase in the temperature is attended by the disappearance of the positive magnetoresistance component for sample no. 2. However, unlike sample no. 1, the positive magnetoresistance component again arises at temperatures above 50 K (Fig. 9b). It can be seen that the local minimum in the magnetoresistance curve at this temperature is shifted with respect to  $B = 0$  and is located approximately at  $B = 0.07$  T when the magnetic field changes from 1.2 T toward negative fields. The change in the magnetic field in the opposite direction leads to a symmetrical shift of the local minimum toward positive magnetic fields.

The positive magnetoresistance component is observed for the samples of the third group over the

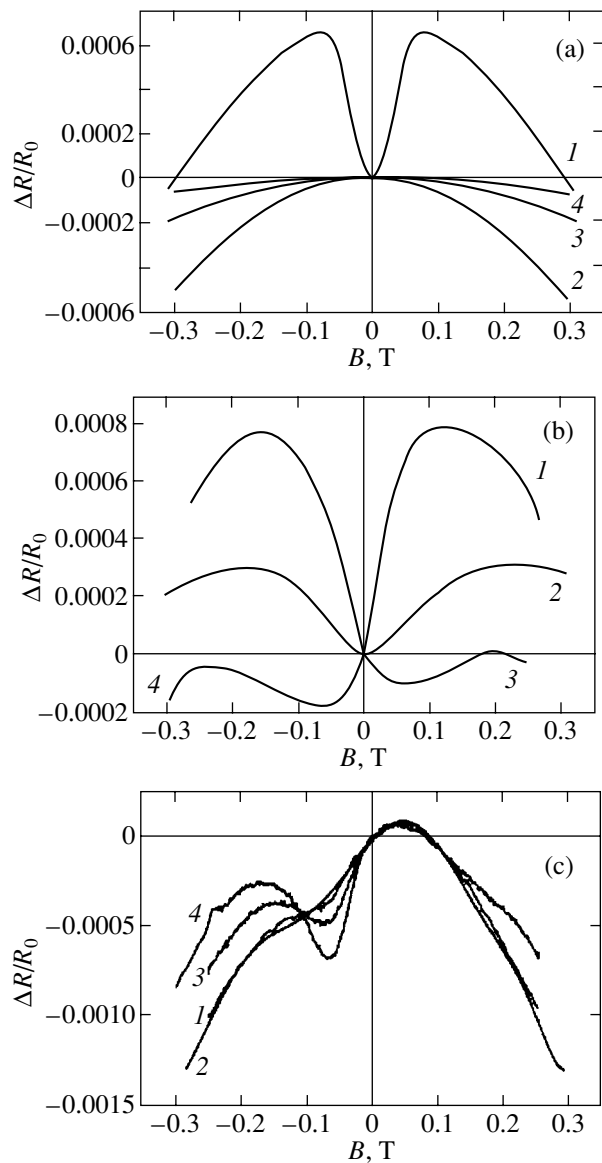


**Fig. 9.** Magnetic-field dependences of the magnetoresistance for cobalt-containing carbon fibers of (a) the first, (b) second, and (c) third groups at different temperatures in weak fields. Curves 1–4 are measured at the same temperatures as those in Fig. 8.

entire temperature range  $2 \text{ K} \leq T \leq 100 \text{ K}$  (Fig. 9c). However, the magnetic-field dependence of the magnetoresistance substantially changes in the range of weak magnetic fields: as the temperature decreases, the pronounced local minimum shifted with respect to  $B = 0$  at high temperatures (Fig. 9c, curves 3, 4) is smeared and manifests itself as a plateau in the curves  $R(B)$  at low temperatures (Fig. 9c, curves 1, 2). The direction of the shift of the local minimum in the magnetoresistance curves depends on the prehistory. As a consequence, there occur hysteresis phenomena in the magnetoresistance of the samples of the third group (Fig. 10).

## 5. DISCUSSION

It is evident that the differences in the magnetization, the temperature dependence of the resistance, and the magnetoresistance of the samples of the three groups under investigation are associated primarily with the cobalt content in the  $\text{Co}_x\text{C}_{1-x}$  fibers and the degree of coagulation of the cobalt clusters in the carbon matrix. The samples of the first group with a low cobalt content correspond to the dielectric side of the metal–dielectric transition and are characterized by a logarithmic temperature dependence of the resistance. This dependence is predicted for two-dimensional disordered systems [10, 11] and is not typical of three-dimensional systems, including the  $\text{Co}_x\text{C}_{1-x}$  fibers studied in our work. The reason for this behavior of the dependence  $R(T)$  is still unclear. Peng *et al.* [12] observed the logarithmic dependence  $R(T)$  is observed for three-dimensional films of  $\text{Co}_x(\text{CoO})_{1-x}$  granular metals. It was established that the logarithmic dependence  $R(T)$  is observed only in the case when individual clusters are separated by a very thin layer of a tunnel-transparent dielectric or metal point contacts.

Two mechanisms responsible for the logarithmic dependence  $R(T)$  with a negative temperature coefficient of resistance are known for two-dimensional disordered systems: a weak localization due to the interference of electron wave functions [11] and an alternative effect associated with the Coulomb electron–electron interaction [10]. These effects manifest themselves differently in the magnetic field. The magnetic field suppresses the weak localization and leads to negative magnetoresistance. At the same time, a moderate magnetic field does not affect the electron–electron interaction. The experimental data obtained allow us to draw the inference that the weak localization mechanism occurs for  $\text{Co}_x\text{C}_{1-x}$  fibers of the first and second groups at low temperatures. Actually, the spin–orbit interaction suppressing the interference of the wave functions owing to the spin reorientation upon scattering results in the antilocalization of electrons and, hence, in alternating magnetoresistance [13]. Therefore, the observed positive magnetoresistance associated with the spin–orbit scattering in the  $\text{Co}_x\text{C}_{1-x}$  fibers at low temperatures and the deviation of  $R(T)$  from the logarithmic dependence at the lowest temperatures count in favor of the weak localization mechanism. The spin-dependent electron scattering by magnetic clusters, i.e., the giant magnetoresistance, can also contribute to the negative magnetoresistance. However, since the conductivity of the carbon matrix is low and has a nonmetallic character, it can be assumed that this contribution is not dominant for the samples of the first group.

The cobalt content  $x$  in the samples of the second group is equal to 0.185–0.198. The temperature dependence of the resistance for the samples of this group at high temperatures is characteristic of metallic conductivity. At  $T < 45$  K, the weak localization proceeding in

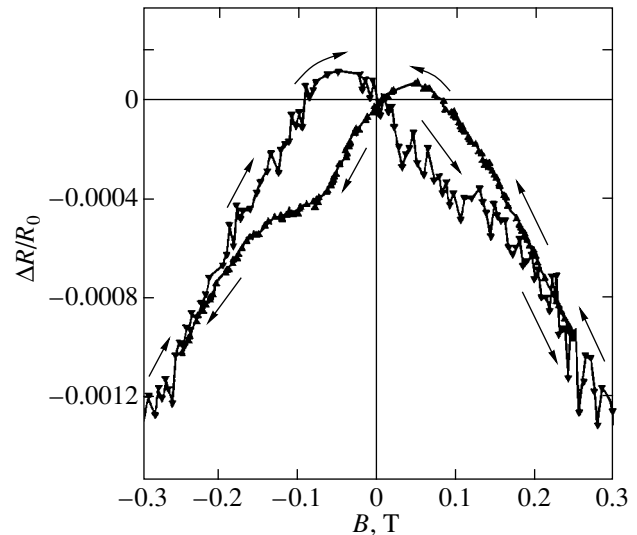


Fig. 10. Magnetoresistance hysteresis loop for a sample of the third group at  $T = 4.2$  K.

the samples leads to a logarithmic temperature dependence of the resistance (Fig. 7, curve 2). As a consequence, at low temperatures and in weak magnetic fields, the positive magnetoresistance manifests itself owing to the spin-orbit scattering. With an increase in the temperature, the positive component of the magnetoresistance decreases and vanishes, as is the case with samples of the first group. However, unlike the latter samples, the positive magnetoresistance component for the samples of the second group again appears at  $T > 45$  K in the form of a maximum shifted with respect to  $B = 0$ , thus reflecting the domination of the metallic conductivity upon the suppression of weak localization due to an increase in the temperature.

The cobalt content  $x$  in the samples of the third group varies from 0.251 to 0.60, which exceeds the percolation threshold for three-dimensional systems. In this case, individual cobalt clusters coalesce into continuous metallic percolation channels. The metallic conductivity in these samples manifests itself in the positive temperature coefficient of resistance and the residual resistance at low temperatures.

As was noted above, the magnetic-field dependences of the magnetoresistance for  $\text{Co}_x\text{C}_{1-x}$  fibers of the third group exhibit a complex behavior due to a superposition of the positive and negative components. Examination of the magnetoresistance demonstrates that the minimum of the positive magnetoresistance component is shifted to the magnetic field  $B_S = 0.078$ – $0.08$  T with respect to  $B = 0$ , whereas the minimum of the negative magnetoresistance component is observed at  $B = 0$  over the entire temperature range. It should be noted that the direction of the shift of the positive magnetoresistance component at a minimum with respect to  $B = 0$  is determined by the direction of the magnetic field scanning (see Fig. 10). Therefore, it can be

assumed that the positive magnetoresistance is associated with the remanent magnetization that results from the formation of an infinite cobalt cluster and is observed for the samples of the given group. The remanent magnetization is characteristic of ferromagnetic films and wires, whereas the positive magnetoresistance in these systems is a manifestation of the anisotropic magnetoresistance [14–16]. As the temperature decreases, the pronounced local minimum in the curves  $R(B)$  in the vicinity of  $B = B_S$  transforms into a plateau (Fig. 9c). This change in the shape of the curves  $R(B)$  is caused by an increase in the negative magnetoresistance component with a decrease in the temperature, because the positive magnetoresistance component only weakly depends on the temperature. The plateau at  $B = B_S$  in the magnetoresistance curves for sample no. 3 appears at temperatures for which the slopes of the curves  $R(B)$  for the positive and negative magnetoresistance components become equal in magnitude.

The specific feature of the studied fibers is that the positive magnetoresistance component is found in a magnetic field applied perpendicularly to the fiber. The positive magnetoresistance component in granular ferromagnetic films is observed only in the case when the magnetic field is aligned along the direction of current flow, i.e., along the film plane. It is reasonable to assume that the clusters in the fibers under consideration form a three-dimensional percolation network built up of metallic channels whose resistance can strongly fluctuate over the fiber bulk. In this network, the current predominantly flows along the fiber; however, there are regions in which the current, to a greater or lesser extent, flows normally to the fiber axis, i.e., along the magnetic field. These regions in the three-dimensional network of metallic percolation channels are responsible for the positive component of the anisotropic magnetoresistance in the magnetic field perpendicular to the fiber.

The remanent magnetization of these network regions leads to a shift of the minimum of the positive magnetoresistance component with respect to  $B = 0$ . Since the remanent magnetization of the formed infinite cluster does not result in a shift of the negative magnetization component, we can state that this component is unrelated to the anisotropic magnetoresistance. We believe that the negative magnetoresistance component is associated with the spin-dependent electron scattering by cobalt clusters, i.e., with the giant magnetoresistance effect, even though this effect in the  $\text{Co}_x\text{C}_{1-x}$  fibers is far from giant, because the parameters of the system (the size of magnetic clusters and the intercluster distance) are not optimum for the manifestation of the effect. The weak manifestation of the giant magnetoresistance effect and the superposition of the negative and positive magnetoresistance components were observed earlier in granular ferromagnetic films with a high content of the magnetic component [15]. The large size of magnetic clusters and the small free

path in the carbon matrix account for the small negative magnetoresistance and the absence of the hysteresis in the  $\text{Co}_x\text{C}_{1-x}$  fibers studied. Note also that the negative magnetoresistance can also be due to the suppression of the weak localization by the magnetic field; however, the contributions of the aforementioned two processes cannot be separated because of the small negative magnetoresistance.

It is of interest to consider the change in the origin of the positive magnetoresistance for samples of the second group under variations in temperature. It can be expected that the system of magnetically interacting clusters will become ferromagnetically harder with a decrease in the temperature. However, the shift of the minimum in the positive-magnetoresistance curves for samples of the second group due to the manifestation of bulk ferromagnetic properties and, correspondingly, the magnetization hysteresis occurs at high temperatures. This fact can be explained by the change in the magnetic interaction between the magnetic clusters. The anisotropic magnetoresistance effect for samples of the second group (Fig. 9b, curve 3) is observed at the same temperatures as the crossover from the weak localization mechanism to metallic conductivity (Fig. 7, curve 2). Whether or not this coincidence is accidental is unclear. Possibly, the exchange interaction, which is responsible for the magnetic ordering in the ensemble of the cobalt clusters and, hence, for the manifestation of collective ferromagnetic properties, proceeds through the exchange of free electrons between the clusters. At low temperatures, the weak localization results in a decrease in the electron exchange rate, which should weaken the indirect magnetic exchange interaction between the cobalt clusters. Therefore, these clusters in the  $\text{Co}_x\text{C}_{1-x}$  fibers behave as a system of noninteracting magnetic clusters. At high temperatures, the suppression of the weak localization leads to an enhancement of the exchange interaction and the fibers exhibit collective ferromagnetic behavior and, consequently, the anisotropic magnetoresistance.

## 6. CONCLUSION

Thus, it has been demonstrated that cobalt clusters can be produced in a carbon matrix upon heat treatment of carboxylated cellulose in which cobalt cations are introduced through the ion-exchange sorption. This makes it possible to control the structuring of the carbon matrix and to prepare different composite carbon materials. In particular, these materials can (i) possess both superparamagnetic and ferromagnetic properties, (ii) have positive and negative temperature coefficients of resistance and the conductivity typical of metals and dielectrics, and (iii) exhibit different mechanisms of the magnetoresistance. These materials can find application in devices of magnetic recording, storage, and reading of information.

## ACKNOWLEDGMENTS

We are grateful to H. Micklitz (Köln University, Germany) for the opportunity to perform low-temperature measurements.

This work was supported by the Belarussian State Committee of Science and Engineering, Belarussian State University (project no. 934/06), and the Bundesministerium für Forschung und Technologie (project no. WEI-002-99).

## REFERENCES

1. I. M. L. Billas, A. Chatelain, and W. A. Heer, *Science* **265** (5172), 1682 (1994).
2. J. Q. Xiao, *Phys. Rev. Lett.* **68** (25), 3220 (1992).
3. J. S. Helman and B. Abeles, *Phys. Rev. Lett.* **37** (21), 1429 (1976).
4. A. E. Berkowitz, J. R. Mitchel, M. J. Carey, *et al.*, *Phys. Rev. Lett.* **68** (25), 3745 (1992).
5. A. Naudon, D. Babonneay, D. Petroff, and A. Vaures, *Thin Solid Films* **319** (1-2), 81 (1998).
6. A. Santos, J. D. Ardisson, E. B. Tambourgi, and W. A. A. Macedo, *J. Magn. Magn. Mater.* **177-181** (1), 247 (1998).
7. B. Weitzel, A. Schreyer, and H. Micklitz, *Europhys. Lett.* **12** (2), 123 (1990).
8. K. Kuriyama and M. S. Dresselhaus, *J. Mater. Res.* **7** (4), 940 (1992).
9. X. M. Lin, C. M. Sorensen, K. J. Klabunde, and G. C. Hajipanayis, *J. Mater. Res.* **14** (4), 1542 (1999).
10. B. L. Altshuler, A. G. Aronov, and P. A. Lee, *Phys. Rev. Lett.* **44** (19), 1288 (1980).
11. P. A. Lee and T. V. Ramakrishnan, *Rev. Mod. Phys.* **57** (2), 287 (1985).
12. D. L. Peng, K. Symiyama, T. J. Konno, *et al.*, *Phys. Rev. B* **60** (3), 2093 (1999).
13. G. Bergmann, *Phys. Rep.* **107** (1), 1 (1984).
14. A. Gerber, A. Milner, I. Ya. Korenblit, *et al.*, *Phys. Rev. B* **57** (21), 13667 (1998).
15. A. Gerber, A. Milner, B. Groisman, *et al.*, *Phys. Rev. B* **55** (10), 6446 (1997).
16. H. Weiforth, Ch. Somsen, B. Rellinghaus, *et al.*, *IEEE Trans. Magn.* **34** (4), 1132 (1998).

*Translated by O. Borovik-Romanova*

---

## MAGNETISM AND FERROELECTRICITY

---

# Stoner–Wohlfarth-Type Behavior of a Close-Packed Array of High-Anisotropy Hexaferrite Nanoparticles

Z. V. Golubenko\*, A. S. Kamzin\*\*, L. P. Ol'khovik\*, M. M. Khvorov\*,  
Z. I. Sizova\*, and V. P. Shabatin\*\*\*

\* Karazin Kharkov National University, pl. Svobody 4, Kharkov, 61077 Ukraine

\*\* Ioffe Physicotechnical Institute, Russian Academy of Sciences, Politekhnicheskaya ul. 26, St. Petersburg, 194021 Russia

\*\*\* Moscow State University, Vorob'evy gory, Moscow, 119899 Russia

Received August 20, 2001; in final form, October 11, 2001

**Abstract**—Magnetization and remagnetization processes in a close-packed nanodispersed barium hexaferrite powder sample in the magnetically stable state were analyzed. Reversibility effects were discussed in terms of interparticle interaction. Judging from the magnetization curve and the parameters characterizing remagnetization irreversibility, the sample under study is a model system of small Stoner–Wohlfarth particles. © 2002 MAIK “Nauka/Interperiodica”.

## 1. INTRODUCTION

Experimental studies of the properties of magnetic powder materials used in nano- and microelectronics pass, as a rule, over the problem of model approximation of objects as complex as highly dispersed systems. Generalization of results of investigations and establishment of the causes of observed deviations from theoretical predictions are complicated because of the size and, in specific cases, chemical-composition distributions of particles.

The investigation of systems of single-domain nano- and micrometer particles includes two basic aspects: revealing of the possible occurrence of a superparamagnetic state of particles with a volume close to critical under a temperature–field exposure, and analysis of the influence of the rough free surface of particles on their properties. Some of the results of our study were reported earlier in [1, 2]. The emphasis in this paper is on model approximation of an object, refinement of the nature of magnetization and remagnetization in fields of various strength, and determination of the parameters of these processes.

## 2. SAMPLE PREPARATION

We studied hexagonal barium ferrite with an unsubstituted magnetic  $\text{BaFe}_{12}\text{O}_{19}$  host in the form of a nanodispersed powder produced using cryochemical technology [3]. Barium and iron nitrates highly soluble in water were used as initial components. The solution concentrations were 1–2 and 0.3–0.32 mol/l for  $\text{Fe}(\text{NO}_3)_3$  and  $\text{Ba}(\text{NO}_3)_2$  solutions, respectively. The solutions were mixed in a stoichiometric (for the end product) ratio (6 : 1). The solution, in the form of a monodisperse flow of drops, was subjected to cryocrystallization followed by sublimation drying. To stabilize

the chemical system homogeneity at the subsequent technological stages, complex formation was used. Citric acid was used as a complexing agent. The produced salt mixture was annealed without flux at  $T = 1173$  K for 2 h. The chosen technological conditions allowed complete ferritization and crystallization of particles with an average size of 60 nm in the basal plane and an aspect ratio of 2–3. X-ray and Mössbauer studies of the powder sample at room temperature do not detect any unintentional phases or para- or superparamagnetic particles.

## 3. MAGNETIZATION CURVES

The measurements were carried out with a thermally demagnetized close-packed (packing factor  $p$  of approximately 0.4) powder sample. Figure 1 displays an experimental magnetization curve measured at 300 K; the material is in a magnetically stable state. This curve, in contrast to the case of a macroscopic analogous crystal in fields up to 4 kOe, exhibits a linear increase in the magnetization followed by a drastic growth. The magnetization change in fields above 8 kOe indicates that in a field equal to the macroscopic-crystal anisotropy field ( $H_a = 17.8$  kOe), there is no saturation. Figure 1 also shows a magnetization curve calculated theoretically in the Stoner–Wohlfarth (SW) model for a system of randomly oriented identical non-interacting magnetically uniaxial single-domain particles under the assumption of homogeneous rotation of their magnetization vectors [4]. For convenience of comparison, the anisotropy field of the SW model system is assumed to be that of barium ferrite and the magnetization is given in relative units. One can see that the experimental dependence correlates well with the calculated SW curve. The shift of the position of the mag-

netization jump in the experimental curve to weaker fields with respect to the jump in the calculated curve is due to the fact that the sample under study is characterized by an effective-anisotropy-field distribution of particles in the range  $H_a = 8\text{--}18$  kOe [2].

To establish the nature of the magnetization process for various portions of the experimental curve, partial and major hysteresis loops were studied (the latter is shown in Fig. 1). From the data obtained, the dependence of the magnetization reversal field  $H_S$  on the amplitude of the magnetizing field  $H$  was determined (Fig. 2). One can see that the field  $H_S$  is zero for magnetizing-field amplitudes up to 3.0 kOe; i.e., the magnetization reversal proceeds without hysteresis. Hence, the initial linear portion of the magnetization curve corresponds to reversible processes of magnetization vector rotation.

As is known, the field value separating the regions of reversible and irreversible rotation (threshold field  $H_0$ ) for a magnetically uniaxial particle depends on the orientation of the easy magnetization axis and on the value of the anisotropy field [5]. The minimum ( $H_0^{\min} = H_a/2$ ) and maximum ( $H_0^{\max} = H_a$ ) threshold fields are characteristic of particles with an easy-axis orientation  $\theta = 45^\circ$  and  $\theta = 0^\circ, 90^\circ$  with respect to the field, respectively. In the case of chaotically oriented particles with a unique value of  $H_a$ , particles with easy-axis orientations different from  $\theta = 45^\circ$  are gradually involved in irreversible rotation as the magnetizing field increases from  $H = H_a/2$  up to  $H = H_a$ .

In considering the threshold fields for the system under study, one should also take into account the distribution of the anisotropy fields of particles and the effect of thermal fluctuations. According to the classification from [6], the particles of the system at hand are small SW particles. The criterion is the ratio between the actual volume  $V$  of particles and the critical volume  $V_S$  for the transition from the magnetostable to superparamagnetic state. Particles for which  $V_S < V < 1000 V_S$  are referred to as small. This condition is met at 300 K not only for the finest ( $V/V_S \sim 3.5$ ) and intermediate ( $V/V_S \sim 130$ ) but also for the largest ( $V/V_S \sim 600$ ) particles of the system under study. As the ratio  $V/V_S$  decreases, the threshold field is reduced and its dependence on the angle  $\theta$  is flattened in comparison to that for large SW particles ( $V/V_S \rightarrow \infty$ ) [7]. The latter factor makes it possible to consider the magnetic behavior of the disordered system under study to be similar to the behavior of particles oriented at an angle  $\theta = 45^\circ$ . From the above discussion, it becomes clear why the lower boundary of the threshold field range is  $H_0^{\min} \sim H_a^{\max}$  and the dependence of the magnetization reversal field on the magnetizing-field amplitude is saturated at a field of the order of 9 kOe rather than at  $H_a^{\max} = 17.8$  kOe (Fig. 2).

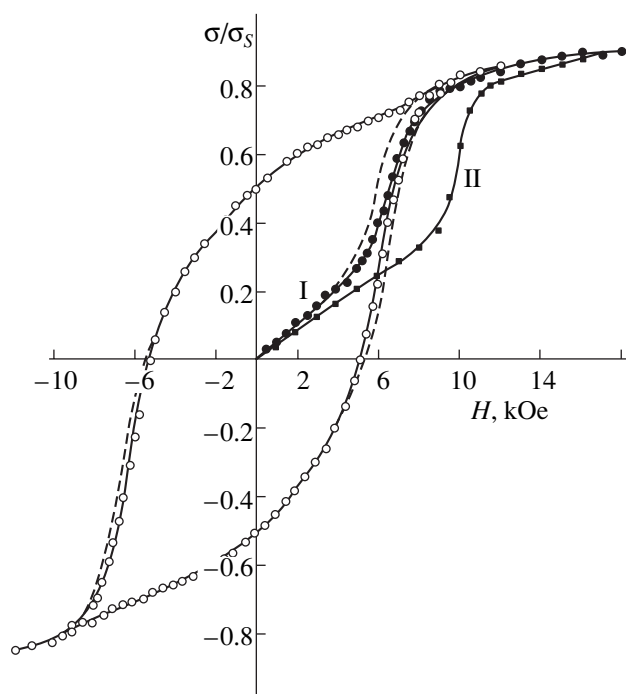


**Fig. 1.** Normal magnetization curve and major hysteresis loop of a nanodispersed powder sample of barium hexaferrite at 300 K: (I) experiment and (II) calculated magnetization curve. Dashed curves are the magnetization curve and hysteresis loop taking into account the interparticle interaction.

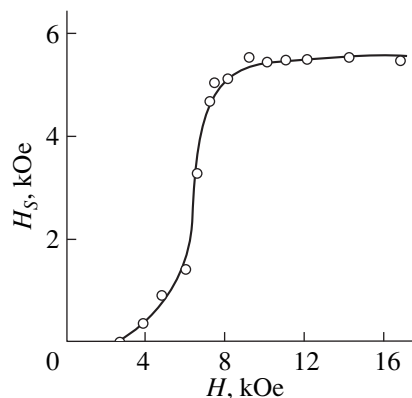


**Fig. 2.** Dependence of the magnetization reversal field on the magnetizing field amplitude at 300 K.

The limiting value of the magnetization reversal field  $H_S$  is the coercivity  $H_C$ , which is an important parameter characterizing the magnetic state of particles and powder quality in terms of a model approximation. According to [4], the coercivity for an array of chaotically oriented identical noninteracting single-domain particles is related to the effective anisotropy field as

$$H_C = 0.48H_a, \quad (1)$$

where the effective anisotropy field is given by

$$H_a = H_K - NI_S. \quad (2)$$

Here,  $H_K$  is the magnetocrystalline anisotropy field and  $NI_S$  is the shape anisotropy field.

Equation (2) is valid for microcrystalline powders of  $\text{BaFe}_{12}\text{O}_{19}$  ferrite. As shown in [8], the anisotropy field measured using various methods in these materials is, on the average, 13.8 ( $\langle d \rangle = 0.11 \mu\text{m}$ ) and 13.65 kOe ( $\langle d \rangle = 0.42 \mu\text{m}$ ). In this case, the shape anisotropy field ( $NI_S \sim 4.8$  kOe) is responsible for the decrease in the anisotropy field in comparison with the case of a macroscopic crystal.

For the nanocrystalline system studied in this work, the average effective anisotropy field is close to that of the above-mentioned microcrystalline systems ( $\langle \tilde{H}_a \rangle = 12.4$  kOe). As in the case of microcrystals, the dominant contribution to the magnetic anisotropy comes from the magnetocrystalline anisotropy. However, the shape anisotropy field of platelike particles of the system under study, even with the maximum aspect ratio  $d/h = 3$ , is an order of magnitude weaker than the magnetocrystalline anisotropy field ( $H_K = 17.8$  kOe,  $NI_S \cong 1.8$  kOe); the surface anisotropy is responsible for the decrease in the effective anisotropy field in this case.

The coercivity found in this work from the major hysteresis loop is 5.3 kOe.

The underestimated values of  $H_C$  in comparison with the value given by Eq. (1) are usually explained by such causes as the presence of multidomain or superparamagnetic particles [9–11]. As indicated above, the size of particles in the system under study does not exceed the critical size for the single-domain state ( $d = 1.3 \mu\text{m}$  [12]) and all of the particles are in the magnetically stable state at 300 K. Taking into account that in the sys-

tem at hand the particle volume is close to its critical value, the influence of thermal fluctuations should be considered above all.

According to [7], the true average anisotropy field  $\langle H_a \rangle$  of the system of particles is related to the experimentally observed field  $\langle \tilde{H}_a \rangle$  as

$$\langle H_a \rangle = Z \langle \tilde{H}_a \rangle, \quad (3)$$

where the coefficient  $Z$  is determined by thermal fluctuations and can be found from the equation

$$(Z - 1)Z^{-0.3} = \left( \frac{50kT}{\langle V \rangle I_S \langle \tilde{H}_a \rangle \mu_0} \right)^{0.7}. \quad (4)$$

Here,  $k$  is the Boltzmann constant,  $\langle V \rangle$  is the average volume of particles of the system,  $I_S$  is the magnetization, and  $\mu_0$  is the vacuum permeability.

Our numerical calculations gave the value  $Z = 1.04$ , which corresponds to the true anisotropy field  $\langle H_a \rangle = 12.9$  kOe and the coercivity  $H_C = 5.5$  kOe. The disagreement between the value of  $H_C$  found with account of thermal fluctuations and the value determined by formula (1) with  $\langle H_a \rangle$  substituted for the true anisotropy field ( $H_C = 6.2$  kOe) necessitates estimation of the role of the interparticle interaction.

#### 4. INTERPARTICLE MAGNETIC INTERACTION

It is generally believed that the magnetic interaction between small particles of a close-packed system can significantly affect its properties. The interaction can be either positive or negative, promoting a sample magnetization or demagnetization, respectively. As indicated in [13], both interaction types take place in the systems of barium hexaferrite particles; however, as a rule, one of these types dominates.

In this study, in order to estimate the interparticle magnetostatic interaction in a nanocrystalline close-packed powder sample of barium hexaferrite, we employed a technique based on measurement of the field dependence of the remanent magnetizations  $m_r(H) = \sigma_r(H)/\sigma_r(\infty)$  and  $m_d(H) = \sigma_d(H)/\sigma_d(\infty)$ . The isothermal remanent magnetization  $\sigma_r$  is measured on a thermally demagnetized sample by cycling the partial and major hysteresis loops with a gradual increase in the measuring field amplitude;  $\sigma_r(\infty)$  is the value of  $\sigma_r = f(1/H)$  dependence to an infinite field. The remanent magnetization  $\sigma_d$  is produced by magnetizing the sample to saturation followed by a field decrease down to zero, then reversing the field sign (direction) and increasing the field to a preset value, and then turning the field off. The quantity  $\sigma_d(\infty)$  is analogous to  $\sigma_r(\infty)$  and is an extrapolated value of  $\sigma_d$  in an infinite field.

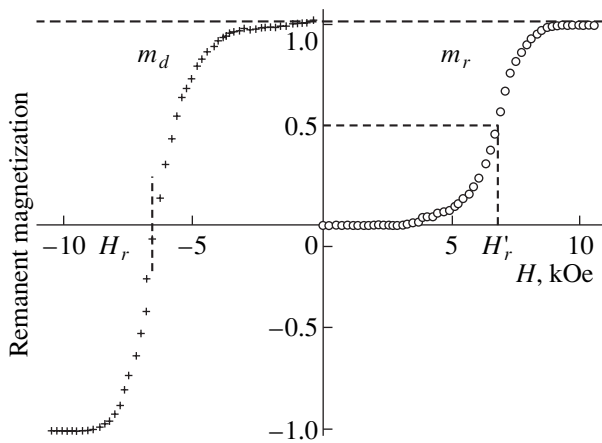


**Fig. 3.** Field dependences of the remanent magnetizations  $m_r$  and  $m_d$ .

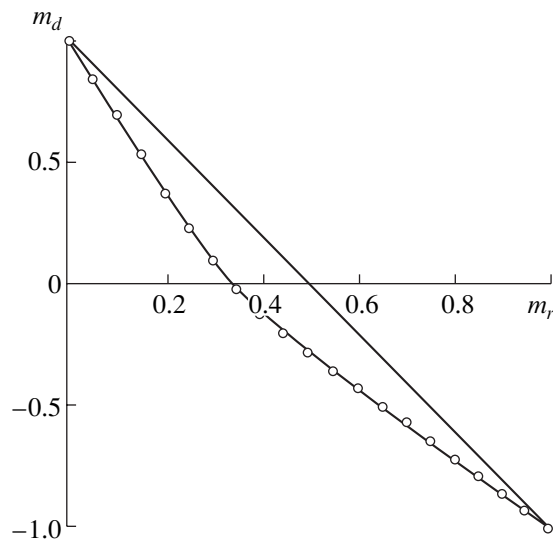


Fig. 4. Henkel plot.

According to [14], the  $m_r(H)$  and  $m_d(H)$  dependences for a system of noninteracting magnetically uniaxial single-domain particles are related as

$$m_d(H) = m_r(\infty) - 2m_r(H) = 1 - 2m_r(H). \quad (5)$$

Any deviation from linearity in the  $m_d(H) = f(m_r(H))$  graph (Henkel plot [15]) indicates interaction between the particles.

Figure 3 shows the experimental field dependences of  $m_r$  and  $m_d$ , and Fig. 4 presents a Henkel plot constructed on their basis for the powder sample under study. The concavity of the experimental  $m_d = f(m_r)$  curve with respect to a straight line indicates that the negative interaction dominates in the array of particles.

Since the Henkel plot compares the remanent magnetizations  $m_r$  and  $m_d$  in the same field, we also analyzed the magnetization and remagnetization processes by using an additional, more informative technique [16] in which the deviation from Eq. (5) is considered as a function of the applied field:

$$\Delta m(H) = m_d(H) - [1 - 2m_r(H)]. \quad (6)$$

One can see from the dependence shown in Fig. 5 that the effect of the interaction manifests itself in the field range 3–9 kOe, which, according to the data of Fig. 2, corresponds to irreversible magnetization processes. The maximum interaction ( $\Delta m = -0.34$ ) is observed for fields of 6–6.5 kOe. The portions of the normal magnetization curve and of the saturation hysteresis loop taking the interparticle interaction into account are indicated in Fig. 1 by dashed lines. It turns out that the negative interaction, as a destabilizing factor, manifests itself only in the region of the magnetization jump, while the threshold fields and coercivity are almost unaffected by the interaction in the system at hand. For example, the correction to the value  $H_C =$

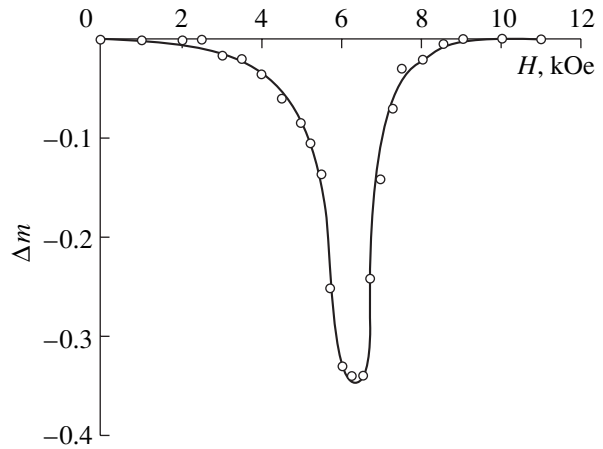


Fig. 5. Modified Henkel plot (Kelly plot [16]).

5.3 kOe can be as small as 100 Oe. As a result, the true coercivity found when taking into account thermal fluctuations and the interparticle interaction is equal to 90% of the theoretical value.

## 5. CONCLUSION

Thus, we have shown that the magnetic behavior of a nanodispersed powder sample of high-anisotropy barium hexaferrite can be rather well described by the classical model as applied to an array of small Stoner–Wohlfarth particles. This allows one to conclude that magnetization proceeds via coherent rotation in particles with a volume close to the critical value.

The negative interparticle magnetic interaction detected in the close-packed array of disordered nanocrystals manifests itself in the field range corresponding to irreversible magnetization and has no appreciable effect on either the shape of the magnetization curve or the values of the coercivity and critical fields characterizing the magnetization mechanism.

## ACKNOWLEDGMENTS

One of the authors (A.S. Kamzin) acknowledges the support of the Russian Foundation for Basic Research, project no. 01-02-17889.

## REFERENCES

1. L. P. Ol'khovik, Z. I. Sizova, Z. V. Golubenko, and T. G. Kuz'micheva, *J. Magn. Magn. Mater.* **183**, 181 (1998).
2. Z. V. Golubenko, A. S. Kamzin, L. P. Ol'khovik, *et al.*, *Fiz. Tverd. Tela (St. Petersburg)* **40** (10), 1894 (1998) [*Phys. Solid State* **40**, 1718 (1998)].

3. T. G. Kuz'micheva, L. P. Ol'khovik, and V. P. Shabatin, Ukraine Patent No. 1724584 C 01 G 49/00 (1990).
4. E. C. Stoner and E. P. Wohlfarth, IEEE Trans. Magn. **MAG-27** (4), 3469 (1991).
5. S. Chikasumi, *The Physics of Ferromagnetism. Magnetic Characteristics and Engineering Applications* (Syokabo, Tokyo, 1984; Mir, Moscow, 1987).
6. H. Pfeiffer, Phys. Status Solidi A **120**, 233 (1990).
7. H. Pfeiffer, Phys. Status Solidi A **118**, 295 (1990).
8. P. Görnert, W. Schüppel, E. Sinn, *et al.*, J. Magn. Magn. Mater. **114**, 193 (1992).
9. K. Haneda and H. Kojima, J. Am. Ceram. Soc. **57**, 68 (1974).
10. P. Görnert, E. Sinn, W. Schüppel, *et al.*, IEEE Trans. Magn. **26** (1), 12 (1990).
11. C. D. Mee and J. C. Jeschke, J. Appl. Phys. **34**, 1271 (1963).
12. K. Goto, M. Ito, and T. Sakurai, Jpn. J. Appl. Phys. **19**, 1339 (1980).
13. X. Batlle, M. Garcia del Muro, and A. Labarta, Phys. Rev. B **55** (10), 6440 (1997).
14. E. P. Wohlfarth, J. Appl. Phys. **29**, 595 (1958).
15. O. Henkel, Phys. Status Solidi **7**, 919 (1964).
16. P. E. Kelly, K. O'Grady, P. I. Mayo, and R. W. Chantrell, IEEE Trans. Magn. **MAG-25**, 3881 (1989).

*Translated by A. Kazantsev*

---

## MAGNETISM AND FERROELECTRICITY

---

# Evolution of Dynamic Spiral Domains over a Period of an Alternating Magnetic Field

M. V. Logunov and M. V. Gerasimov

Mordovian State University, ul. Bol'shevistskaya 68, Saransk, 430000 Russia

e-mail: logunov@mrsu.ru

Received October 15, 2001

**Abstract**—The stroboscopic method was applied to study the evolution of dynamic spiral domains in garnet ferrite films in an ac magnetic field. The spiral-domain shape was shown to change significantly within a field period; the basic shape transformations take place in the phase range  $-\pi/4$  to  $+\pi/4$  with respect to the polarity inversion time. During the spiral-domain formation or decay, the area and shape of a hysteresis loop of the film region containing the domain gradually change. The upper boundary of the frequency range in which spiral domains form was established to be associated with transformations of the domain wall structure. © 2002 MAIK “Nauka/Interperiodica”.

### 1. INTRODUCTION

Spiral domains represent an interesting case of the ordered domain structure of a magnetic material, attracting the attention of many researchers. Dynamic spiral domains can be formed in uniaxial magnetic films in certain frequency and amplitude ranges of an ac magnetic field [1–4]. Spiral domains can also be formed in a pulsed field [4–7], in a quasi-static field [8, 9], under laser radiation [10], in two-layer films [11], and in very thin films [12].

Available experimental data on dynamic spiral domains in an ac magnetic field are not strictly related to the field phase. Due to poor temporal resolution, micrographs of domain structures often display an integral state of the structure over a time comparable to or exceeding a field period. Therefore, we can no more than speculate on the correspondence between domain structure micrographs and the remagnetization phase, which makes the interpretation of experimental data more complicated. In particular, there is no unambiguous answer to the question of whether the spiral-domain formation in an ac magnetic field (of frequency  $f \sim 10^2$ – $10^3$  Hz) is controlled by the dynamic mechanisms of domain wall motion or if it is a superposition of quasi-static processes producing insignificant variations from one field period to another. The remagnetization mechanisms determining the boundaries of the frequency range in which dynamic spiral domains occur are also unclear.

This work is aimed at a direct study of the formation mechanisms of dynamic spiral domains. To this end, we studied the evolution of these domains over a period of the ac magnetic field by detecting dynamic domain structures using the stroboscopic method.

### 2. EXPERIMENTAL

Dynamic spiral domains were studied with a magneto-optical setup using the Faraday effect. The setup allows one to record hysteresis loops in the field frequency range  $f = 10^{-4}$ – $2 \times 10^5$  Hz and to simultaneously view images of dynamic domain structures corresponding to various portions of a hysteresis loop by using the stroboscopic method with a temporal resolution of  $0.8 \mu\text{s}$  [13]. A transversely pumped (by microwave radiation) helium–neon laser with a modulated supply voltage was used as a pulsed light source [14]. Adaptable variation of the laser switching mode made it possible to apply the stroboscopic method with a tuned strobing multiplicity,  $K_{\text{st}} = 1, 2, 3, \dots$ . To detect nonrecurring processes when recording dynamic domain structures using a video camera, we selected the setup operating condition by varying the strobing multiplicity such that the dynamic domain structure was recorded in one video frame over one laser pulse.

In addition to the conventional method of recording dynamic hysteresis loops from an oscilloscope screen when a sequence of loops for many remagnetization cycles is included in a single frame, the setup allows one to strobe and video record a dynamic hysteresis loop for a single remagnetization cycle. To this end, we synchronized the laser pulse in phase and duration with a field period by tuning the pulse duration.

The ac magnetic field was produced by Helmholtz coils 2.5 mm in diameter applied perpendicular to the film plane. A sample area 1.5 mm in diameter was studied.

Single-crystal garnet ferrite films were used as samples. To compare our results with the available data on

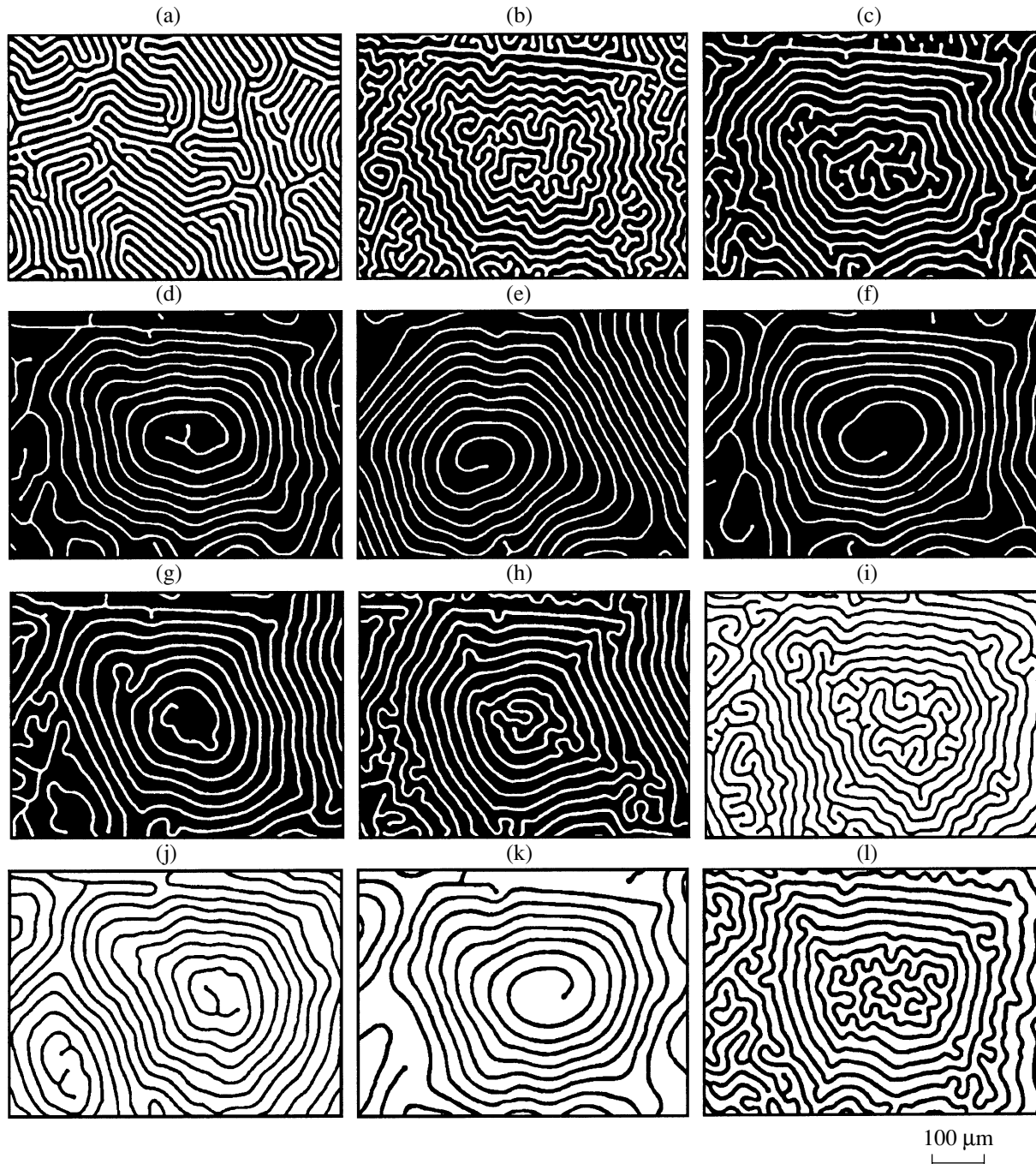


**Fig. 1.** (a) Static ( $H = 0$ ) and (b–l) dynamic domain structures in a garnet ferrite film corresponding to various phases of an applied ac magnetic field with frequency  $f = 2$  kHz and amplitude  $H_M = 38$  Oe: (b)  $0^\circ$ , (c)  $30^\circ$ , (d)  $60^\circ$ , (e)  $90^\circ$ , (f)  $100^\circ$ , (g)  $125^\circ$ , (h)  $135^\circ$ , (i)  $200^\circ$ , (j)  $224^\circ$ , (k)  $292^\circ$ , and (l)  $328^\circ$ .

spiral domains, we chose a  $(\text{Tm,Bi})_3(\text{Fe,Ga})_5\text{O}_{12}$  film with parameters comparable to those of the samples studied in [2–4, 15–17], namely, thickness  $h = 5.8 \mu\text{m}$ , equilibrium width of stripe domains  $w = 8.7 \mu\text{m}$ , saturation magnetization  $M_s = 10$  G, uniaxial anisotropy constant  $K_u = 1.3 \times 10^4 \text{ erg cm}^{-3}$ , and damping constant  $\alpha = 0.09$ .

### 3. EXPERIMENTAL RESULTS

In an equilibrium state, the film possessed a domain structure in the form of stripe or labyrinth domains (Fig. 1a). To achieve an equilibrium state, the structure was placed in an ac magnetic field with a frequency  $f = 50$  Hz and with an amplitude slowly decreasing to zero.

Spiral domains were formed in the field frequency range  $f = 0.5\text{--}5$  kHz at the field amplitudes  $H_M = 43 \pm 5$  Oe. Stripe domains can be twisted into microspirals in a significantly wider range of the field frequency (0.1–20 kHz); however, we did not take into account spiral domains with a number of turns less than two. In this case, the longest lifetime (3–8 s) and the shortest expectation time (5–8 s) of the spiral structure were observed at the frequency  $f \sim 2$  kHz. Therefore, this frequency was chosen for the study of the spiral-domain evolution over a field period (Figs. 1b–11). The time separation between video frames is 80 field periods. Since the spiral-domain lifetime (elapsed from its nucleation to decay) is about  $10^4$  field periods, the number of spiral turns changes insignificantly for several tens of periods.

Spiral domains could also be formed in higher-frequency fields [4, 17], up to  $f \sim 100$  kHz. However, this requires a dc bias field  $H_b$ , applied perpendicular to the film plane; this field must increase and, simultaneously, the ac field amplitude  $H_M$  must decrease with increasing frequency. The field amplitude  $H_M$  and the field  $H_b$  varied steadily (as in [4]) as the frequency was increased; no frequency ranges in which nucleation of spiral domains was impossible [17] were observed. In the whole frequency range, the maximum magnetic field  $H_M + H_b$  applied to the film corresponded to the hysteresis transition region between a uniformly magnetized state and a labyrinth domain structure [4].

The spiral domains shown in Figs. 1b–11 are most typical of the indicated magnetic-field phases. The domains were formed in the same region of the sample at different instants of time. The spiral twist direction can vary since the dc bias field  $H_b$  is zero [3].

At the instant of field polarity inversion, a spiral domain is strongly distorted (Fig. 1b). As the field increases, the amplitude of quasiperiodic distortions of the spiral turns and their “appendixes” (branches) decrease (Fig. 1c). Spiral-turn smoothing is virtually completed at a phase of  $60^\circ$  (Figs. 1b–1d). After the peak field is passed, small-scale untwisting of the spiral center takes place (Fig. 1f) and is followed by distortion of spiral turns (Figs. 1g, 1h). As the field polarity is inverted (in the next field half-cycle), the pattern repeats (Figs. 1i–11). Thus, a significant change in the spiral domain shape takes place within the magnetic-field period, with the number of spiral turns remaining virtually unchanged.

The shape of domains of the same polarity changes differently as the field varies within a half-cycle: bending distortions increase as the field decreases (Figs. 1g, 1h, 1i), and appendixes are formed as the field increases (Figs. 1c, 1i).

The hysteresis loop shape is closely related to the spiral-domain formation [4, 15]. The major and minor hysteresis loops of a film under a quasi-statically varied magnetic field are similar to those typical of garnet fer-

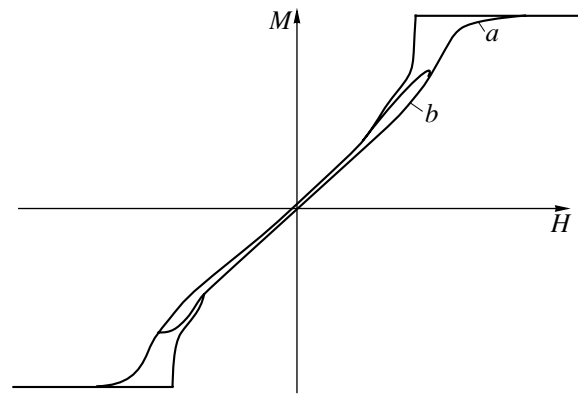


**Fig. 2.** Major ( $H_M = 120$  Oe) (curve *a*) and minor ( $H_M = 38$  Oe) (curve *b*) hysteresis loops of a garnet ferrite film in the case of a quasi-statically varying magnetic field.

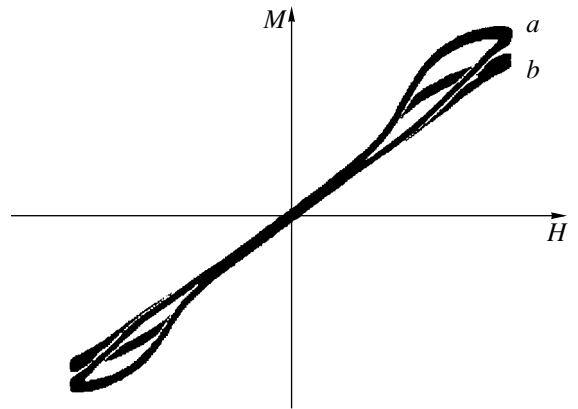


**Fig. 3.** Minor hysteresis loops in an ac magnetic field with amplitude  $H_M = 38$  Oe and frequency  $f = 2$  kHz for the same film area occupied by labyrinth domains (curve *a*) or a spiral domain (curve *b*).

rite films with a low coercive field (Fig. 2; the loop recording time is about 200 s). During the formation or decay of a spiral domain in the ac field, we recorded a hysteresis loop simultaneously with domain detection by focusing a laser beam onto the sample area occupied by a spiral. The hysteresis loop area gradually changed for a few seconds when the spiral formed and curled. Certainly, the loop area changed in steps from one field period to another. However, as strobing of dynamic hysteresis loops for individual remagnetization cycles showed, the step size is insignificant. At the field frequency  $f \sim 2$  kHz, the steps are inappreciable when hysteresis loops are observed on the oscilloscope screen

and manifest themselves as an increase in the oscilloscope beam diameter in separate portions of a loop.

As in [15], hysteresis loops had the least area in the case of the spiral domain structure (Fig. 3, curve *b*). An increase in the loop area and in the maximum film magnetization (Fig. 3, curve *a*) corresponds to spiral decay and transition to the labyrinth domain structure. No loop jumps as observed in [15] were found. The hysteresis loop of the spiral domain is characterized by a downward deviation of the ascending loop branch from the hysteresis loop branch of the stripe domain structure (Fig. 3). The deviation is smaller than the theoretically calculated value [18].

#### 4. DISCUSSION

Compression and expansion of a stripe domain forming a spiral within a period of the magnetic field are accompanied by a change in the structure of its domain walls and, hence, by redistribution of the effective mass along the walls. This is indicated by the formation of appendixes in the spiral domain regions, which are clearly distinguishable over part of the magnetic-field period (Figs. 1c, 1i). Earlier, the formation of lateral appendixes was observed in studying spiral-domain formation, but only under a pulsed field during the pulse [6, 7] or after the pulse was turned off (in a frozen structure) [4, 5].

The formation of spiral-domain appendixes and branches is due to the finite saturation velocity of domain walls [19], which was, according to high-speed photography data with an exposure time of 5 ns [20],  $V_s \sim 10 \text{ m s}^{-1}$  for our sample. Notwithstanding the low average velocity of domain walls over a field period at the frequency  $f \sim 2 \text{ kHz}$ , separate regions of the spiral domain, due to jumplike motion, reach a critical velocity  $V_{cr}$  (during jumps) at which the domain wall structure changes and wall regions with different effective masses (and, hence, different velocities) arise. We observed such phenomena both at the spiral-domain center during the spiral formation or its decay and at the periphery during the transformation of branches. The jumps are caused by local pinning of domain walls (at film defects) and their breaking away under changes in the instantaneous values of the ac field, as well as by the hysteresis of the transformation of stripe magnetic domains into bubble domains and vice versa [21].

The probability that the critical velocity  $V_{cr}$  will be reached during jumplike motion of a domain wall is relatively high. According to our calculations carried out using various models of domain wall motion [19], the critical velocity for the sample at hand is reached in a driving field  $H_{cr} = 1.2\text{--}2 \text{ Oe}$ , which is comparable to the coercive field for the film ( $H_c \sim 0.6 \text{ Oe}$  for a quasi-static hysteresis loop and  $H_c > 1 \text{ Oe}$  for a dynamic loop, at  $f > 0.1 \text{ kHz}$ ).

It is noteworthy that the upper boundary  $f_h$  of the frequency range in which spiral domains form in an ac magnetic field is due to the dynamic properties of domain walls and depends on the maximum rate of the magnetic-field variation. As the field frequency increases, the hysteresis loop area increases; furthermore, the transformation of the structure of dynamic domain walls and the formation of regions with different effective masses in domain walls result not only in branching but also (even more frequently) in breaking of stripe domains (as in the case of formation of bubble magnetic domains in a pulsed field [19]). These processes prevent the formation of a spiral domain, which is, in fact, a long curled stripe domain. To find a generalized parameter defining the boundaries of the frequency range in which spiral domains form is an objective of further investigations. Difficulties encountered in reaching this goal can be associated with significant variations in the shape and parameters of spiral domains, as well as in the amplitude of domain wall vibrations, that are produced by changes in the magnetic-field frequency.

#### ACKNOWLEDGMENTS

This study was supported by the Russian Foundation for Basic Research, project no. 98-02-03325.

#### REFERENCES

1. S. M. Hanna, F. J. Friedlaender, R. L. Gunshor, and H. Sato, *IEEE Trans. Magn.* **MAG-19** (5), 1802 (1983).
2. G. S. Kandaurova and A. E. Sviderskiĭ, *Pis'ma Zh. Éksp. Teor. Fiz.* **47** (8), 410 (1988) [*JETP Lett.* **47**, 490 (1988)].
3. G. S. Kandaurova and A. E. Sviderskiĭ, *Zh. Éksp. Teor. Fiz.* **97** (4), 1218 (1990) [*Sov. Phys. JETP* **70**, 684 (1990)].
4. I. E. Dikshteĭn, F. V. Lisovskiĭ, E. G. Mansvetova, and E. S. Chizhik, *Zh. Éksp. Teor. Fiz.* **100** (5), 1606 (1991) [*Sov. Phys. JETP* **73**, 888 (1991)].
5. F. V. Lisovskiĭ and E. G. Mansvetova, *Fiz. Tverd. Tela (Leningrad)* **31** (5), 273 (1989) [*Sov. Phys. Solid State* **31**, 876 (1989)].
6. A. V. Nikolaev, V. N. Onishchuk, and A. S. Logginov, in *Proceedings of the XV School-Workshop "Novel Magnetic Materials for Microelectronics," 1996*, p. 398.
7. M. V. Chetkin, A. I. Akhutkina, and T. V. Shapaeva, *Mikroelektronika* **27** (5), 396 (1998).
8. M. V. Logunov and V. V. Randoshkin, in *Proceedings of the XVII All-Union Conference on Physics of Magnetic Phenomena, Kalinin, 1988*, p. 235.
9. A. P. Ges', V. V. Fedotova, A. K. Bogush, and T. A. Gorbachevskaya, *Pis'ma Zh. Éksp. Teor. Fiz.* **52** (9), 1079 (1990) [*JETP Lett.* **52**, 476 (1990)].
10. B. E. Argyle and J. C. De Luca, *IEEE Trans. Magn.* **MAG-17** (1), 1141 (1981).
11. I. B. Puchalska, *J. Appl. Phys.* **50** (3), 2242 (1979).
12. E. Yn. Vedmedenko, A. Ghasali, and J.-C. S. Lévy, *Phys. Rev. B* **59** (1), 3329 (1999).

13. M. V. Logunov and M. V. Gerasimov, in *Abstracts of EASTMAG-2001, Yekaterinburg, 2001*, p. 281.
14. A. P. Naumov and V. V. Korovin, *Prib. Tekh. Éksp.*, No. 2, 162 (1988).
15. G. S. Kandaurova and V. Kh. Osadchenko, *Pis'ma Zh. Tekh. Fiz.* **20** (21), 24 (1994) [*Tech. Phys. Lett.* **20**, 864 (1994)].
16. G. S. Kandaurova, V. Kh. Osadchenko, A. A. Rusinov, and E. A. Rusinova, *Pis'ma Zh. Éksp. Teor. Fiz.* **63** (6), 453 (1996) [*JETP Lett.* **63**, 478 (1996)].
17. G. S. Kandaurova and A. A. Rusinov, *Pis'ma Zh. Éksp. Teor. Fiz.* **65** (1), 60 (1997) [*JETP Lett.* **65**, 63 (1997)].
18. V. E. Ivanov and G. S. Kandaurova, in *Abstracts of EASTMAG-2001, Yekaterinburg, 2001*, p. 141.
19. A. P. Malozemoff and J. C. Slonczewski, *Magnetic Domain Walls in Bubble Materials* (Academic, New York, 1979; Mir, Moscow, 1982).
20. M. V. Logunov, V. V. Randoshkin, and V. V. Sigachev, *Prib. Tekh. Éksp.*, No. 5, 247 (1985).
21. F. A. De Jonge and W. F. Druyvesteyn, *Festkörperprobleme* **12**, 531 (1972).

*Translated by A. Kazantsev*

## MAGNETISM AND FERROELECTRICITY

# Magnetic Phase Transitions in Amorphous Systems with Competing Exchange Interactions

V. I. Belokon' and K. V. Nefedev

Far East State University, ul. Sukhanova 8, Vladivostok, 690000 Russia

e-mail: belokon@ifit.phys.dvgu.ru

Received October 15, 2001

**Abstract**—A method is proposed for analyzing magnetic phase transitions within the Ising model under the conditions of competing direct and indirect exchange interactions. It is demonstrated that the competition of exchange interactions leads to a reentrant phase transition between the ferromagnet and spin glass near the percolation threshold below the Curie temperature. © 2002 MAIK “Nauka/Interperiodica”.

### 1. INTRODUCTION

Although spin-glass systems have been intensively studied over many years [1], their properties in the vicinity of the percolation threshold have yet to be explained reasoning from the essentially different (and, sometimes, mutually exclusive) assumptions put forward [2–4]. In particular, Efimova and Ustimenkova [5] and Delyagin *et al.* [6] proposed a number of alternative explanations of the formation of magnetic structures with the properties of the so-called reentrant spin glasses, in which the second magnetic phase transition to the spin-glass state is observed at a temperature below the Curie point. In the present paper, the possibility of the magnetic phase transitions occurring in amorphous alloys with competing exchange interactions is considered in the framework of the Ising model.

### 2. THE DISTRIBUTION FUNCTION OF INTERACTION FIELDS

Earlier [7, 8], we demonstrated that the distribution function for random interaction fields  $W(H)$  in an amorphous ferromagnet is determined by the following relationship:

$$W(H) = \int A(\rho) \exp\{-i\rho H\} d\rho,$$

where

$$A(\rho) = \exp\{-n^* a\},$$

$$a = \int [1 - \exp\{i\rho\varphi(\mathbf{m}, \mathbf{r})\}] \tau(\mathbf{m}) d\mathbf{m} dV,$$

$n^* = \frac{N}{V}$  is the number of ferromagnetic atoms per unit volume,  $\varphi(\mathbf{m}, \mathbf{r})$  describes the law of their interaction, and  $\tau(\mathbf{m})$  is the particle distribution function with

respect to the magnetic moments, which, in the Ising model, has the following form:

$$\tau(\mathbf{m}) = \frac{1}{m^2} \delta(m - \mu) \frac{1}{\sin^2 \vartheta} [\alpha \delta(\vartheta) + \beta \delta(\vartheta - \pi)] \frac{1}{2\pi}. \quad (1)$$

Here,  $\mu$  is the magnetic moment per atom,  $\vartheta$  is the angle responsible for the orientation of  $\mathbf{m}$  with respect to the  $Z$  axis,  $\alpha + \beta = 1$ , and  $(\alpha - \beta)$  is the relative magnetic moment of the system. Within the approximation in which the expression for  $a$  contains only the terms quadratic in  $\rho$ , we obtain the relationship

$$W(H) = \frac{1}{\sqrt{\pi B}} \exp\left\{-\frac{[H - H_0(\alpha - \beta)]^2}{B^2}\right\},$$

where

$$H_0 = -n^* \int_V \varphi(\mathbf{r}) dV, \quad B^2 = 2n^* \int_V \varphi^2(\mathbf{r}) dV.$$

The advantage of this relationship over those used earlier in the spin glass theory is that the basic characteristics of the distribution function  $H_0$  and  $B$  are related through the interaction law  $\varphi(\mathbf{r})$ .

After averaging of the relative magnetic moment  $(\alpha - \beta)$  in terms of the Gibbs distribution and over configurations, the self-consistent equation for  $\langle \bar{\alpha} - \bar{\beta} \rangle$  takes the form

$$\langle \bar{\alpha} - \bar{\beta} \rangle \equiv M = \int_{-\infty}^{\infty} \tanh\left\{\frac{\mu H}{kT}\right\} W(H, M) dH$$

or

$$M = \frac{1}{\sqrt{\pi B}} \int_{-\infty}^{\infty} \tanh\left\{\frac{\mu(H + H_0 M)}{kT}\right\} \exp\left\{-\frac{H^2}{B^2}\right\} dH. \quad (2)$$

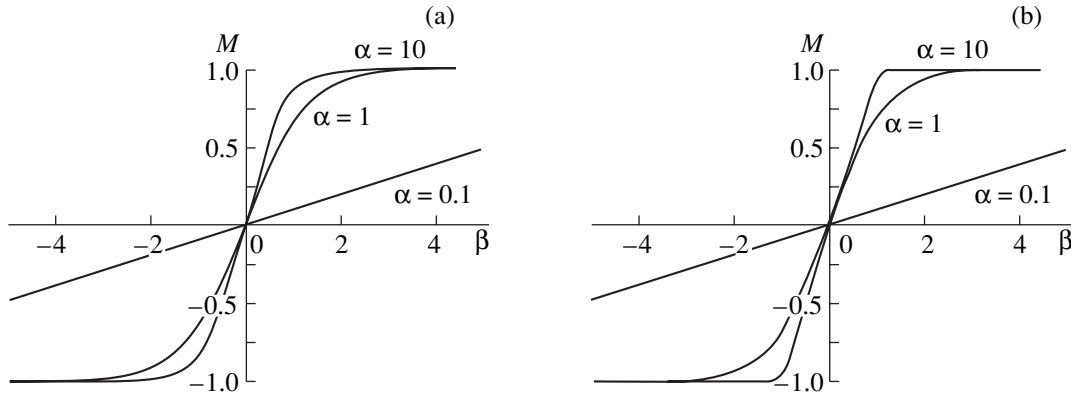


**Fig. 1.** Dependences  $M(\beta)$  calculated with the use of (a) the Gaussian function and (b) the step function substituted for the Gaussian function.

If we replace the Gaussian function by the approximate function

$$f(H, B) = \begin{cases} 0, & H^2 > B^2 \\ \frac{1}{2B}, & H^2 < B^2, \end{cases}$$

Eq. (2) for small  $M$  can be represented in the form

$$M = M \frac{H_0}{B} \tanh \left\{ \frac{\mu B}{kT} \right\}. \quad (3)$$

The insignificant loss of accuracy due to the above replacement is outweighed by the simplicity of the subsequent estimates. This error can be estimated by solving Eq. (2) numerically for two different distribution functions. Figure 1 represents the results of the calculation for different values of  $\alpha = \frac{mB}{kT}$  (the variable  $\beta$  is defined by the expression  $\beta = H_0 \frac{M}{B}$ ).

It follows from Eq. (3) that the solution with non-zero  $M$  (ferromagnetism) becomes possible only under the condition

$$\frac{H_0}{B} \geq 1. \quad (4)$$

In this case, the Curie point can be determined from the relationship

$$\frac{H_0(T_c)}{B(T_c)} \tanh \left\{ \frac{\mu B(T_c)}{kT_c} \right\} = 1. \quad (5)$$

For  $\frac{H_0}{B} < 1$ , a decrease in the temperature can result only in the transition to the spin-glass state.

### 3. COMPETING INTERACTIONS

In the case when the two exchange mechanisms described by different laws, namely,  $\varphi_1(\mathbf{r})$  and  $\varphi_2(\mathbf{r})$ , take place simultaneously, the parameters of the distribution function can be expressed as

$$H_0 = -n^* \int_V (\varphi_1(\mathbf{r}) + \varphi_2(\mathbf{r})) dV, \quad (6)$$

$$B^2 = 2n^* \int_V (\varphi_1(\mathbf{r}) + \varphi_2(\mathbf{r}))^2 dV,$$

or

$$H_0 = H_{0,1} + H_{0,2}, \quad B = (B_1^2 + B_2^2 + B_{12})^{1/2}.$$

Here,  $H_{0,1}$ ,  $B_1$  and  $H_{0,2}$ ,  $B_2$  are the corresponding parameters for each type of interaction and

$$B_{12} = 4n^* \int_V \varphi_1 \varphi_2 dV \quad (7)$$

is the interference integral.

It is evident that the different temperature dependences of the parameters  $H_0$  and  $B$  can lead to a sufficiently complex (nonmonotonic) behavior of the function

$$F(T) = \frac{H_0(T)}{B(T)} \tanh \left\{ \frac{\mu B(T)}{kT} \right\}. \quad (8)$$

The points of intersection of this function with the line  $F = 1$  determine the temperatures of the magnetic phase transitions.

We consider the following competing interactions: (i) the direct exchange, which is described by the function

$$\varphi_1 = \begin{cases} -f_0, & 0 < R < 2R_0 \\ 0, & R > 2R_0, \end{cases} \quad (9)$$

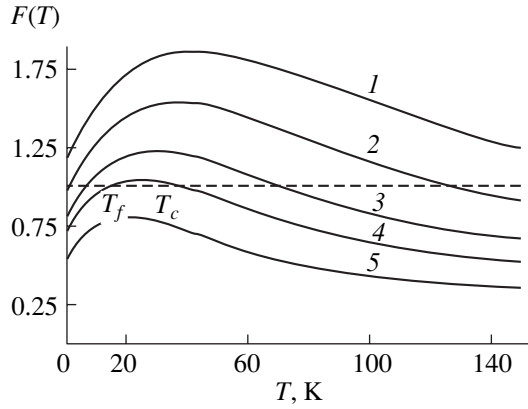


**Fig. 2.** Curves  $F(T)$  for different concentrations of magnetic atoms  $n^*$ ,  $10^{28} \text{ m}^{-3}$ : (1) 4, (2) 3, (3) 2, (4) 1.5, and (5) 1. The temperature range below the point  $T_f$  point of the second intersection of the line  $F(T) = 1$  corresponds to the reentrant spin glass.

where  $R_0$  is comparable to the atomic size in order of magnitude; (ii) the Ruderman–Kittel–Kasuya–Yosida (RKKY) exchange interaction

$$\varphi_2 = -bk_F^4 R_0^4 \frac{\sin(2k_F R) - 2k_F R \cos(2k_F R)}{(2k_F R)^4}; \quad (10)$$

and (iii) the indirect exchange in semiconductors (see [9])

$$\varphi_3 = -dk_F^4 R_0^4 \frac{\exp\{-(k_F R)^2\}}{k_F R}. \quad (11)$$

Here,

$$k_F = \sqrt{\frac{2m^*kT}{\hbar^2}},$$

where  $m^*$  is the effective electron mass.

In the above relationships, the parameters  $f_0$ ,  $b$ , and  $d$  characterize the intensity of the interaction and are chosen in such a manner that, in the vicinity of the concentration  $n_p^*$ , which provides the percolation transition for the direct exchange, any one of these interactions leads to a Curie temperature of the order of 100 K.

The percolation threshold is determined from the condition

$$\frac{H_{0,1}}{B_1} = 1.$$

Taking into account that the minimum distance between atoms is of the order of  $R_0$ , we obtain

$$H_0 = n^* \int_{R_0}^{2R_0} f_0 dV = 7f_0 n^* \frac{4}{3} \pi R_0^3,$$

$$B^2 = 14f_0^2 n^* \frac{4}{3} \pi R_0^3,$$

$$\frac{H_0}{B} = \sqrt{\frac{7}{2}} n^* \frac{4}{3} \pi R_0^3 = 1,$$

$$c_p = n^* \frac{4}{3} \pi R_0^3 = \frac{2}{7},$$

where  $c_p$  is the relative volume concentration of ferromagnetic atoms.

For  $R_0 = 10^{-10} \text{ m}$ , we have  $n_p^* \sim 3 \times 10^{28} \text{ m}^{-3}$ . The function  $F(T)$  for the cases of competing interactions  $(\varphi_1, \varphi_2)$  and  $(\varphi_1, \varphi_3)$  was calculated in the vicinity of  $n_p^* \sim 10^{28} \text{ m}^{-3}$  at  $f_0 = 10^2$  and  $b = d = 5 \times 10^4$ . The effective mass  $m^*$  was assumed to be equal to the electron mass. The results of calculations at different  $n^*$  for the case of competing interactions  $(\varphi_1, \varphi_2)$  are presented in Fig. 2. As is seen from this figure, there exists a concentration range in which the ferromagnet–spin glass transition can occur at a temperature  $T = T_f$  below the Curie point. In the temperature range  $T > T_c$ , the difference between the paramagnet and the spin glass is determined by the maximum exchange field  $B$ ; more specifically, the condition  $\frac{\mu B}{kT} \ll 1$  corresponds to the paramagnet, whereas the condition  $\frac{\mu B}{kT} \geq 1$  determines the region of existence of the spin glass. A similar result was obtained for the competing interactions  $(\varphi_1, \varphi_3)$ ; in this case,  $T_c$  somewhat increases.

#### 4. CONCLUSION

Thus, the competition of direct and indirect exchange interactions in the vicinity of the percolation threshold for amorphous semiconducting alloys can lead to a reentrant phase transition between the ferromagnet and spin glass at temperatures below the Curie point.

#### REFERENCES

1. I. Ya. Korenblit and E. F. Shender, *Usp. Fiz. Nauk* **157**, 267 (1989) [*Sov. Phys. Usp.* **32**, 139 (1989)].
2. K. Binder and A. P. Young, *Rev. Mod. Phys.* **58**, 801 (1986).
3. M. Gabay and G. Toulouse, *Phys. Rev. Lett.* **47**, 201 (1981).
4. P. A. Beck, *Phys. Rev. B* **32**, 7255 (1985).
5. N. N. Efimova and M. B. Ustimenkova, *Zh. Éksp. Teor. Fiz.* **114**, 2065 (1998) [*JETP* **87**, 1122 (1998)].
6. N. N. Delyagin, G. M. Gurevich, A. L. Erzinkyan, *et al.*, *Zh. Éksp. Teor. Fiz.* **109**, 1451 (1996) [*JETP* **82**, 783 (1996)].
7. V. I. Belokon' and S. V. Semkin, *Zh. Éksp. Teor. Fiz.* **102**, 1254 (1992) [*Sov. Phys. JETP* **75**, 680 (1992)].
8. V. I. Belokon' and K. V. Nefedev, *Zh. Éksp. Teor. Fiz.* **120**, 156 (2001) [*JETP* **93**, 136 (2001)].
9. S. Methfessel and D. C. Mattis, in *Handbuch der Physik*, Vol. 18, Part 1, Ed. by H. P. J. Wijn (Springer-Verlag, Berlin, 1968), p. 389.

Translated by O. Moskalev

---

## MAGNETISM AND FERROELECTRICITY

---

# Crystallization of Ba–Me Hexagonal Ferrite Thin Films

A. S. Kamzin\*, Fulin Wei\*\*, Zheng Yang\*\*, and Xiaoxi Liu\*\*

\* Ioffe Physicotechnical Institute, Russian Academy of Sciences,  
Politekhnicheskaya ul. 26, St. Petersburg, 194021 Russia

\*\* Research Institute of Magnetism and Magnetic Materials, Lanzhou University, Lanzhou,  
230000 Republic of China

e-mail: KAMZIN@spb.cityline.ru

Received November 2, 2001

**Abstract**—Thin films of Ba–Me ferrites are synthesized by reactive rf diode sputtering of a  $\text{BaO} \cdot n\text{Fe}_2\text{O}_3$  ceramic target. Quartz plates subjected to preliminary annealing are used as substrates. The influence of the barium ion content on the crystalline and magnetic properties and the microstructure of the prepared films is investigated, and the interrelation between the quantity  $dH_c/dT$  and the microstructure of the film is considered. The prepared films satisfy the requirements for materials used as information carriers with a superhigh recording density. © 2002 MAIK “Nauka/Interperiodica”.

## 1. INTRODUCTION

Thin magnetic films are promising materials for use as information carriers with high and superhigh recording densities. This necessitates comprehensive investigations of their properties and the development of new technologies for manufacturing thin magnetic films with specified parameters. The main objective of these investigations is to increase the data recording density. One way to increase the recording density is to decrease the distance between the recorder and the information carrier. For this purpose, information carriers need to possess high mechanical strength and chemical durability. Films of Ba–Me hexagonal ferrites exhibit high resistance to mechanical actions; however, the coercive forces of these films are insufficiently strong to provide data recording with high and superhigh densities. Moreover, it is important to decrease the manufacturing cost of Ba–Me ferrite films.

The possibility of using thin films of Ba–Me hexagonal ferrites of the chemical formula  $\text{BaFe}_{12}\text{O}_{19}$  in data recording with high and superhigh densities has long since been demonstrated (see, for example, [1–3] and references therein). However, stringent requirements on the properties of hexagonal ferrite films used as storage media necessitate their growth on single-crystal substrates prepared from garnets or other ferrites. In turn, this appreciably increases the net cost of the films at the expense of the single-crystal substrates alone. Matsuoka *et al.* [4] showed that Ba–Me ferrite films whose properties satisfy the rigid requirements on data recording with a superhigh density can be synthesized on amorphous quartz plates. These findings gave impetus to a search for new inexpensive substrates and the development of techniques for synthesizing Ba–Me ferrite films on these substrates. Chen *et al.* [5] proved that the properties of Ba–Me ferrite thin films substantially

depend on their chemical composition. Nonetheless, even despite the large number of works dealing with Ba–Me ferrite films, the processes of crystallization and formation of complex oxide compounds (such as ferrites) in the form of thin films are still not clearly understood.

In the present work, we investigated the influence of the barium ion content on the crystalline and magnetic properties and the microstructure of Ba–Me ferrite thin films synthesized on amorphous substrates. Moreover, we analyzed how the quantity  $dH_c/dT$  (where  $H_c$  is the coercive force) affects the microstructure of the film.

## 2. SAMPLE PREPARATION AND EXPERIMENTAL TECHNIQUE

Thin films of Ba–Me ferrites were synthesized by reactive rf diode sputtering of a Ba–Me ceramic ferrite target in a gaseous mixture of Ar and  $\text{O}_2$  in the ratio 3.5 : 0.5 (mTorr). Quartz plates subjected to preliminary annealing were used as substrates for film deposition. Targets were prepared in the form of  $\text{BaO} \cdot n\text{Fe}_2\text{O}_3$  ceramic pellets annealed for 5 h in a mixture of  $\text{BaCO}_3$  and  $\text{Fe}_2\text{O}_3$  taken in appropriate proportion. After deposition, the films were annealed for 1 h at a temperature of 800°C with the aim of forming crystal and magnetic structures of the required quality, which was established experimentally. The thickness of the prepared films was approximately equal to 100 nm.

The film composition was determined using inductively coupled plasma mass spectrometry (ICP-MS). The crystal structure of the prepared films was investigated by x-ray diffraction. The magnetic structure of the films was analyzed using Auger-electron and conversion-electron Mössbauer spectroscopy. The magnetic properties and their temperature dependences

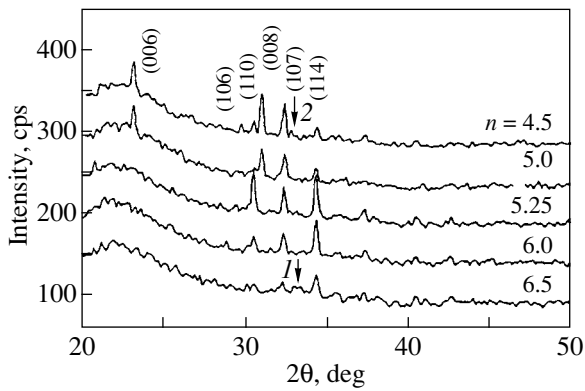


**Fig. 1.** X-ray diffraction spectra of  $\text{BaO} \cdot n\text{Fe}_2\text{O}_3$  films. The concentrations  $n = 4.5, 5.0, 5.25, 6.0,$  and  $6.5$  are determined using inductively coupled plasma mass spectrometry (ICP-MS). The parenthetic numbers correspond to the reflections assigned to the Ba–Me hexagonal ferrite. Arrows 1 and 2 indicate the reflections attributed to  $\text{Fe}_2\text{O}_3$  and  $\text{BaOFe}_2\text{O}_4$ , respectively.

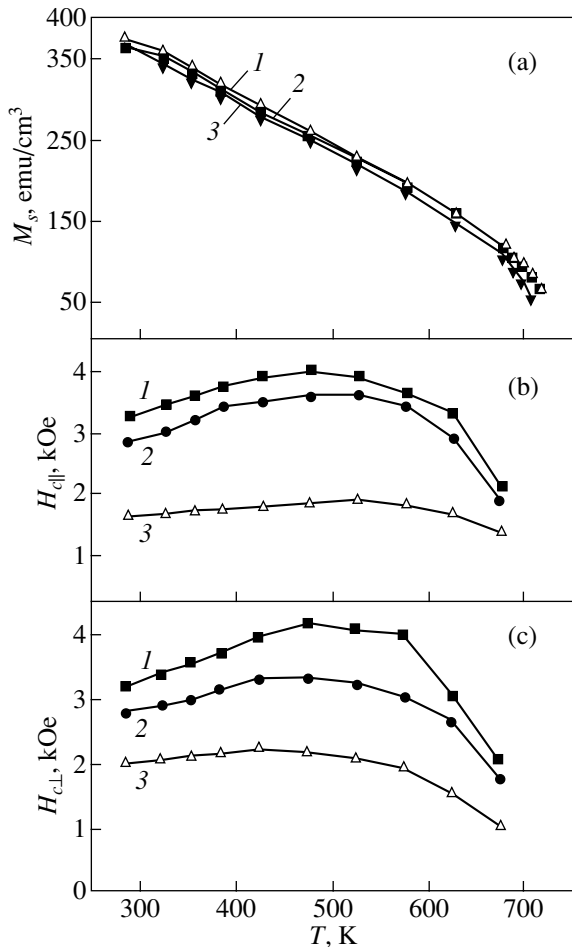


**Fig. 2.** (a) Temperature dependences of the saturation magnetization  $M_s$  and temperature dependences of the coercive force measured in a magnetic field applied (b) parallel and (c) perpendicular to the growth plane of the  $\text{BaO} \cdot n\text{Fe}_2\text{O}_3$  films at  $n = (1) 5.0, (2) 5.5,$  and  $(3) 6.0$ .

were measured on a vibrating-sample magnetometer. The surface morphology of the films was examined using an electron microscope.

### 3. RESULTS AND DISCUSSION

Figure 1 shows the x-ray diffraction spectra of  $\text{BaO} \cdot n\text{Fe}_2\text{O}_3$  films. The concentrations  $n = 4.5, 5.0, 5.25, 6.0,$  and  $6.5$  were determined by inductively coupled plasma mass spectrometry. Analysis of the x-ray diffraction spectra depicted in Fig. 1 revealed that broad peaks with maxima in the  $2\theta$  range of  $22^\circ$  are attributed to reflections from the substrate. As is seen from this figure, the (008) reflection dominates in the spectrum of the  $\text{BaO} \cdot 4.5\text{Fe}_2\text{O}_3$  film. This indicates that, for  $\text{BaO} \cdot n\text{Fe}_2\text{O}_3$  films at  $n = 4.5$ , the crystallographic axis  $C$  is perpendicular to the growth plane of the film. Moreover, the x-ray diffraction spectrum of the  $\text{BaO} \cdot 4.5\text{Fe}_2\text{O}_3$  film exhibits reflections of moderate intensity which correspond to the  $\text{BaFe}_2\text{O}_4$  ferrite. This can be explained by the fact that the content of barium ions in this compound is relatively high and exceeds their content in the stoichiometric compound  $\text{BaO} \cdot 6.0\text{Fe}_2\text{O}_3$ . An increase in the concentration  $n$  leads to an increase in the intensity of the reflection assigned to the (110) plane, which suggests a deviation of the crystallographic axis  $C$  from the normal to the growth plane of the film. It can be seen that the (110) reflection dominates in the spectrum of the  $\text{BaO} \cdot n\text{Fe}_2\text{O}_3$  film at  $n = 5.25$ ; i.e., for the  $\text{BaO} \cdot 5.25\text{Fe}_2\text{O}_3$  composition, the  $C$  axis is predominantly oriented along the film plane. The x-ray diffraction spectrum of the  $\text{BaO} \cdot 6.5\text{Fe}_2\text{O}_3$  film is characterized by the reflection attributed to hematite. This can be associated with the deviation of the  $\text{BaO} \cdot 6.5\text{Fe}_2\text{O}_3$  composition from stoichiometry, as was also noted in [5].

Figure 2 depicts the temperature dependences of the saturation magnetization and the coercive force measured in a magnetic field applied parallel and perpendicular to the growth plane of the  $\text{BaO} \cdot n\text{Fe}_2\text{O}_3$  films at different concentrations  $n$ . The temperature dependences of the saturation magnetization  $M_s$  measured with the use of the vibrating-sample magnetometer upon heating from room temperature to 700 K are displayed in Fig. 2a. It can be seen that, for all the ferrite films under investigation, the saturation magnetization  $M_s$  almost linearly decreases with an increase in the temperature. For films with concentrations  $n = 5.0, 5.5,$  and  $6.0$ , the value of  $dM_s/dT$  remains unchanged.

The concentration dependences of the saturation magnetization  $M_s$  and the coercive force measured in a magnetic field applied parallel and perpendicular to the growth plane of the  $\text{BaO} \cdot n\text{Fe}_2\text{O}_3$  films are plotted in Fig. 3. As the concentration  $n$  increases, the saturation magnetization  $M_s$  increases (Fig. 3, curve 1) and reaches a maximum value of  $\sim 370 \text{ emu/cm}^3$  at  $n = 5.25$ . A further increase in the concentration  $n$  results in a

decrease in the magnetization  $M_s$ . It can be assumed that low values of  $M_s$  at  $n < 4.5$  and  $n > 6.0$  are associated with the presence of the paramagnetic phase in these compositions. This inference is in agreement with the results obtained from analyzing the x-ray diffraction spectra.

Let us now consider the concentration dependences of the coercive force measured in a magnetic field applied parallel and perpendicular to the growth plane of the  $\text{BaO} \cdot n\text{Fe}_2\text{O}_3$  films (Fig. 3, curves 2, 3). As can be seen, an increase in the concentration  $n$  leads to a decrease in the coercive force measured both parallel and perpendicular to the growth plane. At room temperature, the value of  $dH_c/dT$  decreases with an increase in the concentration  $n$ . It is worth noting that the smaller the value of  $dH_c/dT$ , the higher the bit density—an important parameter of information carriers (in our case, the  $\text{BaO} \cdot n\text{Fe}_2\text{O}_3$  films). By analogy with [6], we analyzed our results within an approach described in [7] and revealed that, for the Ba–Me ferrite films under investigation, the above parameter depends solely on the crystal grain shape. According to electron microscopic data, the  $\text{BaO} \cdot n\text{Fe}_2\text{O}_3$  ferrite films with a high content of barium ions (at small concentrations  $n$ ) are characterized by small-sized grains and, at  $n \leq 5.0$ , predominantly contain crystal grains of platelet shape. At  $n \geq 6$ , the mean size of crystal grains in the ferrite films substantially increases and exceeds 200 nm. Crystal grains of needle shape with a length-to-diameter ratio of  $\sim 6$  dominate in the Ba–Me films at  $n \geq 6$ . It seems likely that, at  $n \geq 6$ , the grain size exceeds the size of single domains and the existence of domain walls in the crystal grains leads to a decrease in the coercive force of these films. For concentrations  $n \geq 6$ , the coercivity in the film plane is higher than that in the perpendicular direction. The opposite situation occurs at  $n \leq 5.75$ ; i.e., the coercive force measured in a magnetic field applied parallel to the growth plane of the film is weaker than that applied in a direction perpendicular to this plane. Therefore, we can draw the conclusion that the concentration  $n$  is a controlling factor responsible for the orientation of the  $C$  axis in the synthesized films of  $\text{BaO} \cdot n\text{Fe}_2\text{O}_3$  ferrites.

It is well known that the phase composition of the materials under investigation and the orientation of the magnetic moments in the samples can be determined directly from Mössbauer measurements. For this reason, the prepared films were examined by Mössbauer spectroscopy with recording of conversion electrons and Auger electrons in a backscattering geometry [8]. The latter circumstance stems from the fact that traditional Mössbauer spectroscopy with recording of gamma radiation in a transmission geometry cannot be used for thin films, because, in this case, the signal-to-noise ratio is very small. Figure 4 displays the Mössbauer spectra of  $\text{BaO} \cdot 4.5\text{Fe}_2\text{O}_3$  ferrite films prepared at room temperature and subjected to annealing for 1 h

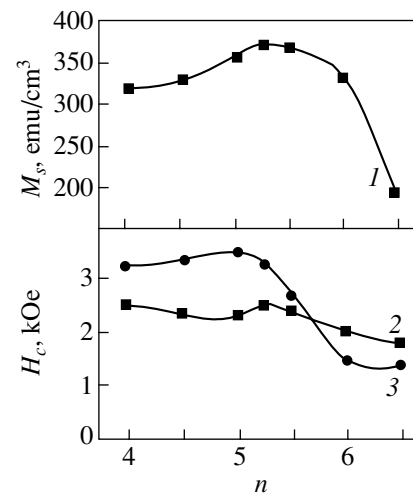


Fig. 3. (1) Concentration dependence of the saturation magnetization  $M_s$  and concentration dependences of the coercive force measured in a magnetic field (2) perpendicular and (3) parallel to the growth plane of the  $\text{BaO} \cdot n\text{Fe}_2\text{O}_3$  films.

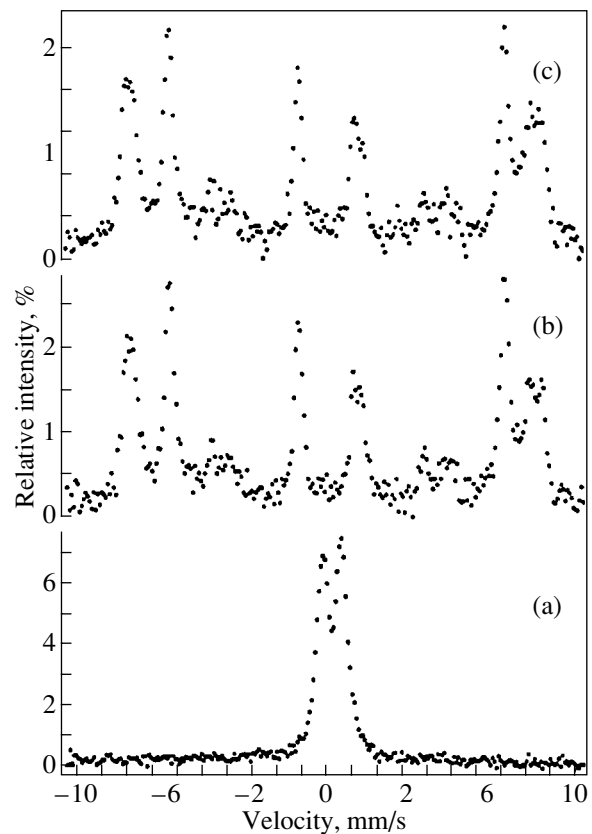


Fig. 4. Mössbauer spectra of  $\text{BaO} \cdot 4.5\text{Fe}_2\text{O}_3$  ferrite films after annealing for 1 h at temperatures of (a) 700, (b) 800, and (c) 900°C.

at different temperatures. The wave vector of gamma radiation is perpendicular to the growth plane of the films.

As is seen from Fig. 4a, the Mössbauer spectrum of the  $\text{BaO} \cdot 4.5\text{Fe}_2\text{O}_3$  ferrite film subjected to annealing at a temperature of  $700^\circ\text{C}$  represents a doublet. Similar spectra are observed for ferrite films either not subjected to annealing or annealed at temperatures below  $700^\circ\text{C}$  for 1 h. The isomer shifts (0.25 mm/s) with respect to Fe and quadrupole splittings (0.75 mm/s) calculated from these spectra (Fig. 4a) coincide with those obtained for Ba–Me ferrite films immediately after their synthesis through radio-frequency sputtering [9] and correspond to the parameters of Ba–Me nonmagnetic bulk amorphous ferrites [10].

After annealing of the  $\text{BaO} \cdot 4.5\text{Fe}_2\text{O}_3$  ferrite film at a temperature of  $800^\circ\text{C}$ , the Mössbauer spectrum exhibits Zeeman splitting (Fig. 4b). A similar spectrum is observed for the  $\text{BaO} \cdot 4.5\text{Fe}_2\text{O}_3$  ferrite film subjected to annealing at  $900^\circ\text{C}$  (Fig. 4c). A computer-assisted least-squares analysis of the experimental Mössbauer spectra demonstrated that the films under investigation belong to the Ba–Me hexagonal ferrite [11]. Mössbauer lines attributed to other phases, including the  $\text{BaFe}_2\text{O}_4$  ferrite, were not found to within an error of 5%. The effective magnetic fields at Fe nuclei in  $4f_1$ ,  $4f_2$ , and  $12k$  sublattices were determined from the spectra and amounted to  $342 \pm 5$ ,  $348 \pm 5$ , and  $327 \pm 5$  kOe, respectively.

It can be seen from Figs. 4b and 4c that the intensities of the second and fifth components of the Zeeman sextets are relatively low. This indicates that the magnetic moments in the studied material slightly deviate from the wave vector of gamma radiation, which is perpendicular to the film plane. The angle  $\theta$  determines the orientation of the magnetic moments in the crystal with respect to the wave vector of gamma radiation and can be calculated from the Mössbauer spectra according to the following formula (see, for example, [12]):

$$\begin{aligned} \theta &= \arccos\left(\frac{4A_{1.6} - 3A_{2.5}}{4A_{1.6} + 3A_{2.5}}\right)^{1/2} \\ &= \arcsin\left(\frac{(3/2)A_{2.5}/A_{1.6}}{1 + (3/4)A_{2.5}/A_{1.6}}\right)^{1/2}, \end{aligned} \quad (1)$$

where  $A_{1.6}$  stands for the intensities of the first and sixth lines and  $A_{2.5}$  are the intensities of the second and fifth lines. The angle  $\theta$  calculated from formula (1) is equal to  $30^\circ \pm 7^\circ$ .

An examination of the  $\text{BaO} \cdot 4.5\text{Fe}_2\text{O}_3$  ferrite films under the electron microscope revealed that these films consist of platelike grains. Earlier [8], it was shown that, in Ba–Me hexagonal ferrites, the magnetic

moments are aligned along the crystallographic axis  $C$ . As follows from analyzing the results of electron microscopy and Mössbauer spectroscopy, in the majority of platelike grains forming the  $\text{BaO} \cdot 4.5\text{Fe}_2\text{O}_3$  film under investigation, the  $C$  axis is oriented normally to the growth plane of the film.

#### 4. CONCLUSION

Thus, our investigation has demonstrated that thin films of Ba–Me hexagonal ferrites whose properties satisfy the requirements for information carriers with a superhigh recording density can be synthesized through reactive rf diode sputtering onto an amorphous annealed quartz substrate followed by annealing.

#### ACKNOWLEDGMENTS

This work was supported by the National Scientific Foundation of China and the Russian Foundation for Basic Research (project no. 01-02-17889).

#### REFERENCES

1. M. Matsuoka, Y. Hoshi, M. Naoe, and S. Yamada, *IEEE Trans. Magn.* **18**, 1119 (1982).
2. D. E. Speliotis, *IEEE Trans. Magn.* **23**, 3134 (1987).
3. Xiaoyu Sui, Matthias Scherge, Mark H. Kryder, *et al.*, *J. Magn. Mater.* **155**, 132 (1996).
4. M. Matsuoka, M. Naoe, and Y. Hoshi, *IEEE Trans. Magn.* **21**, 1474 (1985).
5. V. J. Chen, D. E. Laughlin, X. Ma, and M. H. Kryder, *J. Appl. Phys.* **81**, 4380 (1997).
6. Xiaoxi Liu, Jianmin Bai, Fulin Wei, *et al.*, *J. Magn. Mater.* **212**, 273 (2000).
7. A. A. Aharoni, *Introduction to the Theory of Ferromagnetism* (Oxford Univ. Press, Oxford, 1996).
8. A. S. Kamzin and L. A. Grigor'ev, *Pis'ma Zh. Tekh. Fiz.* **16** (16), 38 (1990) [*Sov. Tech. Phys. Lett.* **16**, 616 (1990)].
9. P. Gerard, E. Lacroix, G. Marest, *et al.*, *Solid State Commun.* **71**, 52 (1989).
10. L. Fa-Shen, Z. Rong-Jie, L. Jand-Zhong, and Y. Zheng, *Hyperfine Interact.* **41**, 491 (1988).
11. Sh. Sh. Bashkirov, A. B. Liberman, and V. I. Sinyavskii, *Magnetic Microstructure of Ferrites* (Kazan. Univ., Kazan, 1978).
12. *Chemical Applications of Mössbauer Spectroscopy: A Collection of Articles*, Ed. by V. I. Goldanskii and R. H. Herber (Academic, New York, 1968; Mir, Moscow, 1977).

*Translated by O. Borovik-Romanova*

---

## MAGNETISM AND FERROELECTRICITY

---

# Spin-Wave Resonance in Magnetic Films under Conditions of the Skin Effect

R. N. Nosov and D. I. Sementsov

Ul'yanovsk State University, Ul'yanovsk, 432700 Russia

e-mail: sdi@sdi.ulsu.ru

Received November 15, 2001

**Abstract**—The spin-wave resonance spectrum of a ferromagnetic film magnetized normally to its surface is investigated as a function of the finite depth of penetration of the high-frequency field into the film with due regard for damping in the spin system and different types of surface-spin pinning. The exact numerical solution of the equation of motion for magnetization is obtained by considering the finite thickness of the skin layer. For a substantially inhomogeneous distribution of the high-frequency field over the layer thickness, the change in the resonance shape at frequencies close to the ferromagnetic resonance frequency is observed in addition to the broadening of all the resonance peaks and the decrease in their amplitudes. © 2002 MAIK “Nauka/Interperiodica”.

### 1. INTRODUCTION

It is known that a necessary condition for excitation of spin-wave resonance in a uniformly magnetized film by a homogeneous high-frequency field is the surface anisotropy of the film. The surface anisotropy differs from the bulk anisotropy and determines the character and degree of spin pinning on the film surface. In many works [1–5], the influence of the boundary conditions on the spin-wave resonance spectrum has been analyzed taking into account the specific features of the spin-wave resonance for different types of surface-spin pinning and damping in the spin system. However, the fact that the high-frequency field penetrates into a conducting sample to a finite depth, thus breaking the homogeneity of the magnetization distribution, has been disregarded by the majority of authors. A consistent analysis of the skin effect, which is important for high-conductivity films, necessitates simultaneous solution of the electromagnetic equation and the equation of motion for magnetization. In general, this leads to a bicubic dispersion equation and a cumbersome solution of the boundary-value problem even for a semi-infinite medium and special cases of total surface-spin pinning or its absence [6]. In this respect, approximate analytical methods of analyzing the spin-wave resonance spectra of conducting films have assumed particular importance.

If the mean free path of conduction electrons is considerably less than the depth  $\delta$  of penetration of the electromagnetic field into a metal, the normal skin effect takes place and the skin depth is determined by the expression  $\delta = c/\sqrt{2\pi\sigma\omega\mu}$ , where  $c$  is the velocity of light in free space,  $\omega$  is the field frequency, and  $\sigma$  is

the conductivity of the metal. The magnetic permeability  $\mu$  of the sample is a function of the frequency and accounts for the magnetic characteristics, geometry, and orientation of the sample with respect to the external magnetic field. For magnetic films with the thickness  $L \sim 10^{-5}$  cm and the conductivity  $\sigma \geq 10^{17}$  s $^{-1}$ , the skin depth can be of the same order of magnitude even at room temperature due to high values of the high-frequency permeability ( $\mu \gg 1$ ). In the case when the film thickness satisfies the condition  $L \geq \delta$ , the distributions of both the microwave field and magnetization cannot be considered to be homogeneous over the film thickness. This circumstance can lead to a modification of the spin-wave modes and a decrease in their amplitudes compared to those in the case  $\delta \gg 1$ .

### 2. GENERAL EQUATIONS AND RELATIONSHIPS

Let us consider a film magnetized normally to its surface by an external field  $\mathbf{H}_0$  along the easy magnetic axis. Since the film possesses axial symmetry, it is convenient to describe the deviation of the magnetic moment  $\mathbf{M}$  from the equilibrium moment  $\mathbf{M}_0$  in terms of the circular projections  $m^\pm = m_x \pm im_y$ . If the microwave field is also circularly polarized ( $h^\pm = h_x \pm ih_y$ ) and harmonically depends on time, the equation of motion for the component  $m^+ \equiv m$ , which is responsible for free oscillations of the spin system, takes the form

$$\frac{d^2 m}{dz^2} + v^2 m = -\frac{h(z)}{\alpha}. \quad (1)$$

Here, the wave number of the spin wave is determined by the relationship

$$v^2 = \frac{(1 - i\xi)\omega - \omega_0}{\alpha\gamma M_0}, \quad (2)$$

where  $\omega_0 = \gamma(H_0 + \beta M_0 - 4\pi M_0)$  is the frequency of uniform (ferromagnetic) resonance;  $\alpha$  and  $\beta$  are the exchange interaction constant and magnetic anisotropy constant, respectively;  $\gamma$  is the gyromagnetic ratio; and  $\xi$  is the damping parameter. Let us represent the dependence of the microwave field on the coordinate in the form

$$\mathbf{h}(z) = \mathbf{h}_0 \exp[(z - L)/\delta]. \quad (3)$$

Here, it is accepted that the origin of coordinates is located at the center of a layer with thickness  $2L$ . Taking into account that the high-frequency permeability  $\mu$ , which enters into the definition of the depth  $\delta$  of penetration of the microwave field into the metal, is a complex quantity, we obtain

$$\frac{1}{\delta} = \frac{1}{\delta_0}(g - ip), \quad (4)$$

where  $\delta_0 = c/\sqrt{2\pi\sigma\omega}$  is the penetration depth without regard for the magnetic properties of the metal,

$$g = |\mu|^{1/2} \cos \varphi, \quad p = |\mu|^{1/2} \sin \varphi, \\ |\mu| = (\mu'^2 + \mu''^2)^{1/2}, \quad \varphi = \frac{1}{2} \arctan(\mu''/\mu').$$

Next, we take into account that the high-frequency permeability can be expressed as  $\mu = 1 + 4\pi\chi$ , where  $\chi$  is the complex high-frequency susceptibility. Hence, the real and imaginary parts of the magnetic permeability involved in expression (4) can be represented by the relationships  $\mu' = 1 + 4\pi\chi'$  and  $\mu'' = 4\pi\chi''$ . Therefore, in order to calculate the depth of penetration of the microwave field into the layer, it is necessary to determine the high-frequency susceptibility  $\chi$ . In turn, this calls for solving the equation of motion for magnetization (1). Making allowance for the inhomogeneous distribution of the microwave field, which is defined by relationship (3), the exact solution to Eq. (1) can be obtained only by numerical methods.

We will seek the exact solution to Eq. (1) with the following boundary conditions for magnetization:

$$\frac{dm}{dz} \pm d_i m|_{z=\pm L} = 0, \quad (5)$$

where  $d_i$  stands for the parameters of spin pinning on the layer surface. The total spin pinning is observed at  $d_i \rightarrow \infty$  and is absent on the corresponding surface of the layer at  $d_i = 0$ .

### 3. HIGH-FREQUENCY SUSCEPTIBILITY OF THE LAYER

Simultaneous solution of Eqs. (1) and (5) in terms of Eq. (3) gives the expression for the high-frequency magnetization:  $m(z) = \chi(z)h_0$ . Averaging the high-frequency magnetization  $m(z)$  over the layer thickness and taking into account that  $\langle m \rangle = \chi h_0$ , we obtain the following general relationship for the high-frequency susceptibility of the layer, which does not depend on the coordinate but does depend on the parameters of the magnetic subsystem, layer thickness, frequency, and conductivity:

$$\chi = G \left\{ \frac{a - be^{-2L/\delta}}{v\delta^2 [d_1 d_2 + v(d_1 + d_2) \cot 2vL - v_2]} - 1 + e^{-2L/\delta} \right\}, \quad (6)$$

where  $a = (v + d_1 \tan vL)(1 + d_2 \delta)$ ,  $b = (v + d_2 \tan vL) \times (1 - d_1 \delta)$ , and  $G = \delta^3/2\alpha L(1 + v^2\delta^2)$ . It should be remembered that the quantity  $\delta$  in expression (6) is a complex function of the frequency and is determined by relationship (4), which involves both the real and imaginary parts of the high-frequency susceptibility  $\chi$ . In order to obtain an approximate analytical representation of the spin-wave resonance spectrum with the use of relationships (4) and (6), the complex parameter  $\delta$  can be determined using an approximate expression for the susceptibility  $\chi_{\text{homog}}$ . This expression corresponds to the homogeneous distribution of the microwave field over the layer thickness and can be derived from relationship (6) at  $\delta \rightarrow \infty$  in the following form:

$$\chi_{\text{homog}} = \frac{1}{2\alpha v^2} \times \left\{ \frac{v(d_1 + d_2) + 2d_1 d_2 \tan vL}{vL[d_1 d_2 + v(d_1 + d_2) \cot 2vL - v^2]} - 2 \right\}. \quad (7)$$

In our recent work [7], we applied expression (7) to analyze thoroughly the spin-wave resonance spectrum for a layer characterized by a homogeneous distribution of the high-frequency field and finite degrees of surface-spin pinning. As will be shown below, the approximate solution thus obtained agrees well with the exact numerical solution of the problem under consideration.

Let us now consider the most important special cases of resonant susceptibility of the spin system at a finite skin depth  $\delta$ , which follow from relationship (6). For symmetric boundary conditions ( $d_1 = d_2 = d$ ), the susceptibility of the spin system can be represented as

$$\chi = G(1 - e^{-2L/\delta}) \left[ \frac{(v + d \tan vL)(1 + d\delta \coth L/\delta)}{v\delta^2 (d^2 + 2vd \cot 2vL - v^2)} \right]. \quad (8)$$

The situation with the total pinning of surface spins ( $d \rightarrow \infty$ ) is of particular interest. The susceptibility of the spin system takes the form

$$\chi = G(1 - e^{-2L/\delta}) \left( \frac{\tan vL}{v\delta} \coth L/\delta - 1 \right), \quad (9)$$

and the position of resonance peaks corresponding to spin-wave modes (in the absence of damping) is determined by the wave numbers  $v_p = \pi(1 + 2p)/2L$ , as is the case with the homogeneous distribution of the high-frequency field over the layer thickness.

In the case of asymmetric pinning ( $d_1 = -d_2 = d$ ), the high-frequency susceptibility has the form

$$\chi = G(1 - e^{-2L/\delta}) \times \left[ \frac{(\delta d - 1)(v + d \tan vL \coth L/\delta)}{v\delta^2(v^2 + d^2)} - 1 \right]. \quad (10)$$

For the total asymmetric pinning, the expression for  $\chi$  coincides with relationship (9).

For completely free surface spins ( $d_1 = d_2 = 0$ ), the resonant susceptibility of the layer takes the form

$$\chi = \frac{\delta}{2\alpha v^2 L} (e^{-2L/\delta} - 1), \quad (11)$$

from which it follows that the spectrum contains only the "uniform" mode ( $v \rightarrow 0$ ).

Among the asymmetric cases of surface-spin pinning, the most interesting situation corresponds to the total pinning of spins on one of the layer surfaces and to the absence of spin pinning on the other surface ( $d_1 \rightarrow \infty$ ,  $d_2 = 0$ ). In this case, the expression for the high-frequency susceptibility takes the form

$$\chi = G(1 - e^{-2L/\delta}) \left( \frac{\delta v e^{-2L/\delta} + \tan vL}{\delta^2 v^2 \cot 2vL} - 1 \right). \quad (12)$$

The position of spin-wave modes is specified by the wave numbers  $v_p = \pi(1 + 2p)/4L$ ; in this case, the number of maxima in the spin-wave resonance spectrum is doubled in comparison with the case of symmetric pinning.

In order to determine the position, amplitude, and width of the line corresponding to the resonant mode in the spin-wave resonance spectrum with damping in the spin system, it is necessary to derive the imaginary part of the susceptibility  $\chi''$  for each of the above cases, because  $\chi''$  determines the absorbed power per unit volume ( $P = \omega h^2 \chi''/2$ ). Since the wave number  $v$  and parameter  $\delta$  are the complex quantities determined by relationships (2) and (4), the appropriate expressions for  $\chi''$  appear rather cumbersome. In the simplest case of the absence of surface-spin pinning ( $d_1 = d_2 = 0$ ),

which is described by relationship (11), the susceptibility  $\chi''$  satisfies the expression

$$\chi''(\omega) = \frac{\gamma M_0 2L p (\omega - \omega_0) + (\delta_0 - 2Lg)\xi\omega}{\xi\omega_0 (\omega - \omega_0)^2 + \xi^2\omega^2}. \quad (13)$$

At the resonance frequency  $\omega = \omega_0$ , we obtain the imaginary part of the susceptibility for the amplitude of the uniform mode:

$$\chi''(\omega_0) = \frac{\gamma M_0}{\xi\omega_0} \left( 1 - \frac{2L}{\delta_0} g \right). \quad (14)$$

Hence, it follows that, as the depth of penetration of the microwave field into the sample increases, the amplitude for the ferromagnetic resonance peak increases and, at  $\delta_0 \rightarrow \infty$ , reaches the susceptibility  $\chi''_m = \gamma M_0/\xi\omega_0$ . Note that the broadening and shift of the resonance curve due to changes in the penetration depth are virtually absent because the parameter of magnetic damping is fixed and is unrelated to the conductivity  $\sigma$ .

#### 4. NUMERICAL ANALYSIS

The above analysis can be illustrated using the frequency dependences of the susceptibility  $\chi''$ , which were obtained by numerical calculation and plotted on a semilogarithmic scale. In our case, the frequency dependence is taken to mean a dependence of the susceptibility  $\chi''$  on the normalized detuning  $\Delta\omega/\omega_0$ , where  $\Delta\omega = \omega - \omega_0$ . For the calculation, we chose the following parameters of the permalloy film:  $M_0 = 10^3$  G,  $\alpha = 10^{-12}$  cm<sup>2</sup>,  $\xi = 10^{-2}$ ,  $L = 2 \times 10^{-5}$  cm, and  $\omega_0 = 3 \times 10^{10}$  s<sup>-1</sup>. The required changes in the depth of penetration of the high-frequency field into the sample were obtained by varying the conductivity. For all the dependences given below (Figs. 1–3), the conductivity was taken to be  $\sigma = (1, 50, \text{ and } 1000) \times 10^{15}$  s<sup>-1</sup> (curves 1–3). The solid lines represent the results of exact numerical calculations, and the dashed lines correspond to the results of approximate calculations. The exact numerical calculation implies a procedure in which the parameter  $\delta$  at a given frequency is calculated from the values of  $\chi'$  and  $\chi''$  obtained at the preceding step of calculation. The step of frequency detuning is chosen such that it provides as small changes in the aforementioned quantities as possible. Curves 1, which correspond to  $\sigma = 10^{15}$  s<sup>-1</sup>, coincide to within high accuracy for both the exact and approximate calculations. This is associated with the distribution of the microwave field over the layer thickness actually being homogeneous. The time of the exact numerical calculation substantially exceeds the time of the approximate calculation.

Figure 1 shows the resonance curves  $\chi''(\omega)$  at  $d_1 = d_2 = 0$ . As in the case of the homogeneous field distribution  $h(t)$ , the absence of spin pinning leads to the disappearance of the spin-wave spectrum and to excitation of a single mode characterized by the exponential

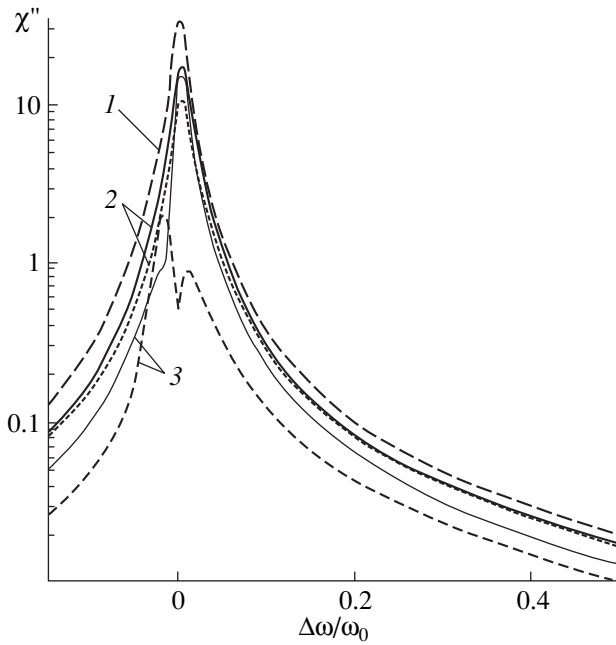


**Fig. 1.** Spin-wave resonance spectra in the absence of spin pinning on the layer surfaces ( $d_1 = d_2 = 0$ ) at different conductivities  $\sigma$ ,  $10^{15} \text{ s}^{-1}$ : (1) 1, (2) 50, and (3) 1000. Solid lines represent the results of exact calculations, and dashed lines are the results of approximate calculations.

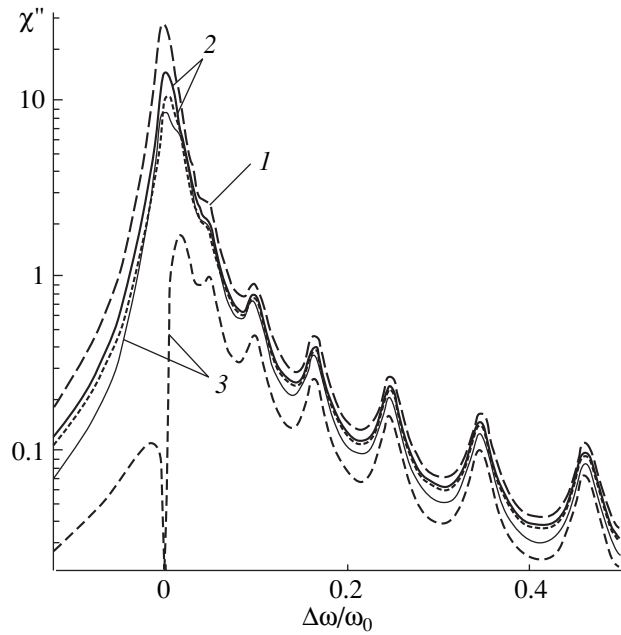


**Fig. 2.** Spin-wave resonance spectra for total symmetric pinning of surface spins ( $d_1 = d_2 \rightarrow \infty$ ). Designations of curves 1–3 are the same as in Fig. 1.

decay of the amplitude of in-phase oscillations of magnetization over the layer thickness. An increase in the conductivity  $\sigma$  brings about a decrease in the penetration depth of the field  $h(t)$  and, consequently, a decrease in the amplitude of the resonance curve. At frequencies close to the frequency of uniform ferromagnetic resonance, the resonance shape somewhat changes, because it is at this frequency that the quantity  $\text{Re}(\delta^{-2})$ , which is proportional to  $\mu''$ , becomes zero.

The dependences  $\chi''(\omega)$  for the total symmetric pinning ( $d_1 = d_2 \rightarrow \infty$ ) and limiting asymmetric pinning ( $d_1 = 0, d_2 \rightarrow \infty$ ) of surface spins are shown in Figs. 2 and 3, respectively. The number of spin-wave modes at the symmetric boundary conditions is equal to half the number of modes in the case of the asymmetric boundary conditions. However, the amplitude of these modes in the former case is substantially higher than that in the latter case. This is associated with the fact that, in the case of asymmetric boundary conditions, spins are pinned only at one surface of the layer.

In addition to the changes in the amplitude, there occur a shift of the resonance curves and their broadening, which are determined by the relationships

$$\Delta\omega_\delta = \frac{\alpha\gamma M_0}{\delta_0^2}(p^2 - g^2), \quad \Delta\Gamma_\delta = \frac{2\alpha\gamma M_0}{\delta_0^2}pg. \quad (15)$$

These quantities are small at the chosen parameters on the given scale. However, detailed analysis of the spin-

wave resonance spectrum at frequencies close to  $\omega_0$  revealed that an increase in the conductivity  $\sigma$  leads to a shift of the uniform mode toward the range of positive  $\Delta\omega_\delta$ , i.e., toward the range of bulk modes.

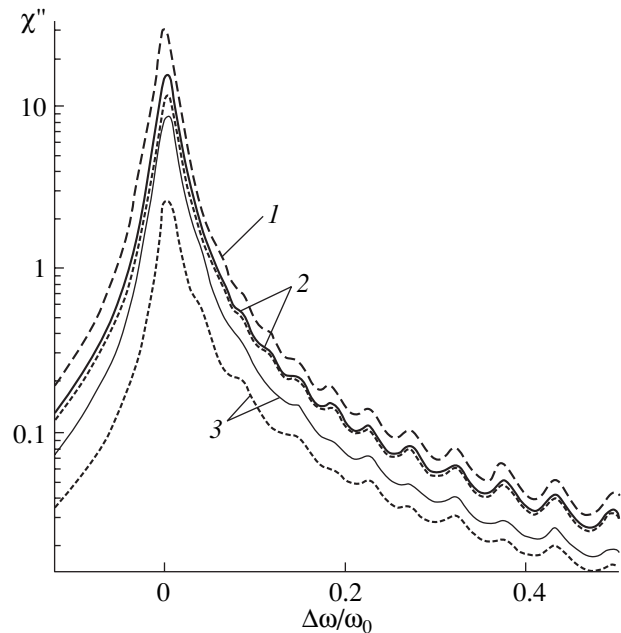


**Fig. 3.** Spin-wave resonance spectra for total asymmetric pinning of surface spins ( $d_1 = 0, d_2 \rightarrow \infty$ ). Designations of curves 1–3 are the same as in Fig. 1.

## 5. CONCLUSION

The above analysis has demonstrated that the conductivity of metallic magnetic layers most strongly affects the character of the spin wave spectrum in the frequency range in which the skin effect leads to an inhomogeneous field distribution over the layer thickness. In this case, the distinctive feature of the spin-wave resonance spectrum is a slight change in the resonance shape in the frequency range of the uniform ferromagnetic resonance in addition to the broadening, shift, and decrease in the amplitude for all the spin-wave modes. The observed change in the resonance shape stems from the fact that the parameter  $\delta$  is a complex quantity. This parameter determines the depth of penetration of the high-frequency field into the magnetic material and depends on its magnetic susceptibility. At frequencies close to the uniform resonance frequency, the real part of the susceptibility becomes zero, which results in a sharp increase in the penetration depth and deviation of the resonance curve from the Lorentzian shape.

## REFERENCES

1. A. G. Gurevich and G. A. Melkov, *Magnetic Oscillations and Waves* (Nauka, Moscow, 1994).
2. Yu. A. Korchagin, R. G. Khlebopros, and N. S. Chistyakov, Preprint IFSO-10 (Krasnoyarsk, 1978).
3. D. I. Sementsov, Fiz. Tverd. Tela (Leningrad) **16** (2), 938 (1974) [Sov. Phys. Solid State **16**, 604 (1974)].
4. L. V. Lutsev and Yu. M. Yakovlev, Fiz. Tverd. Tela (Leningrad) **30** (6), 1675 (1988) [Sov. Phys. Solid State **30**, 965 (1988)].
5. S. L. Vysotskiĭ, G. T. Kazakov, M. L. Kats, and Yu. A. Filimonov, Fiz. Tverd. Tela (St. Petersburg) **35** (5), 1190 (1993) [Phys. Solid State **35**, 606 (1993)].
6. A. I. Akhiezer, V. G. Bar'yakhtar, and S. V. Peletminskii, *Spin Waves* (Nauka, Moscow, 1967; North-Holland, Amsterdam, 1968).
7. R. N. Nosov and D. I. Sementsov, Fiz. Tverd. Tela (St. Petersburg) **42** (8), 1430 (2000) [Phys. Solid State **42**, 1471 (2000)].

*Translated by N. Korovin*

---

**MAGNETISM  
AND FERROELECTRICITY**

---

## Effect of Thermal Instability on the Magnetic Properties of $\text{Cu}_{1-x}\text{Zn}_x\text{Cr}_2\text{Se}_4$ Solid Solutions

N. B. Ivanova, N. V. Kazak, S. G. Ovchinnikov, and E. P. Popel

*Kirenskiĭ Institute of Physics, Siberian Division, Russian Academy of Sciences,  
Akademgorodok, Krasnoyarsk, 660036 Russia*

*e-mail: dir@iph.krasn.ru*

Received November 19, 2001

**Abstract**—Annealing in vacuum is found to affect magnetic order in polycrystalline  $\text{Cu}_{1-x}\text{Zn}_x\text{Cr}_2\text{Se}_4$  samples ( $x = 0.88, 0.90$ ). Samples subjected to heat treatment exhibit a temperature dependence of dynamic magnetic susceptibility characteristic of a non-single-phase magnetic state. The annealing-induced magnetic order is assigned to the zinc off-stoichiometry formed in the process. © 2002 MAIK “Nauka/Interperiodica”.

### 1. INTRODUCTION

The  $\text{Cu}_{1-x}\text{Zn}_x\text{Cr}_2\text{Se}_4$  solid solutions have been attracting interest due to the rich variety of magnetic states these solutions feature upon different substitutions  $x$  [1–3]. This diversity is due to the strong difference in magnetic properties between the extreme compounds in the series, namely,  $\text{CuCr}_2\text{Se}_4$  (ferromagnetic semimetal with  $T_C \sim 420$  K) and  $\text{ZnCr}_2\text{Se}_4$  (helical antiferromagnet with  $T_N \sim 20$  K). The competition between the exchange interactions in the solid solutions gives rise to nontrivial magnetic properties. Of particular interest is the alternation of magnetic phases in the concentration interval from 1.0 to 0.8, where gradual substitution of copper for zinc offers a possibility of observing the following magnetic states successively: simple spin spiral, ferromagnetic spiral, spin glass, ferromagnetic spiral, and collinear ferromagnetism [4].

In our earlier comprehensive investigation [5] of the concentration-driven phase transition in  $\text{Cu}_{1-x}\text{Zn}_x\text{Cr}_2\text{Se}_4$ , we measured the magnetic properties of this solid solution in the 0.8–0.9 concentration interval with a small step of 0.02. Polycrystals were prepared by the authors of [6] using solid-phase technology, which is described in considerable detail in [6]. The substituent concentration  $x_c = 0.88$  was established to be critical. Indeed, all compounds with  $x < x_c$  are ferromagnets with a Curie temperature of 370–420 K, a sample with  $x = 0.88$  possesses a weak room-temperature magnetic moment, and an  $x = 0.9$  sample undergoes only an antiferromagnetic transition at the same temperature as the extreme compound  $\text{ZnCr}_2\text{Se}_4$ .

The magnetic transition from a helical structure in  $\text{ZnCr}_2\text{Se}_4$  to a ferromagnetic structure in  $\text{CuCr}_2\text{Se}_4$  in this series of compounds is accompanied by a change over from semiconducting to semimetallic conduction. Thus, to fully understand the nature of the concentration-driven phase transitions in  $\text{Cu}_{1-x}\text{Zn}_x\text{Cr}_2\text{Se}_4$ , one

has to make a comprehensive investigation of both the magnetic and electrical properties. This raises the problem of thermal stability of these solid solutions, as electrical measurements on polycrystals are made on pressed and sintered powder samples. This problem was discussed earlier in [6], where studies of the thermal stability of  $\text{Cu}_{1-x}\text{Zn}_x\text{Cr}_2\text{Se}_4$  compositions in air were carried out at temperatures ranging from 500 to 920 K. It was found that up to temperatures of about 650 K, selenium is detached and a selenium-deficient spinel forms [6]. Above 650 K, oxide compounds were observed to form. This study was aimed at establishing whether the heat treatment used in sintering a powder sample results in a noticeable change in its physical properties, primarily in its magnetic properties, and, hence, at estimating the possible effect of the off-stoichiometry caused by the heat treatment.

### 2. EXPERIMENTAL TECHNIQUE

The samples, pressed into rectangular parallelepipeds measuring  $2 \times 2 \times 4$  mm, were placed in quartz ampules evacuated to  $10^{-3}$  mm Hg. One sample lot was annealed at  $T_1 = 850$  K (anneal 1); the other, at  $T_2 = 1150$  K (anneal 2). The samples were annealed for two hours, and the operating temperature was reached in three hours of uniform heating. After this, the samples were allowed to cool in the furnace.

The temperature-dependent real part of magnetic susceptibility  $\chi'$  of the samples subjected to heat treatment was measured using the dynamic ac bridge technique. The sample temperature was varied by blowing it with a stream of heated air in a cylindrical flow-through cryostat with measuring coils mounted on its outer wall. The bridge unbalance was measured with a UNIPAN 232B phase-sensitive nanovoltmeter.

The electrical resistance  $R(T)$  was measured using the dc four-probe method. The contacts, made of

indium paste, were arranged along a straight line on the larger face of the sample. The current was supplied over thin copper wires 0.06 mm in diameter. The measurements in the cooling runs were also carried out in a flow-through cryostat, and the samples were heated in an unsealed quartz ampoule in a muffle furnace.

### 3. RESULTS

The magnetic measurements carried out after the annealing revealed that all the samples of the lot under study exhibit spontaneous magnetism with a clearly pronounced ferromagnetic component. This is also valid for compositions with a high zinc concentration,  $x = 0.88$  and  $0.90$ , of which the former had an extremely low magnetization before the annealing and the latter was fully paramagnetic at room temperature. Magnetic ordering occurred during both anneals *1* and *2*. The samples of these two compositions demonstrated similar temperature dependences of the dynamic magnetic susceptibility  $\chi'$ . The measurements made on the sample with  $x = 0.88$  are displayed in Fig. 1, which shows, for comparison,  $\chi'(T)$  curves for compositionally similar samples  $\text{Cu}_{0.14}\text{Zn}_{0.86}\text{Cr}_2\text{Se}_4$  and  $\text{Cu}_{0.16}\text{Zn}_{0.84}\text{Cr}_2\text{Se}_4$  measured before the heat treatment. We readily see from Fig. 1 that the magnetic susceptibility of the annealed sample (curve *1*), as well as  $\chi'(T)$  of the  $\text{Cu}_{0.14}\text{Zn}_{0.86}\text{Cr}_2\text{Se}_4$  stoichiometric composition, vanishes at a temperature close to  $T_C$  of the original compound  $\text{CuCr}_2\text{Se}_4$ . Note that curve *1* follows a pattern characteristic of a non-single-phase magnetic state of a sample and lies between curves *2* and *3* for the samples with  $x = 0.86$  and  $0.84$ , respectively.

The measurements of the temperature dependence of electrical resistance showed that the samples can be divided into two groups. With increasing temperature, the electrical resistance decreases in samples with  $x \geq 0.88$  and increases in the other samples. Figures 2a and 2b display the  $R(T)$  relations measured for two similar compositions,  $x = 0.88$  and  $0.86$ , respectively, featuring different types of conduction.

### 4. DISCUSSION

As already mentioned, it was shown in [6] that annealing  $\text{Cu}_{1-x}\text{Zn}_x\text{Cr}_2\text{Se}_4$  solid solution samples in air up to temperatures of 750–900 K brings about only detachment of selenium, without any visible indications of chemical activity of the Cu and Zn ions. Compositions with a high zinc content were observed to have the highest thermal stability. For instance, the oxidation of  $\text{Cu}_{0.2}\text{Zn}_{0.8}\text{Cr}_2\text{Se}_4$  started at 920 K. Thus, one might expect that a short annealing in vacuum at a lower temperature (anneal *1*) would not produce a noticeable off-stoichiometry in copper or zinc. However, susceptibility measurements showed that the annealed samples (after either of anneals *1* or *2*) approached, in magnetic properties, the compositions

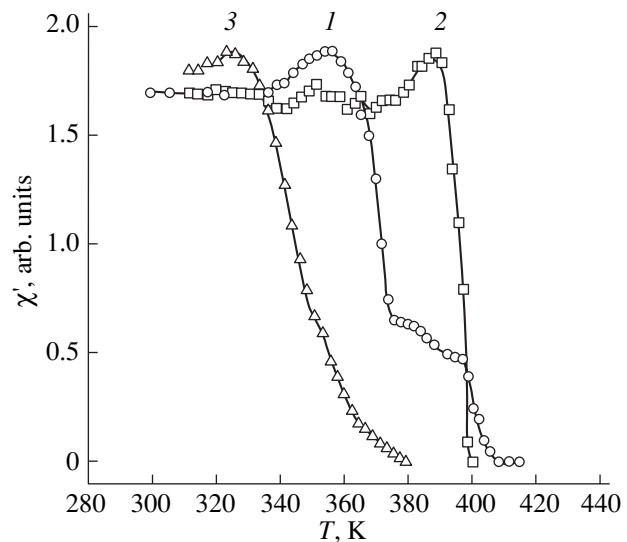


**Fig. 1.** Temperature dependences of the magnetic susceptibility for (*1*) annealed  $\text{Cu}_{0.12}\text{Zn}_{0.88}\text{Cr}_2\text{Se}_4$  and (*2*, *3*) the original  $\text{Cu}_{0.14}\text{Zn}_{0.86}\text{Cr}_2\text{Se}_4$  and  $\text{Cu}_{0.16}\text{Zn}_{0.84}\text{Cr}_2\text{Se}_4$  samples, respectively.

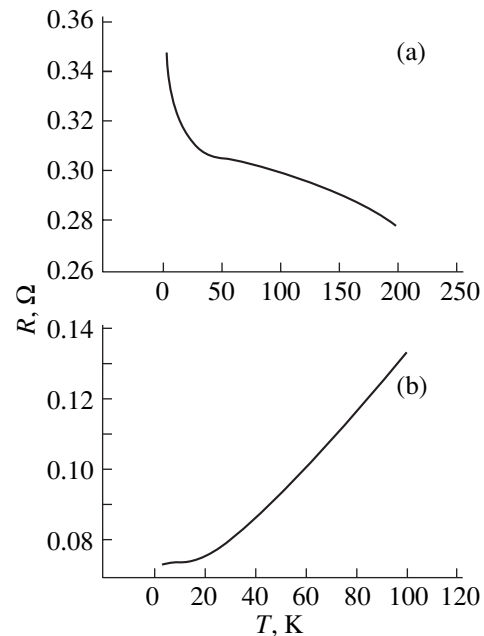


**Fig. 2.** Temperature dependences of the electrical resistance of annealed samples (a)  $\text{Cu}_{0.12}\text{Zn}_{0.88}\text{Cr}_2\text{Se}_4$  and (b)  $\text{Cu}_{0.14}\text{Zn}_{0.86}\text{Cr}_2\text{Se}_4$ .

with a lower zinc content, which suggests that the composition shifted toward the zinc-deficient spinel as a result of annealing. Note that the expected selenium deficiency cannot apparently initiate the onset of ferromagnetism, because the ferromagnetism of  $\text{CuCr}_2\text{Se}_4$  is due to the high hole concentration in the valence band.

The additional electrons appearing as a result of selenium deficiency entail partial compensation and, hence, weakening rather than enhancement of the magnetic properties.

One more important result of this study consists in supporting the assumption made in [5] that the concentration-driven magnetic transition within the critical concentration region in  $\text{Cu}_{1-x}\text{Zn}_x\text{Cr}_2\text{Se}_4$  occurs through separation of the compound into two magnetic phases, namely, a ferromagnetic phase with a high  $T_C$  and an antiferromagnetic phase. This is argued for by the observation that the Curie temperature for the heat-treated samples, as well as for the untreated  $x = 0.86$  sample, is close to  $T_C$  of the extreme compound in the series,  $\text{CuCr}_2\text{Se}_4$ , although the content of copper in them is considerably lower than that of zinc. Also, the heat-treated samples with  $x = 0.88$  and  $0.90$  behave as semiconductors. It is this combination of properties, according to [7], that is characteristic of a magnet with highly conducting ferromagnetic particles embedded in a weakly conducting antiferromagnetic matrix.

Thus, our heat treatment of  $\text{Cu}_{1-x}\text{Zn}_x\text{Cr}_2\text{Se}_4$  samples apparently resulted in a compositional shift toward a spinel which is deficient not only in selenium but also in zinc. The reason for this probably lies in the high volatility of zinc subjected to annealing in vacuum. Indeed, the boiling point of pure zinc drops from 1210 K at a pressure of  $10^3$  mm Hg to 565 K at  $10^{-3}$  mm Hg, which is substantially below the anneal temperature used in the study. Because the study was carried out in the critical concentration region, a slight change

in the composition apparently produced a substantial change in the physical properties. One can thus conclude that even short anneals, such as those needed to sinter  $\text{Cu}_{1-x}\text{Zn}_x\text{Cr}_2\text{Se}_4$  samples for resistance measurements, should be performed under an intentionally produced excess zinc-vapor pressure.

#### ACKNOWLEDGMENTS

This study was supported by the Russian Foundation for Basic Research, project no. 99-02-17405.

#### REFERENCES

1. S. Jusczyk, J. Krok, I. Okonska-Kozłowska, *et al.*, *Phase Transitions* **2**, 67 (1981).
2. J. Krok, J. Spalek, S. Juszczuk, and J. Warczewski, *Phys. Rev. B* **28** (11), 6499 (1983).
3. J. Krok, S. Juszczuk, J. Warczewski, *et al.*, *Phase Transitions* **4**, 1 (1983).
4. T. Gron, H. Duda, and J. Warczewski, *Phys. Rev. B* **41** (18), 12424 (1990).
5. A. D. Balaev, É. G. Zhukov, N. B. Ivanova, *et al.*, *Fiz. Tverd. Tela (St. Petersburg)* **43** (6), 1053 (2001) [*Phys. Solid State* **43**, 1089 (2001)].
6. É. G. Zhukov, E. S. Populyak, G. S. Varnakova, and V. A. Fedorov, *Zh. Neorg. Khim.* **38**, 167 (1993).
7. É. L. Nagaev, *Physics of Magnetic Semiconductors* (Nauka, Moscow, 1979).

*Translated by G. Skrebtsov*

---

**MAGNETISM  
AND FERROELECTRICITY**

---

## Structure and Temperature Dependence of the Magnetization of the DyFe<sub>11</sub>Ti Nanocrystalline Compound

**G. F. Korznikova\*, Kh. Ya. Mulyukov\*, I. Z. Sharipov\*,  
S. A. Nikitin\*\*, and I. S. Tereshina\*\*\***

\* *Institute of Metal Superplasticity Problems, Russian Academy of Sciences,  
ul. Khalturina 39, Ufa, 450001 Bashkortostan, Russia*

\*\* *Moscow State University, Vorob'evy gory, Moscow, 119899 Russia*

\*\*\* *Baïkov Institute of Metallurgy and Materials Technology, Russian Academy of Sciences,  
Leninskii pr. 49, Moscow, 119911 Russia*

*e-mail: korznikova@anrb.ru*

Received November 19, 2001

**Abstract**—The coercive force, the temperature dependence of the magnetization, and the structure of a DyFeTi alloy based on the DyFe<sub>11</sub>Ti compound with an excess content of  $\alpha$ -Fe in the initial coarse-grained, nanocrystalline, and submicrocrystalline states are investigated experimentally. It is found that, in the submicrocrystalline sample, the coercive force is three times stronger and the temperature of the first spin-reorientation transition is 20 K higher than those in the coarse-grained sample. In the nanocrystalline sample, the coercive force is five times stronger than that in the coarse-grained sample, the first spin-reorientation transition is not revealed, and the transition at the Curie temperature is smeared. It is demonstrated that the changes observed in the magnetic properties are unrelated to the phase transformations but stem from the small size of crystal grains and high imperfection of the structure. The thermal instability of the DyFe<sub>11</sub>Ti compound is observed in submicrocrystalline and nanocrystalline states. © 2002 MAIK “Nauka/Interperiodica”.

### 1. INTRODUCTION

Intermetallic compounds based on 3d transition metals and rare-earth elements have been intensively studied in recent years because their magnetic properties are of considerable interest both in basic research and from the practical standpoint. In particular, Clark [1] revealed that RFe<sub>2</sub> compounds exhibit a giant magnetostriction at room temperature. Permanent magnets with record-high characteristics were obtained from rare-earth compounds with 3d elements. It is also known that the magnetic properties of ferromagnets are determined by their structure in many respects. This is especially true for ferromagnetic samples in nanocrystalline and submicrocrystalline states. For example, compared to coarse-grained samples, in nanostructured samples, the coercive force of pure Dy and Tb increases thousandfold [2, 3]; the magnetization of Dy [2], Tb [3], and Gd [4] decreases severalfold; the points of magnetic transformations are shifted [2, 3]; and the magnetic ordering in these metals changes in character [5]. In our recent work [6], we found that, in the triple intermetallic compound GdTiGe, the transition to a nanocrystalline state leads to a transformation of the crystal lattice and, correspondingly, to substantial changes in the magnetic properties. Until presently, triple rare-earth compounds with 3d elements and an RFe<sub>11</sub>Ti-type structure had not been adequately studied, even though these materials are very promising for use

as permanent magnets [7]. For example, Tereshina *et al.* [8, 9] revealed that single-crystal DyFe<sub>11</sub>Ti can undergo two spin-reorientation transitions (at 120 and 248 K). However, the properties of these compounds in nanocrystalline and submicrocrystalline states are not understood.

The present paper reports on the results of experimental investigations into the magnetic properties and the structure of a DyFeTi alloy in nanocrystalline and submicrocrystalline states. For comparison, we studied a coarse-grained sample of the same composition.

### 2. SAMPLE PREPARATION AND EXPERIMENTAL TECHNIQUE

The experiments were performed with a DyFeTi alloy (5.2 at. % Dy, 88.2 at. % Fe, and 7.1 at. % Ti) prepared by induction melting. Prolonged homogenization of this alloy at a high temperature resulted in the formation of the triple compound DyFe<sub>11</sub>Ti with a ThMn<sub>12</sub>-type structure. An excess iron content in the alloy brought about the precipitation of  $\alpha$ -Fe. This slightly increased the plasticity of the material and made severe deformation of the ingots possible.

Samples with a nanocrystalline structure were prepared from a homogenized ingot subjected to severe plastic deformation through torsional strain with the use of Bridgman anvils under a pressure of 8 GPa at

Coercive forces of DyFeTi alloy samples in different crystalline states

Measurement temperature, K	$H_c$ , kA/m		
	coarse-grained samples	submicrocrystalline samples	nanocrystalline samples
298	3.2	6.1	6.6
78	8.2	25.2	41.6

room temperature with a rotation through an angle of  $10\pi$ . The choice of severe plastic deformation as the method of nanostructuring of the studied samples was made for the following reasons: (i) this method does not introduce contaminants into the initial material, and (ii) severe plastic deformation makes it possible to obtain nonporous samples that do not need to be further compacted for structural and magnetic measurements. Samples with a submicrocrystalline structure were produced by grinding a coarse-grained sample in an agate mortar in a protective medium. The submicrocrystalline powder with a particle size of less than  $1\ \mu\text{m}$  was separated through sedimentation. The size of powder particles was determined on a JSM-840 scanning electron microscope.

The magnetization curves and temperature dependences of the magnetization of the samples under inves-

tigation were obtained on a vibrating-sample magnetometer in a magnetic field of  $1.6 \times 10^3$  kA/m. The temperature was measured using a copper thermal resistor. The temperature dependence of the magnetization at high temperatures was measured using an automated magnetic microbalance under vacuum with a residual pressure of  $1.3 \times 10^{-2}$  Pa in a magnetic field of 250 kA/m in the temperature range 78–1070 K. In this case, the temperature measurements were performed with a chromel–alumel thermocouple.

The microstructure of the nanocrystalline samples was examined using a JEM 2000EX transmission electron microscope. The chemical composition of the samples was determined on a JSM-840 scanning electron microscope with a Link attachment.

### 3. EXPERIMENTAL RESULTS

**3.1. Coercive force.** Earlier [8], it was shown that  $R\text{Fe}_{11}\text{Ti}$  compounds exhibit a strong uniaxial magnetocrystalline anisotropy. Therefore, these compounds in a nanocrystalline state should possess a strong coercive force. In this respect, we measured the coercive force  $H_c$  of DyFeTi alloy samples in different crystalline states at temperatures of 298 and 78 K. The results of measurements are presented in the table. It is seen from the table that, at 298 K, the coercive force  $H_c$  of an unstrained coarse-grained sample does not exceed 3.2 kA/m, whereas the coercive forces of submicrocrystalline and nanocrystalline samples are equal to 6.1 and 6.6 kA/m, respectively. A decrease in the temperature leads to an increase in the coercive force  $H_c$  of all the studied samples; however, the maximum increase in  $H_c$  is observed in the nanocrystalline state (by a factor of more than six).

**3.2. Temperature dependence of the magnetization.** Figure 1 depicts the temperature dependences of the magnetization  $\sigma(T)$  measured in the magnetic field  $H = 250$  kA/m for samples in different crystalline states. It can be seen from Fig. 1 that, in all the crystalline states, the temperature dependences of the magnetization exhibit complex behavior: as the temperature increases, the magnetization increases, passes first through a maximum at 250 K and then through an inflection at 350 K, drastically decreases at 550 K, and becomes zero at 1040 K. It should be noted that the position of the maximum in the dependence  $\sigma(T)$  measured upon heating is determined by the crystalline state of the sample; specifically, the maxima in the dependences  $\sigma(T)$  for coarse-grained and nanocrystalline samples are observed at 250 and 275 K, respectively. For a submicrocrystalline sample, the dependence  $\sigma(T)$  exhibits a broad maximum at 310 K. The inflection in the vicinity of 350 K is well defined for the coarse-grained sample (Fig. 1a), less pronounced for the nanocrystalline sample (Fig. 1c), and is absent for the submicrocrystalline sample (Fig. 1b). Although the decrease in the magnetization in all the crystalline

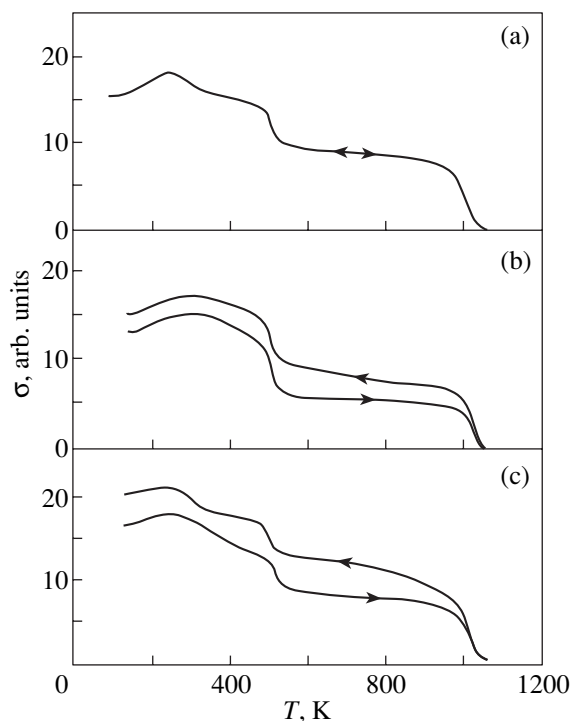


**Fig. 1.** Temperature dependences of the magnetization  $\sigma(T)$  measured in the magnetic field  $H = 250$  kA/m for (a) coarse-grained, (b) submicrocrystalline, and (c) nanocrystalline samples.

states occurs at approximately the same temperature (550 K), which corresponds to the Curie point of the  $\text{DyFe}_{11}\text{Ti}$  phase, the slope of the curve  $\sigma(T)$  depends on the crystalline state of the sample; in particular, the curve  $\sigma(T)$  for the coarse-grained sample has a very steep slope, whereas the slope of the curve  $\sigma(T)$  for the nanocrystalline sample is slightly flattened. For all the samples, the magnetization reduces to zero at the same temperature (1040 K), which corresponds to the  $\alpha$ -Fe phase (Fig. 1).

In order to elucidate the thermal stability of the studied compound in different crystalline states, the temperature dependences  $\sigma(T)$  were measured upon cooling of the samples after high-temperature heating. The curves  $\sigma(T)$  obtained upon heating and cooling of the samples completely coincide only for the coarse-grained sample (Fig. 1a). For submicrocrystalline and nanocrystalline samples, the curves  $\sigma(T)$  measured upon cooling lie slightly above the heating curves and the aforementioned specific features in the cooling curves are more pronounced. As the temperature decreases, the dependence  $\sigma(T)$  for the nanocrystalline sample (Fig. 1c) becomes similar to the dependence  $\sigma(T)$  for the coarse-grained sample (Fig. 1a).

It can be seen that the first spin-reorientation transition (at 120 K) does not manifest itself in the curves  $\sigma(T)$  depicted in Fig. 1. This can be associated with the fact that the magnetic field strength (250 kA/m) used in the magnetization measurements with the magnetic microbalance is not very high. For this reason, the temperature dependences of the magnetization  $\sigma(T)$  were also measured in stronger magnetic fields ( $H = 1.6 \times 10^3$  kA/m). These dependences are displayed in Fig. 2. As is seen, the first spin-reorientation transition manifests itself as a slight kink in the curves  $\sigma(T)$ . This kink is observed at 115 K for the coarse-grained sample and at 135 K for the submicrocrystalline sample. As regards the nanocrystalline sample, no kink is found in the curve  $\sigma(T)$  and the magnetization smoothly increases in the temperature range of the first spin-reorientation transition.

**3.3. Structural investigations.** Figure 3 displays the electron microscope image of the microstructure and the electron diffraction pattern of the nanocrystalline sample. The size of crystal grains was estimated from the bright-field images and amounted to 20–30 nm. An examination of the electron microscope image revealed a high defect density within the crystal grains. It can be seen that crystal grains have broad and diffuse boundaries. The electron diffraction pattern taken from a  $0.5\text{-}\mu\text{m}^2$  section of the nanocrystalline sample has the shape of a ring. This suggests large grain-boundary angles.

The mean size of crystal grains in the submicrocrystalline sample was determined using a scanning electron microscope and amounted to 1  $\mu\text{m}$ .

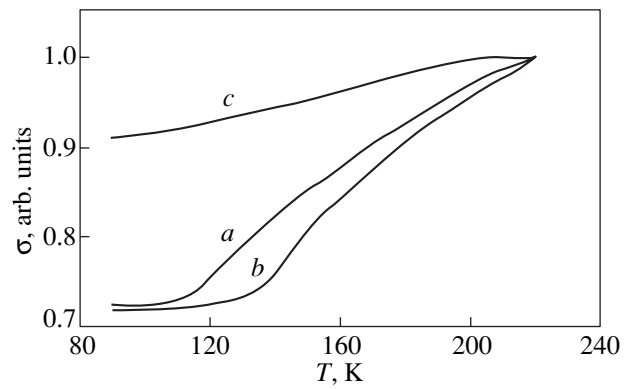


**Fig. 2.** Temperature dependences of the magnetization  $\sigma(T)$  measured in the magnetic field  $H = 1.6 \times 10^3$  kA/m for (a) coarse-grained, (b) submicrocrystalline, and (c) nanocrystalline samples.

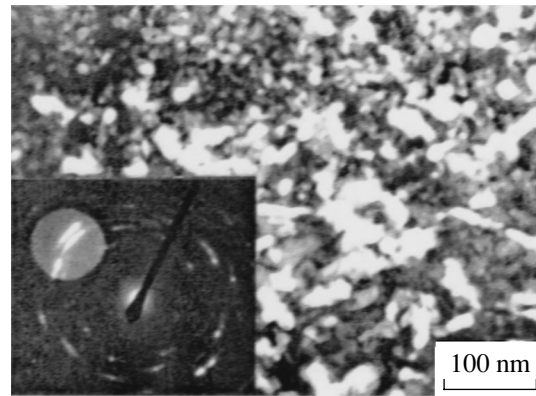


**Fig. 3.** Electron microscope image of the nanocrystalline structure of the studied compound.

#### 4. DISCUSSION

The results of our investigations demonstrate that the magnetic properties of the  $\text{DyFeTi}$  alloy in different crystalline states differ significantly. The coercive force  $H_c$  of the submicrocrystalline sample is less than that of the nanocrystalline sample. At a temperature of 78 K, the coercive forces of these samples are three and five times stronger than that in the coarse-grained sample, respectively. Such an increase in the coercive force can be associated with the small size of crystal grains. This assumption is confirmed by the fact that, in the nanocrystalline state, the smaller the grain size, the stronger the coercive force  $H_c$ . However, the measured values of  $H_c$  proved to be considerably less than the coercive forces predicted from the single-domain theory for the  $\text{DyFe}_{11}\text{Ti}$  compound with strong anisotropy. This can be explained by the fact that microcrystals of the  $\text{DyFe}_{11}\text{Ti}$  phase with a high coercivity are surrounded

by the  $\alpha$ -Fe soft magnetic phase which encourages magnetization reversal of DyFe<sub>11</sub>Ti crystal grains in weaker magnetic fields. The presence of the  $\alpha$ -Fe soft magnetic phase in the composition of the studied alloy is indicated by the temperature dependences of the magnetization (Fig. 1).

As was noted above, the temperature dependences of the magnetization of the DyFe<sub>11</sub>Ti compound in all the crystalline states under investigation exhibit similar behavior. However, some portions of these curves show specific features associated with the small size of the crystal grains involved. In particular, the smoother decrease in the magnetization of the nanocrystalline sample [the curve  $\sigma(T)$  measured upon heating] in the vicinity of the Curie temperature of the DyFe<sub>11</sub>Ti phase is indirect evidence that the crystal lattice of this phase is substantially distorted and that the interatomic distances vary within a certain range. This brings about local changes in the exchange interaction, which, in turn, leads to smearing of the transition from the ferromagnetic order to the paramagnetic state of the DyFe<sub>11</sub>Ti phase. This inference is supported by the fact that, for the submicrocrystalline sample with intermediate-sized grains, the slope of the curve  $\sigma(T)$  in the vicinity of the Curie point of the DyFe<sub>11</sub>Ti phase slightly exceeds the slope for the nanocrystalline sample and is less than that for the coarse-grained sample.

It seems likely that the lattice distortions and the small size of crystal grains affect not only the exchange interaction, which determines the Curie temperature, but also the magnetocrystalline anisotropy constants. The effect of the lattice distortions and the grain size on the anisotropy constants can be judged from the temperatures of the spin-reorientation transitions, because they are determined primarily by the ratio of the first to the second magnetic anisotropy constants. Apparently, this circumstance accounts for both the shift of the kink in the curve  $\sigma(T)$  for the submicrocrystalline sample toward the high-temperature range and its smearing for the nanocrystalline sample (Fig. 2).

The shift and smearing of the maximum attributed to the second spin-reorientation transition in the nanocrystalline sample can also be explained by the weakening of the magnetic anisotropy due to lattice imperfection in the bulk and at the boundaries of nanocrystals.

The fact that the curves  $\sigma(T)$  measured upon heating and cooling of the coarse-grained sample completely coincide with each other indicates the thermal stability of the composition under investigation. For submicrocrystalline and nanocrystalline states, the curves  $\sigma(T)$

measured upon cooling of the samples after high-temperature heating lie above the heating curves due to the precipitation of  $\alpha$ -Fe. This suggests that the DyFe<sub>11</sub>Ti compound in submicrocrystalline and nanocrystalline states possesses a low thermal stability. Moreover, high-temperature heating leads to recrystallization of the nanocrystalline sample, as judged from the recovery of the curve  $\sigma(T)$  below the Curie temperature of the DyFe<sub>11</sub>Ti phase.

## 5. CONCLUSION

Thus, it has been demonstrated that, upon the transition to the nanocrystalline state, the temperatures of spin-reorientation transitions increase, the coercive force enhances, and the thermal stability of the studied alloy decreases.

## ACKNOWLEDGMENTS

This work was supported by the Russian Foundation for Basic Research, project no. 00-02-17723.

## REFERENCES

1. A. E. Clark, in *Handbook on the Physics and Chemistry of Rare Earths*, Ed. by K. A. Gshneidner, Jr. and J. Eyring (North-Holland, Amsterdam, 1979), pp. 231–258.
2. Kh. Ya. Mulyukov, G. F. Korznikova, and S. A. Nikitin, *J. Appl. Phys.* **79** (11), 8584 (1996).
3. Kh. Ya. Mulyukov, G. F. Korznikova, I. Z. Sharipov, and S. A. Nikitin, *Nanostruct. Mater.* **8** (7), 953 (1997).
4. Kh. Ya. Mulyukov, G. F. Korznikova, and S. A. Nikitin, *J. Magn. Magn. Mater.* **153**, 241 (1996).
5. Kh. Ya. Mulyukov, I. Z. Sharipov, G. F. Korznikova, and S. A. Nikitin, *Fiz. Tverd. Tela (St. Petersburg)* **38** (12), 3602 (1996) [*Phys. Solid State* **38**, 1963 (1996)].
6. G. F. Korznikova, Kh. Ya. Mulyukov, S. A. Nikitin, and Yu. A. Ovchenkova, *Fiz. Tverd. Tela (St. Petersburg)* **43** (4), 683 (2001) [*Phys. Solid State* **43**, 710 (2001)].
7. S. P. Efimenko, Yu. K. Kovneristyĭ, and I. M. Milyaev, *Fiz. Khim. Obrab. Mater.* **3**, 82 (1998).
8. I. S. Tereshina, S. A. Nikitin, N. Yu. Pankratov, *et al.*, in *Proceedings of the Moscow International Symposium on Magnetism (MISM 99), Moscow, 1999*, p. 364.
9. I. S. Tereshina, I. V. Telegina, and K. P. Skokov, *Fiz. Tverd. Tela (St. Petersburg)* **40** (4), 699 (1998) [*Phys. Solid State* **40**, 643 (1998)].

*Translated by O. Borovik-Romanova*

---

## MAGNETISM AND FERROELECTRICITY

---

# Interface-Induced States with an Incommensurate Spin-Density Wave in Fe/Cr-Type Multilayers

V. N. Men'shov and V. V. Tugushev

Russian Research Centre Kurchatov Institute, pl. Akademika Kurchatova 1, Moscow, 107207 Russia

e-mail: sasha@mail.mics.msu.su

Received July 6, 2001; in final form, December 27, 2001

**Abstract**—A model is proposed for magnetic ordering in Fe/Cr-type multilayers substantially above the Néel temperature of bulk chromium. Redistribution of the charge (and, hence, spin) density near the Fe/Cr interfaces gives rise to the formation of an essentially inhomogeneous spin-density-wave (SDW) state in the chromium spacer. The spatial structure of the antiferromagnetic order parameter in thick spacers is described. The SDW contribution to the effective exchange coupling between the moments in adjacent iron layers is calculated. The data obtained are used in the interpretation of experimental data on the tunneling spectroscopy of trilayers and neutron diffraction from Fe/Cr superlattices. © 2002 MAIK “Nauka/Interperiodica”.

### 1. INTRODUCTION

Multilayer structures (multilayers) containing transition metals have been recently attracting considerable interest due to their unusual magnetic and kinetic properties. This interest is focused primarily on Fe/Cr-type structures with alternating ferro- and antiferromagnetic layers of iron and chromium [1, 2]. The discovery that the effective coupling between the moments of adjacent Fe layers oscillates in sign depending on the thickness  $L$  of the Cr spacer and the temperature  $T$  should in itself be worthy of close attention [3, 4] because of the considerable significance of this effect from both the standpoint of fundamental science and applications. However, after a number of other features in the magnetic properties of the Fe/Cr structures were revealed (phase slip of the effective exchange, the existence of short and long periods of its oscillations, the formation of noncollinear structures, exchange shift of the hysteresis loop, giant magnetoresistance, etc.), it became clear that one here deals with a new class of objects, which requires individual investigation with the inclusion of a theoretical analysis.

Even a cursory glance at the magnetic phase diagram derived from neutron diffraction and magneto-optical measurements [5–7] supports the need for such a study. For instance, the reason for the existence of two critical temperatures,  $T_1(L)$  and  $T_2(L)$ , that depend differently on the chromium spacer thickness  $L$  is unclear. It is also not understood why there is a strong difference in the properties between multilayers with thick ( $L > L^*$ ) and thin ( $L < L^*$ ) spacers, where  $L^*$  is a critical thickness of about 30 chromium monolayers. Systems with  $L > L^*$  exhibit two antiferromagnetic phases in the chromium spacer; one of them [the so-called low-temperature phase, occurring for  $T < T_2(L)$ ] can be tentatively identified with the corresponding phase in bulk

chromium, while the other [high-temperature phase, existing for  $T_2(L) < T < T_1(L)$ ] has no bulk counterpart. For  $L < L^*$ , only the high-temperature phase persists; it exists below the  $T_1(L)$  line down to very low temperatures. Recall that  $T_1(L)$  is of the order of 550 K; it rises sharply for  $L < L^*$  while remaining nearly unchanged for  $L \gg L^*$ ; at the same time,  $T_2(L)$  drops to zero and does not exist for  $L < L^*$  while tending to the bulk value  $T_2(L \gg L^*) \cong T_N = 311$  K for  $L/L^* \rightarrow \infty$ .

There are sound grounds to believe that the properties of the Fe/Cr(100)-type multilayers are directly connected with the formation, in the chromium spacer, of a peculiar antiferromagnetic order of the type of a spin density wave (SDW) [8] whose structure depends strongly on the perfection of the Fe/Cr interface and on the temperature and thickness of the spacer itself. There is still no adequate theoretical model that could consistently explain the bulk of available experimental observations and support these conjectures. While there are numerical calculations of the ground-state magnetization distribution inside the chromium spacer (see, e.g., [9]), they are not applicable to the complex thermodynamics of magnetic structures in the multilayers studied. The variational approach [10] to description of the magnetic structure inside the chromium spacer, which is based on a straightforward analogy to bulk systems, is not capable of accounting even for the existence of two transition temperatures and of the critical thickness of the spacer, to say nothing of finer details in the magnetic phase diagram. Furthermore, this approach ignores the complex character of spin density redistribution near the Fe/Cr interfaces on the scale of the correlation length of antiferromagnetism in chromium, which depends on temperature and determines the region where short-range order with SDW is formed at

various temperatures, in particular, above the bulk Néel point.

We suggest here a possible scenario for the formation of a strongly inhomogeneous high-temperature SDW phase in the chromium spacer. The main mechanism responsible for the onset of such an antiferromagnetic order at a temperature  $T_1$  substantially in excess of  $T_N = 311$  K consists, in our opinion, in the redistribution of the charge (and, hence, spin) density in the chromium layers adjoining the interface. This redistribution results in a change in electronic polarizability, parameters of the energy spectrum, and band occupation on the scale of the Debye screening length  $l_d$  near the Fe/Cr interface; accordingly, the condition of the paramagnetic phase instability (the generalized Stoner criterion) against SDW formation in the near-surface chromium layers changes. An analysis made within this approach provides a straightforward explanation for the existence of the near-surface antiferromagnetic transition and permits one to estimate its temperature  $T_1$  and find the characteristic spatial scale  $D \sim L^*/2$  of the forming state.

Unfortunately, there are strong factors that do not permit description of magnetic ordering with SDW throughout the temperature interval from  $T_1$  to  $T_2$  within a single analytical procedure. First, as the temperature decreases from  $T_1$  to  $T_2$ , the order parameter  $\Delta(x)$  (the spin density amplitude expressed in energy units;  $x$  is the coordinate reckoned from the spacer center,  $x < L/2$ ) can be far from small near the Fe/Cr interface; as a result, the condition  $\Delta(x) \ll \pi T$ , which is used in deriving the Ginzburg–Landau expansion for the free-energy functional and is valid for  $T \approx T_1$ , is no longer applicable for all  $x$ . Second, even if for some reason  $\Delta(x)$  remains sufficiently small in comparison with  $\pi T$  for all  $x$  [in the bulk of a thick spacer, where  $\Delta(x)$  decays exponentially with distance away from the interfaces, this condition is always satisfied], it becomes necessary, as the temperature decreases from  $T_1$  to  $T_2$ , to take into account terms of higher order in  $\Delta(x)$  in the Ginzburg–Landau expansion. The fact is that it is in this temperature interval that the coefficient of the lowest order gradient term reverses sign from positive to negative, which, as is well known [11, 12], accounts for the formation of the incommensurate SDW structure in bulk chromium. Thus, when describing antiferromagnetic spin-density configurations in Fe/Cr multilayers with the temperature varying in the interval  $T_1 > T > T_2$  and when crossing over from the boundaries of the spacer to its inner layers, one has to take into account the radical change in the significance of the various terms in the thermodynamic potential of the system.

As we will show below, the profile of the order parameter  $\Delta(x)$  across the spacer thickness changes strongly with decreasing temperature; indeed, while for  $T \leq T_1$ , the SDW amplitude decays exponentially away from the Fe/Cr interfaces over a length  $\xi(t)$  which is

larger than or of the order of  $D$ , the sharp falloff of  $\Delta(x)$  near the interfaces is replaced at lower temperatures, in the case of a thick spacer with  $L > L^*$ , by a smoother decay accompanied by oscillations on the scale of the correlation length  $\xi(T) \gg D$ , where  $\xi(T) = \xi_0(T/T_N - 1)^{-1/2}$  and  $\xi_0$  is the coherence length, which in chromium equals, according to various estimates, seven to ten monolayers; i.e.,  $\xi_0 < D \sim L^*/2$ . Assuming the interfaces separating the chromium and iron layers to be ideally plane, the formation of only collinear SDW structures in the chromium spacer (which may change their symmetry relative to  $x = 0$  with variations in the thickness  $L$  and temperature  $T$ ) appears energetically preferable. We believe that this feature can provide a clue to the experimentally observed phase slip [1, 4] in the effective moment coupling at the adjacent iron layers.

Following the universally accepted terminology, we shall call  $T_2(L)$  the Néel temperature  $T_N$  while bearing in mind that the identification of these quantities is formally valid only in the limit  $L/\xi \rightarrow \infty$  under periodic boundary conditions imposed on the order parameter, i.e.,  $T_2(\infty) = T_N$ .

## 2. FORMATION OF A CHARGE-INDUCED PROXIMITY SDW STATE NEAR AN Fe/Cr INTERFACE

Let us consider the structural unit of a Fe/Cr(100)-type multilayer system representing a trilayer made up of two iron films sandwiching a chromium spacer. In the high-temperature domain  $T > T_N$ , the paramagnetic phase of bulk chromium is stable against magnetic ordering; however, the presence of the Fe/Cr interfaces can disrupt this stability. The origin of the SDW state above the Néel point can be qualitatively understood already in terms of the simple model of a plane defect placed in a one-dimensional medium with a free-energy density [12]:

$$f(x) = c_1 \Delta^2 + c_2 v_F^2 \Delta'^2 + c_2 \Delta^4 + \frac{c_3}{2} v_F^4 \Delta''^2 + c_3 \Delta^6 + c_3 v_F^2 [2(\Delta \Delta')^2 + 3\Delta^2 \Delta'^2]. \quad (1)$$

Equation (1) is based on the well-known Landau–Ginzburg expansion for the free energy of an SDW system in powers of the order parameter  $\Delta(x)$ , which is made under the assumption that  $|\Delta(x)| \ll \pi T$  and  $|\Delta'(x)| \ll \pi T/\xi_0$ . This expansion is derived directly from the microscopic SDW model, in which the origin of the antiferromagnetic instability is connected with nesting of the electron and hole parts of the metal Fermi surface in the paramagnetic phase. Here,  $v_F$  is the Fermi velocity of the quasiparticles and  $c_1$ ,  $c_2$ , and  $c_3$  are coefficients depending on the temperature and band-structure parameters;  $c_1$  and  $c_2$  can reverse their sign under the variation of temperature, and the coefficient  $c_3$  is always positive [11, 12]. In this section, we consider the region of fairly high temperatures in which  $(c_1, c_2) > 0$ ;

in these conditions, the equilibrium value of the order parameter corresponding to a minimum of functional (1) is zero, which is certain to correspond to the paramagnetic phase. In this case, the part of the free energy that is connected with the defect potential and is not contained in Eq. (1) plays a decisive role in SDW formation. We shall approximate the Fe/Cr(100) interface with an ideal smooth plane placed perpendicular to the structure growth direction  $\mathbf{n}_x$  and assume the chromium spacer thickness to be large enough (a more rigorous criterion is introduced later on) to exclude the mutual influence of the opposite interfaces. The potential simulating the interface interaction with the itinerant component of spin density forming the SDW will be assumed to fall steeply near the defect as compared with the slowly varying order parameter  $\Delta(x)$ . The contribution from the plane defect placed at the origin  $x = 0$  to the thermodynamic potential of the system can be written, with due inclusion of the above approximations, in the form

$$\Omega_d = \frac{\nu}{2}\Delta^2(0) - \mathbf{A}\Delta(0). \quad (2)$$

The coefficients  $\nu$  and  $\mathbf{A}$  can be obtained in the microscopic model [12] and are of different physical origin. The term quadratic in  $\Delta(0)$  in Eq. (2) describes the effect of Coulomb interaction and charge redistribution near the Fe/Cr interface. Estimation of coefficient  $\nu$  made within the model proposed in [12] yields  $\nu \approx -U\bar{N}/|\delta|$  for  $|\delta| \sim \pi T$ , where  $U = 4\pi q_s e/l_d$ ,  $q_s$  is the surface charge,  $l_d$  is the Debye length in the spacer metal,  $\bar{N}$  is the averaged density of states in the electron and hole parts of the Fermi surface possessing the nesting property, and  $\delta$  is the difference (expressed in energy units) between the occupations of these parts by quasiparticles. In our case,  $\delta < 0$  and  $|\delta| < 0.05$  eV,  $\pi T < 0.2$  eV, and  $U\bar{N} \sim 1$ ; i.e.,  $\nu > 20$  eV $^{-1}$ . Note that the negative sign of the parameter  $\nu$  corresponds to electrons flowing from Fe into Cr. The term linear in  $\Delta(0)$  in Eq. (2) derives from the exchange interaction between the Fe and Cr spins in the monolayers adjacent to the interface. Coefficient  $\mathbf{A}$  takes into account the possible formation of a localized moment in the first Cr monolayer adjoining an Fe layer [2]. The antiferromagnetic coupling between the nearest neighbor iron and chromium moments can reduce the effective interface moment, which affects the itinerant component of spin density in more distant chromium layers, thus producing a specific magnetic screening. Estimation of coefficient  $\mathbf{A}$  made in terms of the model of [12] yields  $A \approx JS_0\bar{N}$ , where  $J$  is the exchange integral and  $S_0$  is the effective moment of the interface. In our case, it appears reasonable to use the estimate of  $J$  made for bulk  $\text{Cr}_{1-x}\text{Fe}_x$  alloys, namely,  $|J\bar{N}| < 0.05$ , which yields  $A < 0.1$ , because  $S_0 < S_{\text{Fe}}$ , where  $S_{\text{Fe}} \cong 2.2\mu_B/\text{atom}$  is the iron moment at  $T \sim 400\text{--}600$  K. Thus, the Cou-

lombic term [quadratic in  $\Delta(0)$ ] can noticeably exceed the exchange term [linear in  $\Delta(0)$ ], at least for values of  $\Delta(0)$  (greater than  $10^{-2}$  eV) that are not overly small, in the high-temperature domain of  $\pi T \approx 0.2$  eV where  $\Delta \ll \pi T$ . In the approach proposed here, the term quadratic in  $\Delta(0)$  is the main contribution and drives the near-surface transition to the SDW state at the temperature  $T_1 > T_N$ . We shall call this state charge-induced. Note that the term linear in  $\Delta(0)$  in Eq. (2), while not driving the transition with  $T$ , induces a small-amplitude SDW component at any temperature. This additional, exchange-induced, proximity SDW component should be taken into account only above or in the immediate vicinity of the near-surface transition temperature  $T_1$  where the charge-induced SDW component is either very small or absent altogether [a case realistic enough under the condition  $\Delta(0) < 10^{-2}$  eV]. It may be expected that this approach, taking into account primarily the term quadratic in  $\Delta(0)$  in Eq. (2), will bring about more or less reasonable qualitative results for the high-temperature region far from the Néel point of interest here.

Let us describe the formation of the charge-induced SDW near a plane defect by using a model expression for the thermodynamic potential:

$$\Omega = \int_0^\infty f(x)dx + \Omega_d, \quad (3)$$

where we retain in  $\Omega_d$  only the first term of Eq. (2), which is proportional to  $\sim \nu\Delta^2(0)$ , with  $\nu < 0$ . Consider the case of temperatures  $T > T^*$  high enough to justify neglect of terms proportional to  $c_3$  in the  $f(x)$  expansion of Eq. (1) (the temperature  $T^*$  is estimated in the next section). Treating Eq. (3) as a functional of  $\Delta(x)$ ,  $\Omega = \Omega[\Delta]$ , we can find its stationary function in the class of linearly polarized SDW envelopes in the form

$$\Delta(x) = \mathbf{n} \frac{v_F}{\xi} \sinh^{-1} \left( \frac{x}{\xi} + \phi \right), \quad \tanh \phi = \frac{D}{\xi}, \quad (4)$$

where  $\mathbf{n}$  is the unit polarization vector,  $\xi(T) v_F \sqrt{c_2/c_1}$  is the correlation length, and  $D = 2c_2 v_F^2 / \nu$  is a characteristic scale, which, by analogy with the terminology accepted in the theory of surface superconductivity [13], we shall call the interpolation length. Within the model used, the length  $D$  is only weakly temperature-dependent. Solution (4) is valid for  $D/\xi \leq 1$ ; for  $D/\xi > 1$ , only the trivial solution  $\Delta(x) \equiv 0$  exists.

Equation (4) suggests the following scenario of the system behavior. For temperatures  $T > T_1$  [which is equivalent to the condition  $\xi(T) < D$ ], only the paramagnetic phase is stable. Below the temperature  $T_1$ , which satisfies the equality

$$\xi(T) = D, \quad (5)$$

the near-surface SDW described by Eq. (4) forms; thereby, equality (5) can be considered a specific Stoner

criterion for antiferromagnetism in a semi-infinite system described by Eq. (3). As the temperature decreases below  $T < T_1$  [or  $\xi(T) > D$ ], a spin density distribution  $\Delta(x)$ , which falls off sharply in amplitude for  $x \gg D$  while varying only weakly on the spatial scale  $x \ll D$ , forms near the plane defect. It goes without saying that a more consistent description of the behavior of the order parameter  $\Delta(x)$  in the high-temperature domain near the Fe/Cr interfaces would require the introduction of a number of complications into the simplest model (3). One would have first of all to cross over from a semi-infinite medium with one defect to a spacer of thickness  $L$  bounded on both sides in the  $\mathbf{n}_x$  direction by plane defects. Criterion (5) is valid in this case only in the limit  $\xi/L \rightarrow 0$ , while in a more general case, the transition temperature depends in a more complicated way on the spacer thickness,  $T_1 = T_1(L)$ . These complications do not affect the qualitative pattern and were considered in detail in [14]. In our case, it is important to understand the origin of the proximity SDW and to estimate the critical temperature  $T_1$  of its onset and its characteristic spatial scale  $D$ . Following these estimates, we shall subsequently use approximations to construct a model of spin density distribution across the chromium spacer for temperatures which, while being fairly low compared to  $T_1$ , would nevertheless correspond to the paramagnetic phase of bulk chromium ( $T > T_N$ ). The approach based on the relation between  $T_1 \approx 550$  K and  $T_N = 311$  K and on the existence of a short-range order on the scale  $D \sim (L^*/2) \approx 10\text{--}15$  chromium monolayers is applicable at least up to thick spacers with  $L > L^*$ .

### 3. SPATIAL SPIN-DENSITY DISTRIBUTION FAR FROM THE Fe/Cr INTERFACES

In the temperature region  $T_N < T < T_1$ , we consider the chromium spacer of thickness  $L > L^*$  in an Fe/Cr(100) multistructure as consisting conventionally of layers of a strong and a weak antiferromagnet. The terms strong and weak relate to the regions adjoining the interfaces and those far in the bulk of the spacer, respectively. We shall assume that all the temperature-induced changes in the order parameter  $\Delta(x)$  occurring in the interval of temperatures (of interest to us here) sufficiently low in comparison with  $T_1$ , take place only in the domain of weak antiferromagnetism with an effective thickness  $2l = L - L^*$ .

The region of strong antiferromagnetism of thickness  $L^*$ , which adjoins the technological interfaces, is only a small fraction of the total chromium spacer thickness and separates the deep layers of chromium from the Fe/Cr interfaces. We shall assume that within the strong-antiferromagnet layers, the amplitude of the charge-induced SDW is temperature-independent and that its formation at temperatures considerably above  $T_N$  is described by nonlinear equations with self-consistent sources at the boundaries, solution of which (as

already pointed out) is a fairly complicated problem in itself. Moreover, for  $T \ll T_1$ , the SDW amplitude near the interfaces is  $\Delta(\pm L) \sim v_F/D(T_1)$  and can turn out to be not at all small as compared to  $\pi T$ , which may make the Ginzburg–Landau expansion throughout the  $|x| < L/2$  spacer inapplicable. Nevertheless, within the weak-antiferromagnetism region, we still have  $|\Delta(x)| \ll \pi T$ , so that one can use Eq. (1) for the free-energy density. Because the temperature region within which we use this expression is now different, the relations between the coefficients  $c_1$ ,  $c_2$ , and  $c_3$  also change. Naturally,  $c_1$  and  $c_3$  are positive as before; however, the parameter  $c_2(T)$  decreases strongly and can even reverse sign as the temperature varies between  $T_1$  and  $T_N$ , so that the terms containing  $c_3$  cannot, generally speaking, be neglected. This makes finding the optimum SDW structure  $\Delta(x)$  an extremely complex problem. There is, however, a simplifying factor which permits one to retain only the terms lowest (quadratic) in  $\Delta(x)$  in the  $f(x)$  expansion of Eq. (1), albeit with some restrictions. The fact is that, in contrast to the situation considered in the preceding section, there is no charge transfer and no Coulomb interaction at the conventional interface separating the strong antiferromagnet from the weak one (these ferromagnets differ in the SDW amplitudes only). Therefore, the surface contribution to the thermodynamic potential of the weak antiferromagnet can be written simply in an approximation linear in  $\Delta(x)$ :

$$\Omega_s = -\frac{1}{2}[\mathbf{B}(l)\Delta(l) + \mathbf{B}(-l)\Delta(-l)], \quad (6)$$

where  $l$  is one half of the effective spacer thickness. Within the specified temperature region, any spin density distribution across the spacer thickness can be represented as the sum of a slowly varying [on the scale of the correlation length  $\xi(T)$ ] and a rapidly varying part [on a scale less than or of the order of the interpolation length  $D < \xi(T)$ ]. By averaging over the rapidly varying part of the order parameter, which is concentrated within a distance  $D \sim L^*/2$  from the interfaces, we obtain for the small, slowly varying component an effective Hamiltonian with a term linear in  $\Delta(\pm l)$  and given by Eq. (6), where the coefficient  $\mathbf{B}(\pm l)$  can be estimated (to within a factor) as  $B \equiv |\mathbf{B}(\pm l)| \approx U_0^{-1} \int |\Delta(x)| dx$ , with  $U_0$  being the effective SDW potential in chromium equal to 0.3–0.5 eV (for more details, see [11]); the integration is performed over the interval  $l < x < L/2$ . An order-of-magnitude estimate of the coefficient  $B \sim (\pi T_1/U_0) \approx 0.5\text{--}1.0$  does not contain any smallness; therefore, the exchange term  $\Omega_s$  in Eq. (6) is a source of the order parameter in the bulk of the spacer for  $|x| < l$ .

We write the thermodynamic potential of the SDW system in the weak-antiferromagnetism region in the form

$$\Omega[\Delta] = \frac{1}{2} \int_{-l}^l f(\Delta, \Delta', \Delta'') dx + \Omega_s[\Delta], \quad (7)$$

where  $f$  and  $\Omega_s$  are given by Eqs. (1) and (6), respectively. Presented in this form, Eq. (7) simulates the effect of the exchange field of the Fe layers on SDW formation in the Cr spacer, although the effective thickness  $2l$  and the effective exchange potential  $B(\pm l)$  naturally have totally different meanings here. In particular,  $B \neq 0$ , even if we formally put the magnetic moment of the Fe layer equal to zero. Actually, the thermodynamic potential was chosen in the form of Eq. (7) in order to be able, after conditional variation of the bulk part [the integral of the density  $f(x)$ ] of the functional  $\Omega[\Delta]$  for given SDW amplitudes near the Fe/Cr interfaces (where the Ginzburg–Landau expansion is either invalid or its analysis would be too cumbersome), to derive the optimum configuration of the order parameter  $\Delta(x)$  in the bulk of the chromium spacer from the linear equation. Considered from the formal standpoint, this corresponds to excitation of the long-wavelength  $\Delta(x)$  component by an external (with respect to the region of weak antiferromagnetism) exchange field  $\mathbf{B}(\pm l)$ , which is generated near the Fe/Cr interfaces at a high temperature  $T \approx T_1$  by the mechanism outlined in the preceding section.

To find the extremals of functional  $\Omega[\Delta]$  of Eq. (7), we make a few additional simplifying assumptions. We shall consider only transverse-polarized SDW structures and assume the  $\Delta(x)$  vector to be orthogonal to the multilayer growth direction  $\mathbf{n}_z$ :

$$\Delta(x) = n_z \Delta_z + n_y \Delta_y, \quad (8)$$

where  $\{\mathbf{n}_x, \mathbf{n}_y, \mathbf{n}_z\}$  is the basis of the orthogonal reference frame. We also restrict ourselves to  $\Delta(x)$  dependences with a symmetric modulus,  $|\Delta(x)| = |\Delta(-x)|$ . We choose the angle  $\varphi$  ( $0 \leq \varphi \leq \pi$ ) between vectors  $\mathbf{B}(l)$  and  $\mathbf{B}(-l)$  to which the directions of the SDW vectors  $\Delta(l)$  and  $\Delta(-l)$  are rigidly related at the boundaries of the weak antiferromagnetism region. This angle is assumed to be a fixed external parameter for the present. The  $\mathbf{n}_z$  axis from which the angle  $\varphi$  is reckoned is chosen conveniently so as to group the solutions for the extremals of functional  $\Omega[\Delta]$  according to boundaries of two types, namely, type I

$$\begin{aligned} \Delta_z(l) &= \Delta_z(-l) = |\Delta(l)| \cos(\varphi/2), \\ \Delta_y(l) &= -\Delta_y(-l) = |\Delta(l)| \sin(\varphi/2) \end{aligned} \quad (9)$$

and type II

$$\begin{aligned} \Delta_z(l) &= -\Delta_z(-l) = |\Delta(l)| \cos(\varphi/2), \\ \Delta_y(l) &= \Delta_y(-l) = |\Delta(l)| \sin(\varphi/2). \end{aligned} \quad (10)$$

We shall have to analyze only type I solutions, because solutions of type II are equivalent to those of type I under the substitution  $z \longleftrightarrow y$ . Conditions (9) or (10) correspond to a noncollinear SDW structure whose polarization vector in the chromium spacer turns continuously (from one monolayer to another) from the angle  $-\varphi/2$  for  $x = -l$  to  $\varphi/2$  for  $x = l$ .

Consider first the temperature interval  $T_N < T < T^*$ , wherein coefficient  $c_2$  is either positive and comparatively small or negative and terms proportional to  $c_3$  have to be retained in expansion (1). By varying functional  $\Omega[\Delta]$  of Eq. (7), we obtain the Euler–Lagrange equation

$$c_3 v_F^4 \Delta^{(4)} - 2c_2 v_F^2 \Delta'' + 2c_1 \Delta = 0 \quad (11)$$

subject to the boundary conditions

$$\Delta_z''(\pm l) = 0, \quad \Delta_y''(\pm l) = 0, \quad (12)$$

$$\pm B = [2c_2 v_F^2 \Delta_z'(\pm l) + c_3 v_F^4 \Delta_z'''(\pm l)] \cos(\varphi/2) \quad (13)$$

$$\pm [2c_2 v_F^2 \Delta_y'(\pm l) - c_3 v_F^4 \Delta_y'''(\pm l)] \sin(\varphi/2).$$

The fundamental system of solutions to Eq. (11) can be written as

$$\begin{aligned} \Delta_1(x) &= \sin \beta x \sinh \alpha x, & \Delta_2(x) &= \cos \beta x \cosh \alpha x, \\ \Delta_3(x) &= \sin \beta x \cosh \alpha x, & \Delta_4(x) &= \cos \beta x \sinh \alpha x, \end{aligned} \quad (14)$$

where the quantities  $\alpha^{-1}$  and  $\beta^{-1}$  are the correlation lengths of amplitude and phase fluctuations of the order parameter:

$$v_F \alpha = \left[ \frac{1}{2} \left( \sqrt{\frac{2c_1}{c_3} + \frac{c_2}{c_3}} \right) \right]^{1/2}, \quad (15)$$

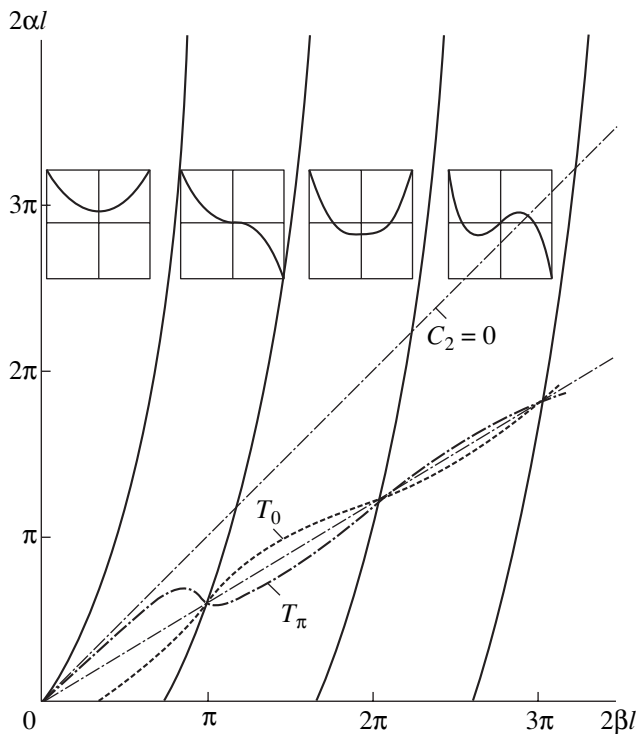
$$v_F \beta = \left[ \frac{1}{2} \left( \sqrt{\frac{2c_1}{c_3} - \frac{c_2}{c_3}} \right) \right]^{1/2}.$$

Solutions of type I have the form

$$\begin{aligned} \Delta_z(x) &= A_1 \Delta_1(x) + A_2 \Delta_2(x), \\ \Delta_y(x) &= A_3 \Delta_3(x) + A_4 \Delta_4(x), \end{aligned} \quad (16)$$

where the constants  $A_i$ , according to boundary conditions (12) and (13), are

$$\begin{aligned} A_1 &= A_0 \cos(\varphi/2) (\sin^2 \beta l + \sinh^2 \alpha l) \\ &\times [2\alpha \beta \sin \beta l \sinh \alpha l - (\alpha^2 - \beta^2) \cos \beta l \cosh \alpha l], \\ A_2 &= A_0 \cos(\varphi/2) (\sin^2 \beta l + \sinh^2 \alpha l) \\ &\times [2\alpha \beta \cos \beta l \cosh \alpha l + (\alpha^2 - \beta^2) \sin \beta l \sinh \alpha l], \\ A_3 &= A_0 \sin(\varphi/2) (\cos^2 \beta l + \sinh^2 \alpha l) \\ &\times [2\alpha \beta \sin \beta l \cosh \alpha l - (\alpha^2 - \beta^2) \cos \beta l \sinh \alpha l], \\ A_4 &= A_0 \sin(\varphi/2) (\cos^2 \beta l + \sinh^2 \alpha l) \\ &\times [2\alpha \beta \cos \beta l \sinh \alpha l + (\alpha^2 - \beta^2) \sin \beta l \cosh \alpha l], \\ A_0 &= 2B [v_F^4 c_3 (\alpha^2 + \beta^2) P(\varphi)]^{-1}. \end{aligned} \quad (17)$$



Phase diagram of induced SDW states in the chromium spacer above the bulk Néel temperature.

Here,  $P(\varphi)$  is the determinant of the coupled equations for  $A_i$  ( $i = 1, 2, 3, 4$ ):

$$\begin{aligned}
 P(\varphi) = & \cos^2(\varphi/2)(\sin^2\beta l + \sinh^2\alpha l) \\
 & \times [\beta(3\alpha^2 - \beta^2)\sinh 2\alpha l + \alpha(3\beta^2 - \alpha^2)\sin 2\beta l] \\
 & + \sin^2(\varphi/2)(\cos^2\beta l + \sinh^2\alpha l) \\
 & \times [\beta(3\alpha^2 - \beta^2)\sinh 2\alpha l - \alpha(3\beta^2 - \alpha^2)\sin 2\beta l].
 \end{aligned} \tag{18}$$

Note two fundamental circumstances connected with relations (17) and (18). First, for  $\alpha l \rightarrow \infty$ , all coefficients  $A_i$  tend to zero exponentially ( $\exp(-2\alpha l) \rightarrow 0$ ), such that in the thermodynamic limit there are no SDW states of the type of Eq. (16). Second, for a negative coefficient  $c_2$ , the determinant  $P(\varphi)$  in Eq. (18) reverses sign and vanishes at a temperature  $T_\varphi$ , which exceeds the Néel temperature  $T_N$  in an infinite sample specified by Eq. (15) for  $\alpha = 0$ :  $2c_1c_3 = c_2^2$ . This means that even in the absence of an external source ( $\mathbf{B} = 0$ ), the system can become unstable with respect to the formation of unique nonuniform SDW states, whose origin derives essentially from the spacer being limited purely geometrically on both sides in the  $\mathbf{n}_x$  direction. The amplitude of such states (we call them topological) oscillates with a period  $\sim \beta^{-1}$  and decays over a length  $\sim \alpha^{-1}$  ( $\beta > \alpha$ ) away from the interfaces into the spacer. The solution of the equation  $P(\varphi) = 0$  gives the temperature  $\max\{T_\varphi(l)\}$  above which such topological states cannot

exist. It is this temperature, rather than  $T_N$ , that limits, from below, the region of applicability of the approach based on Eqs. (11)–(13). As  $l \rightarrow \infty$ , the quantity  $T_\varphi(l)$  approaches the value  $T_\varphi(\infty)$  asymptotically, which does not depend on  $\varphi$  and is given by the equality  $3\alpha^2 - \beta^2 = 0$  or, which is the same,  $c_1c_3 = 2c_2^2$ . Note that, as follows from the expressions for the coefficients  $c_1$ ,  $c_2$ , and  $c_3$  given in [12], we have  $T_\varphi(\infty) > T_N$  for  $c_2 < 0$ . For finite values of  $l$ , the function  $T_\varphi(l)$  is fairly complex; indeed, it oscillates near the  $T_\varphi(\infty)$  line and crosses it at the nodes  $2\beta l_n = \pi n$  ( $n = 0, 1, 2, \dots$ ). The figure qualitatively presents the  $T_0(l)$  and  $T_\pi(l)$  relations corresponding to the lines of instability with respect to the formation of topological collinear states with a symmetrical and an antisymmetrical SDW envelope  $\Delta(x)$ , respectively. Note that the  $T_\pi(l)$  line exists down to very small  $l$ ; for  $\beta l \ll 1$ , the equation for  $T_\pi(l)$  simplifies greatly,  $3v_F^2c_2 = c_1l^2$ . By contrast, the  $T_0(l)$  line exists only at values of  $l$  in excess of a certain critical value; in the limit  $\beta l \ll 1$ , there is no instability against the formation of a symmetrical collinear topological state above  $T_N$ . For  $0 < \varphi < \pi$ , the  $T_\varphi(l)$  curves always lie in the interval between  $T_0(l)$  and  $T_\pi(l)$ .

As the temperature increases, we reach the region of  $c_2 > 0$ , where the determinant  $P(\varphi)$  of Eq. (18) can be only positive. The structure of the order parameter is changed (compared to that for  $c_2 < 0$ ) toward slower oscillations against the background of a sharper drop in amplitude as one moves away from the layer interfaces. In the  $\beta/\alpha \rightarrow 0$  limit (which is equivalent to  $2c_1c_3 \rightarrow c_2^2$  for  $c_2 > 0$ ), we obtain the temperature  $T = T^*$ , which it appears only natural to choose as an estimate of the above conventional boundary. Above  $T^*$ , the terms of expansion from (1) that are proportional to  $c_3$  become insignificant; therefore, by dropping the corresponding terms in Eqs. (11) and (13) and taking into account condition (9), we find the components of the noncollinear structure (8) of type I for the given parameters  $\varphi$  and  $B$ :

$$\begin{aligned}
 \Delta_z(x) &= b \cos(\varphi/2) \sinh\left(\frac{1}{\xi}\right) \cosh\left(\frac{x}{\xi}\right), \\
 \Delta_y(x) &= b \sin(\varphi/2) \cosh\left(\frac{1}{\xi}\right) \sinh\left(\frac{x}{\xi}\right), \\
 b &= \frac{B\xi}{c_2 v_F^2} \left( \cosh\left(\frac{2l}{\xi}\right) - \cos\varphi \right)^{-1}.
 \end{aligned} \tag{19}$$

In the high-temperature phase  $T_1 > T > T^*$ , it is possible to make a self-consistent calculation with an effective exchange potential  $\mathbf{B}(\pm l)$  in Eq. (6) in an explicit way. To do this, we construct linear combinations of SDW envelopes in the form of Eq. (4) which are localized at

the boundaries of a thick spacer ( $L \gg \xi$ ). For small arguments  $|x| \ll L - \xi$ , the symmetric combination coincides with function  $\Delta_c(x)$  and the antisymmetric one coincides with function  $\Delta_s(x)$  in Eq. (19) if we set

$$B = \frac{4v_F^2 c_2}{\xi^2} \left( \frac{\xi - D}{\xi + D} \right)^{1/2}. \quad (20)$$

Equality (20) relates the exchange constant  $B$  at the boundary between the weak and the strong antiferromagnetism to the charge density redistribution near the Fe/Cr interface through the interpolation length  $D(v)$ .

Thus, within the temperature interval  $\max\{T_\phi(L)\} < T < T_1(L)$ , only SDW states associated with the decrease in surface energy at the expense of an external (with respect to the spacer) charge perturbation in near-interface layers and ordered nonuniformly over the Cr spacer thickness can exist. It appears natural to call such states induced, because they vanish in the absence of external sources, as opposed to the topological states, which form spontaneously for  $T \leq T_\phi(L)$ . The latter states can exist only if the following two factors are present simultaneously: (i) the system must be bounded on both sides along the SDW wave vector direction, and (ii) the free-energy functional must have a specific form of Eq. (1) containing a negative lowest order gradient term  $c_2(\Delta'(x))^2$  predetermining instability with respect to the formation of an incommensurate SDW structure in the volume and a positive higher order gradient term  $c_3(\Delta''(x))^2$  stabilizing this structure. No topological SDW states will form in the absence of either of these factors. Unfortunately, the scope of this publication does not allow us to consider the situation at  $T < \max\{T_\phi(l)\}$ , because this would require taking into account higher powers of  $\Delta(x)$  in expansion (1) and would strongly complicate all calculations. Thus, the restriction  $T > \max\{T_\phi(l)\}$ , under which we have  $P(\phi) > 0$  for all  $\phi$  and  $l$ , is of fundamental significance and is assumed subsequently to hold.

#### 4. EFFECTIVE EXCHANGE ENERGY AND PHASE SLIP

It can readily be shown that the equilibrium thermodynamic potential  $\Omega[\Delta]$  of Eq. (7) is expressed through the SDW amplitude at the boundary as  $\Omega = -B|\Delta(l)|/2$ . In the temperature region  $\max\{T_\phi\} < T < T^*$ , straightforward calculation of the order parameter configuration using Eqs. (9) and (16) made with coefficients  $A_i$  of Eq. (17) yields the following relation for  $\Omega$  as a function of the parameter  $\phi$ :

$$\Omega(\phi) = -\frac{\Gamma}{P(0)\cos^2(\phi/2) + P(\pi)\sin^2(\phi/2)}, \quad (21)$$

where  $P(0)$  and  $P(\pi)$  are the values of the determinant in Eq. (18) for  $\phi = 0$  and  $\pi$ , respectively, and  $\Gamma$  does not

depend on the angle  $\phi$  and can be written as

$$\begin{aligned} \Gamma &= -P(0)\Omega(0) = -P(\pi)\Omega(\pi) \\ &= \frac{2B^2\alpha\beta}{c_3 v_F^4 (\alpha^2 + \beta^2)} \end{aligned} \quad (22)$$

$$\times (\sinh^2 \alpha l + \sin^2 \beta l) (\sinh^2 \alpha l + \cos^2 \beta l).$$

In the temperature region of interest here,  $\Gamma$ ,  $P(0)$ , and  $P(\pi)$  are positive; i.e., the gain in energy is the highest either at  $\phi = 0$  or at  $\phi = \pi$ .

The choice of the solution corresponding to the chosen value of  $\phi$  depends on the formulation of the problem. We may recall that the region of weak-antiferromagnetic order described here is connected with the Fe layer spins indirectly through the strong order regions. If the  $\phi$  angle is fixed by an exchange mechanism coupling the iron moments which is not related to SDW formation in the spacer (for instance, coupling through the paramagnetic parts of the chromium itinerant-electron Fermi surface [8, 11]) or by an external magnetic field, then the problem of the choice of the optimum SDW structure can be solved using Eqs. (14)–(18); as for Eqs. (21) and (22), they are not needed in the further commentary.

By contrast, if the energy gained in the formation of antiferromagnetic order in the chromium spacer is large enough, then the relative magnitude of  $\Omega(0)$  and  $\Omega(\pi)$  determines the type of the SDW collinear structure and, accordingly, the mutual orientation of the iron magnetic moments in adjacent layers. Considered in terms of the above model with an additional vector  $\mathbf{B}$ , which has the symmetry of the order parameter in the commensurate SDW state, the state with  $\phi = \pi$  corresponds to the ferromagnetic orientation of Fe moments for an even number of Cr monolayers in the spacer and to the antiferromagnetic orientation if the number of Cr monolayers is odd. If  $\phi = 0$ , the ferro- and antiferromagnetic orientations of the Fe moments in the above reasoning should be reversed. Consider that the SDW-induced contribution to the effective exchange energy is usually calculated as the difference

$$E_{\text{ex}} = \Omega(0) - \Omega(\pi) = \Gamma \frac{D(0) - D(\pi)}{D(0)D(\pi)}, \quad (23)$$

where  $E_{AF} - E_F = (-1)^{N+1} E_{\text{ex}}$  is the difference between the energies of states with antiferromagnetic and ferromagnetic configurations of iron moments in adjacent layers and  $N$  is the number of chromium monolayers in the spacer. The sign of  $E_{\text{ex}}$  is determined by the relative magnitude of  $P(0)$  and  $P(\pi)$  and depends on the spacer thickness and temperature. The  $P(0) - P(\pi)$  difference vanishes if the equality

$$\tan(2\beta l) = \frac{\beta 3\alpha^2 - \beta^2}{\alpha 3\beta^2 - \alpha^2} \tanh(2\alpha l) \quad (24)$$

is met. The solution to Eq. (24) can be conveniently plotted on the  $(2\beta l, 2\alpha l)$  plane (see figure); this solution represents a family of curves starting at the nodes  $2\beta l = \pi n$  ( $n = 0, 1, 2, \dots$ ) on the  $T_\phi(l)$  line of topological instability and reaching the asymptotic behavior  $2\beta l = \pi(n + 1) - 3\beta/\alpha$  for  $\beta/\alpha \rightarrow 0$ . Each curve can be identified with its temperature-dependent  $l_n(T)$  (which has no simple analytical form). For a fixed temperature, the quantities  $L_n(T) \equiv 2(l_n(T) + D)$  are essentially the spacer thicknesses at which the phase of the effective exchange  $(-1)^{N+1}E_{\text{ex}}$  undergoes a slip (in the regular sign alternation), with the number of monolayers  $N$  changing by one [1, 2, 4]. Each phase slip line  $l_n(T)$  is formally a line of thermodynamic equilibrium between collinear phases with an even and an odd order parameter,  $\Omega(0) = \Omega(\pi)$ . As the length  $l$  passes through the point  $l_n(T)$ , function  $\Delta(x)$  acquires or loses one zero. For illustration, the insets to the figure qualitatively show the  $\Delta(x)$  distributions in a spacer with an effective half-thickness  $l$ , which for small  $n$  is confined within an interval  $(l_n(T), l_{n+1}(T))$ . Assuming  $2l_n \approx dN_n$ , where  $d$  is the distance between adjacent chromium monolayers, one can estimate the critical monolayer numbers at which the effective exchange phase undergoes the first, second, and subsequent slips. Because the  $\alpha(T)$  and  $\beta(T)$  quantities given by Eq. (15) are temperature-dependent, the numbers  $N_n(T)$  also vary with temperature. It is easy to verify that in the temperature region of interest to us here, the phase correlation length  $\beta^{-1}(T)$  increases, whereas the amplitude correlation length  $\alpha^{-1}(T)$  decreases with increasing  $T$ , which is associated with the behavior of the coefficient  $c_2(T)$  described above. Thus, the critical numbers  $N_n(T)$  grow with temperature and, in addition, as follows from Eq. (24), we have  $N_n(T) \approx nN_1(T)$  ( $n = 1, 2, \dots$ ); i.e., as the number of monolayers in the chromium spacer varies, the effective exchange phase should slip with a close-to-regular periodicity.

We note that the zero line of phase slippage  $l_0(T)$  exists only for  $c_2 > 0$  and has the form  $l_0(T) = \sqrt{3/2} \xi(T)$  for  $(\alpha l, \beta l) \ll 1$ . However, if  $\beta$  becomes imaginary, which corresponds to the temperature rising above  $T^*$ , then Eq. (24) has no solutions and there is no phase slip effect. This is in accord with the finding that the most energetically favorable state in the high-temperature region  $T_1 > T > T^*$  is always a state with a symmetric SDW envelope. Indeed, the thermodynamic potential for structure (19)

$$\Omega(\varphi) = -\frac{B^2 \xi}{4c_2 v_F^2} \frac{\sinh(2l/\xi)}{\cosh(2l/\xi) - \cos \varphi} \quad (25)$$

has a minimum at the point  $\varphi = 0$ .

As follows from Eqs. (21)–(23) and (25), effective exchange through a thick chromium spacer decays exponentially with increasing  $L$  on the scale length of

amplitude SDW fluctuations:  $\alpha^{-1}(T)$  for  $\max\{T_\phi\} < T < T^*$  and  $\xi(T)$  for  $T^* < T < T_1$ .

The present model of an SDW state in Fe/Cr-type multilayers, which is strongly nonuniform over the chromium spacer thickness, can be useful in the interpretation of some experimental results obtained in investigating these systems. We have in mind here primarily investigation of the magnetic structure of multilayers with thick spacers ( $L > 20$ – $30$  chromium monolayers) performed at high temperatures (150 to 550 K). Polarized neutron reflection experiments [7] (see also reviews [1, 2]) made on Fe/Cr(100) superlattices have revealed two antiferromagnetic transitions in the chromium spacer. The first of them is described in [7] as a gradual transition from the state with an incommensurate SDW to a state with a commensurate SDW (but, possibly, strongly nonuniform over the spacer thickness). For instance, the diffraction pattern obtained with a quasi-momentum  $Q = (100)\pi/(2d)$  on a sample with  $L = 56$  monolayers featured two satellites that approached each other with the temperature increasing from 175 to 310 K. The other transition is identified on the  $(T, L)$  plane of the magnetic phase diagram with a fairly distinct boundary at  $T_1(L) \approx 500$  K above which the central peak disappears; this boundary is interpreted in [7] as corresponding to the transition between the commensurate SDW and the paramagnetic state. We note that the results obtained in neutron diffraction and kinetic measurements on superlattices apparently depend strongly on the quality of the Fe/Cr interface; as a result, in some experiments (e.g., [5]), where the samples were grown in other conditions, one observed only one (low-temperature) incommensurate-SDW phase at  $T < T_N(L)$  in spacers with a  $L > 30$  monolayer thickness. Measurements of the conductivity and magnetization hysteresis made in [15] on epitaxial superlattices of a different composition, Fe/Cr $_{1-x}$ Fe $_x$ (100) with  $x = 0.06$ , showed the existence of two antiferromagnetic transition temperatures in a thick ( $L > 24$  monolayers) spacer. The lower of these temperatures,  $T_N$ , is associated with the transition to a state with a uniform SDW, which is of the type of the  $AF_0$  phase in bulk dilute Cr $_{1-x}$ Fe $_x$  alloys; the other critical temperature  $T_0$  (or  $T_1$  in our notation), lying, as a rule, 150 K above  $T_N$ , corresponds to the transition from the nonuniform SDW state to the paramagnetic phase.

One can thus maintain that experiments carried out on superlattices indicate the existence in the temperature region  $T_N(L) < T < T_1(L)$  of a nonuniform antiferromagnetic phase which has no counterparts in bulk chromium. Unfortunately, it will likely not prove possible to reproduce the fine spatial structure of the SDW envelope that determines this nonuniformity from neutron diffraction data. It is possible to detect only a strong broadening of the central peak within the interval  $T_N(L) < T < T_1(L)$  in the neutron diffractogram near the quasi-momentum  $Q = (100)\pi/(2d)$  associated with the existence of some short-range antiferromagnetic

order and, apparently, with a large diffuse contribution to neutron scattering.

Tunneling spectroscopy measurements performed on the so-called optimized Fe/Cr/Fe(100) trilayers with a wedge-shaped spacer and a high-quality interface structure (see references in reviews [1, 2]), which cannot be reached in Fe/Cr superlattices, turned out to be more informative as to details on the SDW spatial structure. Those experiments studied the effective exchange coupling of ferromagnetic iron layers through a chromium spacer and, in particular, the role played in this coupling by antiferromagnetic ordering inside the spacer. It was found that, instead of the expected alternation of ferro- and antiferromagnetic relative moment orientation of the iron layers with variation of the number of chromium monolayers  $N$  by one, the phase undergoes slippage at room temperature (i.e., irregular reversal of the exchange sign) at  $N_i = 24, 44$ , and  $64$  ( $i = 1, 2, 3$ ); if the spacer thickness exceeds  $\approx 75$  monolayers, magnetic coupling between the layers virtually disappears. The first point of phase slip  $N_1(T)$  is seen to increase monotonically with temperature from 24 to 38 monolayers up to 550 K, as though it continues the corresponding dependence of the half-period of the long-wavelength SDW envelope above  $T_N$  in the  $AF_1$  phase of bulk chromium [8]. While the data available on the  $N_{2,3}(T)$  relations are less definite, they indicate, on the whole, a rise in  $N_i(T)$  at temperatures  $T > T_N(L)$ .

Within the model proposed here, the results of the  $N_i(T)$  measurements can be unambiguously considered as arguing for the existence in a chromium spacer above  $T_N(L)$  of a transversely polarized SDW with long-wavelength modulation along the growth direction of the structure, with the values of  $N_i$  being connected in a straightforward way with the nodes of the SDW at which its amplitude vanishes. The fact that we did not experimentally observe the  $N_0(T)$  line, which appears formally in our model, may be due either to the real temperature of the onset of the proximity SDW state  $T_1(L)$  lying lower than the zero-phase-slip temperature calculated by us or to the  $N_0(T)$  line being in the region of the  $(T, L)$  parameters that is beyond the scope of applicability of our model.

## ACKNOWLEDGMENTS

One of the authors (V.V.T.) is indebted to N.M. Kreĭnes and other participants of the seminar on the physics of magnetic phenomena, IPP RAS, for valuable discussions.

This study was partially supported by the Russian Foundation for Basic Research, project no. 01-02-16175.

## REFERENCES

1. D. T. Pierce, J. Unguris, R. J. Celotta, and M. D. Stiles, *J. Magn. Magn. Mater.* **200** (2), 290 (1999).
2. H. Zabel, *J. Phys.: Condens. Matter* **11** (3), 9303 (1999).
3. S. Parkin, N. More, and K. Roche, *Phys. Rev. Lett.* **64** (10), 2304 (1990).
4. J. Unguris, R. J. Celotta, and D. T. Pierce, *Phys. Rev. Lett.* **69** (5), 1125 (1992).
5. E. E. Fullerton, S. D. Bader, and J. L. Robertson, *Phys. Rev. Lett.* **77** (7), 1382 (1996).
6. E. E. Fullerton, K. T. Riggs, C. H. Sowers, and S. T. Bader, *Phys. Rev. Lett.* **75** (2), 330 (1995).
7. A. Schreyer, C. F. Majkrzak, T. Zeidler, *et al.*, *Phys. Rev. Lett.* **79** (24), 4914 (1997).
8. E. Fawcett, H. L. Albrts, V. Yu. Galkin, *et al.*, *Rev. Mod. Phys.* **66** (1), 25 (1994).
9. A. M. Niklasson, B. Johansson, and L. Nordstrom, *Phys. Rev. Lett.* **82** (22), 4544 (1999).
10. Z. P. Shi and R. S. Fishman, *Phys. Rev. Lett.* **78** (7), 1351 (1997); R. S. Fishman and Z. P. Shi, *Phys. Rev. B* **59** (14), 13849 (1999); R. S. Fishman, *J. Phys.: Condens. Matter* **13** (2), R235 (2001).
11. V. V. Tugushev, in *Electronic Phase Transitions*, Ed. by W. Hanke and Yu. V. KopaeV (North-Holland, Amsterdam, 1992), *Modern Problems in Condensed Matter Sciences*, Vol. 32, p. 239.
12. A. I. Buzdin, V. N. Men'shov, and V. V. Tugushev, *Zh. Ėksp. Teor. Fiz.* **91** (6), 2204 (1986) [*Sov. Phys. JETP* **64**, 1310 (1986)].
13. V. P. Mineev and K. V. Samokhin, *Introduction to the Theory of Unusual Superconductivity* (Mosk. Fiz.-Tekhnol. Inst., Moscow, 1998).
14. M. Avignon, V. Men'shov, and V. Tugushev, *Europhys. Lett.* **56** (1), 132 (2001).
15. E. E. Fullerton, C. H. Sowers, and S. D. Bader, *Phys. Rev. B* **56** (9), 5468 (1997).

*Translated by G. Skrebtsov*

---

## MAGNETISM AND FERROELECTRICITY

---

# Effect of Annealing on the Self-Poled State in Thin Ferroelectric Films

I. P. Pronin\*, E. Yu. Kaptelov\*, E. A. Tarakanov\*, and V. P. Afanas'ev\*\*

\*Ioffe Physicotechnical Institute, Russian Academy of Sciences,  
Politekhnicheskaya ul. 26, St. Petersburg, 194021 Russia

\*\*St. Petersburg State Electrical Engineering University, St. Petersburg, 197376 Russia

Received November 13, 2001

**Abstract**—It is shown that high-temperature treatment of self-poled lead zirconate–titanate films containing an excess of lead oxide, followed by prolonged storage at room temperature, results in a charge redistribution in the near-electrode regions of ferroelectric films. Such heat treatment destroys, as a rule, the self-poled state and removes the dielectric nonuniformity. A model of a thin-film ferroelectric capacitor is proposed which makes it possible to reproduce variations in the  $P$ – $V$  hysteresis loop shape and capacity–voltage ( $C$ – $V$ ) characteristics, as well as in the frequency-dependent pyroelectric response (LIMM). The effect of the interface and grain boundaries on the onset of the self-poled state, its variation, and destruction is discussed in terms of the proposed model. © 2002 MAIK “Nauka/Interperiodica”.

## 1. INTRODUCTION

One of the most interesting properties of thin ferroelectric films is the formation of the self-poled state in some of them. The poled state sets in in a film without application of any external electric field after the film has crystallized and become ferroelectric. The self-poled state can be observed in ferroelectric films irrespective of their composition, crystal structure, and the method of preparation used [1–9]. Self-polarization is actually an interface effect [1, 2]. This state can be induced, in particular, by a field of electrons trapped in surface states on a ferroelectric–bottom electrode interface [3, 4]. Another viewpoint on the nature of the self-poled state relates this state to mechanical stresses present in ferroelectric films [7]. The internal electric field, which manifests itself in the shift of hysteresis loops and  $C$ – $V$  characteristics, is correctly considered to be an attribute of self-poling [2] and is due to the migratory polarization which screens the self-polarization [3].

Nevertheless, the origin of self-poling is still far from being clear and requires additional studies. Among the problems which have to be refined are (1) the role played by Schottky barriers at the interfaces of a thin-film ferroelectric capacitor [1]; (2) the effect of the film crystal structure, for instance, the predominant onset of self-poling in thin films of lead zirconate–titanate solid solutions  $\text{PbZr}_{1-x}\text{Ti}_x\text{O}_3$  (PZT) in the tetragonal phase ( $x \geq 0.47$ ), compared with the rhombohedral compositions ( $x \leq 0.47$ ) [1, 2, 10]; (3) the size effects (depending, in particular, on the relation between the grain size and thickness of polycrystalline films) and their manifestations in the film properties; and (4) the

reasons for self-poling destruction under film annealing [1, 10, 11].

We present here an analysis of the onset of the self-poled state and of its variation and destruction in PZT films subjected to heat treatment.

## 2. FILM PREPARATION AND COMPOSITION AND EXPERIMENTAL TECHNIQUES

The films prepared by using radio-frequency magnetron sputtering of a ceramic target of composition  $\text{PbZr}_{0.54}\text{Ti}_{0.46}\text{O}_3 + 10 \text{ mol } \% \text{ PbO}$  contained an excess of lead oxide  $\text{PbO}$ , which is known [3, 11–14] to stimulate the onset of the self-poled state in these films. Films of thickness 0.7–1.0  $\mu\text{m}$  were deposited on a cold substrate (130°C) and subjected to heat treatment at 550°C. We believe [3] that the role of the lead oxide excess in PZT films can be reduced, in particular, to the extraction of a certain amount of oxygen atoms (which are mobile in the perovskite structure) from the perovskite lattice, as a result of which the ferroelectric layer becomes doped by oxygen vacancies and features  $n$ -type conduction. Platinum films were used as the top and bottom electrodes. The area of the capacitor structure was determined by the dimensions of the top electrode, whose diameter was 130  $\mu\text{m}$ .

The dielectric hysteresis loops of thin-film ferroelectric capacitors were studied using a modified Sawyer–Tower circuit at a frequency of 50 Hz, their voltage–capacity characteristics were obtained with an E7-12 digital bridge at a frequency of 1 MHz, and the frequency-dependent pyroelectric response (LIMM) was measured and processed following the technique described in detail in [15, 16].

### 3. EXPERIMENTAL RESULTS

We showed earlier that the self-poled state in PZT films is distributed nonuniformly over the film thickness and is concentrated in the film region adjacent to the bottom electrode (curve 1 in Fig. 1) [3]. A weakly polarized region with oppositely directed polarization was located close to the top electrode. This distribution of the self-polarization was reflected in the asymmetric hysteresis loops (Fig. 2a) and voltage–capacity characteristics (Fig. 3a).

A comparison of the polarization distribution curves obtained by biasing the film with an external dc voltage of +20 or –20 V (curves 2, 3 in Fig. 1) with the self-poling curve (curve 1 in Fig. 1) showed the self-poled state not to extend over more than 10–15% of the film volume. Despite a fairly strong polarizing field (200 kV/cm) being applied to the film, the maximum in the polarization distribution is seen to remain shifted toward the bottom electrode. This shift becomes stronger after application of a positive voltage (curve 2 in Fig. 1).

The results of LIMM measurements made on the films, which were poled by a voltage of +20 and –20 V at a temperature of 280°C and in the course of subsequent cooling and then storage for 24 h at room temperature, are represented by curves 4 and 5 in Fig. 1. The degree of polarization of such samples is seen to increase substantially compared to that reached in normal conditions. The LIMM amplitudes in the PZT film near the top electrode were almost identical when polarized by pulses of either polarity. At the same time, the amplitude of the positive signal near the bottom electrode is noticeably larger than that of the negative signal, which may be due to the existence of a residual space charge near the bottom electrode.

Heat treatment of self-poled PZT films at 100 and 200°C did not affect the shape of the  $P$ – $V$  and  $C$ – $V$  curves. Annealing the films at a higher temperature (300°C), which is close to the Curie point, resulted in their depolarization and a noticeable change in the shape of the hysteresis loops (Fig. 2b) and  $C$ – $V$  characteristics (Fig. 3b). The hysteresis loops and the voltage–capacity characteristics assumed their normal, i.e., symmetric, form. Prolonged storage of such PZT films at room temperature produced waists in the hysteresis loops (Fig. 2c, storage  $4 \times 10^7$  s), which is frequently seen in polycrystalline ceramic ferroelectrics [17], with additional extrema appearing in the  $C$ – $V$  characteristics (Fig. 3c).

The hysteresis loop shape of self-poled films depended on the amplitude of the ac voltage used. For instance, application of an ac voltage 20 V in amplitude reduced the loop asymmetry (Fig. 4a) in comparison with that at 10 V (Fig. 2a) but did not result in a complete disappearance of the internal bias field. Consecutive measurement of  $C$ – $V$  curves made on the same sample revealed that as the number of polarization

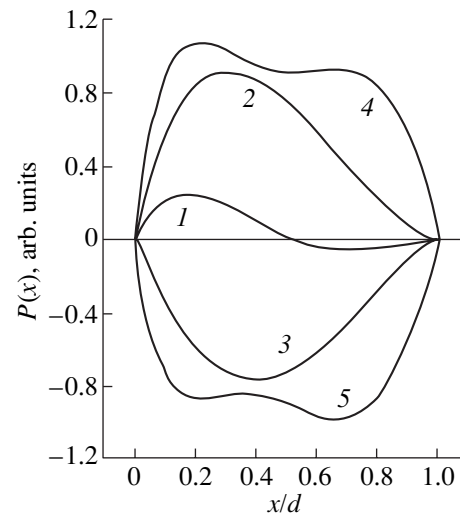


**Fig. 1.** Polarization distribution in a PZT film over its thickness ( $d = 1 \mu\text{m}$ ): (1) self-poled state; (2) after application of a voltage +20 V or (3) –20 V for 30 min at room temperature; (4) after application of +20 V or (5) –20 V at 280°C and field cooling to room temperature.

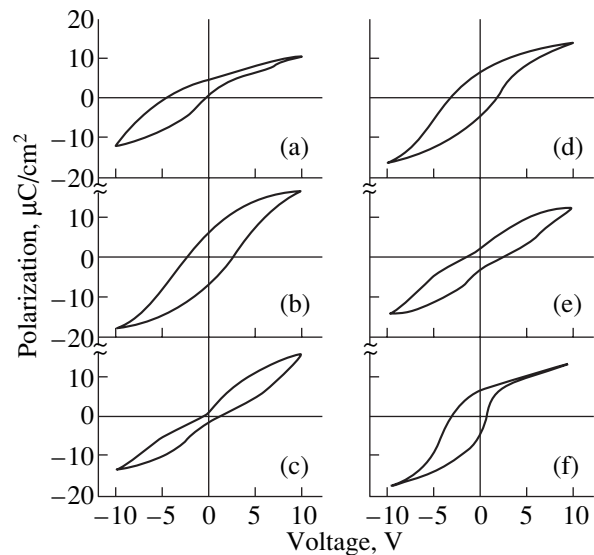


**Fig. 2.** Hysteresis loops of a self-poled film 1  $\mu\text{m}$  thick deposited at 130°C: (a, d, e) before annealing, the loops are observed with a probability of 80, 15, and 5%, respectively; with a capacitor array; (b) immediately after film annealing at 300°C; (c) after film storage for 14 months at room temperature; and (f) the hysteresis loop of a self-poled PZT film of thickness 0.7  $\mu\text{m}$  deposited at a temperature of 200°C.

switching cycles increases, the shape of the  $C$ – $V$  curves changes (Fig. 3c), making them smoother (Fig. 3d).

The experiments showed that the dielectric characteristics of an array of capacitor structures based on a self-poled PZT film exhibit a significant scatter over the film area (Figs. 2a, 2d, 2e). For instance, identical capacitor structures exhibited hysteresis loops of three

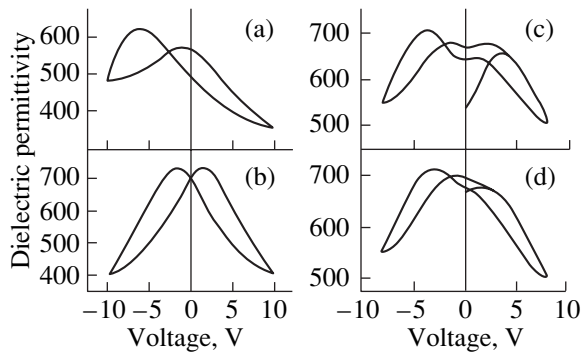


**Fig. 3.**  $C$ - $V$  characteristics of a self-poled PZT film (a) immediately after its formation, (b) after annealing at 300°C, and (c, d) after one-month storage of the annealed film in the first and second cycles of bias voltage variation, respectively.

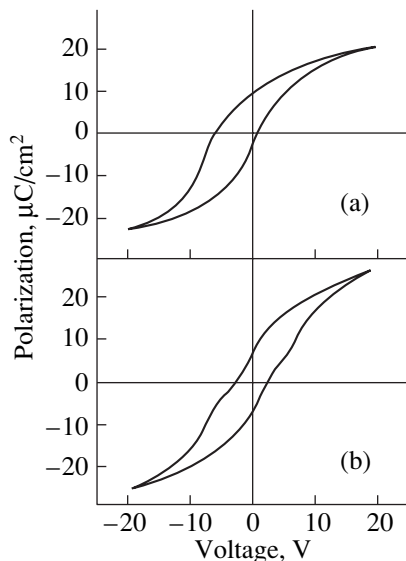


**Fig. 4.** Hysteresis loops of a self-poled PZT film in a strong electric field (20 V) (a) after film formation and (b) after annealing at 300°C and prolonged storage.

types with different degrees of asymmetry, from loops with a strong internal field  $E_{\text{int}} = 25$  kV/cm (Fig. 2a) to nearly symmetric ones with waists (Fig. 2e). Increasing the substrate temperature from 130 to 200°C upon deposition of the ferroelectric layer gave rise to a better uniformity of the dielectric characteristics over the film area, as well as to a growth in dielectric permittivity (from 450 to 750). A typical hysteresis loop for such a film is shown in Fig. 2f.

#### 4. DISCUSSION OF RESULTS

To explain the above experimental results, we propose a model whose essence is illustrated in Figs. 5 and 6. The model postulates the following assumptions,

which were made on the basis of previous studies. (1) PZT films have a predominantly columnar structure characterized by a distinctly oriented texture, e.g., along  $\langle 111 \rangle$  [12, 18, 19]. (2) Due to an oxygen deficiency, the films feature  $n$ -type conduction [3, 20, 21]. (3) Localized states are distributed nonuniformly over the film thickness and concentrate at the interfaces of the thin-film ferroelectric capacitor, where the charge builds up [22]. (4) Self-poling is screened by migratory polarization [17].

Figure 5 schematically shows the distribution of the self-poled state and of the screening space charge over the PZT film thickness (a) before annealing and (b) after annealing and prolonged storage at room temperature.

Before annealing, the poled region in the film is concentrated primarily near the bottom interface of the structure (Fig. 5a). This is due to the fact that the perovskite phase in the PZT film crystallized without the top electrode; this electrode was deposited on the already formed film at a substrate temperature of 100–120°C [3]. The reason for the shift in the  $P$ - $V$  and  $C$ - $V$  characteristics toward negative voltages is that the migratory polarization screens the spontaneous polarization (Figs. 2a, 2f, 3a).

The internal field in the capacitor structures characterized by an asymmetric hysteresis loop (Fig. 2a) can be as high as 25 kV/cm. Such a field can be generated by the charge of the electrons trapped in the surface states. We estimate the density of this charge to be approximately  $5 \mu\text{C}/\text{cm}^2$ . The density of surface states at the interface will be about  $3 \times 10^{13} \text{ cm}^{-2}$  in this case, which correlates well with the data from [23] and corresponds to a volume density of defects of  $10^{18} \text{ cm}^{-3}$ .

According to our model, as a result of high-temperature annealing, the charged localized states at the interfaces become partially depleted due to the disappearance of spontaneous polarization and the released charges are distributed uniformly over the film thickness. When cooled subsequently to below the Curie temperature, the electrons trapped in surface states of the bottom and top interfaces polarize the near-electrode regions of the ferroelectric film. Poled states forming near the interface initiate migratory polarization, which eventually gives rise to the formation of space charge in the near-electrode regions screening spontaneous polarization (Fig. 5b). Therefore, the hysteresis loops and the  $C$ - $V$  characteristics, which exhibit the usual symmetric form immediately after annealing (Figs. 2b, 3b), transform with time to assume the shape illustrated in Figs. 2c and 3c. A waist appears in the  $P$ - $V$  curves, and the  $C$ - $V$  characteristics exhibit additional extrema, which reflect that the migratory polarization screens oppositely poled regions in the ferroelectric film near the electrodes. Thus, annealing and subsequent storage of a film in normal conditions bring about charge redistribution between the top and bottom interfaces and in the volume of the structure. The time

required for the space charge to build up is apparently determined by the low migration rate of charged oxygen vacancies at room temperature.

However, within this concept, one cannot explain the observed nonuniformity of dielectric parameters over the film area and the existence of a poled volume at the top interface of the self-poled film. The experimental results, as a whole, can be interpreted if one assumes that there are structural defects in the film which interfere with the migration of charged particles between the electrodes of the thin-film capacitor.

We believe that such structural defects could be, in the simplest case, transverse grain boundaries parallel to the plane of the capacitor structure (Fig. 6). Grain boundaries can be initiated by film lattice imperfections, such as inclusions of a foreign phase, lattice misfit between the top electrode and the perovskite film, and mechanical stresses. In our case, the formation of transverse boundaries in a PZT film can be related to the presence of a substantial excess of lead oxide, which precipitates at grain boundaries in the volume of the film in the course of perovskite phase formation and suppresses the growth of perovskite nuclei through the film thickness. Figures 6b–6e illustrate the possible arrangement of transverse boundaries over the film thickness. Let us consider the way in which these boundaries can affect hysteresis loops in self-poled ferroelectric films before and after their annealing.

If there are no transverse boundaries across the film (Fig. 6a), charge migration from the interior of the film to traps at the bottom electrode does not meet with obstacles. After the transition to the ferroelectric phase, the region of the film near the bottom interface polarizes to the maximum extent. To this state of the capacitor structure corresponds the strongly asymmetric hysteresis loop shown in Figs. 2a and 2f.

The self-poled film volume at the bottom interface contracts when a transverse boundary forms a two-grain structure (Fig. 6b), because in this case only part of the charges can reach the traps at the bottom interface. This trend becomes stronger as the grain boundary moves toward the bottom interface (Figs. 6c, 6d). If at least part of the charge from the volume of the grain becomes localized in the surface traps, the film region near the free surface will also become poled. In this case, the hysteresis loops will be less asymmetric (Figs. 2d, 2e). If, after deposition of the top electrode, the top interface traps still retain a considerable charge, a loop with a waist can form (Fig. 2e). An increase in the number of grain boundaries (Fig. 6e) tends to make the loops more symmetrical, reduce the polarization of the near-electrode regions of the PZT film, and, accordingly, reduce and, possibly, suppress self-poling. Therefore, the shape of the hysteresis loop will be determined by the relationship between the volumes of individual crystallites and the number of structural defects within the capacitor area (Figs. 6a–6e).

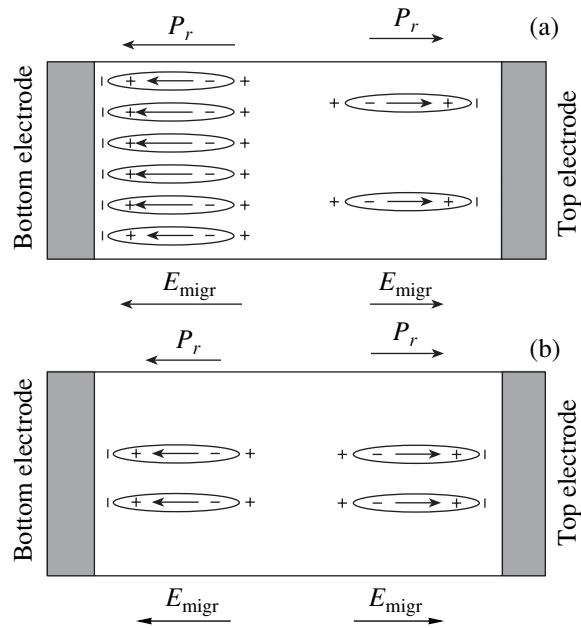


**Fig. 5.** Schematic distribution pattern of the poled state ( $P_r$  is residual polarization) and space charge ( $E_{migr}$  is the migratory polarization field) at the interfaces of a thin-film ferroelectric capacitor made of a self-poled PZT film (a) after film formation and (b) after annealing and prolonged storage at room temperature.

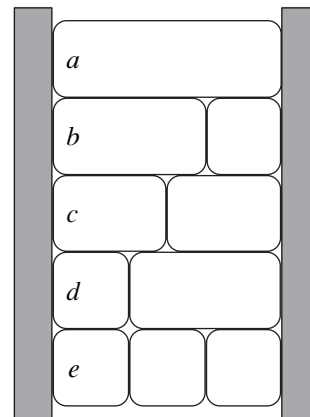


**Fig. 6.** Schematic of a PZT film with different arrangements of transverse grain boundaries over the film thickness.

High-temperature annealing of films containing the above types of structural defects makes the hysteresis loops more symmetrical (Fig. 2b). In particular, in the absence of transverse boundaries, part of the charges become distributed with equal probability between the top and bottom interfaces and polarize the near-interface film regions. Subsequent prolonged storage of such films at room temperature results in the formation of a screening space charge and, accordingly, of waists in the hysteresis loops (Fig. 4b). At the same time, it

may be conjectured that when a film contains grain boundaries shifted toward either electrode, the film can retain noticeable self-poling, as was observed in [1].

As mentioned above, increasing the substrate temperature from 130 to 200°C removes dielectric nonuniformity over the film area and increases the dielectric permittivity from 450 to 750, with the hysteresis loops taking on a distinct asymmetric shape (Fig. 2f). We assign these changes to a decrease in the amount of excess lead in deposited PZT films; this situation is frequently encountered when applying ion plasma methods to ceramic target sputtering. The probability of formation of oppositely poled regions in such films reduces to a minimum, and their crystal structure can be described by the scheme in Fig. 6a.

The above reasoning was made under the assumption that after the annealing, the top and the bottom interfaces of a thin-film ferroelectric capacitor become identical in terms of their density of states. One cannot, however, exclude the possibility that the hysteresis loop asymmetry that is retained in some cases can be associated with there being a difference in the density of charged states between these interfaces. One should, therefore, perform a more comprehensive study of the PZT film structure, interfaces, and their relation to the parameters of capacitor structures.

## 5. CONCLUSION

The results obtained permit the following conclusion. High-temperature annealing of self-poled PZT films brings about destruction of the self-poled state and removes the dielectric nonuniformity over the film area, which is connected with charge redistribution between the top and bottom interfaces of the thin-film ferroelectric capacitor.

The specific features of charge redistribution in a film can be explained within a model which assumes that there are transverse grain boundaries in a ferroelectric film that suppress charge migration between the capacitor electrodes.

The existence of transverse grain boundaries in textured PZT films originates from inclusions of the excess lead oxide phase.

## ACKNOWLEDGMENTS

This study was supported by the Russian Foundation for Basic Research (project no. 01-02-17799) and the Ministry of education of the RF (grant no. EOO-3.4-350).

## REFERENCES

1. A. L. Kholkin, K. G. Brooks, D. V. Taylor, *et al.*, *Integr. Ferroelectr.* **22**, 525 (1998).
2. R. Bruchhaus, D. Pitzer, M. Schreiter, and W. J. Wersing, *J. Electroceram.* **3** (2), 151 (1999).
3. I. P. Pronin, E. Yu. Kaptelov, E. A. Tarakanov, *et al.*, *Fiz. Tverd. Tela (St. Petersburg)* **44** (4), 739 (2002) [*Phys. Solid State* **44**, 769 (2002)].
4. V. P. Afanas'ev, A. A. Petrov, I. P. Pronin, *et al.*, *J. Phys.: Condens. Matter* **13** (39), 8755 (2001).
5. D. Dimos, W. L. Warren, M. B. Sinclair, *et al.*, *J. Appl. Phys.* **76** (7), 4305 (1994).
6. N. F. Foster, *J. Appl. Phys.* **40**, 420 (1969).
7. G. Suchanek, R. Koehler, P. Padmini, *et al.*, *Surf. Coat. Technol.* **116–119**, 1238 (1999).
8. M. Adachi, T. Matsuzaki, N. Yamada, *et al.*, *Jpn. J. Appl. Phys.* **26**, 550 (1987).
9. C. H. Choi and J. Lee, *J. Phys. IV* **8**, 109 (1998).
10. E. G. Lee, J. K. Lee, J.-Y. Kim, *et al.*, *J. Mater. Sci. Lett.* **18**, 2025 (1999).
11. S. Okamura, S. Miyata, Y. Mizutani, *et al.*, *Jpn. J. Appl. Phys., Part 1* **38** (9B), 5364 (1999).
12. V. P. Afanas'ev, G. N. Mosina, A. A. Petrov, *et al.*, *Pis'ma Zh. Tekh. Fiz.* **27** (11), 56 (2001) [*Tech. Phys. Lett.* **27**, 467 (2001)].
13. M. Watamori, M. Isono, H. Madono, *et al.*, *Appl. Surf. Sci.* **142**, 422 (1999).
14. M. Kobune, H. Ishito, A. Mineshige, *et al.*, *Jpn. J. Appl. Phys., Part 1* **37** (9B), 5154 (1998).
15. S. B. Lang, *Ferroelectrics* **106**, 269 (1990).
16. G. Suchanek, Th. Sandner, R. Kohler, *et al.*, in *Proceedings of Eleventh IEEE International Symposium on Applications of Ferroelectrics, Montreux, Switzerland, 1998*, p. 187.
17. K. Okazaki, *Ceramic Engineering for Dielectrics* (Tokyo, 1969; Énergiya, Moscow, 1976), translated from Japanese.
18. R. E. Jones, *Solid State Technol.* **40** (10), 201 (1997).
19. R. J. Waser, *J. Eur. Ceram. Soc.* **19**, 655 (1999).
20. J. J. Lee, C. I. Thio, M. Bhattacharya, and S. B. Desu, *Mater. Res. Soc. Symp. Proc.* **361**, 241 (1995).
21. V. V. Prisedsky, V. I. Shishnovsky, and V. V. Klimov, *Ferroelectrics* **17**, 465 (1978).
22. V. P. Afanas'ev, E. Yu. Kaptelov, G. P. Kramar, *et al.*, in *Proceedings of the 12th International Symposium "Thin Films in Electronics"* (IPTs "Kontrast," Khar'kov, 2001), p. 195.
23. V. I. Dimza and A. É. Krumin', *Avtometriya*, No. 5, 14 (1981).

*Translated by G. Skrebtsov*

---

**MAGNETISM  
AND FERROELECTRICITY**

---

# Specific Features of the Electrical Properties upon Smeared Phase Transitions in Multicomponent Ferroelectric Ceramics Based on Lead Zirconate Titanate

**A. I. Burkhanov\*, A. V. Shil'nikov\*, Yu. N. Mamakov\*, and G. M. Akbaeva\*\***

\* Volgograd State Architecture and Building Academy, Akademicheskaya ul. 1, Volgograd, 400074 Russia

\*\* Research Institute of Physics, Rostov State University, pr. Stachki 194, Rostov-on-Don, 344090 Russia

e-mail: postmaster@vgasa.ru

Received June 14, 2001; in final form, November 15, 2001

**Abstract**—The reverse dependences of the permittivity  $\epsilon'_r(E_-)$  and the polarization and depolarization currents in multicomponent ferroelectric ceramics based on lead zirconate titanate (PZT) are investigated over a wide range of temperatures. The results obtained make it possible to separate the effects associated with the phase transformation and the effects predominantly caused by the switching of the domain structure in the studied material. The assumption is made that two smeared phase transitions occur in the system under consideration. © 2002 MAIK “Nauka/Interperiodica”.

## 1. INTRODUCTION

It is known (see, for example, [1]) that relaxor ferroelectrics have two characteristic temperatures, namely,  $T_m$  and  $T_d$ . The temperature  $T_m$  corresponds to a maximum of the permittivity  $\epsilon'$  and depends on the frequency of the measuring field. The temperature  $T_d$  is the temperature at which the preliminarily polarized sample undergoes depolarization upon heating. It is worth noting that the temperature  $T_d$  is universally less than the temperature  $T_m$  (see, for example, the detailed investigations performed by Zuo-Guang Ye and Hans Schmid [2] for a model relaxor—the lead magnesium niobate  $\text{PbMg}_{1/3}\text{Nb}_{2/3}\text{O}_3$  (PMN)). In our earlier works [3–5], we demonstrated that similar characteristic temperatures are also observed in multicomponent ferroelectric ceramics based on lead zirconate titanate (PZT). However, according to [3–5], the behavior of a number of physical parameters characterizing the polarization in the temperature range from  $T_m$  to  $T_d$  for this multicomponent system significantly differ from the behavior of these parameters, for example, for the well-known PLZT relaxor [6]. In particular, with a change in the frequency from 1 to 1000 Hz, the shift of the temperature  $T_m$  for the multicomponent ferroelectric ceramics is equal to 4 K [7, 8], whereas this shift for the PLZT-9/65/35 ceramics is as large as 10–11 K [6]. Moreover, even at infralow frequencies, the multicomponent ceramics does not exhibit double polarization loops typical of relaxors at  $T \geq T_d$ . At the same time, the temperature dependences of the effective permittivity  $\epsilon'_{\text{eff}}(T)$  determined from analysis of the polarization loops [3, 4] are characterized by two maxima: one maximum is observed in the vicinity of the

temperature  $T_d$  and the other maximum occurs in the vicinity of the temperature  $T_m$ . It should be noted that, in the case of the PZT multicomponent ceramics [3, 4], unlike conventional relaxors based on lead magnesium niobate (see, for example, [9, 10]), an increase in the field amplitude (in the amplitude range covered) brings about a substantial decrease only in the temperature of the additional maximum in the vicinity of  $T_d$  in the dependence  $\epsilon'_{\text{eff}}(T)$  without a change in the temperature of the maximum in the range of  $T_m$ .

Toshio Ogawa and Ayako Yamada [11] performed an x-ray structure investigation into the switching effects in tetragonal ferroelectric ceramics based on lead zirconate titanate and revealed the specific features in the behavior of the intensity of maxima in the diffraction pattern. In [11], these features were attributed to 90° rotations of domains. In the authors' opinion, this should result either in a change in the shape of the polarization loops or in the appearance of double maxima in the reverse dependences of the permittivity  $\epsilon'_r(E_-)$ . Therefore, in ferroelectric ceramics, unlike relaxors, anomalies in the dielectric properties can be associated both with the domain dynamics and with the phase transitions [3, 4, 12].

In this respect, the aim of the present work was to analyze thoroughly the reverse dependences  $\epsilon'_r(E_-)$  in the range of the characteristic temperatures  $T_d$  and  $T_m$  and to investigate the polarization and depolarization currents in the multicomponent ferroelectric ceramics in order to separate the effects associated with phase transformations. In other words, we made efforts to separate the effects typical of relaxor ferroelectrics from the effects predominantly caused by the switching

of the domain structure in multicomponent ferroelectric ceramics.

## 2. SAMPLE PREPARATION AND EXPERIMENTAL TECHNIQUE

The reverse (field) dependences of the permittivity  $\epsilon'_r(E_-)$  were measured by the bridge method at a frequency of 1 kHz with a stepwise variation in the bias field  $E_-$ . The measuring field strength  $E_0$  did not exceed 1 V/cm. The temperature dependences of the current  $I(T)$  were obtained using a V7-30 electrometer under the following conditions: (i) upon heating after annealing for 1 h at  $T > T_m$  and subsequent cooling to room temperature ( $T_r$ ), (ii) upon heating after ageing for one month at  $T_r$ , and (iii) upon heating after cooling of a sample from  $T > T_m$  to  $T_r$  in a dc electric field. The heating was carried out at  $E = E_- = 0$ . In all cases, the heating rate was approximately equal to 1 K/min. The samples used in measurements had the form of plane-parallel plates prepared from the PZT-based soft ferroelectric ceramics belonging to multicomponent systems of the  $\text{PbTiO}_3\text{-PbZrO}_3\text{-PbNb}_{2/3}\text{Zn}_{1/3}\text{O}_3\text{-PbW}_{1/2}\text{Mg}_{1/2}\text{O-PbW}_{3/5}\text{Li}_{2/5}\text{O}_3$  type with a  $\text{PbTiO}_3$  content of 34.89 mol % [13] (hereafter, designated as PKR<sup>1</sup>.) The measurements were performed with samples  $5 \times 5 \times 1$  mm in size. Electrodes were applied by burning-in silver.

## 3. RESULTS AND DISCUSSION

Figure 1 displays the dependences  $\epsilon'_r(E_-)$  at temperatures below  $T_d$  ( $T = 298, 373, \text{ and } 439$  K), in the vicinity of  $T_d$  ( $T = 450$  K), and above  $T_d$  ( $T = 472, 479, 484, \text{ and } 493$  K). The temperatures  $T = 484$  and  $493$  K are higher than the temperature  $T_m$  for this material at a frequency of 1 kHz ( $T_{m(1\text{ kHz})} \approx 483$  K [4]). In our previous work [8], the temperature  $T_d$  was determined using the method proposed by Isupov [1]: the temperature  $T_d$  was taken as the temperature at a minimum of the frequency of piezoelectric resonance. For the ceramics under investigation, this temperature was estimated to be  $T \approx 449$  K. Figure 1 also shows the temperature dependences of the effective coercive field  $E_c(T)$  (curve 1) and the critical field  $E_{\text{ind}}(T)$  (curve 2). The effective coercive field  $E_c(T)$  was determined from the positions of the maxima in the dependence  $\epsilon'_r(E_-)$ . The critical field  $E_{\text{ind}}(T)$  corresponds to the appearance of a pronounced nonlinearity (a kink) in the dependence  $\epsilon'_r(E_-)$  in the temperature range  $T > T_m$ .

<sup>1</sup> The notation PKR (piezoelectric ceramics, Rostov) was introduced by the designers of the aforementioned ferroelectric ceramics at the Research Institute of Physics of the Rostov State University. Patents have been taken out for many ferroelectric ceramics similar in composition to that used in the present work: PKR-1, PKR-8, PKR-7M, and others.

It can be seen from Fig. 1 that a number of reverse dependences  $\epsilon'_r(E_-)$  (at  $T = 298, 373, \text{ and } 472$  K) exhibit anomalies in the form of local minima which arise after preliminary polarization of the sample in a dc field  $E_- > |E_{\text{min}}|$  (where  $E_{\text{min}}$  is the field strength  $E_-$  corresponding to the permittivity  $\epsilon'_r(E_-)$  at a minimum). These anomalies are characterized by the following feature: as the temperature increases, the minimum of the permittivity  $\epsilon'_r(E_-)$  arises at all the temperatures, except for the temperature range in the vicinity of  $T_d$  and  $T \geq T_m$ . It should also be noted that the fields corresponding to the appearance of these anomalies substantially exceed the fields at which the permittivity  $\epsilon'_r(E_-)$  reaches maxima; i.e., they are stronger than the effective coercive fields for this material. It seems likely that these features are caused by the following factors.

(1) A gradual increase in the permittivity  $\epsilon'_r(E_-)$  with a decrease in the magnitude of the polarizing field  $E_-$  from  $-E_{\text{max}}$  to zero is most likely due to an increasing contribution to the permittivity from non-180-degree domain walls (the main contribution) and 180-degree domain walls of both "persistent" and newly arising domains. New, usually tapered, domains [14] appear in ferroelectric ceramics upon switching off the external field  $E_-$  owing to residual mechanical stresses and, possibly, remanent electric fields, which lead to a partial breakdown of nearly single-domain states formed in strong fields  $E_-$ . The application of the electric field  $E_-$  with opposite sign encourages the growth of these domain and the formation of new  $a$  domains and a number of  $c$  domains. In electric fields  $E_- \approx E_c$ , the domain walls of these domains make the maximum contribution, which is reflected in the appearance of the maximum in the dependence  $\epsilon'_r(E_-)$  at the given field strength ( $E_- \approx E_c$ ).

(2) A further increase in the magnitude of the field  $E_-$  (above the maximum of  $\epsilon'_r$ ) is attended by a considerable decrease in the permittivity  $\epsilon'_r(E_-)$ . This can be explained by the rotation of non-180-degree domains (i.e., by the transformation of  $a$  domains into  $c$  domains with a substantially smaller permittivity  $\epsilon'$  [15]) and a further formation of the 180-degree domain structure, which results in pinning of 90-degree domains and piezoelectric clamping of 180-degree antiparallel domains (the well-known Drougard–Joung effect [16]). Note that the switching of domain walls due to the Drougard–Joung effect attains a maximum when the numbers of these antiparallel domains are equal to each other. In our case, this situation is observed at a certain field  $E_- > E_c$  and leads to the appearance of the minimum in the curve  $\epsilon'_r(E_-)$  (Fig. 1). The stronger fields  $E_-$  give rise to a unipolar domain state, and the clamping of domains is eliminated in part. As a consequence, the

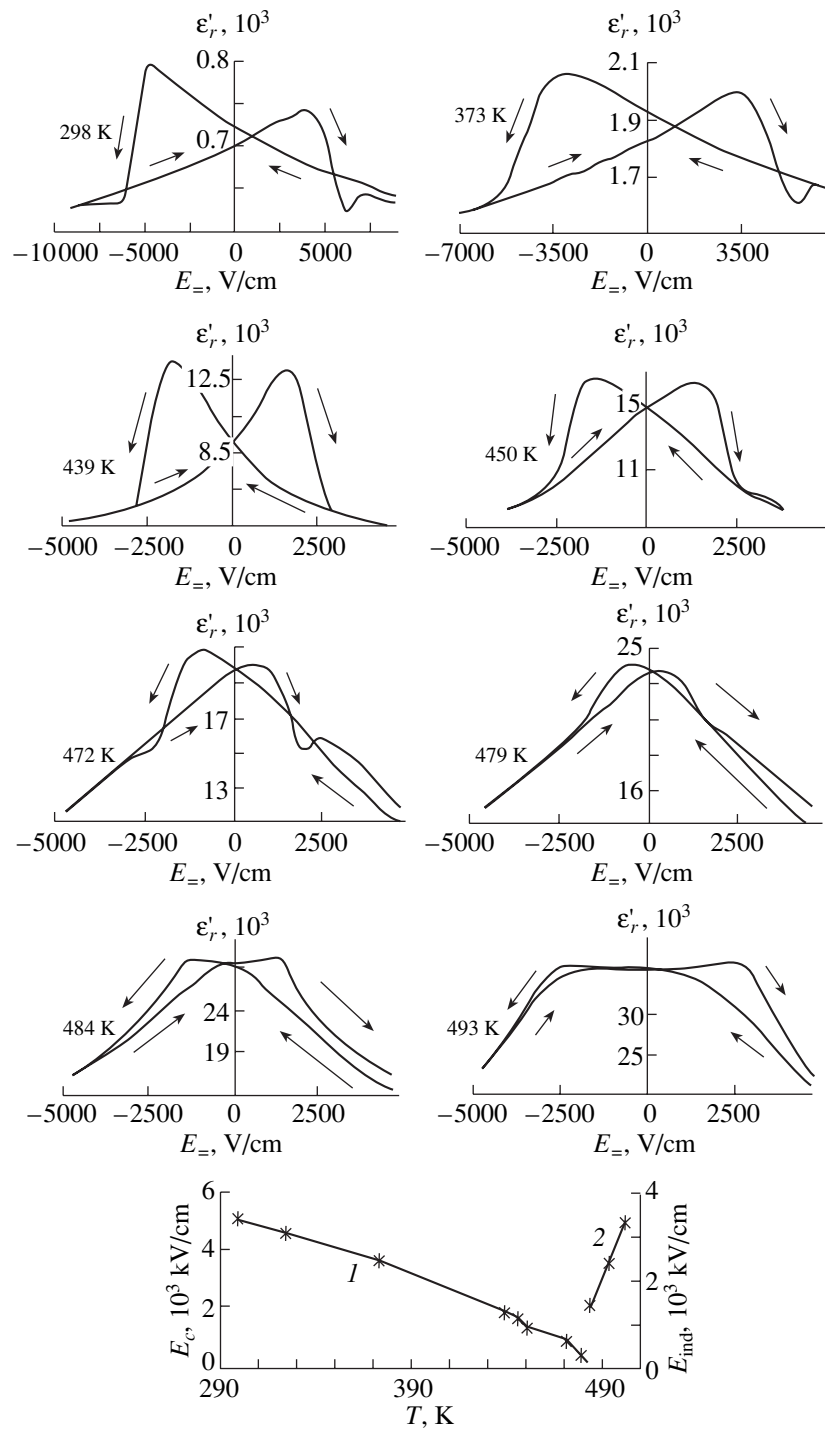


**Fig. 1.** Reverse dependences  $\epsilon'_r(E_{\pm})$  at different temperatures and the temperature dependences of (1) the coercive field  $E_c(T)$  and (2) the induction field  $E_{ind}(T)$  for the multicomponent ferroelectric ceramics based on lead zirconate titanate.

permittivity  $\epsilon'_r(E_{\pm})$  slightly increases and the local minimum in the curve  $\epsilon'_r(E_{\pm})$  at  $E_{\pm} > E_c$  becomes more pronounced (Fig. 1). A further decrease in the permittivity  $\epsilon'_r(E_{\pm})$  at  $E_{\pm} \rightarrow +E_{max}$  is primarily caused by a

decrease in the concentration of domain walls upon polarization of the material in a strong bias field.

Since no local minimum in the dependence  $\epsilon'_r(E_{\pm})$  is revealed at temperatures close to the  $T_d$  point, the tem-

perature  $T_d$  can be treated as the most probable temperature of a smeared phase transition from one ferroelectric phase (hypothetically, rhombohedral) to another ferroelectric phase (hypothetically, tetragonal). The same situation was observed for ferroelectric ceramics of this type in our previous works [3, 4]. It should be emphasized that the x-ray diffraction investigation performed by Konstantinov *et al.* [17] revealed a smeared phase transition of this kind in another PZT-based multicomponent system (similar to that studied in the present work), namely, PKR-7M. Note that the aforementioned smeared phase transition occurs irrespective of whether or not the bias field  $E_-$  is applied to the sample. In our case, the behavior of the dependence  $\epsilon_r'(E_-)$  can only suggest that, in the range of the hypothetical smeared phase transition, relatively weak external (electric or mechanical) fields can rather easily change the phase (domain) state of the material owing to an appreciable lability of the crystal lattice. As a result, in the transition range (i.e., at  $T \approx T_d$ ), the processes associated with changes in the phase and domain states in the piezoelectric ceramics under investigation can be superimposed on one another and lead to a certain “weakening” (suppression) of the clamping of 180-degree antiparallel domains. However, in the case when the temperature reaches the range of the existence of the stable crystal and domain structures, the Drougard–Joung effect again rather clearly manifests itself, as can be seen from the curves  $\epsilon_r'(E_-)$  in the temperature range  $T_d < T < T_m$  (Fig. 1). Aleshin and Luchaninov [18] carried out a numerical simulation of the domain clamping and proved that the clamping effect weakens at a high mobility (compliance) of domain (interphase) boundaries. Making allowance for the fact that such a high compliance is achieved in the vicinity of any phase transition, the above factors responsible for the disappearance of the local minimum in the dependence  $\epsilon_r'(E_-)$  at temperatures  $T \approx T_d$  and  $T \approx T_m$  suggest the occurrence of a phase transition in the vicinity of  $T_d$ , which is in good agreement with the inferences drawn in [18].

In the temperature range  $T \geq T_m$ , the heating of the material studied can be attended by a phase transition from the tetragonal ferroelectric phase to a macroscopically nonpolar phase, as is the case with PKR-7M [17]. Earlier [19], we demonstrated that the temperature range  $T \geq T_m$  in ceramics of this type can be characterized as the range of existence of a superparaelectric phase. The superparaelectric phase can be considered a paraelectric phase with fluctuating polar nanoregions [20] which are responsible for the extremely high polarizability of the material. This inference agrees well with the structural data obtained in [17] for PKR-7M, according to which the cubic phase and the so-called secondary phase composed of an aggregate of polar microregions coexist in the temperature range from  $T_m$  to temperatures more than 100 K above the  $T_m$

point. In the present work, the high polarizability of the system at  $T > T_m$  can be judged from the behavior of the reverse dependences  $\epsilon_r'(E_-)$  at temperatures that correspond to the appearance of a pronounced nonlinearity in the curve  $\epsilon_r'(E_-)$  at certain fields  $E_- = E_{\text{ind}}$ . As is clearly seen from the temperature dependence  $E_{\text{ind}}(T)$  plotted in Fig. 1 (curve 2), the field  $E_{\text{ind}}$  increases with an increase in the temperature. In our opinion, this field represents an induction field in which the macroscopically polar phase is induced from the nonpolar phase in much the same manner as in relaxors.

Therefore, unlike the aforementioned relaxors with a sole strongly smeared phase transition [2, 7, 10], in the piezoelectric ceramics, we deal with two smeared phase transitions: one transition occurs in the vicinity of the temperature  $T_d$  and is associated with the coexistence of two ferroelectric phases, and the other (conventional) transition is observed in the vicinity of  $T_m$ . Note that the temperature  $T_m$  for the piezoelectric ceramics under investigation can, to some extent, characterize the mean temperature of the high-temperature smeared phase transition.

The assumption that the piezoelectric ceramics undergoes two phase transitions can be confirmed, in particular, by the behavior of the dependence  $E_c(T)$  (Fig. 1, curve 1). It is seen from Fig. 1 that this dependence at temperatures  $T_d$  and  $T_m$  exhibits clearly defined steps, which, as a rule, are observed upon phase transitions [14].

The results of investigations into the influence of the sample prehistory on the polarization and depolarization currents in the piezoelectric ceramics (Fig. 2) also indicate that this material can undergo two smeared phase transitions. As is clearly seen from Figs. 2b–2d, the long-term ageing (like the application to the field) leads to the appearance of two anomalies in the form of maxima in the curve  $I(T)$ ; more specifically, one maximum is observed in the vicinity of the temperature  $T_d$  and the other maximum is located in the vicinity of the temperature  $T \approx T_m$  determined at a frequency of 1 kHz. It should be noted that, in the case of preliminary thermal annealing, the maximum in the dependence  $I(T)$  is observed only at a temperature  $T \approx T_{m(1 \text{ kHz})}$  (Fig. 2a). Similar results were obtained in our recent studies on electric currents in different ferroelectric ceramics with smeared phase transitions, namely, in PLZT-8/65/35, lead barium scandium niobate (PBSN-4) [21, 22], and SBN-75 single crystals [23]. In these works, the above behavior of the dependence  $I(T)$  was explained by the fact that, in the course of ageing, specific polar clusters (microelectrets [24, 25] or the so-called tweed structures [26]) are formed over a wide range of smeared phase transition temperatures. Most likely, these clusters are typical of heterogeneous structures, i.e., the structures characterized by the coexistence of different phases. This is particularly supported by the fact that structures of the tweed type were found for the first

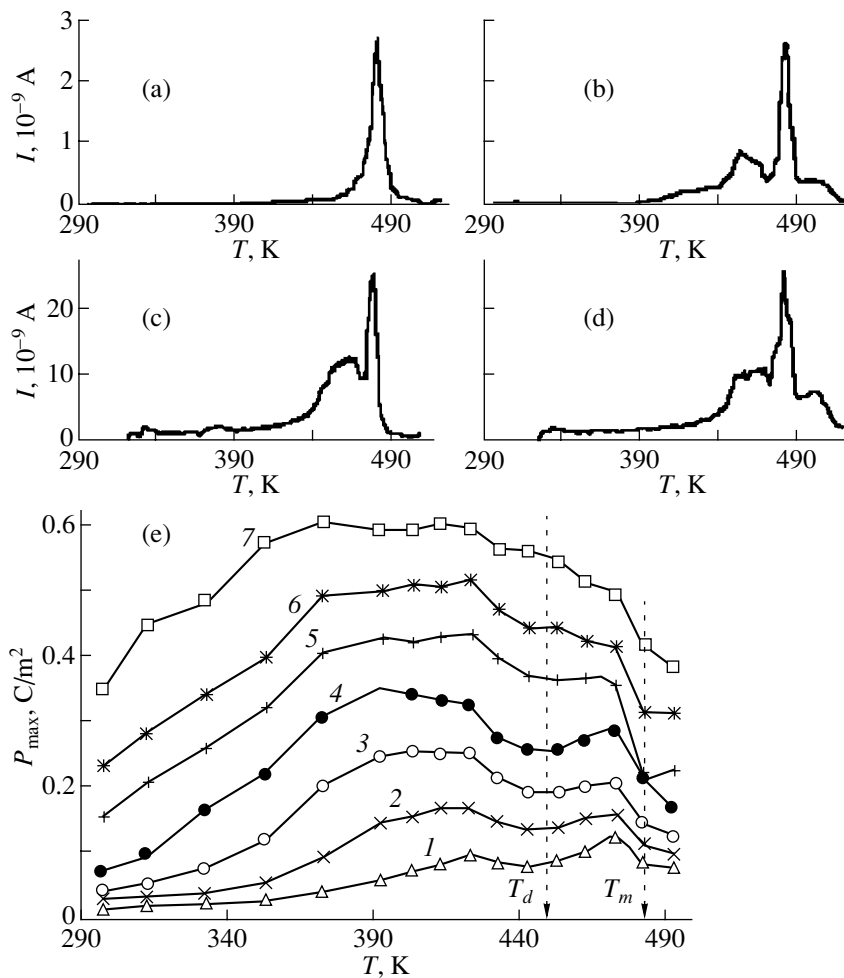


**Fig. 2.** Temperature dependences of (a–d) the current  $I(T)$  and (e) the maximum polarization  $P_{\max}(T)$  for the multicomponent ferroelectric ceramics based on lead zirconate titanate. The currents are measured upon heating of samples with different prehistories: (a) after annealing for 1 h at  $T > T_m$  and cooling to room temperature ( $T_r$ ), (b) after annealing at  $T > T_m$  and ageing for one month at  $T_r$  without preliminary polarization, (c) after cooling of the sample from  $T > T_m$  to  $T_r$  in the dc electric field  $E_{\pm} = 2.23$  kV/cm, and (d) after cooling of the sample from  $T > T_m$  to  $T_r$  in the dc electric field  $E_{\pm} = -4.46$  kV/cm. The polarizations  $P_{\max}$  are determined according to the data taken from [4] on polarization loops measured at a frequency of 0.1 Hz and different fields  $E_0$ , V/cm: (1) 1730, (2) 3400, (3) 4243, (4) 5072, (5) 5937, (6) 6785, and (7) 8412.

time in martensitic materials (see, for example, [27]). The coexistence of the polar and nonpolar phases over a very wide range of temperatures (down to liquid-helium temperature) is characteristic of the aforementioned ferroelectric materials with smeared phase transitions. In our case (piezoelectric ceramics), two different polar phases coexist in the vicinity of the temperature  $T_q$ . This can result in the formation of mesoscopic structures, such as microelectrets, fractal clusters, tweeds, etc. In turn, the formation of these structures can be attended by an increase in the internal electric fields inducing self-polarization processes. The fact that, during ageing, the thermally annealed piezoelectric ceramic sample becomes partially unipolar due to the induction of considerable internal fields is confirmed by the qualitative similarity of the behavior of the currents in this sample and the sample preliminarily

polarized in an external electric field (Figs. 2c, 2d). Although the currents in the latter case are several times heavier, they are comparable to those in the aged sample. In our opinion, this could indicate that the internal fields induced in the material during ageing are comparable to the fields generated as a result of polarization in an external field.

Therefore, we can state that the anomalies observed in the current in the temperature range  $T \approx T_d$  upon heating of the polarized or aged sample are caused by the change in the polarization state of the material due to the phase transition. This inference is supported by the behavior of the temperature dependences of the maximum polarization  $P_{\max}(T)$  for the given piezoelectric ceramics (Fig. 2e). The polarizations  $P_{\max}$  were determined according to the data taken from our earlier work

[4], in which we analyzed the temperature evolution of the polarization loops at different frequencies and amplitudes of the measuring field (the polarizations  $P_{\max}$  at a frequency of 0.1 Hz are presented in Fig. 2e).

It can be seen from Fig. 2e that certain of the dependences  $P_{\max}(T)$  are characterized by a temperature range (433–463 K) in which the anomalies manifest themselves in the form of local minima or plateaus. The temperature that corresponds to the beginning of the steepest decrease (step) in the polarization  $P_{\max}(T)$  virtually coincides with the temperature at which the current  $I(T)$  noticeably increases in the range  $T \leq T_d$ . The second (high-temperature) step in the dependence  $P_{\max}(T)$  is observed in the vicinity of the high-temperature maximum in the dependence  $I(T)$  (i.e., at  $T \approx T_{m(1 \text{ kHz})}$ ). It should be emphasized that the current was measured under dynamic conditions upon heating at the rate  $V_T = 1 \text{ K/min}$ , whereas the polarization  $P_{\max}(T)$  was determined under quasi-static conditions (the rate was decreased to 0.1 K/min in measurements of the polarization loop family at a specified temperature [4]). It is quite possible that this is the reason for the shift of both the low-temperature and high-temperature maxima in the dependence  $I(T)$  toward the high-temperature range with respect to the temperatures of the steps in the curves  $P_{\max}(T)$ . Indeed, it is well known (see, for example, [28]) that the heating rate substantially affects not only the magnitude of the current but also the position of the maximum in the dependence  $I(T)$  [the higher the heating rate, the higher the temperature of the maximum in the curve  $I(T)$ ].

At the same time, it should be noted that an increase in the field amplitude  $E_0$  in measurements of the polarization loops leads to a considerable increase in the maximum polarization  $P_{\max}(T)$ . The polarization  $P_{\max}(T)$  in the temperature range of the plateau increases more rapidly compared to that in the range of the high-temperature step. As a consequence, the local minimum or the plateau in the dependence  $P_{\max}(T)$  gradually disappears in the strongest fields. Specifically, only the high-temperature step and one very smeared maximum can be distinguished in curve 7 (Fig. 2e). This increase in the polarization  $P_{\max}(T)$  with an increase in the amplitude  $E_0$  is governed primarily by the dynamics of domain and interphase boundaries in the course of polarization and polarization switching. A similar inference was made in our earlier work [29], in which we investigated the PZT germanium-doped multicomponent ferroelectric ceramics related to the material studied in the present work. In [29], it was also established that the positions of plateaus or additional maxima in the temperature dependences of the effective permittivity  $\epsilon_{\text{eff}}^*(T) = P(T)/E_0$  substantially depend on both the field  $E_0$  and the measurement conditions (heating–cooling). For example, the temperature hysteresis of the effective permittivity  $\epsilon_{\text{eff}}^*(T)$  in the vicinity of the

low-temperature anomaly of  $\epsilon_{\text{eff}}^*(T)$  reached as high as 10 K, whereas the high-temperature maximum of  $\epsilon_{\text{eff}}^*(T)$  shifted by no more than 5 K.

Therefore, the data obtained in the present work, together with the results of other studies concerning multicomponent systems based on lead zirconate titanate, allow us to make the inference that the specific features revealed in the dielectric and polarization characteristics of the piezoelectric ceramics in the vicinity of the depolarization temperature  $T_d$  are associated with the phase transformation. Since the hypothetical structural phase transformation is a transition between two ferroelectric phases, the domain structure also undergoes transformation (we emphasize that this structure does not disappear, as is the case with relaxors at the temperature  $T_d$ ). On the other hand, as was noted by Isupov [30], the role played by the ceramic nature of the material under investigation (grain misorientation, spread in composition, etc.) in the electrical properties cannot be ruled out.

#### 4. CONCLUSIONS

Thus, the results of our investigation can be summarized as follows.

(1) It is established that, in bias fields  $E_- > E_c$ , the reverse dependences  $\epsilon_r'(E_-)$  for the multicomponent ferroelectric ceramics based on lead zirconate titanate exhibit local minima due to piezoelectric clamping of antiparallel domains. These minima are observed in the entire temperature range, except for the temperatures close to  $T_d$  and  $T_m$ .

(2) The anomalies of the polarization and depolarization currents are revealed at  $T \approx T_d$  and  $T \approx T_m$ . The character of the anomalies observed in the currents at  $T \approx T_d$  is essentially dependent on the prehistory of the material.

(3) The assumption is made that the ferroelectric ceramics studied undergo two smeared phase transitions. One (low-temperature) transition occurs in the vicinity of  $T \approx T_d$  and represents the transition between two ferroelectric phases. The other (high-temperature) transition observed in the vicinity of the temperature  $T_m$  at a maximum of the permittivity is the transition from the ferroelectric phase to the superparaelectric (pseudocubic) phase.

#### REFERENCES

1. V. A. Isupov, *Izv. Akad. Nauk, Ser. Fiz.* **57** (3), 23 (1993).
2. Zuo-Guang Ye and Hans Schmid, *Ferroelectrics* **145**, 83 (1993).
3. A. V. Shil'nikov, I. V. Otsarev, V. N. Nesterov, *et al.*, *Izv. Akad. Nauk, Ser. Fiz.* **62** (7), 1334 (1998).
4. A. D. Danilov, A. V. Shil'nikov, A. I. Burkhanov, *et al.*, *Izv. Akad. Nauk, Ser. Fiz.* **64** (6), 1233 (2000).

5. Yu. N. Zakharov, G. M. Akbaeva, V. Z. Borodin, *et al.*, *Izv. Akad. Nauk, Ser. Fiz.* **64** (7), 1446 (2000).
6. A. I. Burkhanov, Author's Abstract of Candidate's Dissertation (Voronezhskii Politekhnikeskii Inst., Voronezh, 1989).
7. A. V. Shil'nikov, A. D. Danilov, A. I. Burkhanov, *et al.*, in *Abstract Book of the II International Seminar on Relaxor Ferroelectrics, Dubna, 1998*, p. 47.
8. A. V. Sopit, A. G. Luchaninov, A. V. Shil'nikov, and A. I. Burkhanov, *Izv. Akad. Nauk, Ser. Fiz.* **64** (8), 1658 (2000).
9. A. K. Tagantsev and A. E. Glazounov, *J. Korean Phys. Soc.* **32**, S951 (1998).
10. A. I. Burkhanov, A. V. Shil'nikov, A. V. Sopit, and A. G. Luchaninov, *Fiz. Tverd. Tela (St. Petersburg)* **42** (5), 910 (2000) [*Phys. Solid State* **42**, 936 (2000)].
11. Toshio Ogawa and Ayako Yamada, *J. Korean Phys. Soc.* **32**, S724 (1998).
12. A. V. Shil'nikov, I. V. Otsarev, A. I. Burkhanov, *et al.*, *Ferroelectrics* **247**, 205 (2000).
13. G. M. Akbaeva, A. Ya. Dantsiger, and O. N. Razu-movskaya, in *Proceedings of International Conference "Electroceramics IV," Aachen, Germany, 1994*, Book 1, p. 535.
14. F. Jona and G. Shirane, *Ferroelectric Crystals* (Pergamon, Oxford, 1962; Mir, Moscow, 1965).
15. B. Jaffe, W. R. Cook, and H. Jaffe, *Piezoelectric Ceramics* (Academic, New York, 1971; Mir, Moscow, 1974).
16. M. E. Drougard and D. R. Joung, *Phys. Rev.* **94** (6), 1561 (1954).
17. G. Konstantinov, Ya. Bogosova, and M. Kupriyanov, *Ferroelectrics* **131**, 193 (1992).
18. V. I. Aleshin and A. G. Luchaninov, *Vestn. Voronezh. Gos. Tekh. Univ., Materialoved.*, No. 1.8, 53 (2000).
19. A. V. Shil'nikov, I. V. Otsarev, A. I. Burkhanov, *et al.*, *Ferroelectrics* **235**, 125 (1999).
20. E. Cross, *Ferroelectrics* **151**, 305 (1994).
21. A. I. Burkhanov and A. V. Shil'nikov, in *Abstract Book of the III International Seminar on Relaxor Ferroelectrics, Dubna, 2000*, p. 95.
22. A. V. Shil'nikov, A. I. Burkhanov, Yu. N. Mamakov, *et al.*, *Izv. Akad. Nauk, Ser. Fiz.* **65** (8), 1142 (2001).
23. R. E. Uzakov, A. I. Burkhanov, and A. V. Shil'nikov, *J. Korean Phys. Soc.* **32**, S1016 (1998).
24. A. I. Burkhanov, in *Proceedings of the International Workshop "Relaxation Phenomena in Defect Structures of Solids," Voronezh, 1996*, Part 1, p. 89.
25. A. I. Burkhanov, A. V. Shil'nikov, and R. É. Uzakov, *Kristallografiya* **42** (6), 1069 (1997) [*Crystallogr. Rep.* **42**, 993 (1997)].
26. D. Viehland, M. Y. Kim, Z. Xu, and Jie-Fang Li, in *Proceedings of International Conference "Electroceramics V," University of Aveiro, Portugal, 1996*, Book 1, p. 97.
27. I. M. Robertson and C. M. Wayman, *Philos. Mag. A* **48**, 421 (1983); **48**, 443 (1983); **48**, 629 (1983).
28. Yu. A. Gorokhovatskiĭ and G. A. Bordovskii, *Thermoactivated Current Spectroscopy of High-Resistance Dielectrics and Semiconductors* (Nauka, Moscow, 1991).
29. A. V. Shil'nikov, I. V. Otsarev, A. I. Burkhanov, *et al.*, *Ferroelectrics* **222**, 311 (1999).
30. V. A. Isupov, *Fiz. Tverd. Tela (Leningrad)* **22**, 172 (1980) [*Sov. Phys. Solid State* **22**, 98 (1980)].

*Translated by O. Borovik-Romanova*

## MAGNETISM AND FERROELECTRICITY

# Piezoresistive Effect in Polycrystalline Ferroelectric Semiconductors

A. N. Pavlov and I. P. Raevskii

Research Institute of Physics, Rostov State University, pr. Stachki 194, Rostov-on-Don, 344104 Russia

Received November 30, 2001

**Abstract**—The influence of domain reorientations on the piezoresistivity of polycrystalline ferroelectric semiconductors under mechanical stresses is investigated. It is demonstrated that the inclusion of 90° domain reorientations in the analysis of the potential barriers formed at the grain boundaries leads to correct determination of the magnitude and sign (positive under compression and negative under tension) of the piezoresistive coefficients for BaTiO<sub>3</sub>. © 2002 MAIK “Nauka/Interperiodica”.

### 1. INTRODUCTION

Polycrystalline ferroelectric semiconductors that exhibit the so-called effect of the positive temperature coefficient of resistance, or the posistor effect (i.e., a drastic increase in the electrical resistance  $R$  upon transition from a ferroelectric state to a paraelectric state), also manifest the piezoresistive effect (pressure dependence of the resistance  $R$ ) [1]. The piezoresistive effect is characterized by the piezoresistive coefficient  $\pi = (1/R)(\partial R/\partial \sigma)$ , where  $\sigma$  is the mechanical stress. For polycrystalline ferroelectric semiconductors, the piezoresistive coefficient  $\pi$  substantially increases (to  $10^3$  cm<sup>2</sup>/MN) at temperatures close to the ferroelectric–paraelectric phase transition temperature  $T_c$  [1] as compared to the coefficients  $\pi$  for other materials. For example, the piezoresistive coefficient  $\pi$  for germanium and silicon at 20°C does not exceed 10 cm<sup>2</sup>/MN and decreases proportionally to  $T^{-1}$  [2]. Capurso and Schulze [3] noted that, for polycrystalline ferroelectric semiconductors, the piezoresistive coefficient measured along the compression axis over the entire temperature range under investigation satisfies the condition  $\pi = \pi_c > 0$  (Fig. 1a, curve 1). Guntersdorfer and Heywang [4] revealed that, at higher applied pressures, the coefficient  $\pi_c$  changes sign with variations in the temperature (Fig. 1b). A similar inversion of the sign of the piezoresistive coefficient  $\pi$  measured along the compression axis was observed by Gurevich [5]. It was found that the piezoresistive coefficient measured along the tension axis has negative sign:  $\pi = \pi_t < 0$  [5] (Fig. 1a, curve 2); the same sign of the coefficient  $\pi$  measured normally to the compression axis is observed for polycrystalline ferroelectric semiconductors under uniaxial compression [5]. As was shown in [3], a decrease in the posistor effect of polycrystalline ferroelectric semiconductors is attended by a decrease in the piezoresistivity at temperatures close to the  $T_c$  point. In [6–8], the behavior of the piezoresistive coefficient  $\pi$  in the paraelectric phase was satisfactorily described in

the framework of the Heywang model [9] and the thermodynamic theory of ferroelectricity [10]. However, the temperature behavior of the piezoresistive coefficient  $\pi$  in the ferroelectric phase, i.e., the drastic increase in the value of  $\pi$  as the temperature  $T_c$  is

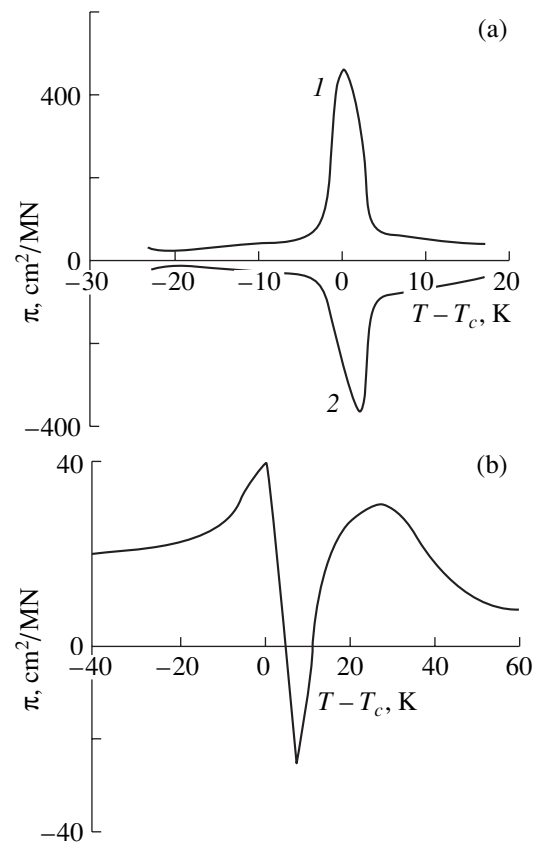


**Fig. 1.** Typical temperature dependences of the piezoresistive coefficients  $\pi$  for BaTiO<sub>3</sub> under (a) (1) uniaxial compression and (2) uniaxial tension at  $\sigma = 10$  MPa [3] and (b) uniaxial compression at  $\sigma = 25$  MPa [4].

approached (Fig. 1a), has defied explanation in terms of the Heywang model [9]. In our earlier work [11], we found experimentally that the domain reorientations have an extremely strong effect on the resistance  $R$  of polycrystalline ferroelectric semiconductors. In this respect, the purpose of the present work was to analyze theoretically how the transformation of the domain structure under external mechanical stresses affects the piezoresistive coefficient  $\pi$ .

## 2. DESCRIPTION OF THE MODEL

For polycrystalline ferroelectric semiconductors, the resistance  $R$  is determined primarily by potential barriers formed at the grain boundaries owing to localized charged states of the acceptor type with the number density  $N_s$  and activation energy  $E_s$  [9]. The resistivity  $\rho$  of a crystal grain at small strengths of an external field inducing an electric current can be represented by the relationship

$$\rho = \frac{l_s}{qN_d k T \mu d} \exp \frac{q\phi_0}{kT}. \quad (1)$$

Here,  $\phi_0$  is the potential  $\phi$  at the grain boundary,  $\mu$  is the mobility of free charge carriers,  $q$  is the elementary charge,  $N_d$  is the number density of donors with a low activation energy,  $k$  is the Boltzmann constant,  $T$  is the temperature,  $d$  is the crystal grain size, and  $l_s$  is the thickness of the Schottky region, whose depletion in mobile charge carriers leads to complete neutralization of the surface charge at the grain boundary. The system of equations for determining the potential  $\phi_0$  involves

$$\nabla\phi = -E, \quad (2)$$

$$\epsilon_0 \nabla E = Q - \nabla P, \quad (3)$$

$$l_s Q = qn_s = \frac{qN_s}{1 + \exp[(E_F - E_s + q\phi_0)/kT]} \quad (4)$$

and the equation of state of the polarization  $P$ . The last equation takes into account the influence of an electric field of the charged grain boundary and can be derived from the minimum condition for the elastic thermodynamic potential  $\Phi$ , which can be written in the following form [8–10, 12]:

$$\begin{aligned} \Phi = & \frac{1}{2}\alpha(P_1^2 + P_2^2 + P_3^2) + \frac{1}{4}\beta_1(P_1^4 + P_2^4 + P_3^4) \\ & + \beta_2(P_1^2 P_2^2 + P_2^2 P_3^2 + P_1^2 P_3^2) + \frac{1}{6}\gamma_1(P_1^6 + P_2^6 + P_3^6) \\ & + \gamma_2(P_1^4(P_2^2 + P_3^2) + P_2^4(P_1^2 + P_3^2) + P_3^4(P_1^2 + P_2^2)) \\ & + \gamma_3 P_1^2 P_2^2 P_3^2 - (E_1 P_1 + E_2 P_2 + E_3 P_3) \\ & - q_{11}(\sigma_1 P_1^2 + \sigma_2 P_2^2 + \sigma_3 P_3^2) - q_{12}(\sigma_1(P_2^2 + P_3^2) \end{aligned} \quad (5)$$

$$\begin{aligned} & + \sigma_2(P_1^2 + P_3^2) + \sigma_3(P_1^2 + P_2^2)) \\ & - q_{44}(\sigma_4 P_2 P_3 + \sigma_5 P_1 P_3 + \sigma_6 P_1 P_2). \end{aligned}$$

Here,  $Q$  is the space-charge density in the Schottky region,  $E$  is the electric field strength,  $\epsilon_0$  is the dielectric constant,  $n_s$  is the density of filled localized states at the grain boundary, and  $E_F$  is the Fermi energy. For donor states with a low activation energy, the space-charge density is determined as  $Q = qN_d$ .

The potential barrier height  $q\phi_0$  depends on the degree of screening of localized charged states. The screening is provided both by conduction electrons with the number density  $N_d$  and through the response of the ferroelectric system. The low resistivity  $\rho$  in the ferroelectric phase, as compared to that in the paraelectric phase, indicates the important role played by screening processes due to the existence of the order parameter (the spontaneous polarization  $P_s$ ) and states corresponding to different directions of the spontaneous polarization  $P_s$  in the ferroelectric phase. The transition from one state to another (i.e., the polarization switching initiated by an external action, namely, the electric field  $E_b$  at the grain boundary) brings about the formation of an antiparallel domain with a zigzag domain wall [12]. Within this domain wall, the fields induced by a change in the direction of the polarization  $P$  and those created by the response of the electronic subsystem of the Schottky region, for the most part, compensate each other. Consequently, the resultant field is determined by thermoactivated processes responsible for changes in the direction of the spontaneous polarization  $P_s$  and is equal to the coercive field. After complete polarization switching, polarization occurs in fields whose strength is appreciably larger than that of the coercive field, because the polarization processes, unlike the polarization switching, are not attended by a thermoactivated transformation of the domain structure [12]. The posistor effect is observed in the case when the thickness  $l_s$  of the Schottky region does not exceed the size of the polarization switching region. In the ferroelectric state, the potential  $\phi_0$  is predominantly governed by the polarization switching and, at the same direction of the spontaneous polarization  $P_s$  in crystal grains with respect to their boundaries, can be approximated by the relationship

$$\phi_0 \approx l_s E_c \approx \frac{N_s E_c}{N_d}. \quad (6)$$

Here,  $E_c$  is the coercive field in which the spontaneous polarization  $P_s$  changes its direction due to thermoactivated processes [12]. The number density  $N_s$  is constant for a particular composition of the material. The coercive field  $E_c$  depends on the orientation of the spontaneous polarization  $P_s$  of the domains with respect to the grain boundaries, because this field is determined by the difference between the depths of the potential wells

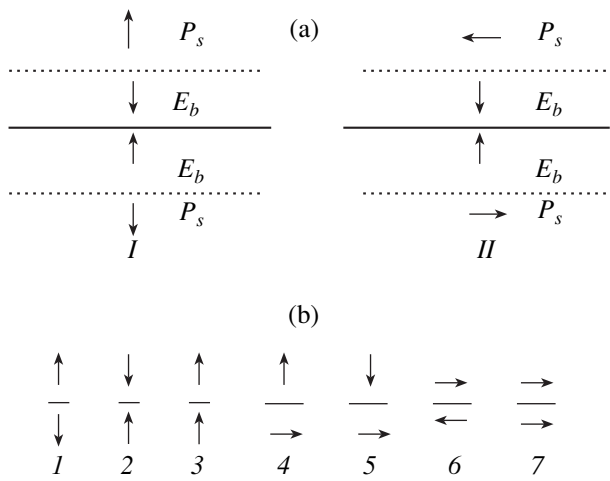


**Fig. 2.** Schematic representation of (a) the orientations of the spontaneous polarization  $P_s$  and the electric field  $E_b$  (arrows) with respect to the grain boundary (solid lines) and the Schottky region boundary (dotted lines) and (b) the orientations of the polarization  $P_s$  (arrows) in the bulk of adjacent crystal grains with respect to the grain boundary (solid lines).

for the states involved in the phase transition [12]. Specifically, for the tetragonal phase, the coercive field  $E_c = E_{c180}$  at a  $180^\circ$  reorientation of the spontaneous polarization  $P_s$  is equal to half the field  $E_c = E_{c90}$  at a  $90^\circ$  reorientation of the polarization  $P_s$ , even though the mechanical clamping of the domains upon  $90^\circ$  reorientation is disregarded. Therefore, the potential barrier  $q\phi_0$  depends on the mutual orientation of the spontaneous polarization  $P_s$  in the bulk of the adjacent crystal grains and on the electric field  $E_b$  induced by localized charged states at the grain boundaries. In particular, the potential barrier  $q\phi_0$  for the antiparallel orientation of  $P_s$  and  $E_b$  is less than that for the perpendicular orientation. As a result, the resistance  $R$  for charge transfer through the boundary of crystal grains with the spontaneous polarization  $P_s$  of configuration *I* (Fig. 2a) is less than that of configuration *II*. Note that crystal grains in a nonpolarized stress-free state have a complex domain structure. Let us now consider a ferroelectric placed in

Calculated resistivities  $\rho$  at the boundaries of crystal grains with different configurations of the orientations of the spontaneous polarization  $P_s$  (Fig. 2b)

Configuration no.	$\rho_i, \Omega \text{ cm}$	$n$
<i>I</i>	116	1
2	$9 \times 10^6$	1
3	$3.3 \times 10^4$	2
4	512	8
5	$8.3 \times 10^5$	8
6, 7	$10^5$	16

a rectangular system of coordinates. It is assumed that, in the ferroelectric under consideration, an electric current flows along the  $OY$  axis and a grain boundary (across which the current flows) lies in the  $XOZ$  plane. The main configurations that characterize the orientation of the spontaneous polarization  $P_s$  in adjacent crystal grains in the  $YOX$  plane are depicted in Fig. 2b. Moreover, proper allowance must be made for equivalent configurations (with respect to the potential barrier height) obtained from different combinations of rotations of configurations 3–7 (Fig. 2b) about the  $OX$  axis through an angle of  $180^\circ$  and about the  $OY$  axis through angles of  $90^\circ$ ,  $180^\circ$ , and  $270^\circ$ . From relationships (1)–(5), we calculated the resistivities of  $\text{BaTiO}_3$  crystal grains with potential barriers corresponding to different configurations with the following parameters:  $d = 5 \times 10^{-3} \text{ cm}$  [3],  $N_s = 3 \times 10^{14} \text{ cm}^{-2}$ ,  $E_s = 0.9 \text{ eV}$  [9],  $N_d = 4 \times 10^{17} \text{ cm}^{-3}$ ,  $E_{c180} = 480 \text{ V cm}^{-1}$  [10],  $\mu = 0.5 \text{ cm}^2 \text{ V}^{-1} \text{ s}^{-1}$  [13], and  $T = T_c - 5 \text{ K}$ . The results of these calculations are presented in the table ( $n$  is the number of equivalent configurations). The required coefficients of the thermodynamic potential (5) used to determine the polarization  $P$  were taken from [10]. The number densities  $N_s$  and  $N_d$  were determined by the best fitting of the calculated results to the experimental data obtained by Capurso and Schulze [3]. In this case, the constraints providing the validity of relationship (6) are satisfied. It should be noted that, in the nonpolarized stress-free state, all the configurations are equally probable and the resistivity  $\rho$  is inversely proportional to the electrical conductivity to which each configuration (Fig. 2b, configurations *I*–7) makes a contribution proportional to  $n$ . Hence, the resistivity  $\rho$  of the ferroelectric tetragonal phase in the stress-free state can be represented by the expression

$$\rho^{-1} = (\rho_1^{-1} + 8\rho_4^{-1})/36, \quad (7)$$

where  $\rho_1$  and  $\rho_4$  are the lowest resistivities for domain configurations shown in Fig. 2b.

According to Subbarao *et al.* [14], the application of the uniaxial stress  $\sigma$  brings about  $90^\circ$  rotations of the spontaneous polarization  $P_s$  of the domains involved. The most intensive rotations are observed in the phase transition range in which the degree of tetragonality of the crystal lattice decreases significantly. Let  $A$  be the fraction of domains in which  $90^\circ$  rotations of the polarization  $P_s$  occur under pressure ( $0 \leq A \leq 1$ ). For small fractions  $A$ , simultaneous rotations of the polarization  $P_s$  in adjacent domains involved in configurations *I*–7 (Fig. 2b) are improbable; hence, the change in the contribution of each configuration to the conductivity is proportional to  $A$ . With due regard for the data presented in the table, the resistivities of the ferroelectric tetragonal phase under uniaxial compression ( $\rho_c$ ) and uniaxial tension ( $\rho_t$ ) can be written as

$$\rho_c^{-1} = \rho^{-1} - A(\rho_1^{-1} + 2\rho_4^{-1})/18, \quad (8)$$

$$\rho_t^{-1} = \rho^{-1} + A(\rho_1^{-1} + 2\rho_4^{-1})/9. \quad (9)$$

Within the proposed model, the appropriate transformation of the relationship  $\pi = (\rho_\sigma - \rho)(\rho\sigma)$  (where  $\rho_\sigma$  and  $\rho$  are the resistivities under mechanical stresses and in the stress-free state, respectively) gives the following formulas for describing the piezoresistivity in the ferroelectric tetragonal phase:

$$\pi_c = \frac{A}{\sigma(K_c - A)}, \quad (10)$$

$$K_c = \frac{\rho_1^{-1} + 8\rho_4^{-1}}{2(\rho_1^{-1} + 2\rho_4^{-1})} \quad (11)$$

for uniaxial compression and

$$\pi_t = -\frac{A}{\sigma(K_t + A)}, \quad (12)$$

$$K_t = \frac{\rho_1^{-1} + 8\rho_4^{-1}}{4(\rho_1^{-1} + 2\rho_4^{-1})} \quad (13)$$

for uniaxial tension along the direction of the electric current.

### 3. COMPUTATIONAL RESULTS

In our calculations, we used relationships (10) and (11) and the experimental x-ray diffraction data on the degree of  $90^\circ$  domain reorientation under pressure in the tetragonal phase of the barium titanate ferroelectric ceramics at temperatures far from the phase transition range ( $A = 0.2$  at  $\sigma \cong 35$  MPa and  $T = 20^\circ\text{C}$ ) [14] and obtained the piezoresistive coefficient  $\pi_c \sim 190$  cm<sup>2</sup>/MN for BaTiO<sub>3</sub>. This value is in reasonable agreement with the experimental piezoresistive coefficient  $\pi_{c, \text{exp}} \sim 200$  cm<sup>2</sup>/MN determined for barium titanate ferroelectric ceramics at  $T = 20^\circ\text{C}$  in [1]. According to formulas (10)–(13), we have  $\pi_c > 0$ ,  $\pi_t < 0$ , and  $\pi_c > \pi_t$ , which also agrees well with the experimental data obtained in [3] (Fig. 1a). A comparison with the experimental data at  $\sigma = 10$  MPa leads to the following estimates:  $A \approx 0.3$ – $0.4$  at  $T = T_c$  and  $A \approx 0.06$  at  $T = T_c - 5$  K. Figure 3a shows the calculated dependences of the piezoresistive coefficient  $\pi$  on the fraction  $A$  for BaTiO<sub>3</sub> at  $\sigma = 10$  MPa and  $T = T_c - 5$  K. The calculated temperature dependences of the coefficient  $\pi$  at  $\sigma = 10$  MPa are plotted in Fig. 3b. The numerical calculations were performed with fractions  $A = 0.4$  at  $T = T_c$  and  $A = 0.06$  at temperatures below  $T_c$ . For temperatures corresponding to the paraelectric phase, the piezoresistive coefficient  $\pi$  was calculated using relationships (1)–(5). As can be seen from Figs. 1 and 3, our theoretical results (Fig. 3b) are in qualitative agreement with the experimental data (Fig. 1a). Therefore, the proposed model can be used in a more detailed analysis of the factors responsible for the piezoresistivity.

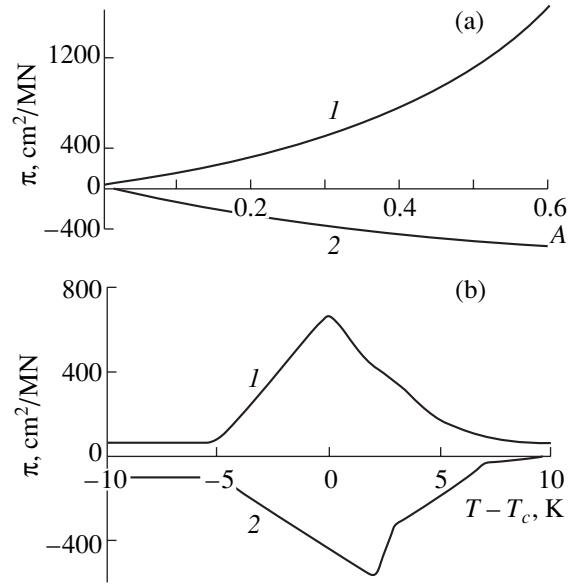


**Fig. 3.** Calculated dependences of the piezoresistive coefficient  $\pi$  on (a) the fraction of domains  $A$  at  $T = T_c - 5$  K and (b) the temperature  $T$  under (1) uniaxial compression and (2) uniaxial tension at  $\sigma = 10$  MPa.

Let us now analyze how the uniaxial compression and uniaxial tension along the direction of the electric current affect the electrical resistance of the ferroelectric tetragonal phase. Under compression,  $90^\circ$  rotations of the polarization  $P_s$  occur in domains at the boundary specifying the barrier to electric current. This leads to a decrease in the fraction of configurations 1 and 4 and an increase in the fraction of configurations 6 and 7 (Fig. 2b). As a result, we have  $\rho_c < \rho$  and  $\pi_c > 0$  (Figs. 1a, 3b, curves 1) because of the low values of  $q\phi_0$  for configurations 1 and 4 and high values of  $q\phi_0$  for configurations 6 and 7 (see table). The opposite situation occurs under uniaxial tension along the direction of the electric current; in this case, we obtain  $\rho_t < \rho$  and  $\pi_t < 0$  (Figs. 1a, 3b, curves 2). The same effect is observed under uniaxial compression in a direction perpendicular to the direction of the electric current. Now, we consider the influence of uniaxial compression and uniaxial tension along the direction of the electric current on the electrical resistance of the paraelectric phase. In the paraelectric phase, the spontaneous polarization in the bulk of crystal grains is absent; i.e.,  $P_s = 0$ . However, the ferroelectric polarization can be induced in the Schottky region by the electric field of grain boundaries at  $E > E_{pi}$  [portions  $A_i B_i$  ( $i = 1, 2, 3$ ) in Fig. 4]. This polarization contributes to the screening of the potential barrier. The compression hinders induction of the polarization along the compression direction by the electric field of grain boundaries, because the field  $E_{p3}$  of the transition to the induced ferroelectric state (Fig. 4, curve 3) is stronger than the field  $E_{p2}$  in the absence of mechanical stresses (Fig. 4, curve 2). Con-

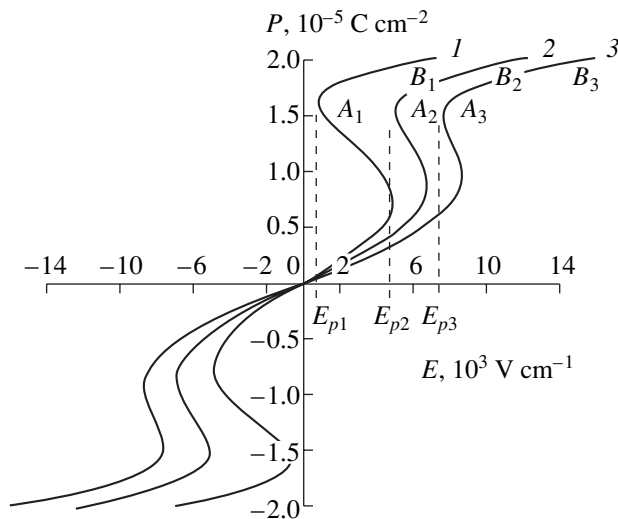


**Fig. 4.** Dependences of the polarization  $P$  on the electric field strength  $E$ : (1) uniaxial tension at  $\sigma = 10 \text{ MPa}$ , (2) the stress-free state, and (3) uniaxial compression at  $\sigma = 10 \text{ MPa}$ .  $T = T_c + 5 \text{ K}$ .

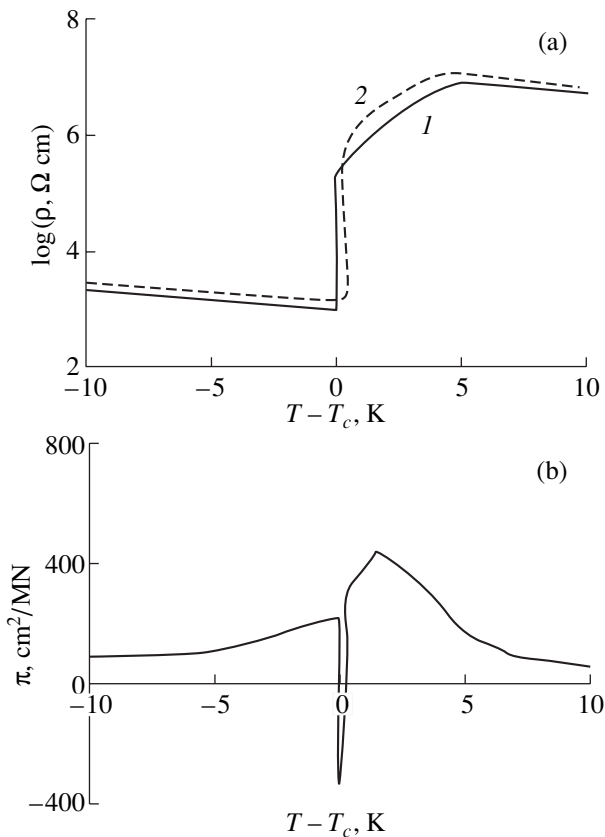


**Fig. 5.** (a) Calculated temperature dependences of the resistivity  $\rho$  (1) in the stress-free state and (2) under uniaxial compression at  $\sigma = 30 \text{ MPa}$  and (b) the calculated temperature dependence of the piezoresistive coefficient  $\pi$  under uniaxial compression at  $\sigma = 30 \text{ MPa}$ .

sequently, the degree of screening of the potential barrier decreases under uniaxial compression and  $\pi_c > 0$  (Fig. 1a, curve 1). The tension in the paraelectric phase facilitates induction of the polarization along the tension direction by the electric field of grain boundaries, because the field  $E_{p1}$  of the transition to the induced ferroelectric state (Fig. 4, curve 1) is weaker than the field  $E_{p2}$ . Therefore, under uniaxial tension, the degree of screening of the potential barriers along the direction of the electric current increases and  $\pi_t < 0$  (Figs. 1a, 3b, curves 2).

In polycrystalline ferroelectrics, the uniaxial compression affects the crystal grain volume and leads to an increase in the temperature  $T_c$  by  $\Delta T_c$ . As a consequence, in the limited temperature range  $T \in (T_c, T_c + \Delta T_c)$ , the resistivity  $\rho_c$  (Fig. 5a, curve 2) appears to be less than the resistivity  $\rho$  of the paraelectric phase in the stress-free state (Fig. 5a, curve 1); hence, we have  $\pi_c < 0$  (Fig. 5b). A theoretical estimate in terms of the thermodynamic potential (5) for uniaxial compression at high pressures ( $\sigma = 30 \text{ MPa}$ ) gives  $\Delta T_c = 21 \text{ K}$ . This value considerably exceeds  $\Delta T_c = 0.5 \text{ K}$ , which is calculated from the relationship  $\Delta T_c = 3.31 \times 10^{-16} \sigma$  obtained experimentally in [1]. This difference can be explained by ignoring the mechanical clamping of domains in the theoretical estimate. In our calculations of the resistivity  $\rho_c$  and the piezoresistive coefficient  $\pi_c$  for uniaxial compression at  $\sigma = 30 \text{ MPa}$ , we used the experimental value  $\Delta T_c$ . The results of these calculations are displayed in Fig. 5. The temperature dependence of the coefficient  $\pi_c$  at high pressures ( $\geq 30 \text{ MPa}$ ) exhibits complex behavior (Figs. 1b, 5b). For the ferroelectric phase at temperatures far from the temperature  $T_c$ , the change in the direction of the spontaneous polarization  $P_s$  under uniaxial compression results in a positive piezoresistive coefficient ( $\pi_c > 0$ ). In the phase transition range, an increase in the temperature  $T_c$  under compression leads to a change in the sign of the piezoresistive coefficient ( $\pi_c < 0$ ). In the paraelectric phase, the compression hinders the polarization and, correspondingly, the screening of the potential barriers along the direction of the electric current; consequently, the piezoresistive coefficient is positive ( $\pi_c > 0$ ). Since  $\Delta T_c$  is small at pressures  $\leq 10 \text{ MPa}$  and the resistance  $R$  increases gradually, no inversion of the sign of the coefficient  $\pi_c$  occurs in the vicinity of  $T_c$  and  $\pi_c > 0$  over the entire temperature range (Figs. 1a, 3b, curves 1). The uniaxial tension affects the crystal grain volume and leads to an increase in the temperature  $T_c$  for configuration 1 (Fig. 2b), providing the best screening of the potential barriers along the direction of the electric current; hence, we have  $\rho_t < \rho$ . As a result, under uniaxial tension, the negative piezoresistive coefficient ( $\pi_t < 0$ ) is observed over the entire ranges of temperatures and pressures (Figs. 1a, 3b, curves 2).

## 4. CONCLUSIONS

Thus, it has been demonstrated that, in polycrystalline ferroelectric semiconductors, the resistivity and the order parameter ( $P_s$ ) are affected by the same factors, because the screening of the potential barriers induced by charged grain boundaries is governed, to a large extent, by local perturbations of the spontaneous polarization  $P_s$  [12]. Consequently, the resistivity appears to be sensitive to external mechanical stresses due to both transformation of the domain structure under stresses and changes in the temperature range of the existence of the order parameter. In the case when the direction of the spontaneous polarization  $P_s$  in adjacent crystal grains is opposite to the direction of the electric field induced by the boundaries of these grains, the potential barrier heights are less than those in the case when these directions are perpendicular to each other.

As a result,  $90^\circ$  rotations of the polarization  $P_s$  in a number of domains under external uniaxial mechanical stresses lead to an increase in the electrical resistance  $R$  along the compression axis, whereas the electrical resistance along the tension axis decreases; moreover, the piezoresistive coefficient proves to be dependent on the degree of transformation of the domain structure.

## REFERENCES

1. O. Saburi, K. Wakino, and N. Fuzikawa, in *Semiconductors Based on Barium Titanate* (Tokyo, 1977; Énergoizdat, Moscow, 1982), p. 13, translated from Japanese.
2. K. Seeger, *Semiconductor Physics* (Springer-Verlag, Berlin, 1974; Mir, Moscow, 1977).
3. J. S. Capurso and W. A. Schulze, *J. Am. Ceram. Soc.* **81** (2), 337 (1998).
4. M. Guntersdorfer and W. Heywang, *Solid-State Electron.* **10**, 1117 (1967).
5. V. M. Gurevich, *Electroconductivity of Ferroelectrics* (Izd. Komiteta Standartov, Moscow, 1969).
6. A. Amin, *Phys. Rev. B* **40** (17), 11603 (1989).
7. A. B. Alles, M. W. Murphy, J. J. Symanski, *et al.*, *J. Appl. Phys.* **77** (10), 5322 (1995).
8. J. S. Capurso and W. A. Schulze, *J. Am. Ceram. Soc.* **87** (2), 347 (1998).
9. W. Heywang, *J. Am. Ceram. Soc.* **47** (10), 484 (1964).
10. G. A. Smolenskii, V. A. Bokov, V. A. Isupov, N. N. Kraïnik, R. E. Pasyukov, and M. S. Shur, *Ferroelectrics and Antiferroelectrics* (Nauka, Leningrad, 1971).
11. I. P. Raevskii, E. I. Bondarenko, A. N. Pavlov, *et al.*, *Fiz. Tverd. Tela (Leningrad)* **26** (4), 1219 (1984) [*Sov. Phys. Solid State* **26**, 741 (1984)].
12. A. N. Pavlov, I. P. Raevskii, and V. P. Sakhnenko, *Fiz. Tverd. Tela (St. Petersburg)* **42** (11), 2060 (2000) [*Phys. Solid State* **42**, 2123 (2000)].
13. Z. M. Lekhtser and É. V. Bursian, *Ferroelectrics* (LGPI, Leningrad, 1978), pp. 89–110.
14. E. C. Subbarao, M. C. McQuarry, and W. R. Buessem, *J. Appl. Phys.* **28** (10), 1194 (1957).

*Translated by O. Borovik-Romanova*

## MAGNETISM AND FERROELECTRICITY

# Ferroelectric Phase Transitions in $\text{Pb}_{0.96}\text{Ba}_{0.04}\text{Sc}_{0.5}\text{Nb}_{0.5}\text{O}_3$ and $\text{Pb}_{0.94}\text{Ba}_{0.06}\text{Sc}_{0.5}\text{Nb}_{0.5}\text{O}_3$ Solid-Solution Single Crystals

L. S. Kamzina\*, I. P. Raevskii\*\*, V. V. Eremkin\*\*, and V. G. Smotrakov\*\*

\*Ioffe Physicotechnical Institute, Russian Academy of Sciences,  
Politekhnicheskaya ul. 26, St. Petersburg, 194021 Russia

\*\*Institute of Physics, Rostov State University, Rostov-on-Don, 344090 Russia

Received October 23, 2001; in final form, December 18, 2001

**Abstract**—The optical properties of  $\text{Pb}_{0.96}\text{Ba}_{0.04}\text{Sc}_{0.5}\text{Nb}_{0.5}\text{O}_3$  (PBSN-4) and  $\text{Pb}_{0.94}\text{Ba}_{0.06}\text{Sc}_{0.5}\text{Nb}_{0.5}\text{O}_3$  (PBSN-6) single-crystal solid solutions were studied for the first time. It was shown that the spontaneous phase transition occurring in PBSN-4 with no electric field present is accompanied by a sharp minimum in optical transmission, which indicates the percolation nature of the transition. No sharp changes were observed in the temperature dependence of optical transmission in PBSN-6 single crystals with no electric field applied. However, a very weak electric field,  $\sim 0.4$  kV/cm, is sufficient to induce the ferroelectric state in PBSN-6 single crystals. It was shown that the destruction of the induced ferroelectric state is a first-order phase transition which is accompanied by an anomalously narrow peak in the small-angle light scattering intensity (or by a minimum in optical transmission) and occurs through the percolation mechanism. © 2002 MAIK “Nauka/Interperiodica”.

### 1. INTRODUCTION

The properties of compositionally ordered ferroelectrics, to which  $\text{PbB}'_{1/2}\text{B}''_{1/2}\text{O}_3$ -type compounds belong (where  $B'$  stands for Sc and  $B''$  stands for Nb, Ta), have recently attracted the increasing interest of researchers. This may be attributed primarily to the observation that the properties of these substances can change from those characteristic of normal ferroelectrics to relaxor properties without a change in their chemical composition. As a result of a high-temperature phase transition of the order–disorder type in the  $B'$  and  $B''$  ion distribution over equivalent crystallographic positions, the degree of order ( $s$ ) of the  $B'$  and  $B''$  ions in a compound can be different, depending on the actual thermal treatment of the samples or the growth temperature regime chosen [1, 2]. The lead scandiumniobate  $\text{PbSc}_{1/2}\text{Nb}_{1/2}\text{O}_3$  (PSN) single crystals belong to this class. Crystals with long-range order ( $s \approx 1$ ) undergo a sharp phase transition and do not exhibit the main features inherent in relaxor compounds. When the crystal is in a disordered state ( $s \rightarrow 0$ ), the ferroelectric phase transition becomes diffuse, but even in this case, a spontaneous phase transition from the relaxor (microdomain) to a macrodomain ferroelectric state takes place below the temperature at which the dielectric permittivity  $\epsilon$  is maximum. This spontaneous transition is identified with a jump in the temperature dependence  $\epsilon(T)$  [3] and with a small-angle light scattering (SAS) peak, which indicates the percolation nature of the phase transition [4, 5]. The relaxor state in partially ordered compounds ( $0 < s < 1$ ) exists in a fairly broad temperature region, thus offering a unique possibility to follow the relation between the conventional ferroelec-

tric and the relaxor behavior in one and the same compound, both in zero electric field and under the action of an external factor.

However, obtainment of a stable relaxor state similar to that observed in lead magnesiumniobate (PMN), a classical relaxor, has not been successful even with the  $\text{Sc}^{3+}$  and  $\text{Nb}^{5+}$  ions arranged in total disorder [6]. For a stable relaxor behavior to set in, the lattice must be additionally disordered. By increasing the lead vacancy concentration in ceramic PSN samples from a nominal level of 0.2–0.5 to 1.4–2 at. %, a quenched relaxor state can seemingly be reached. However, a spontaneous phase transition, although strongly diffused, does occur [6]. It remains unclear at what defect concentration the relaxor state can be quenched.

To enhance the relaxor properties in the PSN ceramic, an attempt was made in [7, 8] to partially substitute isovalent Ba ions for the Pb ions. The motivation was as follows: (i) in the case of a partial substitution of barium for lead, the concentration and uniformity of distribution of isovalent impurities is easier to control than in the case of lead vacancies, and (ii) it may be expected that as the barium content is increased, the stability of the relaxor state in PSN will gradually increase up to total quenching of this state.

Performing such studies on ceramic samples with different barium contents has met with obstacles because of the difficulties in obtaining  $\text{Pb}_{1-x}\text{Ba}_x\text{Sc}_{0.5}\text{Nb}_{0.5}\text{O}_3$  (PBSN) equilibrium solid solutions; these difficulties stem from the PSN and  $\text{BaSc}_{0.5}\text{Nb}_{0.5}\text{O}_3$  (BSN) having substantially different reactivities [9]. This difficulty was overcome by growing single-crystal samples of the  $\text{P}_{1-x}\text{B}_x\text{SN}$  solid solutions ( $0 < x < 0.58$ ) [10, 11]. The

temperature dependence of  $\epsilon$  of crystals with  $0 \leq x \leq 0.04$  was found to exhibit, slightly below the temperature at which the permittivity is maximum, a spontaneous phase transition from the relaxor to a macrodomain state, in which the features of both the normal ferroelectric and the relaxor behavior are retained. The spontaneous phase transition becomes manifest as a jump in  $\epsilon$  and the onset of birefringence [11]. Crystals with  $x > 0.08$  exhibited a typically relaxor behavior. Crystals with  $x = 0.06$  (PBSN-6) were assigned a particular place. These crystals occupied an intermediate position between crystals with normal ferroelectric properties (low barium content) and high-Ba-content compounds possessing typical relaxor properties. As a result, PBSN-6 crystals had a low enough threshold field to allow transition to the macrodomain ferroelectric state [12]. It is such compounds with a low threshold field that are most interesting from the standpoint of studying the effect of a static electric field on the dielectric and optical properties, because the field will affect the relaxor properties and the character of the spontaneous ferroelectric transition differently. The temperature dependences of the dielectric permittivity of PBSN-4 ( $x = 0.04$ ) and PBSN-6 single crystals and the effect of a static electric field on these dependence were studied in [11, 12]. The observed anomalies were not always distinct enough, which made their experimental detection difficult.

Optical methods, more specifically, optical transmission and SAS, are more sensitive in studying the processes occurring in phase transitions. These methods were employed by us to advantage in investigating the spontaneous ferroelectric phase transition in PSN and PST crystals [5, 13, 14] and the induced phase transition in the PMN and PZN relaxors [15]. The temperature dependence of the SAS intensity measured on stoichiometric PST and PSN crystals with different extents of ionic disorder exhibited a narrow peak at the temperature of the spontaneous ferroelectric phase transition in the absence of an electric field; in the PMN crystals, a narrow SAS peak was found to exist only with an electric field applied. If the phase transition is of the percolation type, then the average size of the new-phase cluster at the percolation threshold approaches the side of the sample and a large-scale nonuniform structure forms; in this case, the phase transition should be accompanied by the appearance of anomalously narrow SAS peaks and, hence, of a minimum in optical absorption. The presence of peaks in the temperature dependence of the SAS intensity indicates a percolation character of the transition between the relaxor and ferroelectric states. A theoretical description of anomalous light scattering in the vicinity of first- and second-order phase-transition temperatures in crystals with large-scale inhomogeneities can be found in [16].

The purpose of this study was to investigate the effect of a static electric field on the behavior of the ferroelectric and relaxor states in single crystals of both

PBSN-6 (in which a weak electric field is needed to induce a ferroelectric phase transition) and PBSN-4 (which exhibits a ferroelectric phase transition and relaxor behavior even in the absence of an electric field).

## 2. SINGLE-CRYSTAL GROWTH AND EXPERIMENTAL TECHNIQUE

PBSN-4 and PBSN-6 single crystals were grown by mass crystallization. The growth technique used and the x-ray and dielectric studies of these crystals were described in [10, 11]. The crystal samples, 0.3- to 0.8-mm thick plates with [100] faces, were transparent and yellowish in color. All measurements were carried out on samples that were not subjected to mechanical processing. A static electric field was applied in the [100] direction, and light was propagated along [001]. The electric field was applied in various regimes, namely, field-heating after field-cooling (FHaFC) and field-heating after zero-field-cooling (FHaZFC). After each field application, the subsequent measurement was preceded by annealing of the sample at 500°C for an hour. To obtain reproducible results and to avoid dielectric ageing (an effect observed in PBSN-6 crystals [11]), the dielectric and optical measurements were performed directly following the sample annealing. We studied optical transmission and SAS, which was measured in the transmission geometry [17]. The optical measurements were made with a He-Ne laser. The dielectric measurements were carried out at a frequency of 1 kHz. The sample temperature variation rate was 1.5 to 4.5°C/min.

## 3. EXPERIMENTAL RESULTS AND DISCUSSION

Figure 1 presents temperature dependences of the dielectric permittivity and optical transmission obtained on PBSN-4 single crystals under heating and cooling with no electric field applied. When the sample is heated, optical transmission curve 2 clearly shows a minimum at a temperature  $\sim 52^\circ\text{C}$ , whereas curve 1 exhibits only a fast rise (jump) in  $\epsilon$  at this temperature ( $T_s$ ), which is the point of spontaneous phase transition from the macrodomain to relaxor state [11]. As follows from [11], PBSN-4 crystals exhibit frequency dispersion of  $\epsilon$  and an increase in the temperature of the permittivity maximum with increasing measurement field frequency. Unlike  $T_{\epsilon_{\text{max}}}$ , the temperature position of the jump in  $\epsilon$  is virtually frequency-independent. The non-relaxation character of the spontaneous transition is supported by our optical and dielectric measurements, more specifically, by the coincidence between the minimum-transmission temperature  $T_s$  at zero field frequency and the fast rise in  $\epsilon$  at  $T_s$  at a frequency of 1 kHz. The minimum in optical transmission (or the maximum in SAS) indicates the formation of a large-scale inhomogeneous structure at this temperature and

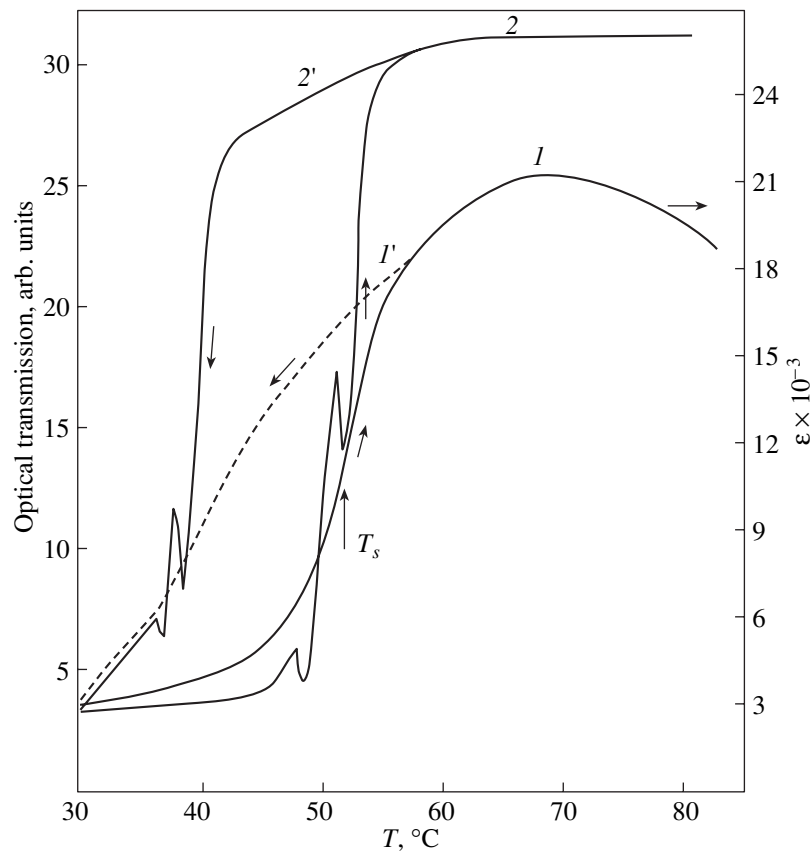


**Fig. 1.** Temperature dependences of (*I*, *I'*) dielectric permittivity and (*2*, *2'*) optical transmission obtained on single-crystal PBSN-4 under (*I*, *2*) heating and (*I'*, *2'*) cooling.

the onset of a spontaneous percolation-type phase transition. The temperature hysteresis of  $\sim 13^\circ\text{C}$  observed in the optical and dielectric measurements (Fig. 1) is one of the main features of a first-order phase transition. The temperature of the spontaneous transition is  $\sim 20^\circ\text{C}$

lower than the temperature of the maximum in  $\epsilon$ , which indicates that the relaxor state exists in this crystal in a fairly broad temperature interval. The temperature dependences of optical transmission for the PBSN-4 and PSN [5] crystals are identical.

The situation with the PBSN-6 crystal is radically different (Fig. 2). In the absence of an electric field, the optical transmission grows fairly smoothly with increasing temperature without any jumps and clearly pronounced maxima (curve *I*), a feature characteristic of purely relaxor compounds. The weak maxima at 28 and  $45^\circ\text{C}$  are most likely associated with the samples being inhomogeneous. The temperature dependence of  $\epsilon$  exhibits no significant anomalies other than the clearly seen maximum (curve *2*).

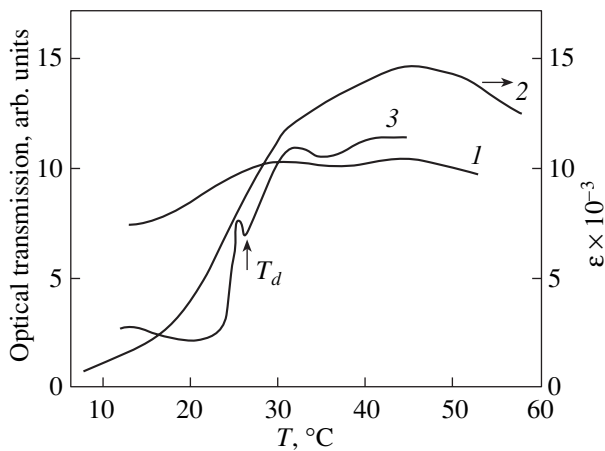


**Fig. 2.** Temperature dependences of (*I*, *3*) optical transmission and (*2*) dielectric permittivity ( $f = 1$  kHz) measured on a PBSN-6 single crystal in an electric field  $E_{\perp}$  equal to (*1*, *2*) 0 and (*3*) 0.45 kV/cm.

The pattern of optical transmission seen in the PBSN-6 crystal changes in an electric field. When an electric field  $E < E \approx 0.3$  kV/cm is applied in the FHaZFC regime, the transmission pattern does not show any changes as compared with the zero-field case. An electric field of  $E \sim 0.4$  kV/cm is high enough to change the character of the temperature dependence of optical transmission (curve *3*); namely, a jump in the intensity is observed and a minimum appears at a temperature of  $\sim 27^\circ\text{C}$ . The pattern of optical transmission in PBSN-6 in an electric field becomes similar to that

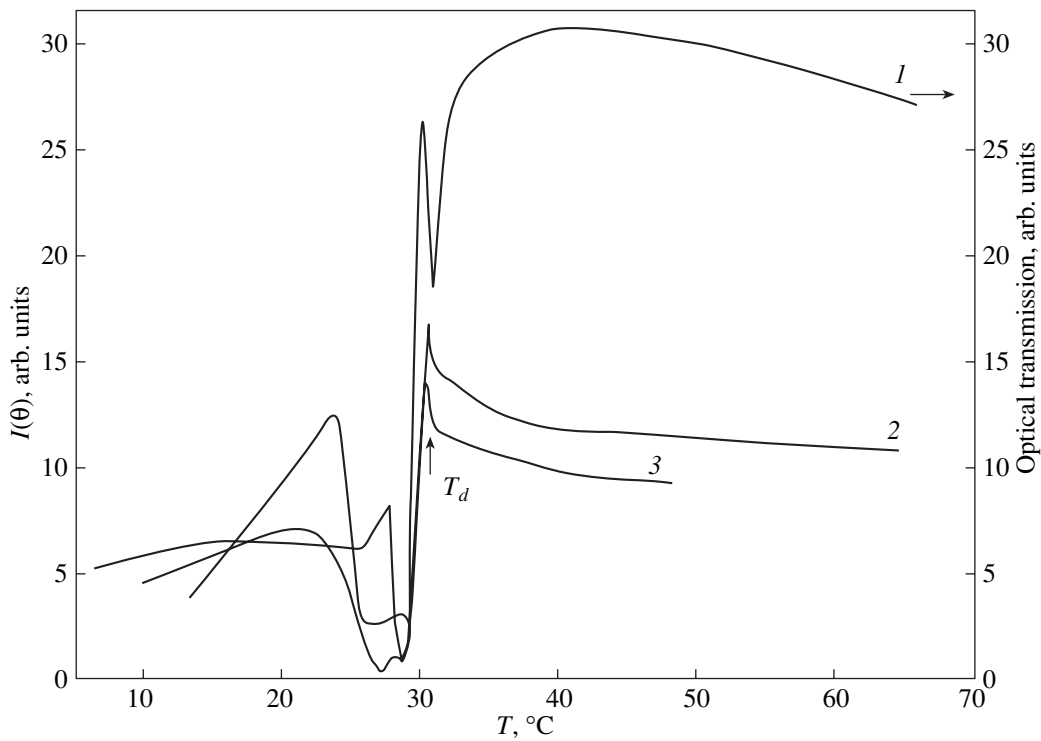


**Fig. 3.** Temperature dependences of (1) optical transmission and (2, 3) small-angle light scattering measured on a PBSN-6 single crystal in an electric field of 3.5 kV/cm applied under different conditions: (1, 2) FHazFC and (3) FHazFC. Scattering angle 30'.

for the PBSN-4 crystal with no electric field applied (curve 2 in Fig. 1). The observed minimum signals the formation of an induced large-scale structure and a ferroelectric state in an electric field in excess of a threshold level. The temperature position of the observed anomaly coincides with the depolarization temperature  $T_d$ , which was derived from dielectric measurements [11], and can be identified with destruction of the electric-field-induced ferroelectric phase.

The anomalies in the temperature dependences of optical transmission and of SAS intensity become more distinct in higher electric fields. Figure 3 displays temperature dependences of the optical transmission and SAS intensity  $I_\theta$  measured in the PBSN-6 crystal in an electric field of 3.5 kV/cm in both field application regimes, FHazFC and FHazFC. As seen from Fig. 3, at a certain temperature  $T_d$  corresponding to destruction of the ferroelectric state under cooling, the temperature dependence of the SAS intensity exhibits a narrow peak, indicating the percolation nature of this transition (curve 3). This temperature coincides, for the same electric field, with the destruction temperature of the ferroelectric state in the FHazFC regime. It should be noted that we did not succeed in deriving the temperature at which the ferroelectric state is induced in the FHazFC regime from our experiments on optical transmission carried out at a fixed sample heating rate. This is probably associated with the fact that, as follows from [12], the formation of the ferroelectric state is a

kinetic phase transition and requires a fairly long time for the equilibrium to set in.

In fields above 2 kV/cm, the depolarization temperature  $T_d$  increases linearly with the field in the PBSN-6

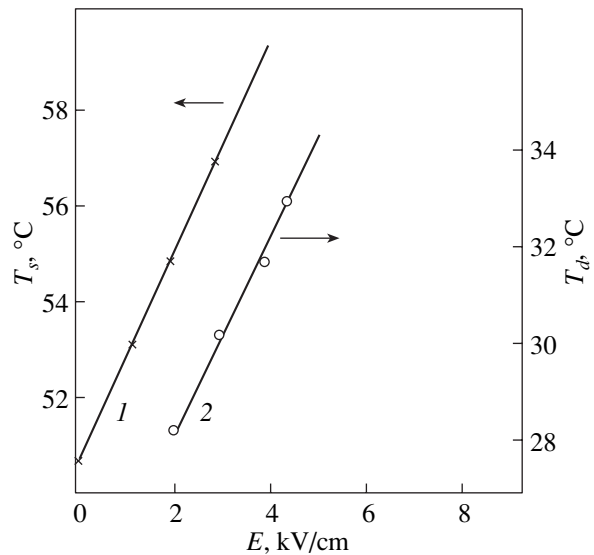


**Fig. 4.** Temperatures of (1) the spontaneous phase transition  $T_s$  for the PBSN-4 crystal and (2) destruction of the field-induced ferroelectric state  $T_d$  for PBSN-6 plotted as functions of the electric field.

crystal (curve 2 in Fig. 4). The temperature  $T_d$  was derived from the position of the maximum in the temperature dependence of the SAS intensity measured in various electric fields. Interestingly, in fields  $0.4 < E < 2$  kV/cm, the temperature  $T_d$  was virtually independent of the electric field. This is most likely connected with the samples being inhomogeneous. The peak in the temperature dependence of the SAS intensity at the destruction temperature of the field-induced ferroelectric phase, as well as the linear dependence of this temperature on electric field in fields above 2 kV/cm, implies that this transition is of the percolation nature and is first order. The occurrence of such a “weak” first-order transition during the destruction of the field-induced ferroelectric phase in the PLZT 9/65/35 ceramic was reported in [18]. We note that the transition from the field-induced ferroelectric to ergodic relaxor phase in the classical relaxors PMN and PZN is not of the percolation type [15].

The observed difference in the nature of the phase transition associated with destruction of the field-induced ferroelectric phase in PBSN-6 single crystals and in the classical relaxor PMN may originate from the fact that PBSN-6 single crystals are at the boundary of stability separating normal ferroelectrics from relaxors. When the barium concentration in PBSN increases and the relaxor state becomes more stable, the phase transition involving destruction of the field-induced ferroelectric state will apparently occur in the same way as it does in the PMN. Further studies are needed to support this conjecture. A linear dependence of the spontaneous phase-transition temperature on electric field was also observed by us within the field interval covered in PBSN-4 crystals (curve 1 in Fig. 4) and is similar to the corresponding relation for pure PSN [5].

#### ACKNOWLEDGMENTS

This study was supported by the Russian Foundation for Basic Research, project nos. 01-02-17801, 01-03-33119.

#### REFERENCES

1. N. Setter and L. E. Cross, *J. Appl. Phys.* **51** (8), 4356 (1980).

2. V. G. Smotrakov, I. P. Raevskii, M. A. Malitskaya, *et al.*, *Izv. Akad. Nauk SSSR, Neorg. Mater.* **19** (1), 123 (1983).
3. F. Chu, I. M. Reaney, and N. Setter, *J. Appl. Phys.* **77** (4), 1671 (1995).
4. L. S. Kamzina and A. L. Korzhenevskii, *Ferroelectrics* **131**, 91 (1992).
5. L. S. Kamzina and N. N. Kraïnik, *Fiz. Tverd. Tela (St. Petersburg)* **42** (9), 1664 (2000) [*Phys. Solid State* **42**, 1712 (2000)].
6. F. Chu, I. M. Reaney, and N. Setter, *Ferroelectrics* **151** (1–4), 343 (1994).
7. M. Ya. Dambekalne, K. Ya. Borman, A. R. Shternberg, *et al.*, *Izv. Ross. Akad. Nauk, Ser. Fiz.* **57** (3), 78 (1993).
8. C. Malibert, B. Dkhil, J. M. Kiat, *et al.*, *J. Phys.: Condens. Matter* **9**, 7485 (1997).
9. I. P. Pronin, T. Ayazbaev, N. V. Zaitseva, *et al.*, *Neorg. Mater.* **32** (12), 1528 (1996).
10. I. P. Raevskii, V. G. Smotrakov, V. V. Eremkin, *et al.*, *Ferroelectrics* **247** (1–3), 27 (2000).
11. I. P. Raevskii, V. V. Eremkin, V. G. Smotrakov, *et al.*, *Fiz. Tverd. Tela (St. Petersburg)* **42** (1), 154 (2000) [*Phys. Solid State* **42**, 161 (2000)].
12. I. P. Raevskii, M. A. Malitskaya, E. S. Gagarina, *et al.*, *Ferroelectrics* (in press).
13. L. S. Kamzina and A. L. Korzhenevskii, *Fiz. Tverd. Tela (St. Petersburg)* **34** (6), 1795 (1992) [*Sov. Phys. Solid State* **34**, 957 (1992)]; L. S. Kamzina, A. L. Korzhenevskii, N. N. Kraïnik, and L. M. Sapozhnikova, *Izv. Akad. Nauk SSSR, Ser. Fiz.* **54** (4), 614 (1990).
14. L. S. Kamzina and A. L. Korzhenevskii, *Pis'ma Zh. Éksp. Teor. Fiz.* **50** (3), 146 (1989) [*JETP Lett.* **50**, 163 (1989)].
15. L. S. Kamzina and N. N. Krainik, *Ferroelectrics* **223**, 27 (1999).
16. A. L. Korzhenevskii, *Fiz. Tverd. Tela (Leningrad)* **29** (9), 2754 (1987) [*Sov. Phys. Solid State* **29**, 1583 (1987)].
17. L. S. Kamzina, A. L. Korzhenevskii, and O. Yu. Korshunov, *Fiz. Tverd. Tela (St. Petersburg)* **36** (2), 479 (1994) [*Phys. Solid State* **36**, 264 (1994)].
18. V. Bobnar, Z. Kutnjak, R. Pirc, and A. Levstik, *Phys. Rev. B* **60** (9), 6420 (1999).

*Translated by G. Skrebtsov*

---

---

**LOW-DIMENSIONAL SYSTEMS  
AND SURFACE PHYSICS**

---

---

## Penetration of a Symmetric Light Pulse through a Wide Quantum Well

L. I. Korovin<sup>1</sup>, I. G. Lang<sup>1</sup>, D. A. Contreras-Solorio<sup>2</sup>, and S. T. Pavlov<sup>2,3</sup>

<sup>1</sup> Ioffe Physicotechnical Institute, Russian Academy of Sciences, Politekhnikeskaya ul. 26, St. Petersburg, 194021 Russia

<sup>2</sup> Escuela de Fisica de la UAZ, Apartado Postal c-580, Zacatecas, 98060 Mexico

<sup>3</sup> Lebedev Institute of Physics, Russian Academy of Sciences, Leninskii pr. 53, Moscow, 117924 Russia

e-mail: ilang@dor.ioffe.rssi.ru

e-mail: pavlov@ahobon.reduaz.mx

Received October 25, 2001

**Abstract**—The reflection, transmission, and absorption of a symmetric electromagnetic pulse whose carrier frequency is close to the frequency of the interband transition in a quantum well are calculated. The energy levels in the quantum well are assumed to be discrete, and one excited level is taken into account. Consideration is given to the case of a sufficiently wide quantum well when the pulse wavelength corresponding to the carrier frequency is comparable to the quantum well width and when allowance should be made for the dependence of the matrix element of the interband transition on the photon wave vector. The calculations are performed with due regard for the difference between the refractive indices of the material of the quantum well and the barrier at an arbitrary ratio of the reciprocal radiative to nonradiative lifetimes of the excited level of the electronic system. It is demonstrated that the inclusion of the spatial dispersion and the difference in the refractive indices most strongly affects the reflection of the electromagnetic pulse, because the reflection due to interband transitions in the quantum well is accompanied by an additional reflection from the quantum well boundaries. Compared to the previously considered model, the most radical changes in the reflection are observed in the case when the reciprocal nonradiative lifetime of the excited state is substantially longer than the reciprocal radiative lifetime. © 2002 MAIK “Nauka/Interperiodica”.

### 1. INTRODUCTION

In recent years, a number of works have been devoted to the investigation of variations in the shape of a light pulse in its penetration through a quantum well [1–7]. Consideration has been given to an asymmetric exciting pulse with a steep edge [1–3] and a symmetric pulse [4, 5]. In [1, 2, 5], analysis was performed under the assumption that the carrier frequency  $\omega_l$  of the exciting pulse is close to the frequency  $\omega_0$  of the electronic excitation (a two-level system). A three-level system [7] and a system with many excited states [3, 6] have also been studied. The results obtained in these works are valid for relatively narrow quantum wells when the following inequality is satisfied:

$$\kappa d \ll 1, \quad (1)$$

where  $d$  is the quantum well width and  $\kappa$  is the magnitude of the photon wave vector corresponding to the carrier frequency of the symmetric pulse. In actual fact, the parameter  $\kappa d$  in the aforementioned works was taken equal to zero and the calculated reflectance, absorptance, and transmittance were independent of the quantum well width  $d$ . The magnitude  $\kappa$  can be numerically estimated from the lasing wavelength of a gallium arsenide heterolaser. This wavelength is estimated to be  $0.8\mu$ , and the corresponding energy  $\hbar\omega_l$  is equal

to 1.6 eV. If the refractive index of the quantum well material is taken as  $n = 3.5$ , we have  $\kappa = n\omega_l/c = 2.8 \times 10^5 \text{ cm}^{-1}$ , where  $c$  is the velocity of light in free space. For the quantum well width  $d = 500 \text{ \AA}$ , we obtain the parameter  $\kappa d = 1.4$ . Therefore, in the case of sufficiently wide quantum wells, the contribution of the spatial dispersion of waves forming the exciting pulse can be significant.

For wide quantum wells, the inequality  $d \gg a_0$  (where  $a_0$  is the lattice constant) is very strong and the penetration of a pulse through the quantum well can be described by the Maxwell equations for a continuous medium. This approach requires inclusion of the difference between the refractive indices of the barrier and the quantum well. As a consequence, there should appear an additional reflection from the quantum well boundaries. This reflection decreases with a decrease in the parameter  $\kappa d$  but, in the range  $\kappa d \geq 1$ , in certain cases, can be equal or exceed the reflection due to resonant transitions in the quantum well. The change in the reflection of the light wave is accompanied by a change in its transmission. Therefore, account must be taken of both the difference in the refractive indices of the barrier and the quantum well and the dependence of the reflection and transmission on the parameter  $\kappa d$ . The aim of the present work was to analyze how these two factors affect the shape of the light pulse reflected

from a quantum well and the light pulse passed through it.

We consider a system composed of a deep semiconductor quantum well located in the range  $0 \leq z \leq d$  and two semi-infinite barriers. Analysis is carried out for an intrinsic semiconductor at zero temperature under the following assumptions: (i) the exciting light pulse propagates along the  $z$  axis from negative values of  $z$ , (ii) the barriers are transparent to the pulse, and (iii) the pulse is absorbed in the quantum well, thus inducing resonant interband transitions. Only the states in which one electron transfers from the valence band to the conduction band with the formation of a hole in the valence band are considered to be excited. It is assumed that  $\omega_l \cong \omega_g$  (the band gap in the quantum well is defined as  $E_g = \hbar\omega_g$ ) and a small fraction of valence electrons participates in the absorption. These electrons are located near the extremum of the band and can be adequately described by the effective mass method. For deep quantum wells, the electron tunneling into the barrier, in this case, can be ignored and the barrier can be regarded to be free of electrons. Moreover, the energy levels close to the quantum well bottom can be treated within the approximation of an infinitely deep well. The system under consideration is inhomogeneous. Since inequality (1) does not hold for wide quantum wells, the optical characteristics of this system should be determined from the solution of the Maxwell equations in which the current and charge densities should be expressed by the relationships derived in the framework of the microscopic approach [8, 9].

The final results are obtained for one discrete level of the electronic system in the quantum well. The influence of other levels on the reflection and absorption of light can be disregarded when the carrier frequency  $\omega_l$  is sufficiently close to the excitation frequency  $\omega_0$  of the chosen level and the other levels are sufficiently far from this level. The exciton levels in a zero magnetic field or the levels in a strong magnetic field perpendicular to the quantum well plane are discrete in the quantum well under the condition  $\hbar\mathbf{K}_\perp = 0$ , where  $\hbar\mathbf{K}_\perp$  is the vector of the total quasi-momentum of an electron-hole pair in the quantum well plane. As an example, we will examine the level of an electron-hole pair in a strong magnetic field aligned parallel to the  $z$  axis without regard for the Coulomb interaction between the electron and the hole. This interaction is considered a weak perturbation for sufficiently strong magnetic fields and not very wide quantum wells [10]. However, the exciton effect does not lead to radical changes in the results obtained and only affects the reciprocal radiative lifetime  $\gamma_r$  of the electronic excitation in the quantum well. The same is also true for the exciton levels in a zero magnetic field.

## 2. THE ELECTRIC FIELD INDUCED BY A PENETRATING PULSE

Let us assume that a symmetric exciting pulse is incident on a single quantum well from negative values of  $z$ . The circularly polarized electric field that corresponds to this pulse can be represented in the form

$$\mathbf{E}_0(z, t) = \mathbf{e}_l E_0 \exp(-i\omega_l t) \times \{ \Theta(p) e^{-\gamma_l p/2} + [1 - \Theta(p)] e^{\gamma_l p/2} \} + \text{c.c.} \quad (2)$$

Here,  $E_0$  is the real amplitude,  $p = t - v_1 z/c$ ,

$$\mathbf{e}_l = (\mathbf{e}_z \pm i\mathbf{e}_y)/\sqrt{2} \quad (3)$$

is the unit vector of circular polarization,  $\mathbf{e}_x$  and  $\mathbf{e}_y$  are the real unit vectors,  $v_1$  is the refractive index of the barrier,  $\Theta(p)$  is the Heaviside function, and the parameter  $\gamma_l$  determines the rise and decay of the symmetric pulse. The Fourier transform of the function  $\mathbf{E}_0(z, t)$  has the form

$$\mathbf{E}_0(z, \omega) = \exp(i\kappa_1 z) \{ \mathbf{e}_l E_0(\omega) + \mathbf{e}_l^* E_0(-\omega) \}, \quad (4)$$

$$E_0(\omega) = E_0 \gamma_l / [(\omega - \omega_l)^2 + (\gamma_l/2)^2],$$

where  $\kappa_1 = v_1 \omega/c$ .

In our earlier work [11], we solved the problem of the penetration of a monochromatic electromagnetic wave through a quantum well with due regard for the spatial dispersion of the wave. In [11], we obtained the relationship for the density of the high-frequency current induced by the propagating wave in the quantum well. For one excited level and circularly polarized incident waves, the current density can be written as

$$\bar{\mathbf{J}}(z, t) = (1/2\pi) \int_{-\infty}^{\infty} d\omega \exp(-i\omega t) \bar{\mathbf{J}}(z, \omega),$$

$$\bar{\mathbf{J}}(z, \omega) = -\frac{\mathbf{e}_l \gamma_r v \omega}{4\pi} \times \Phi(z) \left[ \frac{1}{\omega - \omega_0 + i\gamma/2} + \frac{1}{\omega + \omega_0 + i\gamma/2} \right]$$

$$\times \int_0^d dz' A(z', \omega) \Phi(z') + \text{c.c.} = \mathbf{e}_l \bar{\mathbf{J}}(z, t).$$

The interband transition energy that corresponds to the chosen excited state is defined by the expression

$$\hbar\omega_0 = \hbar\omega_g + \varepsilon(m_v) + \varepsilon(m_c) + \hbar\Omega_\mu(n + 1/2), \quad (6)$$

where  $\varepsilon(m_c)$  [ $\varepsilon(m_v)$ ] is the energy of an electron (a hole) with the quantum number  $m_c$  ( $m_v$ ) in the quantum-well level,  $\Omega_\mu = |e|H/\mu c$  is the cyclotron frequency,  $e$  is the elementary charge,  $H$  is the strength of a constant magnetic field,  $\mu = m_e m_h / (m_e + m_h)$ ,  $m_e$  ( $m_h$ ) is the effective

electron (hole) mass,  $n$  is the Landau quantum number, and  $\gamma$  is the reciprocal nonradiative lifetime of the excited state. Within the approximation of an infinitely deep well, we have

$$\Phi(z) = (2/d) \sin(\pi m_c z/d) \sin(\pi m_v z/d). \quad (7)$$

In expression (5), we introduced the reciprocal radiative lifetime  $\gamma_r$  of the electron-hole pair in the magnetic field at  $\kappa d = 0$ , that is,

$$\gamma_r = (2e^2/\hbar c v)(p_{cv}^2/m_0 \hbar \omega_g)(|e|H/m_0 c), \quad (8)$$

where  $m_0$  is the mass of a free electron. Furthermore, we introduced the scalar  $A(z, \omega)$  related to the Fourier transform of the vector potential  $\mathbf{A}(z, \omega)$  through the expression

$$\mathbf{A}(z, \omega) = \mathbf{e}_l A(z, \omega) + \mathbf{e}_l^* A(z, -\omega). \quad (9)$$

The electric field vector  $\mathbf{E}(z, \omega)$  is described by a formula similar to expression (9). Relationship (5) is valid for heavy holes in crystals with a zinc blende structure when the  $z$  axis is aligned along the fourfold symmetry axis [12, 13]. The real constant  $p_{cv}$  entering into the formula for the reciprocal lifetime  $\gamma_r$  is associated with the momentum interband matrix element for two degenerate bands, that is,

$$\mathbf{p}_{cv}^{I,II} = p_{cv}(\mathbf{e}_x \mp i\mathbf{e}_y)/\sqrt{2}.$$

The current density  $\bar{\mathbf{J}}(z, t)$  satisfies the condition  $\text{div} \bar{\mathbf{J}}(z, t) = 0$ , and hence, the induced charge density is  $\rho(z, t) = 0$ . Then, we can use the gauge:  $\varphi(z, t) = 0$ , where  $\varphi(z, t)$  is the scalar potential, and

$$\begin{aligned} \mathbf{E}(z, t) &= (-1/c)(\partial \mathbf{A}/\partial t), \\ \mathbf{E}(z, \omega) &= (i\omega/c)\mathbf{A}(z, \omega). \end{aligned} \quad (10)$$

Since  $\mathbf{E}(z, \omega) \sim \mathbf{A}(z, \omega)$ , instead of the equation for  $A(z, \omega)$ , it is convenient to solve a similar equation for the scalar  $E(z, \omega)$ . This equation can be written in the form

$$\begin{aligned} d^2 E(z, \omega)/dz^2 + \kappa^2 E(z, \omega) &= -(4\pi/c)\bar{J}(z, \omega), \\ \kappa &= v\omega/c. \end{aligned} \quad (11)$$

Note that, in relationship (5) for  $\bar{J}(z, \omega)$ ,  $A(z', \omega)$  should be replaced by  $E(z', \omega)$  with the use of expression (10).

Equation (11) is integro-differential. The solution of Eq. (11) can be formally represented as the sum of the general solution of a homogeneous equation and the particular solution of a nonhomogeneous equation.

Then, Eq. (11) transforms into the Fredholm integral equation of the second kind,<sup>1</sup>

$$\begin{aligned} E(z, \omega) &= C_1 e^{i\kappa z} + C_2 e^{-i\kappa z} \\ &- \frac{i(\gamma_r/2)F(z)}{\omega - \omega_0 + i\gamma/2} \int_0^d dz' E(z', \omega) \Phi(z'). \end{aligned} \quad (12)$$

This equation is valid at frequencies  $\omega$  close to  $\omega_0$ , because it was derived without regard for the nonresonant term  $\omega + \omega_0 + i\gamma/2$  in relationship (5) for the current density  $\bar{\mathbf{J}}(z, \omega)$ . Ignoring the nonresonant term is equivalent to having the inequality  $(\omega - \omega_0)/\omega_0 \ll 1$ . Therefore, the theory becomes inadequate at  $\omega - \omega_0 \approx \omega_0$ ; however, this frequency range is very far from the resonance frequency  $\omega_0$  and is of no interest. In the case of the time representation, the inadequacy of the theory manifests itself at times  $t \leq t_0 = \omega_0^{-1}$ . For  $\hbar\omega_0 = 1.6$  eV, we obtain  $t_0 = 4 \times 10^{-16}$  s. The arbitrary constants  $C_1$  and  $C_2$  are determined from the boundary conditions in the planes  $z = 0$  and  $z = d$ , and the function  $F(z)$  has the form

$$F(z) = e^{i\kappa z} \int_0^z dz' e^{-i\kappa z'} \Phi(z') + e^{-i\kappa z} \int_z^d dz' e^{i\kappa z'} \Phi(z'). \quad (13)$$

At  $\gamma_r \ll \gamma$ , the integral term in Eq. (12) can be treated as a small perturbation. Hence, it is sufficient to allow for the first approximation with respect to this term. The radiative broadening of the energy levels in quasi-two-dimensional systems results from the breaking of the translational symmetry in a direction perpendicular to the plane of the quantum well [15, 16]. For high-quality quantum wells, the scattering by inhomogeneities of the quantum well boundaries can make a small contribution to the nonradiative broadening of the level. The same is also true for the scattering by phonons and impurities at low temperatures and small impurity concentrations. As a consequence, it can turn out that  $\gamma_r \geq \gamma$ . In this case, the solution of Eq. (12) cannot be limited to the first iteration and requires summation of the complete iteration series. It can be demonstrated that this series is reduced to a geometric progression and the solution can be written in the form [11]

$$\begin{aligned} E(z, \omega) &= C_1 e^{i\kappa z} + C_2 e^{-i\kappa z} - \frac{i(\gamma_r/2)F(z)}{\omega - \omega_0 + i(\gamma + \gamma_r \epsilon)/2} \\ &\times \int_0^d dz' (C_1 e^{i\kappa z'} + C_2 e^{-i\kappa z'}) \Phi(z'). \end{aligned} \quad (14)$$

<sup>1</sup> A similar equation for an inversion layer was considered in [14]. The exact solution of Eq. (12) for a monochromatic exciting wave was obtained in [11].

The complex quantity  $\varepsilon$  defined as

$$\varepsilon = \varepsilon' + i\varepsilon'' = \int_0^d dz' \Phi(z') F(z') \quad (15)$$

characterizes the change in the broadening and the shift in the level due to spatial dispersion of the wave. In the limiting case  $\kappa d = 0$ , we have  $\varepsilon = \delta_{m_c m_v}$ . For barriers without induced current, instead of Eq. (11), the following equation holds:

$$d^2 E(z, \omega) / dz^2 + \kappa_1^2 E(z, \omega) = 0, \quad (16)$$

$$z \leq 0, \quad z \geq d, \quad \kappa_1 = v_1 \omega / c.$$

The solution of this equation has the form

$$E^l(z, \omega) = E_0(\omega) e^{i\kappa_1 z} + C_R e^{-i\kappa_1 z}, \quad (17)$$

$$z \leq 0; \quad E^r(z, \omega) = C_T e^{i\kappa_1 z}, \quad z \geq d.$$

In the expression for  $E^l(z, \omega)$ , the first term is the scalar amplitude of the Fourier transform of the exciting pulse and  $C_R$  and  $C_T$  determine the amplitudes of the wave reflected from the quantum well and the wave transmitted through the well, respectively. The coefficients  $C_1$ ,  $C_2$ ,  $C_R$ , and  $C_T$  depend on the frequency  $\omega$  and are deduced from the continuity conditions for  $E(z, \omega)$  and  $dE(z, \omega)/dz$  at the boundaries  $z = 0$  and  $z = d$ . As a result, we found

$$C_1 = (2E_0(\omega)/\Delta) e^{-i\kappa d} [1 + \zeta + (1 - \zeta)\mathcal{N}],$$

$$C_2 = -(2E_0(\omega)/\Delta)(1 - \zeta)[e^{i\kappa d} + \mathcal{N}], \quad (18)$$

$$C_R = E_0(\omega)\rho/\Delta,$$

$$C_T = 4E_0(\omega)\zeta e^{-i\kappa d} [1 + e^{-i\kappa d}\mathcal{N}]/\Delta,$$

$$\Delta = (\zeta + 1)^2 e^{-i\kappa d} - (\zeta - 1)^2 e^{i\kappa d} - 2(\zeta - 1)\mathcal{N}[(\zeta + 1)e^{-i\kappa d} + \zeta - 1], \quad (19)$$

$$\rho = 2i(\zeta^2 - 1)\sin\kappa d + 2[(\zeta^2 + 1)e^{-i\kappa d} + \zeta^2 - 1]\mathcal{N}.$$

In relationships (18) and (19), we introduced the following designations:

$$\zeta = \kappa/\kappa_1 = v/v_1, \quad (20)$$

$$\mathcal{N} = -i(\gamma_r/2)F^2(0)/[\omega - \omega_0 + i(\gamma + \gamma_r\varepsilon)/2]. \quad (21)$$

The function  $E_0(\omega)$  is defined by formula (4). It follows from expressions (13) and (15) that, at  $m_c = m_v = m$  (the allowed interband transition in the limiting case  $\kappa d = 0$ ), the functions  $F(z)$  and  $\varepsilon$  can be written as

$$F(z) = iB[2 - \exp(i\kappa z) - \exp(i\kappa(d - z)) - (\kappa d/\pi m)^2 \sin^2(\pi m z/d)], \quad (22)$$

$$F(0) = F(d) = iB[1 - \exp(i\kappa d)], \quad (23)$$

$$B = (4\pi^2 m^2/\kappa d)/[4\pi^2 m^2 - (\kappa d)^2],$$

$$\varepsilon' = F^2(0)\exp(-i\kappa d) = 4B^2 \sin^2(\kappa d/2), \quad (24)$$

$$\varepsilon'' = 2B[1 - B\sin\kappa d - 3(\kappa d)^2/8\pi^2 m^2].$$

According to formula (17), the Fourier transform of the electric field vector  $\mathbf{E}^r(z, \omega)$  on the right of the quantum well is given by

$$\mathbf{E}^r(z, \omega) = \exp(i\kappa_1 z)[\mathbf{e}_l C_T(\omega) + \mathbf{e}_l^* C_T(-\omega)], \quad (25)$$

$$z \geq d.$$

The Fourier transform of the electric field vector  $\mathbf{E}^l(z, \omega)$  on the left of the quantum well involves the components associated with the exciting pulse field [expression (4)] and the reflected wave field  $\Delta\mathbf{E}^l(z, \omega)$  and is described by the relationship

$$\mathbf{E}^l(z, \omega) = \mathbf{E}_0(z, \omega) + \Delta\mathbf{E}^l(z, \omega), \quad (26)$$

$$\Delta\mathbf{E}^l(z, \omega) = \exp[-(i\kappa_1 z)][\mathbf{e}_l C_R(\omega) + \mathbf{e}_l^* C_R(-\omega)], \quad (27)$$

$$z \geq d.$$

### 3. THE CHANGE-OVER TO THE TIME REPRESENTATION

In the time representation, the electric field vector of the pulse transmitted through the quantum well, according to relationship (17), has the form ( $p = t - z v_1/c$ )

$$\mathbf{E}^r(z, t) = \mathbf{e}_l \mathbf{E}^r(z, t) + \text{c.c.},$$

$$E^r(z, t) = (1/2\pi) \int_{-\infty}^{+\infty} d\omega \exp(-i\omega p) C_T(\omega), \quad z \geq d. \quad (28)$$

In a similar way, the field vector of the pulse reflected from the quantum well is written as

$$\Delta\mathbf{E}^l(z, t) = \mathbf{e}_l \Delta\mathbf{E}^l(z, t) + \text{c.c.}, \quad (29)$$

$$\Delta E^r(z, t) = (1/2\pi) \int_{-\infty}^{+\infty} d\omega \exp(-i\omega s) C_R(\omega), \quad z \leq d,$$

where  $s = t + z v_1/c$ . After substitution of  $E_0(\omega)$  defined by expression (4) and  $\mathcal{N}(\omega)$  represented by formula (21) into relationships (18), the functions  $C_T(\omega)$  and  $C_R(\omega)$  take the form

$$C_T(\omega) = \frac{4E_0\gamma_l\zeta \exp(-i\kappa_1 d)}{\mathcal{L}\mathcal{D}} \times \frac{\omega - \omega_0 - \gamma_r\varepsilon''/2 + i\gamma/2}{(\omega - \omega_l)^2 + (\gamma_l/2)^2}, \quad (30)$$

$$C_R(\omega) = \frac{E_0 \gamma_l}{\mathcal{L} \mathcal{D}} \times \frac{\mathcal{B}[\omega - \omega_0 - \gamma_r \varepsilon''/2 + i(\gamma + \gamma_r \varepsilon')/2] - i \mathcal{B}_1 \gamma_r \varepsilon'/2}{(\omega - \omega_l)^2 + (\gamma_l/2)^2}, \quad (31)$$

$$\mathcal{D} = \omega - \omega_0 - \gamma_r \mathcal{F}_1/2 + i(\gamma + \gamma_r \mathcal{F}_2)/2, \quad (32)$$

$$\mathcal{L} = (1 + \zeta)^2 \exp(-i\kappa d) - (1 - \zeta)^2 \exp(i\kappa d), \quad (33)$$

$$\mathcal{B} = -2i(1 - \zeta^2) \sin \kappa d, \quad (34)$$

$$\mathcal{B}_1 = 2[1 + \zeta^2 - (1 - \zeta^2) \exp(i\kappa d)],$$

$$\mathcal{F}_1 = \varepsilon'' - \frac{2\varepsilon'(1 - \zeta^2) \sin \kappa d}{1 + \zeta^2 + (1 - \zeta^2) \cos \kappa d}, \quad (35)$$

$$\mathcal{F}_2 = \frac{2\zeta \varepsilon'}{1 + \zeta^2 + (1 - \zeta^2) \cos \kappa d}.$$

In integrals (28) and (29), the integrands have the poles  $\omega = \omega_l \pm i\gamma_l/2$  and, in addition, the pole determined by the equation  $\mathcal{D} = 0$  in the lower half-plane  $\omega$ . In the strict sense, the functions  $\mathcal{F}_1$  and  $\mathcal{F}_2$  entering into  $\mathcal{D}$  [see formula (32)] depend on  $\omega$ , because the magnitude of the wave vector  $\kappa = v\omega/c$  is a function of  $\omega$ . However, reasoning from the assumptions made in deriving relationship (12), the frequency  $\omega$  should not differ strongly from the frequency  $\omega_0$ . Therefore, the equation  $\mathcal{D} = 0$  can be solved using only the first iteration. As a result, we obtain the following pole in the lower half-plane:

$$\omega = \omega_0 - \gamma_r \mathcal{F}_1(\omega_0) - i(\gamma + \gamma_r \mathcal{F}_2(\omega_0))/2. \quad (36)$$

By using the approximate pole (36), we obtain

$$\kappa = \kappa_0 = v\omega_0/c, \quad \kappa_l = \kappa_{l0} = v_l \omega_0/c. \quad (37)$$

On the other hand, the poles  $\omega = \omega_l \pm i\gamma_l/2$  lead to  $\kappa = \kappa_l = v\omega_l/c$  and  $\kappa_l = \kappa_{l1} = v_l \omega_l/c$ . Since the theory holds true when the inequality  $(\omega_l - \omega_0)/\omega_0 \ll 1$  is satisfied, hereafter, we assume that  $\kappa_l = \kappa_0 = \kappa$  and  $\kappa_{l1} = \kappa_{l0} = \kappa_l$ .

After integration over the frequency  $\omega$ , the scalar functions  $E^r(z, t)$  and  $\Delta E^l(z, t)$  take the form

$$E^r(z, t) = (4\zeta E_0/\mathcal{L}) \exp(-i(\omega_l p + \kappa_l d)) \times \{ [1 - \Theta(p)] \exp(\gamma_l p/2) W_T(\gamma_l) + \Theta(p) \varepsilon_T \}, \quad (38)$$

$$\Delta E^l(z, t) = (E_0/\mathcal{L}) \exp(-i\omega_l s) \times \{ [1 - \Theta(s)] \exp(\gamma_l s/2) W_R(\gamma_l) + \Theta(s) \varepsilon_R \}, \quad (39)$$

where the functions  $\varepsilon_T$  and  $\varepsilon_R$  are defined by the identical formulas

$$\varepsilon_{T(R)} = e^{-\gamma_l p(s)/2} W_{T(R)}(-\gamma_l) - e^{i(\Delta\omega - \gamma_r \mathcal{F}_1/2)p(s)} \times W'_{T(R)} e^{-(\gamma + \gamma_r \mathcal{F}_2)p(s)/2}. \quad (40)$$

In relationships (38)–(40), we introduced the following notation:

$$\Delta\omega = \omega_l - \omega_0, \quad (41)$$

$$W_T(\gamma_l) = [\Delta\omega - \gamma_r \varepsilon''/2 + i(\gamma + \gamma_l)/2]/\Omega(\gamma_l), \quad (42)$$

$$W_R(\gamma_l) = \{ \mathcal{B}[\Delta\omega - \gamma_r \varepsilon''/2 + i(\gamma + \gamma_l + \gamma_r \varepsilon')/2] - i\gamma_r \varepsilon' \mathcal{B}_1/2 \}/\Omega(\gamma_l), \quad (43)$$

$$W'_T = -i(\gamma_r/2) [\mathcal{F}_2 - i(\varepsilon'' - \mathcal{F}_1)] \left( \frac{1}{\Omega(-\gamma_l)} - \frac{1}{\Omega(\gamma_l)} \right), \quad (44)$$

$$W'_R = -i(\gamma_r/2) \{ \mathcal{B}[\varepsilon' - \mathcal{F}_2 + i(\varepsilon'' - \mathcal{F}_1)] + \varepsilon' \mathcal{B}_1 \} \times \left( \frac{1}{\Omega(-\gamma_l)} - \frac{1}{\Omega(\gamma_l)} \right), \quad (45)$$

$$\Omega(\gamma_l) = \Delta\omega - \gamma_r \mathcal{F}_1/2 + i(\gamma + \gamma_l + \gamma_r \mathcal{F}_2)/2. \quad (46)$$

Note that allowance made for the dependence of  $\kappa$  on  $\omega$  leads to the replacement of the variable  $p$  by  $p' = p + t_1$  in expression (38) for the scalar function  $E^r(z, t)$ . Here,  $t_1 = v_1 d/c$  is the time the light takes to propagate through the quantum well. Consequently, the inclusion of the dependence of  $\kappa$  on  $\omega$  manifests itself only in the case when  $p \leq t_1$ . At  $d = 500 \text{ \AA}$  and  $v_1 = 3$ , we obtain  $t_1 = 5 \times 10^{-16} \text{ s} \cong t_0$ . The approximate equality  $t_1 \cong t_0$  indicates that allowance made for the dependence of  $\kappa$  on  $\omega$  in calculation of integrals (28) and (29) leads to exceeding the required accuracy, because, in this case, the corrections are of the same order of magnitude as those ignored when deriving formula (12). The expressions deduced for  $E^r(z, t)$  and  $\Delta E^l(z, t)$  are rather cumbersome, and their analytical examination is complicated. Therefore, of special interest are the two limiting cases for which these expressions are simplified substantially. If the medium is homogeneous (i.e.,  $v_1 = v$ ), we obtain

$$\kappa_l = \kappa, \quad \mathcal{L} = 4 \exp(-i\kappa d),$$

$$\mathcal{B} = 0, \quad \mathcal{B}_1 = 4, \quad \mathcal{F}_1 = \varepsilon'', \quad \mathcal{F}_2 = \varepsilon'$$

and expressions (38) and (39) transform into the relationships

$$E^r(z, t) = E_0(z, t) + \Delta E^r(z, t) = E_0(z, t) - E_0(i\gamma_r \varepsilon'/2) \exp(-i\omega_l p) \times \{ [1 - \Theta(p)] \exp(\gamma_l p/2)/\Omega(\gamma_l) + \Theta(p) \varepsilon \}, \quad (47)$$

$$\Delta E^l(z, t) = -E_0(i\gamma_r \varepsilon'/2) \exp(-i(\omega_l s - \kappa d)) \times \{ [1 - \Theta(s)] \exp(\gamma_l s/2)/\Omega(\gamma_l) + \Theta(s) \varepsilon \}, \quad (48)$$

where the function  $\Omega(\gamma_l)$  defined by formula (46) transforms into the function

$$\Omega(\gamma_l) = \Delta\omega - \gamma_r \varepsilon''/2 + i(\gamma + \gamma_l + \gamma_r \varepsilon')/2 \quad (49)$$

and the function described by expression (40) takes the form

$$\epsilon = \exp(-\gamma_l t/2)/\Omega(-\gamma_l) - \exp[i(\Delta\omega - \gamma_r \epsilon''/2)t] \times \exp[-(\gamma + \gamma_r \epsilon')t/2] \{ \Omega(-\gamma_l)^{-1} - \Omega(\gamma_l)^{-1} \}. \quad (50)$$

The parameter  $t$  in formula (50) is as follows:  $t = p$  for  $E'$  and  $t = s$  for  $\Delta E^l$ . The function  $\Delta E^r(z, t)$  determines the distortion of the exciting pulse transmitted through the quantum well.

It is seen from relationships (47) and (48) that the inclusion of the spatial dispersion in the case of the homogeneous medium leads to a shift in the frequency  $\omega_0$  by  $\gamma_r \epsilon''/2$  and the replacement of  $\gamma_r$  by  $\tilde{\gamma}_r = \gamma_r \epsilon'$ . The quantity  $\tilde{\gamma}_r$  coincides with the reciprocal radiative lifetime calculated in [3, 7] for an electron-hole pair in a strong magnetic field at  $\mathbf{K}_\perp = 0$  for an arbitrary value of  $\kappa d$ . When the spatial dispersion is disregarded (i.e., at  $\kappa d = 0$ ), according to formulas (24), we have  $\epsilon' \rightarrow 1$  and  $\epsilon'' \rightarrow 0$  and expressions (47) and (48) transform into the relationships derived in [5] for the case of a homogeneous medium in the absence of spatial dispersion. Formulas (47) and (48) coincide with similar expressions obtained in [5] [formula (15)] provided that, in these expressions, the transition frequency  $\omega_0$  is considered to mean  $\omega_0 + \gamma_r \epsilon''/2$  and  $\gamma_r$  is replaced by  $\tilde{\gamma}_r$ . It is also of interest to analyze the limiting case of a weak spatial dispersion when  $\kappa d \rightarrow 0$  but the medium is inhomogeneous (i.e.,  $v_1 \neq v$ ). This situation can arise with comparatively narrow quantum wells. Setting  $\kappa d = 0$  in formulas (38) and (39), we obtain  $\mathcal{L} = 4\zeta$ ,  $\mathcal{R} = 0$ ,  $\mathcal{B}_1 = 4\zeta^2$ ,  $\mathcal{F}_1 = 0$ ,  $\mathcal{F}_2 = \zeta$ , and

$$\Delta E^r(z, t) = (-iE_0 \gamma_r \zeta/2) \exp(-i\omega_l p) \quad (51)$$

$$\times \{ [1 - \Theta(p)] \exp(\gamma_l p/2)/\Omega(\gamma_l) + \epsilon'(p)\Theta(p) \},$$

$$\epsilon'(p) = \exp(-\gamma_l p/2)/\Omega(-\gamma_l) \quad (52)$$

$$- \exp[i\Delta\omega p - (\gamma + \gamma_r \zeta)p/2] (\Omega(-\gamma_l)^{-1} - \Omega(\gamma_l)^{-1}).$$

In the given case, the function  $\Omega(\gamma_l)$  is represented as

$$\Omega(\gamma_l) = \Delta\omega + i(\gamma + \gamma_l + \gamma_r \zeta/2) \quad (53)$$

and the difference between  $\Delta E^l(z, t)$  and the corresponding function described by expression (51) resides in the replacement of  $p$  by  $s$ . It can be seen that the inhomogeneity of the medium without regard for the spatial dispersion results only in the substitution of  $\gamma_r \zeta$  for  $\gamma_r$ , i.e., in the substitution of  $v_1$  for  $v$  in expression (8) for  $\gamma_r$ . Formulas (51) and (52) coincide with the relationships deduced in [5] if  $\gamma_r$  is replaced by  $\zeta \gamma_r$  in these relationships. Since the condition  $\zeta \cong 1$  is met in real systems, the inhomogeneity of the medium makes only a small contribution. The passage to the limit  $\gamma_l \rightarrow 0$  implies the change-over to a monochromatic exciting wave. In this limiting case, formulas (38) and (39) are reduced to the expressions obtained in [11].

#### 4. REFLECTION AND TRANSMISSION OF AN EXCITING PULSE

The energy flux  $\mathbf{S}(p)$  corresponding to the electric field of the exciting pulse can be written in the form

$$\mathbf{S}(p) = (\mathbf{e}_z/4\pi)(c/v_1)(\mathbf{E}_0(z, t))^2 = \mathbf{e}_z S_0 P(p), \quad (54)$$

where  $S_0 = cE_0^2/(2\pi v_1)$  and  $\mathbf{e}_z$  is the unit vector along the  $z$  axis. The dimensionless function  $P(p)$  determines the spatial and time dependences of the energy flux of the exciting pulse, that is,

$$P(p) = (\mathbf{E}_0(z, t))^2/S_0 \quad (55)$$

$$= \Theta(p)e^{-\gamma_l p} + [1 - \Theta(p)]e^{\gamma_l p}.$$

By analogy with expression (54), the transmitted flux, i.e., the flux on the right of the quantum well, can be represented as

$$\mathbf{S}^r(z, t) = (\mathbf{e}_z/4\pi)(c/v_1)(\mathbf{E}^r(z, t))^2 = \mathbf{e}_z S_0 \mathcal{T}(p). \quad (56)$$

The reflected flux (on the left of the quantum well) has the form

$$\mathbf{S}^l = -(\mathbf{e}_z/4\pi)(c/v_1)(\Delta \mathbf{E}^l(z, t))^2 = -\mathbf{e}_z S_0 \mathcal{R}(s). \quad (57)$$

The dimensionless functions  $\mathcal{T}(p)$  and  $\mathcal{R}(s)$  determine the fractions of the transmitted and reflected energies of the exciting pulse.

By analogy with [5], the absorbed energy flux  $\mathbf{S}^a$  can be defined as the difference between the flux  $\mathbf{S} + \mathbf{S}^l$ , which is incident on the quantum well from the left at  $z = 0$ , and the flux  $\mathbf{S}^r$ , which leaves the well toward the right at  $z = d$  at the same instant of time  $t$ ; that is,

$$\mathbf{S}^a(t) = \mathbf{S}(t) + \mathbf{S}^l(t) - \mathbf{S}^r(t). \quad (58)$$

With the use of definitions (54)–(58), the flux  $\mathbf{S}^a(t)$  can be represented as

$$\mathbf{S}^a(t) = \mathbf{e}_z S_0 [P(t) - \mathcal{R}(t) - \mathcal{T}(t)]. \quad (59)$$

The fraction of the absorbed energy  $\mathcal{A}(t)$  is defined using the equality  $\mathbf{S}^a(t) = \mathbf{e}_z S_0 \mathcal{A}(t)$ . As a result, we have

$$\mathcal{A}(t) = P(t) - \mathcal{R}(t) - \mathcal{T}(t). \quad (60)$$

Formula (60) can be generalized if the planes in which the fluxes are considered are displaced by  $z = -z_0$  toward the left of the quantum well and by  $z_0$  toward the right of the quantum well ( $z_0 > 0$ ). Then, instead of relationship (60), we obtain

$$\mathcal{A}(x) = P(x) - \mathcal{R}(x) - \mathcal{T}(x), \quad (61)$$

where  $x = p = s = t - v_1|z_0|/c$ . The relationships for the quantities  $\mathcal{T}$ ,  $\mathcal{R}$ , and  $\mathcal{A}$  are expressed through the scalar functions  $E^r(z, t)$  and  $\Delta E^l(z, t)$  according to the general formulas (38) and (39). These relationships are very cumbersome and are not presented in this work. The quantities  $P(t)$ ,  $\mathcal{T}(t)$ , and  $\mathcal{R}(t)$  are universally pos-

itive, whereas the absorptance  $\mathcal{A}(t)$  can be positive or negative. The negative absorptance at a certain instant of time  $t$  suggests that the electronic system of the quantum well gives away the energy accumulated at the preceding instants of time.

### 5. TIME DEPENDENCE OF THE REFLECTANCE, TRANSMITTANCE, AND ABSORPTANCE IN THE CASE OF TRUE RESONANCE $\omega_l = \omega_0$

First, we analyze the limiting case  $\gamma \gg \gamma_r$ . The fields  $\mathbf{E}^r(z, t)$  and  $\Delta \mathbf{E}^l(z, t)$  defined by expressions (38) and (39) can be represented as the series

$$\mathbf{E}^r(z, t) = \mathbf{E}_0^r(z, t) + (\gamma_r/\gamma)\mathbf{E}_1^r(z, t) + \dots, \quad (62)$$

$$\Delta \mathbf{E}^l(z, t) = \Delta \mathbf{E}_0^l(z, t) + (\gamma_r/\gamma)\Delta \mathbf{E}_1^l(z, t) + \dots, \quad (63)$$

where

$$\mathbf{E}_0^r(z, t) = \mathbf{e}_l(4\zeta E_0/\mathcal{L}) \exp[-i(\omega_l p + \kappa_1 d)] \{ [1 - \Theta(p)] \times \exp(\gamma_l p/2) + \Theta(p) \exp(-\gamma_l p/2) \} + \text{c.c.}, \quad (64)$$

$$\Delta \mathbf{E}_0^l(z, t) = -\mathbf{e}_l(\mathcal{B} E_0/\mathcal{L}) \exp(-i\omega_l s) \{ [1 - \Theta(p)] \times \exp(\gamma_l s/2) + \Theta(s) \exp(-\gamma_l s/2) \} + \text{c.c.} \quad (65)$$

correspond to the transmitted and reflected pulses at  $\gamma_r = 0$ , i.e., when the absorption in the quantum well is absent.

In the limiting cases  $\kappa d \neq 0$  and  $\zeta = 1$  or  $\kappa d = 0$  and  $\zeta \neq 1$ , we have  $\Delta E_0^l(z, t) = 0$ , because, according to formula (34),  $\mathcal{B} = 0$ . In the former case, this is explained by the fact that the medium becomes homogeneous. In the latter case, the amount of the material in the quantum well is very small and the transmitted wave does not interact with it. In these limiting cases, from relationship (57), we obtain  $\mathcal{R}(t) \sim (\gamma_r/\gamma)^2$ ; i.e., the reflectance is a small quantity. When changing over to the general case  $\kappa d \neq 0$  and  $\zeta \neq 1$ , the reflectance  $\mathcal{R}(t)$  takes the form

$$\mathcal{R}(t) = S_0^{-1} [(\Delta \mathbf{E}_0^l(s))^2 + 2(\gamma_r/\gamma)(\Delta \mathbf{E}_0^l(s)\Delta \mathbf{E}_1^l(s))]. \quad (66)$$

As a consequence, the reflectance appreciably increases owing to the first term in expression (66). As regards the transmittance  $\mathcal{T}(t)$ , in the limiting cases  $\kappa d = 0$  or  $\zeta = 1$ , we found that  $\mathcal{T}(t) = P(t)$ . When changing over to the general case, the transmittance changes only slightly, because the multiplier  $16\zeta/|\mathcal{L}|^2$  does not differ significantly from unity.

Figure 1 displays the time dependences of the dimensionless transmittance  $\mathcal{T}$ , absorptance  $\mathcal{A}$ , and reflectance  $\mathcal{R}$  for different values of the parameters  $\kappa d$  and  $\zeta$ . It is seen from Fig. 1a that the curve  $\mathcal{T}(t)$  at  $\kappa d = 0$  and  $\zeta = 1$  virtually coincides with that at  $\kappa d = 1.5$  and  $\zeta = 1.1$ . The same holds true for the absorptance  $\mathcal{A}(t)$ . As can be seen from Fig. 1b, the reflectance is a small

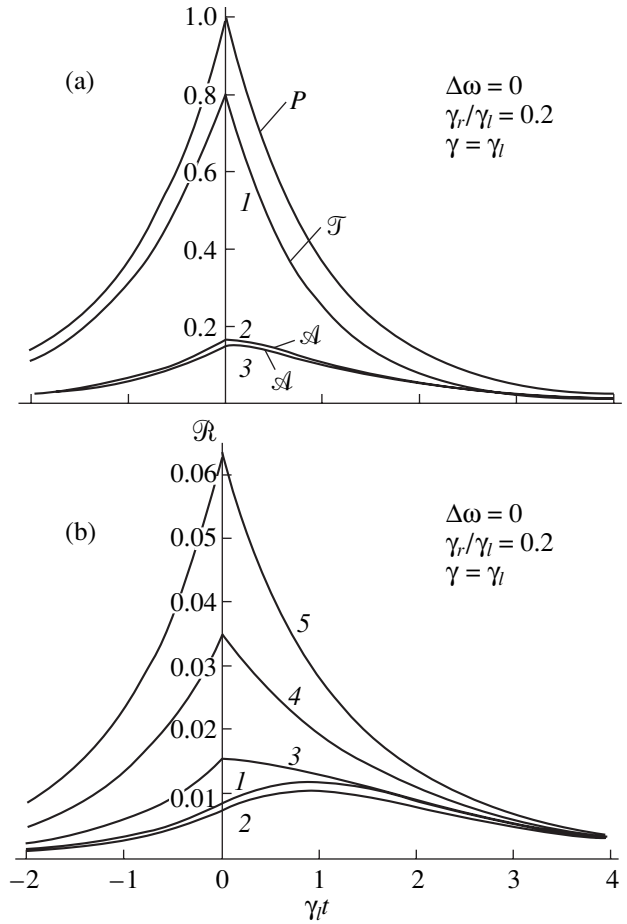


**Fig. 1.** Dependences of the transmittance  $\mathcal{T}$ , the absorptance  $\mathcal{A}$ , and the reflectance  $\mathcal{R}$  of the symmetric exciting pulse  $P$  on the dimensionless time  $\gamma t$  in the case of true resonance and  $\gamma_r \ll \gamma$ . (a) (1)  $\zeta = 1$ ,  $\kappa d = 0$  and  $\zeta = 1.1$ ,  $\kappa d = 1.5$ ; (2)  $\zeta = 1$  and  $\kappa d = 0$ ; and (3)  $\zeta = 1.1$  and  $\kappa d = 1.5$ . (b) (1)  $\zeta = 1$  and  $\kappa d = 0$ , (2)  $\zeta = 1$  and  $\kappa d = 1.5$ , (3)  $\zeta = 1.1$  and  $\kappa d = 1.5$ , (4)  $\zeta = 1.2$  and  $\kappa d = 1.5$ , and (5)  $\zeta = 1.3$  and  $\kappa d = 1.5$ .

quantity and substantially depends on the parameter  $\zeta$  at  $\kappa d = 1.5$ : a change in  $\zeta$  from 1 to 1.3 leads to an eight-fold increase in the reflectance  $\mathcal{R}(t)$

In the limiting case  $\gamma_r \gg \gamma$ , the induced fields are comparable in magnitude to the field of the exciting pulse and, hence, the shape of the pulse transmitted through the quantum well changes very strongly. It can be seen from Fig. 2 that, under these conditions, the transmittance  $\mathcal{T}$  is small and the reflectance  $\mathcal{R}$  is predominant. In our previous work [5], we introduced the notion of singular points in the time dependences of the functions  $\mathcal{T}$ ,  $\mathcal{A}$ , and  $\mathcal{R}$ . In particular, one of these points (the total reflection point of the first kind) is defined by the conditions  $\mathcal{R}(t_0) = P(t_0)$  and  $\mathcal{T}(t_0) = \mathcal{A}(t_0) = 0$  (Fig. 2a). At  $\zeta \neq 1$  and  $\kappa d \neq 0$  (Fig. 2b), other conditions, namely,  $\mathcal{T}(t_0) + \mathcal{A}(t_0) = 0$  and  $\mathcal{R}(t_0) = P(t_0)$ ,

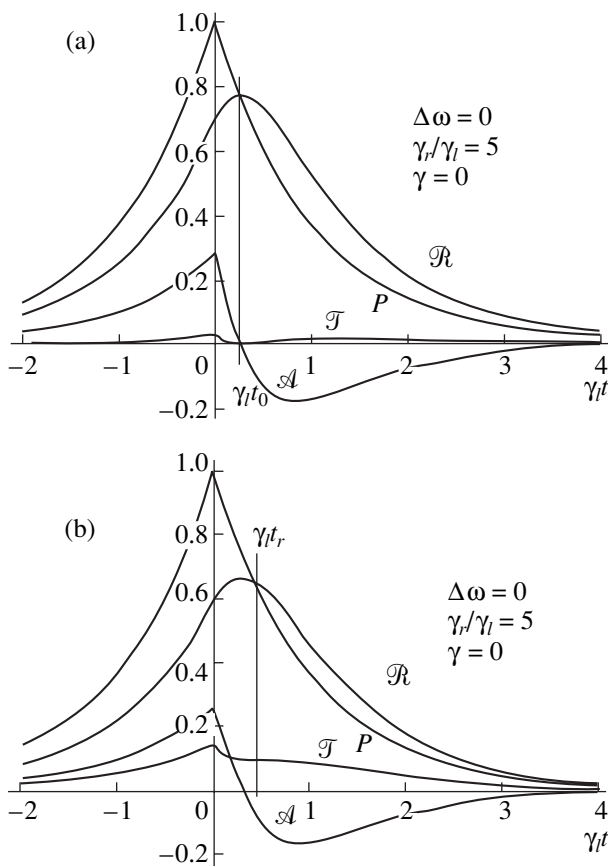


**Fig. 2.** Time dependences of the functions  $P$ ,  $\mathcal{R}$ ,  $\mathcal{A}$ , and  $\mathcal{T}$  in the case of true resonance and  $\gamma_r \ll \gamma_l$ . (a)  $\zeta = 1$  and  $\kappa d = 0$  and (b)  $\zeta = 1.1$  and  $\kappa d = 1.5$ .  $\gamma_l t_0$  and  $\gamma_l t_r$  are the singular points of total reflection of the first and second kinds, respectively.

are satisfied at the total reflection point. This means that the absorptance is negative  $\mathcal{A}(t) < 0$ ; i.e., the system generates radiation accumulated at earlier instants of time. Therefore, the change-over to the general case results in the appearance of a singular point, which, according to the classification proposed in [5], is the total reflection point of the second kind. Note also that the transmittance shown in Fig. 2b is several times larger than that in Fig. 2a. Consequently, in this case, too, the inhomogeneity of the medium and the spatial dispersion substantially affect only small quantities, which are represented by the transmittance  $\mathcal{T}(t)$  in the given limiting case.

**6. DEVIATION OF THE CARRIER FREQUENCY FROM THE RESONANCE FREQUENCY**

In [5], it was demonstrated that the deviation  $\Delta\omega$  of the carrier frequency from the resonance frequency leads to oscillations of the quantities  $\mathcal{A}(t)$  and  $\mathcal{R}(t)$  with time. However, the oscillations could be observed only at small values of  $\mathcal{A}(t)$  and  $\mathcal{R}(t)$ . On the other

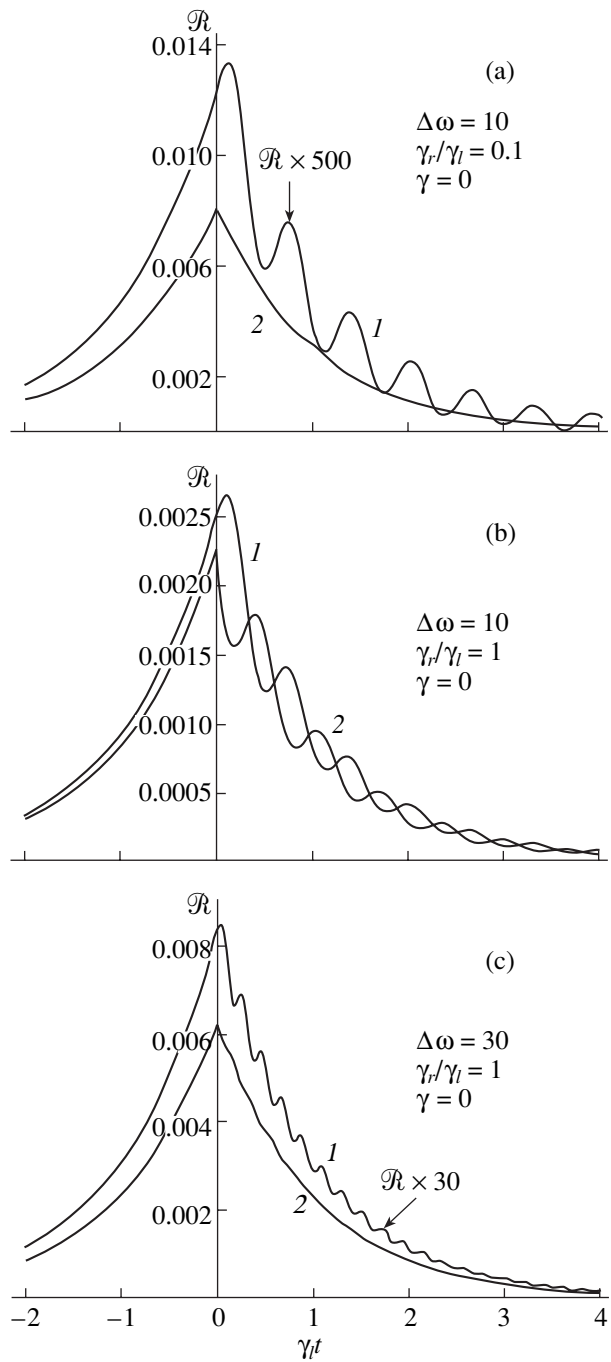


**Fig. 3.** Time dependences of the reflectance in the case of deviation of the carrier frequency from the resonance frequency at  $\gamma = 0$  and (a)  $\Delta\omega = 10$  and  $\gamma_r/\gamma_l = 0.1$ , (b)  $\Delta\omega = 10$  and  $\gamma_r/\gamma_l = 1$ , and (c)  $\Delta\omega = 30$  and  $\gamma_r/\gamma_l = 1$ . (1)  $\zeta = 1$  and  $\kappa d = 0$  and (2)  $\zeta = 1.1$  and  $\kappa d = 1.5$ .

hand, the inclusion of the inhomogeneity of the medium and the spatial dispersion results in the appearance of an additional reflection from the quantum well boundaries. Its magnitude can exceed the oscillating component of the reflectance  $\mathcal{R}(t)$ . The effect of the inhomogeneity of the medium and the spatial disper-

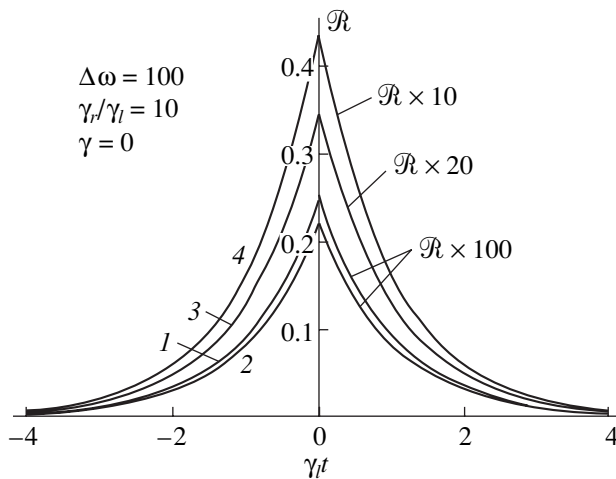


**Fig. 4.** Time dependences of the reflectance in the case of a strong deviation of the carrier frequency from the resonance frequency at (1)  $\zeta = 1$  and  $\kappa d = 0$ , (2)  $\zeta = 1.1$  and  $\kappa d = 1.5$ , (3)  $\zeta = 1.2$  and  $\kappa d = 1.5$ , and (4)  $\zeta = 1.3$  and  $\kappa d = 1.5$ .

sion of the light wave on the reflectance  $\mathcal{R}(t)$  is illustrated in Fig. 3. The most noticeable changes are observed at  $\gamma_r/\gamma_l \ll 1$ , i.e., for a short exciting pulse. It is seen from Fig. 3a that, compared to the reflectance at  $\zeta = 1$  and  $\kappa d = 0$ , the reflectance  $\mathcal{R}(0)$  increases by a factor of more than 300 and no oscillations can be distinguished as a consequence of their low amplitude. In the intermediate case  $\gamma_r = \gamma_l$  (Fig. 3b), the changes are insignificant and the oscillations are clearly seen in the curve corresponding to  $\zeta = 1.1$  and  $\kappa d = 1.5$ . In Fig. 3c, the reflectance  $\mathcal{R}(0)$  increases by a factor of 22 and the oscillations can be distinguished. As regards the absorptance, the oscillating curves  $\mathcal{A}(t)$  weakly change in the inhomogeneous medium. This is explained by the fact that the absorption in the quantum well is caused by the quantum transitions, which only slightly depend on the refractive index.

Figure 4 shows the curves  $\mathcal{R}(t)$  at  $\gamma_r \gg \gamma_l$  (a long exciting pulse) and  $\Delta\omega \neq 0$ . However, in this case, the reflection oscillations are virtually indistinguishable. As is seen from Fig. 4, allowance made only for the spatial dispersion leads to a decrease in the reflectance as compared to the reflectance at  $\kappa d = 0$ . This is associated with a decrease in the effective reciprocal radiative lifetime  $\gamma_r \epsilon'$ , because  $\epsilon'$  is a decreasing function of the parameter  $\kappa d$ . The change-over to the inhomogeneous medium results in an increase in the reflectance. The larger the parameter  $\zeta$ , the greater the increase in the reflectance.

## 7. CONCLUSIONS

The results obtained allowed us to draw the general conclusion that the inclusion of the inhomogeneity of the medium and the spatial dispersion of the plane waves forming the exciting pulse most strongly affects

the reflection. The changes are most pronounced in the case when the reflection associated with the interband transitions in the quantum well is relatively weak and masked by a stronger reflection from the quantum well boundaries. This situation occurs in the limiting case  $\gamma \gg \gamma_r$  at true resonance  $\Delta\omega = 0$  and in the other limiting case  $\gamma \ll \gamma_r$  when the carrier frequency deviates from the resonance frequency. Noteworthy also is the dependence of the reflectance on the parameter  $v/v_1$ , which becomes more pronounced due to the reflection from the quantum well boundaries. The change in the transmittance is also observed only in the case when the value of  $\mathcal{T}$  is small.

In real semiconductor heterostructures, impurity electrons of the barrier transfer to the quantum well and distort its square shape in the vicinity of the boundaries. Therefore, the theory developed above is valid for sufficiently pure materials and wide quantum wells when the size of distorted boundary regions is small compared to the quantum well width. Moreover, the theory holds true for deep quantum wells in which the location of the first levels and the corresponding wave functions only slightly differ from those in an infinitely deep quantum well. Since the theory allows for only one excited level, the energy separation between the adjacent levels in the quantum well should be larger than the width of the level under consideration and the energy width of the exciting pulse. These conditions impose a restriction on the quantum well width from above. For example, at  $d = 500 \text{ \AA}$  and  $m_c = 0.06m_0$ , the difference between the energies of the two lowest quantum-well levels is equal to approximately  $10^{-3} \text{ eV}$ .

## ACKNOWLEDGMENTS

This work was supported by the Russian Foundation for Basic Research (project no. 00-02-16904) and the International Scientific and Technical Program "Physics of Solid-State Nanostructures" (project no. 97-1099). S.T. Pavlov acknowledges the support and hospitality of Zacatecas University and the Consejo Nacional de Ciencia y Tecnología (CONACyT). D.A. Contreras-Solorio acknowledges the support of the CONACyT (27736-E).

## REFERENCES

1. I. G. Lang, V. I. Belitsky, and M. Gardona, *Phys. Status Solidi A* **164** (1), 307 (1997).
2. I. G. Lang and V. I. Belitsky, *Solid State Commun.* **107** (10), 577 (1998).
3. I. G. Lang and V. I. Belitsky, *Phys. Lett. A* **245** (3–4), 329 (1998).
4. D. A. Contreras-Solorio, S. T. Pavlov, L. I. Korovin, and I. G. Lang, *Phys. Rev. B* **62** (23), 16815 (2000); *cond-mat/0002229*.
5. L. I. Korovin, I. G. Lang, D. A. Contreras-Solorio, and S. T. Pavlov, *Fiz. Tverd. Tela (St. Petersburg)* **42** (12),

- 2230 (2000) [Phys. Solid State **42**, 2300 (2000)]; cond-mat/0006364.
6. I. G. Lang, L. I. Korovin, D. A. Contreras-Solorio, and S. T. Pavlov, Fiz. Tverd. Tela (St. Petersburg) **43** (6), 1117 (2001) [Phys. Solid State **43**, 1159 (2001)]; cond-mat/0004178.
  7. I. G. Lang, L. I. Korovin, D. A. Contreras-Solorio, and S. T. Pavlov, cond-mat/0001248.
  8. C. V. Duke, Phys. Rev. **168**, 816 (1968).
  9. A. Ya. Shik, Fiz. Tverd. Tela (Leningrad) **12** (1), 67 (1970) [Sov. Phys. Solid State **12**, 53 (1970)].
  10. I. V. Lerner and Yu. E. Lozovik, Zh. Éksp. Teor. Fiz. **78** (3), 1167 (1980) [Sov. Phys. JETP **51**, 588 (1980)].
  11. L. I. Korovin, I. G. Lang, D. A. Contreras-Solorio, and S. T. Pavlov, Fiz. Tverd. Tela (St. Petersburg) **43** (11), 2091 (2001) [Phys. Solid State **43**, 2182 (2001)]; cond-mat/0104262.
  12. J. M. Luttinger and W. Kohn, Phys. Rev. **97**, 869 (1955).
  13. I. M. Tsidil'kovskii, *Band Structure of Semiconductors* (Nauka, Moscow, 1978).
  14. L. I. Korovin and B. É. Éshpulatov, Fiz. Tverd. Tela (Leningrad) **21** (12), 3703 (1979) [Sov. Phys. Solid State **21**, 2137 (1979)].
  15. L. C. Andreani, F. Tassone, and F. Bassani, Solid State Commun. **77** (11), 641 (1991).
  16. L. C. Andreani, in *Confined Electrons and Photons*, Ed. by E. Burstein and C. Weisbuch (Plenum, New York, 1995), p. 57.

*Translated by O. Borovik-Romanova*

---

---

**LOW-DIMENSIONAL SYSTEMS  
AND SURFACE PHYSICS**

---

---

# The Effect of Zeeman Splitting on Shubnikov–De Haas Oscillations in Two-Dimensional Systems

S. A. Tarasenko

*Ioffe Physicotechnical Institute, Russian Academy of Sciences,  
Politekhnikeskaya ul. 26, St. Petersburg, 194021 Russia*

*e-mail: tarasenko@coherent.ioffe.rssi.ru*

Received October 29, 2001

**Abstract**—A theory of the Shubnikov–de Haas effect is developed for two-dimensional systems in a tilted magnetic field. The conductivity tensor is calculated for an arbitrary ratio  $r$  of the Zeeman splitting to the cyclotron splitting. Possible anisotropy of the  $g$  factor is taken into account. It is shown that at integer values of  $r$ , the main harmonic dominates in the spectrum of Shubnikov–de Haas oscillations and the phase of the oscillations depends on the parity of  $r$ . At half-integer values of  $r$ , the conductivity oscillations are determined by the harmonics of the second order of smallness. © 2002 MAIK “Nauka/Interperiodica”.

## 1. INTRODUCTION

It is well known that at low temperatures, the conductivity of a degenerate electron gas in a magnetic field oscillates as the field changes (the Shubnikov–de Haas effect). These oscillations are caused by consecutive crossing of the Fermi level by Landau levels in a quantizing magnetic field. In two-dimensional (2D) systems, small-amplitude conductivity oscillations are observed in classical magnetic fields, when  $\omega_c \tau \sim 1$ . Here,  $\omega_c$  is the cyclotron frequency and  $\tau$  is the carrier relaxation time. The corresponding small parameter determining the amplitude of the oscillations is  $\exp(-\pi/\omega_c \tau)$ . The Shubnikov–de Haas effect in 2D systems was theoretically studied in [1, 2], and at present, the measurement of Shubnikov–de Haas oscillations is one of the main methods for characterizing conducting 2D structures.

In addition to the diamagnetic (cyclotron) quantization, splitting of the electron states into spin sublevels occurs in a magnetic field (Zeeman effect). The magnitude of the splitting  $\Delta$  is linear in the magnetic field and determined by the  $g$  factor of the carriers.

In bulk materials, the condition  $\Delta \ll \hbar \omega_c$  is usually satisfied; therefore, the Zeeman splitting does not affect small-amplitude Shubnikov–de Haas oscillations and manifests itself only in extremely strong magnetic fields, when the amplitude of conductivity oscillations becomes large. Galvanomagnetic phenomena in bulk materials with due regard for spin splitting were considered in [3]. In 2D systems, however, a qualitatively new situation arises. By applying a magnetic field at some angle to the plane of a 2D electron gas, one can vary the ratio  $r = \Delta/\hbar \omega_c$  over a wide range, because in the case of strong quantum confinement of the carriers, the cyclotron splitting is determined by the component of the field  $B_{\perp}$  perpendicular to the plane of the electron

gas [4], whereas the Zeeman splitting is determined by the total magnetic field  $\mathbf{B}$ .

If the magnitude of the Zeeman splitting is comparable to the distance between the Landau levels, the character of magnetic oscillations changes significantly. For example, if the cyclotron splitting is two times larger than the Zeeman splitting ( $r \approx 1/2$ ), the oscillations are observed at the double frequency. Similar magnetic-transport measurements in a tilted magnetic field (suggested in [5]) have been actively carried out in recent years and allow one to determine, for example, the  $g$  factors of electrons in quantum wells [6–13]. However, only qualitative treatment of the experimental data is possible, because there is presently no consistent theory of this effect.

The aim of this paper is to develop a theory of the Shubnikov–de Haas effect for 2D systems in a tilted magnetic field. The Zeeman splitting is considered with due regard for possible anisotropy of the electron  $g$  factor. It is assumed that the carriers are scattered by a short-range potential and the spin relaxation time is significantly larger than the momentum relaxation time.

## 2. CALCULATION OF THE CONDUCTIVITY TENSOR

In order to calculate the conductivity tensor in the case where the Shubnikov–de Haas effect takes place, it is convenient to use a diagrammatic technique. With allowance for spin splitting, the Green’s function of noninteracting electrons in an external magnetic field is generally a  $(2 \times 2)$  matrix:

$$\mathcal{G}_{\varepsilon}(\mathbf{r}, \mathbf{r}') = \sum_{n, k_y} \hat{G}_{\varepsilon}(n, k_y) \psi_{nk_y}(\mathbf{r}) \psi_{nk_y}^*(\mathbf{r}'). \quad (1)$$

Here,  $\Psi_{nk_y}(\mathbf{r}) = \phi_{nk_y}(\boldsymbol{\rho}) u(z)$  are the electron coordinate wave functions in a quantum well under an external magnetic field with the vector potential written in the Landau gauge,  $\mathbf{A} = (0, B_{\perp}x, 0)$ ;  $n$  labels the Landau levels;  $k_y$  is the wave vector; and  $u(z)$  is the quantum confinement function. The wave functions of the carriers in the quantum-well plane  $\phi_{nk_y}(\boldsymbol{\rho})$  and the electronic spectrum are determined by the perpendicular component of the field only, because the size-quantization energy is significantly larger than the distance between the Landau levels.

Let us assume that the condition of a good conductor is satisfied for the electron gas,

$$E_F \tau / \hbar \gg 1, \quad (2)$$

and the Fermi energy  $E_F$  is significantly larger than the magnitude of the spin splitting and the energy distance between the Landau levels,

$$E_F \gg \Delta, \hbar \omega_c, \quad (3)$$

where  $\omega_c = eB_{\perp}/mc$  is the cyclotron frequency,  $m$  is the effective electron mass for the in-plane motion,  $e$  is the elementary charge, and  $c$  is the speed of light.

In the case where the electrons are scattered by a system of randomly distributed short-range scatterers and there is no spin relaxation, the matrix  $\hat{G}_{\varepsilon}$  takes the form

$$\hat{G}_{\varepsilon}(n, k_y) = [\varepsilon + E_F - \hbar \omega_c(n + 1/2) - \hat{H}_s - \hat{X}_{\varepsilon}]^{-1}, \quad (4)$$

where  $\hat{H}_s$  is the Hamiltonian responsible for the Zeeman splitting,

$$\hat{H}_s = (\mu_0/2) \sum_{\alpha\beta} g_{\alpha\beta} \hat{\sigma}_{\alpha} B_{\beta}. \quad (5)$$

Here,  $\mu_0$  is the Bohr magneton,  $g_{\alpha\beta}$  is the electron  $g$ -factor tensor,  $\hat{\sigma}_{\alpha}$  is the Pauli matrix, and  $\alpha$  and  $\beta$  are Cartesian coordinates. In the framework of the self-consistent Born approximation, the self-energy  $\hat{X}_{\varepsilon}$  is independent of the index  $n$  [1, 3] and defined by the equation

$$\hat{X}_{\varepsilon} = \frac{\hbar \omega_c}{\pi} \frac{\hbar}{2\tau} \sum_n \hat{G}_{\varepsilon}(n, k_y). \quad (6)$$

In view of Eqs. (4) and (6), the matrix  $\hat{X}_{\varepsilon}$  can be rewritten as

$$\hat{X}_{\varepsilon} = a_{\varepsilon} \hat{I} + b_{\varepsilon} \hat{H}_{\varepsilon} / \Delta, \quad (7)$$

where  $a_{\varepsilon}$  and  $b_{\varepsilon}$  are complex quantities. The spin splitting  $\Delta$  is generally defined by the formula

$$\Delta = \mu_0 \sqrt{\sum_{\alpha} \left( \sum_{\beta} g_{\alpha\beta} B_{\beta} \right)^2}. \quad (8)$$

In the case of natural anisotropy of the  $g$  factor, caused by the presence of a size-quantization axis, we have  $g_{xx} = g_{yy} = g_{\parallel}$ ,  $g_{zz} = g_{\perp}$ , and  $g_{\alpha\beta} = 0$  ( $\alpha \neq \beta$ ) and Eq. (8) takes the form

$$\Delta = \mu_0 \sqrt{g_{\parallel}^2 B_{\parallel}^2 + g_{\perp}^2 B_{\perp}^2}, \quad (9)$$

where  $B_{\parallel}$  is the component of the magnetic field parallel to the plane of the 2D electron gas.

Using the Poisson summation formula

$$\sum_n f(n) = \frac{f(0)}{2} + \sum_{k=-\infty}^{\infty} \int_0^{\infty} dn \exp(2\pi i k n) f(n) \quad (10)$$

and neglecting the first term, one can derive the following closed system of equations for  $a_{\varepsilon}$  and  $b_{\varepsilon}$  from Eq. (6):

$$a_{\varepsilon} = -i \frac{\hbar}{2\tau} \left\{ 1 + 2 \sum_{k=1}^{\infty} \exp \left[ 2\pi i k \left( \frac{E_F + \varepsilon - a_{\varepsilon}}{\hbar \omega_c} - \frac{1}{2} \right) \right] \times \operatorname{sgn} \varepsilon \right\} \cos \left( \pi k \frac{\Delta + b_{\varepsilon}}{\hbar \omega_c} \right) \operatorname{sgn} \varepsilon, \quad (11)$$

$$b_{\varepsilon} = -\frac{\hbar}{\tau} 2 \sum_{k=1}^{\infty} \exp \left[ 2\pi i k \left( \frac{E_F + \varepsilon - a_{\varepsilon}}{\hbar \omega_c} - \frac{1}{2} \right) \operatorname{sgn} \varepsilon \right] \times \sin \left( \pi k \frac{\Delta + b_{\varepsilon}}{\hbar \omega_c} \right).$$

A similar equation for the self-energy part of the Green's function without regard for spin effects was derived, for example, in [14].

In order to calculate the conductivity tensor at an electric-field frequency  $\omega > 0$ , we use the relationship [3, 14]

$$\sigma_{\alpha\beta}(\omega) = \frac{1}{\omega} \operatorname{Tr} \iint d\mathbf{r} d\mathbf{r}' \int_{-\infty}^{\infty} \frac{d\varepsilon}{2\pi} [\hat{J}_{\alpha}(\mathbf{r}) \mathcal{G}_{\varepsilon + \hbar\omega}(\mathbf{r}, \mathbf{r}')] \times [\hat{J}_{\beta}(\mathbf{r}') \mathcal{G}_{\varepsilon}(\mathbf{r}', \mathbf{r})] + \frac{iNe^2}{m\omega} \delta_{\alpha\beta}, \quad (12)$$

where  $\hat{\mathbf{J}}(\mathbf{r})$  is the current-density operator, which is diagonal with respect to the spin indices,

$$\hat{\mathbf{J}}(\mathbf{r}) = -\frac{e}{m} \left[ -i\hbar \nabla + \frac{e}{c} \mathbf{A}(\mathbf{r}) \right] \hat{I}; \quad (13)$$

$N$  is the total electron concentration; and  $\text{Tr}$  implies summation over the spin variables. Below, we investigate the static conductivity and, therefore, consider the frequency  $\omega$  as a small quantity and replace it by zero in the final expressions. Since the components of the conductivity tensor are real at  $\omega = 0$  and related to one another by the relationships  $\sigma_{xx} = \sigma_{yy}$  and  $\sigma_{xy} = -\sigma_{yx}$ , it will suffice to calculate the quantity

$$\sigma = \sigma_{xx} + i\sigma_{xy}. \quad (14)$$

Using the Green's functions in the coordinate representation given by Eq. (1) and the matrix elements of the current-density operator between the eigenstates of an electron in the magnetic field

$$\begin{aligned} \langle n'k_y' | \hat{J}_x | nk_y \rangle &= ie \sqrt{\frac{\hbar\omega_c}{2m}} \\ &\times (\sqrt{n}\sigma_{n',n-1} - \sqrt{n+1}\delta_{n',n+1})\delta_{k_y,k_y'}, \\ \langle n'k_y' | \hat{J}_y | nk_y \rangle &= -e \sqrt{\frac{\hbar\omega_c}{2m}} \\ &\times (\sqrt{n}\sigma_{n',n-1} - \sqrt{n+1}\delta_{n',n+1})\delta_{k_y,k_y'}, \end{aligned} \quad (15)$$

we can write the conductivity  $\sigma$  in the form

$$\sigma = \frac{e^2\omega_c^2}{2\pi\omega} \text{Tr} \sum_n \int_{-\infty}^{\infty} \frac{d\varepsilon}{2\pi} \hat{G}_{\varepsilon+\hbar\omega}(n) \hat{G}_{\varepsilon}(n-1) + \frac{iNe^2}{m\omega}. \quad (16)$$

After summation over the spin indices, the quantity  $\text{Tr} \hat{G} \hat{G}$  can be written as the sum of two terms,

$$\text{Tr} \hat{G}_{\varepsilon+\hbar\omega} \hat{G}_{\varepsilon} = G_{\varepsilon+\hbar\omega}^{(+)} G_{\varepsilon}^{(+)} + G_{\varepsilon+\hbar\omega}^{(-)} G_{\varepsilon}^{(-)}, \quad (17)$$

each of these terms being a product of the functions

$$G_{\varepsilon}^{(\pm)}(n) = [\varepsilon + E_F \mp \Delta/2 - \hbar\omega_c(n+1/2) - X_{\varepsilon}^{(\pm)}]^{-1}, \quad (18)$$

where

$$X_{\varepsilon}^{(\pm)} = a_{\varepsilon} \pm b_{\varepsilon}/2. \quad (19)$$

Using the system of equations (11) for  $a_{\varepsilon}$  and  $b_{\varepsilon}$ , one can derive independent equations for  $X^{(\pm)}$ ,

$$\begin{aligned} X_{\varepsilon}^{(\pm)} &= -i \frac{\hbar}{2\tau} \left\{ 1 + 2 \sum_{k=1}^{\infty} \exp \left[ 2\pi i k \right. \right. \\ &\times \left. \left. \left( \frac{E_F \mp \Delta/2 + \varepsilon - X_{\varepsilon}^{(\pm)}}{\hbar\omega_c} - \frac{1}{2} \right) \text{sgn} \varepsilon \right] \right\} \text{sgn} \varepsilon, \end{aligned} \quad (20)$$

which differ from each other only in the sign of  $\Delta/2$ .

It is obvious that  $G^{(\pm)}$  are the Green's functions of noninteracting spinless electrons in a magnetic field with the effective Fermi energy  $E_F \mp \Delta/2$ , that is, of the particles occupying the upper and lower spin sublevels, and Eqs. (20) are equations for the self-energy parts of

these Green's functions. Thus, Eq. (17) formally demonstrates that the spin subsystems, as one would expect, give independent contributions to the conductivity in the absence of spin relaxation:  $\sigma = \sigma^{(+)} + \sigma^{(-)}$ . In this case, the contribution from each spin subband to the conductivity can be calculated as the conductivity without spin effects  $\tilde{\sigma}$ , in which  $E_F$  is replaced by the energy distance between the Fermi level and the bottom of the spin subband,  $E_F \pm \Delta/2$ :

$$\sigma^{(\pm)} = \tilde{\sigma}(E_F \mp \Delta/2). \quad (21)$$

Summing over the Landau levels by using the Poisson summation formula (10) (detailed calculations without regard for spin effects are presented in [14]) gives the following expression for the conductivity:

$$\sigma^{(\pm)} = \frac{e^2\tau}{\hbar^3\omega} E_F \quad (22)$$

$$\times \int_{-\infty}^{\infty} \frac{d\varepsilon}{2\pi} (X_{\varepsilon+\hbar\omega}^{(\pm)} - X_{\varepsilon}^{(\pm)}) / (\hbar\omega_c + X_{\varepsilon+\hbar\omega}^{(\pm)} - X_{\varepsilon}^{(\pm)}).$$

Expanding the self-energy parts up to the second order in  $\exp(-\pi/\omega_c\tau)$  yields

$$\begin{aligned} X_{\varepsilon}^{(\pm)} &= -i \frac{\hbar}{2\tau} \left\{ 1 + 2 \exp \left( -\frac{\pi}{\omega_c\tau} \right) \right. \\ &\times \exp \left[ 2\pi i \left( \frac{E_F \mp \Delta/2 + \varepsilon}{\hbar\omega_c} - \frac{1}{2} \right) \text{sgn} \varepsilon \right] \\ &+ 2 \left( 1 - \frac{2\pi}{\omega_c\tau} \right) \exp \left( -\frac{2\pi}{\omega_c\tau} \right) \\ &\times \exp \left[ 4\pi i \left( \frac{E_F \mp \Delta/2 + \varepsilon}{\hbar\omega_c} - \frac{1}{2} \right) \text{sgn} \varepsilon \right] \left. \right\} \text{sgn} \varepsilon. \end{aligned} \quad (23)$$

The final expression for the static-conductivity tensor ( $\omega \rightarrow 0$ ), which is correct to the second order in  $\exp(-\pi/\omega_c\tau)$ , is

$$\begin{aligned} \sigma_{xx} &= \frac{Ne^2\tau/m}{1+\Omega^2} \left\{ 1 + \frac{2\Omega^2}{1+\Omega^2} \delta_1 \right. \\ &+ \left. \left[ \frac{2\Omega^2}{1+\Omega^2} \left( 1 - \frac{2\pi}{\Omega} \right) - \frac{(3-\Omega^2)\Omega^2}{(1+\Omega^2)^2} \right] \delta_2 \right\}, \\ \sigma_{xy} &= -\frac{Ne^2\tau\Omega/m}{1+\Omega^2} \left\{ 1 - \frac{1+3\Omega^2}{(1+\Omega^2)\Omega^2} \delta_1 \right. \\ &- \left. \left[ \frac{1+3\Omega^2}{(1+\Omega^2)\Omega^2} \left( 1 - \frac{2\pi}{\Omega} \right) - \frac{1-3\Omega^2}{(1+\Omega^2)^2} \right] \delta_2 \right\}, \end{aligned} \quad (24)$$

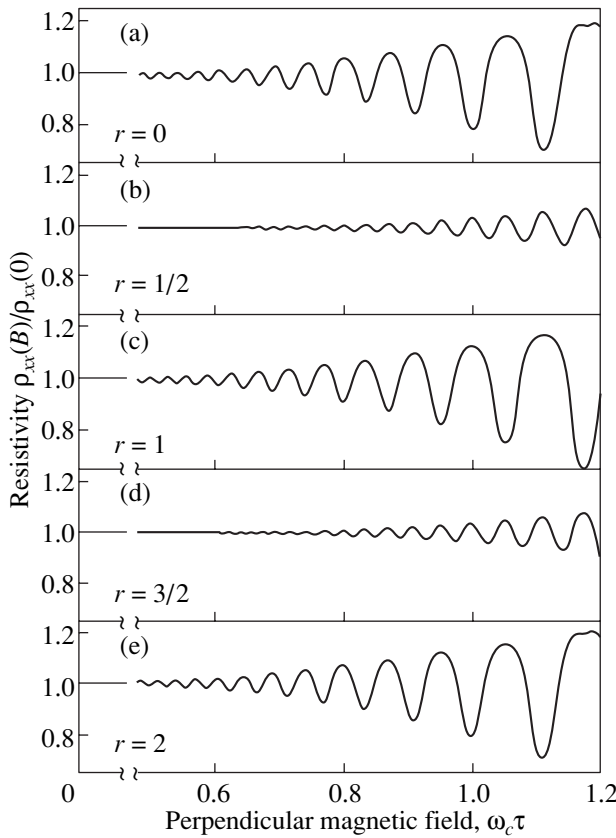


**Fig. 1.** Dependence of the resistivity  $\rho_{xx}$  on magnetic field in the regime of the Shubnikov–de Haas effect for different values of the ratio between the spin and cyclotron splittings of energy levels.

where  $\Omega = \omega_c \tau$  and  $\delta_1$  and  $\delta_2$  are oscillating quantities of the first and second order of smallness, respectively:

$$\delta_1 = 2 \exp\left(-\frac{\pi}{\omega_c \tau}\right) \cos\left(2\pi \frac{E_F}{\hbar \omega_c} - \pi\right) \cos\left(\pi \frac{\Delta}{\hbar \omega_c}\right), \quad (25)$$

$$\delta_2 = 2 \exp\left(-\frac{2\pi}{\omega_c \tau}\right) \cos\left(4\pi \frac{E_F}{\hbar \omega_c}\right) \cos\left(2\pi \frac{\Delta}{\hbar \omega_c}\right).$$

The smearing of the electron distribution at a non-zero temperature leads to temperature damping of the oscillations. A similar calculation of the conductivity tensor at a finite temperature made using the Matsubara diagrammatic technique shows that Eqs. (24) remain unchanged, but extra (conventional) temperature factors appear in the formulas for  $\delta_1$  and  $\delta_2$ :

$$\delta_1 = 2 \exp\left(-\frac{\pi}{\omega_c \tau}\right) \times \cos\left(2\pi \frac{E_F}{\hbar \omega_c} - \pi\right) \cos\left(\pi \frac{\Delta}{\hbar \omega_c}\right) \frac{\lambda}{\sinh \lambda}, \quad (26)$$

$$\delta_2 = 2 \exp\left(-\frac{2\pi}{\omega_c \tau}\right) \times \cos\left(4\pi \frac{E_F}{\hbar \omega_c}\right) \cos\left(2\pi \frac{\Delta}{\hbar \omega_c}\right) \frac{2\lambda}{\sinh 2\lambda},$$

where  $\lambda = 2\pi^2 T / \hbar \omega_c$  and  $T$  is the temperature expressed in energy units.

Equations (24), in combination with Eqs. (26) and (9), describe the magnetoconductivity of two-dimensional systems under the conditions of small-amplitude Shubnikov–de Haas oscillations in a magnetic field of arbitrary direction.

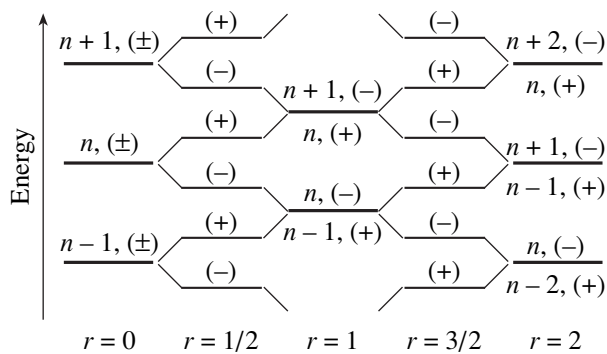
### 3. RESULTS AND DISCUSSION

Figure 1 shows the dependences of the resistivity  $\rho_{xx} = \sigma_{xx} / (\sigma_{xx}^2 + \sigma_{xy}^2)$  on magnetic field at different values of the ratio  $r = \Delta / \hbar \omega_c$ . The dependences were calculated using Eqs. (24) for zero temperature and  $E_F \tau / \hbar = 10$ . In the absence of spin splitting, small-amplitude Shubnikov–de Haas oscillations are determined by the  $\cos(2\pi E_F / \hbar \omega_c)$  harmonic, which is of the first order of smallness in  $\exp(-\pi / \omega_c \tau)$  (Fig. 1a). Multiple harmonics appear only in stronger fields, when the amplitude of oscillations becomes large, and modify the shape of oscillations.

When the spin splitting is comparable to the cyclotron one, the behavior of the Shubnikov–de Haas oscillations qualitatively changes. Since the spin subsystems give additive contributions to the conductivity, the oscillation parameters depend on the relative positions of the Landau levels of the spin subbands. This leads to the appearance of the factors  $\cos(\pi \Delta / \hbar \omega_c)$  and  $\cos(2\pi \Delta / \hbar \omega_c)$  in Eqs. (25) and (26) for the oscillating parts of the conductivity tensor. Figure 2 schematically shows the relative positions of the Landau levels at a certain value of cyclotron splitting and different values of the parameter  $r$ .

At  $r = 1/2, 3/2, \dots$  (half-integer values), the “mismatch” between the Landau levels of the spin subsystems is maximal; that is, the Landau levels of one spin subband are located between the Landau levels of the other subband (Fig. 2). In this case, the contributions from the spin subsystems to the conductivity oscillations cancel out to the first order in  $\exp(-\pi / \omega_c \tau)$ . As a result, the Shubnikov–de Haas effect is determined by the harmonic of the second order of smallness, because the contributions from the spin subsystems to this harmonic coincide when  $r$  is half-integer. Such doubling of the oscillation frequency and a decrease in the amplitude of oscillations are clearly seen in Figs. 1b and 1d.

If the spin splitting is a multiple of the cyclotron splitting (when  $r$  is an integer), the matching of the Landau levels of the spin subsystems occurs (Fig. 2) and the main harmonic again dominates in the spectrum of Shubnikov–de Haas oscillations. However, the positions of the maxima and minima of the resistivity at even (Fig. 1e) and odd (Fig. 1c) values of  $r$  are different, because the positions of the Landau levels differ by  $\hbar \omega_c / 2$  in these two cases (Fig. 2). The second-order har-



**Fig. 2.** Relative positions of the Landau levels of the spin subsystems at different values of the Zeeman splitting.

monics, which slightly change the character of the oscillations, are the same for all integer values of  $r$ .

The Shubnikov–de Haas effect in a tilted magnetic field was experimentally investigated in a number of works [5–13]. The effect of the change in the phase of the main harmonic caused by the transition from an even to an odd value of  $r$  was used to determine the  $g$  factor. In accordance with the results of our calculations, the doubling of the oscillation frequency and a decrease in the amplitude of oscillations were observed when  $r$  was half-integer. The experimental data indicate, however, that the phases of second-harmonic oscillations can be different [9, 11, 12]. In [12], as in our calculations, the extrema of the dependence of  $\rho_{xx}$  on magnetic field at integer values of  $r$  transform to the maxima of the resistivity at half-integer values of  $r$ . In contrast, the data presented in [9, 11] indicate that the phase of the second harmonic is the opposite. Since the phase sign is determined by smooth functions of the magnetic field that are the coefficients of  $\delta_2$  in Eqs. (24), such a difference in the sign is, probably, due to a significant difference between the transport and quantum relaxation times in the structures investigated.

## ACKNOWLEDGMENTS

The author is grateful to N.S. Averkiev and L.E. Golub for useful discussions.

This work was supported by the RF Ministry of Science, the Russian Foundation for Basic Research, INTAS, and the Program of the Presidium of the Russian Academy of Sciences “Quantum Low-Dimensional Structures.”

## REFERENCES

1. T. Ando, *J. Phys. Soc. Jpn.* **37**, 1233 (1974).
2. A. Isihara and L. Smrčka, *J. Phys. C* **19**, 6777 (1986).
3. A. A. Abrikosov, *Zh. Éksp. Teor. Fiz.* **56**, 1391 (1969) [*Sov. Phys. JETP* **29**, 746 (1969)].
4. T. Ando, A. Fowler, and F. Stern, *Rev. Mod. Phys.* **54** (2), 437 (1982).
5. F. F. Fang and P. J. Stiles, *Phys. Rev.* **174**, 823 (1968).
6. T. P. Smith, III and F. F. Fang, *Phys. Rev. B* **35**, 7729 (1987).
7. R. J. Nicholas, R. J. Haug, K. V. Klitzing, and G. Weimann, *Phys. Rev. B* **37**, 1294 (1988).
8. S. J. Koester, K. Ismail, and J. O. Chu, *Semicond. Sci. Technol.* **12**, 384 (1997).
9. D. R. Leadley, R. J. Nicholas, J. J. Harris, and C. T. Foxon, *Phys. Rev. B* **58**, 13036 (1998).
10. W. Pan, D. C. Tsui, and B. L. Draper, *Phys. Rev. B* **59**, 10208 (1999).
11. S. Brosig, K. Ensslin, A. G. Jansen, *et al.*, *Phys. Rev. B* **61**, 13045 (2000).
12. S. A. Vitkalov, H. Zheng, K. M. Mertes, *et al.*, *Phys. Rev. Lett.* **85**, 2164 (2000).
13. V. M. Pudalov, M. Gershenson, H. Kojima, *et al.*, *condmat/0105081*.
14. N. S. Averkiev, L. E. Golub, S. A. Tarasenko, and M. Willander, *J. Phys.: Condens. Matter* **13**, 2517 (2001).

*Translated by A. Poushnov*

---

---

LOW-DIMENSIONAL SYSTEMS  
AND SURFACE PHYSICS

---

---

# Electrical Properties of Tellurium Clusters on the Void Sublattice of an Opal Crystal: The Important Role Played by the Te–SiO<sub>2</sub> Interface

V. A. Berezovets<sup>1,2</sup>, V. N. Bogomolov<sup>1</sup>, I. I. Farbshtein<sup>1</sup>, and V. I. Nizhankovskii<sup>2</sup>

<sup>1</sup>*Ioffe Physicotechnical Institute, Russian Academy of Sciences,  
Politekhnikeskaya ul. 26, St. Petersburg, 194021 Russia  
e-mail: Iosif.Farbshtein@pop.ioffe.rssi.ru*

<sup>2</sup>*International Magnetic Laboratory, Wrocław, 53-421 Poland*

Received October 31, 2001

**Abstract**—The temperature dependences of electrical resistivity and of the Hall effect of nanocluster tellurium crystals obtained by filling the voids in a dielectric (opal) matrix with a melt of pure and doped Te were studied. The Hall hole concentration  $p_{\text{eff}}$  was found to increase anomalously (by more than two orders of magnitude) in a sample prepared from pure Te and cooled to helium temperatures. At  $T = 1.45$  K, the hole concentration in this sample was  $p_{\text{eff}} \cong 6 \times 10^{17} \text{ cm}^{-3}$ . At the same time, the Hall effect in this sample was observed to reverse sign at  $T \cong 200$  K from positive for  $T < 200$  K to negative at higher temperatures. This implies a low impurity concentration ( $N_A$  is less than at least  $10^{15} \text{ cm}^{-3}$ ). A nanocluster crystal of doped Te does not exhibit this anomaly; here, we have  $p_{\text{eff}} \cong 6 \times 10^{17} \text{ cm}^{-3}$  throughout the temperature region covered, as in the original Te. These features are assigned to the formation of a two-dimensional conducting accumulation layer near the Te–amorphous SiO<sub>2</sub> (the opal material) interface at low temperatures; such a layer determines the low-temperature properties of nanocluster crystals prepared from pure Te. Actually, we obtained a model of a three-dimensional structure formed from a two-dimensional film. © 2002 MAIK “Nauka/Interperiodica”.

## 1. INTRODUCTION

Progress made in the growth technologies of synthetic opal [1] has provided a basis for the development of a new class of ordered semiconductor nanostructures, namely, spatially modulated cluster crystals.

Synthetic opal represents a system of silicate spheres of amorphous silicon dioxide, about 200 nm in diameter, that are close-packed, producing an fcc cubic lattice. The material under study is introduced into voids between the spheres. When the voids are filled completely by a metal or semiconductor, the conducting structure thus formed makes up a nanocluster crystal, i.e., a cubic array of octa- and tetrahedral clusters, ~45 and ~85 nm in size (the diameters of inscribed spheres), which share corners [2]. As has been shown by electron microscopy [3], Te introduced into opal crystallizes in the voids between silicate spheres under cooling to form a single-crystal structure corresponding to the tellurium volume lattice, with all clusters having the same crystallographic orientation.

On the other hand, the system of filled voids inside the opal can be considered to be a regular honeycomb structure, with the cells separated by holes corresponding to points of contact between the silicate spheres, which represents an inverted opal lattice [4]. In a real opal, the diameter of these holes varies depending on the technology of preparation. In the sample studied in [5], the diameter was estimated as 2 nm. Thus, the

material embedded in the opal contacts with the matrix material over an extremely large area.

There were grounds to believe that this circumstance would play a decisive role in the electrical properties of a tellurium cluster crystal, because the surface of crystalline tellurium is known to support the formation of an accumulation layer [6].

This publication is the first report of an investigation into the electrical resistivity and Hall effect of samples prepared by injecting original Te doped to various levels into opal performed over a broad range of temperatures and magnetic fields in order to reveal the role played by the Te–silicon dioxide interface in the properties of nanocluster tellurium crystals.

## 2. EXPERIMENT

Nanocluster crystals were prepared by injecting pure melted Te with a residual hole concentration  $p(77 \text{ K}) \sim 10^{14} \text{ cm}^{-3}$  (sample 1) and doped Te with  $p(77 \text{ K}) \approx 5 \times 10^{17} \text{ cm}^{-3}$  (sample 2) under pressure into a matrix (synthetic opal). In the first case, the electron gas (holes) in the original material remained nondegenerate down to helium temperatures. In the second case, the holes are degenerate at low temperatures ( $T < 100$  K).

The samples intended for electrical measurements were  $2 \times 3 \times 8$ -mm rectangular parallelepipeds prepared by mechanical processing of synthetic opal crys-

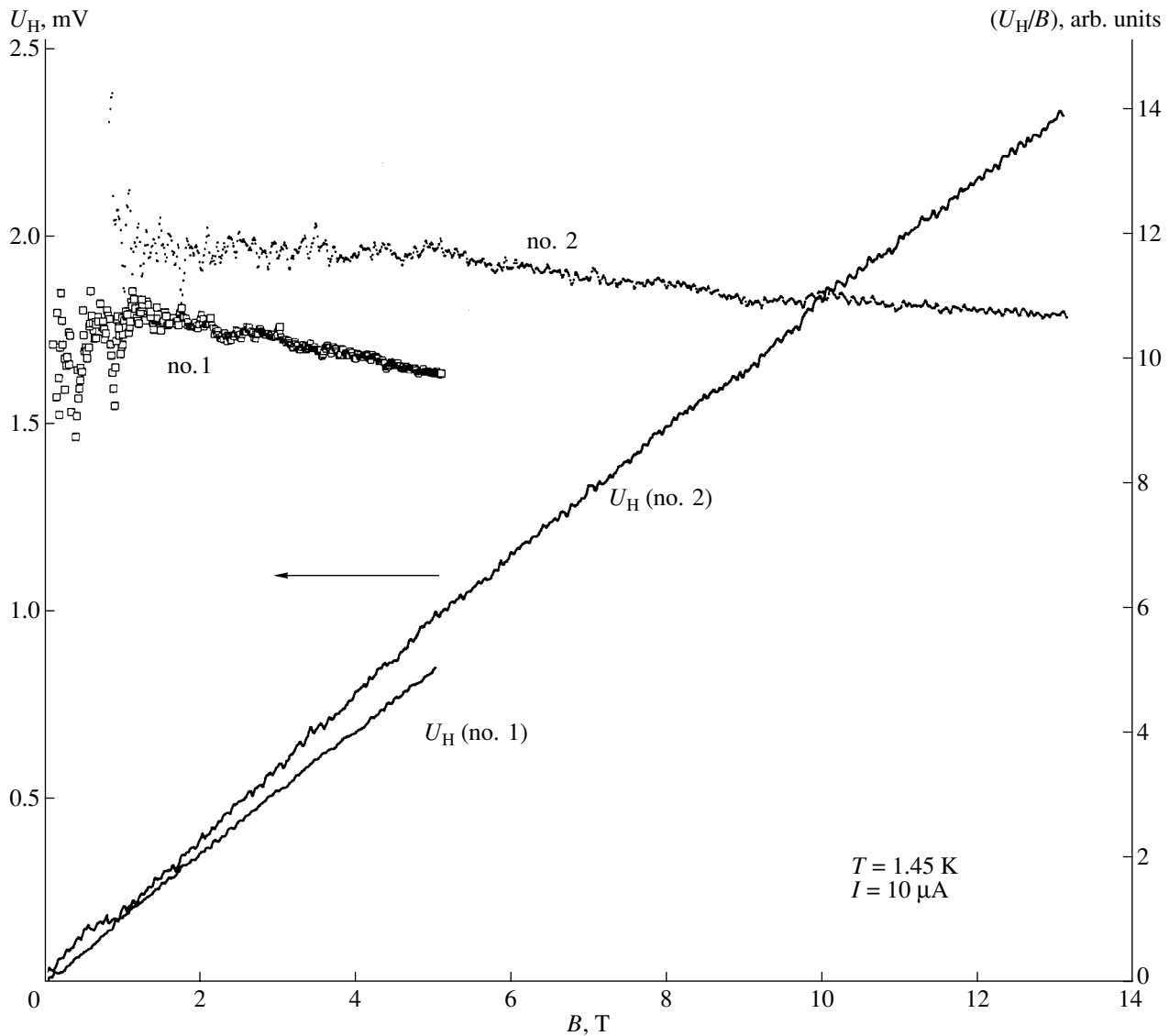


**Fig. 1.** Hall voltage  $U_H$  vs. magnetic-field plots obtained at  $T = 1.4$  K on samples 1 [ $U_H$  (no. 1)] and 2 [ $U_H$  (no. 2)]. Also shown is the magnetic-field dependence of the ratio  $U_H/B \sim R_{\text{eff}}$  for these samples.

tals following tellurium injection. No purposeful alignment of the  $C_3$  crystallographic axis of tellurium with respect to the parallelepiped edges was made. The contacts were prepared by gold deposition through a mask. The electrical resistivity and Hall effect measurements on the cluster samples discussed here were carried out in the magnetic-field range 0–12 T at temperatures of 1.4–300 K with an 11-Hz ac current. The current did not exceed  $10 \mu\text{A}$ . The magnetic field was generated by a superconducting coil, and the measured signal was entered into a computer.

The measurements were conducted at the International Laboratory of Strong Magnetic Fields and Low Temperatures in Wrocław, Poland.

Figure 1 shows the Hall voltage  $U_H$  measured as a function of magnetic field at  $T = 1.4$  K on samples of

both types. The voltages are seen to depend approximately linearly on the magnetic field and to be similar in magnitude. Calculation of the ratio  $U_H^{(i)}/B^{(i)}$  ( $i$  is the number of a data point), which is proportional to the effective Hall coefficient  $R_{\text{H,eff}}$ , revealed a certain decrease in  $R_{\text{H,eff}}$  with increasing magnetic field (Fig. 1). We note that the magnitude of  $R_{\text{H,eff}}$  differs markedly from the microscopic value for bulk tellurium in clusters not only because of the sample size differing geometrically from the total size of the Te clusters (the filling factor), but also as a result of the topological properties of the Te cluster sublattice in opal voids and as a consequence of the Te– $\text{SiO}_2$  interface affecting the conductivity, a point which we touch on later. The rough calculation of the effective hole concentration  $p_{\text{eff}}$

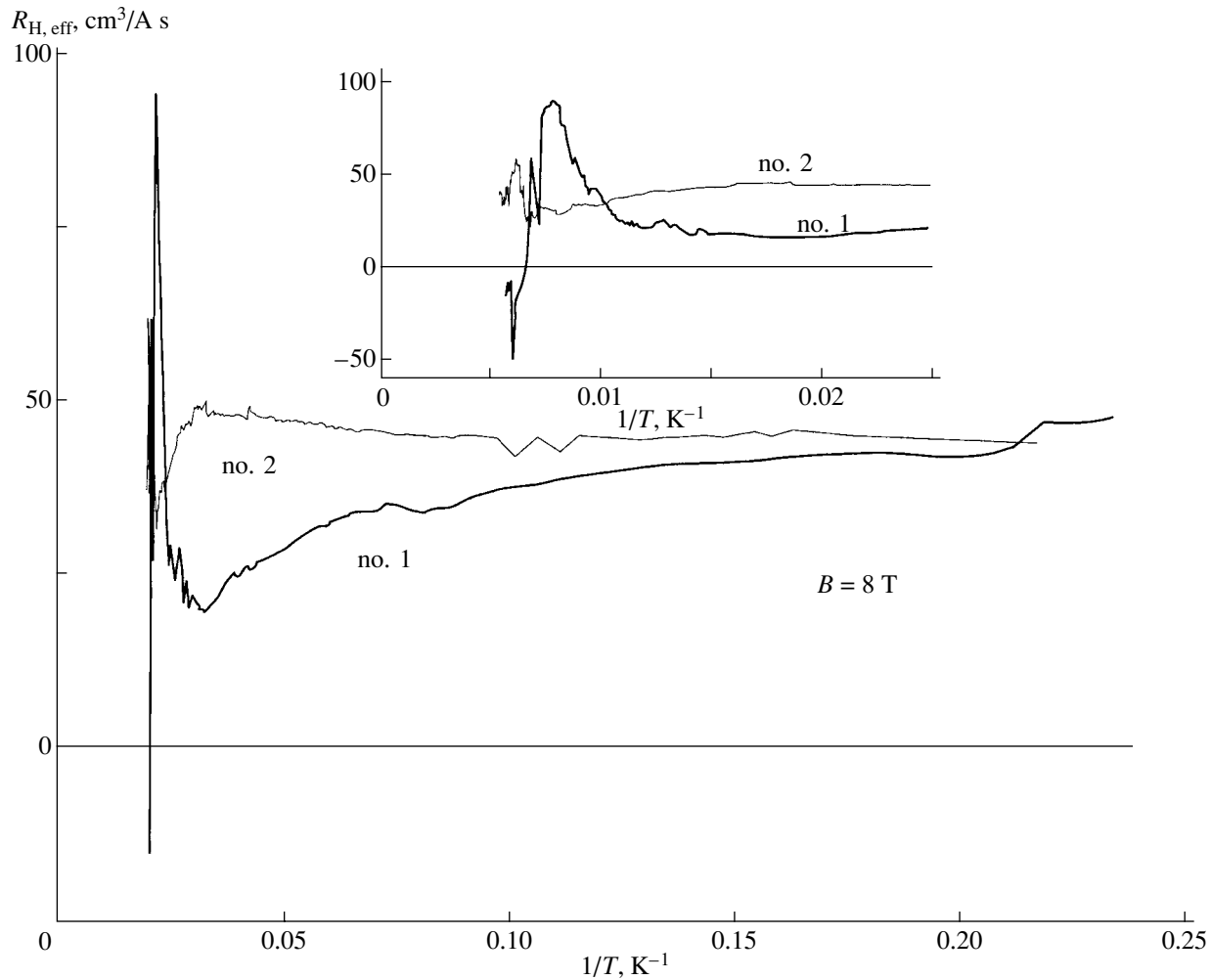


**Fig. 2.** Dependence of the effective Hall coefficient  $R_{H, \text{eff}}$  of samples 1 and 2 on reciprocal temperature. The measurements were performed at  $B = 8$  T.

took into account only the filling factor ( $\sim 25\%$  of the sample volume).

The experiment showed that  $p_{\text{eff}}$  at  $T = 1.45$  K is approximately the same ( $\sim 5.5 \times 10^{17} \text{ cm}^{-3}$ ) for both samples (the magnetic-field-averaged values obtained at 1.45 K are  $p_{\text{eff}} = 6.11 \times 10^{17} \text{ cm}^{-3}$  for sample 1 and  $5.23 \times 10^{17} \text{ cm}^{-3}$  for sample 2). One might thus conclude that the severe technological conditions followed in Te injection into the opal (temperature  $T \sim 600^\circ\text{C}$  and hydrostatic pressure  $P \sim 3$  kbar) favor impurity introduction into the starting material (the doping level of the pure material increases by three orders of magnitude). This conclusion, however, proved to be wrong. Check measurements of  $R_H$  performed on fragments of the starting material after removal from a high-pressure chamber showed the hole concentration of the undoped starting Te to have increased only to  $p(77 \text{ K}) \sim 10^{15} \text{ cm}^{-3}$ .

Figure 2 presents the  $R_{H, \text{eff}}(1/T)$  temperature dependences for both samples measured in a magnetic field of

80 T. The value of  $R_{H, \text{eff}}(77 \text{ K})$  obtained for sample 2 yields  $p_{\text{eff}} \approx 5 \times 10^{17} \text{ cm}^{-3}$  and varies only weakly up to room temperature.  $R_{H, \text{eff}}$  of sample 1, prepared from pure Te, almost coincides below 10 K with the value measured on sample 2. However, as the temperature of sample 1 is increased,  $R_{H, \text{eff}}$  reverses its sign at  $T_{\text{in}} \approx 200$  K from positive (for  $T < T_{\text{in}}$ ) to negative for  $T > T_{\text{in}}$ .

The temperature dependence of effective electrical resistivity ( $\rho_{\text{eff}}$ ) of both samples is displayed graphically in Fig. 3. While the  $\rho_{\text{eff}}(T)$  relation for sample 2 has a metallic character (it grows monotonically with temperature),  $\rho_{\text{eff}}$  of sample 1 decreases with increasing temperature.

### 3. DISCUSSION

The sign reversal of  $R_{H, \text{eff}}$  observed in sample 1 is typical of  $p$ -type semiconductors with a low acceptor concentration  $N_A$  and indicates a transition to mixed conduction with increasing temperature, i.e., to thermal

activation of electrons with a mobility  $u_n$  higher than that of holes,  $u_p$ .

The temperature of the Hall coefficient sign reversal can be used for independent determination of  $N_A$  without recourse to absolute values of the semiconductor electrical characteristics. In the case of a cluster crystal, this approach acquires specific significance, because the result does not depend here on the topological characteristics of the object.<sup>1</sup>

In general, the magnitude and sign of the Hall coefficient  $R(H)$  depend on the contributions provided by all active groups of carriers to the conductivity in a magnetic field:

$$R(H) = \frac{\sigma(H)_{xy}^2}{\sigma(H)_{xx}^2 + \sigma(H)_{xy}^2}, \quad (1)$$

where  $\sigma_{xy} = \sum \sigma_{xy}^i$  and  $\sigma_{xx} = \sum \sigma_{xx}^i$ .

In the case of a magnetic field tending to zero, Eq. (1) for the standard band-structure model can be presented in the form

$$R = -\frac{A}{ec} \frac{nu_n^2 - pu_p^2}{(nu_n + pu_p)^2}, \quad (2)$$

where  $u_n$  and  $u_p$  are the mobilities of the electrons and holes, respectively;  $n$  and  $p$  are their respective concentrations; and  $A$  is a coefficient of order unity which depends on the scattering mechanism and the statistics of carriers.

By combining the condition of the zero Hall coefficient

$$p/n = (u_n/u_p)^2 = b^2 \quad (3)$$

with the charge neutrality equation

$$(p + N_A)n = n_i^2,$$

$$n_i^2 = np = (N_c N_v)^3 T^{3/2} \exp(E_g/2kT), \quad (4)$$

one can determine the concentration of the ionized acceptor impurity  $N_A$  at the temperature of the Hall coefficient sign reversal. Calculations made for tellurium at  $T_{in} = 200$  K in this model yield  $N_A \cong 1.8 \times 10^{14} \text{ cm}^{-3}$ .

We used here  $u_n/u_p \cong 1.6$  and  $m_n^* m_p^* = 0.076 m_0^2$  [7]. Note that  $R(T)$  of single-crystal Te samples with a concentration  $p(77 \text{ K}) \cong 1 \times 10^{14} \text{ cm}^{-3}$  does indeed reverse sign at  $T_{in} \cong 200$  K (see, e.g., [8]).

The value of  $N_A$  thus obtained corresponds to the residual hole concentration  $p(77 \text{ K})$  in the starting

<sup>1</sup> When determining the microscopic characteristics, the topological features of a nanocluster crystal can be roughly included within a simplified geometric model, for instance, a model of spheres connected by cylindrical channels [2], paralleled by simultaneous measurement of the resistance, Hall effect, and magnetoresistance in a weak magnetic field.

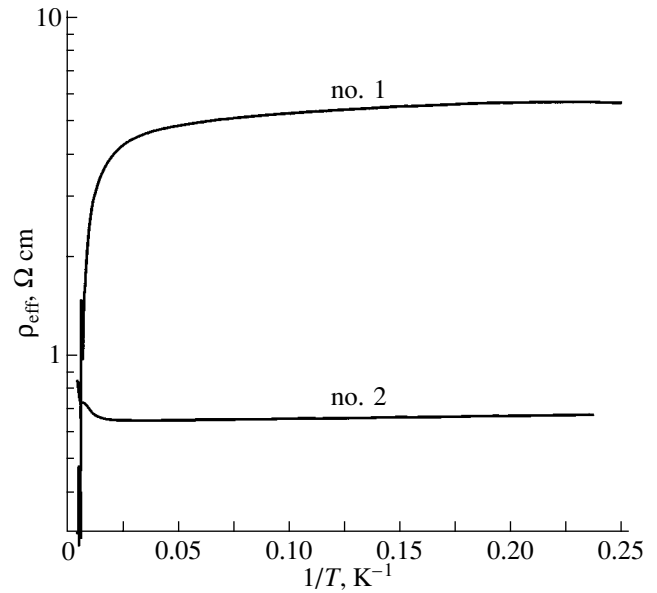


**Fig. 3.** Electrical resistivity  $\rho_{\text{eff}}$  of samples 1 and 2 measured as a function of reciprocal temperature.

material and is at odds with the low-temperature measurements presented graphically in Fig. 1. This suggests a qualitative conclusion that the value of  $R_{H, \text{eff}}$  measured on the undoped starting material at low temperatures (Fig. 1) cannot be identified with the concentration of three-dimensional (3D) holes in the bulk of Te clusters.

No such phenomenon was observed in the Te cluster crystal prepared from a strongly doped material. In this case, as expected,  $R_{H, \text{eff}}$  remains virtually temperature-independent up to 300 K. This appears only natural, because at high values of  $N_A$ , the  $R_H$  sign reversal occurs at substantially higher temperatures.

We propose the following model to account for these contradictory results.

It is known that the free surface of single-crystal tellurium is always coated by a thin ( $\sim 2$  nm thick) film of natural tellurium oxide  $\text{TeO}_2$ . This oxide is a dielectric with a large band gap width. It is because of the existence of the Te– $\text{TeO}_2$  interface on the Te surface that a layer of thickness of the order of 10 nm with an enhanced content of free two-dimensional (2D) holes (size-quantized accumulation layer, AL) forms on the Te surface [6]. The hole concentration in the AL as derived from the Shubnikov–de Haas effect is approximately  $10^{12} \text{ cm}^{-2}$  (or  $p \approx 10^{18} \text{ cm}^{-3}$ , if reduced to three-dimensional volume), and the mobility of the 2D holes exceeds that of holes in the volume by nearly an order of magnitude [9]. If the Te– $\text{SiO}_2$  (opal) contact produces an effect similar to that of Te– $\text{TeO}_2$ , a layer with an enhanced hole concentration should also form in the Te– $\text{SiO}_2$  interface. Recalling that a cluster crystal has an extremely large Te– $\text{SiO}_2$  interface, one readily

comes to the conclusion that the major contribution to the electrical conductivity and Hall effect at helium temperatures is due to charge carriers in the AL. In this case, the value of  $R_{H, \text{eff}}$  measured at low temperatures contains, according to Eq. (1), contributions from 2D holes in the AL and from 3D holes in the bulk of the clusters, as in the case of bulk Te samples with a surface AL [6]. As the temperature increases and the system crosses over to the state of mixed conduction, the concentration of free carriers (primarily, of electrons) increases, the screening length decreases rapidly, and the AL disappears. Therefore, for  $T > 100$  K, we deal already with volume conduction, where Eq. (2) is appropriate for the Hall coefficient. In a Te cluster crystal prepared from a strongly doped material, an AL does not form at all, because the screening length for doped Te is small and the surface layer does not contain allowed states.

This model provides an explanation for the fact that the temperature dependences of electrical resistivity  $\rho(T)$  of the samples studied follow different patterns (Fig. 3). In sample 1,  $\rho(T)$  has a semiconducting character with a transition to intrinsic conductivity at high temperatures, whereas sample 2, because of the electron gas being strongly degenerate, behaves as a dirty metal. One can thus conclude that the major contribution to low-temperature galvanomagnetic effects is due to 3D carriers in the sample with doped tellurium and to 2D holes in the AL on the Te–SiO<sub>2</sub> interface in the “pure” sample. According to Eq. (1), the value of  $R_{\text{eff}}$  measured on sample 1 at low temperatures is determined by the sum  $\sigma_{xy}(2D) + \sigma_{xy}(3D)$  and depends primarily on the concentration of 2D holes in the AL.

The two-group conductivity model proposed for the Te cluster crystal at helium temperatures is also argued for by the above-mentioned slight decrease in  $R_{H, \text{eff}}$  observed to occur with increasing magnetic field (Fig. 1). Indeed, in accordance with Eq. (1), an increase in the magnetic field brings about a decrease in the relative contribution from the group of fast charge carriers to  $\sigma_{xy}$  and, accordingly, a decrease in  $R_{\text{eff}}$ . For sample 1, such carriers are 2D holes. In sample 2, the role of the second group of carriers is apparently played by holes residing in regions of size comparable to the extension in space of their wave functions but possessing a considerably lower mobility.

As a result of the Te cluster crystals having a large surface area in the opal matrix, the main carrier scattering mechanism here involves the Te–SiO<sub>2</sub> interface. Estimation of the hole mobility in the samples studied yielded  $u_{\text{eff}}(\text{sample 1}) = 10 \text{ cm}^2/(\text{V s})$  and  $u_{\text{eff}}(\text{sample 2}) = 100 \text{ cm}^2/(\text{V s})$ . No such low mobility has thus far been observed in Te. The interface mechanism of scattering is also indicated by the fact that the mobility in the dirty sample is an order of magnitude higher than that in the pure one, where the electrical conductivity is determined by the interface charge carriers.

An interface or a thin interlayer of modified tellurium separating the sublattice of octahedral and tetrahedral tellurium clusters from the amorphous SiO<sub>2</sub> spheres making up the opal lattice forms an interface bubble lattice. An earlier publication [10] described a silicon bubble lattice obtained by Si deposition on the inner opal surface. In our case, the physical properties of such an interface bubble lattice are determined by both the contact effects between the Te sublattice and the SiO<sub>2</sub> spheres and the symmetry of the opal lattice and of its three-dimensional volume replica (Te sublattice). In the case of *n*- and *p*-cluster sublattices, the interface will represent a large-area *p*–*n* junction, which can be treated as a superrectifier or a supercapacitor [11].

#### ACKNOWLEDGMENTS

This study was supported by the Russian Foundation for Basic Research (project no. 00-02-16894), the Ministry of Science and Industry (grant no. 97-1041), and the Basic Research Program of the Presidium of the RAS “Low-Dimensional Structures.”

#### REFERENCES

1. V. G. Balakirev, V. N. Bogomolov, V. V. Zhuravlev, *et al.*, *Kristallografiya* **38** (3), 111 (1993) [*Crystallogr. Rep.* **38**, 348 (1993)].
2. V. N. Bogomolov and T. M. Pavlova, *Fiz. Tekh. Poluprovodn. (St. Petersburg)* **29** (5), 826 (1995) [*Semiconductors* **29**, 428 (1995)].
3. V. N. Bogomolov, L. M. Sorokin, D. A. Kurdyumov, *et al.*, *Fiz. Tverd. Tela (St. Petersburg)* **39** (11), 2090 (1997) [*Phys. Solid State* **39**, 1869 (1997)].
4. C. M. Sotomayor Torres, T. Maka, M. Müller, *et al.*, in *Proceedings of the 8th International Symposium “Nanostructures: Physics and Technology,” St. Petersburg, Russia, 2000*, p. 224.
5. V. N. Bogomolov, L. S. Parfen'eva, I. A. Smirnov, *et al.*, *Fiz. Tverd. Tela (St. Petersburg)* **44** (1), 175 (2002) [*Phys. Solid State* **44**, 181 (2002)].
6. V. A. Berezovets, I. I. Farbshtein, and A. L. Shelankov, *Fiz. Tverd. Tela (Leningrad)* **25** (5), 2988 (1983) [*Sov. Phys. Solid State* **25**, 1725 (1983)].
7. M. V. Glushkov, E. S. Itskevich, Yu. V. Kosichkin, *et al.*, *Zh. Éksp. Teor. Fiz.* **71** (9), 1239 (1976) [*Sov. Phys. JETP* **44**, 648 (1976)].
8. H. Roth, *J. Phys. Chem. Solids* **8**, 525 (1959).
9. V. A. Berezovets and I. I. Farbshtein, *Fiz. Tekh. Poluprovodn. (St. Petersburg)* **29** (5/6), 965 (1995) [*Semiconductors* **29**, 500 (1995)].
10. V. N. Bogomolov, N. F. Feoktistov, V. G. Golubev, *et al.*, *Inst. Phys. Conf. Ser.* **164**, 533 (1999).
11. V. N. Bogomolov, *Phys. Rev. B* **51** (23), 17040 (1995).

*Translated by G. Skrebtsov*

**LOW-DIMENSIONAL SYSTEMS  
AND SURFACE PHYSICS**

# Dynamic Fluctuation Electromagnetic Interaction of a Nonrelativistic Quadrupole Particle with a Flat Surface

A. A. Kyasov and G. V. Dedkov

*Kabardino-Balkar State University, ul. Chernyshevskogo 173, Nalchik, 360004 Russia*

*e-mail: dv\_dedkov@mail.ru*

Received November 22, 2001

**Abstract**—Within the framework of the nonrelativistic fluctuation electromagnetic theory, relationships for the quadrupole–quadrupole contribution to the tangential and normal components of the force acting on a particle moving parallel to the polarizing surface are derived for the first time. Consideration is given to the cases when the particle possesses a permanent quadrupole moment or a fluctuation quadrupole moment and the surface is characterized by a local dielectric function. © 2002 MAIK “Nauka/Interperiodica”.

## 1. INTRODUCTION

As far as we know, all theoretical investigations into the interaction of moving neutral particles with a surface have hitherto been performed only within the dipole approximation (see, for example, [1–4]), specifically for the cases of particles with both a permanent dipole moment (a polar molecule, etc.) and a fluctuation moment (an atom in the ground state, etc.). However, there exists a diversity of molecules with a zero dipole moment  $\mathbf{d}$  but with a nonzero quadrupole moment  $Q_{ik}$  and higher-order multipole moments. For example, among these molecules are all homonuclear molecules ( $H_2$ ,  $N_2$ ,  $O_2$ , etc.) [5]. Spherical particles that have no permanent multipole moments possess the fluctuation moments  $\mathbf{d}^{sp}$ ,  $Q_{ik}^{sp}$ , and  $L_{ijk}^{sp}$  with zero mean values but with nonzero mean squares [5, 6]. This provides interaction of the spherical particles with each other and with the surface at distances considerably longer than the interatomic distances. Despite the fact that the dipole contribution to the fluctuation interaction of spherical particles with the surface dominates in the vicinity of the van der Waals minimum, the inclusion of higher-order multipole moments is of the utmost significance [6].

The purpose of the present work is to develop the nonrelativistic theory of dynamic interaction between neutral particles and a surface [2–4] with inclusion of a permanent quadrupole moment or a fluctuation quadrupole moment.

## 2. THE PARTICLE WITH A PERMANENT QUADRUPOLE MOMENT (A QUADRUPOLE MOLECULE)

By analogy with the approach developed in [2–4], we consider a point particle with the quadrupole moment  $Q_{ik}$  that moves in vacuum with the nonrelativ-

istic velocity  $V$  along the  $x$  axis aligned parallel to a flat surface bounding a semi-infinite medium with the permittivity  $\epsilon(\omega)$ . The particle and the surface are separated by a distance  $z_0$ . The space density of bound charges of the quadrupole particle can be represented in the form [6]

$$\rho(x, y, z, t) = \frac{1}{3} \nabla_i \nabla_k \times \{ \delta(x - Vt) \delta(y) \delta(z - z_0) Q_{ik} \}. \quad (1)$$

It should be noted that the quadrupole moment tensor involved in expression (1) is defined as

$$Q_{ik} = \frac{1}{2} \int \rho(r') (3x'_i x'_k - \delta_{ik} r'^2) d^3 r'. \quad (2)$$

This expression differs from the most universally accepted definition [7, 8] by a multiplier of 1/2. Definition (2) used in [5, 6] is more convenient in terms of the spherical tensor formalism.

With due regard for expression (1), the Poisson equation for the electric potential can be written in the form

$$\Delta \varphi(x, y, z, t) = -\frac{4\pi}{3} \nabla_i \nabla_k \times \{ \delta(x - Vt) \delta(y) \delta(z - z_0) Q_{ik} \}. \quad (3)$$

After the Fourier transformation of both sides of Eq. (3) with respect to components of the two-dimensional wave vector  $(k_x, k_y)$  in a plane of the surface, we have

$$\left( \frac{d^2}{dz^2} - k^2 \right) \varphi_{\omega \mathbf{k}}(z) = \frac{8\pi^2}{3} \delta(\omega - k_x V) \times \{ (k_x^2 Q_{xx} + k_y^2 Q_{yy} + 2k_x k_y Q_{xy}) \delta(z - z_0) - (2ik_x Q_{xz} + 2ik_y Q_{yz}) \delta'(z - z_0) - Q_{zz} \delta''(z - z_0) \}. \quad (4)$$

The solution of Eq. (4) for the Fourier component of the induced potential has the following form (for more details, see the Appendix):

$$\begin{aligned} \varphi_{\omega\mathbf{k}}(z) = & \frac{4\pi^2}{3k} \delta(\omega - k_x V) \Delta(\omega) \exp(-k(z + z_0)) \\ & \times \{k_x^2 Q_{xx} + k_y^2 Q_{yy} + 2k_x k_y Q_{xy} \\ & - 2ik_x Q_{xz} - 2ik_y Q_{yz} - k^2 Q_{zz}\}, \end{aligned} \quad (5)$$

$$\text{where } \Delta(\omega) = \frac{\varepsilon(\omega) - 1}{\varepsilon(\omega) + 1}.$$

Note that the components of the tensor  $Q_{ik}$  in Eqs. (4) and (5) can also be calculated in the coordinate system related to the particle, because they do not depend on the shift of the coordinate system provided the particle has zero charge and zero dipole moment [5, 6].

Let us now calculate the lateral ( $F_x$ ) and normal ( $F_z$ ) forces acting on the particle on the side of the induced field of the surface. The Hamiltonian of the interaction of the quadrupole  $Q_{ik}$  with an external electric field can be represented by the expression [6]

$$\mathcal{H} = -\frac{1}{3} Q_{ik} \nabla_k E_i. \quad (6)$$

Taking into account expression (6), we obtain

$$F_x = \frac{1}{3} \nabla_x Q_{ik} \nabla_k E_i = -\frac{1}{3} \nabla_x Q_{ik} \nabla_k \nabla_i \varphi^{\text{in}}, \quad (7)$$

$$F_z = \frac{1}{3} \nabla_z Q_{ik} \nabla_k E_i = -\frac{1}{3} \nabla_z Q_{ik} \nabla_k \nabla_i \varphi^{\text{in}}. \quad (8)$$

It should be remembered that, in relationships (7) and (8), we first perform the differentiation with respect to spatial variables and then substitute the coordinates of the moving particle,  $\mathbf{r}_0(t) = (Vt, 0, z_0)$ .

Next, the induced potential  $\varphi^{\text{in}}$  is expanded in a Fourier integral with respect to spatial and time variables [ $\varphi_{\omega\mathbf{k}}(z)$  is defined by formula (5)] and the resultant expression is substituted into relationships (7) and (8) with due regard for the above remark. Upon integrating by parts and transforming the limits of integration over  $k_x k_y$  to the interval  $(0, \infty)$  with allowance made for the evenness of the real part and the oddness of the imaginary part of the dielectric function  $\varepsilon(\omega)$ , we obtain the following expressions:

$$\begin{aligned} F_x = & -\frac{2}{9\pi} \int_0^\infty \int dk_x dk_y k_x \exp(-2kz_0) \frac{\Delta''(k_x V)}{k} \\ & \times \{k_x^4 Q_{xx}^2 + k_y^4 Q_{yy}^2 + k^4 Q_{zz}^2 + 2k_x^2 k_y^2 (2Q_{xy}^2 + Q_{xx} Q_{yy}) \\ & + 2k_x^2 k^2 (2Q_{xz}^2 - Q_{xx} Q_{zz}) + 2k_y^2 k^2 (2Q_{yz}^2 - Q_{yy} Q_{zz})\}, \end{aligned} \quad (9)$$

$$\begin{aligned} F_z = & -\frac{2}{9\pi} \int_0^\infty \int dk_x dk_y \exp(-2kz_0) \Delta'(k_x V) \\ & \times \{k_x^4 Q_{xx}^2 + k_y^4 Q_{yy}^2 + k^4 Q_{zz}^2 + 2k_x^2 k_y^2 (2Q_{xy}^2 + Q_{xx} Q_{yy}) \\ & + 2k_x^2 k^2 (2Q_{yz}^2 - Q_{xx} Q_{zz}) + 2k_y^2 k^2 (2Q_{yz}^2 - Q_{yy} Q_{zz})\}. \end{aligned} \quad (10)$$

Here, the real and imaginary components of the function  $\Delta(k_x V)$  are denoted by one and two primes, respectively.

Expressions (9) and (10) describe not only the interaction of moving homonuclear molecules with a surface but also the interaction between a surface and more complex molecules (benzene, ethylene, etc.) that possess more than one symmetry axis, a reflection axis, or the center of symmetry. In all the above cases, the first nonzero moment of a particle is the quadrupole moment [5].

In the static case (at  $V = 0$ ), we have  $F_x = 0$  and the integration of expression (10) with respect to wave vectors leads to the relationship for the attractive force

$$\begin{aligned} F_z = & -\frac{5}{192z_0^6} \frac{\varepsilon - 1}{\varepsilon + 1} \\ & \times \{3Q_{xx}^2 + 3Q_{yy}^2 + 8Q_{zz}^2 + 2(2Q_{xy}^2 + Q_{xx} Q_{yy}) \\ & + 8(2Q_{xz}^2 - Q_{xx} Q_{zz}) + 8(2Q_{yz}^2 - Q_{yy} Q_{zz})\}, \end{aligned} \quad (11)$$

where  $\varepsilon$  is the static permittivity. Formula (11) can be appreciably simplified for an axially symmetric molecule whose axis is perpendicular to the surface. In this case, the nondiagonal components of the quadrupole moment tensor are taken as zero and the diagonal components are related through the simple expression [5]

$$Q_{xx} = Q_{yy} = -Q_{zz}/2. \quad (12)$$

By substituting these relationships into expression (11), we have

$$F_z = -\frac{15}{32} \frac{Q_{zz}^2 \varepsilon - 1}{z_0^6 \varepsilon + 1}. \quad (13)$$

Formula (13) can also be derived in a simpler manner as follows. Let us consider a system of three point charges ( $e, -2e, e$ ) whose coordinates on the  $z$  axis are given by  $(z_0 - a, z_0, z_0 + a)$ . In this system, according to definition (2), we have  $Q_{zz} = 2ea^2$ . The image charges in this case are determined as  $\frac{\varepsilon - 1}{\varepsilon + 1} (e, -2e, e)$  [9]. Recall that the energy of the system accounts for the interaction between the charges and their images. By expanding the energy of the system into a series with respect

to the small parameter  $a/z_0$ , to a first nonvanishing approximation, we obtain the expression

$$U(z_0) = -\frac{3e^2a^4\varepsilon - 1}{8z_0^5\varepsilon + 1} = -\frac{3Q_{zz}^2\varepsilon - 1}{32z_0^5\varepsilon + 1}. \quad (14)$$

Taking into account the relationship  $F_z = -\partial U(z_0)/\partial z_0$ , formula (13) immediately follows from expression (14).

### 3. THE PARTICLE WITH A FLUCTUATING QUADRUPOLE MOMENT

Before proceeding to the case of a moving fluctuating quadrupole, we should note that, in addition to the fluctuation quadrupole moment  $Q_{ik}^{\text{sp}}$ , a neutral particle possesses the fluctuation dipole moment  $\mathbf{d}^{\text{sp}}$  (apart from the other fluctuation multipole moments). For a spherical particle in its own coordinate system, no correlation between the fluctuation quadrupole moment  $Q_{ik}^{\text{sp}}$  and the fluctuation dipole moment  $\mathbf{d}^{\text{sp}}$  is revealed [6]. However, upon changing over to another coordinate system through the parallel shift  $\mathbf{r} \rightarrow \mathbf{r}' = \mathbf{r} - \mathbf{b}$ , the components of the quadrupole moment tensor defined by formula (2) can be represented in the form [6]

$$Q_{ik}^{\text{sp}'} = Q_{ik}^{\text{sp}} - \frac{3}{2}(d_i^{\text{sp}}b_k + d_k^{\text{sp}}b_i) + (\mathbf{d}^{\text{sp}}\mathbf{b})\delta_{ik}. \quad (15)$$

From relationship (15), it follows that, in the coordinate system related to the surface, the fluctuation dipole moment correlates with the fluctuation quadrupole moment; i.e.,  $\langle d_i^{\text{sp}'} Q_{ik}^{\text{sp}'} \rangle \neq 0$ . By virtue of this correlation, the total force acting on the moving neutral particle on the side of the surface can be written as

$$F_x = F_x^{d-d} + F_x^{d-Q} + F_x^{Q-Q}. \quad (16)$$

The first term in relationship (16) describes the retarding force within the dipole approximation in the case when the quadrupole and higher-order multipole moments are equal to zero. To the best of our knowledge, all the theoretical works dealing with the calculation of dissipative tangential forces were reduced to analyzing only this contribution. In relationship (16), the second term accounts for the correlation between the dipole moment and the quadrupole moment and the third term describes the quadrupole contribution. Formally, the quadrupole contribution can be obtained from relationship (16) at  $\mathbf{d}^{\text{sp}} = 0$ . In this work, we will restrict our consideration to the case of the purely quadrupole contribution.

For a fluctuating quadrupole moment, the expression for the tangential force takes the form

$$F_x = \frac{1}{3} \langle \nabla_x Q_{ij}^{\text{sp}} \nabla_j E_i^{\text{in}} \rangle + \frac{1}{3} \langle \nabla_x Q_{ij}^{\text{in}} \nabla_j E_i^{\text{sp}} \rangle. \quad (17)$$

In formula (17), the first term describes the contribution of spontaneous fluctuations of the quadrupole moment and the second term accounts for the contribution of the fluctuation electromagnetic field of the surface. The Poisson equation for the Fourier component of the potential  $\varphi_{\omega\mathbf{k}}(z)$  takes the form

$$\begin{aligned} \left( \frac{d^2}{dz^2} - k^2 \right) \varphi_{\omega\mathbf{k}}(z) &= \frac{4\pi}{3} \{ (k_x^2 Q_{xx}(\omega - k_x V) \\ &\times k_y^2 Q_{yy}(\omega - k_x V) + 2k_x k_y Q_{xy}(\omega - k_x V) \\ &\times \delta(z - z_0 - (2ik_x Q_{xz}(\omega - k_x V) \\ &+ 2ik_y Q_y(\omega - k_x V)) \delta'(z - z_0) \\ &- Q_{zz}(\omega - k_x V) \delta''(z - z_0) \}. \end{aligned} \quad (18)$$

The solution of Eq. (18) (see the Appendix) has the following form:

$$\begin{aligned} \varphi_{\omega\mathbf{k}}(z) &= \frac{2\pi}{3k} \Delta(\omega \exp(-k(z - z_0))) \{ k_x^2 Q_{xx}(\omega - k_x V) \\ &+ k_y^2 Q_{yy}(\omega - k_x V) + 2k_x k_y Q_{xy}(\omega - k_x V) \\ &- 2ik_x Q_{xz}(\omega - k_x V) - 2ik_y Q_{yz}(\omega - k_x V) \\ &- k^2 Q_{zz}(\omega - k_x V) \}. \end{aligned} \quad (19)$$

In order to calculate the first term in relationship (17), the quadrupole moment  $Q_{ij}^{\text{sp}}$  is expanded in the Fourier frequency integral and the components of the field  $E_i^{\text{in}}$  are expanded in the Fourier integral with respect to the frequency and the two-dimensional wave vector. Next, the Fourier components of the induced field are expressed in terms of  $\varphi_{\omega\mathbf{k}}$  with due regard for relationship (19). The resultant correlator of the quadrupole moment can be calculated using the fluctuation dissipative relationship [6]

$$\begin{aligned} \langle Q_{ik}^{\text{sp}}(\omega) Q_{lj}^{\text{sp}}(\omega') \rangle &= 2\pi \delta(\omega + \omega') \frac{3\hbar}{4} \coth \frac{\hbar\omega}{2k_B T} \\ &\times \text{Im} \alpha^{(2)}(\omega) \left( \delta_{il} \delta_{kj} + \delta_{ij} \delta_{kl} - \frac{2}{3} \delta_{ik} \delta_{lj} \right), \end{aligned} \quad (20)$$

where  $\alpha^{(2)}(\omega)$  is the quadrupole polarizability. After transformations with allowance made for the evenness of the real parts and the oddness of the imaginary parts of the functions  $\alpha^{(2)}(\omega)$  and  $\varepsilon(\omega)$ , the contribution of spontaneous fluctuations of the quadrupole moment to the tangential force can be written in the form

$$\begin{aligned} F_x^{(1)} &= -\frac{2\hbar}{3\pi^2} \iiint_0^\infty d\omega dk_x dk_y k_x k^3 \exp(-2kz_0) \\ &\times \coth \frac{\hbar\omega}{2k_B T_1} \alpha^{(2)''}(\omega) [\Delta''(\omega + k_x V) - \Delta''(\omega - k_x V)], \end{aligned} \quad (21)$$

where  $T_1$  is the temperature of the particle.

The second term in formula (17) can be calculated using a linear integral relationship between the induced quadrupole moment and the Fourier components of the fluctuation field of the surface. For this purpose, the components of the field  $E_i^{\text{sp}}$  entering into formula (17) are expanded in Fourier integrals with respect to  $\omega$ ,  $k_x$ , and  $k_y$ . The correlators of the spatial derivatives of the surface field, which appear in the course of the calculation, are expressed through the components of the retarded Green's function of a photon in the medium in accordance with the general result of the theory of electromagnetic fluctuations [10]. After transformations similar to those applied to derive relationship (21), we obtain

$$F_x^{(2)} = -\frac{2\hbar}{3\pi^2} \int_0^\infty \int \int d\omega dk_x dk_y k_x k^3 \exp(-2kz_0) \times \coth \frac{\hbar\omega}{2k_B T_2} \Delta''(\omega) [\alpha^{(2)''}(\omega + k_x V) - \alpha^{(2)''}(\omega - k_x V)], \quad (22)$$

where  $T_2$  is the temperature of the surface. By combining expressions (21) and (22), we finally obtain

$$F_x^{Q-Q} = -\frac{2\hbar}{3\pi^2} \int_0^\infty \int \int d\omega dk_x dk_y k_x k^3 \exp(-2kz_0) \times \left\{ \coth \frac{\hbar\omega}{2k_B T_1} \alpha^{(2)''}(\omega) [\Delta''(\omega + k_x V) - \Delta''(\omega - k_x V)] + \coth \frac{\hbar\omega}{2k_B T_2} \Delta''(\omega) [\alpha^{(2)''}(\omega + k_x V) - \alpha^{(2)''}(\omega - k_x V)] \right\}. \quad (23)$$

Similar calculations for the force of attracting the quadrupole to the surface lead to the following formula:

$$F_z^{Q-Q} = -\frac{2\hbar}{3\pi^2} \int_0^\infty \int \int d\omega dk_x dk_y k^4 \exp(-2kz_0) \times \left\{ \coth \frac{\hbar\omega}{2k_B T_1} \alpha^{(2)''}(\omega) [\Delta'(\omega + k_x V) + \Delta'(\omega - k_x V)] + \coth \frac{\hbar\omega}{2k_B T_2} \Delta''(\omega) [\alpha^{(2)'}(\omega + k_x V) - \alpha^{(2)'}(\omega - k_x V)] \right\}. \quad (24)$$

In conclusion, we consider the special cases of formulas (23) and (24), which are important from the practical standpoint. Within an approximation linear in the

velocity, the particle temperature is equal to the surface temperature; hence, it follows from formula (23) that

$$F_x = \frac{15\hbar V}{8\pi z_0} \int_0^\infty d\omega \text{Im} \alpha^{(2)} \left( \omega \text{Im} \Delta(\omega) \frac{d}{d\omega} \coth \frac{\hbar\omega}{2k_B T} \right). \quad (25)$$

Formula (25) is identical in the structure of the frequency integral to the expression for the dipole-dipole force [1, 4]. The only difference is provided by the additional small factor  $\frac{5}{2} a^2/z_0^2$ , where  $a$  is the characteristic linear size of the quadrupole. It is obvious that the parameter  $a/z_0$  characterizes the convergence of the total interaction between the particle and the surface in the case of the expansion into a series in terms of multipole moments.

For a particle at rest ( $V = 0$  and  $T_1 = T_2 = 0$ ), the integration of expression (24) with respect to wave vectors and the rotation of the frequency integration contour through an angle of  $\pi/2$  lead to the following relationship for the force of attracting the particle to the surface:

$$F_z = -\frac{5\hbar}{4\pi z_0} \int_0^\infty d\omega \alpha^{(2)}(i\omega) \Delta(i\omega). \quad (26)$$

From relationship (26), we can readily obtain the standard expression for the conservative interaction potential between the fluctuating quadrupole and the surface [11]:

$$U = -\frac{\hbar}{4\pi z_0} \int_0^\infty d\omega \alpha^{(2)}(i\omega) \Delta(i\omega). \quad (27)$$

#### 4. CONCLUDING REMARKS

It is evident that, in the case  $a/z_0 \ll 1$ , the quadrupole-quadrupole contribution to the normal and tangential forces of the interaction between a moving particle and the surface is negligible compared to the dipole-dipole contribution. However, the structure of the frequency integrals involved in expressions (25)–(27), generally speaking, does not allow us to introduce the small parameter  $a/z_0$  in a formal manner. Consequently, there can occur a situation when the contribution of higher-order multipole moments will appear to be predominant, specifically for the resonance structure of the functions entering into the integrands in expressions (25)–(27).

At  $T_1 = T_2 = 0$ , formula (25) and the dipole-dipole contribution [1, 4] lead to a zero tangential force to the first order in the velocity. In this case, Persson and Volokitin [12] applied the higher-order perturbation theory (based on the dipole approximation) to the determination of the coefficient of internal friction and

obtained a dependence  $\sim z_0^{-10}$ , which was used for the interpretation of experiments on the friction of adsorbates. The inclusion of the multipole moments, which are disregarded by the theory used in [12], as follows from formula (25), makes contributions with a weaker dependence of the forces on the distance. Therefore, the multipole moments cannot be ignored.

It should also be noted that the derived formulas can be easily generalized to the case of nonlocal dielectric surface functions through formal substitution [13].

APPENDIX

SOLUTION OF THE POISSON EQUATION FOR THE FOURIER COMPONENTS OF THE ELECTRIC POTENTIAL INDUCED BY A MOVING MULTIPOLE

For a quadrupole particle, the Poisson equation for the Fourier components of the electric potential coincides with expressions (4) and (18) in the cases of a permanent quadrupole moment and a fluctuating quadrupole moment, respectively. Without loss of generality, these equation can be written as follows:

$$\left(\frac{d^2}{dz^2} - k^2\right)\varphi_{\omega k}(z) = A\delta(z - z_0) + B\delta'(z - z_0) + C\delta''(z - z_0) + D\delta'''(z - z_0), \tag{A1}$$

where  $A, B, C,$  and  $D$  are the  $z$ -independent coefficients and  $k^2 = k_x^2 + k_y^2$ .

The general solution of Eq. (A1) can be represented as the sum of the general solution of the homogeneous equation

$$\varphi_{\omega k}(z) = C_1 \exp(-kz) + C_2 \exp(kz) \tag{A2}$$

and the partial solution of the inhomogeneous equation (A1). The partial solution of the inhomogeneous equation (A1) can be found using a Green's function which corresponds to the formulated problem and satisfies the equation

$$\left(\frac{d^2}{dz^2} - k^2\right)G(z, z') = \delta(z - z'). \tag{A3}$$

By directly substituting into Eq. (A3), we can easily check that the required Green's function has the form

$$G(z, z') = -\frac{1}{2k} \exp(-k|z - z'|). \tag{A4}$$

Then, according to the conventional method of finding partial solutions to equations of type (A1) [14], we

write the convolution of the right side of Eq. (A1) with the Green's function (A4); that is,

$$\varphi_{\omega k}(z) = \int_0^{\infty} G(z, z') [A\delta(z' - z_0) + B\delta'(z' - z_0) + C\delta''(z' - z_0) + D\delta'''(z' - z_0)] dz'. \tag{A5}$$

For calculating the convolution, we use the standard relationships

$$\int_{-\infty}^{+\infty} \delta^{(m)}(x) f(x) dx = (-1)^m \int_{-\infty}^{+\infty} \delta(x) f^{(m)}(x) dx,$$

$$\frac{d}{dx}|x| = \text{sgn}(x),$$

$$\frac{d^2}{dx^2}|x| = 2\delta(x).$$

As a result, from expression (A5), we obtain the partial solution in the following form:

$$\varphi_{\omega k}(z) = \exp(-k|z - z_0|) \left\{ -\frac{A}{2k} + \frac{B}{2} \text{sgn}(z - z_0) - \frac{Ck}{2} + C\delta(z - z_0) + \frac{Dk^2}{2} \text{sgn}(z - z_0) - Dk \text{sgn}(z - z_0)\delta(z - z_0) + D\delta'(z - z_0) \right\}. \tag{A6}$$

A combination of Eqs. (A2) and (A6) results in the general solution of Eq. (A1). The coefficients  $C_1$  and  $C_2$  ( $C_1 = 0$  at  $z < 0$  and  $C_2 = 0$  at  $z > 0$ ) can be determined from the continuity conditions of the potential and the normal component of the electrical induction on the surface  $z = 0$ . As a result, we have

$$C_1 = C_2 = \frac{\epsilon(\omega) - 1}{\epsilon(\omega) + 1} \times \frac{A + Bk + Ck^2 + Dk^3}{2k} \exp(-kz_0). \tag{A7}$$

Next, we eliminate the internal electromagnetic field of the particle [the nonzero term at  $\epsilon(\omega) = 1$ ] from the general solution. Consequently, for the induced potential in the range  $z > 0$ , we have

$$\varphi_{\omega k}(z) = \Delta(\omega) \frac{A + Bk + Ck^2 + Dk^3}{2k} \exp(-k(z + z_0)). \tag{A8}$$

where  $\Delta(\omega) = \frac{\epsilon(\omega) - 1}{\epsilon(\omega) + 1}$ .

Formula (A8) can be easily generalized to the case of multipole moments of an arbitrary order. For this

purpose, given a zero octupole moment  $L_{ikm}$ , the coefficient  $D$  in formula (A8) should be taken as zero.

In the case when the solutions of Eqs. (4) and (18) are represented in terms of formula (A8), we have  $D = 0$  and the coefficients  $A$ ,  $B$ , and  $C$  can be found from direct comparison of the right sides of Eqs. (4) and (18) with formula (A1).

#### REFERENCES

1. M. S. Tomassone and A. Widom, *Phys. Rev. B* **56**, 4938 (1997).
2. A. A. Kyasov and G. V. Dedkov, *Surf. Sci.* **463**, 11 (2000).
3. G. V. Dedkov and A. A. Kyasov, *Fiz. Tverd. Tela (St. Petersburg)* **43** (1), 169 (2001) [*Phys. Solid State* **43**, 176 (2001)].
4. G. V. Dedkov and A. A. Kyasov, submitted to *Phys. Lett. A*.
5. I. G. Kaplan, *Theory of Molecular Interactions* (Nauka, Moscow, 1982; Elsevier, New York, 1986).
6. Yu. S. Barash, *Van der Waals Forces* (Nauka, Moscow, 1988).
7. L. D. Landau and E. M. Lifshitz, *Course of Theoretical Physics, Vol. 2: The Classical Theory of Fields* (Nauka, Moscow, 1973; Pergamon, Oxford, 1975).
8. M. M. Bredov, V. V. Romyantsev, and I. N. Toptygin, *Classical Electrodynamics* (Nauka, Moscow, 1985).
9. I. E. Tamm, *Principles of the Electricity Theory* (Nauka, Moscow, 1976).
10. E. M. Lifshitz and L. P. Pitaevskii, *Course of Theoretical Physics, Vol. 5: Statistical Physics* (Nauka, Moscow, 1978; Pergamon, New York, 1980), Part 2.
11. X. P. Jiang, F. Toigo, and M. W. Cole, *Surf. Sci.* **148**, 21 (1984).
12. B. N. J. Persson and A. I. Volokitin, *J. Chem. Phys.* **103**, 8679 (1995).
13. G. V. Dedkov and A. A. Kyasov, *Pis'ma Zh. Tekh. Fiz.* **27** (8), 68 (2001) [*Tech. Phys. Lett.* **27**, 338 (2001)].
14. V. S. Vladimirov, *Equations of Mathematical Physics* (Dekker, New York, 1971; Nauka, Moscow, 1988).

*Translated by O. Borovik-Romanova*

---

POLYMERS  
AND LIQUID CRYSTALS

---

# The Influence of the Preparation Conditions on the Energy Disorder in Poly(methylphenyl)silane Films

Yu. A. Skryshevski

Institute of Physics, National Academy of Sciences of Ukraine, pr. Nauki 46, Kiev, 03039 Ukraine

e-mail: skrysh@uninet.kiev.ua

Received July 4, 2001; in final form, November 13, 2001

**Abstract**—The photoluminescence ( $T = 5$  K) and absorption ( $T = 295$  K) spectra and thermostimulated luminescence ( $T = 5$ – $300$  K) curves of poly(methylphenyl)silane (*PMPS*) films are investigated as functions of the film thickness, annealing temperature, and oxygen content in air. It is revealed that the optical spectra and thermostimulated luminescence curves of *PMPS* films prepared in air at room temperature undergo changes after annealing at  $T = 370$ – $450$  K. The assumption is made that the observed changes are associated with the formation of long polymer chain segments with a closer packing. This leads to an increase in the density of low-energy states of excitons and charge carriers. It is demonstrated that atmospheric oxygen substantially affects the formation processes and the energy disorder in the films prepared. The *PMPS* films are found to degrade after heating to  $T \geq 500$  K. © 2002 MAIK “Nauka/Interperiodica”.

## 1. INTRODUCTION

Polysilanes are organosilicon polymers in which the chains consist of silicon atoms linked by  $\sigma$  bonds and attached side organic groups. Chromophores in polysilanes are polymer chain segments in which electrons involved in the  $\sigma$  bonds between silicon atoms are delocalized. These segments have different lengths and are separated by topological defects [1, 2]. Polysilanes are characterized by large quantum yields of photoluminescence (PL) [1] and high drift mobilities of holes [3] and hold considerable promise for use as transferring and light-emitting layers in multilayer electroluminescent diodes [4–7].

Under operating conditions, electroluminescent diodes degrade and, in the process, the passage of ultimate currents considerably shortens their service life. According to Kido *et al.* [4] and Suzuki *et al.* [5], the degradation of diodes can be associated with the oxidation of electrodes, deterioration of contacts between layers, morphological changes in the films, and their photodegradation and thermodegradation. Fujii *et al.* [6] and Nespurek *et al.* [7] studied the photoluminescence and electroluminescence spectra of diodes in which poly(methylphenyl)silane (*PMPS*) films served as emitting layers. The photodegradation of *PMPS* films as a function of the temperature, emission wavelength, and atmospheric oxygen content was investigated in detail in [8, 9]. The aim of the present work was to elucidate how the heat treatment conditions affect the luminescent properties and the energy disorder of *PMPS* films. For this purpose, the photoluminescence ( $T = 5$  K) and absorption ( $T = 295$  K) spectra and thermostimulated luminescence (TSL) ( $5$ – $300$  K) curves of *PMPS* films were investigated at different

film thicknesses ( $d = 0.5$ – $30$   $\mu\text{m}$ ), annealing temperatures ( $T_{\text{an}} = 295$ – $570$  K), and oxygen contents in air.

## 2. SAMPLE PREPARATION AND EXPERIMENTAL TECHNIQUE

The polymer films were prepared by pouring toluene solutions of *PMPS* onto fused silica substrates followed by drying in air at room temperature. Moreover, a number of films were produced by drying of a degassed toluene solution of *PMPS* under vacuum with the residual pressure  $P = 100$  Pa. The degassing was carried out as follows. Initially, a quartz cell filled with a *PMPS* solution was held for  $t = 60$  min at  $T = 370$  K. Then, the cell was dipped into liquid nitrogen, the *PMPS* solution was frozen, and air was evacuated from the cell. After the solution was defrozed, the procedures of its freezing and evacuation of air were repeated. The absorption spectra ( $T = 295$  K) were recorded on a KSVU-23 spectrometric computer complex, and the photoluminescence spectra ( $T = 5$  K) were measured on an SDL-1 spectrometer. The photoluminescence was excited by a DRSh-250-3 high-pressure mercury-vapor lamp with a set of absorption glass filters. The low-temperature measurements were performed using an optical helium cryostat with quartz windows and an automatic system of control and stabilization of the temperature which was measured with a thermocouple.

The thermostimulated luminescence curves were measured as follows: the samples in the cryostat at  $T = 5$  K were irradiated with a DRSh-500M mercury lamp at the excitation wavelength  $\lambda_{\text{ex}} = 365$  nm for  $t = 30$  s, were allowed to stand in the dark at this temperature, and were then heated at a constant rate of  $0.15$  K  $\text{s}^{-1}$ . The integrated signal of thermostimulated lumines-

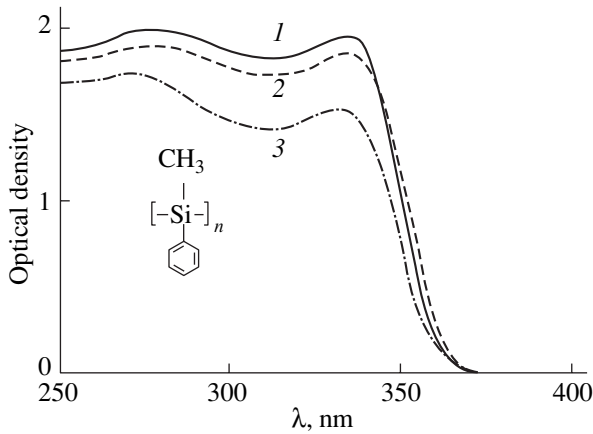


**Fig. 1.** Absorption spectra of the *PMPS* film ( $T = 295$  K,  $d = 5$   $\mu\text{m}$ ) prepared in air at room temperature: (1) prior to annealing and (2, 3) after annealing under vacuum with residual pressure  $P = 100$  Pa for  $t = 60$  min at  $T_{\text{an}} =$  (2) 400 and (3) 550 K. The structural formula of *PMPS* is shown.

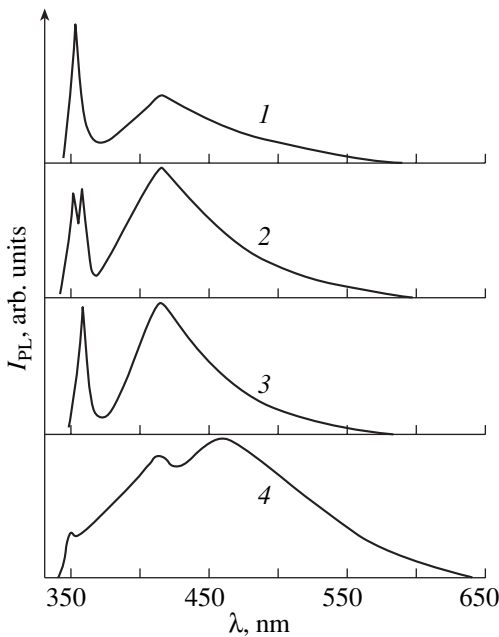


**Fig. 2.** Photoluminescence spectra of *PMPS* films ( $T = 5$  K,  $\lambda_{\text{ex}} = 313$  nm) prepared in air at room temperature: (1, 2) prior to annealing and (3, 4) after annealing under vacuum with residual pressure  $P = 100$  Pa for  $t = 60$  min at  $T_{\text{an}} =$  (3) 400 and (4) 550 K. Film thickness  $d$ : (1) 1 and (2–4) 30  $\mu\text{m}$ .

cence was measured on an automated setup with the use of an FEU-106 photomultiplier operating in a photon-counting mode. The activation energies of charge carrier traps were determined by the fractional thermoluminescence technique based on the temperature modulation of the linear heating of the studied sample [10].

The activation energies  $E_a$  in each thermal cycle were calculated from the relationship

$$E_a(T) = -d[\ln I_{\text{TSL}}(T)]/d(1/kT), \quad (1)$$

where  $I_{\text{TSL}}(T)$  is the thermostimulated luminescence intensity and  $k$  is the Boltzmann constant.

### 3. EXPERIMENTAL RESULTS

Let us first consider the absorption and photoluminescence spectra and the thermostimulated luminescence curves of *PMPS* films prepared from a nondegassed solution in air. At  $T = 295$  K, the absorption spectrum of the *PMPS* film prepared at room temperature consists of two broad structureless bands with maxima at 275 and 337 nm (Fig. 1, curve 1). These bands are associated with the  $\pi \rightarrow \pi^*$  and  $\sigma \rightarrow \sigma^*$  transitions in side phenyl groups and polymer chain segments, respectively [2, 11]. Upon annealing of this film for  $t = 60$  min at  $P = 100$  Pa and  $T_{\text{an}} = 370$ –450 K, i.e., at temperatures either near or above the glass transition point of the *PMPS* polymer ( $T_g = 408$  K [3]), the intensity of both absorption bands in the spectrum slightly decreases and the low-energy edge of the band attributed to the  $\sigma \rightarrow \sigma^*$  transition shifts toward the long-wavelength range (Fig. 1, curve 2). A further increase in the annealing temperature to  $T_{\text{an}} \geq 500$  K brings about a drastic decrease in the intensity of the band attributed to the  $\sigma \rightarrow \sigma^*$  transition and a hypsochromic shift in the location of its maximum. For example, after annealing for  $t = 60$  min at  $T_{\text{an}} = 550$  K, the intensity of the absorption band of the  $\sigma \rightarrow \sigma^*$  transition at a maximum decreases by  $\sim 25\%$  and the hypsochromic shift is approximately equal to 5 nm (Fig. 1, curve 3). These changes become more pronounced with an increase in the temperature  $T_{\text{an}}$  and the annealing time.

Figure 2 displays the photoluminescence spectra of *PMPS* films ( $T = 5$  K,  $\lambda_{\text{ex}} = 313$  nm) at different film thicknesses and different heat-treatment conditions. It is found that the spectra of *PMPS* thin films ( $d = 0.5$ –3  $\mu\text{m}$ ) prepared at room temperature coincide with those of the *PMPS* solution in toluene (the concentration  $C$  is equal to 0.01 wt %) and contain two bands with maxima at  $\lambda_{m1} = 350$ –353 nm and  $\lambda_{m2} = 415$  nm (Fig. 2, curve 1). The short-wavelength band with a half-width of approximately 0.1 eV is assigned to the  $\sigma^* \rightarrow \sigma$  exciton transitions in long chain segments, whereas the long-wavelength band corresponds to the radiative transition from the  $\pi^*$  state to the  $\sigma$  state, which is formed as a result of the  $\sigma$  electron transfer from a chain segment to the  $\pi^*$  orbital of the side phenyl ring [7, 11]. As the film thickness increases to  $d = 5$ –7  $\mu\text{m}$ , the half-width of the exciton band increases by a factor of approximately 1.5. At  $d \geq 7$   $\mu\text{m}$ , this band is split into two components with maxima at  $\lambda_{m1} = 350$  nm and  $\lambda_{m2} = 355$ –358 nm whose intensities are virtually equal to each other (Fig. 2, curve 2). After annealing of

both thin and thick films for  $t = 10\text{--}200$  min at  $P = 100$  Pa and  $T_{\text{an}} = 370\text{--}450$  K, their photoluminescence spectra coincide with each other and consist of two bands with maxima at  $\lambda_{m2} = 355\text{--}358$  nm and  $\lambda_m = 415$  nm (Fig. 2, curve 3).

An increase in the annealing temperature of *PMPS* films to  $T_{\text{an}} = 500\text{--}570$  K at  $P = 10^2\text{--}10^5$  Pa results in more significant changes in the photoluminescence spectra. These changes become more pronounced with an increase in the temperature and time of annealing. In particular, the annealing of the *PMPS* film at  $T_{\text{an}} = 550$  K for  $t = 60$  min brings about an appreciable decrease in the intensity of the exciton band, a hypsochromic shift in the location of its maximum by 5–8 nm, and the appearance of a new broad luminescence band in the visible range with a maximum at  $\lambda_m = 460$  nm (Fig. 2, curve 4). An increase in the annealing temperature to  $T_{\text{an}} = 570$  K is attended by a substantial decrease in the intensity of all the bands in the spectrum, and the photoluminescence almost completely disappears after annealing of the film at this temperature for  $t = 60$  min.

Now, we analyze the thermostimulated luminescence curves for *PMPS* films. It is revealed that the thermostimulated luminescence curves for thin and thick films ( $d = 0.5\text{--}30$   $\mu\text{m}$ ) prepared at room temperature coincide with each other and have the shape of a broad asymmetric peak located in the temperature range  $T = 5\text{--}150$  K with a maximum at  $T_{m1} = 95$  K (Fig. 3, curve 1). It turned out that the thermostimulated luminescence curves measured in this work are similar to those obtained in [8, 12]. As follows from the fractional thermoluminescence measurements, the activation energy  $E_a$  linearly increases with an increase in the temperature (Fig. 3, curve 4) and proves to be  $E_{m1} = 0.21$  eV at a maximum of the thermostimulated luminescence band. The annealing of *PMPS* films at  $T_{\text{an}} = 370\text{--}450$  K and  $P = 100$  Pa for  $t = 10\text{--}200$  min leads to a shift of the thermostimulated luminescence band toward the high-temperature range, and its intensity increases by a factor of two to five (Fig. 3, curve 2). In this case, the maximum of the band is observed at  $T_{m2} = 110$  K and the activation energy  $E_{m2}$  is equal to 0.25 eV. As the annealing temperature increases to  $T_{\text{an}} = 550$  K ( $t = 60$  min), the intensity of the thermostimulated luminescence band at  $T_{m2} = 110$  K decreases and a new high-temperature band appears in the range  $T = 150\text{--}180$  K with a maximum at  $T_{m3} = 160$  K. This indicates the formation of new traps of charge carriers with the activation energy  $E_{m3} = 0.40$  eV (Fig. 3, curve 3).

In order to elucidate how atmospheric oxygen affects the luminescent properties of the *PMPS* polymer, we analyzed the photoluminescence spectra and the thermostimulated luminescence curves for a thick film ( $d = 30$   $\mu\text{m}$ ) annealed at  $T_{\text{an}} = 400$  K and  $P = 100$  Pa for  $t = 60$  min and saturated with oxygen upon holding in air at room temperature for a certain time. First, the

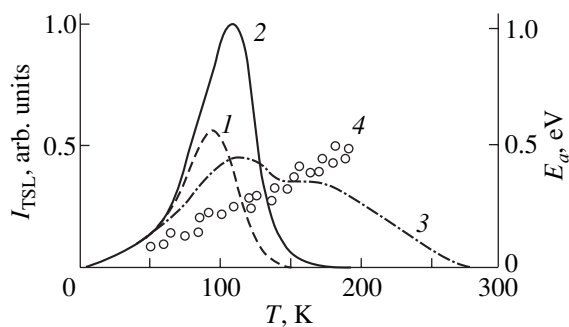


**Fig. 3.** Thermostimulated luminescence curves of the *PMPS* film ( $T = 5$  K,  $\lambda_{\text{ex}} = 365$  nm,  $d = 30$   $\mu\text{m}$ ) prepared in air at room temperature: (1) prior to annealing and (2, 3) after annealing under vacuum with residual pressure  $P = 100$  Pa for  $t = 60$  min at  $T_{\text{an}} =$  (2) 400 and (3) 550 K. (4) Dependence of the activation energy  $E_a(T)$ .

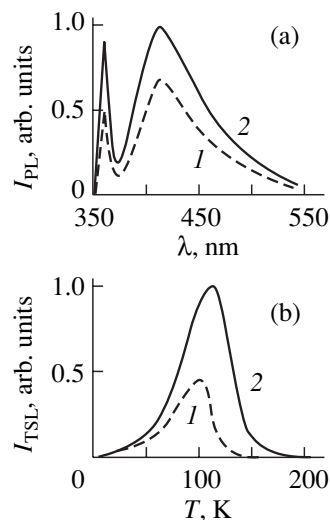


**Fig. 4.** (a) Photoluminescence spectra ( $T = 5$  K,  $\lambda_{\text{ex}} = 313$  nm) and (b) thermostimulated luminescence curves of *PMPS* films ( $d = 30$   $\mu\text{m}$ ) subjected to annealing at  $T_{\text{an}} = 400$  K for  $t = 60$  min: (1) after rapid cooling from room temperature to liquid-helium temperature and (2) after annealing at  $T_{\text{an}} = 300$  K for  $t = 15$  min in a helium atmosphere.

photoluminescence spectrum and the thermostimulated luminescence curve were measured for the film rapidly cooled from room temperature to liquid-helium temperature. Then, the film was annealed in a cryostat in a helium atmosphere at  $T_{\text{an}} = 300$  K for  $t = 15$  min and cooled to  $T = 5$  K and the photoluminescence spectrum and the thermostimulated luminescence curve were recorded again. It was found that, after annealing of the *PMPS* film in a helium atmosphere, the intensities of both the photoluminescence and thermostimulated luminescence bands increase by a factor of 1.5–2. Note that the photoluminescence spectrum remains unchanged (Fig. 4a, curves 1, 2), whereas the thermo-

stimulated luminescence curve for the film containing adsorbed oxygen shifts toward the low-temperature range (Fig. 4b, curves 1, 2). Moreover, it is revealed that the maximum of the exciton photoluminescence band in the spectrum of the *PMPS* film prepared from a degassed solution at room temperature under vacuum with residual pressure  $P = 100$  Pa is observed at  $\lambda_{m2} = 354\text{--}355$  nm and its location remains unchanged after annealing of the film at  $T_{\text{an}} = 370\text{--}450$  K for  $t = 60$  min.

#### 4. DISCUSSION

In disordered organic matrices, only relatively weak forces of intermolecular interaction act between molecules. As a consequence, excitons and charge carriers are localized at molecules of the matrix and exhibit energy distributions that are characterized by the density-of-state functions of excitons and charge carriers, respectively. According to the model proposed by Bassler [13, 14], these functions can be represented by a Gaussian distribution. Specifically, for charge carriers, we can write the relationship

$$\rho(E) = (2\pi\sigma^2)^{-1/2} \exp[-E^2/(2\sigma^2)], \quad (2)$$

where  $E$  is the energy of a charge carrier with respect to the center of the Gaussian distribution with the half-width  $\sigma$ . As follows from the calculations, the parameter  $\sigma_{\text{ex}}$  for excitons is approximately 1.5 times smaller than that for charge carriers [13]. In the model under consideration, it is assumed that the energy disorder in polysilanes is governed by the distributions of chain segments over energies and over local changes in the packing of the polymer chains. In this case, the low-energy edge of the absorption band attributed to the  $\sigma \rightarrow \sigma^*$  transition is determined primarily by the length distribution of chain segments. Within this model, the dynamics of excitonic excitations is treated as migration of excitons from short segments to longer segments with a lower excitation energy. The excitons continue to migrate until their energy becomes equal to an energy  $E_{\text{th}}$ , which is referred to as the mobility threshold. Below the mobility threshold  $E_{\text{th}}$ , the density of states is so low that the migration of excitons becomes impossible and they are localized. Consequently, upon excitation of excitons with energies higher than the mobility threshold, the photoluminescence spectrum does not depend on the excitation wavelength  $\lambda_{\text{ex}}$ . In the case when the excitation energies are less than the mobility threshold  $E_{\text{th}}$ , the photoluminescence spectrum is associated with radiative transitions from states that have already been excited selectively and the Stokes shift between absorption and emission in long segments is absent [15].

In polysilanes, the *trans* planar conformation of chain segments is more energetically favorable and the polymer chains containing segments with this conformation in the solid phase have a closer packing as compared to polymer chains involving segments with a dis-

ordered structure [1, 2]. The calculations demonstrates that, in polysilanes containing chain segments with a disordered structure, the longest segments should adopt a conformation similar to the *trans* planar conformation [1]. As is known [2], *PMPS* polymers can form amorphous films and the *PMPS* chain fragments have a disordered structure. It can be assumed that the structure, the conjugation length, and packing of chain segments in *PMPS* depend on the preparation conditions of the polymer films. Moreover, in the photoluminescence spectrum, the short-wavelength band at  $\lambda_{m1} = 350\text{--}353$  nm corresponds to luminescence of excitons localized at relatively short segments and the long-wavelength band at  $\lambda_{m2} = 353\text{--}358$  nm is attributed to luminescence of excitons localized at longer segments. Analysis of the photoluminescence spectrum (Fig. 2, curve 1) shows that relatively short chain segments are formed in thin films prepared in air at room temperature. The doublet structure of the exciton photoluminescence spectrum of thick films prepared in air at room temperature (Fig. 2, curve 2) indicates that these films contain two types of spatially separated centers of radiative excitonic recombination. These centers are polymer chains with different length distributions of chain segments. It seems likely that the annealing of thin and thick films at  $T_{\text{an}} = 370\text{--}450$  K leads to an increase in the concentration of long segments with a closer packing, as judged from the long-wavelength shift in the low-energy edge of the absorption band assigned to the  $\sigma \rightarrow \sigma^*$  transition (Fig. 1, curves 1, 2). As a result, the energy disorder in the films becomes more pronounced, the density of low-energy states localized at long segments increases, and the maximum of the exciton photoluminescence band is located at  $\lambda_{m2} = 355\text{--}358$  nm (Fig. 2, curve 3).

If the hypothesis that the energy disorder in *PMPS* films prepared at room temperature increases after their annealing at  $T_{\text{an}} = 370\text{--}450$  K holds true, it can be expected that, after annealing of the film, the parameter  $\sigma$  for charge carriers will increase. As a rule, the parameter  $\sigma$  is determined from the temperature dependence of the charge carrier mobility  $\mu$ , which is extrapolated to zero electric field strength [3, 13]; that is,

$$\mu(T) = \mu_0 \exp[-(2\sigma/3kT)^2], \quad (3)$$

where  $\mu_0$  is the mobility in the energetically ordered matrix.

Unlike excitons with a finite lifetime, photogenerated charge carriers in disordered matrices at sufficiently low temperatures are localized at the lowest energy levels described by the density-of-state function [13, 14]. An increase in the temperature results in thermal release of trapped carriers, and radiative recombination of oppositely charged carriers leads to thermostimulated luminescence. Earlier [12, 16–18], it was shown that the shape of the distribution  $\rho(E)$  can be determined from analyzing the thermostimulated luminescence curves; more specifically, the high-tempera-

ture edge of these curves for a number of molecular, doped, carbazoyl-containing, and  $\sigma$ - and  $\pi$ -conjugated polymers can be approximated by the Gaussian function (2). In this case, the parameter  $\sigma$  can be calculated using the following relationship [12, 16, 17]:

$$\sigma = \frac{E_m}{[3 \ln \ln(\Delta t/t_0)]^{1/2} - 1}. \quad (4)$$

Here,  $E_m$  is the activation energy at a maximum of the thermostimulated luminescence curve measured after illumination of the polymer at  $T = 5$  K,  $\Delta t = 10^3$  s is the delay time between the illumination of the polymer and the recording of the thermostimulated luminescence curve, and  $t_0 \approx 10^{-13}$  s is the residence time of carriers in the polymer molecule in the absence of disorder effects.

From relationship (4) and the data presented in Fig. 3 (curves 1, 2), we obtain  $\sigma_1 = 0.10$  eV and  $\sigma_2 = 0.12$  eV. Therefore, the annealing of the *PMPS* film at  $T_{\text{an}} = 400$  K results in an increase in the energy disorder. According to formula (3), the above increase in the parameter  $\sigma$  after annealing of the film implies that the hole mobility at room temperature decreases by a factor of 20. Note that the parameter  $\sigma_1$  determined in the present work agrees well with the parameter  $\sigma_T = 0.093$  eV obtained from the experimental data on the hole mobility in *PMPS* films in [3].

After heating of the *PMPS* films to higher temperatures ( $T_{\text{an}} = 500$ – $570$  K), the changes revealed both in the absorption (Fig. 1, curve 3) and luminescence (Fig. 2, curve 4) spectra and in the thermostimulated luminescence curves (Fig. 3, curve 3) are similar to those observed earlier upon exposure of the *PMPS* films to UV light at room temperature due to photodegradation of the polymer [8, 9]. It is known that photodegradation and thermodegradation of *PMPS* are accompanied by identical chemical reactions due to the following factors: (i) the scission of  $\sigma$  bonds between silicon atoms in the polymer chain, (ii) the formation of cyclic structures, (iii) the cross-linking between polymer chains, and (iv) the incorporation of oxygen into the polymer chain [1, 9]. Reasoning from the results obtained in previous works, we can make the inference that the decrease in the intensity of the absorption band attributed to the  $\sigma \rightarrow \sigma^*$  transition and the decrease in the intensity of the exciton photoluminescence band, which are attended by a hypsochromic shift in their maxima, are caused by the scission of  $\sigma$  bonds between silicon atoms in the polymer chain, whereas the appearance of the new photoluminescence band at  $\lambda_m = 460$  nm and the new thermostimulated luminescence band at  $T_{m3} = 160$  K is associated with the cross-linking between polymer chains [8, 9]. It should be noted that thermodegradation is a completely irreversible process.

It is known that, in polysilanes, adsorbed atmospheric oxygen [20] serves as an electron acceptor and can form weak charge-transfer complexes with mole-

cules of many organic compounds at atmospheric pressure. These complexes are relatively unstable and can easily dissociate upon elimination of oxygen [21]. As was shown in my recent work [22], doping of *PMPS* films by acceptors, namely, 2,7-dinitro-9-fluorenone, 2,4,7-trinitro-9-fluorenone, and 7,7',8,8'-tetracyanoquinodimethane, results in coloration of the films and the appearance of new broad bands in the absorption and photoluminescence spectra due to the formation of weak charge-transfer complexes with segments of the *PMPS* chain. It can be assumed that atmospheric oxygen is also capable of forming weak charge-transfer complexes with *PMPS* chain segments. This accounts for the experimentally observed photoluminescence quenching in the film saturated with atmospheric oxygen (Fig. 4a). The interaction between an electron donor and an electron acceptor is accompanied by partial transfer of the electron density from the donor to the acceptor, and the efficiency of this process increases with a decrease in the ionization potential of the donor [21]. Consequently, it can be expected that the charge-transfer complexes with oxygen molecules will be formed primarily by the longest *PMPS* chain segments on which the lowest energy states of holes are localized. The formation of the charge-transfer complexes between oxygen molecules and the longest segments leads to rearrangement of the energy levels of the segments and a decrease in the density of low-energy states of holes. In turn, this results in a shift of the thermostimulated luminescence curve toward the low-temperature range after saturation of the film with atmospheric oxygen (Fig. 4b).

Thus, the following model can be proposed to explain the changes observed in the morphology and energy disorder in *PMPS* films prepared under different conditions. In thin films ( $d < 7$   $\mu\text{m}$ ) produced from non-degassed solutions at room temperature, atmospheric oxygen forms weak charge-transfer complexes with *PMPS* chain segments. This prevents their close packing, and relatively short segments are predominantly formed in the films. The maximum of the exciton photoluminescence band ( $T = 5$  K) is observed at  $\lambda_{m1} = 350$ – $353$  nm. During the preparation of thick films, the oxygen concentration in the film bulk decreases, which encourages the formation of chain segments with a large conjugation length and regions with a close packing of the polymer chains. As a result, the spatially separated polymer chains with different length distributions of segments are formed and the exciton photoluminescence band is split into a doublet with maxima at  $\lambda_{m1} = 350$  nm and  $\lambda_{m2} = 355$ – $358$  nm. The films prepared at room temperature are characterized by the energy disorder parameter  $\sigma_1 = 0.10$  eV.

The annealing of *PMPS* films at sufficiently high temperatures and a low pressure brings about the decomposition of charge-transfer complexes formed by chain segments with oxygen molecules and the elimination of oxygen. Upon heating to temperatures either

near or above the glass transition point, the mobility of individual fragments of the polymer chains increases and, after cooling of the films, the concentration of long segments with a closer packing increases. This results in a substantial increase in the density of low-energy states of excitons and charge carriers. As a consequence, the maximum of the exciton photoluminescence band is observed at  $\lambda_{m2} = 355\text{--}358$  nm and the energy disorder parameter increases to  $\sigma_2 = 0.12$  eV. After annealing at temperatures above 500 K, the PMPS polymer undergoes thermodegradation.

## REFERENCES

1. R. D. Miller and J. Michl, *Chem. Rev.* **89**, 1359 (1989).
2. M. Pope and C. E. Swenberg, *Electronic Processes in Organic Crystals and Polymers* (Oxford Univ. Press, New York, 1999), pp. 877–901.
3. P. M. Borsenberger and D. S. Weiss, *Organic Photoreceptors for Xerography* (Marcel Dekker, New York, 1998).
4. J. Kido, K. Nagai, Y. Okamoto, and T. Skotheim, *Appl. Phys. Lett.* **59**, 2760 (1991).
5. H. Suzuki, H. Meyer, and S. Hoshino, *J. Appl. Phys.* **78**, 2684 (1995).
6. A. Fujii, K. Yoshimoto, M. Yoshida, *et al.*, *Jpn. J. Appl. Phys.* **35**, 3914 (1996).
7. S. Nespurek, A. Kadashchuk, Yu. Skryshevski, and A. Fujii, *J. Soc. Elect. Mat. Eng.* **9**, 119 (2000).
8. A. Kadashchuk, S. Nespurek, Yu. Skryshevski, *et al.*, *Mol. Cryst. Liq. Cryst.* **355**, 413 (2001).
9. Yu. A. Skryshevskii and A. Yu. Vakhnin, *Fiz. Tverd. Tela* (St. Petersburg) **43**, 569 (2001) [*Phys. Solid State* **43**, 589 (2001)].
10. I. A. Tale, *Izv. Akad. Nauk SSSR, Ser. Fiz.* **45**, 245 (1981).
11. O. Ito, M. Terazima, T. Azumi, *et al.*, *Macromolecules* **22**, 1718 (1989).
12. A. Kadashchuk, N. Ostapenko, V. Zaika, and S. Nespurek, *Chem. Phys.* **234**, 285 (1998).
13. H. Bassler, *Phys. Status Solidi B* **175**, 15 (1993).
14. H. Bassler, in *Disorder Effects on Relaxational Processes*, Ed. by R. Blumen (Springer-Verlag, Berlin, 1994), pp. 485–507.
15. J. R. G. Thorne, S. T. Repinec, S. A. Abrash, *et al.*, *Chem. Phys.* **146**, 315 (1990).
16. A. Kadashchuk, D. S. Weiss, P. M. Borsenberger, *et al.*, *Chem. Phys.* **247**, 307 (1999).
17. A. Kadashchuk, D. S. Weiss, P. M. Borsenberger, *et al.*, *Synth. Met.* **109**, 177 (2000).
18. A. Kadashchuk, Yu. Skryshevski, A. Vakhnin, *et al.*, *Phys. Rev. B* **63**, 115205 (2001).
19. H. K. Kim and K. Matyjaszewski, *J. Polym. Sci., Part A: Polym. Chem.* **31**, 299 (1993).
20. G. Loubriel and J. Zeigler, *Phys. Rev. B* **33**, 4203 (1986).
21. A. V. Vannikov and A. D. Grishina, *Photochemistry of Polymeric Donor–Acceptor Complexes* (Nauka, Moscow, 1984).
22. Yu. A. Skryshevski, *Zh. Prikl. Spektrosk.* **68**, 455 (2001).

*Translated by O. Borovik-Romanova*

## POLYMERS AND LIQUID CRYSTALS

# Deformation of Poly(methyl methacrylate) after Exposure to Radiation and Magnetic Fields

N. N. Peschanskaya\*, A. S. Smolyanskiĭ\*\*, and A. V. Rylov\*\*

\* Ioffe Physicotechnical Institute, Russian Academy of Sciences, Politekhnikeskaya ul. 26, St. Petersburg, 194021 Russia

\*\* Karpov Institute of Physical Chemistry (Obninsk Branch), Obninsk, Kaluzhskaya oblast, 249033 Russia

e-mail: yak@pav.ioffe.rssi.ru

Received September 27, 2001; in final form, December 7, 2001

**Abstract**—It is demonstrated that prolonged treatment in a constant magnetic field considerably increases the creep rate under compression of poly(methyl methacrylate) samples irradiated with gamma-ray doses as high as 100 kGy. For higher irradiation doses, the effect of the magnetic field on the creep rate is insignificant.  
© 2002 MAIK “Nauka/Interperiodica”.

### 1. INTRODUCTION

As a rule, polymers used in recent devices are subjected to fields of different nature simultaneously. In this respect, the study of the mechanical properties of irradiated polymers is an urgent problem, because these properties remain poorly understood. Smolyanskiĭ *et al.* [1] and Borisenko and Zhdanov [2] investigated radiation-chemical processes in polymers under irradiation and in light, magnetic, and temperature fields. The inference was made that radiation-chemical transformations can be enhanced under the action of magnetic fields. It was assumed that changes in the rate of radical reactions can lead to variations in the strength properties of polymers. In our earlier works [3, 4], we experimentally demonstrated that an applied constant magnetic field can substantially affect the stress-strain properties of polymers; moreover, we assumed that the changes in the creep rate in a magnetic field are caused by averaging of local magnetic fields. It was also proven that the strength and stress-strain characteristics of poly(methyl methacrylate) depend on the irradiation dose [5, 6].

In this work, we analyzed the changes in the strain of poly(methyl methacrylate) irradiated with different gamma-ray doses after prolonged exposure to a constant magnetic field. It was demonstrated that the effect of the constant magnetic field on the creep rate depends on the radiation dose absorbed by the polymer under investigation.

### 2. SAMPLES AND EXPERIMENTAL TECHNIQUE

Poly(methyl methacrylate) was studied under conditions of uniaxial compression at a constant load of 80 MPa and a temperature of 300 K. The samples were 6 mm in height and 3 mm in diameter. Before mechanical testing, the samples were placed in a constant mag-

netic field with a strength of 1600 Oe for 1.5 months. Then, the samples were evacuated in ampules and irradiated by different gamma-ray doses with the use of a  $^{60}\text{Co}$  source at a power of 0.4 Gy/s. The reference series of samples was not subjected to the magnetic field. The samples were loaded after the ampules were opened, and the time evolution of their strain under a constant stress was measured. The error in measuring the total creep was equal to 0.05%. The creep curves for the samples treated and not treated in the magnetic field were compared.

### 3. RESULTS AND DISCUSSION

Figures 1–3 depict the creep curves for reference samples and samples treated in the magnetic field at identical irradiation doses. For low irradiation doses,

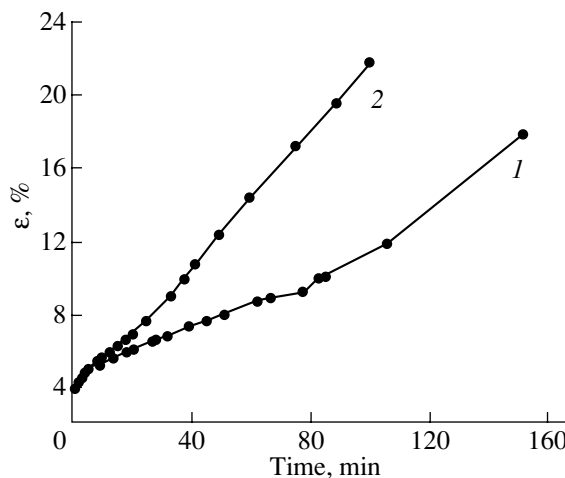


**Fig. 1.** Creep curves for poly(methyl methacrylate) after irradiation with a dose of 10.5 kGy.  $H$ , Oe: (1) 0 and (2) 1600.

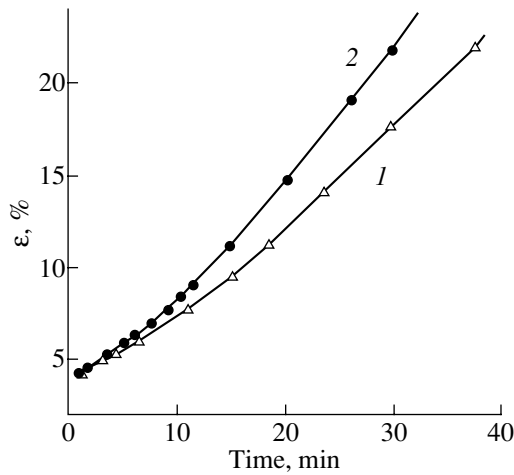


**Fig. 2.** Creep curves for poly(methyl methacrylate) after irradiation with a dose of 156 kGy. *H*, Oe: (1) 0 and (2) 1600.

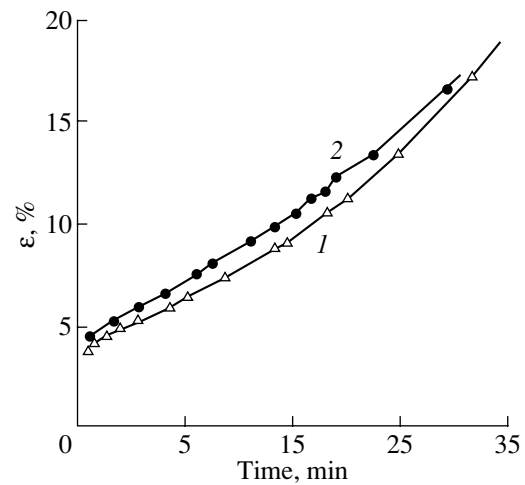


**Fig. 3.** Creep curves for poly(methyl methacrylate) after irradiation with a dose of 350 kGy. *H*, Oe: (1) 0 and (2) 1600.

the constant magnetic field, as a rule, increases the strain rate (curves 2). However, for irradiation doses higher than 107 kGy, the measured and reference curves approach each other.

Earlier [3–6], we examined the individual effects of a constant magnetic field and gamma radiation. It was shown that an increase in the creep rate with an increase in the irradiation dose is associated not only with the plastic shear but also with the extension of large-sized hollow cracks. Note that, usually, the latter phenomenon is not observed under the compression of unirradiated poly(methyl methacrylate) samples. A sharp decrease in the yield strength was observed at irradiation doses above 100 kGy, whereas the scatter of yield strengths increased at irradiation doses of approximately 25 kGy. These effects can be explained by the difference in the radical reactions at different irradiation doses. Prolonged treatment (no shorter than a few days) in a magnetic field at a temperature of 300 K also increased the creep rate (the strain in the same time) for poly(methyl methacrylate) samples [3, 4]. The effect of the constant magnetic field was explained in terms of disordering of the structure (excitation of macromolecules), which is characteristic of the early stages of orientation [3, 4].

Let us now compare the effects of gamma radiation alone and the joint action of gamma radiation and a constant magnetic field on the poly(methyl methacrylate) samples treated according to the above procedure. After irradiation, poly(methyl methacrylate) can be so brittle that it cleaves under compression. For this reason, we observed creep for small strains at which no macroscopic fracture occurred.

Figures 4 and 5 display the creep curves for two series of samples. It can be seen from Fig. 4 that the strain of poly(methyl methacrylate) samples in the same time increases with an increase in the irradiation

dose. However, at irradiation doses of 205 and 350 kGy, the mean strain rate decreases. The same is also true for poly(methyl methacrylate) samples treated in the magnetic field (Fig. 5); however, the deceleration of the process occurs at lower irradiation doses and is more pronounced.

The times of attaining a 10% strain in the samples irradiated with different gamma-ray doses and in the samples treated in the magnetic field are compared in Fig. 6. The shorter the time, the higher the strain rate. As can be seen from Fig. 6, the largest divergence of the two curves is observed at irradiation doses of 10.5 and 107 kGy. A similar result was obtained for strains in the range from 5 to 15%. The higher strains were disregarded because of the distortion of the true strain due to the extension of hollow cracks. Thus, prolonged treatment in a constant magnetic field with a strength of 1600 Oe at a temperature of 300 K substantially affects

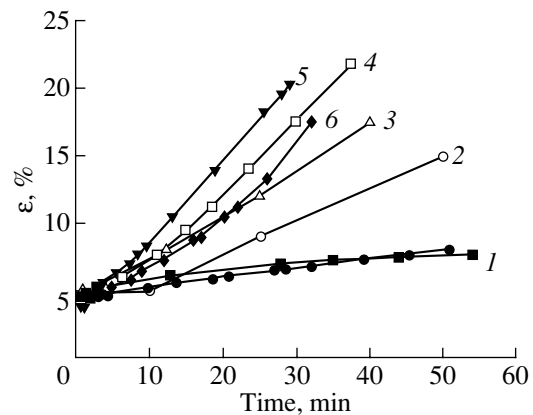


**Fig. 4.** Creep curves for poly(methyl methacrylate) after irradiation with different doses *D*, kGy: (1) 10.5, (2) 29.2, (3) 107, (4) 156, (5) 205, and (6) 350. Curves 1 refer to two different samples.

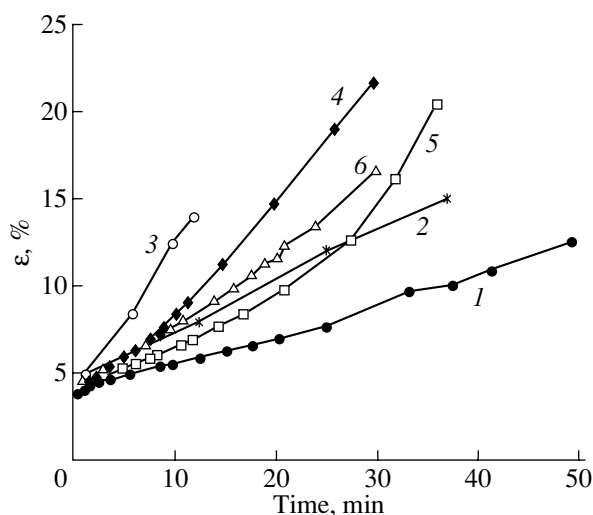


**Fig. 5.** Creep curves for poly(methyl methacrylate) after prolonged exposure to a magnetic field.  $D$ , kGy: (1) 10.5, (2) 29.2, (3) 107, (4) 156, (5) 205, and (6) 350.

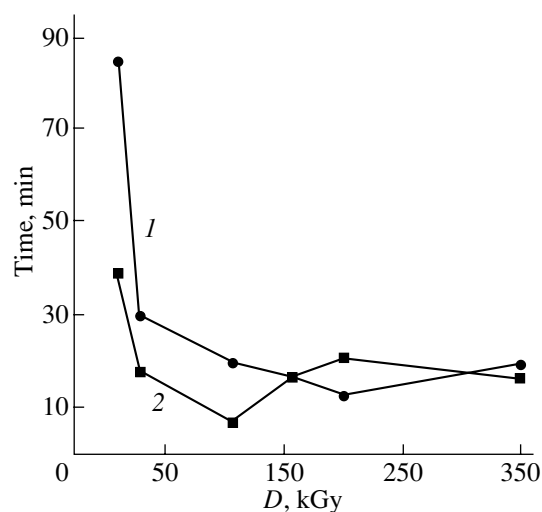


**Fig. 6.** Dependences of the time of attaining a 10% strain in poly(methyl methacrylate) on the irradiation dose.  $H$ , Oe: (1) 0 and (2) 1600.

the creep rate of poly(methyl methacrylate) irradiated with gamma-ray doses as high as 107 kGy.

The intensive formation of hollow cracks that suppress the true strain is observed in the samples irradiated with a dose of higher than 107 kGy. Therefore, we can assert that the magnetic field affects the shear acts associated with the intermolecular interaction. As is seen from Fig. 6, the magnetic field most strongly affects the samples irradiated with doses of 10.5 and 107 kGy. Earlier [6], we noted that the creep rate begins to change after irradiation with a dose of higher than 10.5 kGy; i.e., the influence of the constant magnetic field at this dose of irradiation is not yet complicated by radiation-chemical processes. It was assumed that exposure to gamma radiation with a dose of approximately 25 kGy decreases the molecular mobility, thus initiating, for example, the reaction of radiative linking; consequently, the effect of the constant magnetic field in this range of irradiation doses decreases. Smolyanskii *et al.* [1] also observed a specific feature in the form of a maximum in the radical concentration at a radiation dose of 25 kGy. As was mentioned earlier, the influence of a constant magnetic field on the strain at doses above 107 kGy is suppressed by the fictive strain due to the growth of cracks; as a result, the creep rates (times in Fig. 6) for samples of two types approach each other. It is evident that, even for the same polymer, the critical irradiation doses can vary depending on the conditions of irradiation and heat treatment of the samples, the strength and exposure time of the constant magnetic field, and the measurement temperature of the stress-strain characteristics.

The mechanism of the influence of the constant magnetic field on the creep rate is open to speculation. Diamagnetism is inherent in all solids; however, its mechanism is assumed to be specific to each material.

For complex molecules, diamagnetism is governed not only by electron precession in atoms but also by the polarization of electron clouds in an external magnetic field and by the orbital magnetic moment oriented parallel to the constant magnetic field [7]. Theoretically, the coefficients of magnetic susceptibility are calculated for individual atoms and molecules.

Since the strain is associated with overcoming of the barriers to intermolecular nonchemical interactions and is determined by the degree of molecular mobility [8], it is clear that the constant magnetic field affects the intermolecular bonds and mobility of segments of the polymer chains. In [3], it was demonstrated that the effect of a constant magnetic field on the unirradiated poly(methyl methacrylate) manifests itself in an increase in the creep rate and a decrease in its nonmonotonicity. It was assumed that the constant magnetic field suppresses strong interactions between neighboring molecules. This leads to an increase in the molecular mobility and accelerates shear processes under mechanical stresses. It is also known that polymer molecules are oriented in a constant magnetic field. According to the calculations performed by Rodin [9], the complete orientation of the molecule becomes possible in viscous solutions. In solid polymers [4–6], the orientation is also observed upon prolonged treatment in a magnetic field; however, reasoning from the long times of relaxation of the molecules involved, we can only infer an orientation of individual segments of the macromolecule. Consequently, the orientation influence of the constant magnetic field on the polymer is similar to the influence of the mechanical field. This corresponds to a decrease in the potential barrier to shear acts and to an increase in the strain rate, which is observed experimentally.

The changes observed in radiation-chemical reactions in irradiated polymers under the action of a constant magnetic field have been discussed in the literature. In particular, Borisenko and Zhdanov [2] noted that, upon irradiation of polymers, a constant magnetic field increases the density of paramagnetic centers and stabilizing charged particles and enhances radiation-chemical transformations. The magnetic field can also favor a decrease in the recombination rate of radical pairs. It is not improbable that the variations in chemical reactions under the action of a constant magnetic field can affect the strength properties of the polymers. Actually, the deformation and failure can be considered chemical processes. In this case, the increase in the strain rate (decrease in the time in Fig. 6) agrees with the data obtained in [2].

At present, the mechanism of the influence of a constant magnetic field on the mechanical properties cannot be unambiguously interpreted for the lack of reliable data; however, the changes in the stress-strain characteristics and certain regularities have been established [3, 4]. The results of this work confirm and complement the available data regarding the influence of a constant magnetic field on the properties of diamagnetic materials. It was demonstrated that the effect of a magnetic field on the strain rate of poly(methyl methacrylate) depends on the radiation dose.

## REFERENCES

1. A. S. Smolyanskiĭ, L. A. Znamenskaya, S. S. Zhdanov, *et al.*, *Khim. Vys. Énerg.* **27** (5), 56 (1993).
2. V. I. Borisenko and G. S. Zhdanov, *Khim. Vys. Énerg.* **27** (5), 69 (1993).
3. N. N. Peschanskaya, V. Yu. Surovova, and P. N. Yakushev, *Fiz. Tverd. Tela (St. Petersburg)* **34** (7), 2111 (1992) [*Sov. Phys. Solid State* **34**, 1127 (1992)].
4. N. N. Peschanskaya and P. N. Yakushev, *Fiz. Tverd. Tela (St. Petersburg)* **39** (9), 1690 (1997) [*Phys. Solid State* **39**, 1509 (1997)].
5. N. N. Peschanskaya, A. S. Smolyanskiĭ, and V. Yu. Surovova, *Vysokomol. Soedin., Ser. B* **34** (12), 3 (1992).
6. N. N. Peschanskaya, A. S. Smolyanskiĭ, and V. Yu. Surovova, *Fiz. Tverd. Tela (St. Petersburg)* **35** (9), 2465 (1993) [*Phys. Solid State* **35**, 1222 (1993)].
7. Ya. G. Dorfman, *Diamagnetism and the Chemical Bond* (Fizmatgiz, Moscow, 1961; American Elsevier, New York, 1965).
8. V. A. Stepanov, N. N. Peschanskaya, and V. V. Shpeĭzman, *Strength and Relaxation Phenomena in Solids* (Leningrad, 1984).
9. Yu. P. Rodin, *Mekh. Kompoz. Mater.* **3**, 490 (1991).

*Translated by N. Korovin*

---

## POLYMERS AND LIQUID CRYSTALS

---

# Elastic Properties of Liquid Crystals

A. V. Zakharov\*, M. N. Tsvetkova\*\*, and V. G. Korsakov\*\*

\* Institute for Problems of Mechanical Engineering, Russian Academy of Sciences,  
Bol'shoi pr. 61, Vasil'evskii ostrov, St. Petersburg, 199178 Russia

\*\* St. Petersburg Institute of Technology, Zagorodnyĭ pr. 49, St. Petersburg, 198013 Russia

e-mail: korsakov@tu.spb.ru

Received June 4, 2001

**Abstract**—The structural and elastic properties of 4-*n*'-pentyl-4'-cyanobiphenyl (5CB) in the nematic liquid-crystal phase are investigated in the framework of the statistical–mechanical theory and the molecular dynamics method. © 2002 MAIK “Nauka/Interperiodica”.

### 1. INTRODUCTION

The macroscopic properties of liquid crystals, generally, and the Frank elastic constants, in particular, have been the subject of extensive experimental [1] and theoretical [2] investigations. In many cases, homologs of cyanobiphenyls, specifically of 4-*n*'-pentyl-4'-cyanobiphenyl (5CB), are used as liquid-crystal materials.

Mesogenic molecules of these compounds consist of one or several flexible hydrocarbon chains attached to an elastic polar core. The flexibility of the hydrocarbon chains determines the physical properties of liquid crystals in many respects. Moreover, these molecules possess a sufficiently large dipole moment (~4.5–5.0 D [3]), which is directed from the polar core to the molecular tail, and form a nematic phase in the low-temperature range (295–305 K [1]). The latter circumstance renders these objects very interesting for experimental investigations [4–7]. Direct experimental measurements of the Frank elastic constants are rather complicated and can be performed accurate to within ~20–40% [4, 5]. In this respect, theoretical studies of the elastic liquid-crystal properties in the framework of statistical mechanics [8] or numerical molecular dynamics calculations [9] have assumed a new significance, because these approaches can provide answers to a number of fundamental questions. For example, how much do the microscopic parameters responsible for the character of intermolecular interactions in a liquid-crystal system affect the measured macroscopic characteristics of the real liquid crystal?

In the present work, the above theoretical approaches were used to investigate the elastic properties of liquid crystals. The statistical–mechanical theory is based on the method of conditional distribution functions [10]. This method makes it possible to take into account not only translational and orientational correlations but also mixed correlations of the molecules involved. As a model intermolecular interaction potential, we chose the dipolar Gay–Berne potential [11].

The dipoles were aligned parallel to the long axes of the molecules forming a liquid crystal. The pair and direct correlation functions of the distribution and the orientation distribution function of 5CB molecules in the temperature range corresponding to the nematic phase were calculated in the framework of the statistical–mechanical theory. Moreover, the orientation distribution function and the pair correlation function were obtained by molecular dynamics calculations with the use of realistic intramolecular and intermolecular atom–atom interaction potentials for 5CB [12, 13].

Nowadays, there exist a number of microscopic theories describing the elastic properties of nematic liquid crystals [14–17]. Within these theories, the Frank elastic constants  $K_i$  ( $i = 1, 2, \text{ and } 3$ ) are expressed in terms of the orientation distribution function and the direct correlation function of the nematic liquid crystal. It should be noted that the key problem—the determination of the direct correlation function for a nematic liquid crystal—was solved with different degrees of strictness. In particular, the pair correlation function was obtained in the framework of the statistical–mechanical theory with the inclusion of translational, orientational, and mixed correlations, which made it possible to construct the direct correlation function in the classical Percus–Yevick approximation [18]. In turn, the direct correlation function within the molecular dynamics approach was derived by numerical solution of the Ornstein–Zernike equation [18]; furthermore, the pair correlation function was also determined by the molecular dynamics method. In the latter case, both the direct and pair correlation functions were expressed as power series in spherical functions and the solution of the Ornstein–Zernike equation was limited to the lowest expansion terms.

This paper is organized as follows. Section 2 covers the basic principles of the statistical–mechanical description of the Frank elastic constants for nematic liquid crystals. Section 3 describes the equilibrium statistical–mechanical theory used to calculate the orien-

tation distribution function and the pair correlation function, the numerical solution of the nonlinear integral equations required to construct these functions, and the specific features in molecular dynamics calculations of the pair correlation function and order parameters of a nematic liquid crystal formed by 5CB molecules. Section 4 presents the results of calculations of the Frank elastic constants and the structural properties of 5CB and the basic inferences drawn in this work.

## 2. FRANK ELASTIC CONSTANTS

In a perfect nematic liquid crystal, molecules are predominantly aligned parallel to the director  $\mathbf{n}$  [1, 2]. In the case when the perfect configuration is distorted by either surfaces bounding the nematic liquid crystal or thermal fluctuations, the molecular orientation varies from point to point and the distortion of the director field  $\mathbf{n}(\mathbf{r})$  can be determined by minimizing the free energy density functional

$$f = f_0 + K_{ij}n_{i,j} + K_{ijk}n_{i,jk} + \frac{1}{2}K_{ijkl}n_{i,j}n_{k,l} + \dots, \tag{1}$$

where  $f_0$  is the density functional for the unstrained state;  $K_{ij}$ ,  $K_{ijk}$ , and  $K_{ijkl}$  are the elastic constant tensors; and  $n_{i,j} = \frac{\partial n_i}{\partial x_j}$  [1, 2]. In the bulk of the nematic liquid crystal, we have  $K_{ij} = 0$  and the contributions  $K_{ijk}n_{i,jk}$  can be represented in the form [19, 20]

$$f_{13} + f_{24} = k_{13}\nabla(\mathbf{n} \cdot \nabla\mathbf{n}) - (K_2 + k_{24})\nabla[\mathbf{n} \cdot \nabla\mathbf{n} + \mathbf{n} \times \nabla \times \mathbf{n}]. \tag{2}$$

Moreover, in functional (1), the other important part, which is proportional to the square of the derivative of the director, can be written in the Frank form [14, 15]

$$f_F = \frac{1}{2} \times [K_1(\nabla\mathbf{n})^2 + K_2(\mathbf{n} \times \nabla\mathbf{n})^2 + K_3(\mathbf{n} \times \nabla \times \mathbf{n})^2], \tag{3}$$

where  $K_i$  ( $i = 1, 2,$  and  $3$ ) are the three fundamental elastic constants corresponding to the longitudinal, torsional, and flexural strains.

Therefore, the complete expression for the free energy takes the form

$$F = \int dV f_F + \int dS(f_{13} + f_{24}) + \int dS f_S, \tag{4}$$

where  $f_{13} = k_{13}\mathbf{k} \cdot (\mathbf{n} \cdot \nabla \cdot \mathbf{n})$ ,  $f_{24} = -(K_2 + k_{24})\mathbf{k} \cdot [\mathbf{n}\nabla \cdot \mathbf{n} + \mathbf{n} \times (\nabla \times \mathbf{n})]$ , and  $\mathbf{k}$  is the normal to the surface  $S$  bounding the volume  $V$ .

In recent years, several microscopic approaches to the description of the coefficients  $K_i$  have been proposed [14–17, 19, 21]. Within these approaches, the coefficients  $K_i$  are related to structural characteristics of

the nematic phase, such as the orientation distribution function and the direct correlation function. In the general form, the Frank elastic constants can be represented by the following expressions [14, 15]:

$$K_1 = \frac{k_B T \rho^2}{2} \int r_x^2 C(\mathbf{r}, \mathbf{e}_i, \mathbf{e}_j) f_0'(\cos \beta_i) \tag{5}$$

$$\times f_0'(\cos \beta_j) e_{i,x} e_{j,x} r^2 dr d\Omega_i d\Omega_j,$$

$$K_2 = \frac{k_B T \rho^2}{2} \int r_x^2 C(\mathbf{r}, \mathbf{e}_i, \mathbf{e}_j) f_0'(\cos \beta_i) \tag{6}$$

$$\times f_0'(\cos \beta_j) e_{i,y} e_{j,y} r^2 dr d\Omega_i d\Omega_j,$$

$$K_3 = \frac{k_B T \rho^2}{2} \int r_z^2 C(\mathbf{r}, \mathbf{e}_i, \mathbf{e}_j) f_0'(\cos \beta_i) \tag{7}$$

$$\times f_0'(\cos \beta_j) e_{i,x} e_{j,x} r^2 dr d\Omega_i d\Omega_j,$$

where  $C(\mathbf{r}, \mathbf{e}_i, \mathbf{e}_j)$  is the direct correlation function;  $f_0(\cos \beta_i)$  is the orientation distribution function;  $\beta_i$  is the polar angle, i.e., the angle between the  $z$  axis (coinciding with the director orientation  $\mathbf{n}$ ) and the long axis of the  $i$ th molecule;  $d\Omega_i = \sin \beta_i d\beta_i d\varphi_i$ ;  $d\Omega = \sin \beta_{ij} d\beta_{ij} d\varphi_{ij}$ ;  $\beta_{ij}$  and  $\varphi_{ij}$  are the polar and azimuthal angles of the unit vector  $\mathbf{e} = \mathbf{r}/|\mathbf{r}|$ , respectively;  $\mathbf{r} = \mathbf{r}_i - \mathbf{r}_j$ ;  $\mathbf{r}_i$  and  $\mathbf{r}_j$  are the vectors specifying the coordinates of the centers of mass of the  $i$ th and  $j$ th molecules, respectively;  $T$  is the temperature;  $\rho = N/V$  is the density of the system;  $k_B$  is the Boltzmann constant; and  $f_0'(\cos \beta_i)$  is the derivative of the orientation distribution function with respect to  $\cos \beta_i$ .

There are a number of simplified approaches to the problem of calculating the Frank elastic constants [17, 19–21]. These approaches are based on the approximate calculation of the direct correlation function  $C(\mathbf{r}, \mathbf{e}_i, \mathbf{e}_j) = C(r/\sigma)$ , where  $\sigma$  is the parameter of the Gay–Berne potential [11], which depends on the vectors  $\mathbf{e}_i$  and  $\mathbf{e}_j$  (specifying the orientation of the  $i$ th and  $j$ th molecules, respectively) and the unit vector  $\mathbf{e}$ .

For example, according to the approach developed in our earlier works [8, 17], the Frank elastic constants can be written in the form

$$\frac{K_i}{\bar{K}} = 1 + \lambda(5 - 9z), \tag{8}$$

$$\frac{K_2}{\bar{K}} = 1 - \lambda(1 + 3z), \tag{9}$$

$$\frac{K_3}{\bar{K}} = 1 - 4\lambda(1 - 3z), \tag{10}$$

where

$$z = \frac{\overline{\cos^4 \beta} - \overline{\cos^6 \beta}}{\overline{\cos^2 \beta} - \overline{\cos^4 \beta}}, \quad \lambda = \frac{\omega}{2(3 - \omega)}, \quad \omega = \frac{\gamma^2 - 1}{\gamma^2 + 1},$$

$\gamma = \sigma_{\parallel}/\sigma_{\perp}$  is the length-to-width ratio of the molecule, and

$$\begin{aligned} \bar{K} &= \frac{1}{3}(K_1 + K_2 + K_3) \\ &= B\bar{P}_2^2 \frac{10\bar{P}_2 - 24\bar{P}_4 + 143 - \omega}{105} \frac{1}{6\omega}. \end{aligned} \quad (11)$$

Here, the factor  $B$  has the dimensions of force and is given by

$$B = 3M_4 b^2 \rho^2 \sigma^5 \pi \omega^3 k_B T \frac{1 + (1/14)\omega^2}{(1 - \omega^2)^2}, \quad (12)$$

$$b = 4\pi \sigma_{\perp}^3 \rho \omega^2 M_2 \frac{1 + (3/14)\omega}{(1 - \omega^2)^2}, \quad (13)$$

$$\overline{\cos^2 \beta} = \frac{2\bar{P}_2 + 1}{3},$$

$$\overline{\cos^4 \beta} = \frac{20\bar{P}_2 + 8\bar{P}_4 + 7}{35},$$

$$\overline{\cos^6 \beta} = \frac{110\bar{P}_2 + 72\bar{P}_4 + 16\bar{P}_6 + 33}{231}.$$

The dimensionless parameter  $M_{2L}$  ( $L = 1$  and  $2$ ) is defined as

$$M_{2L} = -\int_0^{\infty} dr C(r) r^{2L}, \quad (14)$$

and

$$\bar{P}_{2L} = \int_0^{\pi} P_{2L}(\cos \beta) f_0(\cos \beta) \sin \beta d\beta \quad (15)$$

are the order parameters of rank  $2L$ . Here,  $P_{2L}(\cos \beta)$  ( $L = 1, 2,$  and  $3$ ) are the Legendre polynomials of even order.

Thus, relationships (8)–(10) allow us to calculate the Frank elastic constants in the case when the order parameters  $\bar{P}_{2L}$ , the orientation distribution function  $f_0(\cos \beta)$ , and the direct correlation function  $C(r)$  are known. Note that the calculation of the first two quantities presents no special problems, whereas the calculation of the direct correlation function for the nematic phase is considerably more complicated.

### 3. CORRELATION FUNCTIONS

The direct correlation functions for such an anisotropic system as the nematic phase of 5CB are calcu-

lated in the framework of two independent approaches: (i) the equilibrium statistical–mechanical theory [8, 17, 22], which is based on the method of conditional distribution functions [10], and (ii) the molecular dynamics method applied to the description of nematic liquid crystals [9, 12, 13]. Within the equilibrium statistical–mechanical theory, we consider a single-component system composed of ellipsoidal molecules of length  $\sigma_{\parallel}$  and width  $\sigma_{\perp}$  in a volume  $V$  at a temperature  $T$ . The volume  $V$  of the system is divided into  $N$  cells, each occupying the volume  $v = V/N$ . As a first approximation, we take into account only states of the system for which each cell contains one molecule [8, 17, 22].

The potential energy of this system can be represented as  $U = \sum_{i < j} \Phi(ij)$ , where  $\Phi(ij)$  is the pair intermolecular potential,  $i \equiv (\mathbf{r}_i, \mathbf{e}_i)$ , and  $\mathbf{r}_i$  and  $\mathbf{e}_i$  are the vectors specifying the position and the orientation of the  $i$ th molecule, respectively. By integrating the quantity  $\exp\left[-\frac{U}{k_B T}\right]$ , which is the density of probability of find-

ing the system at points  $i$  at the temperature  $T$  [10, 18], we can introduce partial distribution functions, namely, the one-particle distribution function  $F(i)$  (the density of probability of finding a particle inside the  $i$ th cell), the pair distribution function  $F(ij)$  (the density of probability of finding two particles in the  $i$ th and  $j$ th cells), etc. [8, 10, 17, 22].

Within this approach, we will restrict our consideration to the case of two-particle correlations. The functions  $F(i)$  and  $F(ij)$  can be expressed in terms of the mean-force potentials [8, 10, 17]

$$F_j(j) = \frac{\Psi_j(j)}{\int_j d(j) \Psi_j(j)}, \quad (16)$$

$$F_{ij}(ij) = F_i(i) F_j(j) V(ij) \Psi_{i,j}(i)^{-1} \Psi_{j,i}(j)^{-1}, \quad (17)$$

where

$$\Psi_j(j) = \prod_{i \neq j} \Psi_{j,i}(j), \quad \int_j d(j) = \int_{\omega} d\mathbf{r}_j d\mathbf{e}_j,$$

$$V(ij) = \exp\left[-\frac{\Phi(ij)}{k_B T}\right],$$

$$\omega = v \otimes \alpha,$$

and  $\alpha$  is the volume associated with the orientation of the  $i$ th molecule. The one-particle function  $F(i)$  automatically satisfies the normalizing condition  $\int_i d(i) F_i(i) = 1$ , and the constraint  $F_i(i) = \int_j d(j) F_{ij}(ij)$ , which relates the one-particle and two-particle func-

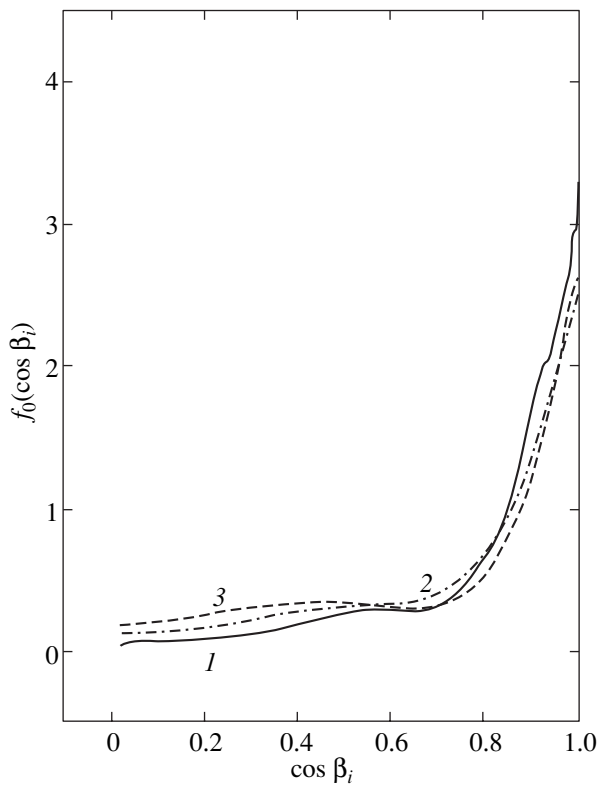


**Fig. 1.** Orientation distribution function for 5CB molecules at  $T = 300$  K according to calculations in the framework of (1) the molecular dynamics method, (2) the statistical-mechanical theory with inclusion of the dipole-dipole interaction, and (3) the statistical-mechanical theory without regard for the dipole-dipole interaction.

tions, allows us to derive the closed integral equation with respect to the mean-force potential [8, 10, 17, 22]:

$$\psi_{i,j}(i) = \int_j d(j) V(ij) \psi_{j,i}^{-1}(j F_j(j)). \quad (18)$$

Equation (18) can only be solved by a numerical method, which is described in detail in [8, 22].

With the use of the solution  $\psi_{i,j}(i)$ , we can calculate the pair correlation function  $F(ij)$  and the orientation distribution function  $f_0(\cos \beta_i) = \int d\mathbf{r}_i \int d\varphi_i F(i)$ , where  $\varphi_i$  is the azimuthal angle of the unit vector  $\mathbf{e}_i$ . In the classical Percus-Yevick approximation [18], the expression for the direct correlation function has the form

$$C_{ij}(ij) = F_{ij}(ij)(1 - V^{-1}(ij)). \quad (19)$$

Here,  $V(ij)$  is the kernel of the integral equation (18), which is determined by the pair intermolecular potential chosen as the sum of the Gay-Berne potential [11] and the dipole-dipole interaction potential:  $\Phi(ij) = \Phi_{GB}(ij) + \Phi_{dd}(ij)$ . The former potential can be written as  $\Phi_{GB}(ij) = 4\epsilon_0\epsilon(R^{-12} - R^{-6})$ , where  $R = (r - \sigma + \sigma_{\perp})/\sigma_{\perp}$ ;

$r = |\mathbf{r}_i - \mathbf{r}_j|$ ; and  $\sigma$  and  $\epsilon$  [11] are the width and the depth of the potential well, respectively. The parameters  $\sigma$  and  $\epsilon$  depend on the orientation of the unit vectors  $\mathbf{e}_i$ ,  $\mathbf{e}_j$ , and  $\mathbf{e}$ ; the geometric parameter  $\gamma$ ; and the exponents  $\nu$  and  $\mu$  in the relationship  $\epsilon = \epsilon_1^{\nu}(\mathbf{e}_i, \mathbf{e}_j)\epsilon_2^{\mu}(\mathbf{e}, \mathbf{e}_i, \mathbf{e}_j)$ . The dipole-dipole interaction potential has the form  $\Phi_{dd}(ij) = \frac{\Delta^2}{r^3}(\mathbf{e}_i \cdot \mathbf{e}_j - 3\mathbf{e}_j \cdot \mathbf{e}\mathbf{e} \cdot \mathbf{e}_j)$ , where  $\Delta$  is the dipole moment of the 5CB molecule ( $\Delta \sim 5$  D [3]).

The intermolecular interaction parameters used in our calculations are as follows:  $\gamma = 3$  ( $\sigma_{\parallel} \approx 1.8$  nm and  $\sigma_{\perp} \approx 0.59$  nm),  $\nu = 2.0$ ,  $\mu = 0.98$ , and  $\epsilon_0 = 2.07 \times 10^{-21}$  J. In addition, we used the following dimensionless parameters: the dimensionless density  $\rho^* = N\sigma_{\perp}^3/N \approx 0.512$  (corresponding to a density of  $10^3$  kg/m<sup>3</sup> for 5CB), the temperature  $\Theta^* = k_B T/\epsilon_0$ , and the dipole moment  $\mu^* = \frac{\Delta}{(\epsilon_0\sigma_{\perp}^3)^{1/2}} \approx 2.5$ . The molecular dynamics calculations included 120 5CB molecules enclosed in a cubic cell with an edge of 3.647 nm, which corresponds to a density of  $10^3$  kg/m<sup>3</sup>. The temperature was maintained at 300 K ( $\Theta^* = 2.0$ ) (for a large canonical ensemble).

The equations of motion were solved using the Verlet algorithm [23] with a time step of 2 fs. The starting configuration corresponded to the smectic phase of 5CB [9]. The orientation of the director  $\mathbf{n}$  was determined with the use of the matrix  $Q_{zz}^{vv'}$  written in the form [24]

$$Q_{zz}^{vv'} = \frac{1}{N_0} \sum_{j=1} \frac{1}{2} (3 \cos \beta_{zv}^j \cos \beta_{zv'}^j - \delta_{vv'}), \quad (20)$$

where  $N_0$  is the number of 5CB molecules and  $\beta_{zv}^j$  is the angle between the long axis of the  $j$ th molecule and the  $v$  axis related to the cubic cell. The molecular coordinates of the system were constructed using the eigenvectors of the tensor of the moment of inertia [9, 12, 13]. By diagonalizing the matrix  $Q_{zz}^{vv'}$ , we obtained three eigenvectors, of which the largest vector corresponds to the orientation of the director  $\mathbf{n}$ . Figure 1 depicts the orientation distribution function  $f_0(\cos \beta_i)$  calculated directly by the molecular dynamics method with due regard for the potential energy involving the intramolecular and intermolecular atom-atom contributions in the system at  $T = 300$  K [9, 12, 13]. The orientation distribution functions derived with the use of the integral equation for polar ( $\mu^* \approx 2.5$ ) and nonpolar ( $\mu^* = 0$ ) systems at  $T = 300$  K are also displayed in Fig. 1. Making allowance for the fact that the calculations were performed using different potentials of the intermolecular interaction, the results obtained by different methods are in good agreement. Moreover, the

order parameters  $\bar{P}_2$  and  $\bar{P}_4$  calculated in the framework of the statistical–mechanical theory ( $\bar{P}_2 = 0.4$  and  $\bar{P}_4 = 0.13$ ) and the molecular dynamics method ( $\bar{P}_2 = 0.504$  and  $\bar{P}_4 = 0.188$ ) were compared with the experimental data obtained by Raman spectroscopy ( $\bar{P}_2 = 0.58$  and  $\bar{P}_4 = 0.14$ ) [25].

It turned out that the results of our calculations deviate from the experimental data only slightly. The pair correlation function  $F(ij)$  of the anisotropic system formed by 5CB molecules at  $T = 300$  K was also calculated using the aforementioned molecular dynamics method. Figure 2 (curve 1) shows the radial distribution function  $G(r) = \int F(ij) d\Omega_i d\Omega_j$ , where  $d\Omega = \sin\beta_{ij} d\beta_{ij} d\phi_{ij}$ .

The Ornstein–Zernike equation relating the direct and pair correlation functions, that is,

$$C(r_{12}) = G(r_{12}) - 1 - \frac{\rho}{4\pi} \int dr_3 C(r_{13})(G(r_{13}) - 1), \quad (21)$$

makes it possible to calculate the direct correlation function with the use of the iterative procedure described in [9]. The radial part of the direct correlation function obtained by solving Eq. (21) numerically is plotted in Fig. 2 (curve 2). Thus, we determined the orientation distribution function  $f_0(\cos\beta_i)$ , the order parameters  $\bar{P}_{2L}$ , and the direct correlation function  $C(r)$ , which are necessary in calculating the Frank elastic constants.

#### 4. RESULTS OF CALCULATIONS OF THE FRANK ELASTIC CONSTANTS AND STRUCTURAL PROPERTIES FOR 5CB

In order to calculate the Frank elastic constants  $K_i$  ( $i = 1, 2,$  and  $3$ ) with the use of relationships (8)–(10), it is necessary to determine the moments  $M_{2L}$  ( $L = 1$  and  $2$ ) of the direct correlation function and the order parameters  $\bar{P}_{2L}$  ( $L = 1, 2,$  and  $3$ ). The moments  $M_{2L}$  were obtained in the framework of both the statistical–mechanical theory with expression (19) and the molecular dynamics method with expression (21). The calculated magnitudes of  $K_i$  ( $i = 1, 2,$  and  $3$ ) in the temperature range corresponding to the nematic phase of 5CB are displayed in Fig. 3.

A comparison shows that the theoretical and experimental results are in reasonable agreement with allowance made for the approximate character of relationships (8)–(10) and the accuracy of the measurements (20–40% [4, 5]). Note that the accuracy in direct measurements of the ratios between the Frank constants  $K_3/K_1$  and  $K_2/K_1$  can be higher than that of the con-

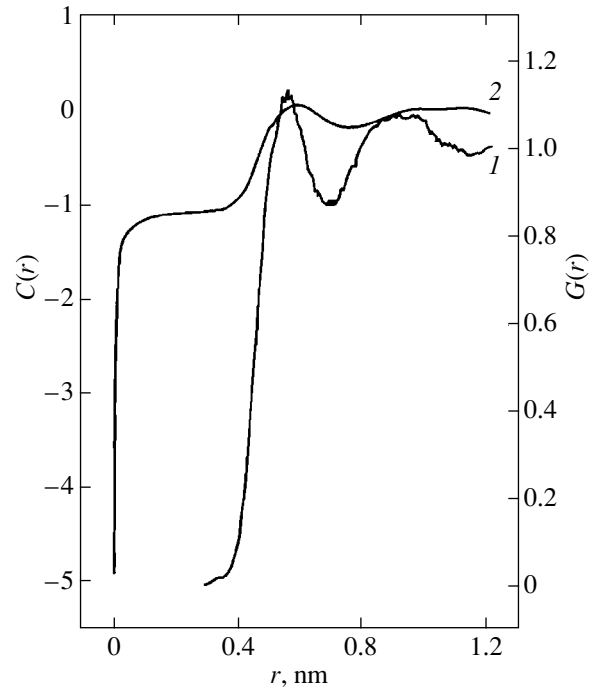


Fig. 2. (1) Radial function  $G(r)$  and (2) direct correlation function  $G(r)$  of the distribution of 5CB molecules at  $T = 300$  K (molecular dynamics calculations).

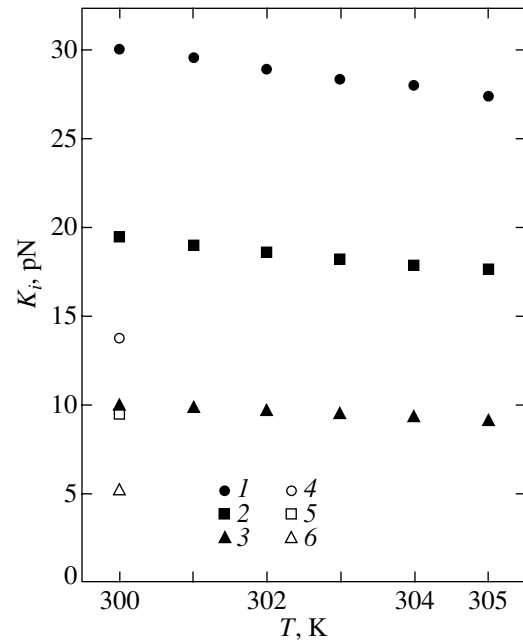


Fig. 3. Temperature dependences of the Frank elastic constants  $K_i$  ( $i = 1, 2,$  and  $3$ ): (1)  $K_3$ , (2)  $K_1$ , and (3)  $K_2$  constants calculated according to relationships (8)–(10) with the direct correlation function obtained from expression (19) and (4)  $K_3$ , (5)  $K_1$ , and (6)  $K_2$  constants calculated according to relationships (8)–(10) with the direct correlation function obtained from expression (21).

Frank elastic constants  $K_i$  ( $i = 1, 2,$  and  $3$ ) and their ratios  $K_2/K_1$  and  $K_3/K_1$  for 5CB at a temperature of 300 K

Frank constants	Theoretical approach		Experiment
	statistical–mechanical theory	molecular dynamics	
$K_1$ , pN	19.4	9.5	10.5
$K_2$ , pN	10.0	5.1	5.4
$K_3$ , pN	30.1	13.8	13.8
$K_3/K_1$	1.55	1.45	1.31
$K_2/K_1$	0.52	0.54	0.51

Note: The calculations were performed according to relationships (8)–(10). The direct correlation function was calculated within two approaches: (i) the statistical–mechanical theory with expression (19) and (ii) the molecular dynamics method with expression (21). The experimental data were obtained by the Fréedericksz transition technique [5].

stants  $K_i$  themselves [1]. The theoretical and experimental data on the Frank constants and their ratios are presented in the table. Knowing the radial parts of the pair and direct correlation functions and using the hyperinterlacing chain approximation [18], we can

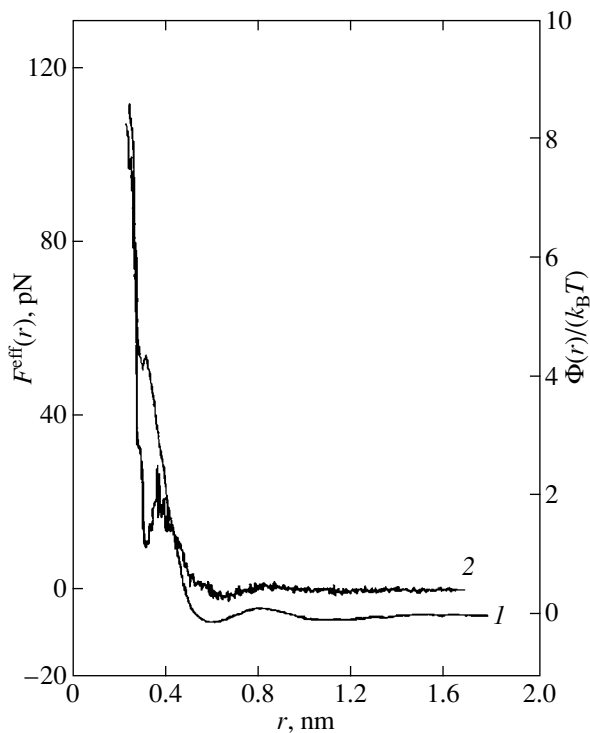


**Fig. 4.** (1) Radial part of the effective intermolecular potential  $\Phi(r)/(k_B T)$  determined using relationship (21) and (2) the effective force  $F^{\text{eff}}(r)$  between two 5CB molecules.

determine the radial part of the effective pair potential  $\Phi(r)$ , that is,

$$\frac{\Phi(r)}{k_B T} = G(r) - 1 - \ln G(r) - C(r) \quad (22)$$

and the effective force  $F^{\text{eff}}(r) = -\frac{d\Phi(r)}{dr} \mathbf{e}$  between two

5CB molecules. The results of calculations are represented in Fig. 4. The potential  $\Phi(r)/k_B T$  is characterized by a pronounced repulsive part at distances up to  $\bar{r} = 0.6$  (which corresponds to the width of the 5CB molecule) and the small potential barrier  $\Delta\Phi = \Phi(0.79) - \Phi(0.59) \cong 0.26k_B T$ . The repulsive force between two 5CB molecules rapidly decreases with an increase in the intermolecular distance and becomes zero at  $\bar{r} \cong 0.6$ . As the distance increases in the range  $0.62 \leq \bar{r} \leq 0.8$ , the molecules are attracted to each other. The maximum attractive force is approximately equal to 2.21 pN at  $\bar{r} \cong 0.8$ . With a further increase in the distance between the molecules, the attractive force rapidly tends to zero. It should be noted that the effective potential  $\Phi(r)$  differs from the Gay–Berne potential  $\Phi_{\text{GB}}(ij)$  in both the potential well depth and the potential barrier. However, structural characteristics, such as the orientation distribution function  $f_0(\cos\beta_i)$  and the order parameters  $\overline{P_{2L}}$ , calculated in the framework of these radically different approaches exhibit a very similar behavior. In turn, this gives grounds to make the inference that the correct inclusion of intermolecular correlations leads to a decrease in the differences associated with the choice of the intermolecular potential. At the same time, structural characteristics such as the Frank elastic constants must be calculated with due regard for the flexibility of the hydrocarbon chains of cyanobiphenyls. This problem is partly solved in the framework of the molecular dynamics approach. As a result, compared to the calculations in terms of the mechanical–statistical theory, the molecular dynamics calculations lead to a better agreement with the experimental data. However, we believe that both approaches open up independent ways of solving the problem concerning the prediction of the structural properties of real liquid crystals.

#### ACKNOWLEDGMENTS

This work was supported by the Ministry of Education of the Russian Federation, Grant for Basic Research in the Field of Natural Science (project no. E00-5.0-154).

#### REFERENCES

1. W. H. de Jeu, *Physical Properties of Liquid Crystal Materials* (Gordon and Breach, New York, 1980).
2. P. G. de Gennes and J. Prost, *The Physics of Liquid Crystals* (Oxford Univ. Press, Oxford, 1995).

3. F. Eikelschulte, S. Yakovenko, D. Paschek, and A. Geiger, *Liq. Cryst.* **27**, 1137 (2000).
4. P. P. Karat and N. V. Madhusudana, *Mol. Cryst. Liq. Cryst.* **40**, 239 (1977).
5. N. V. Madhusudana and R. P. Ratibha, *Mol. Cryst. Liq. Cryst.* **89**, 249 (1982).
6. M. J. Bradshaw, E. P. Raynes, J. D. Bunning, and T. E. Fabver, *J. Phys. (Paris)* **46**, 1513 (1985).
7. M. Hara, J. Hirakata, T. Toyooka, *et al.*, *Mol. Cryst. Liq. Cryst.* **122**, 161 (1985).
8. A. V. Zakharov and S. Romano, *Phys. Rev. E* **58**, 7428 (1998).
9. A. V. Zakharov and A. Maliniak, *Eur. Phys. J. E* **4**, 85 (2001).
10. L. A. Rott, *The Statistical Theory of Molecular Systems* (Nauka, Moscow, 1978).
11. J. G. Gay and B. J. Berne, *J. Chem. Phys.* **74**, 3316 (1981).
12. A. V. Komolkin and A. Maliniak, *J. Chem. Phys.* **101**, 4103 (1994).
13. A. V. Zakharov, A. V. Komolkin, and A. Maliniak, *Phys. Rev. E* **59**, 6802 (1999).
14. A. Poniwierski and J. Stecki, *Mol. Phys.* **38**, 1931 (1979).
15. M. D. Lipkin, S. A. Rice, and U. Mohanty, *J. Chem. Phys.* **82**, 472 (1985).
16. A. M. Somoza and P. Tarazona, *Mol. Phys.* **72**, 911 (1991).
17. A. V. Zakharov, *Physica A (Amsterdam)* **175**, 327 (1991).
18. R. Balescu, *Equilibrium and Nonequilibrium Statistical Mechanics* (Wiley, New York, 1978).
19. J. Steltzer, L. Longa, and H. Trebin, *J. Chem. Phys.* **103**, 3098 (1995).
20. P. I. C. Teixeira, V. M. Pergamenschik, and T. Sluckin, *Mol. Phys.* **80**, 1339 (1993).
21. M. A. Osipov and S. Hess, *Mol. Phys.* **78**, 1191 (1993).
22. A. V. Zakharov, S. Romano, and A. Maliniak, *Phys. Rev. E* **60**, R1142 (1999).
23. M. P. Allen and D. J. Tildesley, *Computer Simulation of Liquids* (Clarendon, Oxford, 1989).
24. R. Eppenga and D. Frenkel, *Mol. Phys.* **52**, 1303 (1984).
25. T. Koboyashi, H. Yoshida, A. D. L. Chandani, *et al.*, *Mol. Cryst. Liq. Cryst.* **136**, 267 (1986).

*Translated by O. Borovik-Romanova*

## FULLERENES AND ATOMIC CLUSTERS

# Discrete and Continuum Models for Calculating the Phonon Spectra of Carbon Nanotubes

S. S. Savinskiĭ and V. A. Petrovskii

Udmurt State University, Krasnoarmeĭskaya ul. 71, Izhevsk, 426034 Russia

Received July 12, 2001; in final form, November 19, 2001

**Abstract**—The vibration spectrum of perfect carbon nanotubes is studied using a two-parametric potential which includes pairwise and three-particle interatomic interactions. This potential was proposed by Keating and allows one to take into account the elasticity of pairwise interatomic bonds and the elasticity associated with a change in the angle between directional interatomic bonds in covalent crystals. Using the Keating potential, the vibration spectrum of a graphite monolayer is calculated and fitted to the vibration spectrum of crystalline graphite, thereby determining the parameters of the potential. With these parameters, the phonon spectra of perfect monolayer graphite nanotubes are calculated. A continuum model, in which a monolayer nanotube is represented as an elastic cylindrical shell of a finite thickness, is also discussed. Within this model, the vibration spectrum of a nanotube is calculated numerically in the long-wavelength limit as a function of the radius and thickness of the nanotube. © 2002 MAIK “Nauka/Interperiodica”.

### 1. INTRODUCTION

Carbon nanotubes were experimentally discovered by Iijima [1] and have attracted considerable attention because of their unique properties, such as high strength and conductivity dependent on the chirality indices of the nanotube, and of their application potential in nanoelectronics. Unfortunately, there is no currently available technology of fabricating a nanotube of a given chirality; nanotubes resulting from thermal decomposition of graphite have uncontrollable dimensions and chirality.

A perfect carbon nanotube can be covered by making screw rotations of a unit cell consisting of two carbon atoms lying on the cylindrical surface. Let  $S(\Delta z, \Delta \varphi)$  be a screw rotation operator that transforms the cylindrical coordinates  $z$  and  $\varphi$  of a point on the cylindrical surface according to the rule  $z, \varphi \rightarrow z + \Delta z, \varphi + \Delta \varphi$ .

We can introduce two linearly independent screw rotation operators  $S_1(\Delta z_1, \Delta \varphi_1)$  and  $S_2(\Delta z_2, \Delta \varphi_2)$  on the nanotube. These operators can be chosen differently. Since screw rotation operators commute, the operator  $S_1^n S_2^m$  (where  $n, m$  are arbitrary integers) transforms the coordinates of an arbitrary point according to the rule  $(z, \varphi) \rightarrow (z + n\Delta z_1 + m\Delta z_2, \varphi + n\Delta \varphi_1 + m\Delta \varphi_2)$ . For certain values of  $n$  and  $m$ , this operator can be equivalent to the identity operator. The minimum values of  $n$  and  $m$  in this case are called the indices of the nanotube and are designated as  $(i_1, i_2)$  in what follows. Since the choice of operators  $S_1$  and  $S_2$  is not unique, there are several different definitions of indices  $(i_1, i_2)$  in the lit-

erature (these indices are also called chirality indices). In this paper, we use the notation from Fig. 1.

Let us discuss how the parameters of the screw rotation operators shown in Fig. 1 can be found for a perfect monolayer nanotube with given chirality indices. Mentally cutting the nanotube along its generator and unbending the tube, we will obtain a strip which can be thought of as part of an infinite graphite monolayer consisting of closely packed regular hexagons of carbon atoms with side  $d_0$ . The screw rotation operators  $S_1$  and  $S_2$  for the nanotube are represented by primitive vectors  $\mathbf{T}_1$  and  $\mathbf{T}_2$  in the plane, and the chirality indices  $i_1$  and  $i_2$  define a vector  $\mathbf{C} = i_1 \mathbf{T}_1 + i_2 \mathbf{T}_2$ ; this vector is perpendicular to two sides of the strip, and its magnitude is equal to the strip width. The parameters  $\Delta \varphi_1$  and  $\Delta \varphi_2$  can easily be related to the projections of the vectors  $\mathbf{T}_1$  and  $\mathbf{T}_2$  onto the vector  $\mathbf{C}$ , while  $\Delta z_1$  and  $\Delta z_2$  are equal to the

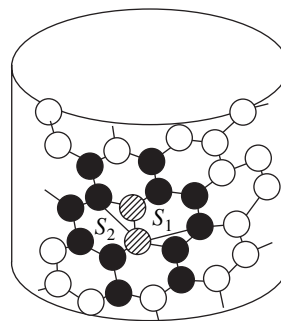


Fig. 1. Atomic structure of a carbon nanotube (schematic).

projections of  $\mathbf{T}_1$  and  $\mathbf{T}_2$  onto the direction of the generator of the nanotube:

$$\Delta\phi_1 = 2\pi\frac{(\mathbf{T}_1 \cdot \mathbf{C})}{C^2}, \quad \Delta\phi_2 = 2\pi\frac{(\mathbf{T}_2 \cdot \mathbf{C})}{C^2},$$

$$\Delta z_1 = (\mathbf{T}_1 \cdot \mathbf{e}_z), \quad \Delta z_2 = (\mathbf{T}_2 \cdot \mathbf{e}_z),$$

where  $\mathbf{e}_z$  is a unit vector parallel to the generator of the lateral surface. Thus, given the value of  $d_0$  and using the above formulas, one can calculate the parameters of the screw rotation operators for a perfect monolayer nanotube from the primitive vectors  $\mathbf{T}_1$  and  $\mathbf{T}_2$  and the vector  $\mathbf{C}$ .

Using the operators  $S_1$  and  $S_2$  introduced above, we can uniquely determine the coordinates of atoms on the surface of the carbon nanotube by expressing them in terms of three numbers  $(n, m, s)$ , where  $n$  and  $m$  are arbitrary integers, except the multiples of the tube indices  $i_1$  and  $i_2$ , and  $s$  takes on two values ( $s = 0, 1$ ) and specifies the atoms in the unit cell of the structure. The cylindrical coordinates of an atom specified by the numbers  $(n, m, s)$  can be found by operating with  $S_1^n S_2^m$  on the  $s$ th atom in the zeroth unit cell of the structure. For notational convenience, we will replace the pair of numbers  $(n, m)$  by one index  $\gamma$ , so that the position of an atom on the nanotube will be specified by the pair of numbers  $(\gamma, s)$ . We also note that the carbon nanotube can be represented as two interpenetrating tubes, with the unit cell of each of these tubes containing one carbon atom.

## 2. DISCRETE MODEL

We numerically calculated the vibration spectrum of the nanotube by using the Keating two-parametric interatomic interaction potential [2], in terms of which the relative interaction energy of atoms of the nanotube can be written as

$$W = \frac{\alpha}{2} \sum_{\gamma s, \gamma' s'} \frac{(\mathbf{r}_{\gamma s, \gamma' s'}^2 - \boldsymbol{\tau}_{\gamma s, \gamma' s'}^2)^2}{\boldsymbol{\tau}_{\gamma s, \gamma' s'}^2} + \frac{\beta}{2} \sum_{\gamma s, \gamma' s', \gamma'' s''} \frac{(\mathbf{r}_{\gamma s, \gamma' s'} \mathbf{r}_{\gamma' s', \gamma'' s''} - \boldsymbol{\tau}_{\gamma s, \gamma' s'} \boldsymbol{\tau}_{\gamma' s', \gamma'' s''})^2}{\boldsymbol{\tau}_{\gamma s, \gamma' s'} \boldsymbol{\tau}_{\gamma' s', \gamma'' s''}}, \quad (1)$$

where  $\alpha$  and  $\beta$  are the stiffness coefficients of the C–C bond stretching and C–C–C bond bending modes of vibration, respectively;  $\boldsymbol{\tau}_{\gamma s, \gamma' s'}$  is the vector connecting the nearest neighbor atoms  $(\gamma, s)$  and  $(\gamma', s')$  in equilibrium positions; and  $\mathbf{r}_{\gamma s, \gamma' s'}$  is the current value of the vector connecting the nearest neighbor atoms. In the first sum in Eq. (1), summation is performed over various pairs of nearest neighbor atoms, while in the second sum, it is performed over various triples of nearest neighbor atoms. When all of the carbon atoms are in their equilibrium positions, characterized by vectors  $\boldsymbol{\tau}_{\gamma s, \gamma' s'}$ , the energy of Eq. (1) is equal to zero.

Let  $\mathbf{U}_{\gamma s}$  be the displacement of an atom from its equilibrium position. Assuming this displacement to be small in comparison with the interatomic distances, we expand the function  $W$  into a Taylor series and keep only second-order terms. In this case, the force acting on a specified atom  $(\gamma, s)$  is a linear function of atomic displacements and the classical equations of motion in this approximation have the form

$$M \ddot{\mathbf{U}}_{\gamma s} = 4\alpha \sum_{\gamma' s'} \frac{(\boldsymbol{\tau}_{\gamma s, \gamma' s'} (\mathbf{U}_{\gamma s} - \mathbf{U}_{\gamma' s'})) \boldsymbol{\tau}_{\gamma s, \gamma' s'}}{\boldsymbol{\tau}_{\gamma s, \gamma' s'}^2} + \beta \sum_{\gamma' s', \gamma'' s''} \frac{(\boldsymbol{\tau}_{\gamma s, \gamma' s'} (\mathbf{U}_{\gamma'' s''} - \mathbf{U}_{\gamma s}) + \boldsymbol{\tau}_{\gamma s, \gamma'' s''} (\mathbf{U}_{\gamma' s'} - \mathbf{U}_{\gamma s})) (\boldsymbol{\tau}_{\gamma s, \gamma' s'} + \boldsymbol{\tau}_{\gamma s, \gamma'' s''})}{\boldsymbol{\tau}_{\gamma s, \gamma' s'} \boldsymbol{\tau}_{\gamma s, \gamma'' s''}} + \beta \sum_{\gamma' s', \gamma'' s''} \frac{(\boldsymbol{\tau}_{\gamma' s', \gamma s} (\mathbf{U}_{\gamma'' s''} - \mathbf{U}_{\gamma' s'}) + \boldsymbol{\tau}_{\gamma' s', \gamma'' s''} (\mathbf{U}_{\gamma s} - \mathbf{U}_{\gamma' s'})) \boldsymbol{\tau}_{\gamma' s', \gamma'' s''}}{\boldsymbol{\tau}_{\gamma' s', \gamma s} \boldsymbol{\tau}_{\gamma' s', \gamma'' s''}}, \quad (2)$$

where  $M$  is the mass of a carbon atom.

Figure 1 schematically depicts two atoms of the zeroth unit cell of the carbon nanotube and the atoms interacting with the zeroth unit cell; the latter atoms are responsible for the terms on the right-hand side of the equations of motion (2) with  $\gamma = 0$  and  $s = 0, 1$ . In Fig. 1, the atoms of the zeroth unit cell are hatched and the atoms of the neighbor unit cells interacting with the zeroth unit cell are represented by black circles.

It should be noted that in the case of a planar carbon structure (graphite monolayer), all of the vectors  $\boldsymbol{\tau}_{\gamma s, \gamma' s'}$  in Eq. (1) lie in the same plane and the restoring force acting on the atoms in the monolayer, according to Eq. (2), has no component along the normal to the monolayer. In the case of the carbon nanotube, the vectors  $\boldsymbol{\tau}_{\gamma s, \gamma' s'}$  do not lie in the same plane and the restoring force acting on an atom on the nanotube surface, according to Eq. (2), can have a nonzero radial component.

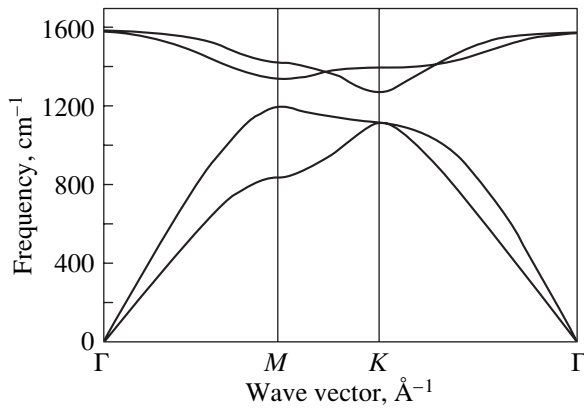


**Fig. 2.** Phonon spectrum of an individual graphite monatomic layer.

We seek a solution to the set of equations (2) in the form

$$\mathbf{U}_{\gamma s} = R_1^n R_2^m \mathbf{A}_s \exp(iqz_\gamma + il\phi_\gamma - i\omega t). \quad (3)$$

It will be recalled that  $\gamma$  stands for  $(n, m)$ ;  $R_1$  and  $R_2$  are the rotation matrices corresponding to the screw rotation operators  $S_1$  and  $S_2$ , respectively;  $\mathbf{A}_0$  and  $\mathbf{A}_1$  are the displacement vectors of the atoms of the zeroth unit cell;  $\hbar q$  is the momentum of a phonon and  $\hbar l$  is the angular momentum of the phonon;  $\omega$  is the frequency; and  $z_\gamma$  and  $\phi_\gamma$  are the cylindrical coordinates of the  $\gamma$ th unit cell on the nanotube surface. Substituting Eq. (3) into Eq. (2) reduces the infinite set of differential equations describing the motion of atoms of the carbon nanotube to the eigenvalue and eigenvector problem for a dynamic  $6 \times 6$  matrix. Given the solution to this problem, one can numerically calculate the dispersion curves and polarization of phonons in the nanotube.

To calculate the phonon spectrum of the carbon nanotube, we need the numerical values of the stiffness coefficients  $\alpha$  and  $\beta$  and the vectors  $\boldsymbol{\tau}_{\gamma s, \gamma' s'}$  characterizing the equilibrium positions of the carbon atoms of the perfect monolayer nanotube in a Cartesian coordinate system. We choose the  $x$  axis to pass through the zeroth-cell atom with index  $s = 0$  and the  $z$  axis to coincide with the nanotube axis. By acting with operators  $S_1$  and  $S_2$  on the coordinates of the two atoms of the zeroth cell, one can determine the Cartesian coordinates of the atoms of the nanotube and then find the equilibrium position vectors  $\boldsymbol{\tau}_{\gamma s, \gamma' s'}$ .

We determined the values of  $\alpha$  and  $\beta$  by solving the set of equations (2) describing atomic oscillation for the case of a plane carbon monolayer. In this case, the rotation matrices in Eq. (3) are equal to the identity matrix and the atomic displacements in the monolayer plane have the form

$$\mathbf{U}_{\gamma s} = \mathbf{A}_s \exp(iq_z z_\gamma + iq_x x_\gamma - i\omega t), \quad (4)$$

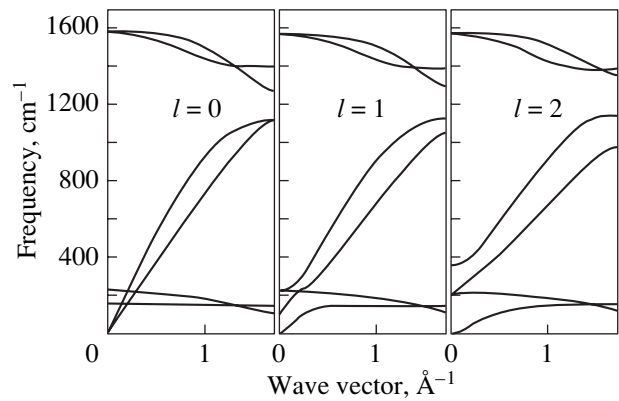


**Fig. 3.** Phonon spectra of a (20, 10) carbon nanotube as calculated within the discrete model for  $l = 0, 1,$  and  $2$ . The nanotube radius is  $R = 6.785 \text{ \AA}$ .

where  $q_x$  and  $q_z$  are the components of the wave vector of a two-dimensional phonon in the  $xz$  coordinate plane coinciding with the monolayer plane. Substituting Eq. (4) into Eq. (2) reduces the infinite set of differential equations to the eigenvector and eigenvalue problem for a dynamic  $4 \times 4$  matrix. By solving this problem, we found the dispersion curves and polarization of two-dimensional phonons in the graphite monolayer. We note that the order of the dynamic matrix of the carbon monolayer is associated with the Keating potential, for which the restoring force acting on an atom displaced along the normal to the monolayer vanishes in the linear approximation and, hence, the component of the atomic displacement vector along the monolayer normal in Eq. (4) is equal to zero. The parameters  $\alpha$  and  $\beta$  are fitted under the assumptions that the frequency of the optical vibration mode at the  $\Gamma$  point in the Brillouin zone of the graphite monolayer equals  $1582 \text{ cm}^{-1}$  [3] and the behavior of the phonon dispersion curves along the  $\Gamma M$ ,  $\Gamma K$ , and  $MK$  directions is similar to that determined from experimental phonon spectra of a graphite crystal [4] for the case where the propagation vectors and the atomic displacement vectors of phonons lie in the graphite atomic sheets. These assumptions are justified, because the interaction between atomic sheets in graphite is relatively weak and the properties of two-dimensional phonons are mainly determined by the elastic moduli of individual carbon monatomic layers. The values of the parameters  $\alpha$  and  $\beta$  thus fitted are  $\alpha = 105216.76 \text{ dyn/cm}$  and  $\beta = 84489.06 \text{ dyn/cm}$  for the equilibrium value of the carbon hexagon side in the monolayer taken to be  $d_0 = 1.418 \text{ \AA}$ . The dispersion curves calculated for two-dimensional phonons in the carbon monolayer are presented in Fig. 2. It follows from Fig. 2 that the velocities of long-wavelength acoustic phonons in the monolayer are  $V_1 = 14.3 \text{ km/s}$  and  $V_2 = 20.7 \text{ km/s}$ . These values are close to the theoretical values of the velocities of long-wavelength phonons in a carbon monolayer presented in [3] and are

equal to  $V_1 = 15.0$  km/s and  $V_2 = 21.1$  km/s. It should be noted that calculations of the vibration spectrum of a graphite monolayer based on the Keating potential were first performed in [5]; those calculations are at variance with the data presented in [3, 4] because of the inadequate values of the parameters  $\alpha$  and  $\beta$  chosen in [5].

We assumed that the parameters  $\alpha$  and  $\beta$  of the Keating potential found for a carbon monolayer can be used to calculate the phonon spectra of carbon nanotubes.

Calculations are performed for a (20, 10) nanotube, for which the data on phonon dispersion are available in the literature. For example, in [3], the phonon spectrum of a (20, 10) nanotube was calculated using only translational symmetry without specifying the quantum numbers of phonons: the longitudinal momentum and angular momentum. The calculated phonon dispersion curves for a nanotube with chirality indices (20, 10) are presented in Fig. 3. The velocities of long-wavelength acoustic phonons with orbital quantum number  $l = 0$  are found to be  $V_1 = 14.1$  km/s and  $V_2 = 20.7$  km/s; these phonons belong to the longitudinal mode (in which atoms are displaced along the axis of the nanotube) and to the shear mode (in which atomic displacements are perpendicular to the nanotube axis). In addition, the nanotube supports a breathing phonon mode with a limiting frequency equal to  $\omega_b = 161.2$  cm<sup>-1</sup>; in this mode, atoms are displaced in the radial direction and their displacements have axial symmetry. An analysis of the dispersion curves in Fig. 3 reveals that near the breathing mode, there is a vibration mode with a limiting frequency 228.7 cm<sup>-1</sup> which corresponds to radial vibrations of the nanotube sublattices relative to each other. In the optical-frequency region, there are modes with limiting frequencies 1575 and 1583 cm<sup>-1</sup> in the long-wavelength limit; these modes correspond to displacements of the nanotube sublattices relative to each other along the axis of the nanotube and to relative rotations of the sublattices.

The dispersion curves for phonons with  $l \neq 0$  are different (Fig. 3).

We compared the numerically calculated frequencies of long-wavelength phonons in the (20, 10) nanotube with the data from [3, 6] obtained using another technique and a potential with many parameters. In those papers, the frequency of the breathing mode in the long-wavelength limit was calculated to be  $\omega_b = 170$  cm<sup>-1</sup> [6] and  $\omega_b = 165$  cm<sup>-1</sup> [3], which is close to our result for this frequency,  $\omega_b = 161.2$  cm<sup>-1</sup>.

### 3. CONTINUUM MODEL

In the continuum model, the carbon nanotube is represented as a cylindrical elastic shell of finite thickness. This approximation is adequate if  $qd_0 \ll 1$  and  $ld_0/R \ll 1$  ( $R$  is the radius of the nanotube), which corresponds to the case where the phonon wavelength is large in

comparison with the interatomic distance. If the vibration amplitude of the thin elastic shell is small compared to the shell thickness, the vibrations of the shell can be described by the linear equations [7]

$$\begin{aligned} \frac{\partial^2 u_z}{\partial z^2} + \frac{1-\mu}{2R^2} \frac{\partial^2}{\partial \varphi^2} u_z + \frac{1+\mu}{2R} \frac{\partial^2 u_\varphi}{\partial \varphi \partial z} - \frac{\mu}{R} \frac{\partial u_r}{\partial z} &= \frac{1}{c^2} \frac{\partial^2 u_z}{\partial t^2}, \\ \frac{1+\mu}{2R} \frac{\partial^2 u_z}{\partial z \partial \varphi} + \frac{1-\mu}{2} \frac{\partial^2 u_\varphi}{\partial z^2} + \frac{1}{R^2} \frac{\partial^2 u_\varphi}{\partial \varphi^2} - \frac{1}{R^2} \frac{\partial u_r}{\partial \varphi} &= \frac{1}{c^2} \frac{\partial^2 u_\varphi}{\partial t^2}, \\ \frac{\mu}{R} \frac{\partial u_z}{\partial z} + \frac{1}{R^2} \frac{\partial u_\varphi}{\partial \varphi} - \frac{u_r}{R^2} & \\ - \frac{h^2}{12} \left( \frac{\partial^2}{\partial z^2} + \frac{1}{2} \frac{\partial^2}{\partial \varphi^2} \right) u_r &= \frac{1}{c^2} \frac{\partial^2 u_r}{\partial t^2}, \end{aligned} \quad (5)$$

where  $\mu$  is the Poisson ratio,  $\rho$  is the density of the material of the shell,  $R$  is the radius of the middle cylindrical surface within the shell,  $h$  is the shell thickness, and  $z$  and  $\varphi$  are the cylindrical coordinates of a point on the middle cylindrical surface within the shell;  $u_z$ ,  $u_\varphi$ , and  $u_r$  are the components of the displacement vector in

the cylindrical coordinate frame; and  $c = \sqrt{\frac{E}{\rho(1-\mu^2)}}$  ( $E$  is the Young modulus).

We seek solutions to Eqs. (5) for the components of the displacement vector in the form

$$\begin{aligned} u_z &= A \exp(-i\omega t + il\varphi + iqz), \\ u_\varphi &= B \exp(-i\omega t + il\varphi + iqz), \\ u_r &= C \exp(-i\omega t + il\varphi + iqz), \end{aligned} \quad (6)$$

where  $A$ ,  $B$ , and  $C$  are constants. By substituting Eqs. (6) into Eqs. (5), we obtain a set of algebraic equations for the constants  $A$ ,  $B$ , and  $C$ . From the condition for a nontrivial solution of these equations to exist, we obtain dispersion relations for elastic waves propagating through the shell.

We note that Eqs. (5) have the following simple particular solutions with  $l = 0$  in the elastic-membrane limit  $h = 0$ .

(1)  $u_z = u_r = 0$  and  $u_\varphi = B \exp(-i\omega t + iqz)$ . In this case, the dispersion relation has the form

$$\omega^2 = \frac{E}{2(1+\mu)\rho} q^2 \quad (7)$$

and the solution describes torsional waves propagating along the elastic shell.

(2)  $u_\varphi = 0$ ,  $u_z = A \exp(i\omega t + iqz)$ , and  $u_r = C \exp(i\omega t + iqz)$ .

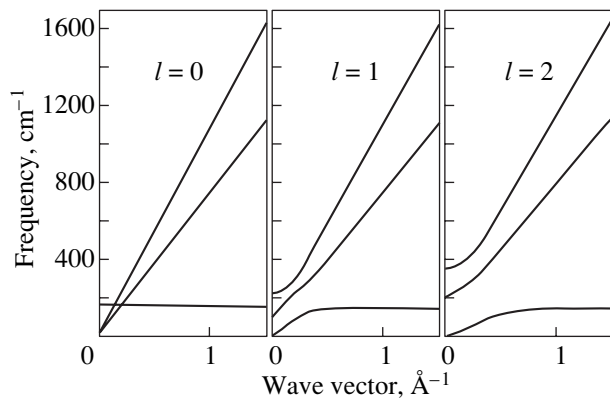


**Fig. 4.** Phonon spectra of a carbon nanotube as calculated within the continuum model for  $l = 0, 1,$  and  $2$ . The nanotube radius is  $R = 6.785 \text{ \AA}$ , and the thickness of the nanotube wall is zero.

This solution describes a wave propagating along the shell. Under the conditions  $gh \ll qR \ll 1$ , the dispersion relations have the form

$$\omega_1^2 = c^2 \left( \frac{1}{R^2} + \mu^2 q^2 \right), \quad \omega_2^2 = \frac{q^2 E}{\rho}. \quad (8)$$

In the case of  $q = 0$ , the wave with frequency  $\omega_1$  is a radial shell vibration ( $A = 0, C \neq 0$ ) and corresponds to the breathing mode. The second of dispersion relations (8) in the case of  $q \sim 0$  corresponds to a longitudinal wave with  $A \neq 0$  and  $C = 0$ .

Generally, the dispersion relations for waves propagating through the elastic shell are found by solving a cubic equation following from Eqs. (5) for the frequency squared  $\omega^2$  at fixed values of  $q$  and  $l$ .

We determined the values of the phenomenological parameters  $\mu$  and  $c$  for the monolayer carbon nanotube by fitting to the long-wavelength phonon spectra calculated within the discrete atomic model in the preceding section. These fitting parameters are found to be  $\mu = 0.065$  and  $c = 20.59 \text{ km/s}$ .

Figure 4 shows phonon spectra of the (20, 10) carbon nanotube calculated numerically within the continuum approximation. The velocities of long-wavelength acoustic phonons with  $l = 0$  are  $V_1 = 14.1 \text{ km/s}$  and  $V_2 = 20.6 \text{ km/s}$ , and the frequency of the breathing mode is  $\omega_b = 161.3 \text{ cm}^{-1}$ . The calculated spectra presented in Fig. 4 correspond to a nanotube of zero thickness  $h = 0$ . In the case of  $h \neq 0$ , the calculated dispersion curve of the breathing mode depends heavily on the thickness of the nanotube. As an illustration, Fig. 5 shows the numerically calculated phonon dispersion curves for a (20, 10) carbon nanotube with  $h/R = 0.295$ .

Thus, the discrete and continuum models of carbon nanotubes considered above may prove useful in analyzing data on Raman scattering on nanotubes, in estimating the lattice heat capacity of an individual nano-

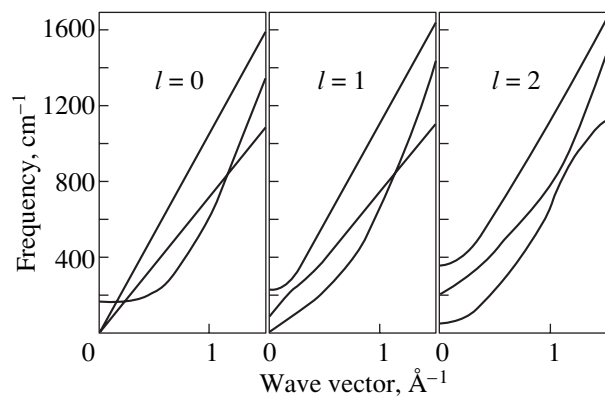


**Fig. 5.** Phonon spectra of a carbon nanotube as calculated within the continuum model for  $l = 0, 1,$  and  $2$ . The nanotube radius is  $R = 6.785 \text{ \AA}$ , and the ratio of the wall thickness of the nanotube equals  $0.295$ .

tube, and in analyzing the electron–phonon interaction in nanotubes.

For example, scattering of an optical photon on a carbon nanotube can be accompanied by the creation or annihilation of a phonon and the photon–phonon interaction must obey certain selection rules following from the conservation of energy, momentum, and angular momentum. A Raman-active phonon mode of a nanotube is a breathing mode; the limiting frequency of this mode (in inverse centimeters) as a function of the nanotube radius (in angstroms) is given by the following formula, as can be seen from Eq. (8):

$$\omega_b = \frac{1093.278}{R}. \quad (9)$$

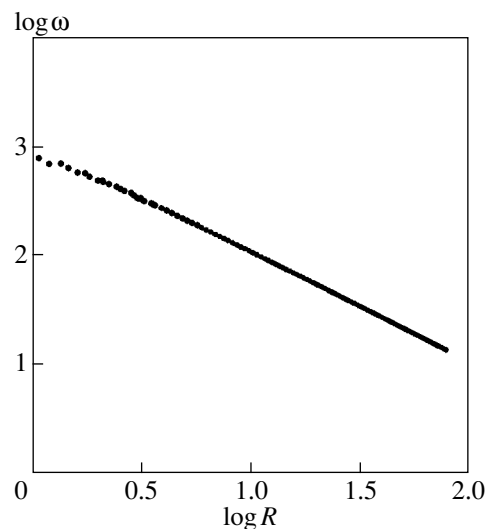


**Fig. 6.** Dependence of the limiting frequency of the breathing mode on the nanotube radius as calculated within the discrete model. The frequency  $\omega$  is measured in inverse centimeters; the radius  $R$ , in angstroms.

Figure 6 shows the dependence of the frequency of the breathing mode on the nanotube radius calculated numerically in the long-wavelength limit within the discrete model. It can be seen from Fig. 6 that a deviation from Eq. (9) is observed only for nanotubes of small radius. Calculations also show that the frequency of the breathing mode virtually does not depend on the nanotube chirality. These data and Eq. (9) can be used to identify carbon nanotubes on the basis of experimental Raman scattering data.

The low-temperature heat capacity of a nanotube can be calculated within the continuum model. In a nanotube at low temperatures, there are acoustic phonons with zero angular momentum and phonons whose frequencies do not vanish in the limit  $q = 0$  and depend on the orbital quantum number  $l$ . The frequency of long-wavelength acoustic phonons can be evaluated from a simple formula,

$$\omega_{0l} \approx \frac{lV}{R}, \quad (10)$$

where  $V$  is the velocity of an acoustic phonon with  $l = 0$ . At low temperatures, phonons are excited with various values of the orbital quantum number  $l$  for which  $\hbar\omega_{0l} \approx k_B T$ , where  $k_B$  is the Boltzmann constant and  $T$  is

the temperature; therefore, anomalies can occur in the temperature dependence of the nanotube heat capacity.

#### ACKNOWLEDGMENTS

This study was partially supported by INTAS, grant no. 97-30810.

#### REFERENCES

1. S. Iijima, *Nature (London)* **354**, 56 (1991).
2. P. N. Keating, *Phys. Rev. B* **145**, 37 (1966).
3. R. Saito, T. Takeya, T. Kimura, *et al.*, *Phys. Rev. B* **57** (7), 4145 (1998).
4. M. S. Dresselhaus, G. Dresselhaus, and P. C. Eklund, *Science of Fullerenes and Carbon Nanotubes* (Academic, New York, 1996).
5. K. C. Hass, *Phys. Rev. B* **46** (1), 139 (1992).
6. V. N. Popov, V. E. van Doren, and M. Balkanski, *Phys. Rev. B* **59** (13), 8355 (1999).
7. A. S. Vol'mir, *Shells in Fluid and Gas Flows (Problems of Aeroelasticity)* (Nauka, Moscow, 1976).

*Translated by Yu. Epifanov*